Synthesis and Photophysical Investigation of Donor-Acceptor-Substituted *meta*- and *para*-Benzene Derivatives

Dissertation zur Erlangung
des naturwissenschaftlichen Doktorgrades der
Julius-Maximilians-Universität Würzburg

vorgelegt von

Julian Schäfer

aus Trier

Würzburg 2017

Eingereicht bei der Fakultät für Chemie und Pharmazie am

08.09.2017

Gutachter der schriftlichen Arbeit

1. Gutachter: Prof. Dr. Christoph Lambert

2. Gutachter: Prof. Dr. Matthias Lehmann

Prüfer des öffentlichen Promotionskolloquiums

1. Prüfer: Prof. Dr. Christoph Lambert

2. Prüfer: Prof. Dr. Matthias Lehmann

3. Prüfer: Prof. Dr. Tobias Hertel

Datum des öffentlichen Promotionskolloquiums

09.11.2017

Doktorurkunde ausgehändigt am

Die vorliegende Arbeit wurde in der Zeit von Oktober 2012 bis August 2017 am Institut für Organische Chemie der Universität Würzburg angefertigt.

Mein besonderer Dank gilt

Herrn Prof. Dr. Christoph Lambert

dafür, dass ich dieses abwechslungsreiche und vielseitige Thema bearbeiten durfte, sowie für die intensive und mit vielen Anregungen und Diskussionen verbundenen Betreuung während dieser Arbeit.

COPYRIGHTS REMARKS

Parts of this thesis have previously been published and are adapted with permission from:

Hole Transfer Processes in *meta*- and *para*-Conjugated Mixed Valence Compounds: Unforeseen Effects of Bridge Substituents and Solvent Dynamics
J. Schäfer, M. Holzapfel, B. Mladenova, D. Kattnig, I. Krummenacher, H. Braunschweig, G. Grampp, C. Lambert
J. Am. Chem. Soc. **2017**, *139*, 6200-6209.

And in the following theses (under supervision of Julian Schäfer):

Synthese von Donor-Akzeptor-Verbindungen mit para-*verknüpfender Benzolbrücke,* W. Wagner, Bachelor Thesis, Julius-Maximilians-Universität Würzburg, **2013**.

Synthese und photophysikalische Charakterisierung von Donor-Akzeptor-substituierten 1,4-Dimethoxybenzolen, M. Krahfuß, Bachelor Thesis, Julius-Maximilians-Universität Würzburg, **2014**.

CONTENTS

Abbreviations

bisTAA	bistriarylamine
BTMA-Cl_2Br	benzyltrimethylammonium dichloroiodate
BTMA-Br_3	benzyltrimethylammonium tribromide
m-CPBA	*meta*-chloroperoxybenzoic acid
CR	charge recombination
CS	charge separated
CT	charge transfer
DMS	dimethyl sulphate
EDG	electron-donating-group
EA	ethyl acetate
EADS	evolution associated difference spectra
EI	electron impact ionization
ENDOR	electron nuclear double resonance
ESA	excited state absorption
ESI	electrospray ionization
ET	electron transfer
EWG	electron-withdrawing-group
GPC	gel permeation chromatography
hfc	hyperfine coupling constant
HT	hole transfer
IVCT	intervalence charge transfer
MALDI	matrix assisted laser desorption/ionization
MBM	metal-bridge-metal junction
MFE	magnetic field effect
MV	mixed valence
NBS	*N*-bromosuccinimide
NCS	*N*-chlorosuccinimide
NDI	1,4,5,8-naphthalene diimide
NIS	*N*-iodosuccinimide
OLED	organic light emitting diode
PE	petrol ether
PCTM	perchlorinated triphenylmethyl
QI	quantum interference
SEC	spectroelectrochemistry
TA	transient absorption

TAA	triarylamine
TBAF	tetrabutylammoniumfluorid
TBAHFP	tetrabutylammonium hexafluorophospate
TD-DFT	time dependent density functional theory
TLC	thin layer chromatography
TM	target molecule
TMSA	trimethylsilylacetylene
TS	transition state
TST	transition state theory
QY	quantum yield

1 INTRODUCTION

1.1 Electron Transfer

In photosynthesis large and highly complex structures are involved in order to generate chemical energy from sunlight. After absorption of a photon, e.g. by a chlorophyll molecule within a light-harvesting complex, the energy is transferred to the photosynthetic reaction center where charge separation occurs.[1-5] Then a cascade of electron transfer (ET) steps is necessary to transport the electron to the cofactor nicotinamide adenine dinucleotide phosphate (abbreviated $NADP^+$) which is reduced to NADPH.[2, 6-8] But how exactly do the charge separation and the subsequent electron transfer steps work in detail? Is it possible to obtain chemical energy with similar effectivness by artificial photosynthesis and which factors influence the efficiency? In order to get closer to an answer to these questions, the fundamental processes must be understood.

Furthermore ET is a process of high importance not only for photosynthesis, but also for several areas of science and technology. Understanding of ET is essential for the optimization of optoelectric devices such as organic light emitting diodes (OLEDs), organic solar cells, phototransistors or other semiconducting nanostructures and for the ongoing miniaturization process of single molecule electronics.[9-22]

Therefore, structures have to be found that reduce the complexity of such problems. Small molecules, which seem to be sufficient in order to investigate ET, can serve as model compounds and help to gain a better understanding of the ET processes occurring. As model structures, molecules consisting of an electron donor (D) and an electron acceptor moiety (A) with a bridging unit (B) connecting the chromophores, hereinafter referred simply as DA compounds, were proven to be successful.[23-26] Absorption of light can lead to a photoinduced ET from the donor to the acceptor, depicted as the first step in Figure 1. This event, in principle, is possible by excitation of the donor, the acceptor or the bridging moiety (the latter is then often defined as a photosensitizer). In neutral DA compounds photoinduced ET leads to a separation of charges, resulting in a positively charged, oxidized donor and a negatively charged, reduced acceptor. Thus, in this charge separated (CS) state a radical pair is formed. After population of this CS state, charge recombination (CR) takes place and finally the initial ground state is formed again. In this way DA compounds provide the possibility to investigate two fundamental ET processes after excitation, first the CS and second the CR.

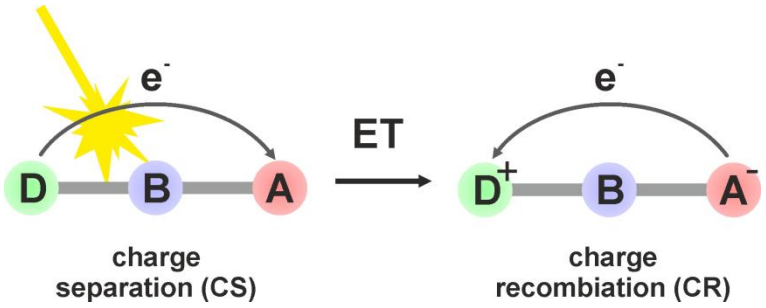

Figure 1: Photoinduced ET transfer processes in donor-bridge-acceptor dyads.

A second substance class widely used to investigate ET phenomena are mixed valence (MV) compounds.[27-29] These molecules can be seen as a sub-class of DA compounds and are defined by an open-shell configuration, thus unpaired electrons are present in the ground state, as well as in all excited states. Mostly, MV compounds consist of two structurally identical redox centers in different formal redox states, connected via a bridging unit (B). Either optically, by absorption of light, or thermally induced, a charge can be transferred from the donor to the acceptor. For a symmetric cationic MV compound the optically induced ET is shown in Figure 2. Here the non-oxidized redox center serves as the electron donor (D) and the oxidized redox center as the acceptor (A).

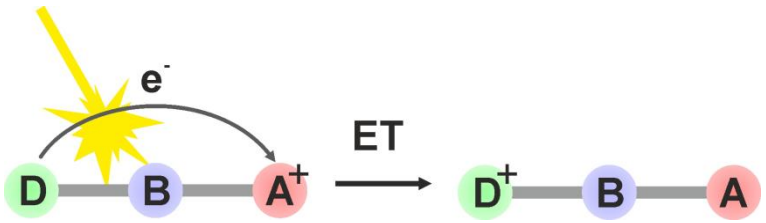

Figure 2: Optically induced ET transfer processes in cationic MV compounds.

The main focus of this thesis is to investigate the influence of the bridging unit (B) in these two substance classes on the occurring ET processes. For this purpose, the most important fundamental ET parameters, such as the transfer mechanism (superexchange vs. hopping), distance between the redox centers, solvent, reorganization energy, electronic coupling, electron transfer barrier, solvent and spin multiplicity, will be introduced and then examined in more detail.

The obtained results will contribute to a better understanding of the fundamentals of charge transfer process in DA compounds and will help to understand how ET could be controllable.

1.2 *Meta*-and *para*-Conjugation

There are many parameters having a decisive influence on ET processes in DA systems. If the compound is dissolved in a solvent, the solvent properties can significantly affect the ET process taking place.[30, 31] However, the structural properties of the compounds seem to be far more important. Here, beside the redox centers and the distance between them, the bridging unit has a strong impact on the CT, since it is able to govern the electronic communication between redox centers. One major key concept in the regulation of ET is to modify the architecture of the bridging moiety in the respective system.[32-39]

Widely used as bridging units are organic structures with π-systems. They provide the possibility to transfer charges over long distances and show a high optical and thermal stability. The size of the bridging moiety and the electronic character can be varied in almost infinite diversity. Nevertheless, the transport through one of the most important aromatic system, namely benzene, still is not completely understood.[39-43] Benzene, whose discovery and characterization marked the beginning of the aromatic chemistry, is one of the smallest π-systems and is intensively studied in a great variety and thus predestined for the investigation of CT. Nevertheless predictions of its behavior as a bridging moiety in DA systems is only possible to a limited extend, and this work is intended to contribute to further understanding in this area.

There are three possible topologies, for the connection of two chromophores to a benzene ring via σ-bonding. As shown in Figure 3, the redox centers can either be directly adjacent to each other - as in the case of the *ortho*-substitution, oriented in a 120° angle to one another - as in the case of *meta*-substitution, or be arranged linearly - in *para*-topology.

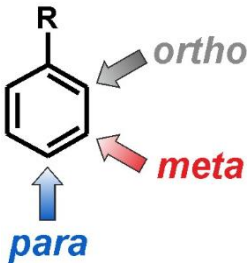

Figure 3: *Ortho*-, *meta*- and *para*-position of a benzene derivative.

If the benzene bridge is now embedded between a donor and an acceptor, an ET between the redox centers can occur. Here, one has to differentiate between two possible transfer mechanisms (Figure 4): I) The coherent super exchange mechanism where the electron is transferred directly from the donor to the acceptor without resting at the bridging unit. In the *ortho*-case the donor and the acceptor can be in very close contact. Here, two different

superexchange reactions can be present at the same time, namely through-bond and the through-space ET.[34, 44] Since the latter case does not include the benzene bridge, the influence of which is to be investigated in this study, the *ortho*-arrangement will not be discussed further. However, the through bond mechanism can be seen as a tunneling process, which is mediated by the virtual states of the bridging unit. II) The incoherent hopping mechanism, where the electron is first transferred to the bridging unit, stays there for a certain time, and is then transferred to the acceptor moiety.

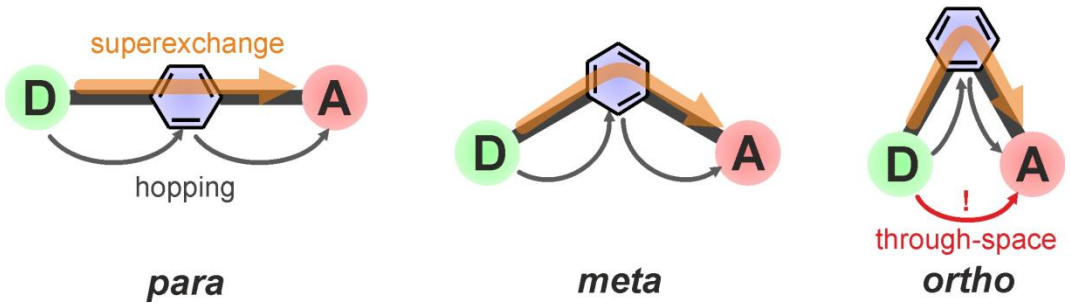

Figure 4: CT via super exchange (orange arrows), hopping (grey arrows) and superexchange through space (red arrow) in *para*-, *meta*- and *ortho*-substituted benzene.

The bridging unit can have a decisive influence on which mechanism dominates, by the energetic position of its frontier orbitals. Figure 5 visualizes the influence of the energetic position of the bridging unit in case of a cationic MV compound with two identical redox centers, where the non-oxidized redox center acts as an electron donor.

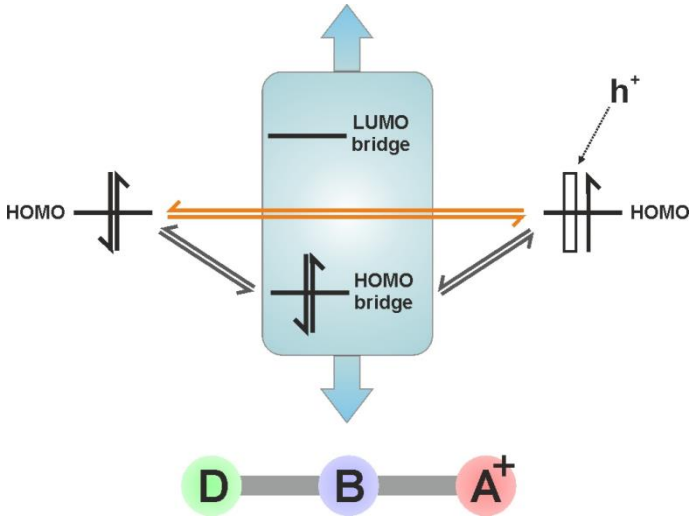

Figure 5: Frontier orbitals for a cationic MV compound and superexchange (orange arrows) and hopping (grey arrows) mechanism. The small rectangle at the right, oxidized moiety, symbolizes the electron hole.

In this context, it is advisable to treat the ET in cationic MV compounds as a hole transfer (HT) from the oxidized to the non-oxidized redox center, which leads to an easier understanding of the occurring CT. The cationic MV compounds investigated in this work will mostly be treated under this assumption.
In MV compounds with low-energy bridge HOMOs, the hole is supposed to be preferably transferred by superexchange mechanism. In MV compounds with high-energy bridge HOMOs the hopping mechanism becomes possible. A variation of the energetic position of bridging unit is possible by e.g. attachment of additional substituents at the bridging unit, which tune the position of HOMO and LUMO. In benzene, electron-donating substituents raise the energy level of the HOMO, which might then be accessible for HT via hopping. However, electron-withdrawing substituents lower the energy of the HOMO, making it unachievable for hopping and thus HT is only possible via superexchange mechanism.[45-48]

The main focus of this work is to investigate the topology dependency in *meta*- and *para*-substituted benzene derivatives, and change of the energetic position by suitable substituents at the benzene unit, in order to obtain a detailed insight on occurring ET and HT processes.

1.3 *Marcus* Theory

Before further discussing HT and ET processes in MV and DA compounds in more detail, a short overview of fundamental ET theories is given, to get a better understanding in ET phenomena and to introduce some basic parameters.
In 1956, the first appropriate model for describing ET processes was introduced by *Marcus*, describing the ET on the basis of two diabatic (formally non-interacting) parabola, which represent the ET as a transition between two free-energy surfaces, of the educt and product states, respectively (Figure 6, blue curves).[49-51] In case of degenerate product and educt states, optically induced, vertical (following *Franck-Condon* principle) excitation with energy λ (green arrow) leads to an ET between the two states. Here, λ is the reorganization energy that consists of two parameters: the internal reorganization energy λ_v, which describes the structural reorganizations taking place after ET, and the outer reorganization energy λ_o, describing the rearrangement of the solvent after ET. In case of non-degeneracy, an energy of $\lambda + \Delta G^{00}$ is needed, with ΔG^{00} being the free-energy difference between product and educt states.
Another possible pathway is given by the thermally induced ET of the charge from the free energy minimum of the educt state along the ET coordinate to the free energy minimum of

the product state, whereby the free energy barrier ΔG^* must be overcome. The size of this barrier is, according to the classical description, given by equation (1):

$$\Delta G^* = \frac{\left(\lambda + \Delta G^{00}\right)^2}{4\lambda} \tag{1}$$

and the rate constant k for thermally induced ET is given by:

$$k = A \times e^{-\frac{\Delta G^*}{k_B T}} \tag{2}$$

where k_B is the *Boltzmann* constant and A a pre-exponential factor. As the further course of this work will prove (see Chapter 3.3.2), for the degenerate MV compounds presented in this work, k can in some cases be determined via ESR spectroscopy and thus it is possible do estimate ΔG^* by ESR measurements at different temperatures.

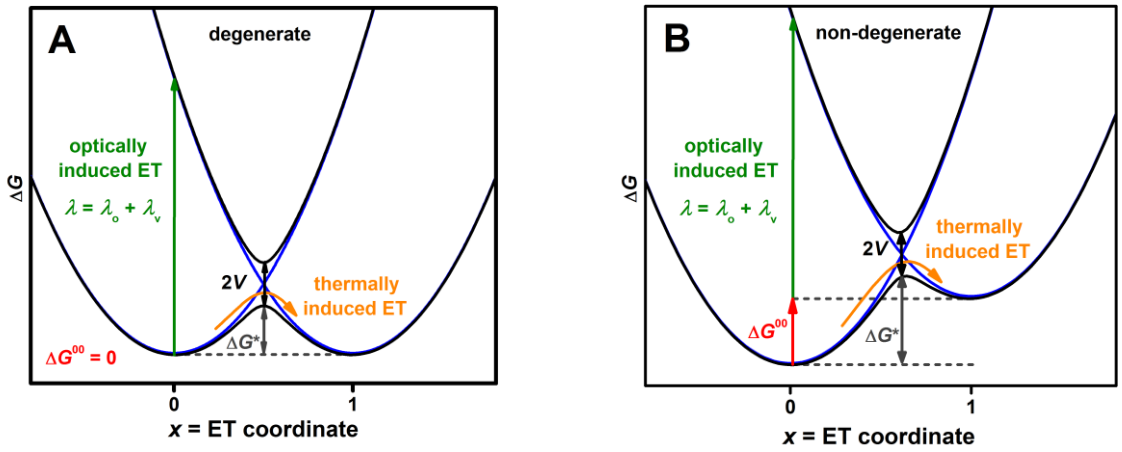

Figure 6: Diabatic (blue lines) and adiabatic (black lines) free energy surfaces of a MV compound with degenerate (A) and non-degenerate (B) states.

In case of a stronger electronic communication between donor and acceptor, one can no longer treat the two states as diabatic. The *Marcus-Hush* theory, which can be seen as an extension to the classical *Marcus* theory, is taking this circumstance into account.[52, 53] The two diabatic states (blue) form two adiabatic states (black curves). Here, the electronic coupling V can be seen as a measure of electronic communication between these states.
For degenerate MV compounds ΔG^* decreases as a result of the coupling V and is now defined as:

$$\Delta G^{*} = \frac{\lambda}{4} - V + \frac{V^2}{\lambda}$$

In optically induced ET, the electronic coupling *V* is related to the so-called intravalence charge transfer band (IVCT) band, an absorption typically in the low-energy side of the spectrum. Thus, as the following work will elucidate in detail, following *Mullikan-Hush* band analysis, *V* and Δ*G** are determined by spectral analysis.[27, 54-56]

1.4 Metal-Bridge-Metal Junction

An alternative to the investigation of ET processes in small molecular systems with donor and acceptor moieties, is to use single-molecule junctions, allowing for a direct observation of the ET by measurements of current-voltage characteristics. These junctions consist of a molecule (bridge) which is connected to two electrodes, by e.g. thiols, isocyanides or diamines as anchor groups. As electrodes, gold electrodes are by far most widely used. Although this technique is different in nature compared to the investigation of donor-bridge-acceptor compounds, similar behaviors are often observed. In 1997 *Tour et al.* reported the realization of a single-molecule junction with benzene-1,4-dithiol covalently bound between two gold electrodes. This gold-sulfur-aryl-sulfur-gold system was designed using so called "mechanically controlled break junction (MCB) technique".[57-62] Here, a gold wire gets coated with e.g. dithiol molecules, which are able to form a self-assembled monolayer (which is then going to be investigated). The wire gets stretched until it breaks, resulting in a tip formation of two breakages. The two tips are slowly brought together, until an onset of conductance is achieved and the metal-bridge-metal junction (MBM) is formed.

Using this approach *Venkataraman et al.* studied a series of substituted benzenes (**A1-5**, Scheme 1) which were linked by two amino functions to the electrodes. It was found that electron-donating substituents provide the possibility to increase the junction conductance, while electron-withdrawing substituents behave oppositely.[63] However, there are, besides the molecule itself, many parameters affecting the conductance of such MBM junctions, such as the kind of anchor group and electrodes used, since different electronic overlaps between electrode and molecule can be achieved, influencing the overall conductance of the metal-molecule-metal junction.[41, 64, 65] Furthermore, the strong covalent bonding to the atomic disordered metallic electrodes can cause significant sample to sample fluctuations, which makes both scientific investigation and engineering of electronics demanding.[58] Nevertheless, in the course of the investigation of a multitude of organic molecules by this method, another important discovery was made, that is a dependency of the conductance in benzene on the topology of the attachment of the anchor groups. Contributions of *Ke et al.*

and *Kiguchi et al.* on *meta*- (**B**$_m$) and *para*-linked (**B**$_p$) benzene, as well as studies of *Ratner et al.* investigating phenyl rings with ethynyl spacers substituted in *meta*- (**C**$_m$) and *para*- (**C**$_p$) positions, reveal a significant decrease of conductivity in the both *meta*-cases.[37, 41, 66] This observation was also made for larger *π*-systems as shown by *Mayor et al.*, where an anthracene unit was connected to two benzenes, each either *meta*- (**F**) or *para*-linked (**G**) to the metal electrodes.[58]

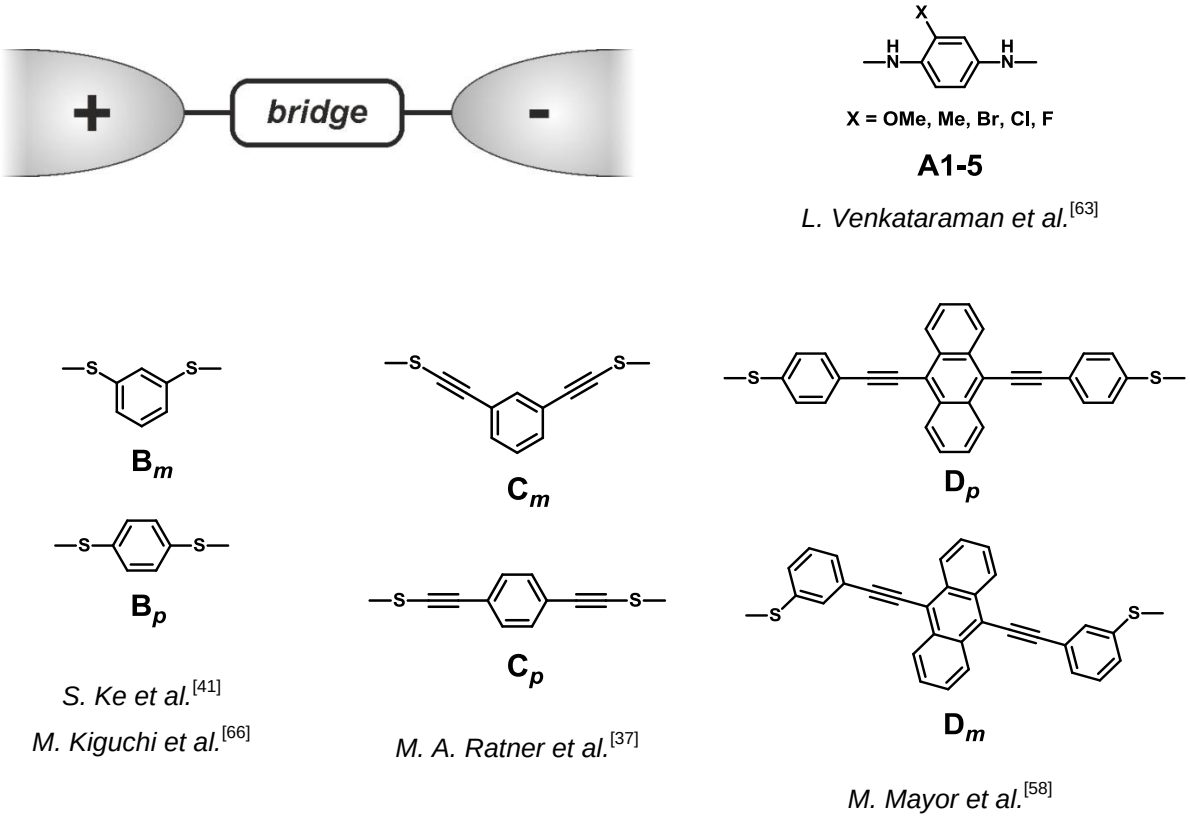

Scheme 1: Selection of single-molecule junctions used in conductance studies.

The observation of the reduced conductivity in the *meta*-compounds required an interpretation of this finding, which is often given by the so-called destructive quantum interference (QI).[39, 41, 67-73] Ab initio calculations of conductance and movement of the wave function of the electron travelling through the molecular system showed that antiresonances may occur when the electron migrates over different pathways of the molecule. This is exemplified for a MBM with benzene bridging unit in Figure 7. In the *para*-case, the electron can travel over two identical pathways from one electrode to the other, resulting in constructive QI and thus a high conductivity. In the *meta*-case, interfering tunneling pathways offered by the bridge orbitals lead to destructive QI of the wave functions and thus a low conductivity. The QI explanation is not restricted for interpretation of conductance in MBM, and has proven to be reliable for the interpretation of ET in organic molecules with donor and

acceptor redox centers instead of electrodes.[74-76] Furthermore the role of QI has been investigated on larger systems with extended aromatic bridging units, like linear rod-like molecular wires or two dimensional graphene-like structures and can help in the prediction of conductivity in comparable structures.[70, 72, 77-79]

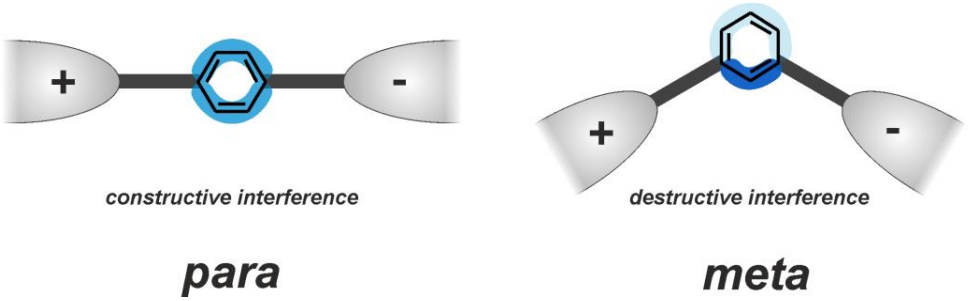

Figure 7: Illustration of constructive (left) and destructive (right) quantum interference in benzene embedded in an MBM, linked in *para*- and *meta*-position, respectively.

1.5 Hole Transfer in Mixed-Valence Compounds

As already mentioned in the first chapter of this work, a more common approach for the investigation of ET over a specific bridging moiety is to use small molecular architectures, such as mixed-valence (MV) compounds. Thus, the metal electrodes are replaced by appropriate molecular electron donor and acceptor components.

In anionic MV compounds with two identical redox centers, the electron is transferred from the reduced to the non-reduced redox center.[80, 81] A literature-known example for investigating the influence of topology on long-range ET on anionic MV compounds is shown in Scheme 2. In this study, perchlorinated triphenylmethyl (PCTM) moieties serve as redox centers.[80] After reduction of one PCTM moiety, optically induced and thermally induced ET were accessible for *para*-compound $\mathbf{E}_p$. In contrast, for the *meta*-connected compound $\mathbf{E}_m$ no indication of an intramolecular ET was found, neither optically nor thermally. This indicates that the coupling in the *meta*-case must be very small.

In cationic MV compounds with two identical redox centers, the hole donor is the oxidized, the hole acceptor the non-oxidized redox center, respectively. Extensive studies of *Nelsen et al.* contributed to the understanding on HT in symmetrically bridged bis-hydrazine radical cations.[82-87] Adding methyl groups to the central benzene ring lead to an energetically favored out-of-plane rotation of the bridging unit, resulting in a decrease of coupling (**F** > **G** > **H**), optically determined by IVCT analysis. Thermally induced HT was investigated by temperature dependent ESR measurements, which revealed the same trend of exchange rates k_{ESR} for **F** to **G**. However, for **H** the ESR rate constant was higher than for **G**, showing

that the HT processes in these molecules cannot be reduced to the rotation parameter. In another contribution on a series of naphthalene bridged bis-hydrazine radical cations, the dependency of the topology of the redox centers was investigated. The optical IVCT analysis of $\mathbf{I_{2,6}}$ showed a 100-fold larger *k* than $\mathbf{I_{1,5}}$, while for the cross conjugated $\mathbf{I_{2,7}}$ the exchange was too small to be detected, which presumably results from a too small coupling *V*. In addition to the optical data, exactly the same trend was found for thermally induced HT by ESR spectroscopy.[82]

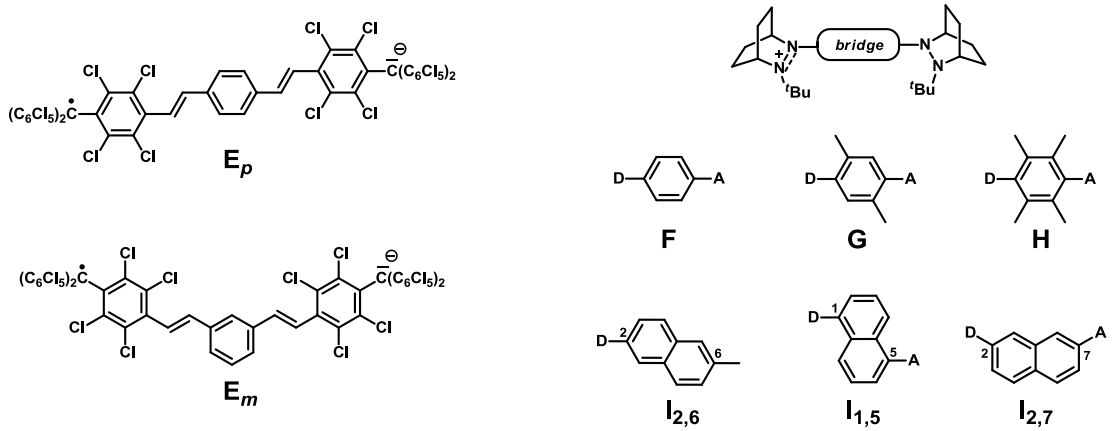

J. Veciana et al.[80] *S. F. Nelsen et al.*[82-87]

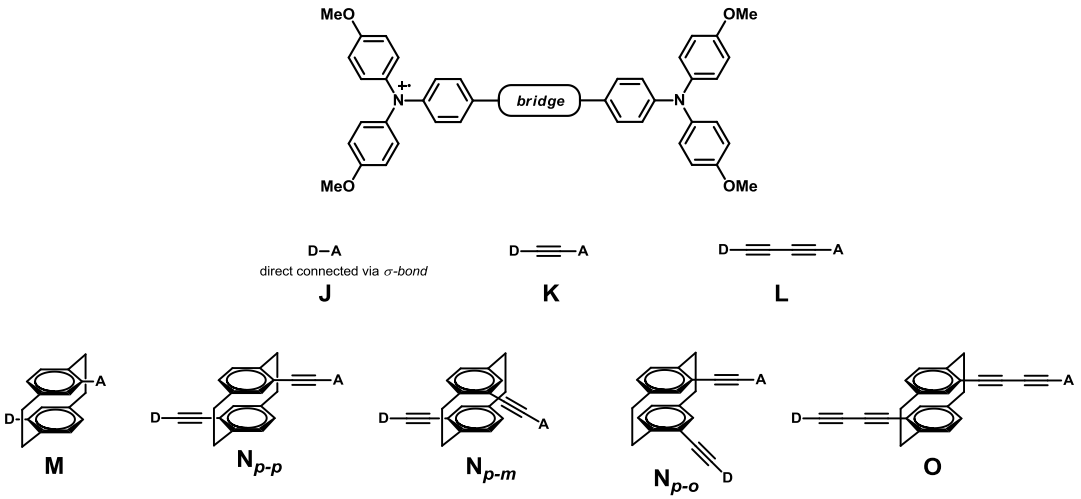

C. Lambert et al. [88-93]

Scheme 2: Example of series of bisPCTM radical anions (**E**), bis-hydrazine radical cations (**F-I**) and bisTAA radical cations (**J-O**).

Bistriarylamine (bisTAA) radical cations are a widely used class of molecules for investigation of HT in organic molecules.[34, 92-94] Triarylamines (TAA) show ideal optical properties, high

stability and their redox potential can easily be tuned by variation of the substituents at the outer *para*-positions of the phenyl groups.[95, 96] Here, in particular the methoxy-substituted TAA should be emphasized, since it is a notably strong electron donor and often used, e.g. by *Lambert et al.*[97-101] Hence, on the basis of this class of compounds, the dependency of the HT when increasing the number of bonds (and thus the distance *d*) between the TAA redox centers from one to (**J**), to three (**K**) and five (**L**) was examined.[90] It was proved, that the exponential dependency of the exchange rare *k* for this superexchange is based on the exponential dependency of the coupling *V* given by equation (3):

$$V = V_0 e^{-\left(\frac{\beta d}{2}\right)} \qquad (3)$$

where β is the '"attenuation factor", and V_0 the hypothetical coupling at $d = 0$. Similar observations were made by *Barlow et al*. on vinylene and phenylene-vinylene bridged TAA as well as by *Lambert et al.* for non-conjugated bridging units based on the paracyclophane moiety. [88-93] *Lambert et al.* also showed, that in the [2,2]-paracyclophanes depicted in Scheme 2 the electronic coupling between the redox centers is significantly decreased in comparison to a conjugated bridging unit, since HT is assigned to occur mostly via through-space interaction between the two benzene units. However, similar exponential dependency on the exchange rate and coupling was found when increasing the HT distance from **M** to **O**.[90] For the [2,2]-paracyclophanes with ethynyl spacers, the optically and thermally induced HT in dependency on topology of the TAA units was investigated intensively. The optical IVCT analysis unraveled that *V* of the *pseudo-meta* MV compound ($\mathbf{N}_{p\text{-}m}$) is much lower than in both, the *pseudo-para*- ($\mathbf{N}_{p\text{-}p}$) and *pseudo-ortho*-case ($\mathbf{N}_{p\text{-}o}$).[90, 102] For the latter one could think of superexchange through-space directly between the TAA units, significantly increasing the exchange interaction. It was found to be in strong contrast to the thermally induced HT rate constant determined by ESR spectroscopy, where the substitution position of the TAA, in either *pseudo-para*- or *pseudo-meta*-position does not have a major impact.[91] This differences of the obtained parameters demonstrates that in some cases the interpretation of the HT processes depends on the respective type of data acquisition and that a general statement about HT processes may not be possible by the sole analysis of the optically induced or thermally induced HT, respectively.

1.6 Electron Transfer in Neutral Donor-Acceptor Compounds

Neutral donor-acceptor (DA) compounds provide the possibility to investigate the charge separation (CS) and the subsequent charge recombination (CR) within one molecular architecture and to evaluate the parameter influencing these processes. After excitation of the donor or the acceptor moiety, ET form the donor to the acceptor can result in the formation of a CS state (Figure 2). This CS state has a finite lifetime and recombines into the ground state. Both, the formation of the CS state and the CR can be strongly dependent on the length, structure and energetic position of the bridging unit and in the following some studies, mostly focused on the CR are presented, in order to evaluate some basic, general trends and insights.

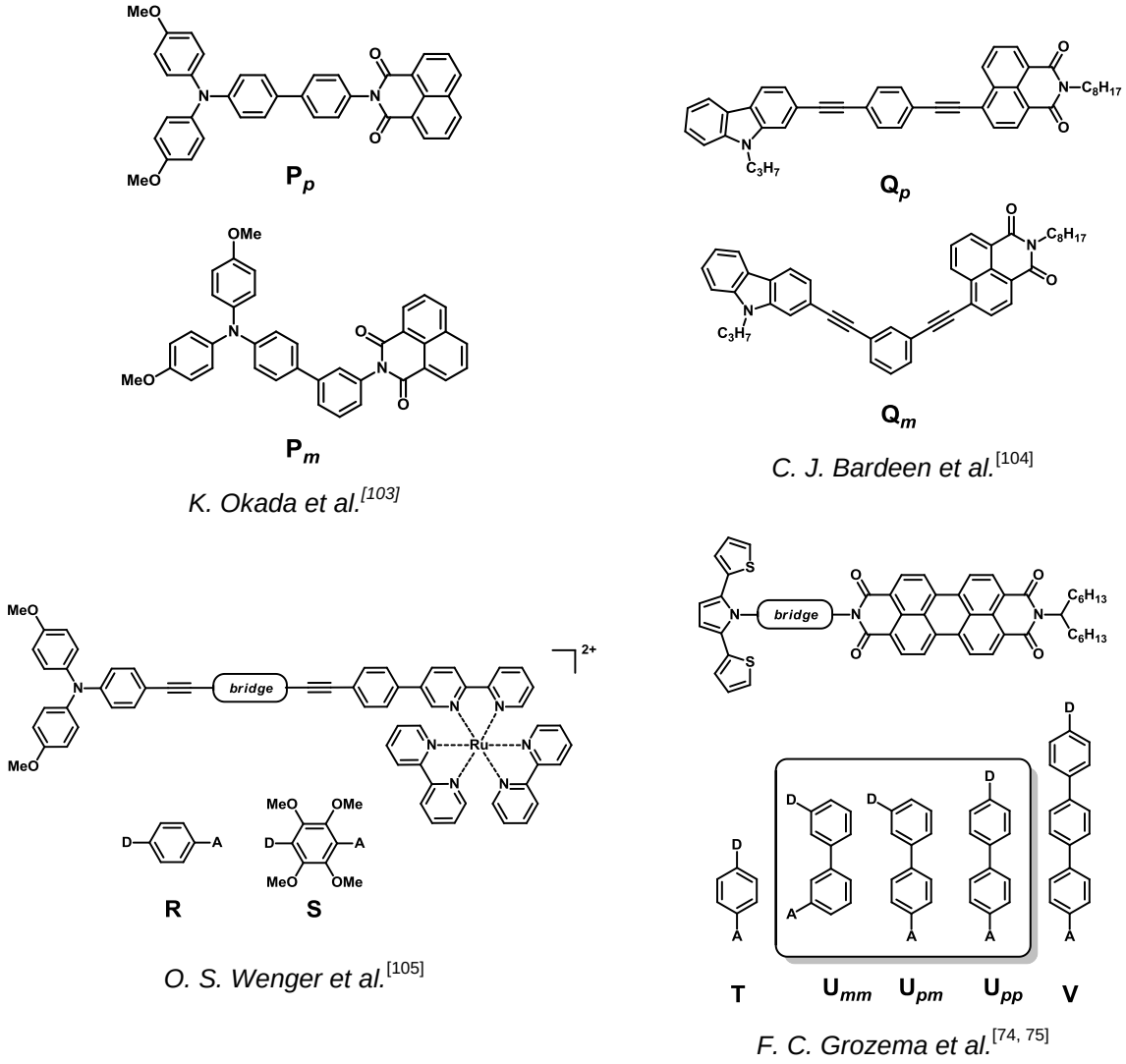

Scheme 3: Overview about some studied DA dyads.

Okada et al. investigated the photoinduced ET in *para*- (**P**$_p$) and *meta*-linked (**P**$_m$) TAA-naphthalene imide dyads where the decay rates of the charge recombination of the *meta*-compound was half as fast as the *para*-compound.[103] Similar observations were made by *Bardeen et al.,* whose study on benzene bridging units with ethynyl spacer and *para*- (**Q**$_p$) or *meta*- (**Q**$_m$) constitution of the chromophores revealed, that the CS time is roughly the same for both dyads, whereas the CR is about 10 times faster in the *para*-compound.[104]

Concerning the electronic position of the bridging unit, *Wenger et al.* investigated the photoinduced ET properties of CR for two donor-bridge-acceptor molecules with TAA as a donor and ruthenium bipyridine redox center as an acceptor. Here, 2,3,5,6-teramethoxybenzene (**R**) permits a more rapid charge transfer of about the factor of 4.5 than an unsubstituted phenylene spacer (**S**). [105]

Recently, *Grozema et al.* presented a combined theoretical and experimental study on HT and ET in donor-bridge-acceptor molecules with a series of *n*-phenylene bridging units, depicted in Scheme 3.[74, 75] While, as expected, exponential distance dependency of the transfer rate was observed ($k_{(T)} > k_{(U)} > k_{(V)}$), contrary to the expectations, a faster HT for the non-linear (**U**$_{mm}$ and **U**$_{pm}$), than for the linear molecules (**U**$_{pp}$) was found experimentally. Furthermore, this finding was not observed in calculations on the conductance of these bridging units in MBM, where the cross conjugated molecules showed lower conductivity. In this study it became clear that HT and ET might behave differently and thus experience different quantum interference effects, depending on the involved bridge orbitals and their symmetry.

1.7 Influence of the Magnetic Field on ET Processes

Besides focusing on conventional approaches of structural optimization to maximize the lifetime of the CS state and minimize CR in DA compounds, one important aspect was neglected so far in this introduction: spin multiplicity.

After excitation of a DA compound, one oxidized and one reduced redox center can be formed and the radical pair in this CS state may form an equilibrium between the singlet and triplet state. This equilibrium is sensitive to an external magnetic field, which can strongly influence the CR dynamics, making this approach a new starting point for the optimization of optoelectronic devices, such as OLEDs or photovoltaics.

The subsequent chapters will evaluate the impact of an external magnetic field on the CT dynamics in more detail in order to help understanding under which conditions a magnetic field effect (MFE) can occur, and how the involved parameters influence this effect.

1.7.1 Degenerate Singlet and Triplet States

The influence of a magnetic field (*B*) on the CS dynamics will first be explained for two quasi-degenerate singlet and triplet states, were the radicals are separated over large distances. At zero magnetic field, the two radical centers behave in the first approximation as being independent and spin-spin dipolar interaction and exchange interaction are negligible. The three triplet CS states as well as the singlet CS state are degenerate (Figure 8, left). Spin interconversion between ^{3}CS states and ^{1}CS state is given by the hyperfine coupling interaction (hfc) of magnetic moments of the nuclei surrounding the respective radical center. This coherent spin-flip is defined by the rate constant k_{ST0} and has a value on the order of 1×10^8 s^{-1}.[106] Charge recombination to the S_0 state is spin forbidden from ^{3}CS states and thus can only take place from the singlet state. Applying a magnetic field induces a splitting of the triplet sublevels into T_+, T_0 and T_- based on the *Zeeman* effect. With increasing *B* the energetic positions of S and T_0 remain unaffected (since $M_s = 0$), while the two triplet states T_- and T_+ linearly fall and rise in energy, respectively. A relaxation mechanism describing the dynamics between the singlet and the triplet sates when applying a strong magnetic field was proposed by *Hayashi and Nagakura* and is depicted in Figure 8 (right).[107-110]

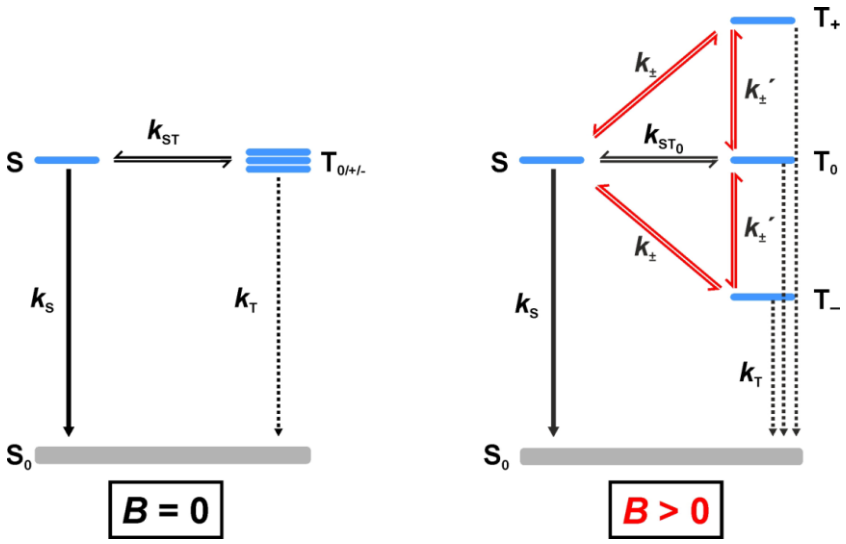

Figure 8: State diagram of the CS state with degenerated singulet and triplet states at zero magnetic field (left) and non-zero field (right).

The formally coherent interconversions between T_+/T_- and S are becoming incoherent governed by a much slower stochastic relaxation process. This interconversion is assigned to the rate constant $k_\pm$. The spin-flip between T_+/T_- and T_0 become incoherent too, and the respective rate constant is denoted as $k_\pm'$. As shown by *Hayashi et al.* $k_\pm'$ and $k_\pm$ are equal

and thus can be merged together to form one rate constant $k_{\pm}$.[107, 110] Since all transitions involving the T_+ and T_- are strongly inhibited when increasing the magnetic field, the total rate of interconversion between singlet and triple states decreases, because the S-T_0 (still described by k_{ST0}) bares the only effective interconversion channel.

In a recent publication of *Lambert et al.* concerning a triad with TAA and NDI redox centers and a central iridium complex as photosensitizer (**W**), it was possible to separate the coherent, hfc driven spin conversion at small magnetic fields from the incoherent relaxation processes at larger fields and therefore obtain detailed information about the involved rates and the energetic situation (Scheme 4). In these systems, applying a magnetic field leads to a prolongation the lifetime of the CS state by a factor of ca. 5.[78, 111]

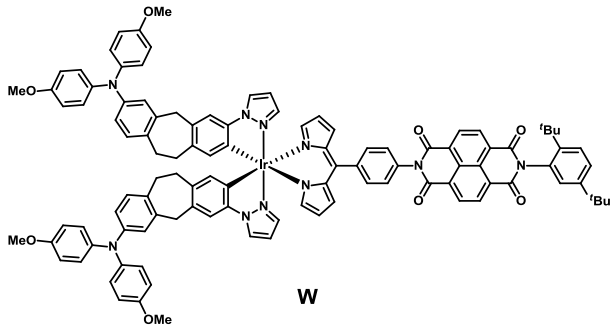

W

C. Lambert et al.[78]

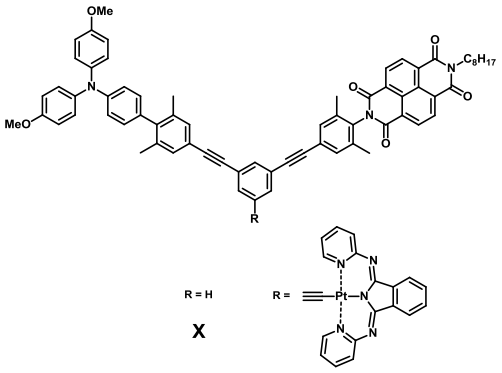

X **Y**

T. Ikoma et al.[112]

Scheme 4: Triad with an iridium complex as photosensitizer (**W**). Triad with benzene bridging unit (**X**) and with an additional palladium complex attached to the bridge (**Y**).

A contribution of *Ikoma et al.* demonstrates the dependency on the initial population of the CS to the CR dynamics.[112] In these studies, dyads consisting of a TAA donor and NDI acceptor were linked in *meta*-position by a benzene unit (**X**). Attachment of a platinum complex (**Y**), linked by an ethynyl group to the central benzene bridging unit, results in a switching of the initial spin state from ^{1}CS to ^{3}CS induced by the heavy-atom effects of the Pt (spin orbit coupling). The spin selective CR and spin relaxation processes remained unaffected by the attachment of the Pt-complex. However, changing the initial population leads to significantly different decay times, especially at higher magnetic fields. In case of the exclusive population of the triplet CS state, 1/3 of the population is initially given to the T_0 state, which can efficiently depopulate by coherent T_0-S spin-flip. But 2/3 of the population initially given to the T_+ and T_- states has to interconvert by incoherent spin relaxation to the T_0 and S states, before CR to the ground state can occur (exclusively from S).

1.7.2 Non-Degenerate Singlet and Triplet States

The influence of a magnetic field (*B*) on the CS dynamics for non-degenerate singlet and triplet states at zero magnetic field will be explained in the following. This situation occurs, if the radical centers are closer to each other. As a result the two radical centers cannot be treated as being independent and exchange interaction cannot be neglected.

Here, the energy difference between singlet and triplet levels is given by E_S-E_T = 2*J*, where *J* is the exchange interaction, which is assumed to be positive in this scenario. If the exchange interaction of the radical pair is much larger than the average hfc, spin interconversion is no longer coherent. In organic radicals the hfc energy is typically about 5.0 mT, which corresponds to a coherent interconversion frequency of ca. 1.4×10^8 s^{-1} between singlet and triplet state.[106]

If *2J* is substantially larger than 5.0 mT the hfc can no longer drive the S-T interconversion. It is then based on an incoherent stochastic relaxation process, which is particularly dominant at larger S-T separations. The latter relaxation process is at least an order of magnitude slower than the coherent spin flip and slows down drastically with increasing S-T separation.

Applying a magnetic field leads to a *Zeeman* splitting of the three sublevels of the triplet manifold T_+, T_0 and T_-, which increases linearly with the field strength *B*. While T_0 remains unaffected by the field being separated from S by 2*J*, the state energies of T_- and T_+ lower and rise in energy, respectively. Here, a new scenario arises from the course of the energy level for T_+. First, at fields smaller than 2*J* the energetic separation S-T_+ decreases with increasing magnetic field. Then, at *B* = 2*J* the T_+ level is isoenergetic to the S level. At fields larger than 2*J* the energetic separation S-T_+ increases with increasing magnetic field

The state diagrams of the CS state with non-degenerate singulet and triplet states at zero magnetic field (left) and non-zero field higher B = *2J* (right) are depicted in Figure 9. It becomes obvious, that at higher fields (B ≠ 0) the interconversion between each T_0, T_+, T_- and S has to be associated with its own rate constant; which are k_{ST0} for S-T_0 (unaffected by magnetic fields), k_+ for S-T_+ and k_- for S-T_-. Since the separation between T_0-T_+ and T_0-T_- have the same magnitude, these interconversions can be described by one rate constant $k_\pm$.

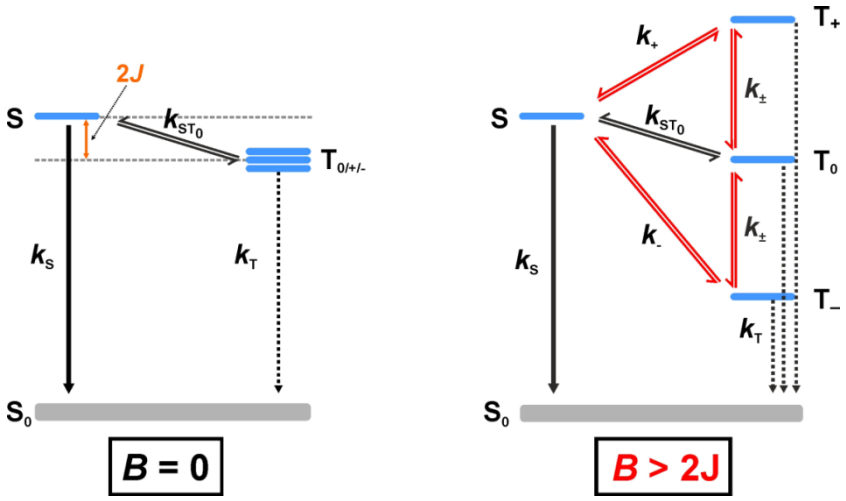

Figure 9: State diagrams of the CS state with non-degenerate singulet and triplet states at zero magnetic field (left) and non-zero field (right).

The lower limit of 2*J* that could be determined with MFE measurements is set by those exchange interactions were hfc occurs efficiently. Thus one can roughly set 5.0 mT as a lower limit. However, in some cases it was possible to determine 2*J* with a few tenths of mT, e.g. 0.4 mT observed in large systems by *Werner et al.*, consisting of zinc porphyrin as a donor and pyromellit diimide as an acceptor with a center to center distance of 22.4 Å (Scheme 5, **Z**).[108] A comparable observation was made in triade **AA** recently studied by *Lambert et al.* where 2*J* was estimated to ca. 3 mT and thus found to lie within the effective hyperfine field, too.[113] The distance between the RP located at the methoxy substituted TAA and the NDI, varies between 22.5 Å and 28.0 Å, since two resonance structures with a stretched or bent conformation were found by calculation.

The singlet-triplet splitting determined for dyads and triads with smaller distance between the RP of ca. 15–20 Å (e.g. **AB–AE**), is typically on the order of a few tenths of mT.[114, 115] The distance dependency on 2*J* was intensively investigated by *Wasielewski et al.,*[114, 116-118] e.g. with studies on a series of donor-bridge-acceptor molecules in which the donor, 3,5-dimethyl-4-(9-anthracenyl)juloidine (DMJ) and the NDI acceptor, were linked by three types of bridging units namely, *p*-phenylethynylene (**AF1–3**, n = 1–3), fluorenone (**AG1–3**, n = 1–3) and *p*-phenylene (**AH1–5**, n = 1–5).

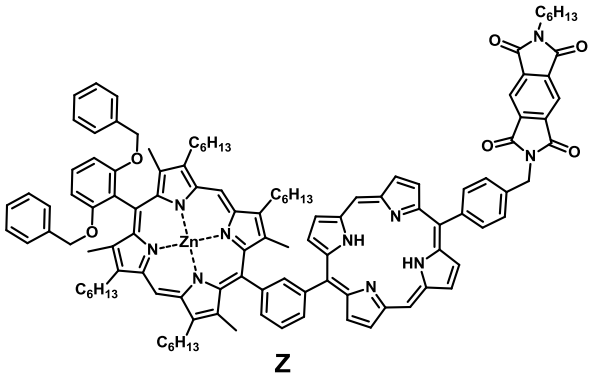

Z

Werner et al.[108]

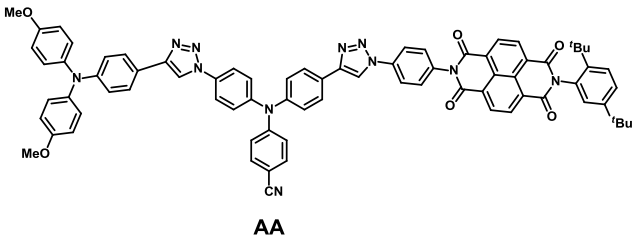

AA

C. Lambert et al.[113]

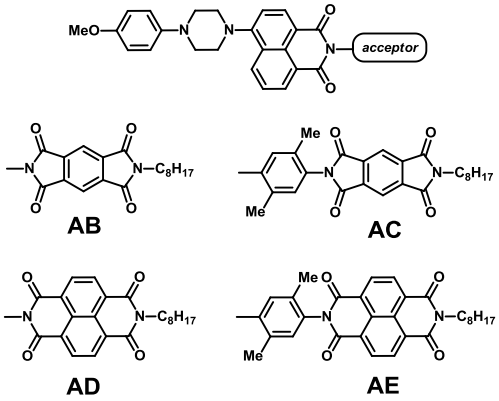

AB **AC** **AD** **AE**

M. R. Wasielewski et al.[114]

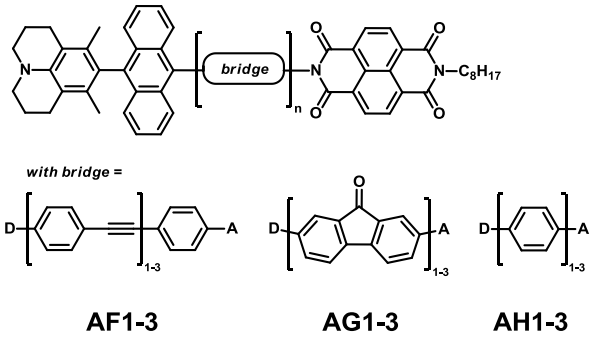

AF1-3 **AG1-3** **AH1-3**

M. R. Wasielewski et al.[114, 116, 117]

Scheme 5: Overview of some donor-acceptor systems in which 2*J* coupling has been investigated.

Wasielewski et al. demonstrated that the exchange interaction depends exponentially on the distance of donor and acceptor radical centers given by equation (4).[119]

$$2J = 2J_0 e^{-\alpha(r_{DA} - r_0)} \quad (4)$$

where r_0 is the *van der Waal* contact distance, r_{DA} the distance between donor and acceptor, $2J_0$ the exchange interaction at r_0 and α a specific decay parameter.

Following an argumentation by *Anderson* based on perturbation theory, the exchange interaction is related to the square of electronic coupling to energetically nearby lying states.[120]

$$2J = E_S - E_T = \left[\sum_n \frac{V^2_{CS,n}}{E_{CS} - E_n - \lambda}\right]_S - \left[\sum_n \frac{V^2_{CS,n}}{E_{CS} - E_n - \lambda}\right]_T \quad (5)$$

Accordingly, 2*J* can be obtained as a sum over all triplet/^{3}CS (e.g. or ^{3}CT/^{3}CS or local-triplet/^{3}CS) and singlet/^{1}CS perbutations, each given by the square of the appropriate *V* divided by the respective energy difference Δ*E*. The latter can be estimated from the appropriate energies E_{cs} and E_n and the reorganization energy *λ*. In some cases it is possible to reduce the perbutation to a single term related to the interaction with the smallest Δ*E* (nearest energy level e.g. a localized triplet state) and express 2*J* simply by equation (6).[106]

$$2J = \frac{V^2_{CS,n}}{E_{CS} - E_n - \lambda} \quad (6)$$

In that way, besides the distance, the electronic communication between redox centers linked by a bridge moiety may modulate the exchange interaction. One has to note that both *V* and thus *J* depend exponentially on the distance between the radical centers, but the distance dependency is significantly different (the distance dependency of *V* is much stronger).[106]

2 SCOPE OF THE WORK

This work aims at contributing to a better understanding of the fundamental aspects that dictate energy transfer processes in organic compounds. Therefore, special attention is paid to the bridging unit connecting the two redox centers, whose properties decisively affect the charge transfer. The work is divided into two main parts which are treated mostly separately and thus will be introduced separately in the following section.

The aim of the first part in this work (Chapter 3) is the synthesis of cationic mixed valence (MV) compounds **pX**$^{\bullet+}$, **mX**$^{\bullet+}$ and **mX46**$^{\bullet+}$ with the general structures shown in Scheme 6. They consist of two triarylamine (TAA) redox centers, which are connected to a central benzene unit via alkyne spacers, either in *meta*- or *para*-position. One redox centers is oxidized, while the other is neutral. If these dyads are now suitably excited (photoinduced or thermally), a superexchange hole transfer (HT) from the oxidized to the non-oxidized TAA occurs. The HT takes place over the bridging unit, whose electron density will be tuned by substituents with electron donating or accepting character attached in the 1,4-position. The substituents, hereafter referred as X, will vary from methoxy, methyl, chloro, cyano, to nitro. Furthermore, to investigate the influence of the substitution pattern of X, for the methoxy and methyl derivatives with *meta*-topology a 4,6-costitution of X will complete the series of MV compounds.
After discussing the synthetic work (3.1), the electrochemical and photophysical properties will be presented. For this purpose, **sX** and **sOMe46** will serve as reference compounds, which will aid in interpreting the results. The HT within the MV compounds (**pX**$^{\bullet+}$, **mX**$^{\bullet+}$ and **mX46**$^{\bullet+}$) will be investigated using of three different approaches. The first approach consists of the determination of the optical induced HT parameters via IVCT analysis is presented (3.3.1). The second approach is the investigation of the thermal HT by temperature dependent ESR measurement is discussed (3.3.2). In the third approach, the data for the HT obtained by TD-TFT calculations will be shown and compared to the experimental results (3.3.3). Finally a discussion of the received data for the HT, also regarding solvent dynamics, will be carried out.

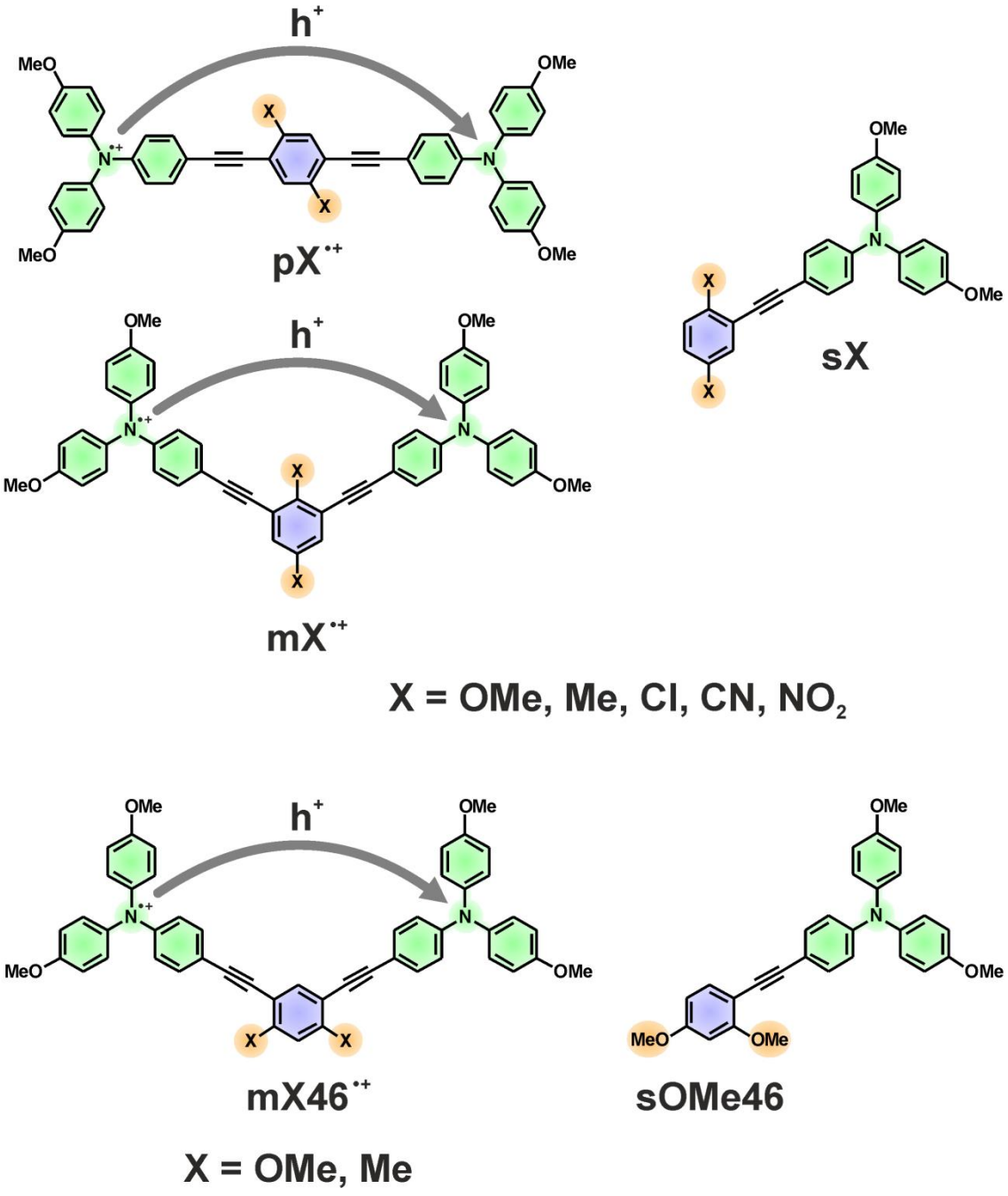

Scheme 6: Bistriarylamine MV compounds **pX**$^{\bullet+}$, **mX**$^{\bullet+}$, **mX46**$^{\bullet+}$ and their respective references **sX** and **sOMe46**.

The aim of the second part (Chapter 4) in this work is the synthesis of neutral donor-acceptor (DA) dyads **pXNDI**, **mXNDI** and **mOMeNDI46**, with structures are shown in Scheme 6. They consist of a triarylamine and a naphthalene diimide moiety, which are connected via alkyne spacers, either in *meta*- or in *para*-position, to a central benzene unit. After excitation a photoinduced charge separation will occur, where the TAA unit will serve as an electron donor and the NDI unit as the acceptor, generating a charge-separated (CS) state (Figure 1). Subsequently, charge recombination, under transfer of an electron from the NDI to the TAA, takes place, forming the ground state.

As in the first theme presented above, the electron density of the bridge will be tuned by substituents X with electron donating or accepting character attached in the 1,4-position, namely methoxy, methyl, chloro, cyano and nitro. Furthermore, to investigate the influence of the substitution pattern of X on the charge transfer dynamics for the methoxy derivatives with *meta*-topology, **mOMeNDI46** with 4,6-constitution of two methoxy units will complete the series of MV compounds.

After discussing the synthetic work (4.1), the electrochemical and photophysical properties will be presented. For this purpose, **sXNDI** and **sOMeNDI** will serve as reference compounds, which will facilitate the interpretation of the results. First the influence of the bridging unit on the charge separation will be investigated by fs-transient absorption (TA) spectroscopy (4.6.3/4), before the charge recombination (CR) dynamics will be discussed (4.6.5/6). This will be done at zero magnetic field and under application of an external magnetic field to detect magnetic field effects (MFE) and get a more detailed understanding on the CR.

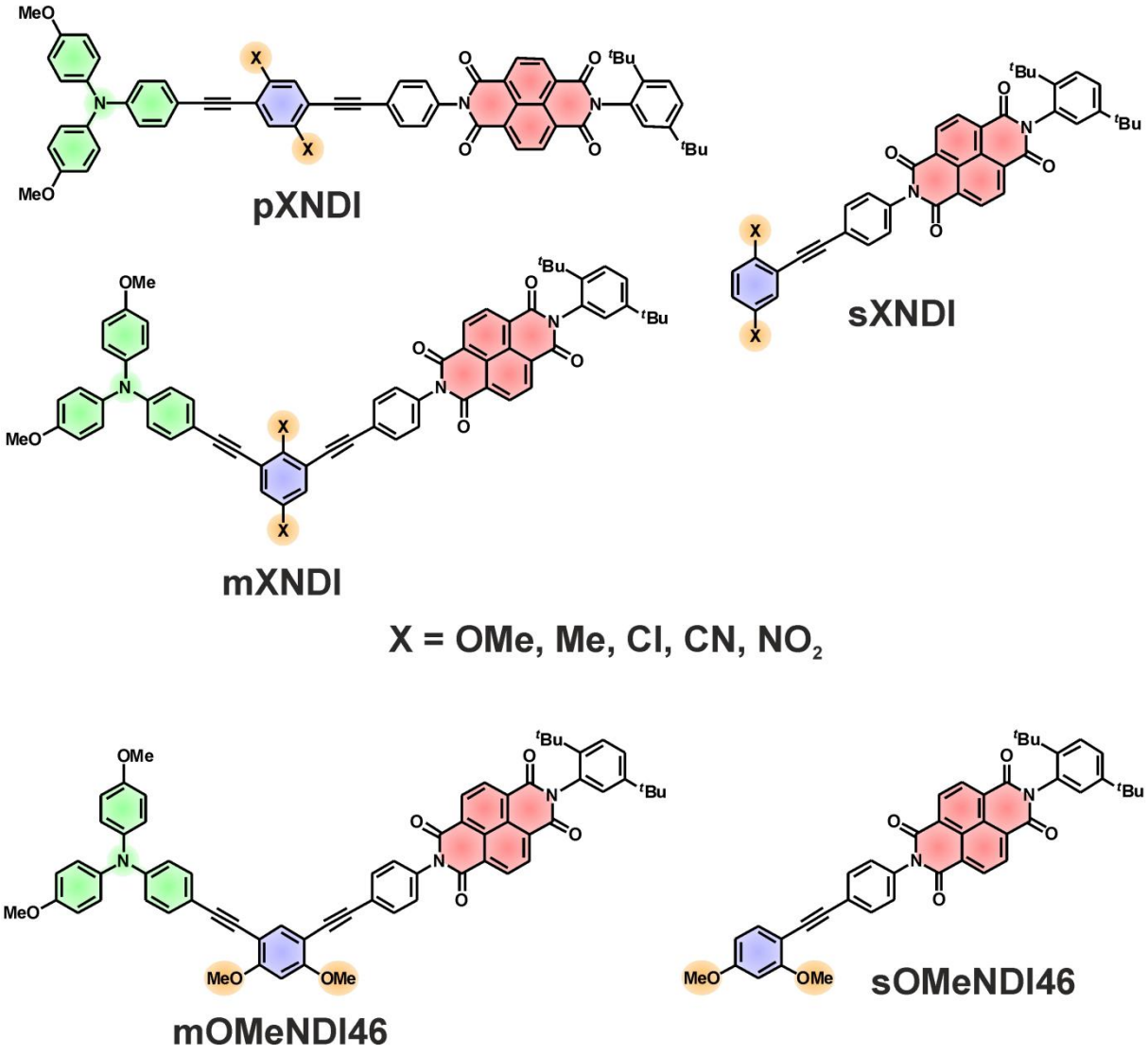

Scheme 7: Dyads **pXNDI**, **mXNDI**, **mOMeNDI46** and their respective references **sXNDI** and **sOMeNDI46**.

3 MIXED-VALENCE COMPOUNDS – RESULTS AND DISCUSSION[1]

3.1 Synthesis

The synthesis of the neutral bistriarylamine (bisTAA) *para*-compounds **pX**, *meta*-compounds **mX**, *meta*-compounds with substituents X in the 4,6-position **mX46** (X= OMe and Me) and their references **sX** and **sOMe46,** respectively, will follow a procedure that has proven to be successful by *Lambert et al.* for the synthesis of wide variety of similar bisTAAs, like cyclophane, anthracene and even benzene bridged bisTAAs.[88, 90, 98, 99, 101] In fact, the synthesis of **pMe** and **pOMe** are already published using this approach.[90, 98]

In Scheme 8 the first step of the retrosynthesis of the bisTAA target molecules (TM) and their references is shown, that is a (or two) C-C bond cleavage between a benzene carbon atom and the ethynyl carbon atom. Since this C-C bond will later be formed by Pd catalyzed *Sonogashira-Hagihara* cross coupling between the two precursors, one (or two) halogen functionality at the benzene moieties and one (or two) acetylene functionalized triarylamine unit (eTAA) are required.

The bromo functionality was preferentially chosen as suitable halogen functionality, since it is known to undergo reliable C-C cross couplings under *Sonogashira-Hagihara* condition.[121, 122] However, as the following description will show, use is also made of the iodine functionality. For the in total 18 different bisTAA/reference compounds that were synthesized, besides the eTAA unit, logically consistent 18 different benzene units already attached with a halogen functionality the later position of the TAA are needed. Also the designation of the benzene units is related to the parental bisTAA/reference. Therefore their acronym will simply be that of the bisTAA/reference with the letter ”b” written before the substituent X (e.g. the bridging unit of **mOMe** is named **mbOMe**).

[1] Reproduced or adapted in parts with permission from the American Chemical Socierty: *Hole Transfer Processes in* meta- *and* para-*Conjugated Mixed Valence Compounds: Unforeseen Effects of Bridge Substituents and Solvent Dynamics,* J. Schäfer, M. Holzapfel, B. Mladenova, D. Kattnig, I. Krummenacher, H. Braunschweig, G. Grampp, C. Lambert, *J. Am. Chem. Soc.* **2017**, *139*(17), 6200-6209. DOI: 10.1021/jacs.7b01650. Copyright © 2017 American Chemical Society.
Parts of this chapter have been investigated in a Bachelor thesis under supervision of J.Schäfer: *Synthese von Donor-Akzeptor-Verbindungen mit* para-*verknüpfender Benzolbrücke,* W. Wagner, Bachelor Thesis, Julius-Maximilians-Universität Würzburg, **2013**.

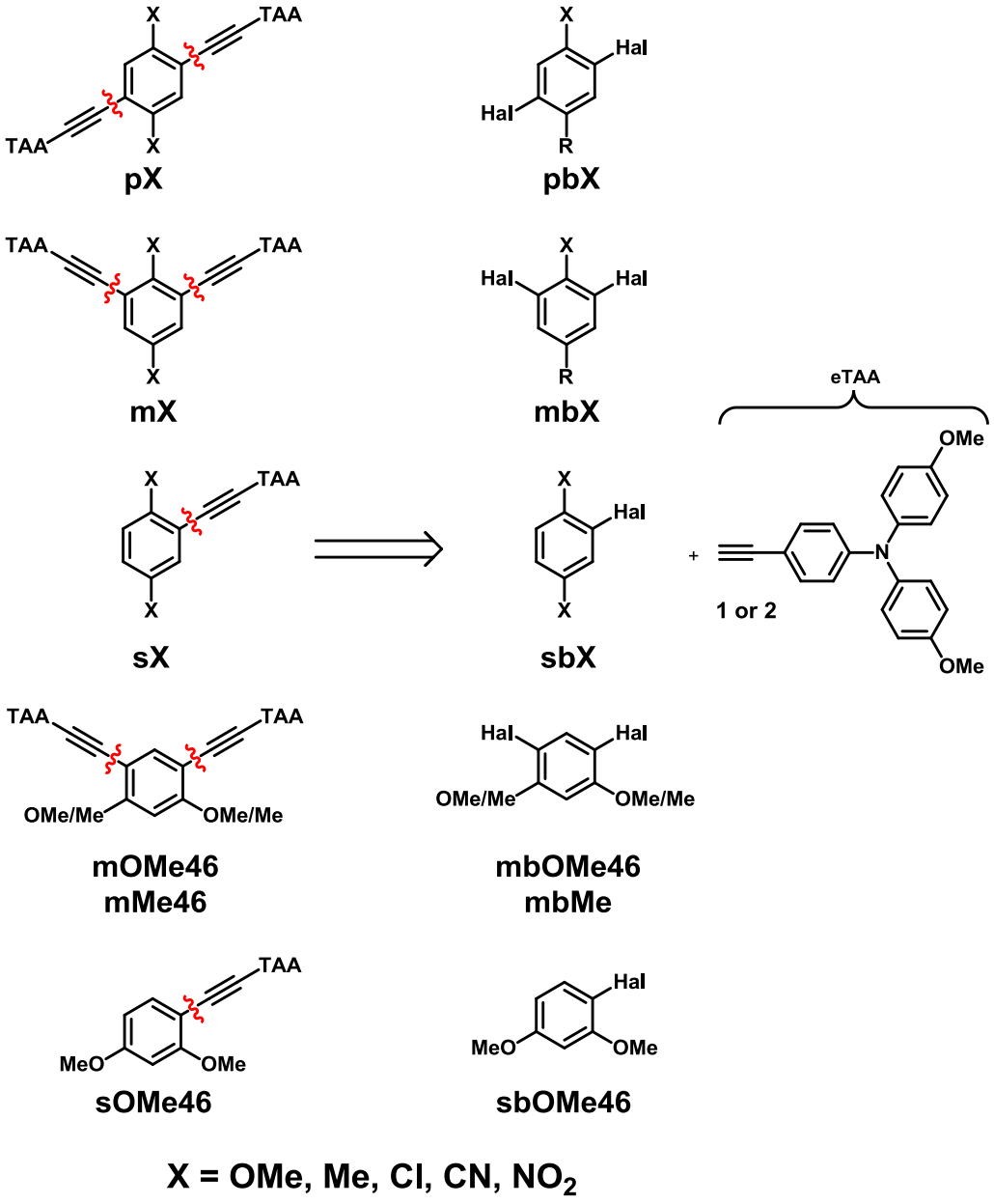

Scheme 8: Retrosynthesis of the bisTAA target molecules and their references.

In the following the synthesis of the neutral bisTAAs and their references is subdivided into three parts. First the synthesis of the TAA donor moiety with ethynyl functionality (eTAA), followed by the synthesis of the whole range of bridging units and finally the Pd-catalyzed *Sonogashira-Hagihara* cross coupling reactions will be explained.

The final MV compounds **pX**$^{\bullet+}$, **mX**$^{\bullet+}$ and **mX46**$^{\bullet+}$, in which the HT is examined, will be generated *in situ* by use of an appropriate oxidant. The procedure of oxidation is explained in the respective chapter.

3.1.1 Synthesis of the Ethynyl Functionalized Triarylamine (eTAA)

The synthesis of the doubly methoxy substituted triarylamine with an ethynyl function attached to one of the aryl unit was first reported by *Lambert et al*.[123] The synthesis started with a ligated catalysis of the *Ullmann* condensation of 4-bromoaniline and two equivalents of 4-iodoanisole, following the procedure of *Goodbrand et al.*[124] (Scheme 9). After recrystallization from EtOH/water, 4-bromo-*N*,*N*-bis(4-methoxyphenyl)aniline (**1**) was obtained in 42 %. Via *Sonogashira-Hagihara* coupling of **1** with trimethylsilylacetylene (TMSA) the ethynyl group was introduced at the TAA moiety with nearly quantitative yield (98 %).

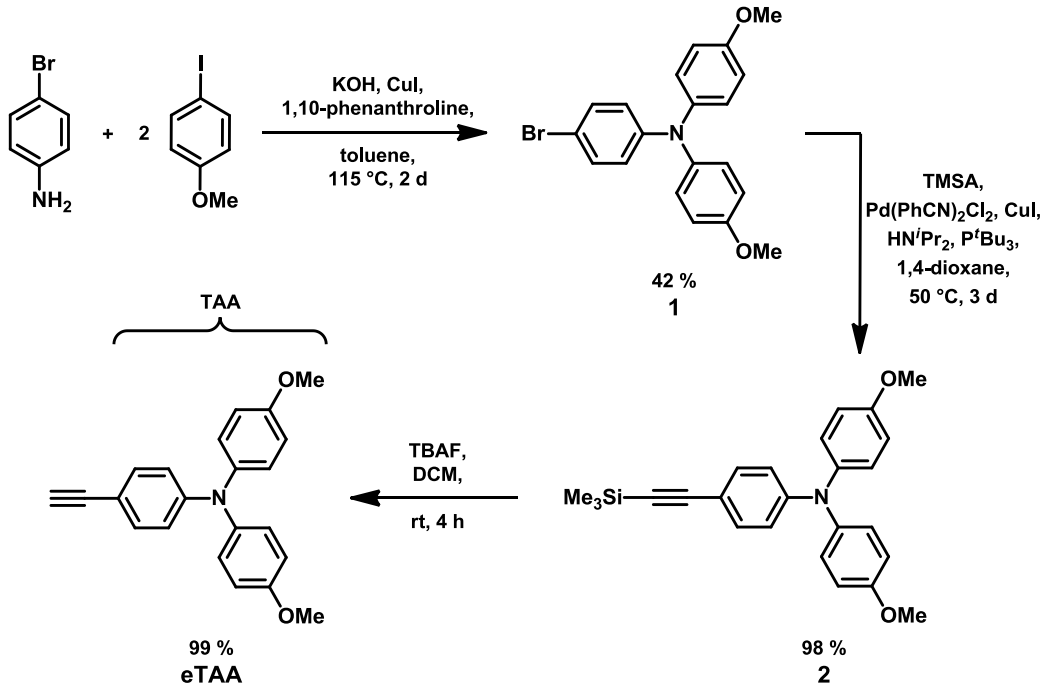

Scheme 9: Synthesis of **eTAA**.

The new functionality was still protected on one end by the trimethylsilyl group. By desylilation of **2** with tetrabutylammoniumfluorid (TBAF) in DCM the ethynyl group was deprotected and **eTAA** was isolated in quantitative yield (99 %).

3.1.2 Synthesis of the Bridging Units

As already mentioned in chapter 3.1 18 different bridging units were necessary to achieve the total range of target molecules (Scheme 8).The synthesis of the non-commercially available bridging units is presented in the following section.

Synthesis of the Bromo-1,4-dimethoxybenzenes Units (sb-/pb-/mbOMe)

Bromination of 1,4-dimethoxybenene with bromine in glacial acetic acid at 0 °C resulted in a mixture of 1,4-dibromo-2,5-dimethoxybenzene (**pbOMe**) and 1-bromo-2,5-dimethoxybenzene (**sbOMe**) in a ratio of 3:1 (Scheme 10). The two benzene derivatives could easily be separated by flash-column chromatography on silica gel.

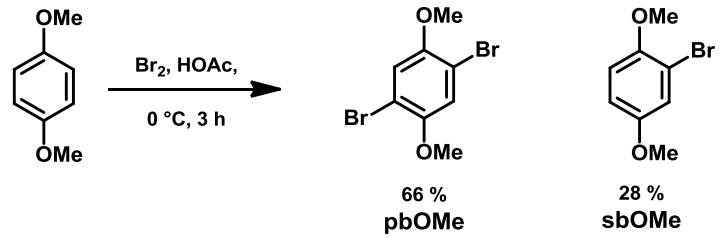

Scheme 10: Synthesis of the dimethoxybenzene units **pb-** and **sbOMe**.

One method of synthesizing **mbOMe** started with the bromination of 2,5-dimethoxyaniline with bromine in DCM (Scheme 11). Then, the 2,4-dibromo-3,6-dimethoxyaniline (**3**) was reduced to **mbOMe**. This recation step proceeds via an *in situ* generated diazonium salt, which was thermally dediazoniated.

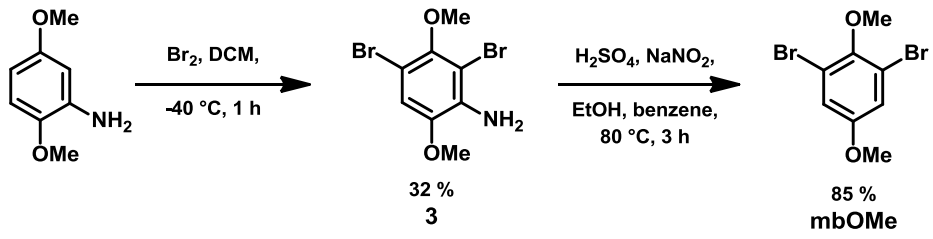

Scheme 11: Synthesis of **mbOMe** by bromination and subsequent oxidation of the aniline.

The disadvantages of this synthesis route were that the workup of the crude aniline product was very time intensive and required the use of large amounts of solvents. The phase

separation in the separation funnel was very poor and particularly a very thick and long column for flash chromatography was needed, which resulted in the consumption of large quantities of solvent. In addition to this the yield of this step (32 %) was non-satisfying.

The alternative starting point for the synthesis of **mbOMe** was the bromination of 4-methoxyphenol. If the bromination was done with bromine at 0 °C under acidic conditions, a mixture of different brominated compounds was formed (Scheme 12). Further workup led to a small amount of a mixture of 2,6-dibromo-4-methoxyphenol and 2,3,6-tribromo-4-methoxyphenol from which the dibromo compound could not be isolated. Therefore, 4-methoxyphenol had to be brominated with BTMA-Br_3 (benzyltrimethylammonium tribromide) to 2,6-dibromo-4-methoxyphenol (**4**) to achieve selective bromination in *meta*-position in good yields (78 %).[125]

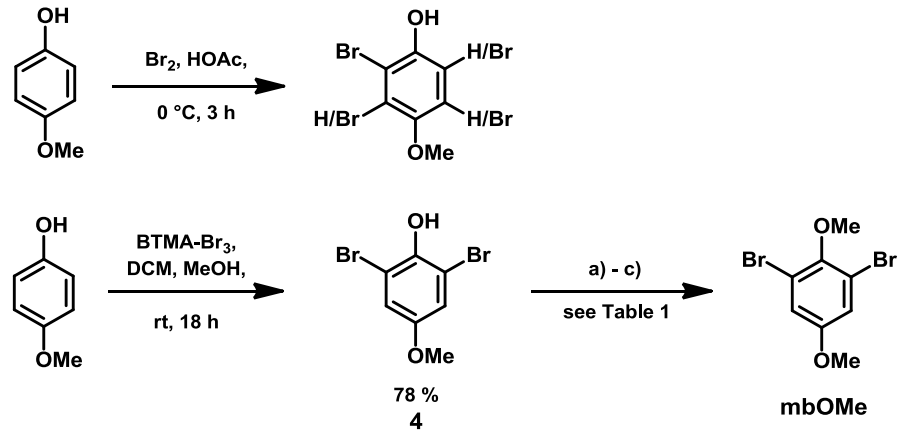

Scheme 12: Synthesis of the dimethoxybenzene unit **mbOMe**.

The following methylation of the hydroxyl group was tested under different conditions (Table 1). With the most efficient methylation reagent, dimethyl sulfate (DMS), it was possible to isolate 1,3-dibromo-2,5-dimethoxybenzene (**mbOMe**) in yields of over 70 %.

Table 1: Methylation of 2,6-dibromo-4-methoxyphenol.

	Reaction Conditions	**Yield in %**
a)	MeI, K_2CO_3, DMF, rt, 12 h	9
b)	MeI, K_2CO_3, acetone, 56 °C, 12 h	17
c)	DMS, NaOH, water, rt, 1 h	71

At this point it is important to mention, that later attemps to couple the bromodimethoxybenzene bridges with **eTAA** by *Sonogashira-Hagihara* coupling failed (see 3.1.3, Scheme 23). Due to the strong electron donating character of the methoxy groups, the electron density at the benzene unit stabilizes the Br-C bond. Consequently, this bond is too stable to react under the condition used in the catalytic cycle.[126] It is assumed that one of the rate-limiting elementary step of the catalytic cycle, presumably the oxidative addition to the Pd, is too slow.[127] However, the I-C bond is much weaker and shows a higher reactivity in *Sonogashira-Hagihara* couplings. For this reason the dimethoxy compounds with iodo (**OMe'**) instead of bromo (**OMe**) atoms had to be synthesized.

Synthesis of the Iododimethoxybenzene Units (pb-/mbOMe' and mbOMe'46)

The iodo compounds 1,4-diodo-2,5-dimethoxybenzene (**pbOMe'**) 1-iodo-2,5dimethoxybenzene (**sbOMe'**) and 1,3-diodo-4,6-dimethoxybenzene (**mbOMe'46**) were obtained by direct iodination of the corresponding dimethoxybenzenes with iodine (Scheme 13).[128-132]

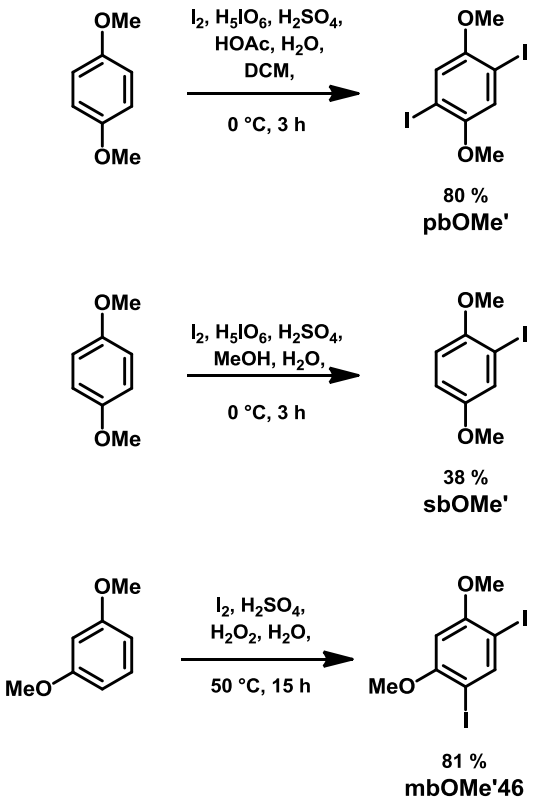

Scheme 13: Synthesis of the iododimethoxybenzenes **pb-/sbOMe'** and **mbOMe'46**.

The iodination of these activated benzenes were done under oxidative, acidic conditions with e.g. H_2O_2 or periodic acid as oxidants and H_2SO_4 as strong acid.[133] While the diiodo compounds **mb/-pbOMe'** were synthesized in good yields (ca. 80 %), the singly substituted compound **sbOMe** was isolated in only 38 % yield.

Synthesis of 1,3-diiodo-2,5-dimethoxybenzene

The first attempts to synthesize 1,3-diiodo-2,5-dimethoxybenzene (**mbOMe'**) started with the iodination of 2,4-dimethoxyaniline (Scheme 14, the shaded reaction step shows the planned synthesis after a successful first step). The latter should be reduced (e.g. under conditions successfully used in Scheme 11) to **mbOMe'**.

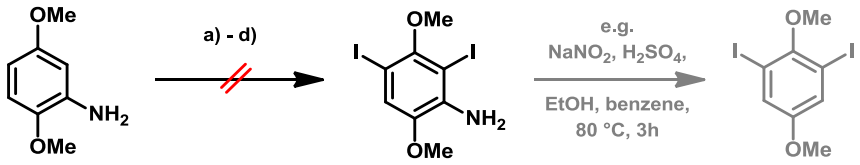

Scheme 14: Planed synthesis of the dimethoxybenzene **mbOMe'**.

Despite the successful bromination of 2,5-dimethoxyaniline, all attempts to iodinate this compound failed. The iodination was tried with iodine, as well with *N*-iodosuccinimide (NIS) under various conditions and reaction times, respectively (Table 2).

Table 2: Tries to diiodinate 2,4-dimethoxyaniline.

	Reaction Conditions	**Yield in %**
a)	I_2, H_2O_2, H_2O, 50 °C, 5–15 h	-
b)	I_2, Na_2CO_3, H_2O, Et_2O, rt, 15 h	-
c)	I_2, H_5IO_6, HOAc, H_2SO_4, H_2O, DCM, 75 °C, 15 h	-
d)	NIS, THF, rt, 2–15 h	-

In all cases the iodination attempts resulted in a formation of a black, barley soluble, tarry solid. Unfortunately, the identification of the unintended reaction or its products was not possible.

A second synthetic route started with the iodination of 2,4-dimethoxyaniline to 1,5-diiodo-4-methoxyaniline (Scheme 15, the shaded reaction steps shows the planed synthesis after a successful first step). The latter should be methylated (e.g. under conditions successfully used in Table 1) to **mbOMe'**.

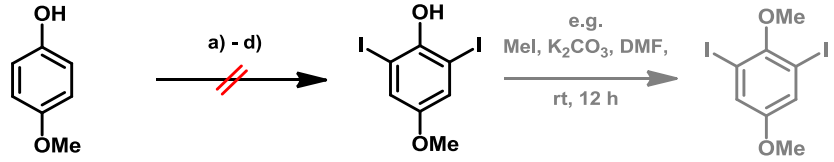

Scheme 15: Planed synthesis of the dimethoxybenzene **mbOMe'**.

As iodination reagents iodine, NIS, benzyltrimethylammonium dichloroiodate (BTMA-Cl_2Br) and a *N*-chlorosuccinimide(NCS)/NaI system were tested. Again, all tries to isolate the diiodinated compound failed.

Table 3: Tries to diiodinate 4-methoxyphenol.

	Reaction Conditions	**Yield in %**
a)	NCIS, NaI, HOAc, 100 °C, 1.5 h	-
b)	NIS, THF, rt, 15 h	-
c)	I_2, H_5IO_6, HOAc, H_2SO_4, H_2O, DCM, 75 °C, 15 h	-
d)	BTMA-Cl_2Br, MeOH, DCM, rt, 1–3 d	-

For these reasons a different approach was chosen. Using the brominated compound **mbOMe** as starting point, a halogen exchange via the organ lithium intermediate was tried (Scheme 16). Hence, **mbOMe** was lithiated with an excess of ^{t}BuLi (3 eq.) at −78 °C and iodine was added. However, only one halogen exchange took place and 1-bromo-3-iodo-2,5-dimethoxybenzene (**5**) was formed exclusively.

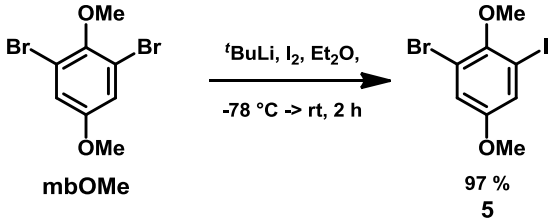

Scheme 16: Halogen exchange with ^{t}BuLi.

The dilithiated intermediate can properly not be generated under this conditions and even with increasing the ^{t}BuLi concentration to a 10 times excess (5 eq.) no **mOMe'** was formed. Finally, **mbOMe'** was synthesized by use of an aromatic *Finkelstein* reaction reported by *Klapars et al.* (Scheme 17).[134] For this purpose **mOMe** was treated with a catalyst system consisting of CuI, NaI and *trans-N,N'*-dimethyl-1,2-cyclohexanediamine in 1,4-dioxane under reflux.

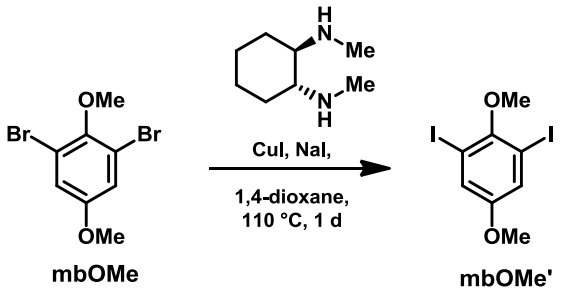

Scheme 17: Copper-catalyzed halogen exchange of **mbOMe** to **mbOMe'**.

As reported in literature, this copper-catalyzed exchange is an equilibrium in which the position of the equilibrium is dependent on the amount of NaI in the reaction. This dependency becomes clear when looking at the three different reaction conditions used (Table 4).

Table 4: Halogen exchange of **mOM**e with CuI, NaI and diamine to **mOMe'**.

	Reaction Conditions			Yield mbOMe' in %
	Eq. CuI	**Eq. Diamine**	**Eq. NaI**	
a)	0.1	0.2	4	< 1
b)	0.2	0.4	15	30
c)	0.2	0.4	40	99

With 4 eq. of NaI only traces of diiodo compound was formed. When increasing the NaI equivalence to 40, the equilibrium shifts drastically to the product side and **mOMe'** was obtained in quantitative yields.

Synthesis of the Dimethylbenzene Units (pb-/mbMe)

2,4-Dibromo-*para*-xylene (**pbMe**) was synthesized by bromination of *para*-xylene with bromine and catalytic amounts of iodine at 0 °C (Scheme 18).

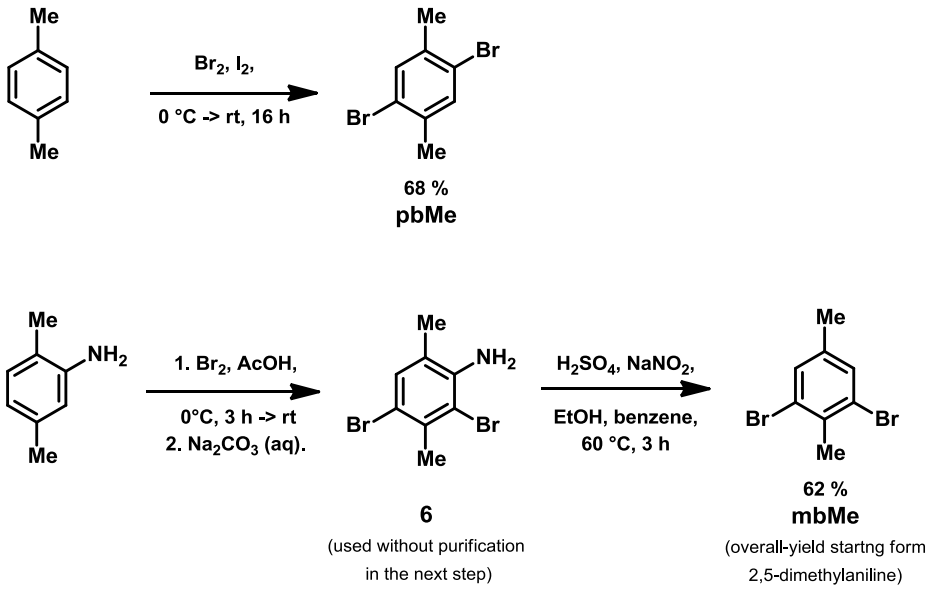

Scheme 18: Synthesis of the dimethylbenzene units **pb-/mbMe**.

To achieve the *meta*-orientation of the bromo atoms, 2,5-dimethylaniline was brominated and the resulting 2,4-dibromo-3,6-dimethylaniline (**6**) was reduced to 2,5-dibromo-*para*-xylene (**mbMe**) via dediazoniation of the diazonium salt.

Synthesis of the Dichlorobenzene Unit (mbCl)

2,5-Dichloroaniline was brominated with two equivalents of *N*-bromosuccinimide (NBS) in THF yielding 79 % of 2,4-dibromo-2,5-dichloroaniline (**7**, Scheme 19). A following dediazoniation via a diazonium salt led to the tetrahalogenated compound 1,3-dibromo-2,5-dichlorobenzene (**mbCl**).

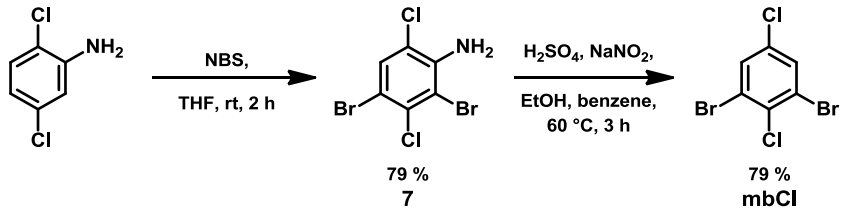

Scheme 19: Synthesis of the dichloro compound **mbCl**.

Synthesis of the Terephthalonitrile Units (sb-/pb-/mbCN)

The first attempt to synthesize the terephthalonitrile compounds started with the oxidation of the corresponding brominated *para*-xylenes (**sb-/pbMe**) with chromium trioxide to obtain the terephthalaldehydes (Scheme 20, the shaded reaction steps shows the planed synthesis after a successful first step).[135] But even with a large excess of oxidizing agent and increasing the temperature and the reaction time, only one methyl group was oxidized to an aldehyde.

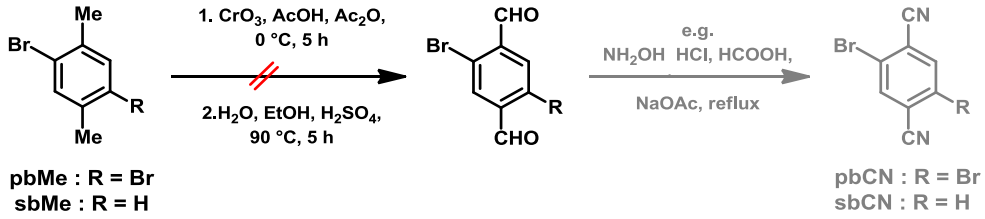

Scheme 20: Oxidation of **sb-** and **pbMe** with chromium trioxide.

The second synthetic route of the dinitril compounds started with the oxidation of the *para*-xylenes (**sb-/pb-/mbMe**) with potassium permanganate in basic conditions under reflux (Scheme 21, Table 5).[136] To get both methyl groups oxidized, a high excess (eightfold) of oxidant and a long reaction time (2 d) was needed. The yield of the terephthalic acids (**8**–**10**) –varied from ca. 40–60 %. A further increase of the reaction time and/or the oxidant did not lead to higher yields. The latter may be due to the fact that the reaction mixture under the given conditions is already saturated with $KMnO_4$.

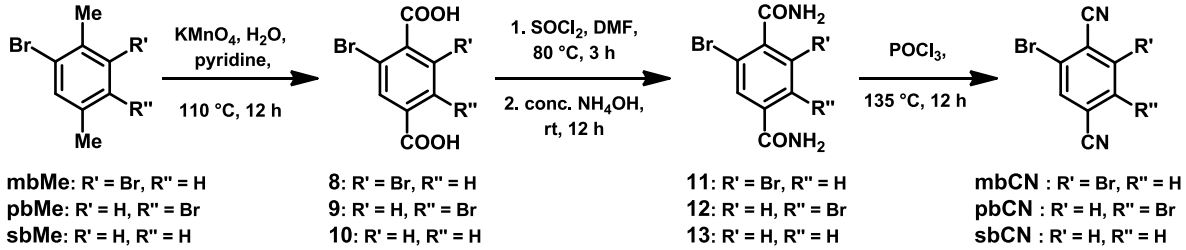

Scheme 21: Synthesis of the terephthalonitrile units **sb-/pb-/mbCN**.

The terephthalic acids (**8**–**10**) were first treated with an excess of thionyl chloride and catalytic amounts of DMF to form the acyl chlorides *in situ*. Treatment with conc. ammonium hydroxide yields the corresponding carboxamides (**11**–**13**).

Table 5: Yields of the synthesis of the terephthalonitrile units **sb-/pb-/mbCN**.

Starting Material	Product Step 1	Yield Step 1 in %	Product Step 2	Yield Step 2 in %	Product Step 3	Yield Step 3 in %
mbMe	**8**	59	**11**	87	**mbCN**	82
pbMe	**9**	42	**12**	56	**pbCN**	82
sbMe	**10**	62	**13**	55	**sbCN**	66

The amide function was converted to the final cyano function by reaction with phosphoryl chloride under reflux. The terephthalonitrile units (**sb-/pb-/mbCN**) were obtained in 60–80 % yield.

Synthesis of the Dinitrobenzene Units (sb-/pb-/mbNO$_2$)

The *para* isomer 2,5-dibromo-1,4-dinitrobenzene (**pbNO$_2$**) was synthesized by dinitration of *para*-dibromobenzene (Scheme 22). The nitration should take place at about 100 °C. At lower temperatures the second nitration is not possible because the activation barrier for the second nitration is too high. At higher temperatures the explosive trinitro compound may be formed.[137] The isolation of **pbNO$_2$** from the mixture of side products (mono- and dinitration) was done by repeated recrystallization from acetic acid and 1,4-dioxane.[138, 139]

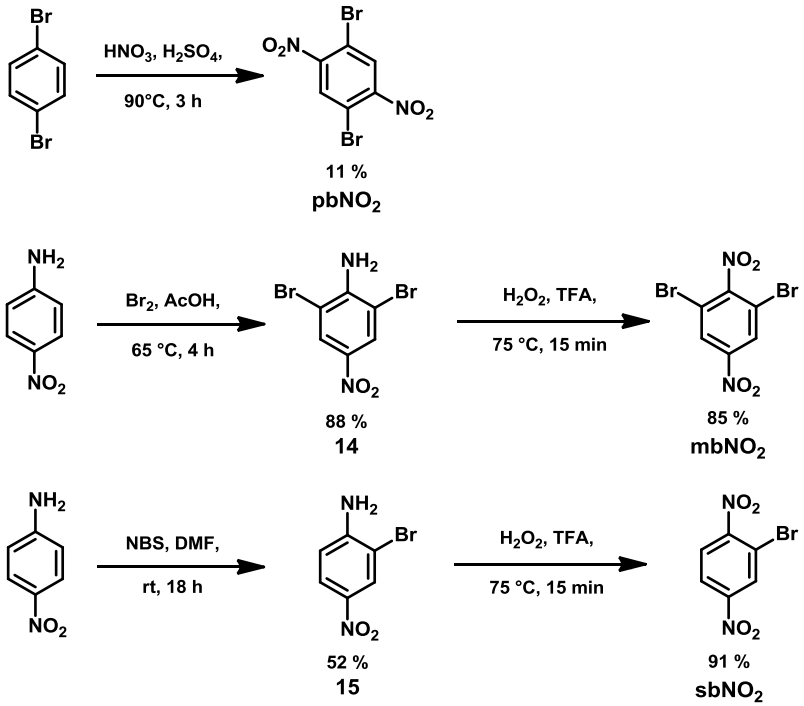

Scheme 22: Synthesis of the dinitro benzenes **pb-/sb-/mbNO$_2$**.

The synthesis of the dinitro benzene unit with *meta*-orientation of the halogen atoms started with the bromination of 4-nitroaniline with bromine in acetic acid. The resulting 2,6-dibromo-4-nitroaniline (**14**) was attempted to be oxidized with *m*CPBA in DCM, but no **mbNO$_2$** formation was observed.[140, 141] In contrary, by oxidation with H_2O_2 under acid conditions 1,3-dibromo-2,5-dinitrobenzene was formed in good yields (**mbNO$_2$**).[142]

The single brominated dinitro compound (**sbNO$_2$**) was made in a similar way as **mbNO$_2$**. Here, 4-nitroaniline was brominated with one equivalent of *N*-bromosuccinimide (NBS) to 2-bromo-4-nitoaniline (**15**) and the amine group was oxidized with hydrogen peroxide, as well.

3.1.3 Synthesis of the Neutral bisTAAs and their Reference Compounds

The neutral bisTAA target molecules (TM) were built up by *Sonogashira-Hagihara* coupling of the bridging units and the triarylamine unit. The methoxy groups in the dimethoxybenzene units cause a high electron density at the benzene system, and as a result these compounds behave differently in the Pd-catalyzed cross coupling reactions. Hence the synthesis of **s-/p-/mOMe** is shown in more detail.

Attempts to synthesize s-/pOMe from sb-/pbOMe

As mentioned briefly above, all attempts to synthesis the triarylamine compounds **pOMe** or **sOMe** starting from the bromo substituted bridging units **sb-/pbOMe** failed (Scheme 23). The respective *Sonogashira-Hagihara* couplings of the bridging units with **eTAA** were tested under various conditions (Table 6). But even though **sb-/pbOMe** are reported in literature to undergo *Sonogashira-Hagihara* coupling with different alkynes, such as ethynylbenzene, TMSA or (1-hydroxy-1-methylethyl)acetylene no coupling with **eTAA** was possible.[143-147]

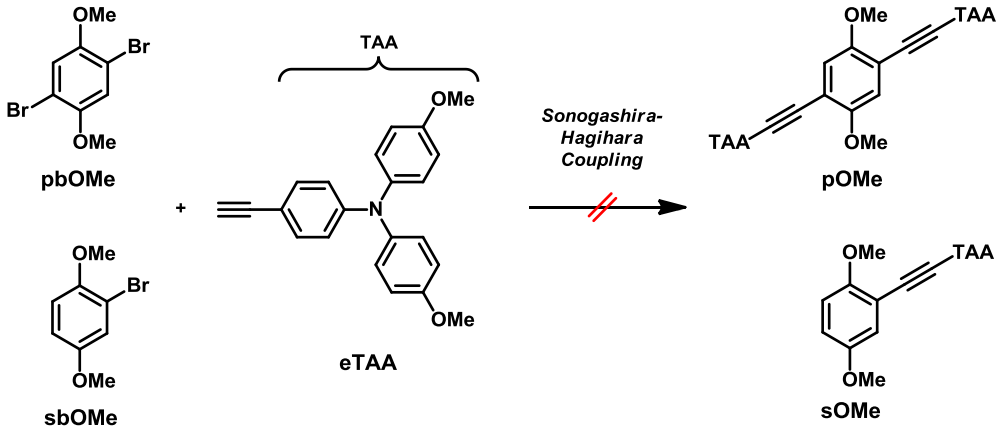

Scheme 23: Attempts to synthesis **p-/sOMe** starting from the bromobenzene bridging units **pb-/sbOMe**.

In all cases the reaction time was varied from 1–3 d. In Addition to that, after 1–2 d 1 eq. **eTAA** was added and after 2–3 d the temperature was increased from 60 °C to 80 °C. The reaction process was checked twice a day by TLC, but in none of the reactions a coupling to the TM **mOMe** or **sOMe** was observed.

Table 6: Conditions tested for the *Sonogashira-Hagihara* reaction of **pb-/sbMe** and **eTAA**.

Reactants	Reaction Conditions
pbOMe + 2.2 eq. TAA	**a)** $Pd(C_6H_5CN)_2Cl_2$, CuI, P^tBu_3, HN^iPr_2, 1,4-dioxane
	b) $Pd(C_6H_5CN)_2Cl_2$, CuI, $[^t(Bu)_3PH]BF_4$, HN^iPr_2, DMF
	c) $Pd(PPh_3)_2Cl_2$, CuI, NEt_3, THF
sbOMe + 1.1 eq. TAA	**d)** $Pd(C_6H_5CN)_2Cl_2$, CuI, P^tBu_3, HN^iPr_2, 1,4-dioxane
	e) $Pd(PPh_3)_2Cl_2$, CuI, NEt_3, THF
	f) $Pd(PPh_3)_2Cl_2$, CuI, NEt_3, toluene

Step-by-Step Synthesis of mOMe via Halogen Exchange

The first successful synthesis route for **mOMe** opened up by the halogen exchange in **mbOMe** when using ^{t}BuLi/I_2 (Scheme 16). Here, one of the two bromo atoms was exchanged by an iodo atom to form **5**, while the other left unchanged. Nevertheless, in **5** one iodine functionality is available, which can undergo *Sonogashira-Hagihara* coupling with **eTAA** to form **16** in high yields (95 %, Scheme 24). Even with an excess of the alkyne (2 eq.) no second substitution took place. Next, a second halogen exchange under the same conditions as shown before (Scheme 16) provided a new iodo functionality. Finally, **18** was used, again in a Pd-catalyzed cross coupling reaction with **eTAA** yielding **mOMe** in 86 %.

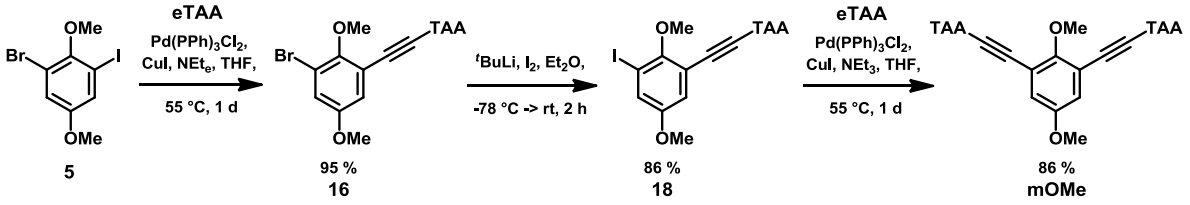

Scheme 24: Stepwise addition of **eTAA** to the dimethoxy benzene unit to form **mOMe**.

Although this step-by-step synthesis works in good yields, many synthesis steps are needed (more precisely 4 starting from **mbOMe**), an advantage of this this synthesis route is the formation of **18** in high yields, which was also needed in chapter 4.1.2 to build the DA molecule **mOMeNDI**.

Synthesis of all Target Molecules in One Step

The synthesis of the methoxy compounds is possible by *Sonogashira*-Hagihara coupling with the iodinated bridging units **sbOMe'**, **pbOMe'**, **mbOMe'**, **sbOMe'46** and **mbOMe'46** (Scheme 25) in one step. The electron donating strength of methyl group in **sb-/pb-/mbMe** and **mbMe46** is significantly lower, compared to the methoxy derivative, thus the cross coupling reaction readily takes place when using the bromo substituted bringing units. Consequently, the same holds true for all other bridging units **sb-/mb-/pbX** with **X** from Me to NO_2.

The best conditions for the *Sonogashira-Hagihara* coupling were identified in several attempts to synthesize the mono- and bistriarylamine functionalized benzenes. For this purpose the catalyst system, the amine base, the solvent and the reaction time were varied. For each substituent OMe to NO_2 a specific *Sonogashira* reaction gave the highest yields, which led to five general procedures (**GP**).The particular reactions conditions and yields of the coupling reactions are summarized in Table 7.

GP_{OMe}: A mixture of the methoxy substituted benzene bridges, $Pd(PPh_3)_2Cl_2$, CuI and of NEt_3 was thoroughly degassed. The amine base NEt_3 is used in a high excess and serves as a base and as well as a solvent. To this mixture a degassed solution of the alkyne **eTAA** was added. Here, the reactions showed a color change from brown to yellow and sometimes an appearance of precipitate within a few minutes, even at rt. TLC analysis indicated that the reactions were almost quantitative after 2–3 h at 60°C. But still all reactions were additionally stirred overnight to achieve a complete as possible reaction. After workup an average yield of about 75 % was accessible.

GP_{Me} and **GPc_l**: The conditions determined for the methyl and the chloro substituted bridges were quite similar and treated in the following together. They included a catalytic system consisting of $Pd(PPh_3)_2Cl_2$ (for Me) or $Pd(C_6H_5CN)_2Cl_2CuI$ (for Cl), CuI, P^tBu_3 and as a base HN^iPr_2. As solvent 1,4-dioxane was used. All components were mixed together and thoroughly degassed. Again, a color change from brown to yellow/green indicated a starting of the reaction. TLC analysis showed that the reactions were completed after stirring at 60 °C for 1–2 d. Nevertheless just moderate yields varying from 32–66 % for the chloro **s-/p-/mCl** and 60–70 % for the methyl compounds **s-/p-/mMe** and **mMe46** were achieved.

GP_{CN} and **GP_{NO_2}**: Nitro and cyano bridges were coupled by use of a catalyst system consisting of $Pd(PPh_3)_2Cl_2$ and CuI in NEt_3. In this suspension the alkyne **eTAA** was added and the mixture was degassed for at least 20 min. Then a degassed solution of the benzene unit in THF for the CN compounds or toluene for the NO_2 compounds was added.

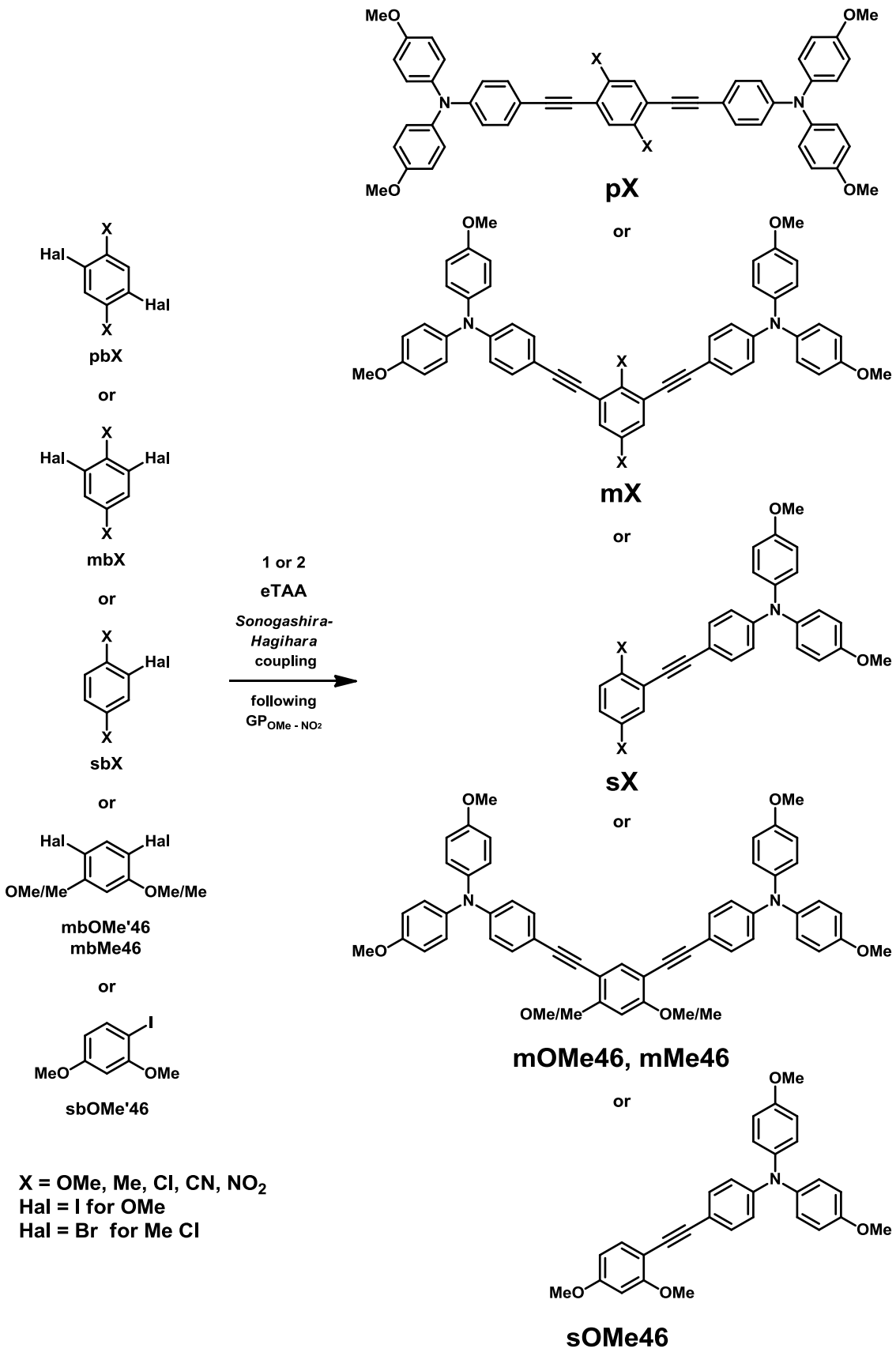

Scheme 25: *Sonogashira-Hagihara* coupling of the bridging units and **eTAA** to form the bisTAAs and their corresponding reference compounds.

After addition of the **sb-/pb-/mbCN** or the **sb-/pb-/mbNO$_2$** the color of the reaction mixtures turned orange-red (in the cyano case) and deep red (in the nitro case) after several hours, indicating that **s-/p-/mCN** and **s-/p-/mNO$_2$** were formed, respectively.

TLC analysis showed that the *Sonogashira* reaction with the cyano benzenes and the reactions with the nitro benzenes were completed after about 8 h and 12 h, respectively. Here the electron withdrawing character of the cyano and especially the nitro function was recognizable. In the latter case, the reactions seemed to be very fast and even the CN function led the reaction time drop to 12 h, which is a time decrease in reaction time by 75 % compared to coupling reactions done with the methyl benzenes.

Nevertheless the coupling reactions were additionally stirred at 60°C overnight or even for two days, in order to achieve complete reaction. The yields of **s-/p-/mCN** varied from 53–93 %.

Table 7: Reaction conditions for *Sonogashira-Hagihara* coupling of the references and bisTAAs.

	Reaction Conditions	Bridge	Eq. eTAA	Product	Yield in %
GP$_{OMe}$	$Pd(PPh_3)_2Cl_2$, CuI, NEt_3, THF, 60 °C, 1 d	**sbOMe'**	1.0	**sOMe**	66
		sbOMe'46	1.1	**sOMe46**	52
		pbOMe'	2.2	**pOMe**	83
		mbOMe'	2.2	**mOMe**	89
		mbOMe'46	2.2	**mOMe46**	88
GP$_{Me}$	$Pd(PPh_3)_2Cl_2$, CuI, P^tBu_3, HN^iPr_2, 1,4-dioxane, 60 °C, 3 d	**sbMe**	1.1	**sMe**	71
		pbMe	2.2	**pMe**	82
		mbMe	2.2	**mMe**	66
		mbMe46	2.2	**mMe46**	60
GP$_{Cl}$	$Pd(C_6H_5CN)_2Cl_2$, CuI, P^tBu_3, HN^iPr_2, 1,4-dioxane, 60 °C, 3 d	**sbCl**	0.9	**sCl**	66
		pbCl	2.0	**pCl**	32
		mbCl	2.0	**mCl**	35
GP$_{CN}$	$Pd(PPh_3)_2Cl_2$, CuI, NEt_3, THF, 60 °C, 1–2 d	**sbCN**	1.0	**sCN**	93
		pbCN	2.0	**pCN**	53
		mbCN	2.2	**mCN**	70
GP$_{NO2}$	$Pd(PPh_3)_2Cl_2$, CuI, NEt_3, toluene, 60 °C, 1 d	**sbNO$_2$**	1.1	**sNO$_2$**	60
		pbNO$_2$	2.2	**pNO$_2$**	59
		mbNO$_2$	2.2	**mNO$_2$**	43

The yields of **s-/p-/mNO$_2$** were significantly lower. A reason for this was the slight sensitivity of these compounds and the resulting decomposition, which complicated the work up process. The decomposition progress could be observed by a color change of the dissolved compound (e.g. in DCM) from red to green. Furthermore the decomposition was detectable by ^{1}H-NMR spectroscopy, which is exemplary shown for **mNO$_2$** in Figure 10. The ^{1}H-NMR spectra show the aromatic region of **mNO$_2$**. Without light exposure the spectrum shows the two typical AA'-BB' systems around 7.2–6.6 ppm and a singlet for the protons at the benzene unit at 8.27 ppm (blue spectrum).

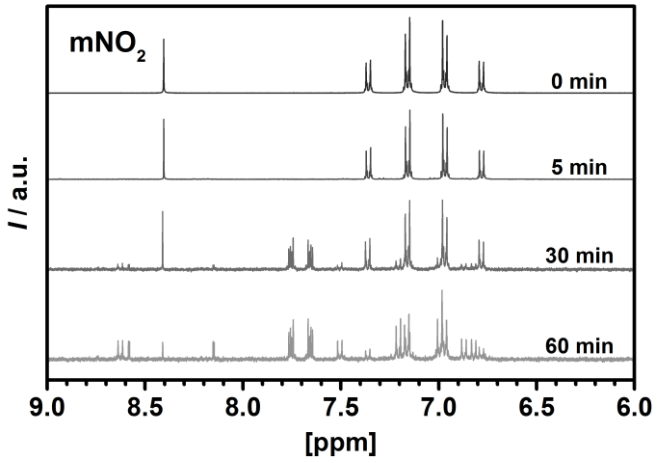

Figure 10: Cutout of the aromatic region of the normalized ^{1}H-NMR spectra of **mNO$_2$** without exposure of light (0 min) and after 5 min, 30 min and 60 min of light exposure.

After irradiation with sunlight (5 min / red spectrum, 30 min / green spectrum and 60 min / purple spectrum) several additional signals at e.g. ca. 8.5, 8.0 and 7.6 ppm appeared, proving decomposition of **mNO$_2$**. Unfortunately an identification of the decomposition product was not possible.

Another aspect which decreased the product yield of the nitro compounds is based on the instability of these compounds during flash column chromatography (even under exclusion of light).

3.2 Investigation of the Neutral Bistriarylamines

3.2.1 Crystal Structure of pOMe

The analysis of the crystallographically determined structure provides the possibility to get information about the structural features of the bisTAAs, which will help to understand the characteristic physicochemical properties.[2]

Later electrochemical measurements such as cyclic voltammetry (3.2.3) and chemical oxidation (3.3.1) will expose, that an isolation of the MV compound is not possible. This is due to an underlying comproportionation equilibrium, caused by a very low electrostatic communication the between the two TAA redox centers, preventing the existence of the exclusively mono oxidized bisTAA **pOMe$^{\bullet+}$**. Therefore, single crystals of the exemplarily chosen neutral bisTAA **pOMe**, which allowed X-ray crystal structure analysis, were prepared. In a good approximation the structural features will be present in **pOMe$^{\bullet+}$**, too and will help to understand the HT taking place there.

The crystallographically-determined structure of **pOMe** is shown in Figure 11. The structure is composed of two identical halves due to its C_2 symmetry. The TAA nitrogen is trigonal-planar surrounded by the three benzene rings with an angular sum of 359.8(4)°, resulting in a propeller-like structure which is typically found for TAA compounds.[149-152] The alkynes are approximately linear, with a C3–C5–C6 angle of 175.2(2)° and a C5–C6–C7 angle of 173.9(2)°, having a slight torsion of 5.8(4)° (for C3–C5–C6–C7). The alkyne unit connects two phenyl moieties (bridging unit and one TAA phenyl), which are consequently almost in plane. By constructing a plane in each of the benzenes rings a torsion angle of 3.36° was found. This geometry may allow a communication between the two molecule moieties (bridge and TAA).

In addition to that, the methoxy groups are planar to the phenyl plane too, since they exhibit a small torsion angle of 9.92(4)° (bridging unit), 17.4(3)° (TAA) and 3.2(2)° (TAA), respectively. This orientation provides the possibility to influence the adjacent π system (e.g. the bridging unit) significantly.

The N-N‘-distance in **pOMe** is 19.216(3) Å. Thus, the HT between the oxidized TAA and the non-oxidized TAA within the MV compound **pOMe$^{\bullet+}$** will have to take place over approximately the same length.

[2] The crystallographic measurement was performed by Dr. Marius Schäfer.[148]

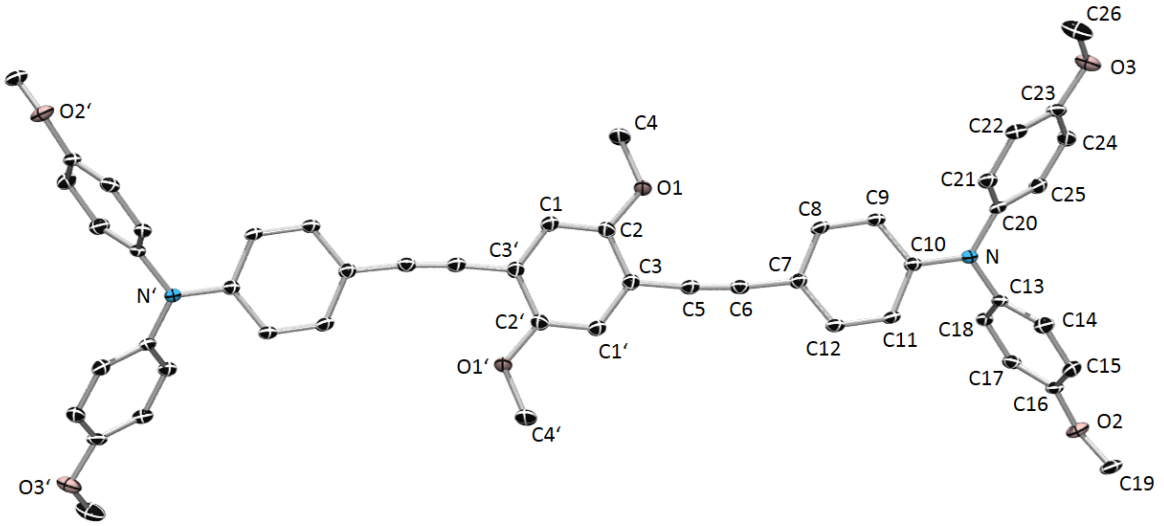

Figure 11: Molecular structure of **pOMe**. Ellipsoids are set at 50% probability; hydrogen atoms and solvent molecules are omitted for clarity. Selected bond lengths [Å] and angles [°]: C1–C2 1.282(3), C2–C3 1.406(3), C3–C4 1.403(3), C4–C5 1.426(2), C5–C6 1.199(2), C6–C7 1.325(2) C2–O 1.362(3), O–C4 1.429(3), C10–N 1.401(2), C13–N 1.430(2), C20–N 1.420(3); C2–O–C4 117.2(2), C3–C5–C6 175.2(2), C5–C6–C7 173.9(2), C10–N–C20 121.8(2), C20–N–C13 119.2(2), C10–N–C20 118.9(2), C16–O2–C19 117.3(2), C23–O3–C26 117.9(2); torsion C1–C2–O1–C4 9.9(2), C3–C5–C6–C7 5.8(4), C15–C15–O2–C19 17.4(3), C22–C23–O3–C26 3.2(2).

3.2.2 Steady-State Absorption Spectroscopy

In order to obtain information about the electronic ground state of the neutral bisTAA compounds steady-state UV/Vis absorption spectra were measured in solvents of different polarity, namely toluene (Figure 13, A–C), *ortho*-dichlorobenzene (*o*DCB, Figure 13, D–F), dichloromethane (DCM, Figure 14, A–C) and acetonitrile (MeCN, Figure 14, D–F). The absorption maxima ($\tilde{\nu}_{max}$ and λ_{max}) and extinction coefficients (ε_{max}) of the characteristic absorption bands for toluene and *o*DCB are listed in Table 8, those for DCM and MeCN in Table 9. The absorption behavior will be discussed exemplary for one solvent in more detail. Since toluene and *o*DCB have a *cut-off point* of ca. 35100 cm^{-1} (285 nm) and 34500 cm^{-1} (290 nm), respectively, some TAA absorptions are not visible.[153, 154] Consequently, the absorption will be discussed itemized in DCM with a *cut-off point* of ca. 43400 cm^{-1} (230 nm).[154] Essential observations can be transferred directly to the other solvents, and the main differences when changing the solvent are worked out later. First the absorption spectra of the references **sX** will be treated, with the insights gained the bisTAAs will be discussed.

Figure 14 A shows the absorption spectra of the reference compounds **sX** in DCM. For **sOMe-sCl** and **sOMe46** one can identify the typically broad π-π*-absorptions of the TAA between 22000–38000 cm^{-1} (454–363 nm). The C_2 symmetry of the TAA results in two possible transitions within the TAA unit (Figure 12), associated with two possible bands: One HOMO → LUMO ($S_0 \rightarrow S_1$) transition with an orientation of the transition moment along the *z*-axis (ethynyl axis) which shows CT character to the benzene and is denoted in following "*z*-band/*z*-transition". For **sOMe–sCl** and **sOMe46** this band has a maximum absorption energy ($\tilde{\nu}_{max}$) of ca. 28000 cm^{-1} (357 nm) and a maximum molar absorption coefficient (ε_{max}) of ca. 30000 M^{-1} cm^{-1}. The second transition is a HOMO → LUMO+1 ($S_0 \rightarrow S_2$) transition along the *x*-axis perpendicular to the before mentioned one, in the π-π*-system of the dianisyl part and is denoted "*x*-band/*x*-transition".[96] For **sOMe–sCl** and **sOMe46** this transition is located at higher energy as a shoulder or a separated band (for **sCl**) at ca. 34000 cm^{-1} (294 nm).
The situation changes when looking at the absorption spectra of **sCN** and **sNO$_2$**. Still they exhibit a *z*-band at ca. 34000 cm^{-1} (294 nm), but the shape and position of the former *x*-band changes drastically. **sCN** shows two absorptions at lower energy with a maximum at 23700 cm^{-1} (422 nm) and 27900 cm^{-1} (358 nm), respectively. For **sNO$_2$** the two absorptions are further separated and bathochromically shifted to 20200 cm^{-1} (495 nm) and 26800 cm^{-1} (373 nm), respectively. These lowest energetic transitions can be assigned to a CT transition including the electron deficient benzene "bridge".

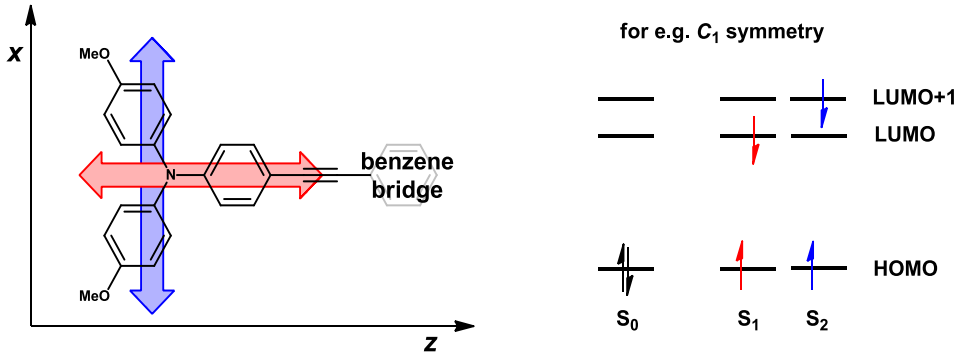

Figure 12: Transition moments of TAA with bridging unit (left). Configuration diagram for the ground and excited states for a TAA with C_1 symmetry (right). Color red indicates the CT-transition, blue the π-π*-transition.

Comparing **sX,** the influences on the absorption features by substituents X at the benzene units becomes obvious. Changing the substituents from electron donating groups (EDG) to EWG is associated with a bathochromic shift. Electron withdrawing groups (EWG, like CN) lower the electron density of the benzene and finally lead to low-lying CT bands, which are now shifted to the visible.[38]

Surprisingly, the absorption maximum of **sOMe** at 27500 cm^{-1} (364 nm) is a lower energy than those of **sMe** and **sOMe46** at 28200 cm^{-1} (355 nm). This circumstance can be explained by the orientation of the methoxy groups. In absence of steric hindrance, that means no substitution in *ortho*-position, methoxy groups prefer a planar over a gauche or perpendicular conformation (see Figure 11), since conjugation between the substituent *p* lone-pair orbital and the organic π system is possible.[155-160] Adjacent substituents may force the methoxy group out of plane, thus the strong electron π donating ability of the methoxy group gets strongly reduced or even prevented.[159, 161-163] Accordingly this particular OMe group acts as an electron acceptor through the oxygen electronegativity. Thus, it is assumed, that in **sOMe** on average one methoxy group is rotated out of plane resulting in a decrease of the absorption maximum to 27500 cm^{-1} (364 nm) and below that of **sMe**. However, in **sOMe46** the electron donating second OMe group in *para*-orientation to the TAA compensates the electron withdrawing effect more efficiently and the absorption maximum is just shifted to 28200 cm^{-1} (355 nm).

From this it can be seen that the strong EDG OMe has the ability to act to as an acceptor and donor and that not only the kind of substituent X (OMe–NO_2) influence the absorption features of **sX**, also the positon of X at the benzene unit plays a crucial role. Contrary to the transition oriented along z-axis, the π-π*-transitions are marginally effected by the substituents, which is visible by the almost same position of the absorption maxima/shoulder at ca. 35000 cm^{-1} (286 nm).

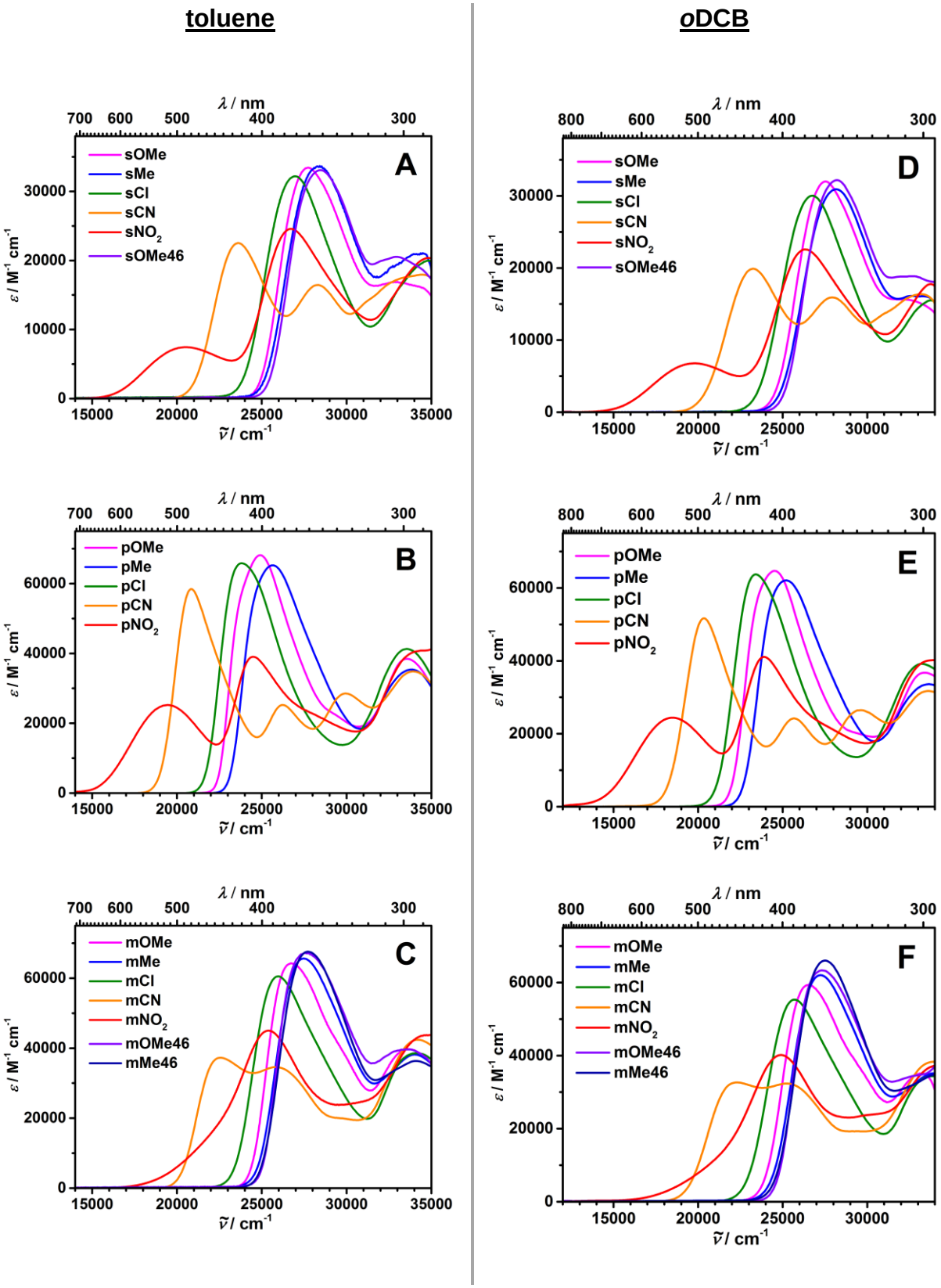

Figure 13: Left: Absorption spectra of the reference compounds **sX** (A), *para*-compounds **pX** (B) and *meta*-compounds **mX** (C) in toluene. Right: Absorption spectra of the reference compounds **sX** (D), *para*-compounds **pX** (E) and *meta*-compounds **mX** (F) in *o*DCB.

Table 8: Absorption maxima ($\tilde{\nu}_{max}$ and λ_{max}) and extinction coefficients (ε_{max}) of the characteristic absorption bands of references **sX**, the *para*-compounds **pX** and the *meta*-compounds **mX** in toluene and *o*DCB.

		$\tilde{\nu}_{max}$ (λ_{max}) / ε_{max} / cm^{-1} (nm) / M^{-1} cm^{-1}	$\tilde{\nu}_{max}$ (λ_{max}) / ε_{max} / cm^{-1} (nm) / M^{-1} cm^{-1}	$\tilde{\nu}_{max}$ (λ_{max}) / ε_{max} / cm^{-1} (nm) / M^{-1} cm^{-1}
Toluene	**sOMe**	-	27500 (364) / 32000	-
	sMe	-	28200 (355) / 30900	-
	sCl	-	26700 (375) / 30000	-
	sCN	23300 (429) / 19900	27900 (358) / 15900	33100 (302) / 16400
	sNO$_2$	19800 (505) / 6800	26600 (376) / 22600	-
	sOMe46	-	28200 (355) / 32200	-
	pOMe	-	24500 (408) / 64700	33300 (300) / 36700
	pMe	-	25300 (395) / 62100	33700 (301) / 33600
	pCl	-	23400 (427) / 63700	33200 (301) / 39200
	pCN[a]	20400 (490) / 51700	25700 (389) / 24200	33700 (301) / 31700
	pNO$_2$	18500 (541) / 24400	23900 (418) / 41100	-
	mOMe	-	26500 (377) / 59300	33300 (300) / 35100
	mMe	-	27200 (368) / 62000	-
	mCl	-	25700 (389) / 55300	-
	mCN	22300 (448) / 32700	25300 (395) / 32400	-
	mNO$_2$	-	24900 (402) / 45000	-
	mOMe46	-	27300 (366) / 63300	-
	mMe46		27500 (364) / 66000	
***o*DCB**	**sOMe**	-	27700 (361) / 33400	-
	sMe	-	28500 (351) / 33100	-
	sCl	-	27000 (370) / 32200	-
	sCN	23600 (423) / 22500	28300 (353) / 16400	-
	sNO$_2$	20500 (488) / 7400	26700 (376) / 24600	-
	sOMe46	-	28500 (351) / 33100	33000 (303) / 20500
	pOMe	-	24900 (402) / 68130	33600 (298) / 38500
	pMe	-	25600 (391) / 65200	33900 (295) / 35400
	pCl	-	23800 (420) / 65800	33600 (298) / 41300
	pCN[b]	20800 (481) / 58400	26200 (382) / 25300	34000 (294) / 34800
	pNO$_2$	19500 (513) / 25200	24500 (408) / 39000	-
	mOMe	-	26800 (373) / 64200	33600 (298) / 39700
	mMe	-	27500 (364) / 65600	34000 (294) / 38200
	mCl	-	26000 (385) / 60500	34100 (293) / 38600
	mCN	22600 (442) / 37300	25800 (386) / 34600	34200 (292) / 42400
	mNO$_2$	-	25400 (394) / 45000	-
	mOMe46	-	27500 (364) / 67300	33400 (299) / 39700
	mMe46	-	27500 (364) / 67300	33400 (299) / 39700

[a]Additional band at 29600 cm^{-1} (338 nm) with ε_{max} of 26500 M^{-1} cm^{-1}. [b]Additional band at 29900 cm^{-1} (334 nm) with ε_{max} of 28500 M^{-1} cm^{-1}.

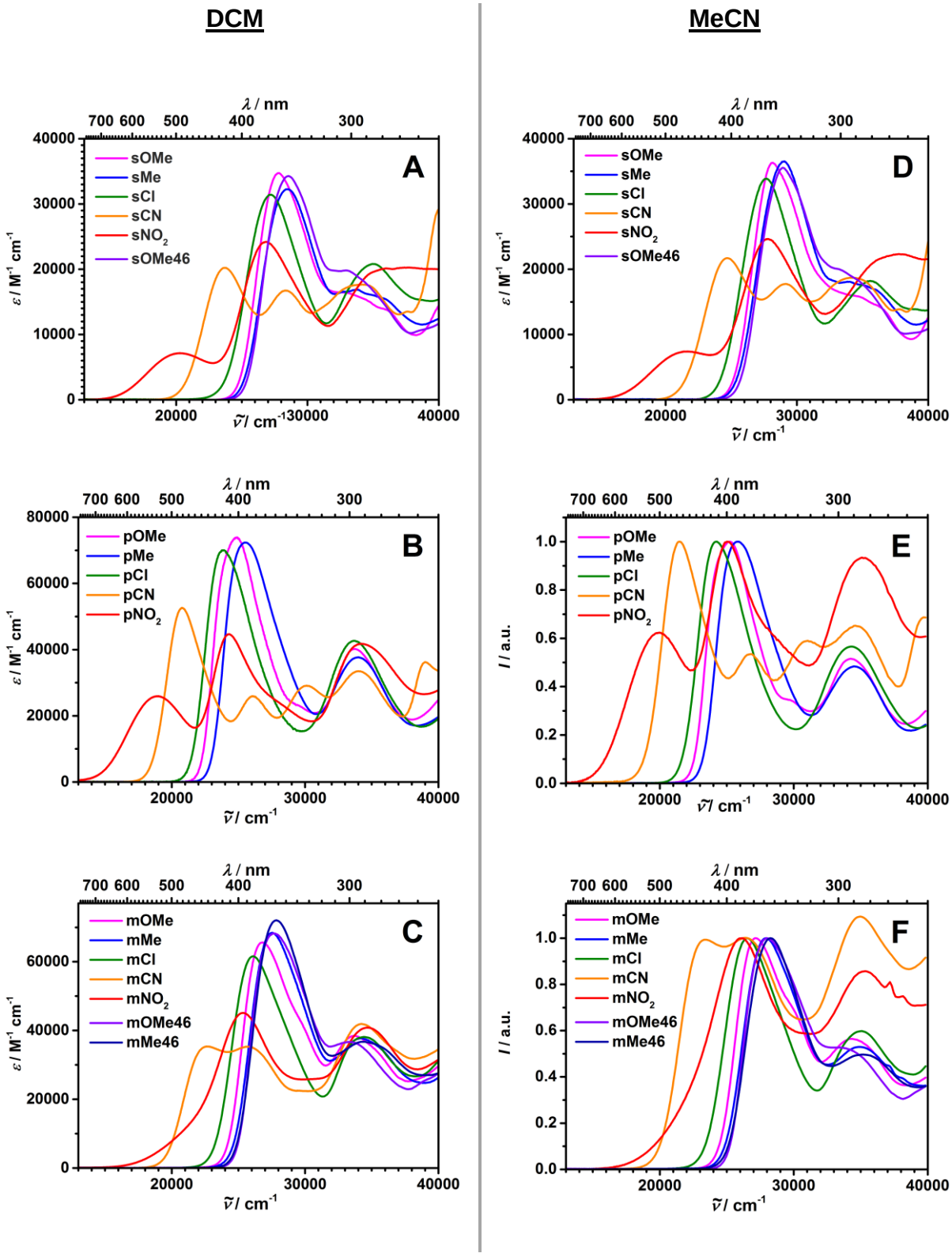

Figure 14: Left: Absorption spectra of the reference compounds **sX** (A), *para*-compounds **pX** (B) and *meta*-compounds **mX** (C) in DCM. Right: Absorption spectra of the reference compounds **sX** (D) in MeCN. Normalized absorption spectra of the *para*-compounds **pX** (E) and *meta*-compounds **mX** (F) in MeCN.

Table 9: Absorption maxima ($\tilde{\nu}_{max}$ and λ_{max}) and extinction coefficients (ε_{max}, not for **p-/mX** in MeCN) of the characteristic absorption bands of references **sX**, the *para*-compounds **pX** and the *meta*-compounds **mX** in DCM and MeCN. Due to solubility problems the determination of the extinction coefficients (ε_{max}) of **p-/mX** in MeCN was not possible.

		$\tilde{\nu}_{max}$ (λ_{max}) / ε_{max} / cm^{-1} (nm) / M^{-1} cm^{-1}	$\tilde{\nu}_{max}$ (λ_{max}) / ε_{max} / cm^{-1} (nm) / M^{-1} cm^{-1}	$\tilde{\nu}_{max}$ (λ_{max}) / ε_{max} / cm^{-1} (nm) / M^{-1} cm^{-1}
DCM	**sOMe**	-	27800 (360) / 34700	-
	sMe	-	28600 (350) / 34300	-
	sCl	-	27200 (368) / 31400	35000 (286) / 20800
	sCN	23700 (422) / 20200	28400 (352) / 16700	34200 (292) / 17700
	sNO_2	20200 (495) / 7100	26800 (373) / 26200	-
	sOMe46	-	28600 (350) / 20200	-
	pOMe	-	24900 (402) / 73900	33800 (296) / 40200
	pMe	-	25600 (391) / 72300	34000 (294) / 37700
	pCl	-	23800 (420) / 70000	33700 (297) / 42700
	pCN[a]	20800 (481) / 52600	26100 (383) / 25900	34000 (294) / 33500
	pNO_2	18900 (529) / 25900	24300 (412) / 44700	34200 (292) / 41800
	mOMe	-	26800 (373) / 65600	33800 (296) / 38400
	mMe	-	27500 (364) / 68400	34100 (293) / 37800
	mCl	-	26100 (383) / 61600	34400 (291) / 38100
	mCN	22700 (441) / 35100	25700 (389) / 35300	34200 (292) / 41900
	mNO_2	-	25300 (395) / 44500	34700 (288) / 40800
	mOMe46	-	27600 (362) / 68200	33200 (301) / 36700
	mMe46	-	27900 (358) / 72000	34500 (290) / 36600
MeCN	**sOMe**	-	28200 (355) / 36300	-
	sMe	-	29000 (345) / 36500	-
	sCl	-	27600 (362) / 33800	35600 (281) / 18200
	sCN	24700 (405) / 21700	29200 (342) / 17700	34200 (292) / 18700
	sNO_2	21600 (463) / 7400	27800 (360) / 24600	37800 (258) / 22300
	sOMe46	-	28900 (346) / 35500	-
	pOMe	-	25300 (395) / -	34300 (292) / -
	pMe	-	25800 (388) / -	34500 (290) / -
	pCl	-	24200 (413) / -	34400 (291) / -
	pCN[b]	21500 (465) / -	26700 (375) / -	34600 (289) / -
	pNO_2	20000 (500) / -	25100 (498) / -	35100 (285) / -
	mOMe	-	27200 (368) / -	34400 (291) / -
	mMe	-	27900 (358) / -	35000 (286) / -
	mCl	-	26500 (377) / -	35100 (285) / -
	mCN	23400 (427) / -	26400 (379) / -	34800 (287) / -
	mNO_2	-	26200 (382) / -	35300 (283) / -
	mOMe46	-	28100 (356) / -	33700 (297) / -
	mMe46		28200 (355) / -	35200 (284) / -

[a]Additional band at 30100 cm^{-1} (332 nm) with ε_{max} of 29100 M^{-1} cm^{-1}. [b]Additional band at 31100 cm^{-1} (322 nm).

The bisTAA compounds **pX** (Figure 14, B), **mX** and **mX46** (Figure 14, C) show analogous absorption behavior compared to the references. All molecules exhibit the typical π-π* band of the TAA at ca. ca. 34000 cm^{-1} (294 nm), showing that the energy of this transition is not influenced by the addition of a second TAA and remains unaffected for all bisTAAs presented. Even more the ε_{max} of this band of the bisTAAs reach values of ca. 40000 M^{-1} cm^{-1} showing that it displays an additive effect (ε_{max} **sX** ca. 20000 M^{-1} cm^{-1}). **p-/mX** with X = OMe–Cl show an intense *z*-band between ca. 24000–28000 cm^{-1} (417–357 nm). Since two TAA units are attached molar absorption coefficients (ε_{max}) of the maxima have a value of ca. 60000 M^{-1} cm^{-1}, indicating that the absorption feature of the bisTAAs behaves additive (ε_{max} **sOMe-Cl**: ca. 30000 M^{-1} cm^{-1}), too. However, the position of the maximum absorption energy ($\tilde{\nu}_{max}$) and the band structure of the bisTAAs are different compared to the references and the additive behavior is observed only very approximately. The differences resulting from the addition of a second TAA to **sOMe-Cl** will be explained by the methoxy compounds in the following. In Figure 15, A the absorption spectra of all OMe compounds in DCM are displayed. Adding a TAA moiety to **sOMe** (27800 cm^{-1} (360 nm)) in the *meta*-position to form **mOMe** (26800 cm^{-1} (373 nm)) is associated with a bathochromic shift of the *z*-band by 1000 cm^{-1}. The same is true for the reference/bisTAA couple **s-/mOMe46** where the absorption is shifted by 1000 cm^{-1}, too (**sOMe46**: 28600 cm^{-1} (360 nm), **mOMe**: 27600 cm^{-1} (373 nm)).

Addition of a second TAA unit in *para*-position shifts the absorption maximum to an even further extent. Compared to **sOMe** (7000 cm^{-1} (370 nm)), $\tilde{\nu}_{max}$ of **pOMe** (24500 cm^{-1} (408 nm)) is bathochromically shifted by 2500 cm^{-1} and the band shape of the absorption is somewhat asymmetric. The comparison of the OMe compounds shows that not only addition of one TAA to **sOMe** influences the characteristic absorption behavior of the TAA units, but also the position of this attachment, and furthermore the position of the substituent X at the benzene bridge influences the absorption properties.

In analogy to references **sOMe** and **sOMe46** the bisTAAs **p-/mOMe** and **mOMe46** show a reduced absorption energy of the *z*-band below those of the corresponding methyl compounds **p-/mMe** and **mMe46**, which might be caused by out of plane rotation of the OMe group. However, aking the crystal structure of **pOMe** into account (Figure 11), one could question the validity of the assertion, since the obtained structure clearly shows the OMe groups been in plane to the benzene bridge.

However, since the molecules are in solution, the situation is different. Studies of *Anderson et al.* showed that OMe groups that are in plane to the aromatic system in crystal, can nevertheless be oriented out of plane in solution (or/and in the gas phase), which is probably the case here and explains the bathochromic shift compared to the methyl compounds.[159]

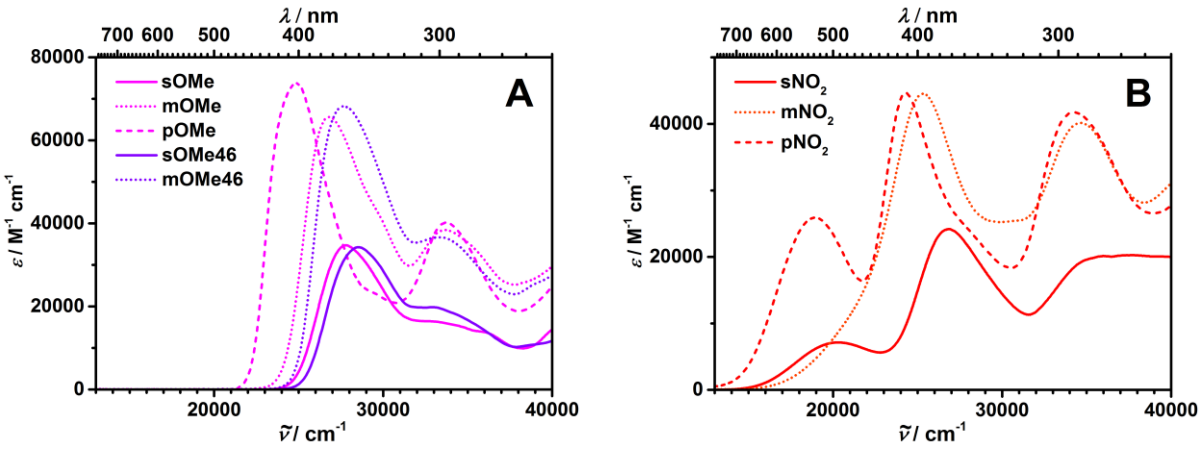

Figure 15: Absorption spectra of the OMe compounds in toluene (A). Absorption spectra of the NO_2 compounds in toluene (B).

For the CN and NO_2 compounds the situation is somehow different: on the one hand $\tilde{\nu}_{max}$ of the lowest lying CT band of **mCN**/**pCN** are bathochromically shifted by about 1000 cm^{-1} / 2900 cm^{-1} (compared to **sCN**, Figure 14), too. On the other hand **mCN** shows two TAA absorptions at 22700 cm^{-1} (441 nm) and 27300 cm^{-1} (389 nm) of the same intensity (ε_{max} ca. 35000 M^{-1} cm^{-1}) with an energetic separation of 3000 cm^{-1} and local minimum in between. The former absorption (compared to **sCN**) at 27900 cm^{-1} (358 nm) is no longer present, whereas in **pCN** this peak is retained. However, in the latter the first excitation at 20400 cm^{-1} (417 nm) is clearly more pronounced (ε_{max} = 53000 M^{-1} cm^{-1}).

All compounds **p-/mX** with X = OMe-CN show the same correlation between the *meta*-/*para*-compounds and the references, namely the *meta*-bisTAAs “behave” more like the double monoTAAs and the *para*-bisTAAs offer a major change in the absorption properties.

The nitro compounds do not show this correlation as can be seen in Figure 15, B. The excitation at 26800 cm^{-1} (373 nm) in **sNO₂** is shifted to 25300 cm^{-1} (402 nm) in **mNO₂** and 24300 cm^{-1} (412 nm) in **pNO₂**. Moreover the CT band with lowest energy in **pNO₂** is shifted to 18900 cm^{-1} (529 nm), whereas in **mNO₂** it is not visible as an isolated band. It is assigned to be shifted close to the second lowest band in **pNO₂** resulting in a broad absorption with a wide edge at lower wavenumbers.

All observations described so far in DCM are also valid for toluene, *o*DCB and MeCN. Since some bisTAAs are not readily soluble in the latter solvent, the xtincion coefficinet ε is imprecise and these spectra are normalized to one.

The molecules show a negative solvatochromism of the characteristic absorptions, meaning an increase of the solvent polarity from nonpolar toluene to polar MeCN results in a hypsochromic shift of all electronic transitions. The *x*-bands possess a hypsochromic shift of approximately 800–1000 cm^{-1} when changing the solvent from toluene to MeCN. A precise

value is hard to discern because of the above mentioned high *cut-off point* of toluene (and *o*DCB).The *z*-band at 28000–30000 cm^{-1} (357–333 nm) is associated with a blue shift of the TAA bands of ca 800 cm^{-1} for the OMe compounds and raises ca. to 1200 cm^{-1} for the NO_2. The low lying CT bands of the cyano and nitro compounds are actually hypsochromically shifted by up to 1500 cm^{-1}, proving a pronounced CT character of these excitations.

3.2.3 Electrochemistry: Cyclic Voltammetry (CV), Square Wave Voltammetry (SWV), Differential Pulse Voltammetry (DPV)

After discussion of the absorption characteristics of the *meta*- and *para*-bisTAAs and their references, the electrochemical properties will be discussed. *Geiger et al.* showed that redox potentials and potential differences are dependent on the solvent, conducting salt, temperature and concentration of the used compounds (and the conducting salt). Hence, no accurate prediction of the electronic coupling *V* based on potential differences is possible.[164] Nevertheless, by analyzing electrochemical properties a rough estimate of the strength of interactions between the bridged triarylamine redox centers is possible. In addition, the data obtained are helpful for subsequent recording of the electron paramagnetic resonance and UV/Vis/NIR spectra of the cationic species. In Figure 16 the cyclic voltammograms (CV) of all TM measured in DCM are displayed. Figure 17 shows the square wave voltammograms (SWV) of the methoxy compounds (A) and the differential pulse voltammograms (DPV) of the nitro compounds (B). The SWV were recorded in order to resolve the process in the oxidative parts in the methoxy compounds. For investigation of the reductive processes within the nitro compounds DPV measurements were performed, since they showed a higer relsolution of the occurring processes than the SWV measurements. The CV, SWV and DPV were measured under argon atmosphere in DCM with TBAHF as supporting electrolyte and referenced against the ferrocen/ferrocenium (Fc/Fc^+) redox couple. All potentials are listed in Table 10. Chemical and electrochemical reversibility of the half-wave potentials were investigated by multi thin layer experiments and measurement at different scan rates, respectively.[165] In the following treatment of the redox behavior, special attention will be given to the half-wave processes referring to the first oxidation of the TAA unit. Their energetic position and behavior play a key role in the possibility to form MV species by oxidation with a suitable oxidizing agent.

Before the examination of the bisTAAs, the reference compounds **sX** will be discussed (Figure 16, A). All references exhibit a half-wave potential $E_{1/2}$ of approximately +300 mV deriving from the first oxidation (Ox1) of the TAA. Another signal at ca. +1000 mV derives from the second oxidation (Ox2) of the TAA unit. The first oxidation is chemically reversible, the second is not. This behavior and the $E_{1/2}$ values are in a typical range for triarylamines with two OMe substituents directly attached to the TAA.[96, 113, 123, 166]

The references with OMe groups at the benzene “bridging unit” **sOMe** and **sOMe46** show additional oxidative processes after the second oxidation of the TAA unit (Figure 17, A). These oxidations are strongly irreversible and related to oxidations of the 2,5- and 4,6-dimethoxybenzene bridges and resulting follow up reactions.[167, 168]

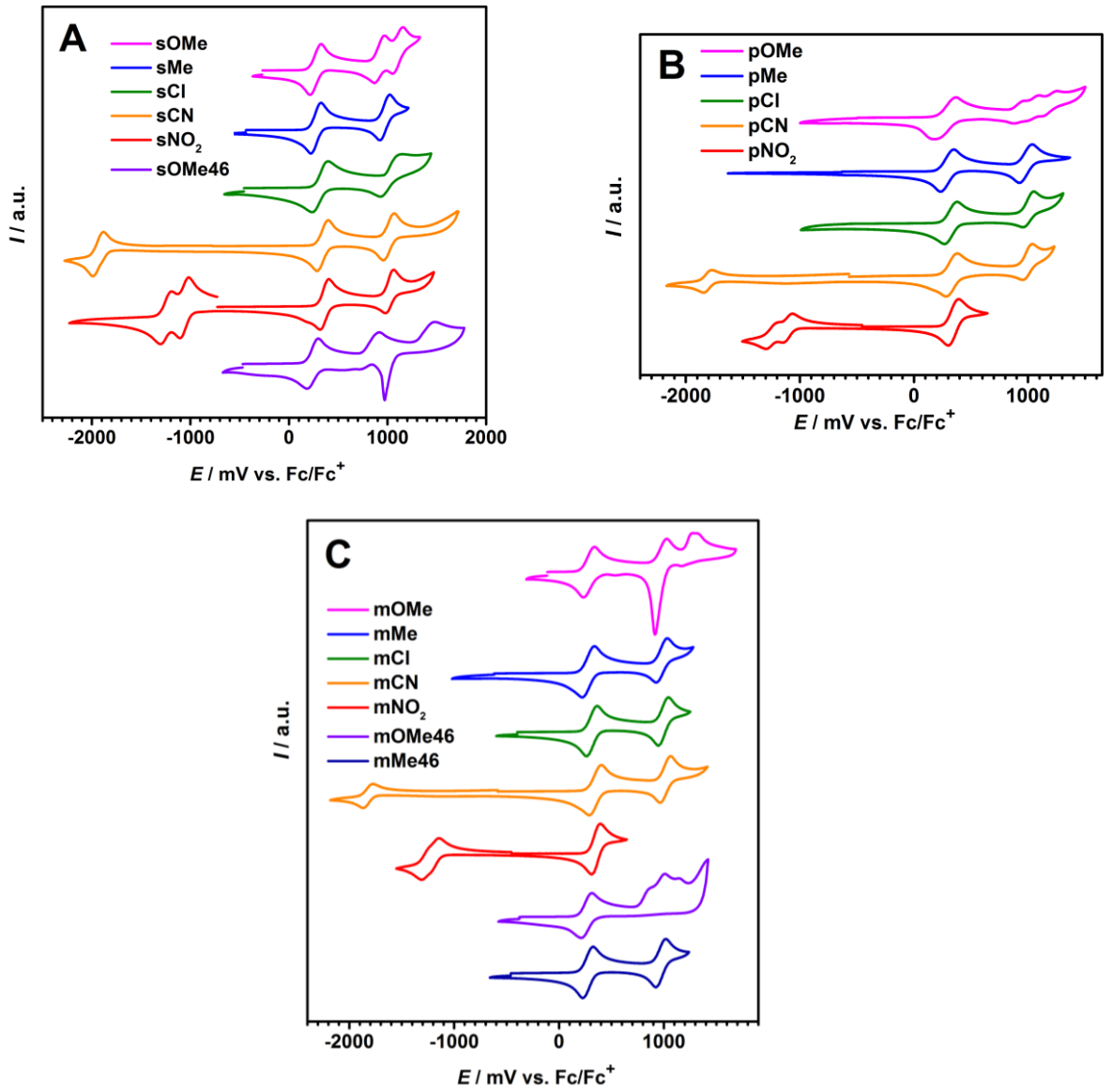

Figure 16: **A**: Cyclic voltammograms of the reference *single*-compounds **sX**. **B**: Cyclic voltammograms of the *para*-compounds **pX**. **C**: Cyclic voltammograms of the *meta*-compounds **mX**. The voltammograms of all compounds **OMe** to **CN** were recorded in DCM/0.2 M TBAHF at a scan rate of 1000 mV s^{-1}. The NO_2 compounds were recorded at a scan rate of 100 mV s^{-1}.

The cyano reference **sCN** shows an irreversible reductive half-wave potential $E_{1/2}$ at −1919 mV which can be assigned to a reduction of one CN group of the benzene bridge.[169, 170] This reduction shows a weak irreversibility under multi-layer thin film experiment. The nitro reference **sNO$_2$** shows two reductive potentials at −1064 mV and −1244 mV which are caused by a succeed reduction of the nitro groups.[171, 172]

The electron-donating-group (EDG) and electron-withdrawing-group (EWG) in **sX** affect the redox potential of the TAA via the benzene unit. This becomes clear when looking at half-

wave of the first oxidation $E_{1/2}$(Ox1). Strong EDG like OMe increase the charge density at the benzene unit and the TAA and therefore the TAA are more readily oxidized. The opposite is true for e.g. **sNO₂**, the EWG NO_2 decreases the charge density at the TAA resulting in a higher half-have potential. One has to note that not only the type of EWG/EDG influences oxidation potentials, but also the position at the benzene unit. In **sOMe** the 2,5-position of the OMe groups lead to a first oxidation of the TAA at +269 mV, in **sOMe46** this potential drops even further to +256 mV, indicating that the 4,6-position raises the electronic communication between the TAA and the OMe groups.

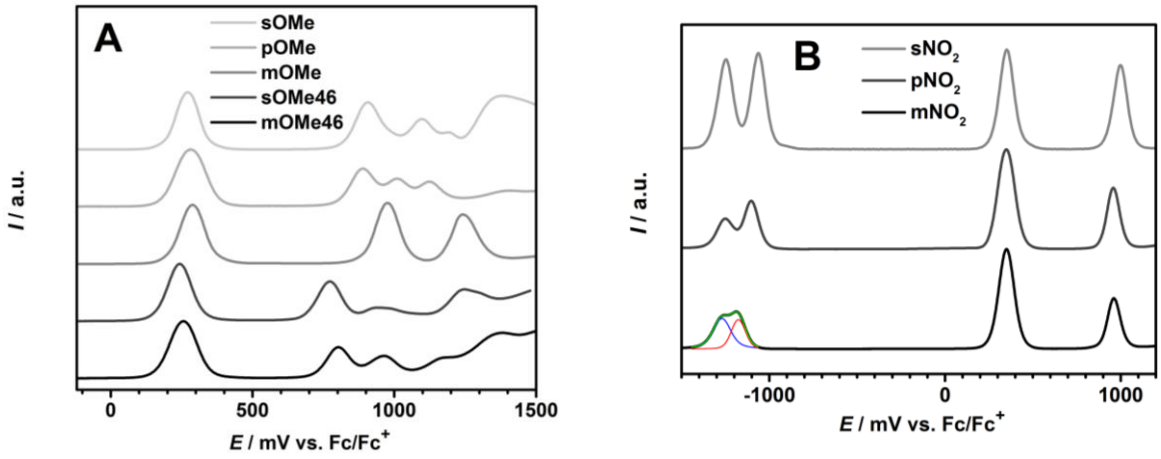

Figure 17: Square wave voltammograms of the OMe compounds in DCM/0.2 M TBAHF at a scan rate of 50 mV s^{-1} (A). Differential pulse voltammograms of the NO_2 compounds in DCM/0.2 M TBAHF at a scan rate of 2 mV s^{-1} (B). The colored lines (blue, red) show the *Voigt* fits of the reductive signals and its resulting cumulative fits (green) for **mNO₂**. All potentials are referenced against Fc/Fc^+.

The potential position of the redox processes of **pX** and **mX** are comparable to those of the references **sX** indicating that the electronic situation is not much effected by addition of a second TAA unit to the bridging unit. Like the single TAA compounds **sX**, the bisTAA **pX** and **mX** possess two oxidation half-wave potentials, the first at ca. +300 mV the second at about +1000 mV. Here the redox signal at ca. +300 mV covers two redox processes associated with the first oxidation of each TAA group. Since the TAA units have a very low electrostatic communication, these two redox processes are hardly separated an appear as a single half-wave potential in the CV.[165] The separation does not seem to be much larger than the statistic value of 35.6 mV at 298 K for two non-interacting redox centers and, therefore, suggests a low electronic coupling causing a superposition of the two signals. In literature, the first half-have potential of *para*-compounds **pOMe** and **pMe** were fitted by digital simulation. A potential difference of 60 mV for **pOMe** and 50 mV for **pMe** underpin a weak coupling between the two TAA redox centers.[90, 98]

Table 10: Redox potentials[a] ($E_{1/2}$) of references **sX**, the *para*-compounds **pX** and the *meta*-compounds **mX** in DCM / 0.2 M TBAHF.

	$E_{1/2}$ / mV							
	Red3[b]	**Red2**[c]	**Red**[d]	**Ox1**	**Ox2**[b]	**Ox3**[b]	**Ox4**[b]	**Ox5**[b]
sOMe	-	-	-	269	907	1096	1191	1374[c]
sMe	-	-	-	280	970	-	-	-
sCl	-	-	-	315	1004	-	-	-
sCN	−1919	-	-	347	990	-	-	-
sNO$_2$	-	−1244	−1064	360	1019	-	-	-
sOMe46	-	-	-	256	804	964[c]	1183[c]	1379[c]
pOMe	-	-	-	280	884[c]	1004[c]	1120[c]	1404[c]
pMe	-	-	-	292	982	-	-	-
pCl	-	-	-	321	1004	-	-	-
pCN	−1787	-	-	343	1000	-	-	-
pNO$_2$		−1249	−1103	345	957[d]	-	-	-
mOMe	-	-	-	287	976[c]	-	-	-
mMe	-	-	-	280	979	-	-	-
mCl	-	-	-	313	998	-	-	-
mCN	−1799	-	-	348	1011	-	-	-
mNO$_2$	-	−1287	−1186	349	966[d]	-	-	-
mOMe46	-	-	-	256	804	964[c]	1183[c]	1379[c]
mMe46	-	-	-	275	969	-	-	-

[a]All potentials are referenced against Fc/Fc^+. [b]Irreversible process. [c]Value determined by SWV. [d]Value determined by DPV.

The same is true for the CV signals at ca +1000 mV, which result from the twofold second oxidation of each TAA. This can also be seen when looking at the SWV of the nitro compounds (Figure 17, B). Integration of the signals in **sNO$_2$** gives ratio of 1:1:1:1, meaning that every process is a single electron reduction/oxidation. The signals of the two nitro groups associated processes show a separation of 180 mV. For **pNO$_2$**, the two oxidation potentials of the nitro groups shift closer together (146 mV). The maxima and area of the two signals in **mNO$_2$** were determined by simulation of this region with two *Voigt* functions. Here the separation is even further decreased to a value of 101 mV. However, integration of the signals in **pNO$_2$** and **mNO$_2$** give a ratio of 1:1:2:2 proving, that the TAA associated signals cover two redox processes.

As **sOMe** and **sOMe46** the *para*- and *meta*-OMe compounds show a variety of oxidations after the second TAA oxidation. They are strongly irreversible and are related to oxidations of the 2,5- and 4,6-dimethoxybenzene bridges and resulting follow up reactions like polymerization at the electrode.[167, 168]

3.3 Investigation of the Hole Transfer (HT)

The hole transfer within the mixed valance (MV) compounds **pX$^{\bullet+}$**, **mX$^{\bullet+}$** (X = OMe–NO_2) and **mX46$^{\bullet+}$** (X = OMe, Me) will be investigated by the use of three different approaches. First, the determination of the optically induced HT parameters via IVCT analysis is presented (3.3.1). Following this, the investigation of the thermal HT by temperature dependent ESR measurement is discussed (3.3.2). Then, the data for the HT obtained by TD-TFT calculations will be shown and compared to the experimental results (3.3.3). Finally a discussion of the obtained data for the HT, which needs to be treadted by an appropriate HT theory (3.3.5), will be presented.

3.3.1 Chemical Oxidation and IVCT Analysis

After discussing the optical properties of the neutral compounds in chapter 3.2.2 the spectroscopic properties of their cationic species will be elucidated in the following. Therefore, a solution of the neutral bisTAA was stepwise oxidized by titration with an oxidant until the dicationic species was formed. UV/Vis/NIR absorption spectra were recorded after each addition. As oxidant a solution of $SbCl_5$ in the respective solvent was chosen. Since $SbCl_5$ is a strong oxidant, the oxidization takes place very quickly and has proven its efficiency in previous measurements.[173] The steady-state optical spectra of the **p-/mX$^{\bullet+}$** and **mX46$^{\bullet+}$** will give information about reorganization energies λ (= $\tilde{\nu}_{max}^{IVCT}$), electronic couplings V_{12} and the HT barrier ΔG^*_{IVCT}. The influence of the solvent on these parameters will be determined by measurements in three solvents of different polarity, namely *o*DCB (Figure 18 / Figure 19), DCM (Figure 20 / Figure 21) and nitrobenzene ($PhNO_2$, Figure 22 / Figure 23). The absorption maxima ($\tilde{\nu}_{max}$ and λ_{max}) and extinction coefficients (ε_{max}) of the characteristic absorption bands of the dicationic *para*-compounds **pX$^{2(\bullet+)}$** the two dicataionic *meta*-series **mX$^{2(\bullet+)}$** and **mX46$^{2(\bullet+)}$** in $PhNO_2$, *o*DCB and DCM are listed in Table 11. The processes occurring during chemical oxidation are quite similar in the different solvents. Thus, the spectra of chemical oxidation for all molecules will be discussed exemplary in *o*DCB (Figure 18 and Figure 19). The essential observations can be transferred directly to the other solvents and the differences when changing the solvent will be examined later.

***o*DCB**

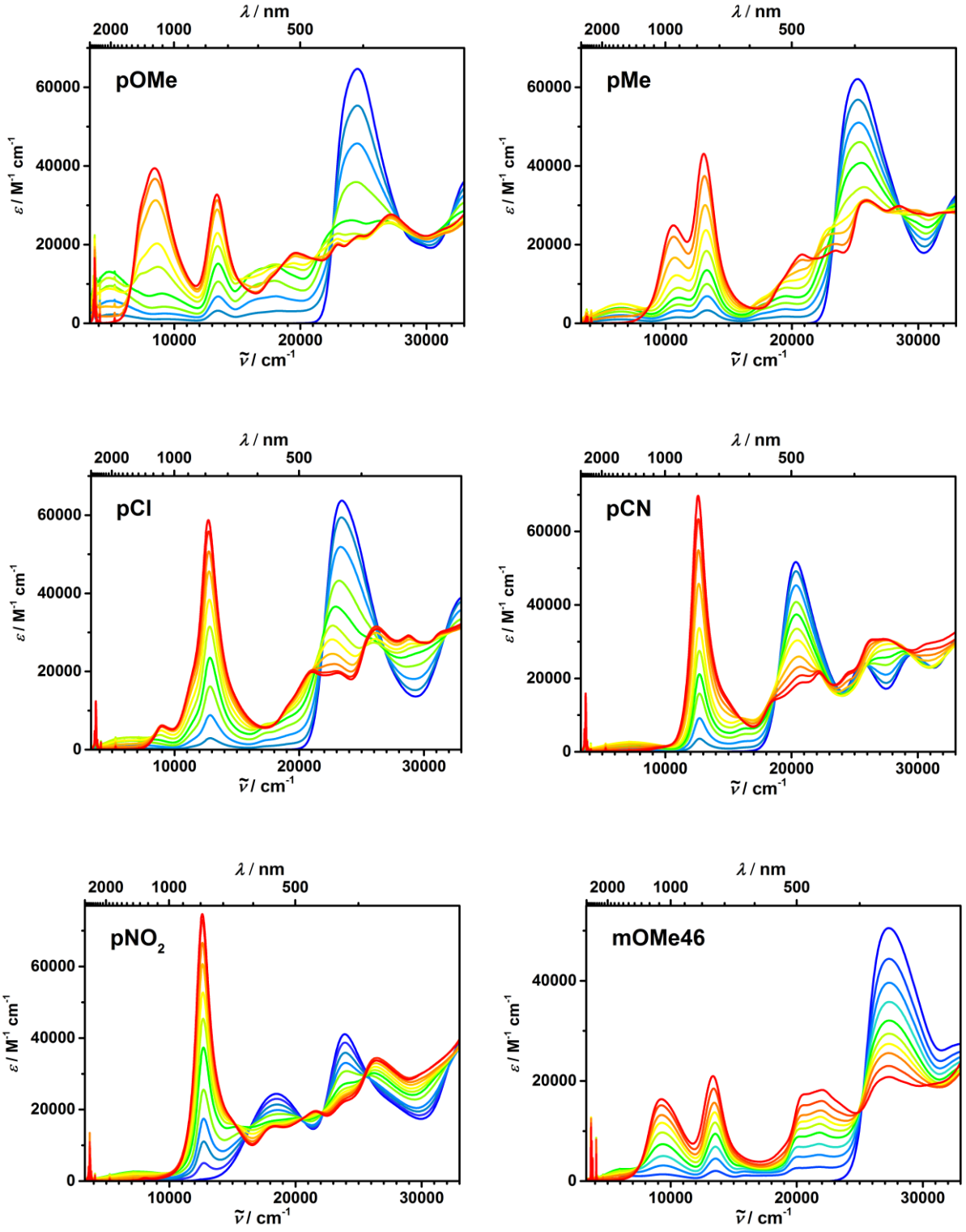

Figure 18: Absorption spectra of the *para*-compounds **pX** and the *meta*-compound **mOMe46** in *o*DCB (ca. 1.5 µM) during stepwise addition of a solution of $SbCl_5$ in *o*DCB (1 mM). Early spectra are depicted in blue and the later spectra in red.

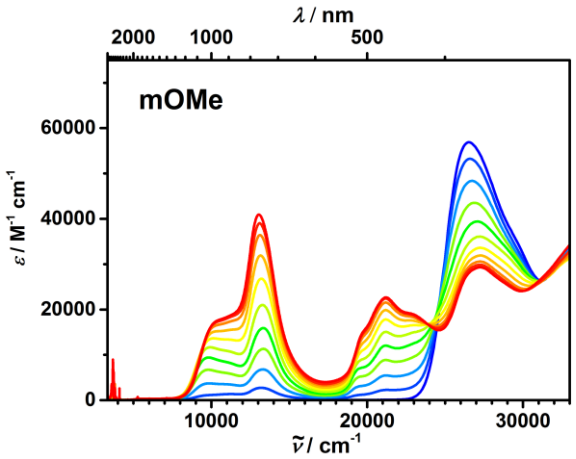
λ / nm
2000
1000
500
mOMe
60000
40000
20000
0
ε / M-1 cm-1
10000
20000
30000
ν̃ / cm-1

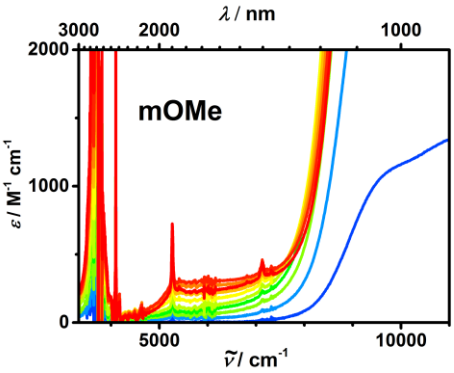
λ / nm
3000
2000
1000
mOMe
2000
1000
0
ε / M-1 cm-1
5000
10000
ν̃ / cm-1

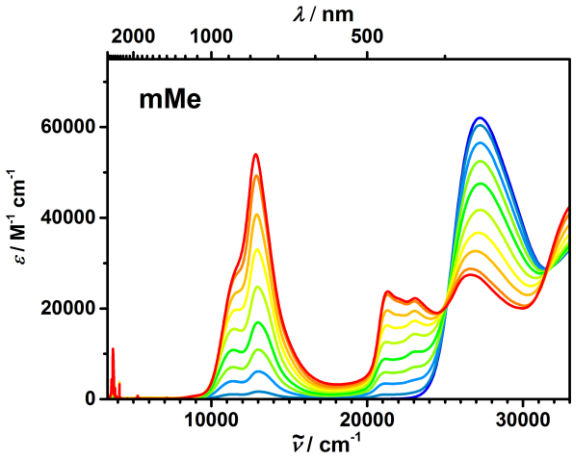
λ / nm
2000
1000
500
mMe
60000
40000
20000
0
ε / M-1 cm-1
10000
20000
30000
ν̃ / cm-1

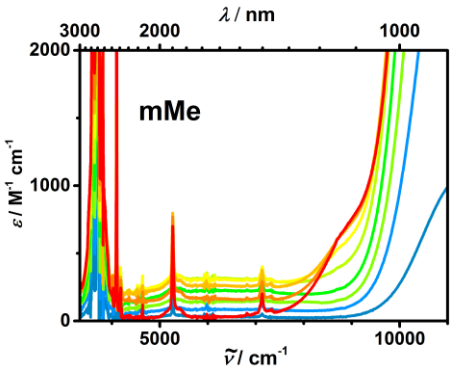
λ / nm
3000
2000
1000
mMe
2000
1000
0
ε / M-1 cm-1
5000
10000
ν̃ / cm-1

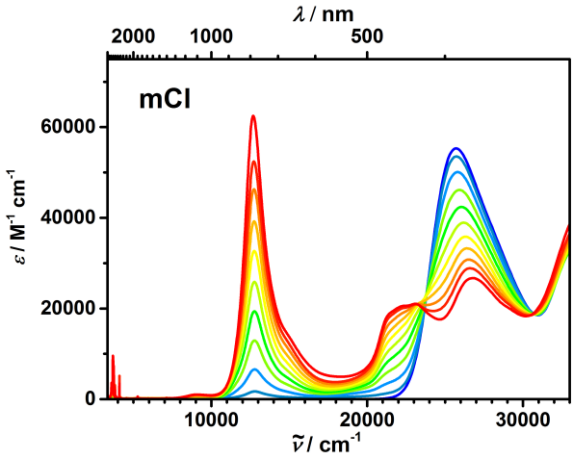
λ / nm
2000
1000
500
mCl
60000
40000
20000
0
ε / M-1 cm-1
10000
20000
30000
ν̃ / cm-1

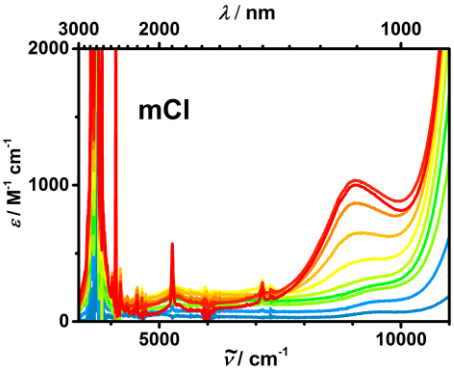
λ / nm
3000
2000
1000
mCl
2000
1000
0
ε / M-1 cm-1
5000
10000
ν̃ / cm-1

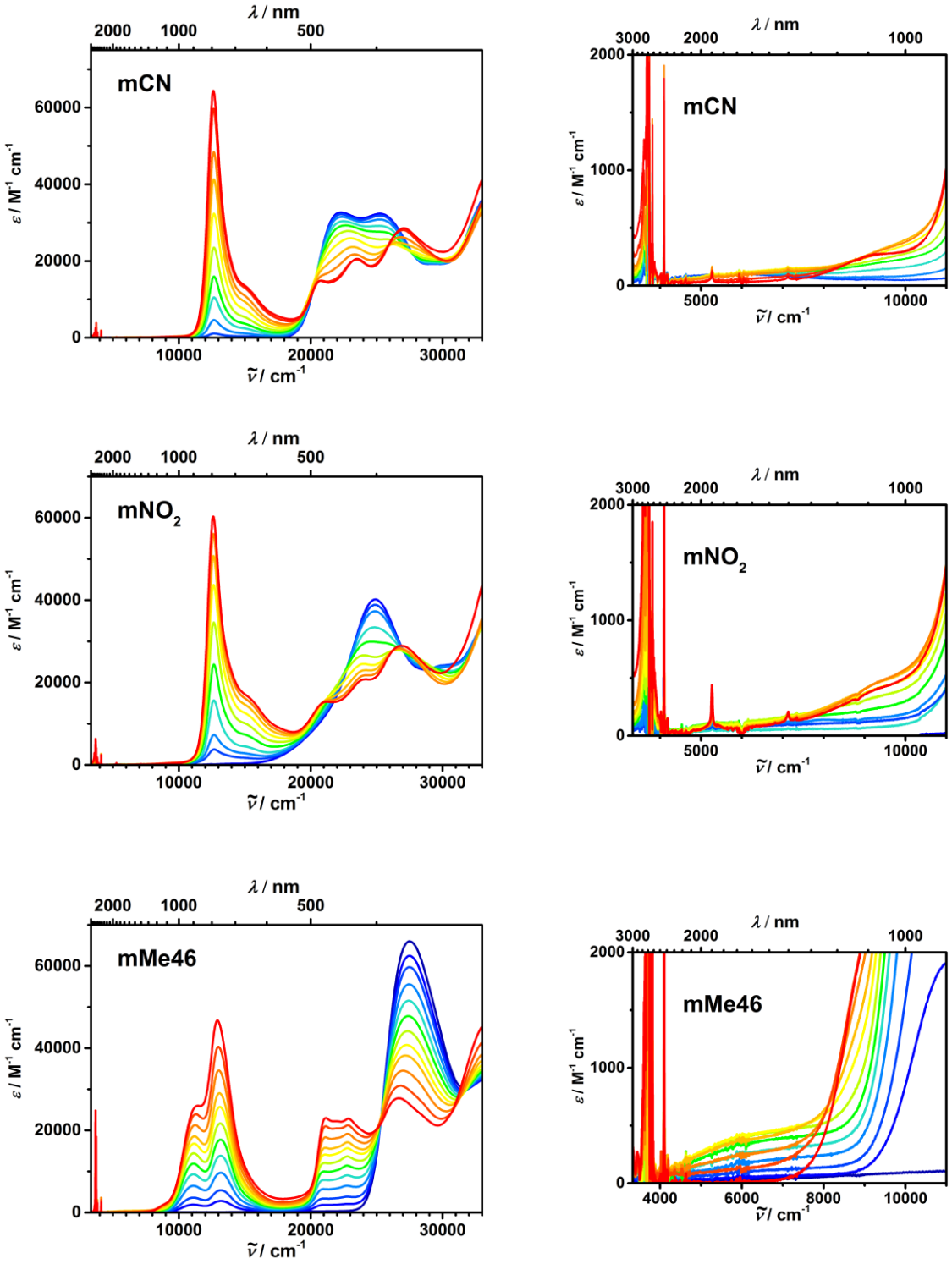

Figure 19: Absorption spectra of the *meta*-compounds **mX** and **mMe46** in *o*DCB (ca. 1.5 µM) during stepwise addition of a solution of $SbCl_5$ in *o*DCB (1 mM). Early spectra are depicted in blue and the later spectra in red. The smaller figures on the right side show the magnified region where the IVCT band is visible.

DCM

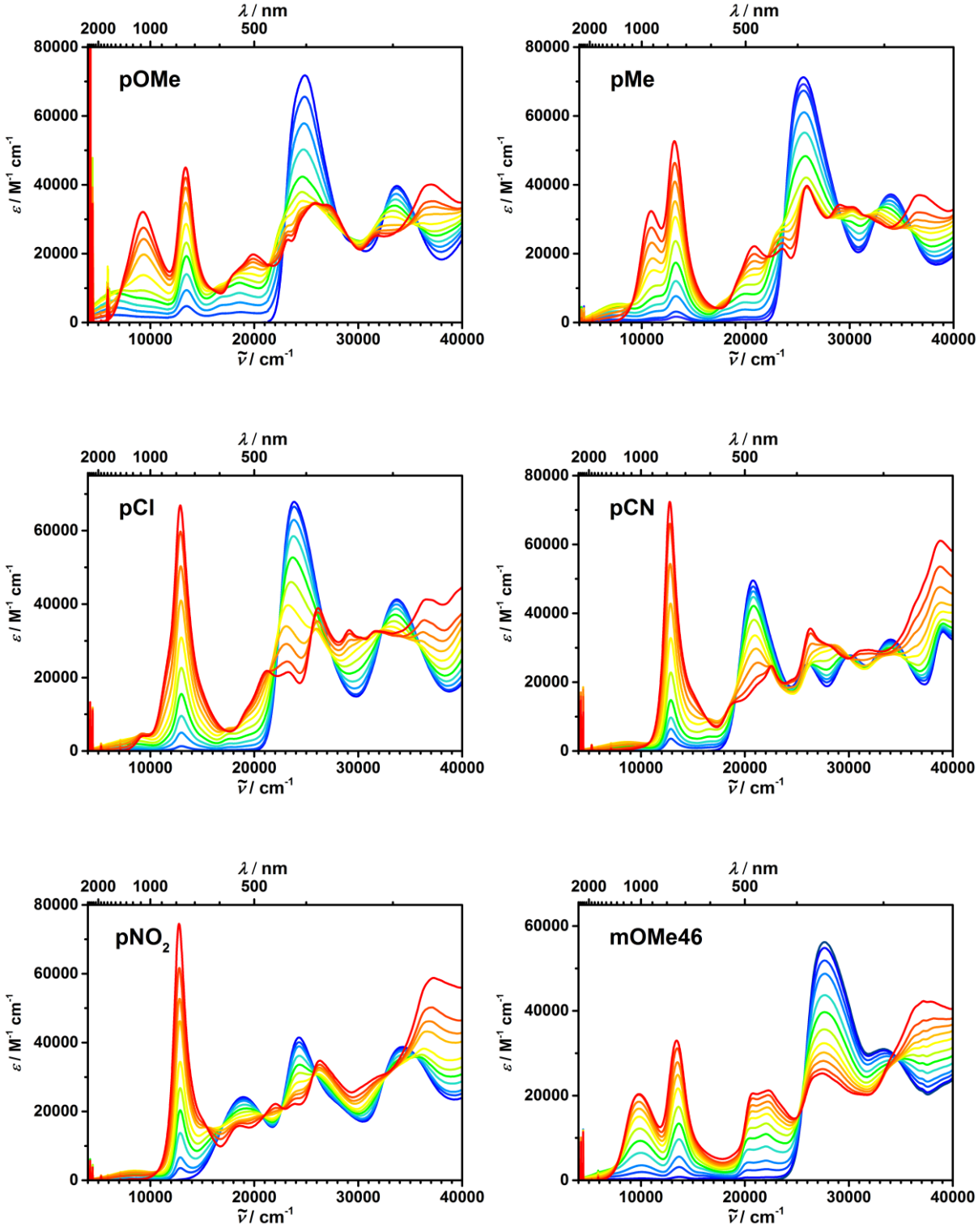

Figure 20: Absorption spectra of the *para*-compounds **pX** and the *meta*-compound **mOMe46** in DCM (ca. 1.5 µM) during stepwise addition of a solution of $SbCl_5$ in DCM (1 mM). Early spectra are depicted in blue and the later spectra in red.

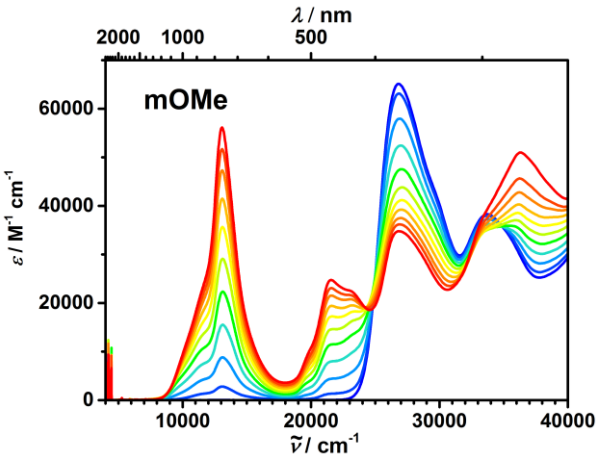
λ / nm
2000 1000 500
mOMe
ε / M⁻¹ cm⁻¹
60000
40000
20000
0
10000 20000 30000 40000
ν̃ / cm⁻¹

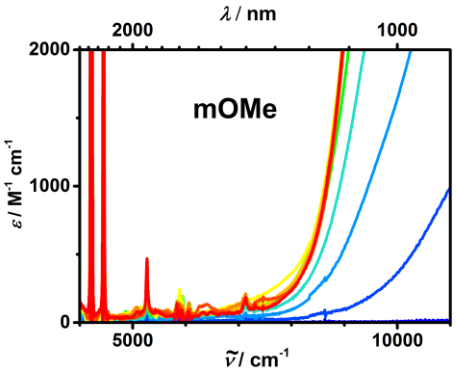
λ / nm
2000 1000
mOMe
ε / M⁻¹ cm⁻¹
2000
1000
0
5000 10000
ν̃ / cm⁻¹

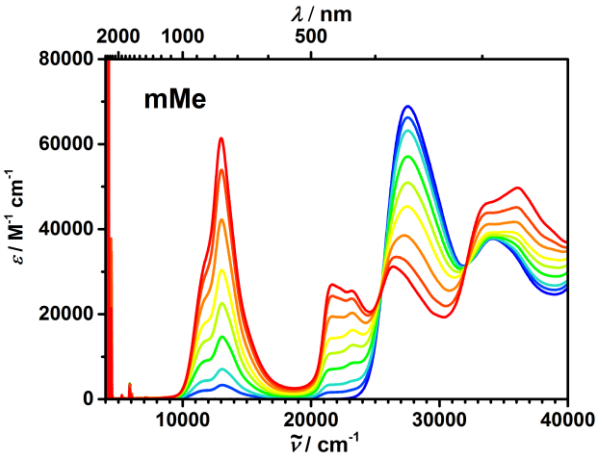
λ / nm
2000 1000 500
mMe
ε / M⁻¹ cm⁻¹
80000
60000
40000
20000
0
10000 20000 30000 40000
ν̃ / cm⁻¹

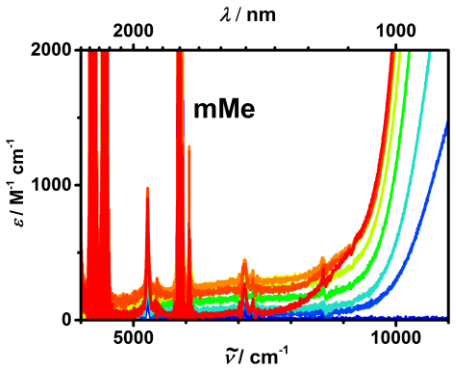
λ / nm
2000 1000
mMe
ε / M⁻¹ cm⁻¹
2000
1000
0
5000 10000
ν̃ / cm⁻¹

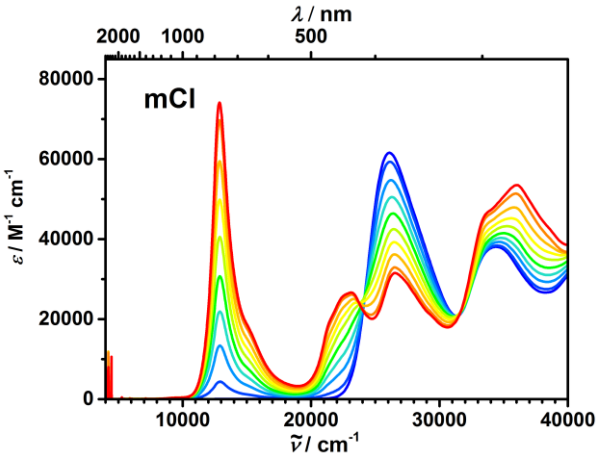
λ / nm
2000 1000 500
mCl
ε / M⁻¹ cm⁻¹
80000
60000
40000
20000
0
10000 20000 30000 40000
ν̃ / cm⁻¹

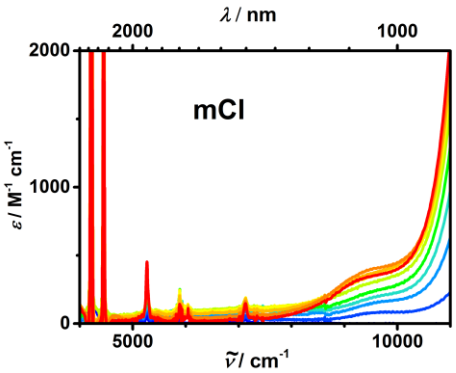
λ / nm
2000 1000
mCl
ε / M⁻¹ cm⁻¹
2000
1000
0
5000 10000
ν̃ / cm⁻¹

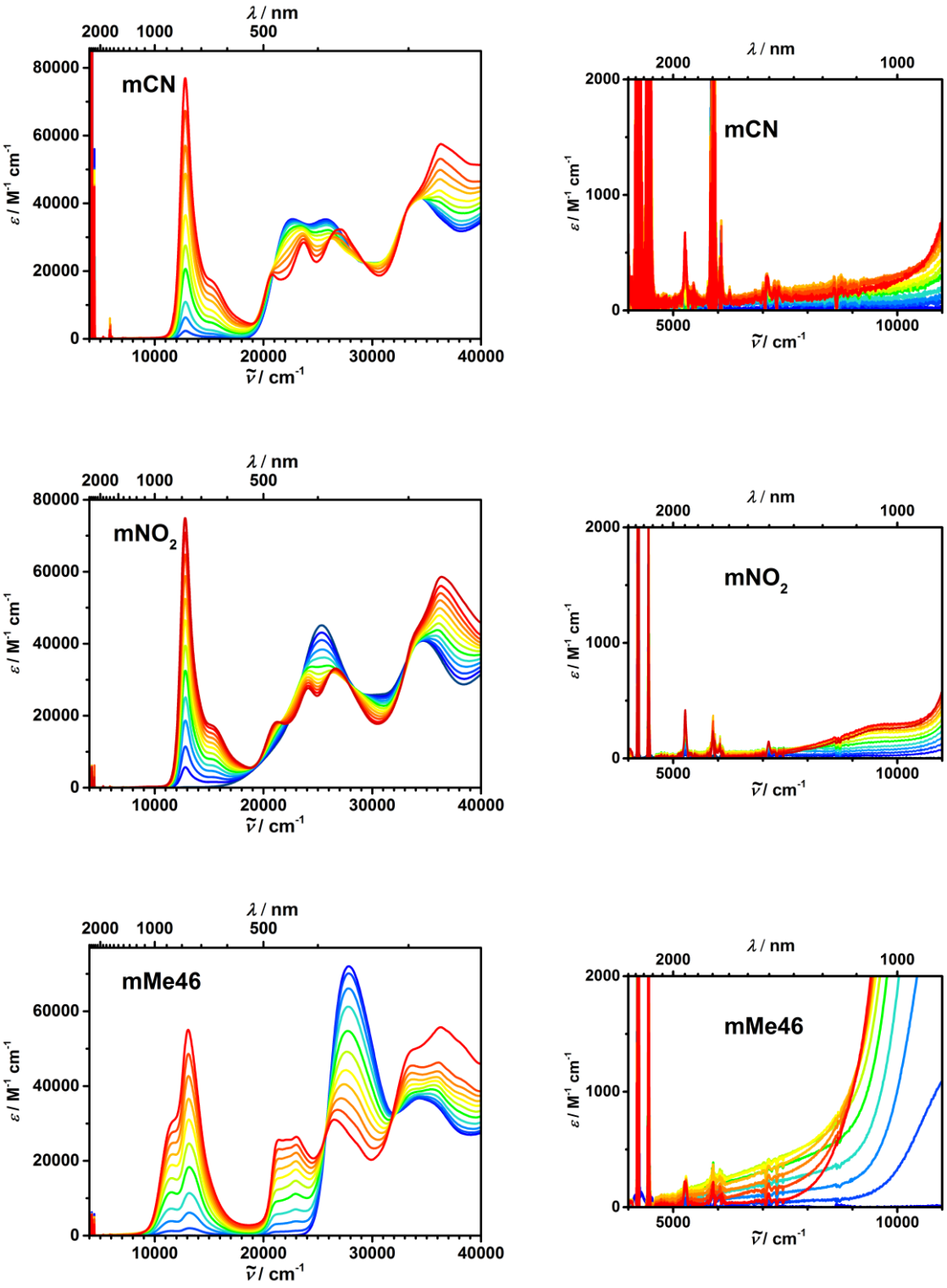

Figure 21: Absorption spectra of the *meta*-compounds **mX** and **mMe46** in DCM (ca. 1.5 µM) during stepwise addition of a solution of $SbCl_5$ in DCM (1 mM). Early spectra are depicted in blue and the later spectra in red. The smaller figures on the right side show the magnified region where the IVCT band is visible.

$PhNO_2$

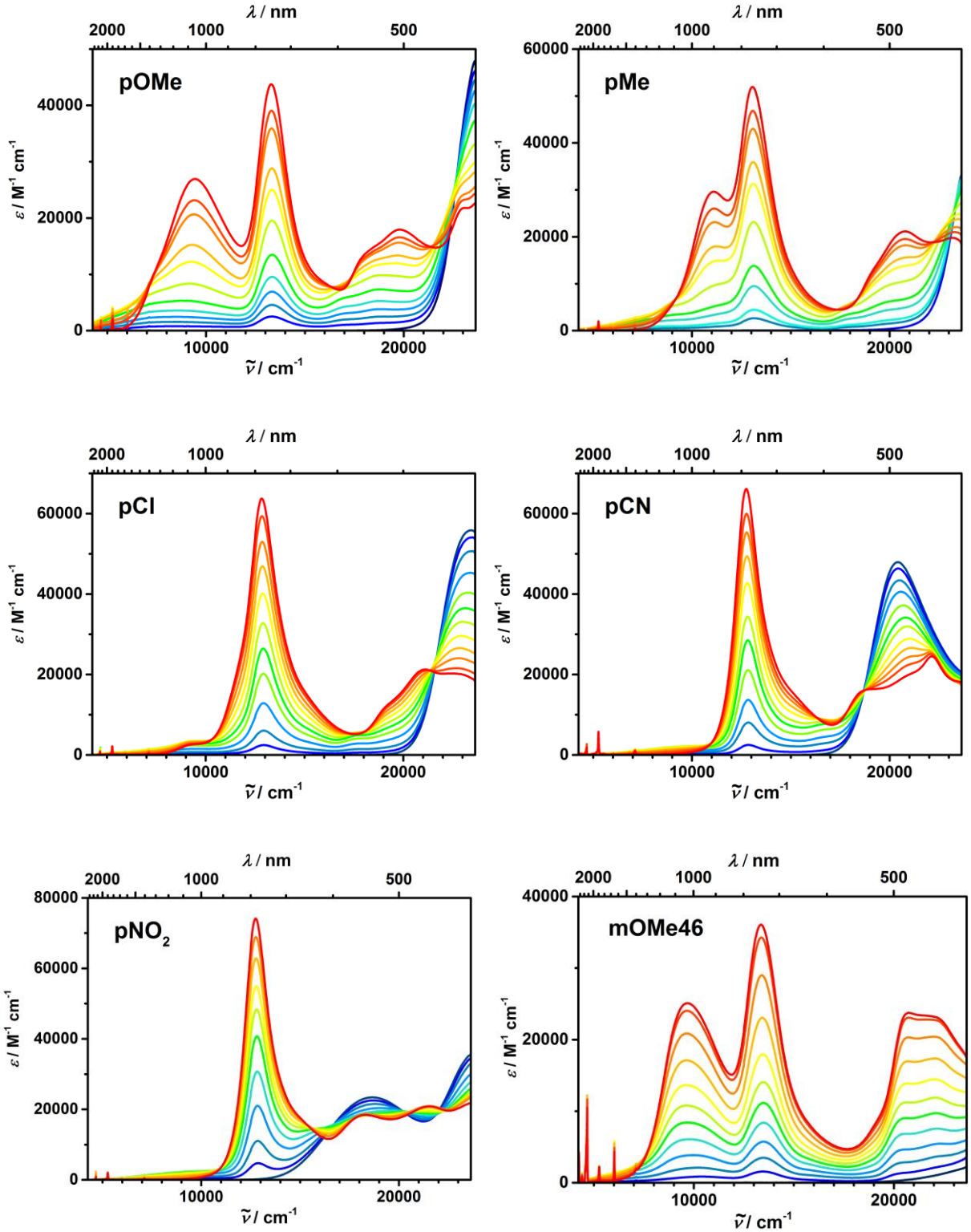

Figure 22: Absorption spectra of the *para*-compounds **pX** and the *meta*-compound **mOMe46** in $PhNO_2$ (ca. 1.5 µM) during stepwise addition of a solution of $SbCl_5$ in $PhNO_2$ (1 mM). Early spectra are depicted in blue and the later spectra in red.

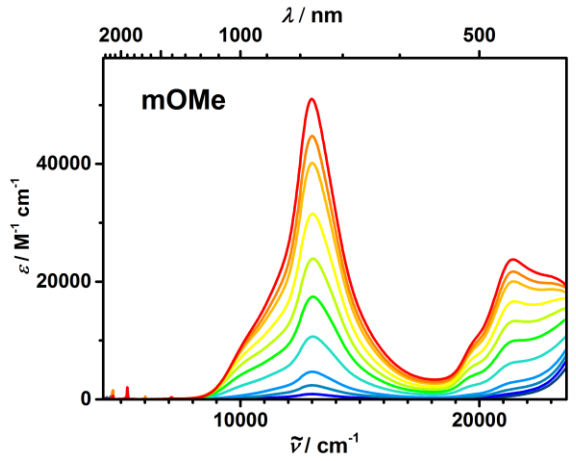
λ / nm
2000
1000
500
mOMe
40000
20000
0
ε / M-1 cm-1
10000
20000
ν̃ / cm-1

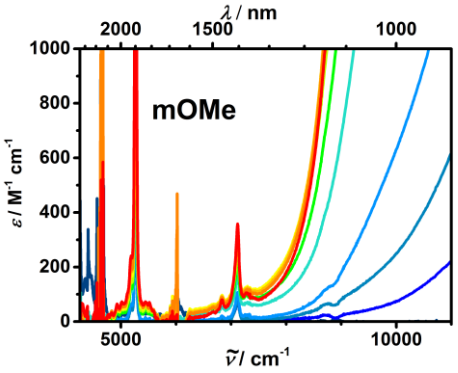
λ / nm
2000
1500
1000
1000
800
600
400
200
0
mOMe
ε / M-1 cm-1
5000
10000
ν̃ / cm-1

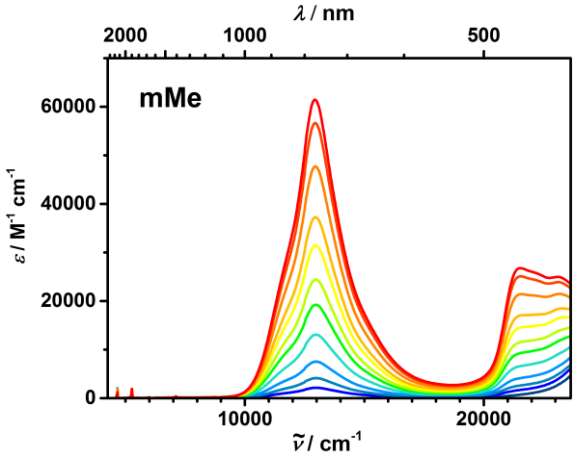
λ / nm
2000
1000
500
mMe
60000
40000
20000
0
ε / M-1 cm-1
10000
20000
ν̃ / cm-1

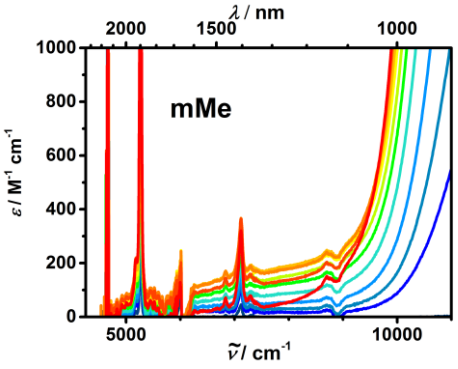
λ / nm
2000
1500
1000
1000
800
600
400
200
0
mMe
ε / M-1 cm-1
5000
10000
ν̃ / cm-1

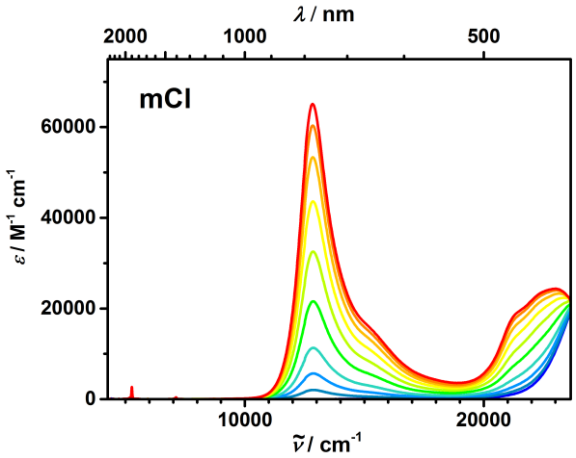
λ / nm
2000
1000
500
mCl
60000
40000
20000
0
ε / M-1 cm-1
10000
20000
ν̃ / cm-1

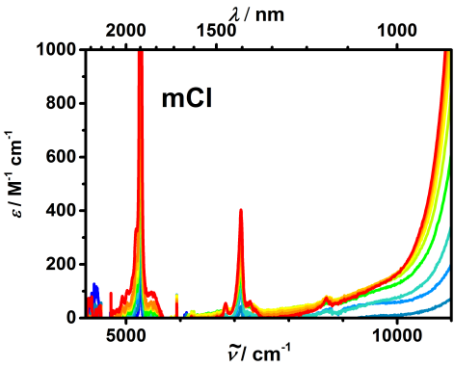
λ / nm
2000
1500
1000
1000
800
600
400
200
0
mCl
ε / M-1 cm-1
5000
10000
ν̃ / cm-1

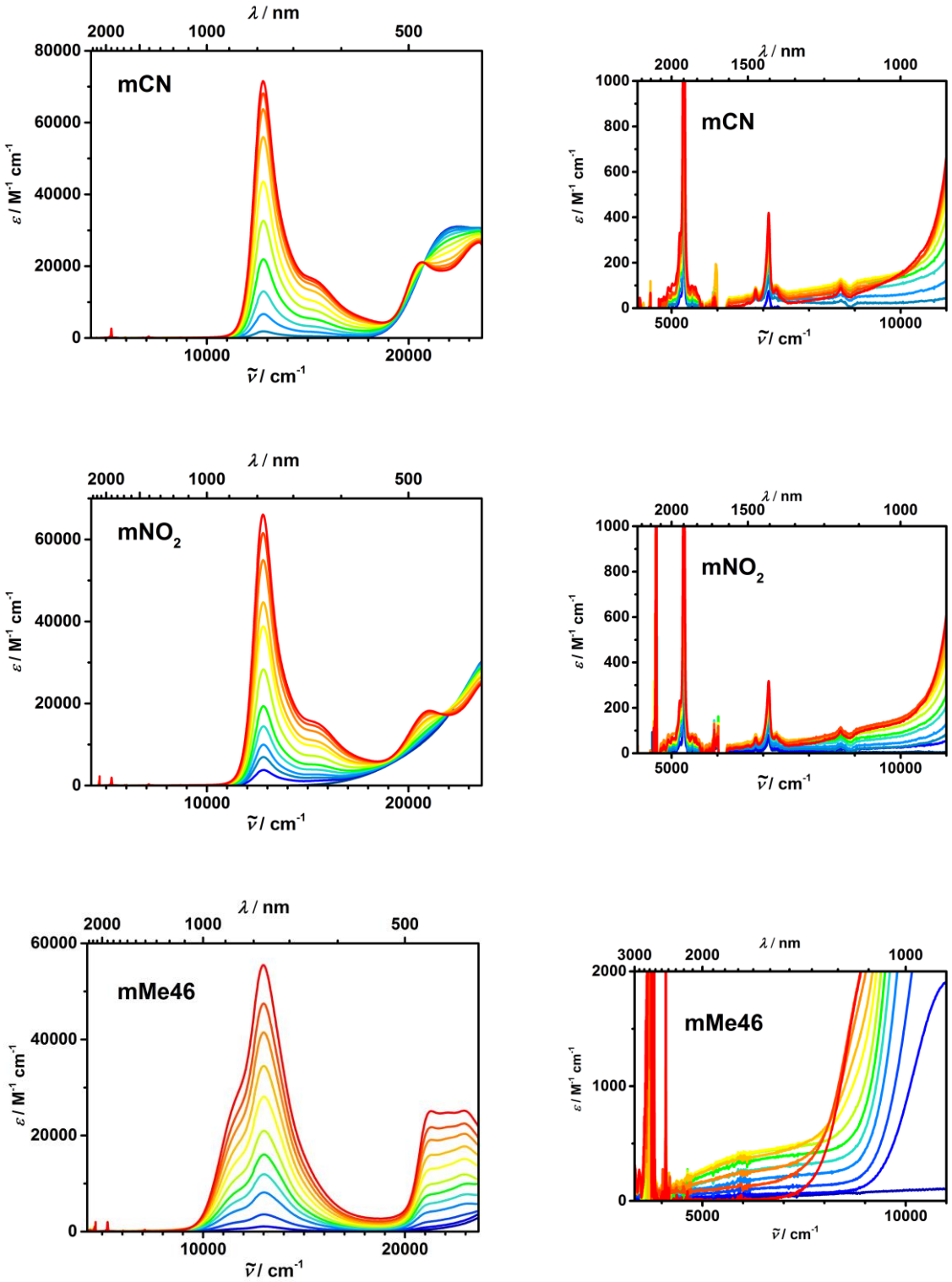

Figure 23: Absorption spectra of the *meta*-compounds **mX** and **mMe46** in $PhNO_2$ (ca. 1.5 µM) during stepwise addition of a solution of $SbCl_5$ in $PhNO_2$ (1 mM). Early spectra are depicted in blue and the later spectra in red. The smaller figures on the right side show the magnified region where the IVCT band is visible

Table 11: Absorption maxima ($\tilde{\nu}_{max}$ and λ_{max}) and extinction coefficients (ε_{max}) of the characteristic absorption bands of the dicationic *para*-compounds **pX$^{2(\bullet+)}$** and *meta*-compounds **mX$^{2(\bullet+)}$** in $PhNO_2$, *o*DCB and DCM.

Solvent		$\tilde{\nu}_{max}$ (λ_{max}) / ε_{max} / cm^{-1} (nm) / M^{-1} cm^{-1}	$\tilde{\nu}_{max}$ (λ_{max}) / ε_{max} / cm^{-1} (nm) / M^{-1} cm^{-1}
***o*DCB**	**pOMe$^{2(\bullet+)}$**	8500 (1176) / 39400	13400 (746) / 32700
	pMe$^{2(\bullet+)}$	10600 (943) / 24900	13000 (769) / 43100
	pCl$^{2(\bullet+)}$	-	12700 (787) / 58700
	pCN$^{2(\bullet+)}$	-	12600 (794) / 69700
	pNO$_2$$^{2(\bullet+)}$	-	12600 (794) / 74600
	mOMe$^{2(\bullet+)}$	-	13100 (763) / 40900
	mMe$^{2(\bullet+)}$	-	12800 (781) / 54000
	mCl$^{2(\bullet+)}$	-	12700 (787) / 62500
	mCN$^{2(\bullet+)}$	-	12600 (794) / 64400
	mNO$_2$$^{2(\bullet+)}$	-	12600 (794) / 60300
	mOMe46$^{2(\bullet+)}$	9300 (1075) / 16400	13400 (746) / 21000
	mMe46$^{2(\bullet+)}$	-	12900 (775) / 46700
DCM	**pOMe$^{2(\bullet+)}$**	9300 (1075) / 32100	13400 (746) / 45000
	pMe$^{2(\bullet+)}$	10900 (917) / 32400	13200 (756) / 52700
	pCl$^{2(\bullet+)}$	-	12700 (775) / 66900
	pCN$^{2(\bullet+)}$	-	12800 (781) / 72300
	pNO$_2$$^{2(\bullet+)}$	-	12800 (781) / 74500
	mOMe$^{2(\bullet+)}$	-	13100 (763) / 55400
	mMe$^{2(\bullet+)}$	-	13000 (769) / 61400
	mCl$^{2(\bullet+)}$	-	12900 (775) / 74100
	mCN$^{2(\bullet+)}$	-	12900 (775) / 76900
	mNO$_2$$^{2(\bullet+)}$	-	12800 (781) / 74900
	mOMe46$^{2(\bullet+)}$	9300 (1075) / 16400	13400 (746) / 20970
	mMe46$^{2(\bullet+)}$	-	13100 (763) / 55000
$PhNO_2$	**pOMe$^{2(\bullet+)}$**	9400 (1064) / 26900	13300 (751) / 43700
	pMe$^{2(\bullet+)}$	11100 (901) / 29600	13100 (763) / 51900
	pCl$^{2(\bullet+)}$	-	12800 (781) / 63700
	pCN$^{2(\bullet+)}$	-	12700 (787) / 66100
	pNO$_2$$^{2(\bullet+)}$	-	12700 (787) / 74100
	mOMe$^{2(\bullet+)}$	-	13000 (769) / 51000
	mMe$^{2(\bullet+)}$	-	13000 (769) / 61400
	mCl$^{2(\bullet+)}$	-	12800 (781) / 65100
	mCN$^{2(\bullet+)}$	-	12800 (781) / 71500
	mNO$_2$$^{2(\bullet+)}$	-	12800 (781) / 66000
	mOMe46$^{2(\bullet+)}$	9700 (1030) / 25100	13400 (746) / 36100
	mMe46$^{2(\bullet+)}$	-	12900 (775) / 46700

During the oxidation of the bisTAA the characteristic bands of the neutral TAA between ca. 20000–30000 cm^{-1} (500–333 nm) vanish (see chapter 3.2.2). Simultaneously, intense absorptions between ca. 6000–16000 cm^{-1} (1666–625 nm) rise, which can be assigned to π–π* TAA radical cation transitions. The collective signal in this area is a result of mainly two excitations: one HOMO → SOMO transition with a transition moment along the *x*-axis and one HOMO−1 → SOMO transition with transition moment oriented along the *z*-axis (alkyne axis / perpendicular to the former, Figure 24).

The HOMO → SOMO transition takes place in the π-π*-system of the dianisyl part of the oxidized TAA and is therefore called the "π-π* band". The HOMO−1 → SOMO transition has CT character and gets influenced by the bridging unit, and is therefore referred to as "bridge band" in the following.

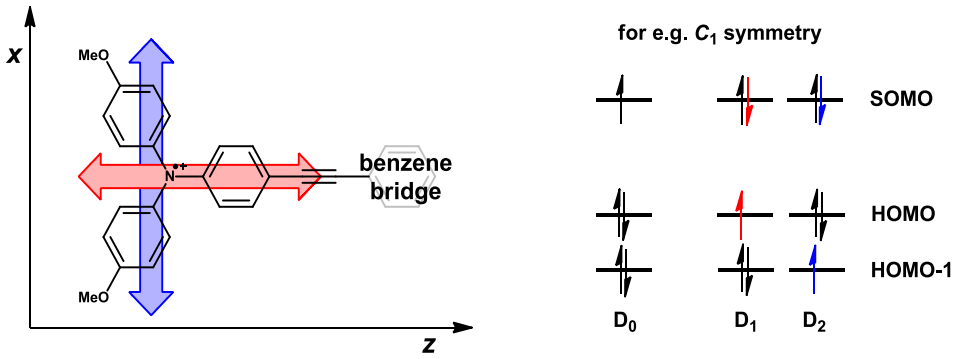

Figure 24: **Left:** Transition moments of TAA radical cation with bridging unit. **Right:** Configuration diagram for the ground and excited states for a TAA radical cation with C_1 symmetry. Red color indicates the bridge-, blue the π-π* band.

The π-π* band is hardly dependent on the substituents X and its orientation of attachment of the EDG/EWG at the bridging benzene unit. In addition to that, the position of the second TAA (*meta* or *para*) does not have a big influence either. The absorption maxima $\tilde{\nu}_{max}$ remain at roughly 13000 cm^{-1} (769 nm) for all $bisTAA^{2(\bullet+)}$. Contrary to this, the position of the bridge band gets influenced by the electronic situation at the bridge and is therefore related to its substituents X, their attachment to the bridge and to the position of the second TAA or $TAA^{\bullet+}$. EDG (like OMe) shift the HOMO−1 → SOMO transition to lower energies, EWG (like NO_2) to higher energies, respectively. In case of the chloro compounds the HOMO and the HOMO−1 are approximately degenerated, and the bridge and π-π* band have about the same energy, thus the absorptions sum up to one intense signal at 13000 cm^{-1} (769 nm) with ε_{max} of the $bisTAA^{2(\bullet+)}$ absorption of ca. 60000 M^{-1} cm^{-1}. The $TAA^{\bullet+}$ absorptions of **m-/pCl$^{2(\bullet+)}$** are accompanied by a small band at 9000 cm^{-1} (1111 nm) whose origin remains unclear. The

bridge bands of the cyano and nitro compounds are hypsochromically shifted and distinguishable as a shoulder at ca. 15000 cm^{-1} (667 nm). Consequently the bridge bands of the methyl and methoxy compounds are bathochromically shifted. For the *meta*-compounds **mOMe$^{2(\bullet+)}$**, **mMe$^{2(\bullet+)}$**, **mMe46$^{2(\bullet+)}$** the transitions are visible as a shoulder at higher wavelengths, in case of the methyl compounds at ca. 11000 cm^{-1} (909 nm) and for the methoxy compound at ca. 10000 cm^{-1} (1000 nm), since OMe being a stronger EDG. For the two *para*-compounds **pOMe46$^{2(\bullet+)}$**, **pMe$^{2(\bullet+)}$** and **mOMe46$^{2(\bullet+)}$** the bridge bands are even shifted further to ca. 9000 cm^{-1} (1111 nm) and can now be identified as separated bands

In the absorption spectra of the dicationic bisTAA species one can identify transitions at ca. 18000–23000 cm^{-1} (556–435 nm). Although no exact assignment was possible, they are assumed to be caused by SOMO → LUMO transition within the TAA radical cation unit, as reported for isoelectronic triarylboranes radical anions.[174, 175]

Upon oxidation of the molecules a broad absorption band in the NIR between ca. 3300–10000 cm^{-1} (3030–1000 nm) first rises and then diminishes again. It is in some cases superimposed by the formerly investigated TAA radical cation bands. This band is related to an intervalence charge transfer (IVCT), which is caused by an optically induced HT from one oxidized TAA to the non-oxidized TAA within the molecule. Its energetic position and intensity gives information about the coupling between the two TAA redox centers. During the oxidation of the bisTAA, first the monocationic species with its IVCT transition is generated. Then, the dicationic bisTAA is formed at the expense of the monocationic species. Since no IVCT transition is possible in this case, it vanishes and is no longer present in the final dicationic spectra. For the *para*-series the IVCT band is clearly visible having an ε_{max} rising from approximately 2000 $M^{-1}\,cm^{-1}$ for **pNO$_2^{\bullet+}$** to 10000 $M^{-1}\,cm^{-1}$ for **pOMe$^{\bullet+}$**, indicating a smaller electronic coupling in the *para*-series containing electron deficient bridges. By contrast, the IVCT bands for the *meta*-series are very weak and are in most cases hard to discern from the baseline. On the left side of Figure 19, the magnified region where the IVCT bands of the *meta*-series are discernable is depicted (without **mOMe46**). They have ε_{max} values of ca. 200 $M^{-1}\,cm^{-1}$, indicating much smaller electronic coupling then the *para*-series. For **mMe46$^{\bullet+}$**, one can see a significant, but still small increased IVCT band. An exception is **mOMe46$^{\bullet+}$**, which also shows a sizable IVCT band.

As mentioned before, the chemical oxidations were performed in solvents of different polarity. The energetic position of the π-π* bands, for both the *meta*- and *para*-series are quasi solvent independent. The absorption maxima just shift about ±100 cm^{-1} when changing the solvent from less polar *o*DCB to the solvents with higher polarity DCM and $PhNO_2$, indicating negligible CT character.

In contrast, the bridge bands of the cationic species of **pOMe**, **pMe** and **mOMe46** show a distinct negative solvatochromism and therefore CT-character. Increasing the solvent polarity

by going from *o*DCB to $PhNO_2$ is associated with a blue shift of 900 cm^{-1} for **pOMe**$^{\bullet+/2(\bullet+)}$, 500 cm^{-1} for **pMe**$^{\bullet+/2(\bullet+)}$ and 400 cm^{-1} for **mOMe46**$^{\bullet+/2(\bullet+)}$. Unfortunately, values of the hypsochromic shift of for the chloro, cyano, nitro compounds and **mMe46**$^{\bullet+/2(\bullet+)}$ are virtually impossible to determine, since the bridge bands are superimposed by the π-π^* bands. Hence, no statement about the CT character of the bridge band for these transitions was possible.

A detailed IVCT band analysis of the MV compounds **pX**$^{\bullet+}$, **mOMe46**$^{\bullet+}$ and **mMe46**$^{\bullet+}$ is presented in the following, since only these bisTAAs show a clearly pronounced IVCT band. It allows the determination of the most fundamental electron transfer parameters: the reorganization energy λ, the electronic coupling matrix element V and the thermal barrier ΔG^*.

During chemical oxidation, the MV compounds exist in a comproportionation equilibrium, as shown in Figure 25, with an equilibrium constant K_D that is given by equation (7).

$$K_D = \frac{[\text{bisTAA}] \times [\text{bisTAA}^{2(\cdot+)}]}{[\text{bisTAA}^{\cdot+}]^2} \tag{7}$$

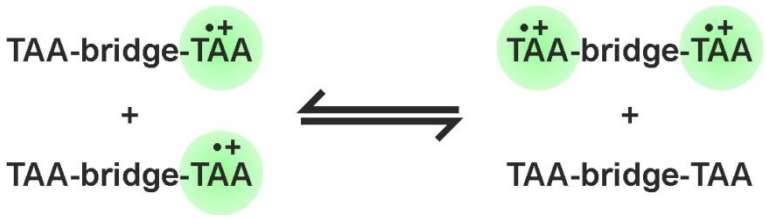

Figure 25: Comproportionation reaction between two cationic bisTAA (left side) and one dicationic and one non-oxidized bisTAA (right side).

For related bisTAA$^{\bullet+}$, K_D amounts to a value of 0.14–0.17 at T = 298 K, meaning that the dynamic equilibrium is on the side of the two singly oxidized TAA.[88, 150] At higher concentrations of monocations (later spectra of chemical oxidation), a considerable amount of dicationic species gets formed. However, the first recorded spectra show only a negligible dicationic contribution to the absorption. Therefore, the monocation spectra were calculated assuming the monocation band possess half the intensity of the dication band (both at ca. 14000 cm^{-1} (714 nm)). The extinction coefficient of the dication band (ε^{2+}_{max}) was divided by 2, yielding the extinction coefficient of the monocation (ε^{+}_{max}, equation (8)). The recorded spectra after the first addition of oxidant were then multiplied by the factor *f*, which represents the relation between ε^{+}_{max} and ε^{+}, to obtain the “pure” monoradical spectra (equation (9)).

$$\varepsilon_{max}^{+} = \frac{\varepsilon_{max}^{2+}}{2} \quad (8)$$

$$f = \frac{\varepsilon_{max}^{+}}{\boldsymbol{\varepsilon}^{+}} \quad (9)$$

For determination of the Gaussian-shaped IVCT bands the reduced spectra ($\varepsilon/\tilde{\nu}$) were fitted by up to four fit functions, since they are sometimes strongly superimposed by TAA associated radical cation bands.[176] The monocation spectra for the *para*-series **pX$^{\bullet+}$**, **mOMe46$^{\bullet+}$** and **mMe46$^{\bullet+}$** and their fits in *o*DCB are depicted in Figure 26, those in DCM in Figure 27 and in $PhNO_2$ in Figure 28. For easier comparison Figure 29 summarizes the radical cation spectra and the respective IVCT fits for all molecules in *o*DCB (A), DCM (B) and $PhNO_2$ (C).

***o*DCB**

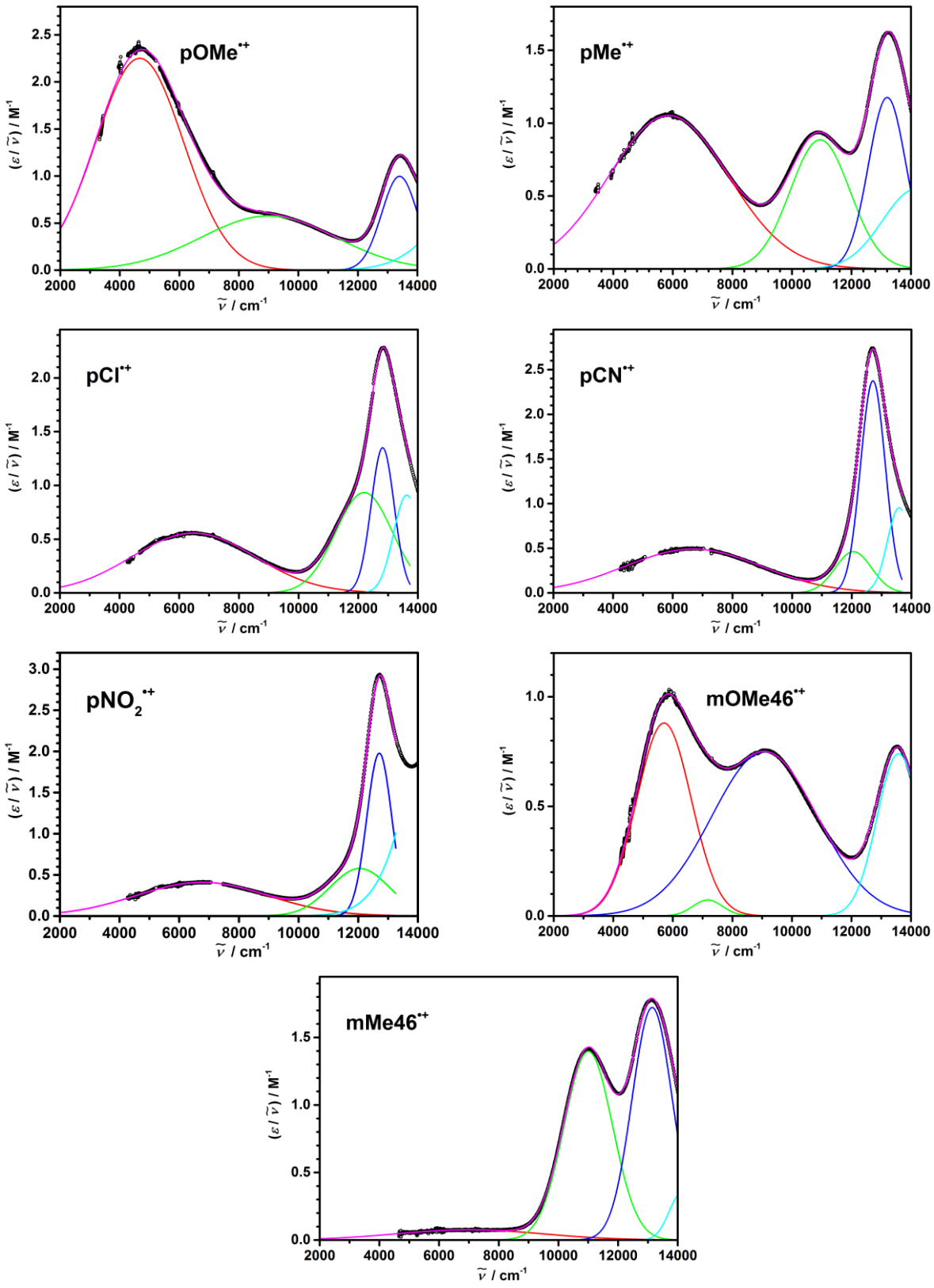

Figure 26: Reduced absorption spectrum of the monocation of **pX**$^{\bullet+}$, **mOMe46**$^{\bullet+}$ and **mMe46**$^{\bullet+}$ in *o*DCB and fit with Gaussian functions. The IVCT band is given in red.

DCM

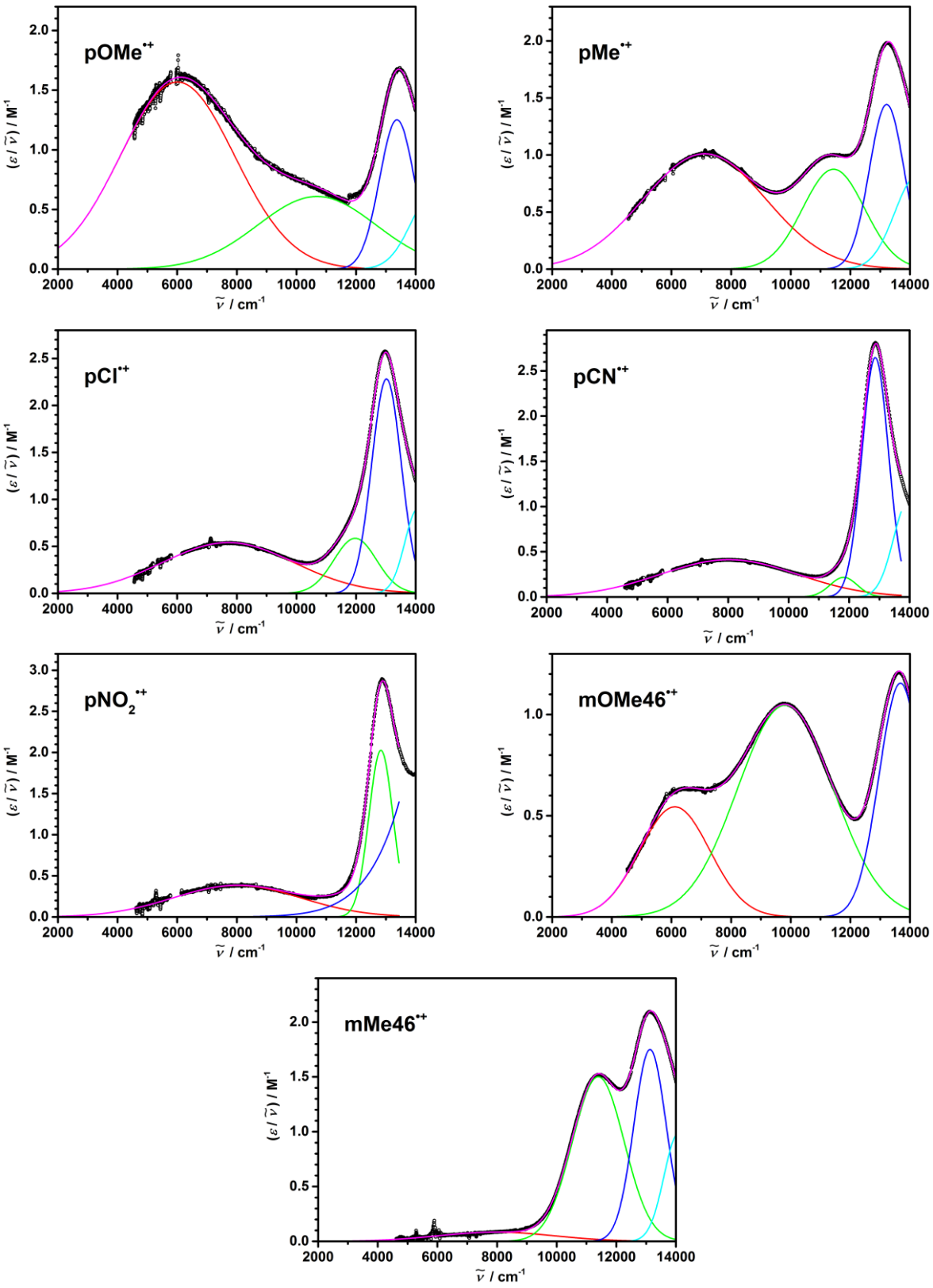

Figure 27: Reduced absorption spectrum of the monocation of **pX**$^{\bullet+}$, **mOMe46**$^{\bullet+}$ and **mMe46**$^{\bullet+}$ in DCM and fit with Gaussian functions. The IVCT band is given in red.

PhNO$_2$

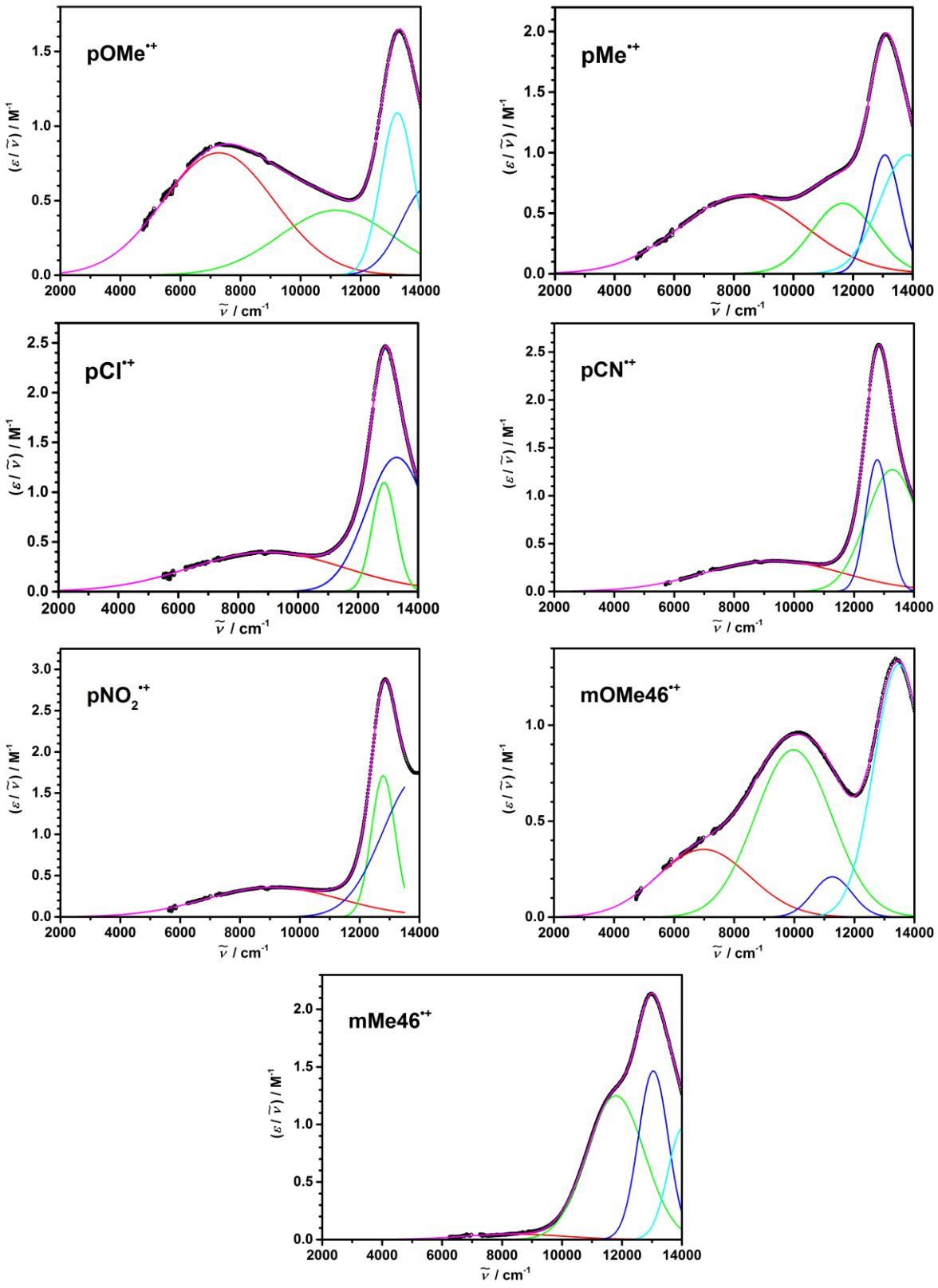

Figure 28: Reduced absorption spectrum of the monocation of **pX$^{\bullet+}$**, **mOMe46$^{\bullet+}$** and **mMe46$^{\bullet+}$** in $PhNO_2$ and fit with Gaussian functions. The IVCT band is given in red.

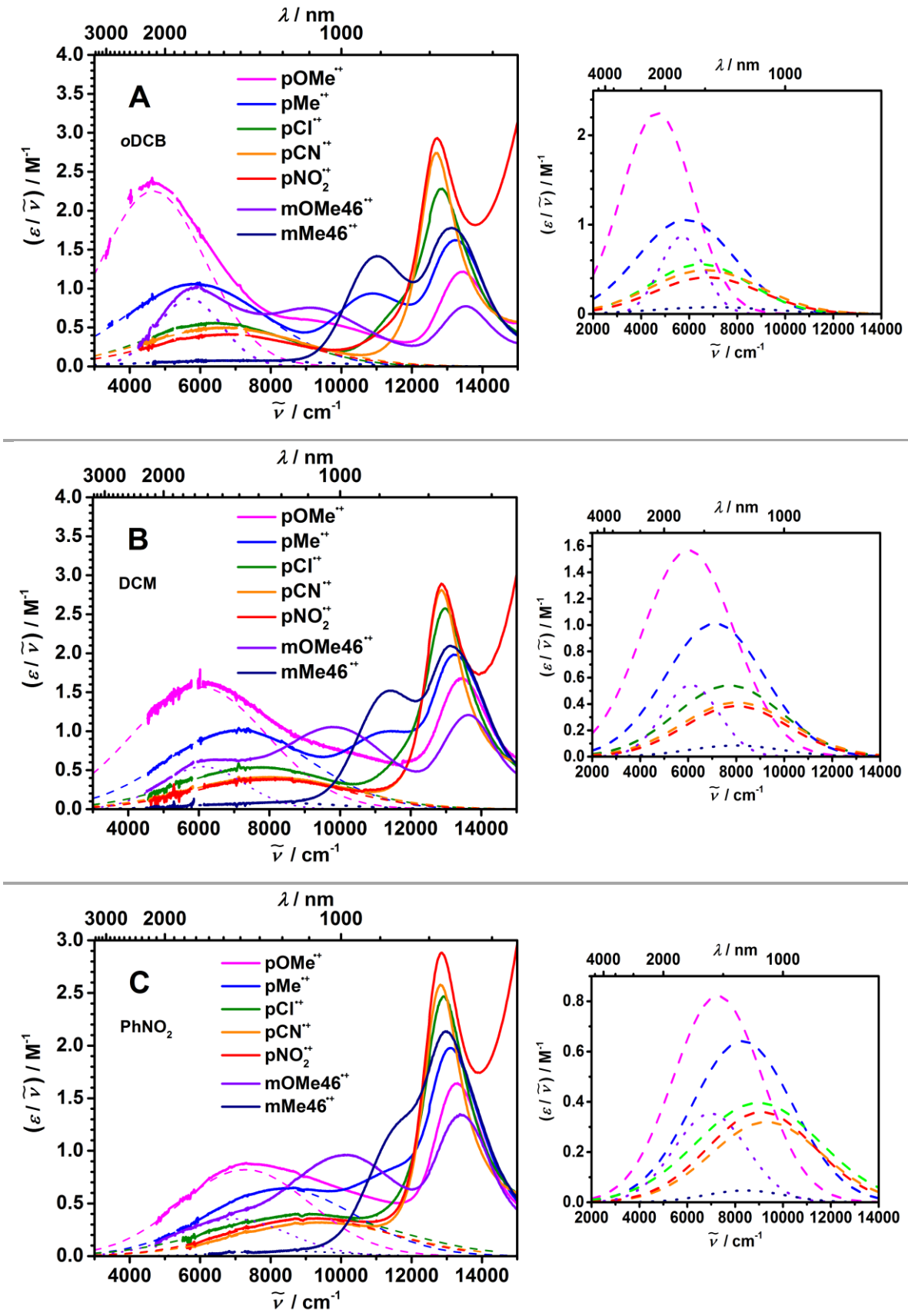

Figure 29: Radical cation spectra and the respective IVCT fits for **pX$^{\bullet+}$**, **mOMe46$^{\bullet+}$** and **mMe46$^{\bullet+}$** in oDCB (A), DCM (B) and $PhNO_2$ (C). The smaller figures on the right side show the magnified region where the IVCT band is visible.

The maxima of the IVCT bands $\tilde{\nu}_{max}^{IVCT}$ of all MV compounds are located in the NIR at ca. 7000–9300 cm^{-1} (1429–1075 nm). The respective positions and intensities strongly depend on the used solvent (see Table 12). *o*DCB has a much smaller solvent reorganization energy than $PhNO_2$. Consequently, the IVCT bands show a strong negative solvatochromism. Increasing the solvent polarity from unpolar *o*DCB to more polar $PhNO_2$ is associated with a hypsochromic shift of the absorption maxima of about 1300 cm^{-1} for the two *meta*-compounds, and even ca. 2600 cm^{-1} for the *para*-series. In addition to that, the intensity of the IVCT band is reduced by about half. In DCM, which is a solvent of intermediate polarity and solvent reorganization energy, the position of the maxima and the intensity of the IVCT band are between those in $PhNO_2$ and *o*DCB.

The substituents X at the benzene bridge also have a great impact on the maxima and the intensity of the IVCT band. Within the *para*-series, the IVCT band shifts to lower energies when increasing the electron donating character of X. The maxima of the IVCT bands of MV compounds with acceptors attached to the central benzene moiety (X = CN–NO_2) have roughly the same energy of ca. 6600 cm^{-1} (1515 nm). However, the IVCT maximum of MV compounds with donors have a much lower energy of 6700 cm^{-1} (1493 nm) for **pMe$^{\bullet+}$** and 4670 cm^{-1} (2100 nm) for **pOMe$^{\bullet+}$**, respectively. This trend of absorption maxima and energy difference of ca. 2000 cm^{-1} (between NO_2 and OMe compound) is present in all solvents.

For the **mX46$^{\bullet+}$** series the situation is a somewhat different. $\tilde{\nu}_{max}^{IVCT}$ of **mMe46$^{\bullet+}$** (7020 cm^{-1} (1706 nm)) has a similar value as **pX$^{\bullet+}$** compounds bearing acceptors, while **mOMe46$^{\bullet+}$** (5700 cm^{-1} (1706 nm)) even reaches a maximum of the absorption similar to those of donor substituted **pX$^{\bullet+}$**.

Mulliken-Hush theory was used to calculate the electronic coupling V_{12} via equation (10).[52, 54-56] The maximum of the IVCT band $\tilde{\nu}_{max}^{IVCT}$ can directly be determied from the IVCT fitting results and the diabatic dipole moment difference $\Delta\mu_{12}$ can be evaluated by using the integral of the IVCT band and equation (11) and (12). On the contrary, the adiabatic dipole moment difference $\Delta\mu_{ab}$ is not accessible by *Mullikan-Hush* band analysis and was determined using DFT calculations (see next section).

$$V_{12} = \frac{\mu_{ab}\tilde{\nu}_{max}^{IVCT}}{\Delta\mu_{12}} \tag{10}$$

$$\Delta\mu_{12} = \sqrt{\Delta\mu_{ab}^2 + 4\mu_{ab}^2} \tag{11}$$

$$\mu_{ab}^2 = \frac{3hc\varepsilon_0 \ln 10}{2000\pi^2 N_A} \frac{9n}{(n^2+2)^2} \int \frac{\varepsilon}{\tilde{\nu}} d\tilde{\nu} \tag{12}$$

Here, μ_{ab} is the adiabatic transition dipole moment, *h* the *Planck* constant, *c* the speed of light in vacuum, ε_0 the vacuum permittivity, N_A the *Avogadro´*s constant, *n* the refractive index of the solvent and $\int \frac{\varepsilon}{\tilde{\nu}} d\tilde{\nu}$ the integral of the reduced IVCT band. The hole transfer (HT) barriers ΔG^* (for the IVCT analysis ΔG_{IVCT}^*) can now be calculated using equation (13).

$$\Delta G^* = \frac{\lambda}{4} - V_{12} + \frac{V_{12}^2}{\lambda} \tag{13}$$

where λ is the reorganization energy which equals the energy at the IVCT maximum $\tilde{\nu}_{max}^{IVCT}$ and comprises a solvent (λ_o) and an inner-sphere (λ_i) part. The evaluated couplings and HT barriers using this approach are given in Table 12.

In $PhNO_2$ the transition moments μ_{ab} in the *para*-series rise continuously with electron donating character of X, from 3.7 D for **pNO$_2$$^{\bullet+}$** to 5.0 D for **pOMe$^{\bullet+}$**. The electronic coupling V_{12} increases slightly from ca. 450 cm^{-1} to 480 cm^{-1} within the acceptor substituted MV compounds (X = NO_2, CN, Cl). Then a faster increase to 550 cm^{-1} for donor substituents (X = OMe, Me) is observed. In agreement, the contrary behavior is also found for the HT barriers. As expected from the obtained electronic couplings, the HT barriers are roughly constant for acceptor substituents (X = NO_2, CN, Cl; about 1850 cm^{-1}) and drop to 1570 cm^{-1} for **pMe$^{\bullet+}$** and 1301 cm^{-1} for **pOMe$^{\bullet+}$**, respectively.

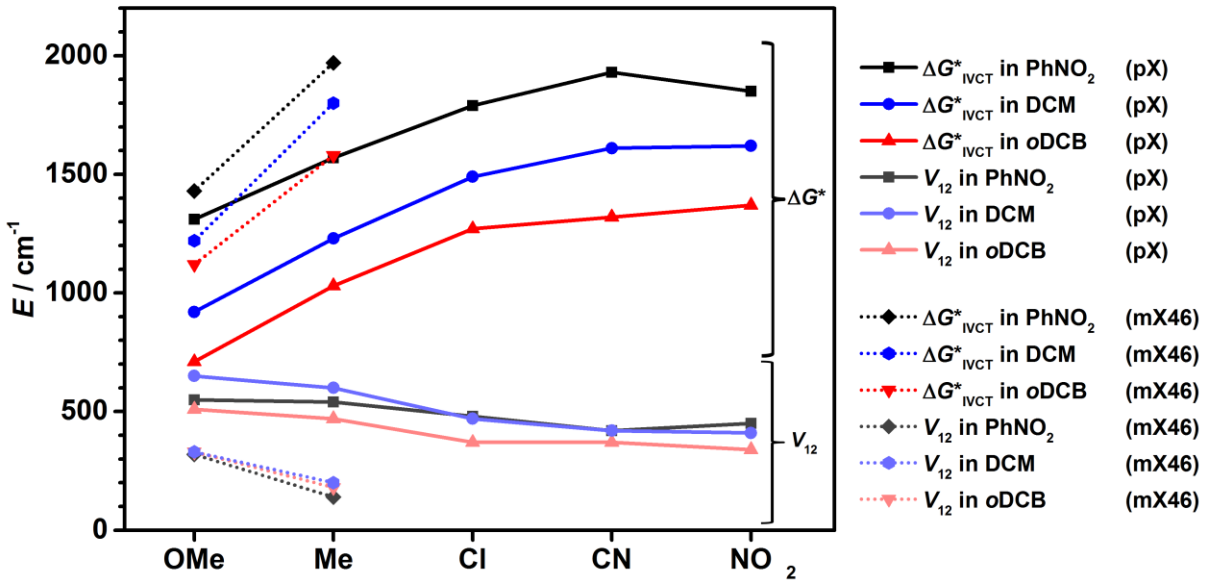

Figure 30: Plot of the electronic couplings V_{12} and HT barriers ΔG^{*} of the *para*-compounds **pX**$^{\bullet+}$ (X = OMe-NO_2, solid lines) and *meta*-compounds **mX46**$^{\bullet+}$ (X = OMe, Me, dotted lines) in $PhNO_2$ (black), *o*DCB (blue) and DCM (red).

The transition moment μ_{ab} and electronic coupling V_{12} of **mMe46**$^{\bullet+}$ (1.1 D, 140 cm^{-1}) are much lower than those of the *para*-series, with a HT barrier ΔG^{*}_{IVCT} of 1970 cm^{-1}. The situation is different for **mOMe46**$^{\bullet+}$. The transition moment (3.0 D) and electronic couplings (320 cm^{-1}) both reach values close to those determined for the MV compounds of the *para*-series with acceptor substituents. However, the HT barriers ΔG^{*}_{IVCT} of 1430 cm^{-1} are much lower than the latter ones, comparable to those of **pOMe**$^{\bullet+}$.

Although exhibiting differences in the absolute magnitude of the determined values, the basic trends in transition moment, electronic coupling and HT barrier can be transferred to the less polar solvents DCM and *o*DCB, too. However, compared to the results in $PhNO_2$, the μ_{ab} values are clearly higher in *o*DCB and DCM. In addition to that the HT barriers in both solvents are significantly smaller, which can be explained by the lower solvent polarity and thus smaller solvent reorganization energy.

The couplings of the *para*-series are slightly lower in *o*DCB than in $PhNO_2$. In DCM a somehow different trend is observed, for MV compounds with acceptor substituents (X = NO_2, CN, Cl) the coupling is lower compared to those determined in $PhNO_2$. However, for all MV compounds with donor substituents (X = OMe, Me) the couplings are higher.

Table 12: Experimental data obtained by IVCT band analysis at 295 K and temperature dependent ESR spectroscopy. Both measurements were done in $PhNO_2$, *o*DCB and DCM.

		IVCT analysis				ESR spectroscopy		
		$\tilde{\nu}_{max}^{IVCT}$ / cm^{-1} [a]	μ_{ab} / D[b]	V_{12} / cm^{-1} [b,c]	ΔG^*_{IVCT} / cm^{-1}	ΔG^*_{ESR} / cm^{-1} [e]	T range / K	k_{ESR} / 10^7 s^{-1}
$PhNO_2$	**mOMe46$^{\bullet+}$**	6980	3.0	320	1430	1970 ± 150	290–315	40
	mMe46$^{\bullet+}$	8410	1.1	140	1970	1360 ± 110	280–300	4.8
	mOMe$^{\bullet+}$	-	-	-	-	1640 ± 30	280–345	1.1
	mMe$^{\bullet+}$	-	-	-	-	1740 ± 20	280–360	2.5
	mCl$^{\bullet+}$	-	-	-	-	1600 ± 70	280–335	1.3
	mCN$^{\bullet+}$	-	-	-	-	1630 ± 20	285–350	1.5
	m$NO_2^{\bullet+}$	-	-	-	-	1790 ± 140	280–320	1.0
	pOMe$^{\bullet+}$	7280	5.0	550	1310	1700 ± 90	280–320	57
	pMe$^{\bullet+}$	8310	4.7	540	1570	1380 ± 60	295–345	35
	pCl$^{\bullet+}$	8980	4.1	480	1790	1420 ± 50	280–325	11
	pCN$^{\bullet+}$	9310	3.5	420	1930	1430 ± 50	280–320	9.9
	p$NO_2^{\bullet+}$	9100	3.7	450	1850	1410 ± 80	280–310	11
DCM	**mOMe46$^{\bullet+}$**	6110	3.4	330	1220	1008 ± 40	235–260	160[e]
	mMe46$^{\bullet+}$	7970	1.7	200	1800	1210 ± 20[j]	240–280[f]	11[e]
	pOMe$^{\bullet+}$	6010	7.4	650	920	660 ± 50[g]	200–230[g]	322[e]
	pMe$^{\bullet+}$	7110	6.2	600	1230	970 ± 20	250–310	114
	pCl$^{\bullet+}$	7710	4.6	470	1490	1020 ± 20[h]	220–250[f]	29[e]
	pCN$^{\bullet+}$	8030	4.1	420	1610	1050 ± 20[i]	220–260[f]	21[e]
	p$NO_2^{\bullet+}$	8010	3.9	410	1620	-	-	-
*o*DCB	**mOMe46$^{\bullet+}$**	5700	3.6	330[d]	1120	970 ± 50	260–300	87
	mMe46$^{\bullet+}$	7020	1.8	180	1580	1080 ± 30	255–275[f]	14[e]
	pOMe$^{\bullet+}$	4670	7.4	510[d]	710	1250 ± 40	260–305[g]	201
	pMe$^{\bullet+}$	5860	5.9	470[d]	1030	-	-	-
	pCl$^{\bullet+}$	6480	4.4	370[d]	1270	900 ± 40	260–280[f]	16[e]
	pCN$^{\bullet+}$	6680	4.3	370	1320	840 ± 60	260–285[f]	14[e]
	p$NO_2^{\bullet+}$	6760	3.9	340[d]	1370	970 ± 20	260–275[f]	16[e]

[a] ±5 %. [b] ±20 %. [c] Calculated by *Mulliken-Hush* theory using experimental data and the DFT computed dipole moment difference $\Delta\mu_{ab}$ (see Table 14). [d] Using DFT computed dipole moment difference in DCM which hardly differs from those in *o*DCB (see Table 15). [e] Extrapolated to 295 K. [f] Rate constants at higher temperature deviate from linearity in the $\ln(k_{ESR}/T^{1/2})$ vs. 1/T plot towards lower rates. [g] Rate constants at higher temperature deviate from linearity in the $\ln(k_{ESR}/T^{1/2})$ vs. 1/T plot towards lower rates.

3.3.2 ESR Analysis

In order to investigate the HT rate constants k_{ESR} and thermal HT barrier ΔG^*_{ESR} of the MV radical cations temperature dependent ESR measurements in different solvents were performed.[3] The procedure to determine the HT rate constants k_{ESR} is briefly explained in the following by example of the CN compounds in *o*DCB. A more detailed description of this procedure, ESR spectroscopic measurements and sample preparation, is given in literature.[88]

The radical cations of **pCN** and **mCN** were generated at a concentration of ca. 1×10^{-4} M by oxidation with tris(bromophenyl)ammonium hexachloroantimonate ("magic blue"). At low temperature the MV compounds shows an unresolved three line spectrum that can tentatively be fitted by use of a single nitrogen hyperfine coupling constant (hfc) of ca. 0.87 mT and $I = 1$ (Figure 32). Upon warming, first the spectra undergo line broadening and at higher temperatures a spectrum of five lines is formed. The five line pattern that can be explained by coupling with two equivalent nitrogen atoms with approximately half the coupling constant from above ($2 \times a_N = 0.4$ mT), meaning the radical is delocalized between the two N of the TAA moieties in the ESR time scale. One would expect a 1:2:3:2:1 intensity pattern for both MV compounds at high temperature, but due to large line width, this pattern was not clearly observable.[36, 88, 93]

The line width in turn depends on the hyperfine coupling components of the surrounding protons. Not accounting their hyperfine interactions would lead to reduced accuracy of the fit. These hfc have to be extracted from the non-exchanging, single centered model compound **sCN**$^{\bullet+}$ experimentally by ENDOR spectroscopy (Figure 31, left). By use of the hfc evaluated from ENDOR spectroscopy a simulation of the non-resolved ESR spectrum of **sCN**$^{\bullet+}$ was possible with high accuracy, proving the correctness of the hfc determination (Figure 31, right). The obtained hfc at 260 K are given in Table 13.

[3] The ESR measurements were done by Dr. Boryana Mladenova[177] and Dr. Ivo Krummenacher.[178] The ESR line shape analysis was performed using a program designed by Dr. Daniel Kattnig.[179]

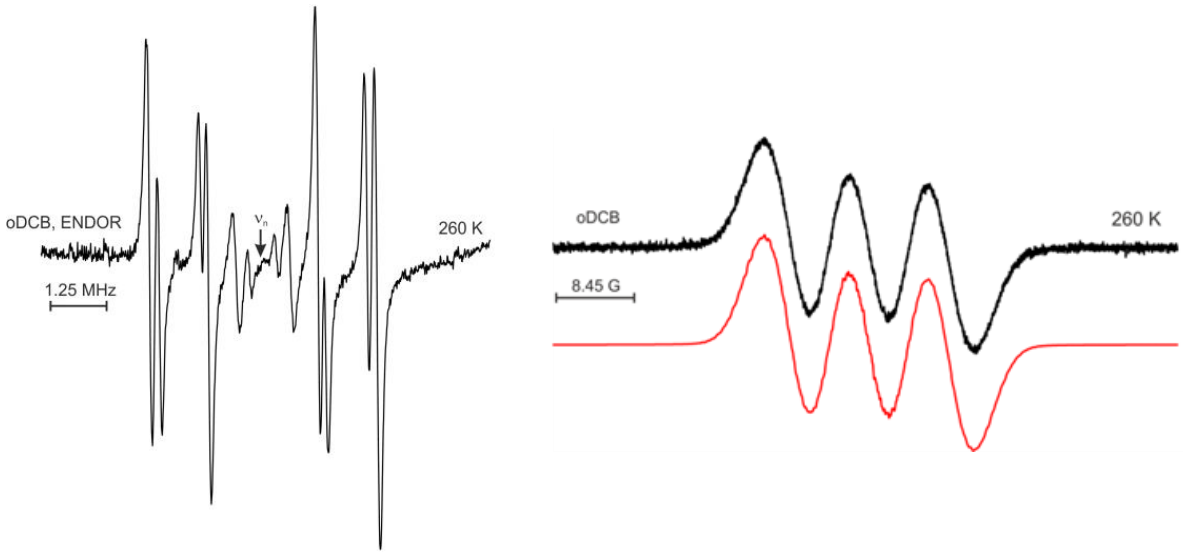

Figure 31: ENDOR spectrum of the reference **sCN**$^{\bullet+}$ in *o*DCB at 260 K (left). ESR spectrum (black) of **sCN**$^{\bullet+}$ in *o*DCB at 260 K (right). The simulation (red) is based on the hyperfine coupling constants obtained by analysis of the ENDOR spectrum.

Table 13: Hyperfine coupling constants determined for the radical cation **sCN**$^{\bullet+}$ from ENDOR spectrum in *o*DCB at 260K.

designation	no. of nuclei	a_i (ENDOR) / mT
N	1	0.848
H_{ortho1}	2	0.181
H_{ortho2}	4	0.165
H_{meta1}	2	0.129
H_{CH3}	6	0.099
H_{meta2}	4	0.057
$H_{bridge1}$	1	0.015
$H_{bridge2}$	1	0.005
$H_{bridge3}$	1	0.085

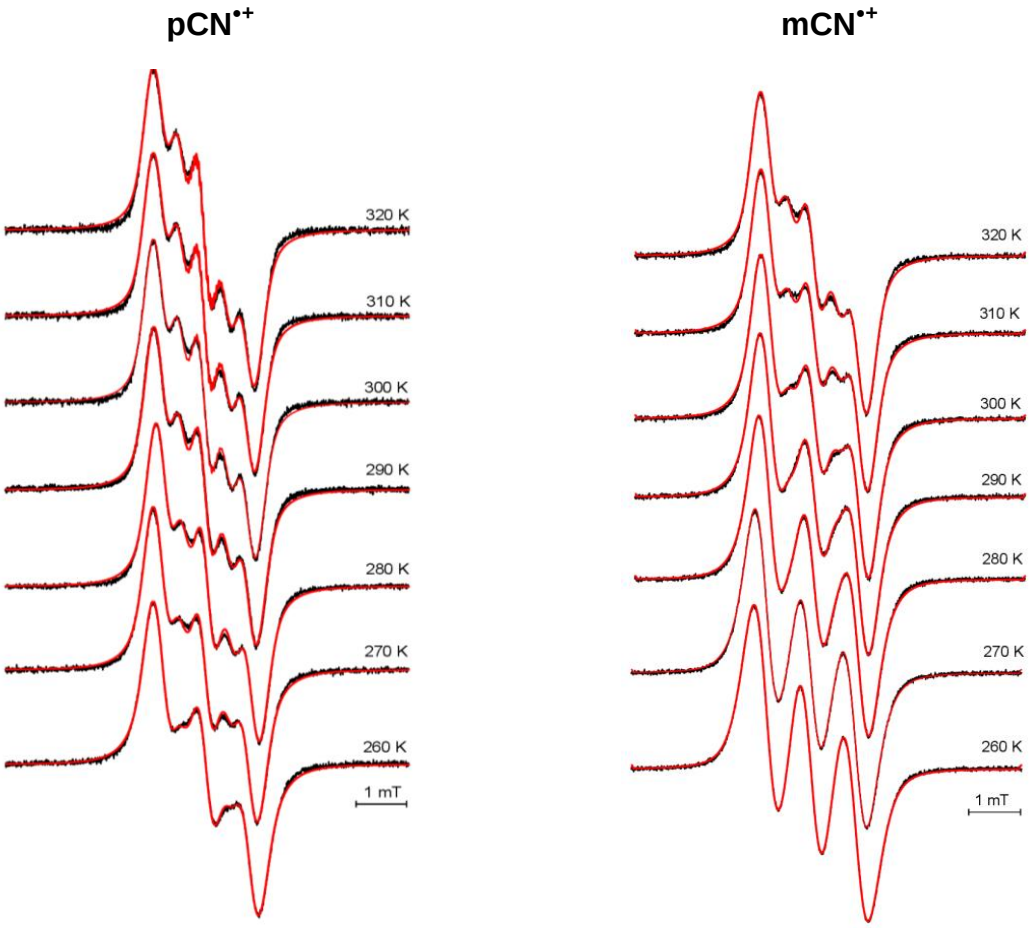

Figure 32: ESR spectra of MV compound **pCN**$^{\bullet+}$ (left) and **mCN**$^{\bullet+}$ (right) in oDCB at various temperatures between 260 K and 320 K. The simulated spectra (red) are based on the hyperfine coupling constants obtained by analysis of the ENDOR spectrum of **sCN**$^{\bullet+}$.

By use of the hfc of **sCN**$^{\bullet+}$ obtained by ENDOR spectroscopy, the ESR spectra of the MV compounds **pCN**$^{\bullet+}$ and **mCN**$^{\bullet+}$ can now be simulated adequately as illustrated in Figure 32 (red lines). In particular, the hfc of two triarylamine *ortho*-protons of the two anisyl groups ($4 \times a_{Hortho1}$ = 0.181 mT) and the two *ortho*-protons of the phenylene ring which is oriented to the bridge ($2 \times a_{Hortho2}$ = 0.165 mT) were used. The nitrogen hfc (ca. 0.8–0.9 mT) was freely fitted for each spectrum at each temperature as it is slightly temperature dependent and shows a weak decrease with increasing temperature. All other hfc are very small and were neglected.

Following this line shape analysis procedure the HT rate constants k_{ESR} at the respective temperature were determined for all MV compounds in $PhNO_2$. The *para*-series, **mOMe46**$^{\bullet+}$ and **mMe46**$^{\bullet+}$ were investigated in *o*DCB and DCM, too. For simulation of the spectra of **mMe46**$^{\bullet+}$, the hfc determined for **sMe**$^{\bullet+}$ were used instead of those for **sMe46**$^{\bullet+}$. The obtained k_{ESR} values for all measurements at 295 K are listed in Table 12.

Activation barriers ΔG^*_{ESR} were then obtained by linear fits of the $\ln(k/T^{1/2})$ vs $1/T$ plots. [36, 88, 91] Some compounds showed instability in *o*DCB and in DCM when reaching rt and above. Therefore, only measurements at lower temperature were used for the determination of ΔG^*_{ESR}. For these bisTAAs, the reported rate constants at 295 K were gained by extrapolation. Several attempts to measure **pMe**$^{\bullet+}$ in *o*DCB and **pNO$_2$**$^{\bullet+}$ in DCM failed, maybe due to the just mentioned instability problems.

Figure 33 exemplarily gives the plots for **p-/mOMe**$^{\bullet+}$ and **p-/mCN**$^{\bullet+}$ in $PhNO_2$. All $\ln(k/T^{1/2})$ vs $1/T$ plots are displayed separately in Figures A1-A7 in the appendix.

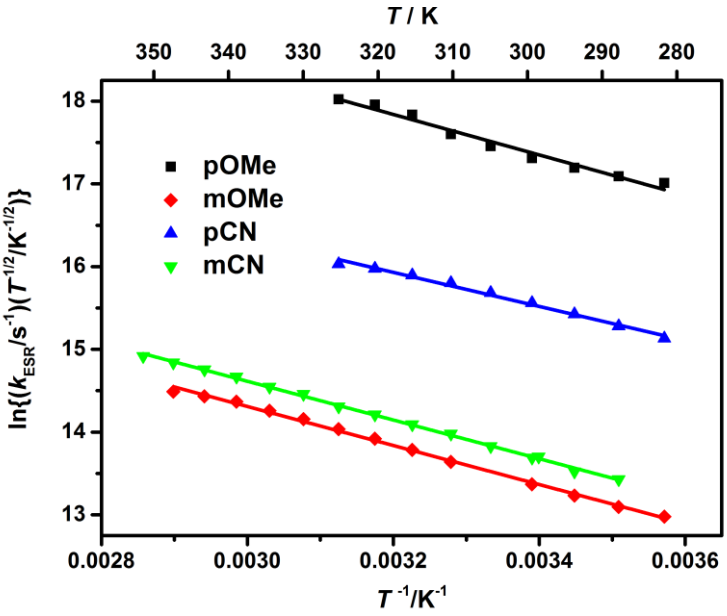

Figure 33: $\ln(k/T^{1/2})$ vs $1/T$ plots for **mOMe46**$^{\bullet+}$ and **mMe46**$^{\bullet+}$ in DCM.

First the results in $PhNO_2$ will be discussed, since only here a comparison with the *meta*-compounds is possible. At 295 K the rate constants of the HT k_{ESR} of the *meta*-series are very similar (ca. 1×10^7–2×10^7 s^{-1}) and seem to be independent of the substituents X at the bridge. Within the *para*-series k_{ESR} is constant for acceptor substituents (X = NO_2, CN, Cl; about 10×10^7 s^{-1}) but increases on going from **pCl**$^{\bullet+}$ to species with donor substituents (Me = 35×10^7 s^{-1}, OMe = 57×10^7 s^{-1}; Figure 34). This demonstrates that strong donor substituents, which increase the electron density at the bridge, can be used to accelerate the HT. In addition to that the rate constants are an order of magnitude larger than those of the *meta*-compounds. A feature that was already observed for other MV compounds in a similar context.[80, 169, 180]

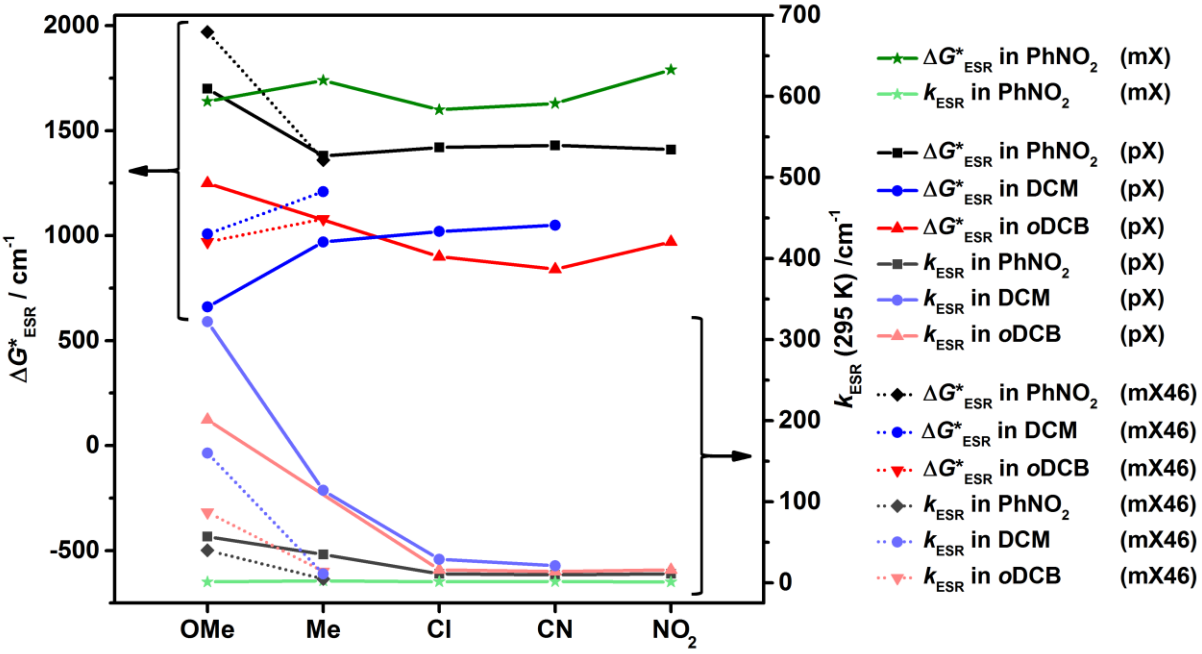

Figure 34: Plot of the electronic couplings HT barriers ΔG^*_{ESR} and rate constants k_{ESR} of the *meta*-compounds **pX**$^{\bullet+}$ (X = OMe-NO_2) in $PhNO_2$ (green).Plot of the electronic couplings HT barriers ΔG^*_{ESR} and rate constants k_{ESR} of the *para*-compounds **mX**$^{\bullet+}$ (X = OMe-NO_2, solid lines) and *meta*-compounds **mX46**$^{\bullet+}$ (X = OMe, Me, dotted lines) in $PhNO_2$ (black), *o*DCB (blue) and DCM (red).

In $PhNO_2$ the HT barriers ΔG^*_{ESR} are almost independent of the substituents for the **mX**$^{\bullet+}$ series (ca. 1680 cm^{-1}). Within the **pX**$^{\bullet+}$ series the barriers are constant for acceptor substituents (X = NO_2, CN, Cl; about 1400 cm^{-1}) and clearly lower than those of the **mX**$^{\bullet+}$ series. The same is true for **pMe**$^{\bullet+}$ and its constitutional isomer **mMe46**$^{\bullet+}$, with HT barriers of 1380 cm^{-1} and 1360 cm^{-1}, respectively. The situation changes drastically when looking at **pOMe**$^{\bullet+}$ and **mOMe46**$^{\bullet+}$. For **pOMe**$^{\bullet+}$ with its strong donor substituents, the barrier is much larger (1700 cm^{-1}) and approaches those of the **mX**$^{\bullet+}$ series. This observation is surprising, because at first, it appears contradictory to the corresponding increase in HT rate. The same is true for **mOMe46**$^{\bullet+}$ which shows a high HT rate and high HT barrier, too. In fact, the barrier is significantly higher than that for all other MV compounds investigated in this study.

In the less polar solvents *o*DCB and DCM the analogous effect concerning the HT rate constants is present. For the **pX**$^{\bullet+}$ series k_{ESR} is almost independent of substituent for X = NO_2 to Cl (and similar in all three solvents) but rises dramatically for X = OMe in *o*DCB and particularly in DCM. Compared to the results in $PhNO_2$, the barriers are significantly lower in *o*DCB. This can be explained by the lower solvent polarity and thus smaller solvent reorganization energy, which is in line with the observations made above for the IVCT band (previous chapter). In DCM the HT barriers for **pX**$^{\bullet+}$ with acceptor substituents (X = Cl–NO_2)

lie between those of $PhNO_2$ and *o*DCB at ca. 1550 cm^{-1}. Surprisingly for **pX$^{\bullet+}$** with donor substituents (X = OMe–Me) the barriers decrease; for **pMe$^{\bullet+}$** to 1230 cm^{-1} and for **pOMe$^{\bullet+}$** drastically to 920 cm^{-1}.

For the **mX46$^{\bullet+}$** series the HT rates k_{ESR} behave analogous to those obtained for $PhNO_2$, starting form ca. 10×10^7 s^{-1} for **mMe46$^{\bullet+}$** (in all three solvents). A significant higher rate constant for **mOMe46$^{\bullet+}$** was found in oDCB (87×10^7 s^{-1}) and especially DCM (160×10^7 s^{-1}). However, the trend of the HT barriers ΔG^*_{ESR} shows the inverse behavior. Increasing the electron donating character of substituent X form Me to OMe is associated with a decrease of the HT barriers from 1210 cm^{-1} in DCM and 1800 cm^{-1} in *o*DCB to 1008 cm^{-1} and 970 cm^{-1}, respectively.

3.3.3 TD-DFT Computations

In order to obtain the computed dipole moment differences $\Delta\mu_{ab}$ between ground and IVCT state, transition moments μ_{ab} and transition energies E_{ab}, UDFT optimizations and TD-DFT computations were performed.[4] The activation barrier ΔG^*_{HM} was evaluated via equation (13) following the *Mulliken-Hush* theory and the computed data. The resulting values for all MV compounds in $PhNO_2$ are summarized in Table 14. For the **mX46**$^{\bullet+}$ series the calculations were extended by the two MV compounds **mCl46**$^{\bullet+}$ and **mCN46**$^{\bullet+}$. The transition state was optimized at constrained geometries, with either C_i or C_s symmetry. The nature of the stationary states was characterized by frequency calculations, which gave one imaginary frequency in most cases. In some cases zero or two imaginary frequencies we obtained. Nevertheless, it was assumed that these structures correspond closely to the true transition state, since the hypersurface is notably shallow in this region.

All MV compounds offer large dipole moment differences $\Delta\mu_{ab}$, which illustrates that the charge distribution is strongly asymmetric and thus one triarylamine is positively charged while the other remains neutral. For the **mX**$^{\bullet+}$ series, the dipole moment difference remains constant at ca. 74 D. On contrary for the **pX**$^{\bullet+}$ series, $\Delta\mu_{ab}$ decreases from 75.0 D to 65.6 D while increasing the electron donating character of X. The **mX46**$^{\bullet+}$ series shows a very moderate increase in the charge delocalization on going from X = CN to Me, whereas the charge delocalization is significantly higher in **mOMe46**$^{\bullet+}$.

The IVCT transition energy E_{ab}, and thus the reorganization energy, decreases with increasing electron-donating character of X. This tendency agrees excellently with the experimental optical studies of the *para*-series, **mOMe46**$^{\bullet+}$ and **mMe46**$^{\bullet+}$, for which experimental data are available. The transition moments μ_{ab} in the *para*-series are much larger than those in the **mX**$^{\bullet+}$ series, reflecting a more efficient electronic coupling V_{12} in the former. The transition moments of **mX46**$^{\bullet+}$ with acceptor substituents (for X = CN and Cl) are small, similar to **mX**$^{\bullet+}$. However those of **mX46**$^{\bullet+}$ with of donor substituents (for X = Me and OMe) rise dramatically to values approaching those of the *para*-series for **mOMe46**$^{\bullet+}$. Using the computed data the electronic couplings V_{12} were estimated by the *Mulliken-Hush* formalism (equation (10) and (11)). As expected the *meta*-series exhibits small couplings between 60 cm^{-1} and 180 cm^{-1} (Figure 35). The couplings are much bigger in the *para*-series, for which V_{12} is ca. 900 cm^{-1} for acceptor substituted MV compounds (X = NO_2 to Cl), but rises clearly for **pMe**$^{\bullet+}$ (1140 cm^{-1}) and **pOMe**$^{\bullet+}$ (1320 cm^{-1}).

The couplings of the *meta*46-series again show intermediate behavior between those of the **mX**$^{\bullet+}$ and **pX**$^{\bullet+}$ series. The magnitude of these couplings places the thermal HT of all

[4] The UDFT optimizations and TD-DFT computations were by Dr. Marco Holzapfel.[181]

compounds in the so-called adiabatic regime. Here, a limiting factor is the motion over the transition state which is possibly subject to solvent dynamics.

The TD-DFT method was also used to estimate the electronic coupling from half of the lowest excitation energy $E_{ab}(TS)/2 = V_{12,TS}$ which was calculated at the HT transition state, which directly corresponds to half the splitting of adiabatic potentials at the avoided crossing. On the one hand the obtained couplings are in good agreement with V_{12} for the *meta*-series **mX$^{\bullet+}$**. On the other hand for **pX$^{\bullet+}$** the calculations seem to exaggerate the influence of the substituents, underestimating the values obtained for X = Cl–NO_2 and overestimating the couplings for **pOMe$^{\bullet+}$**. For the **mX46$^{\bullet+}$** series with X = CN–Me, $V_{12,TS}$ is in reasonable agreement to V_{12}, while for **mOMe46$^{\bullet+}$** the coupling is too high.

Table 14: TD-DFT computed data in $PhNO_2$

		E_{ab} / cm^{-1}	μ_{ab} / D[a]	$\Delta\mu_{ab}$ / D	V_{12} / cm^{-1}	$E_{ab}(TS)/2 = V_{12,TS}$ / cm^{-1}	ΔG^*_{MH} / cm^{-1}	ΔG^*_{TS} / cm^{-1}
mX46	**mOMe46$^{\bullet+}$**	7256	7.57	62.83	850	1137	1063	1005[b]
	mMe46$^{\bullet+}$	8216	2.39	70.23	279	183	1784	1837
	mCl46$^{\bullet+}$	8800	1.09	72.55	133	166	2069	2089[b]
	mCN46$^{\bullet+}$	9442	1.29	72.70	167	221	2196	2151
mX	**mOMe$^{\bullet+}$**	8496	0.55	72.83	64		2061	
	mMe$^{\bullet+}$	8480	1.55	73.76	178	209	1946	2273[c]
	mCl$^{\bullet+}$	8904	0.84	74.61	100	156	2127	2142
	mCN$^{\bullet+}$	9271	1.33	73.83	167	192	2153	2165[b]
	m$NO_2^{\bullet+}$	9382	1.30	74.55	163		2185	
pX	**pOMe$^{\bullet+}$**	7414	12.48	65.57	1319	1825	769	628[c]
	pMe$^{\bullet+}$	8106	10.47	71.51	1139	1094	1048	1119
	pCl$^{\bullet+}$	8829	8.29	76.38	937	581	1370	1482
	pCN$^{\bullet+}$	9237	7.57	77.24	888	415	1506	1622
	p$NO_2^{\bullet+}$	9267	7.85	75.01	950	426	1464	1579

[a]Projection of transition moment onto the dipole moment difference vector $\Delta\mu_{ab}$. [b]Minimum according to frequency calculation. [c]Two imaginary frequencies.

The reorganization energy E_{ab} (= IVCT energy) and the electronic coupling V_{12} can be used to calculate the thermally activated HT barrier ΔG^*_{MH} for the HT process via equation (13). For the **pX$^{\bullet+}$** series, one observes a reduction of the HT barrier from 1464 cm^{-1} to 769 cm^{-1} while increasing the electron donating character of X. This behavior can be explained by an increasing charge delocalization, which results in a smaller effective adiabatic charge

transfer distance $r_{ab} = \Delta\mu_{ab}/e$. As a consequence the reorganization energy $\lambda = E_{ab}$ gets reduced by up to 20% via its solvent part (λ_o) which directly depends on r_{ab} as can be seen in the following equation:[182]

$$\lambda_o = \frac{e^2}{4\pi\varepsilon_0}\left[\frac{1}{2r_a}+\frac{1}{2r_b}-\frac{1}{r_{ab}}\right]\left[\frac{1}{n^2}-\frac{1}{D}\right] \qquad (14)$$

where r_a and r_b are the radii of donor and acceptor (assuming spherical geometry), n is the refraction index and D is the dielectric permittivity of the solvent. This correlation is usually disregarded in standard electron transfer theories in which reorganization energy is treated independent of the electronic coupling. In the **mX**$^{\bullet+}$ systems these effects are less pronounced. The DFT calculations show small and weakly varying electronic couplings V_{12} and a decrease of E_{ab} by only ca. 900 cm^{-1} on going from **mNO$_2$**$^{\bullet+}$ to **mOMe**$^{\bullet+}$, being significantly smaller compared to the decrease of 1900 cm^{-1} in the *para*-series. The **mX46**$^{\bullet+}$ series shows the same behavior as **pX**$^{\bullet+}$, exhibiting a somewhat lower decrease of E_{ab} by 1200 cm^{-1}, but an even stronger increase of V_{12}.

Figure 35 shows a plot of the HT barrier ΔG^*_{MH}, the electronic coupling V_{12}, and the hypothetical barrier in the absence of electronic coupling (= $E_{ab}/4$, see equation (13)) to visualize the dependency between HT barrier and coupling.

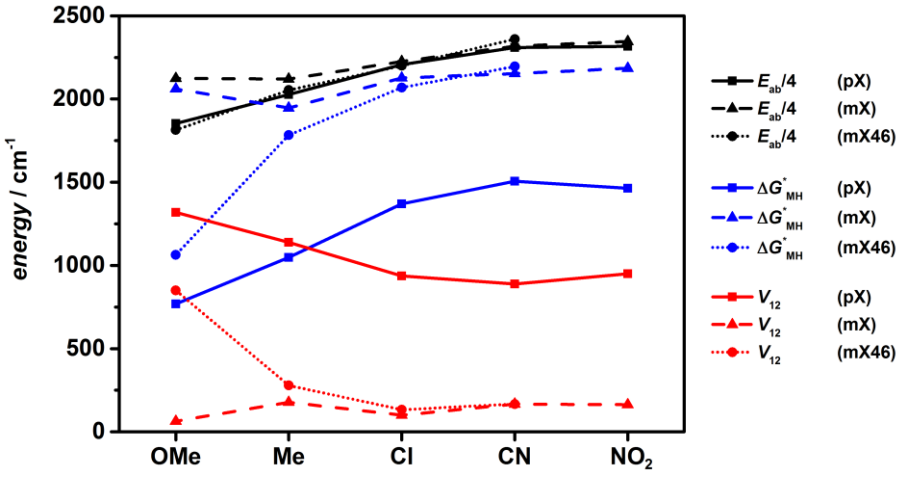

Figure 35: Plot of the DFT computed potential energy parameters $E_{ab}/4$ (black lines), ΔG^*_{MH} (blue lines) and V_{12} (red lines) for **pX**$^{\bullet+}$ (solid lines), **mX**$^{\bullet+}$ (dashed lines) and **mX46**$^{\bullet+}$ (dotted lines) in $PhNO_2$.

For the **mX**$^{\bullet+}$ series $E_{ab}/4$ and ΔG^*_{MH} agree very well. They are almost independent of the substituent and decrease for X = OMe and Me. The couplings remain for all **mX**$^{\bullet+}$

compounds at a low value. However, for **pX$^{\bullet+}$**, E_{ab}/4 decreases just to a small extent, while ΔG^*_{MH} decreases strongly for **pMe$^{\bullet+}$** and **pOMe$^{\bullet+}$**, and simultaneously V_{12} rises by almost the same amount. **mX46$^{\bullet+}$** shows an analogous but even more pronounced behavior. This observation is a focus point of the following discussion (3.3.4) and will lead to the formation of an appropriate rate theory for describing the dynamic HT processes.

Another possibility to estimate the HT barrier is to use the energy difference ΔG^*_{TS} between the optimized ground state structure and the symmetric transition state structure. For all MV compounds in this study, the obtained data for ΔG^*_{TS} are in close agreement to ΔG^*_{MH} (Table 14), which demonstrates the correctness of the underlying assumption of adiabatic Gibbs energy surfaces constructed from harmonic potentials, i.e. *Marcus-Hush* theory, and the applicability of *Mulliken-Hush* theory to estimate the electronic coupling. Nevertheless, at least some differences are discernable. The HT barriers ΔG^*_{TS} and ΔG^*_{MH} (among others) for the *para*-series are plotted in Figure 36, A. For **pX$^{\bullet+}$** with X = NO_2 to Me ΔG^*_{TS} is somewhat higher than ΔG^*_{MH}. However for **pOMe$^{\bullet+}$** the opposite is true. In previous work of *Lambert et al.* reported low lying bridge states for **pOMe$^{\bullet+}$** which distort the ground state hypersurface leading to the appearance of a third minimum on the ground state hypersurface, where the hole is localized at the bridging unit, which might result in a decrease of the TS energy.[98, 183] This finding could play a role in the present study indicating a more complex hypersurface structure at the transition state, which might be shown by the two imaginary frequencies of the "transition state" of **pOMe$^{\bullet+}$** (Table 14).

As already mentioned above, the influence of the solvent dielectric properties on the reorganization energy is one important aspect in *Marcus* ET theory. Thus, the performance of the DFT computations in different solvents for one exemplary chosen MV compound, **pCN$^{\bullet+}$**, was tested.

The calculated values in less polar *o*DCB and in the intermediately polar DCM are listed in Table 15. Although the IVCT band energy E_{ab} (i.e. reorganization energy) is bathochromically shifted, just the values obtained for $PhNO_2$ (9237 cm^{-1}) and DCM (8033 cm^{-1}) are in good agreement to the experimental data. In *o*DCB (8033 cm^{-1} compared to 6680 cm^{-1} in the experiment) the bathochromic shift is clearly too small. In addition to that the transition dipole moments, dipole moments and the electronic coupling are markedly less solvent dependent. Accordingly, the HT barrier drops from $PhNO_2$ to *o*DCB because of (and in the same way as) the smaller IVCT band energy.

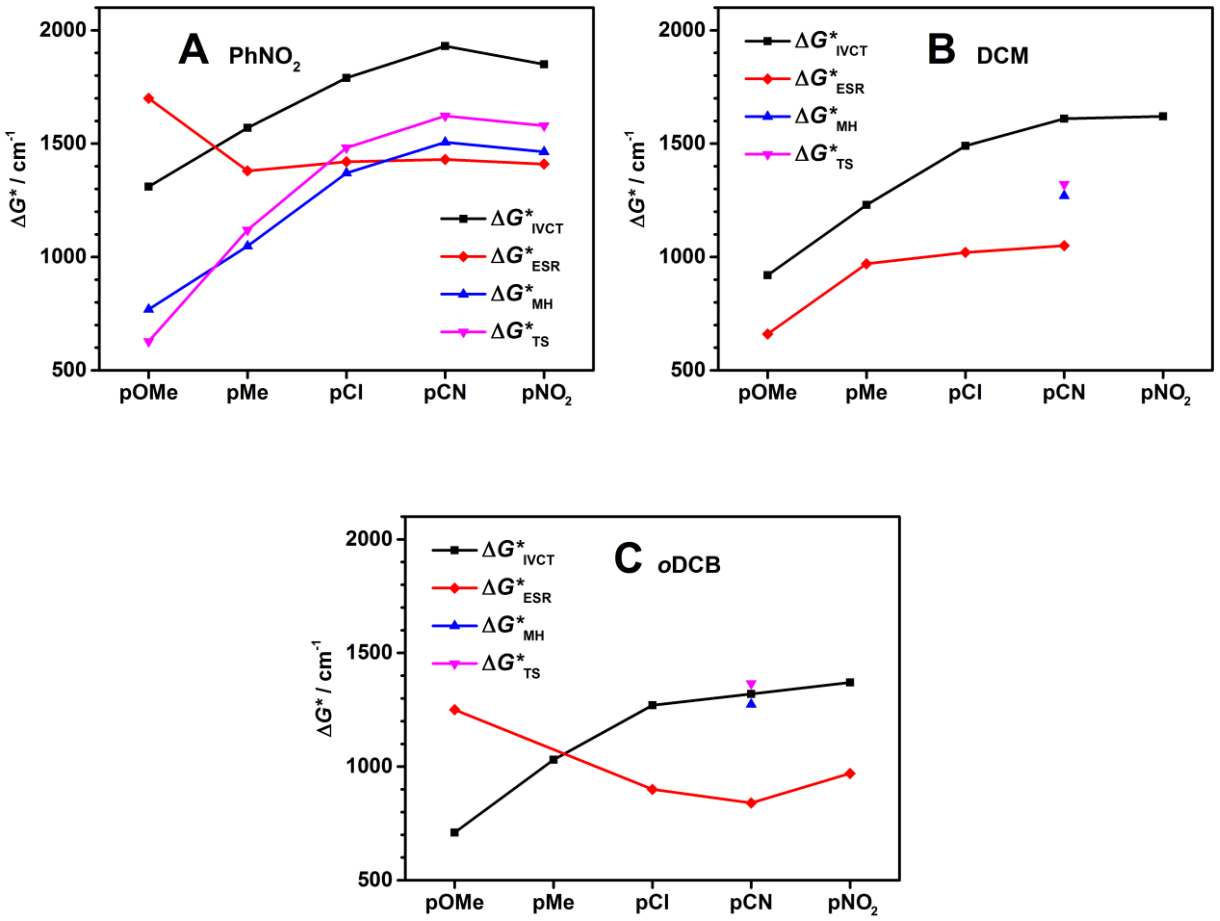

Figure 36: Plot of the hole transfer barriers Δ*G** determined by IVCT analysis (Δ*G**$_{IVCT}$), temperature dependent ESR spectroscopy (Δ*G**$_{IVCT}$), DTF calculation using the *Mulliken-Hush* formalism (Δ*G**$_{MH}$) or calculations at the transition state (Δ*G**$_{TS}$) in $PhNO_2$ (A), DCM (B) and *o*DCB (C).

Table 15: TD-DFT computed data for **pCN**$^{\bullet+}$ in $PhNO_2$, DCM and *o*DCB.

		E_{ab} / cm^{-1}	μ_{ab} / D[a]	$\Delta\mu_{ab}$ / D	V_{12} / cm^{-1}	$E_{ab}(TS)/2 = V_{12,TS}$ / cm^{-1}	ΔG^*_{MH} / cm^{-1}	ΔG^*_{TS} / cm^{-1}
pCN$^{\bullet+}$	$PhNO_2$	9237	7.57	77.24	888	415	1506	1622
	DCM	8026	8.12	77.78	820	760	1270	1321[b]
	*o*DCB	8033	8.10	77.94	817	429	1274	1366[b]

[a]Projection of transition moment on the dipole moment difference vector $\Delta\mu_{ab}$. [b]Minimum according to frequency calculation.

3.3.4 Discussion of the HT Dynamics

In order to explain the observed the HT dynamics within the MV bisTAAs compounds rate constants k_{ESR} and HT barriers ΔG^* (eq. 1) were attempted to be calculated using established electron transfer theories.[30] The most relevant solvent dependent parameter like e.g. longitudinal solvent relaxation time τ_L or dielectric constants of the solvent (ε) for PhNO2, *o*DCB and DCM are listed in Table 16 at the end of this chapter.
The rate constants of electron transfer processes can be defined by equation (15).

$$k = A \times e^{-\frac{\Delta G^*}{k_B T}} \tag{15}$$

In principle four different theories could apply to the HT process in the present setting. These models differ in the pre-exponential factor *A* which is related to the coupling matrix element and the dielectric relaxation properties of the solvent.[184] The four theories are based the assumption of:

1) a strongly diabatic limit, with an electronic coupling $V << k_B T$
2) being strongly adiabatic with a solvent dynamic controlled situation with cusped barrier
3) being strongly adiabatic with a solvent dynamic controlled situation with parabolic barrier
4) adiabatic transition state theory

In case 1), the strong diabatic limit (electronic coupling $V << k_B T$), the prefactor A_{PT} is given by equation (16). It is based on the perturbation theory (therefore PT; *Fermi's Golden Rule*) and depending on the square of the electronic coupling *V*.

$$A_{PT} = \frac{2\pi}{\hbar} \frac{{V_{12}}^2}{\sqrt{4\pi\lambda_o k_B T}} \tag{16}$$

The rates received under this assumption are too high for the MV compounds investigated in this work. Here the electronic coupling *V* is much too high to describe the HT process as diabatic.
In case 2), the strong adiabatic dynamic solvent controlled regime (DSE) with cusped barrier, the prefactor A_{PT} is given by equation (17). It describes a cusped shape of the ground state

free energy surface at the TS and is appropriate for small coupling. Here the prefactor depends mostly on the longitudinal solvent relaxation time τ_L.

$$A_{DSE} = \frac{1}{\tau_L}\sqrt{\frac{\lambda_o}{16\pi k_B T}} \tag{17}$$

Rates received under this assumption are too low for the MV compounds investigated in this work.

In situation 3), the strong adiabatic, solvent friction controlled regime with parabolically shaped free energy surface (PAR) at the TS, the prefactor A_{PAR} is given by equation (18). Just as in 2) solvent controls the dynamics by the longitudinal solvent relaxation time τ_L, but a larger coupling is taken into account by using a parabolically shaped TS surface.

$$A_{PAR} = \frac{1}{\tau_L}\sqrt{\frac{\lambda_o}{8\pi V_{12}} - 1} \tag{18}$$

In case 4), applying adiabatic transition state theory (TST), with uniform motion to the TS, the pre-exponential factor A can be described as a well frequency, following equation 19.[185]

$$A_{TST} = \frac{1}{2\pi}\sqrt{\zeta\frac{k_B T}{I}} \tag{19}$$

$$\text{with } \zeta = \frac{2\varepsilon_s + \varepsilon_\infty}{3\varepsilon_s g}$$

Where ε_s and ε_∞ are the static and optical dielectric constants of the solvent, respectively. *g* is the *Kirkwood* correlation factor and *I* is the average moment of inertia of the solvent molecule, which is given by:

$$I = 2\sqrt{\left(\frac{1}{I_x} + \frac{1}{I_y}\right)} \tag{20}$$

The calculation of the well frequency from the moment of inertia of the solvent was done following eq. 2 and A.4 according to the work of *McManis et al.*[185] The moments of inertia for $PhNO_2$ are $I_x = 652 \times 10^{-47}$ and $I_y = 862 \times 10^{-47}$ kg m^2 which gives an average moment of inertia $I = 742 \times 10^{-47}$ kg m^2.[186] For *o*DCB ($I_x = 1011 \times 10^{-47}$ and $I_y = 578 \times 10^{-47}$ kg m^2)

$I = 736 \times 10^{-47}$ kg m^2 and for DCM (with $I_x = 26.2 \times 10^{-47}$ and $I_y = 273.7 \times 10^{-47}$ kg m^2) $I = 48 \times 10^{-47}$ kg m^2.[187, 188]

Rips and *Jortner* suggested inequalities (22) based on the adiabaticity parameter κ_A to decide upon the electron transfer regime and, thus, which prefactor applies.[189] For κ_A (21) holds:

$$\kappa_A = \frac{4\pi V^2 \tau_L}{\hbar \lambda_o} \tag{21}$$

$$\frac{1}{\pi}\left(\frac{k_B T}{V_{12}}\right)^2 2\zeta\omega_{rot}\tau_L \ll \kappa_A \leq \frac{4\pi}{2\zeta\omega_{rot}\tau_L} \tag{22}$$

$$\text{with } \omega_{rot} = \frac{\hbar}{I}$$

where ω_{rot} is the rotation frequency of the solvent molecules. If κ_A lies in the interval given by inequality (**22**), transition state theory (TST) is valid. If κ_A is smaller than the term of the inequality the HT takes place under diabatic conditions. If κ_A is significantly larger than the right-hand term, it is adiabatic and controlled by solvent dynamics. For most MV compounds here (e.g. with $V_{12} = 200$ cm^{-1}, $\lambda_o = 6000$ cm^{-1}, $\tau_L = 4.3 \times 10^{-12}$ s^{-1}, $I = 742 \times 10^{-47}$ kg m^2, $\varepsilon_s = 35.90$, $\varepsilon_\infty = 3.48$, $g = 1$) the adiabaticity parameter κ_A is larger than unity (e.g. $\kappa_A = 67.8$). Being larger than the left term in inequality (22) (e.g. 0.029), but smaller than the right-hand term (e.g. 147), indicates a uniform adiabatic behavior as described by TST. Contrary if the coupling constant V_{12} is much higher (e.g. 1000 cm^{-1}), the adiabaticity parameter κ_A (e.g. 1697) is much larger than then the right-hand term. Now the solvent controlled dynamics dominate, which is covered by case 3).

For case 3) the temperature dependence of τ_L is given by:[190]

$$\frac{1}{\tau_L} = \frac{1}{\tau_{L0}} e^{\left(-\frac{H_L}{k_B T}\right)} \tag{23}$$

resulting in an increase of the effetive HT barrier by H_L. τ_{L0} and H_L were determined by linear fit of ln ($1/\tau_L$) vs $1/T$ with data calculated by:

$$\tau_L = \left(\frac{\varepsilon_\infty}{\varepsilon_S}\right) \tau_D \tag{24}$$

where τ_D is the *Debye* relaxation time. In this temperature range the barrier H_L amounts to 1439 cm^{-1} ($\tau_{L0} = 3.55 \times 10^{-15}$ s) for nitrobenzene, which was determined using data reported

in literature.[191] However, such a high contribution of H_L to the total barrier would mean that the intrinsic Marcus barrier $E_{ab}/4$ (and thus the reorganization energy) would be unreasonably small.

Case 4) seems to be suitable to estimate the electronic coupling and the reorganization energy from the experimental barriers for electronic couplings on the order of 100–600 cm^{-1} considering the high moment of inertia of nitrobenzene. Following equation (8) with prefactor A_{TST} for the *meta*-series (V_{12} = 200 cm^{-1} and λ_o = 6000 cm^{-1}, λ_v = 2000 cm^{-1}) reasonable rate constants (k_{TST} = 1.5 × 10^7 s^{-1}) and HT barriers (ΔG^* = 1805 cm^{-1}) were obtained in comparison with the experimental data. For the *para*-series (V_{12} to 600 cm^{-1} and λ_o = 6000 cm^{-1}, λ_v = 2000 cm^{-1}) with X = NO_2 to Me reasonable rate constants (k_{TST} = 8.6 × 10^7 s^{-1}) and HT barriers (ΔG^* = 1445 cm^{-1}) were obtained, too. In contrast to this, the remarkably high rate constants and HT barriers of both **pOMe$^{\bullet+}$** and **mOMe46$^{\bullet+}$** could not be modelled adequately solely under use of case 3) or 4).

As already mentioned above, using large coupling constants V_{12} the adiabaticity parameter κ_A is much larger than then the right-hand term in inequality (**22**) hinting to a regime controlled by solvent dynamics. To take the solvent dynamics into account an interpolation between the TST and the PAR regime, as given by equation (25), was done:

$$k = \frac{k_{PAR} \times k_{TST}}{k_{PAR} + k_{TST}} \tag{25}$$

By use of this interpolation (and V_{12} = 1200 cm^{-1} and a somewhat smaller λ_o of 5000 cm^{-1}) reasonable values of k = 74 × 10^7 s^{-1} and ΔG^* = 1700 cm^{-1} were obtained. These values are in much better agreement with the experimental values for **pOMe$^{\bullet+}$** (k_{ESR} = 57 × 10^7 s^{-1}, ΔG^*_{ESR} = 1700 cm^{-1}) and **mOMe46$^{\bullet+}$** (k_{ESR} = 40 × 10^7 s^{-1}, ΔG^*_{ESR} = 1970 cm^{-1}).

The fundamental finding is that apparently the higher electronic coupling in **pOMe$^{\bullet+}$** and **mOMe46$^{\bullet+}$** shifts the system towards the solvent dynamically controlled regime and as a consequence both the barrier *and* the rate constant increase compared with the respective values for **pMe$^{\bullet+}$**. The former increase is caused by the additional activation energy H_L in the pre-exponential term.

To test the validity of the interpretation the values determined for the *para*-series in *o*DCB and DCM solvents were calculated using the same approach. As will be shown in the following, *o*DCB is a significant less polar solvent compared to $PhNO_2$ that nonetheless shows a very similar longitudinal solvently relaxation time τ_L. DCM is less polar than $PhNO_2$, too, but somewhat more polar than *o*DCB. However, the relaxation time is much shorter.

By use of TST for **pNO$_2$$^{\bullet+}$**, **pCN$^{\bullet+}$**, and **pCl$^{\bullet+}$** in *o*DCB (e.g. with V_{12} = 300 cm^{-1}, λ_o = 3500 cm^{-1}, λ_i = 2000 cm^{-1}, I = 736 × 10^{-47} kg m^2, ε_s = 9.93, ε_∞ = 2.03 and g = 1) value of

$k = 50 \times 10^7\ s^{-1}$ and $\Delta G^* = 1091\ cm^{-1}$ were obtained. Although not as satisfactory as in $PhNO_2$, they are in good agreement with the experimental data. However, within TST no reasonable combination of parameters could be found which for **pOMe$^{\bullet+}$**, that reproduced the observed values satisfactorily. On the other hand, the approach of interpolation between the solvent dynamic and the PAR regime results in values which are in good agreement with the experimental data. Applying equation (25) with equations (18), (19) and (23) (with λ_o = 3000 cm^{-1}, V_{12} = 1000 cm^{-1}) and assuming a temperature dependence of the longitudinal solvent relaxation with a somewhat lower barrier of H_L = 1080 cm^{-1} for *o*DCB as $PhNO_2$ gives $k = 176 \times 10^7\ s^{-1}$ and $\Delta G^* = 1278\ cm^{-1}$.Therefore, H_L of oDCB had to be calculated seperatly, since no temperature dependent dielectric data are available in literature. For *o*DCB τ_L at 298 K was estimated from τ_D = 24.8 ps, ε_S = 9.93 and $\varepsilon_\infty = n^2$ with *n*= 1.549 to be 6.0 ps.[56] The viscosity η should have a similar temperature dependence as the *Debye* relaxation time τ_D which in turn has a similar temperature dependence as τ_L (provided that the dielectric permittivities ε_S and ε_∞ have negligible temperature dependence). For $PhNO_2$ a plot of ln(η) with 1/*T* displays a good linear correlation with a barrier of 14.1 kJ mol^{-1}.[192, 193] For *o*DCB the correlation yields a barrier of 10.6 kJ mol^{-1}. Thus, for *o*DCB the rather precise H_L barrier of $PhNO_2$ (17.22 kJ mol^{-1}) was reduced by the same factor by which the viscosity barrier of *o*DCB is smaller than that of $PhNO_2$ which gave H_L = 12.9 kJ mol^{-1} (1080 cm^{-1}). In order to obtain τ_L = 6.0 ps at 295 K the τ_{L0} must be 3.11 x 10^{-14} s.

The barriers and coupling constants for the *para*-series in DCM are good agreement with experiment, too. Assuming similar HT parameters for X = CN and Cl (e.g. with V_{12} = 200 cm^{-1}, λ_o = 4000 cm^{-1}, λ_v = 2000 cm^{-1}, $I = 48 \times 10^{-47}$ kg m^2, ε_S = 8.83, ε_∞ = 1.98 and *g* = 1) TST gives $k = 68 \times 10^7\ s^{-1}$ and $\Delta G^* = 1307\ cm^{-1}$. Although somewhat larger, the data show a satisfying accordance with those observed for X = CN and Cl. Increasing the electronic coupling to $V_{12} = 1200\ cm^{-1}$ (as determined for e.g. **pMe$^{\bullet+}$**) and applying the interpolation between the solvent dynamic TST and the PAR regime approach gives a barrier of 721 cm^{-1} with $k = 1133 \times 10^7\ s^{-1}$.

Thus, in contrast to $PhNO_2$ and *o*DCB, in DCM the barrier in **pX$^{\bullet+}$** becomes smaller with an increasing rate constant. This is caused by the relaxation constant of DCM which impacts the HT by only a small barrier $H_L = 401\ cm^{-1}$, which was determined in analogy to those of *o*DCB: at 298 K τ_L was estimated from τ_D = 2.17 ps, ε_S = 8.83 and ε_∞ = 1.98 to be 0.49 ps.[47, 80, 180] Again assuming that the temperature dependence of the longitudinal relaxation time is the same as that of the Debye relaxation, values of H_L = 401 cm^{-1} and τ_{L0} = 7.05 x 10^{-14} s were obtained.

The obtained data prove that the rise of the HT barrier for **pOMe**$^{\bullet+}$ in $PhNO_2$ and in *o*DCB is indeed caused by the additional barrier exerted by the solvent dynamics. This behavior can now be described accurately by interpolation between the solvent dynamic TST and the PAR regime.

It is important clarify that what was measured by ESR spectroscopy is an "apparent" barrier, calculated as the derivative of $\ln(k_{ESR}/T^{1/2})$ vs. $1/T$. It is a combination of the intrinsic Marcus barrier as defined by equation (13), and when the solvent dynamic regime in entered, a not to be ignored solvent dependent barrier.

Although not directly obvious, in the ESR measurements the intrinsic *Marcus* barrier decreases for both **pOMe**$^{\bullet+}$ and **mOMe46**$^{\bullet+}$ as a result of the deformation of the hypersurface in the TS region, in analogy to the observations from both the analysis of the IV-CT band and the DFT computations. This relationship gets clear when looking at Figure 36. Here, the barriers of the **pX**$^{\bullet+}$ compounds obtained by IVCT analysis, ESR measurements and DFT computations (using MH and TS approach) are plotted for $PhNO_2$ (A), DCM (B), and *o*DCB (C).

Although the HT barrier for the IVCT is significantly higher than the calculated barriers, they three follow the same trend. However, the most interesting aspect is the deviating behavior of the ESR-determined apparent barriers. While there is a very good agreement with the DFT computed values for X = NO_2 to Cl, the transition of the HT mechanism towards the solvent dynamic regime leads to an increase of the apparent barrier for **pMe**$^{\bullet+}$ and, in particular, **pOMe** $^{\bullet+}$. The same holds true for the barriers in *o*DCB, in contrast those determined in DCM. Since the solvent dynamics barrier does not add much to the intrinsic barrier, the overall apparent barriers do not rise for neither for **pMe**$^{\bullet+}$ nor for **pOMe**$^{\bullet+}$.

Table 16: Solvent parameter of $PhNO_2$, *o*DCB and DCM.

	I / 10^{-47} kg m^2	ε_S	ε_∞	g	τ_L / 10^{-12} s	τ_{L0} / 10^{-15} s	τ_D / 10^{-12} s	H_L / cm^{-1}
$PhNO_2$	742	35.9	3.48	1	4.3	3.55		1439
oDCB	736	9.93	2.03	1	6.0	31.1	24.8	1080[b]
DCM	48	8.83	1.98	1	0.49	70.5	2.17	401

3.3.5 Discussion of the Electronic Coupling

The optical IVCT and the thermal ESR analysis revealed, that not only the orientation of the two TAA at the bridging unit, but also the attachment and electron donating/accepting character of the substituent X at the benzene unit is crucial to the HT properties of the MV compounds. This study showed that the rate constant of **mOMe46**$^{\bullet+}$ is similar to **pOMe**$^{\bullet+}$ or **pMe**$^{\bullet+}$, while the rate constant of **mMe46**$^{\bullet+}$ is similar to **pX**$^{\bullet+}$ with X = CN to NO_2. That is not the case for the constitutional isomers **mOMe**$^{\bullet+}$ and **mMe**$^{\bullet+}$, with substituents X in the 1,4-position. Here, the electron donating methoxy or methyl groups have no influence on the bridge resulting in transfer rates identical to **mX**$^{\bullet+}$ with X = CN to NO_2. Placing strong donor substituents in 4,6-position at the central benzene bridge in the *meta*-series can accelerate the HT to enter the regime observed for the *para*-series. This is most likely caused by a surprisingly large electronic coupling in the **mOMe46**$^{\bullet+}$ as can be seen from the data in Table 12 and Table 14.

As shown above, the IV-CT energy at the TS corresponds is twice the electronic coupling V_{12}. This excitation is caused by the promotion of an electron from the β-HOMO to the β-LUMO orbital. These orbitals were calculated by unrestricted UDFT computation, where the α-orbitals contain n and the β–orbitals $n-1$ electrons in different spin orbitals, exemplarily for the methyl substituted MV compounds **mMe46**$^{\bullet+}$, **mMe**$^{\bullet+}$ and **pMe**$^{\bullet+}$. The obtained orbitals are depicted in Figure 37.

Electron donating substituents like Me and in particular OMe exert a destabilizing influence on the MOs, when they are attached to positions with significant orbital coefficient at the benzene bridge. Consequently the β-LUMOs of **mMe46**$^{\bullet+}$, **mMe**$^{\bullet+}$ and **pMe**$^{\bullet+}$ are destabilized, but the magnitude of destabilization varies clearly. For **mMe46**$^{\bullet+}$ and **pMe**$^{\bullet+}$, the destabilization is more pronounced since the two Me groups are each attached to positions with significant orbital coefficient at the benzene bridge. In **mMe46**$^{\bullet+}$ only one of the methyl substituents is attached to a position of this type, destabilizing the orbital to a much lesser extent. In this way, the symmetry of the involved MOs and the position of the substituents play a decisive role in determining the electronic coupling.

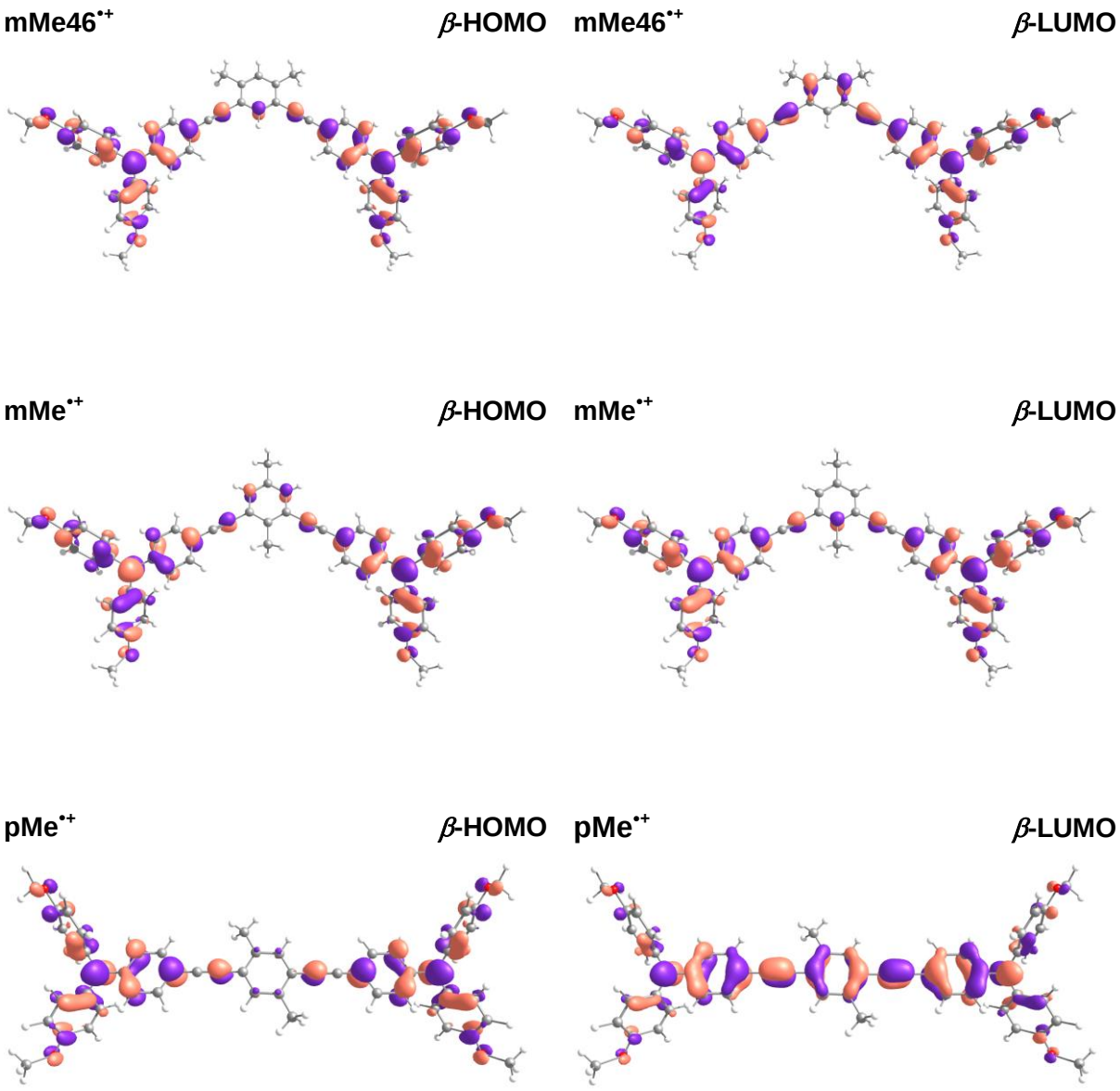

Figure 37: UDFT computed β-HOMO and β-LUMO of **mMe46**$^{\bullet+}$, **mMe**$^{\bullet+}$ and **pMe**$^{\bullet+}$ that are responsible for the lowest energy excitation at the geometry of the TS.

3.4 Conclusions

The main conclusions of this part of the work are summarized in Figure 38, visualizing the unforeseen observation found concerning the HT rate constants k_{ESR} and the apparent (ESR measured) HT barriers ΔG^*_{ESR}. While the HT rate constants and the barriers HT barriers of the *meta*-series are quasi unaffected by the substituents X, for the *para*-series electron donating substituents show a strong impact. Amazingly, the HT rate constants *and* the HT barriers increase simultaneously for **pMe**$^{\bullet+}$ and **pOMe**$^{\bullet+}$ in $PhNO_2$ (and *o*DCB). This finding can be explained by an increasingly important solvent dynamic effect and an additional, effective barrier that is caused by the longitudinal solvent relaxation time.

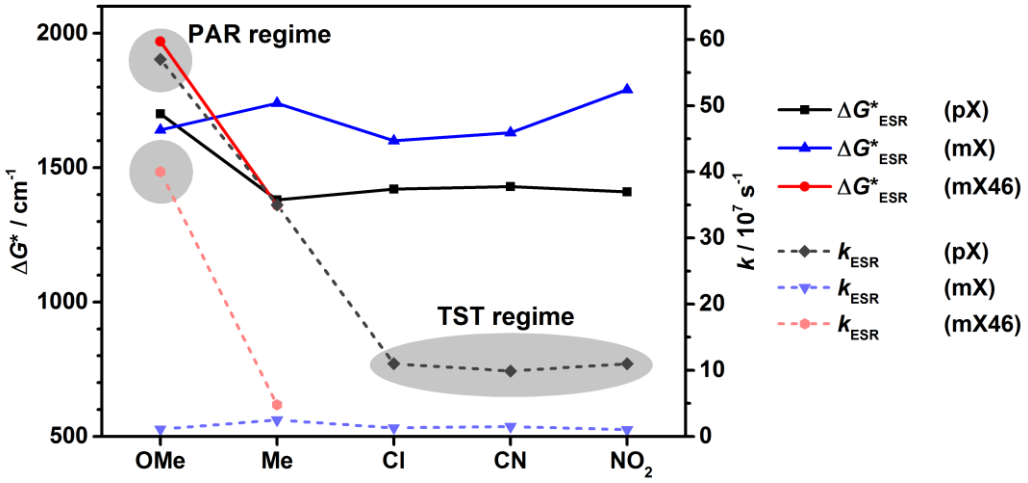

Figure 38: ESR determinated HT barriers ΔG^*_{ESR} (solid lines) and rate constants k_{ESR} (dashed lines) for MV compounds **pX**$^{\bullet+}$ (black), **mX**$^{\bullet+}$ (blue) and **mX46**$^{\bullet+}$ (red) in $PhNO_2$.

Here, a transition of mechanism from the regime where TST applies to the regime where a parabolically (PAR) shaped transition state, in which CT is controlled by solvent dynamics, can clearly be observed. Understandably, this method of approach is limited for reactions in solution. Nevertheless, the findings of this study elucidates the general influence of bridge substituents for any bridge moiety and, thus, is of crucial importance for e.g. organic electronic devices, be it on the molecular level or in the bulk. Here, the HT rate constants can easily be tuned in *para*-conjugated systems by attaching substituents to the bridge units, which is a result of orbital symmetry in the transition state.

While in the **pX**$^{\bullet+}$ series the substituents are attached to positions with a high orbital coefficient at the bridge, due to vanishing orbital coefficients these influences are much weaker in the **mX**$^{\bullet+}$ conjugated systems. The **mX46**$^{\bullet+}$ series shows an intermediate behavior: On the one hand the **mX46**$^{\bullet+}$ series with electron-withdrawing substituents behaves like the

mX$^{\bullet+}$ compounds. On the other hand, with electron-donating substituents they are rather similar to the **pX**$^{\bullet+}$ compounds.

Thereby, the findings in this work complement a study of *Grozema et al.*, presented in the introduction (chapter 1.6), which showed that hole-, electron- and mixed electron/hole-transfer pathways may experience different quantum interference effects depending on the involved bridge orbitals and their symmetry.[74, 75]

Furthermore, this part of the work shows, that the *meta*- or *para*- topology does no longer have to be the decisive factor for CT and can be overruled by substituent effects, which broadens the use of conjugative topologies for new applications such as organic field effect transistors or photovoltaic devices.

4 NEUTRAL DONOR-ACCEPTOR COMPOUNDS - RESULTS AND DISCUSSION[5]

4.1 Synthesis

The synthesis of the neutral *para*- and *meta*-substituted donor-acceptor (DA) compounds **pXNDI** and **mXNDI**, the *meta*-substituted DA compound with methoxy substituents in the 4,6-position **mOMe46NDI** and their references **sXNDI** and **sOMe46**, are presented in the following section. The synthesis of the reference compounds with one TAA attached to the benzene ring (**sX** and **sOMe46**) is presented in section 3.1.3.

The synthesis of the target molecules (TM) has the same approach as the bistriarylamine compounds in chapter 3.1. Indeed, according to this procedure some similar dyads with triarylamine (TAA) as donor and naphthalene diimide (NDI) as acceptor have been synthesized by *Lambert et al.*[102, 150, 166]

In Scheme 26, the first step of the retrosynthesis of the NDI substituted references **sXNDI** and **sOMeNDI46** is shown, which is a C-C bond cleavage between a benzene carbon atom and the ethynyl carbon atom. Since the C-C bond will later be formed by Pd catalyzed *Sonogashira-Hagihara* cross coupling between these two precursors, one halogen functionality at the benzene moiety and one acetylene functionalized naphthalene diimide unit (**eNDI**) are required. The synthesis of all needed (non-commercial available) mono halogenated benzene units is already described in chapter 3.1.2.

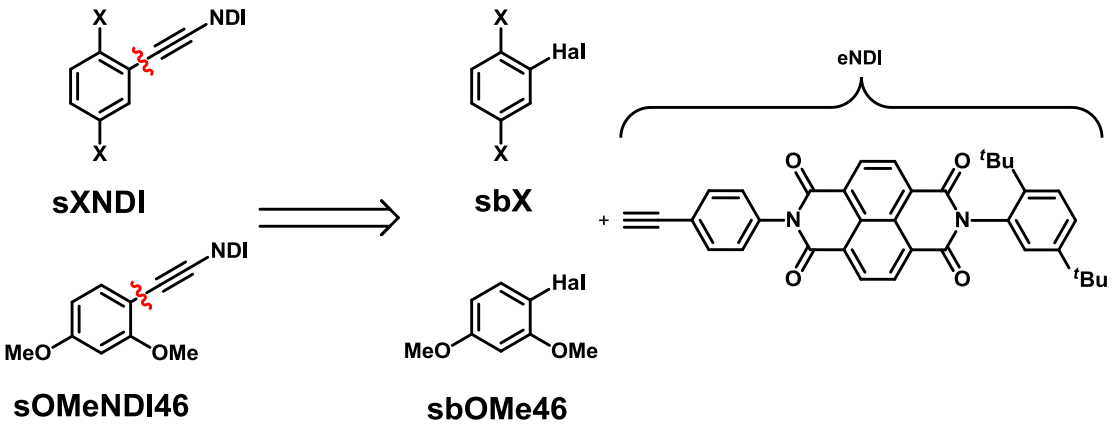

Scheme 26: Retrosynthesis of the NDI substituted references **sXNDI** and **sOMeNDI46**.

[5] Parts of this chapter have been investigated in a Bachelor thesis under supervision of J. Schäfer: *Synthese und photophysikalische Charakterisierung von Donor-Akzeptor-substituierten 1,4-Dimethoxybenzolen*, M. Krahfuß, Bachelor Thesis, Julius-Maximilians-Universität Würzburg, **2014**.

The DA compounds can be obtained by two different approaches, which are illustrated in Scheme 27, where the first two steps of the retrosynthesis of all dyads are shown.

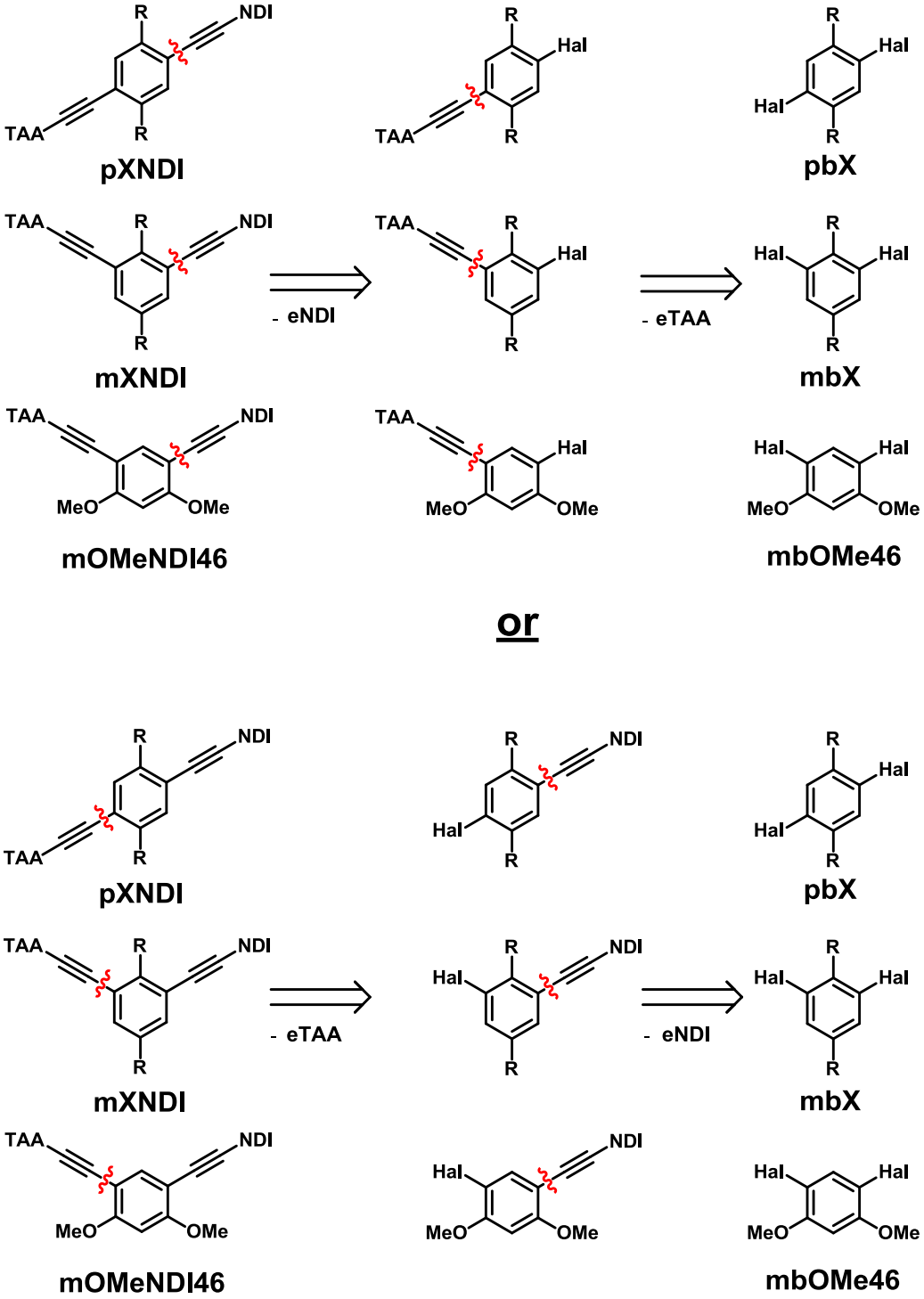

Scheme 27: Two different retrosynthesis routes of the DA compounds **pXNDI**, **mXNDI** and **mOMeNDI46**.

The retrosynthesis starts with one C-C bond cleavage between a benzene carbon atom and the ethynyl carbon atom. There are two possible C-C bonds available, the one connecting the TAA and the one connecting the NDI to the bridge. At this point one of the two synthetic pathways has to be chosen.
The respective C-C bond will later be formed by Pd catalyzed *Sonogashira-Hagihara* cross coupling between the two precursors. Thus, halogen functionality at the benzene moiety and acetylene functionality at either a triarylamine unit (**eTAA**) or a naphthalene diimide unit (**eNDI**) are required. The next retrosynthesis step is again a C-C bond cleavage between a benzene carbon atom the ethyl carbon atom, resulting in the second halogen functionality at the benzene ring and the respective **eNDI** or **eTAA**.
As will be shown later, both synthetic routes were used, depending on the substituent X at the bridging unit. As suitable halogen functionality the bromo functionality was preferentially chosen, since it is known to undergo reliable C-C cross couplings under *Sonogashira-Hagihara* conditions. With regard to the synthesis of the bisTAA compounds and **sX** reference with methoxy groups attached to the central benzene unit (chapter 3.1.3), the iodo functionality was chosen for the methoxy substituted benzenes here, too. The synthesis of all needed (non-commercial available) dihalogenated benzene units and **eTAA** is not discussed here, since it is already described in detail in chapter 3.1.2.

The synthesis of the TM in the following is divided into three parts. First the synthesis of the NDI acceptor moiety with ethynyl functionality, then the synthesis of the references (with NDI unit) and finally the synthesis of DA compounds by Pd-catalyzed cross coupling reactions will be discussed.

4.1.1 Synthesis of the Ethynyl Functionalized Naphthalene Diimide (eNDI)

The naphthalene diimide synthesis was done by reaction under microwave irradiation that is well established in our group (Scheme 28).[78, 113, 166] Accordingly, 2,5-di-*tert*-butylaniline and 4-ethynylaniline were treated with 1,4,5,8-naphthalenetetracarboxylic acid dianhydride in DMF. Two *tert*-butyl groups attached to one benzene ring were chosen since they are known to increase the solubility of **eNDI** and also the final TM.

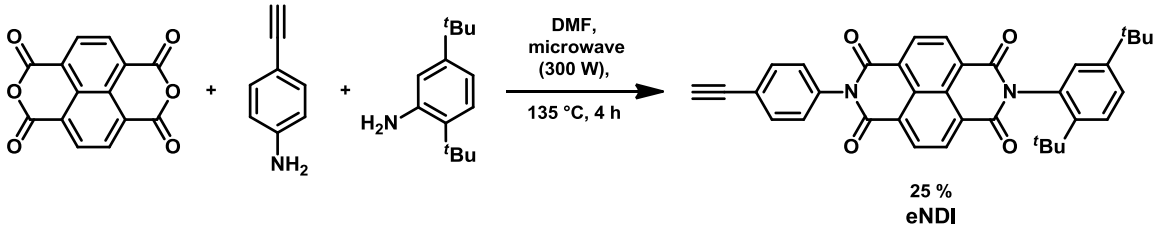

Scheme 28: Synthesis of **eNDI** in a microwave-assisted one-pot synthesis.

Within this dicondensation reaction statistical distribution led to several side products (mono- and dicoupled products) and a product yield of just 25 %. Nevertheless the one-pot synthesis of **eNDI** was preferred to a step-by-step addition of the amines, due to an easier workup procedure of the diimides compared to the naphthalene monoimide compounds and higher time efficiency.

4.1.2 Synthesis of the Dyads and their NDI Substituted References

The synthesis of the dyads **pXNDI**, **mXNDI** and **mOMeNDI46**, as well as the synthesis of the NDI substituted reference compounds **sXNDI** and **sOMeNDI46** is presented in the following. The synthesis of the TAA substituted reference compounds **sX** and **sOMe46** was already discussed in section 3.1.3.

Synthesis of the Reference Compounds sXNDI and sOMeNDI46

The single NDI substituted reference compounds **sXNDI** and **sOMeNDI46** were synthesized by *Sonogashira-Hagihara* coupling of the single iodinated (**sbOMe'** and **sbOMe'46**) or brominated (**sbMe** to **sbNO$_2$**) bridging units and the ethynyl functionalized naphthalene diimide (**eNDI**, Scheme 19).

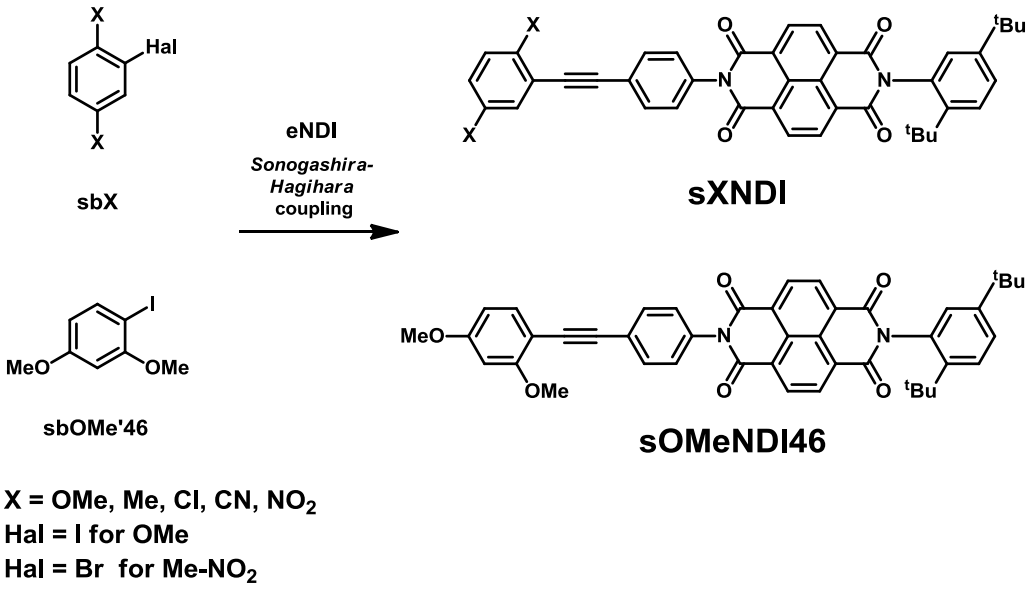

Scheme 29: Synthesis of the **NDI** substituted reference compounds.

The reaction conditions for the Pd-catalyzed couplings were the same as determined for the bisTAA compounds in section 3.1.3 (**GP$_{OMe}$** to **GP$_{NO2}$**) and not further optimized for the reactions shown here (Table 17). One approach for optimizing the couplings could be the variation of the solvent, since in the used solvents **eTAA** provides a higher solubility than **eNDI**. Nevertheless, with 1.0 or 1.1 eq. of **eNDI** under the **GP** conditions, satisfying (60 %, **sOMeNDI**) to good yields (82 %, **sClNDI**) were accomplished.

Table 17: Reaction conditions and yields for the synthesis of the reference compounds **sXNDI** and **sOMeNDI46**.

	Reaction Conditions	Bridge	Eq. eTAA	Product	Yield in %
GP_{OMe}	$Pd(PPh_3)_2Cl_2$, CuI, NEt_3, THF, 60 °C, 1 d	**sbOMe'**	1.1	**sOMeNDI**	60
		sbOMe'46	1.2	**sOMeNDI46**	67
GP_{Me}	$Pd(PPh_3)_2Cl_2$, CuI, P^tBu_3, HN^iPr_2 1,4-dioxane, 60 °C, 1–2 d	**sbMe46**	1.0	**mMe46**	75
GP_{Cl}	$Pd(C_6H_5CN)_2Cl_2$, CuI, P^tBu_3, HN^iPr_2, 1,4-dioxane, 60 °C, 1–2 d	**sbCl**	1.0	**sClNDI**	82
GP_{CN}	$Pd(PPh_3)_2Cl_2$, CuI, NEt_3, THF, 60 °C, 1–2 d	**sbCN**	1.2	**sCNNDI**	74
GP_{NO2}	$Pd(PPh_3)_2Cl_2$, CuI, NEt_3, toluene, 60 °C, 1 d	**$sbNO_2$**	1.0	**sNO_2NDI**	64

Synthesis of the OMe, Me and Cl Substituted Dyads

As already mentioned in the retrosynthesis section in 4.1, there are two possible pathways to synthesize the dyads. Either the TAA or the NDI unit is coupled with the bridge in the first step and the other respective unit in the second step. For this reason the methyl bridging units (**mb-/pbMe**) were tried to be coupled with **eNDI** and **eTAA** under *Sonogashira-Hagihara* coupling conditions, which were proven to be successful in the synthesis of the reference compounds **sX**, as shown in the previous chapter (3.1.3).

Using **GP_{Me}**, that is a catalytic system of $Pd(PPh_3)_2Cl_2$, CuI, P^tBu_3 and HN^iPr_2 in 1,4-dioxane with **pbMe** or **mbMe** and 0.5 eq. of **eNDI**, did not lead to the mono NDI substituted bridge as the main products (Scheme 30, Table 18). There were only traces found by mass spectroscopy, instead the dicoupled products were formed. Consequently, after the first addition of **eNDI** to **pbMe** or **mbMe**, respectively, these monocoupled intermediates must be more reactive than the non-coupled bridge. The same is true for the chloro compounds. Using **GP_{Cl}**, with the catalytic system $Pd(C_6H_5CN)_2Cl_2$, CuI, P^tBu_3 and HN^iPr_2 in 1,4-dioxane, and **pbCl** or **mbCl** and 0.5 eq. of **eNDI** result in the formation of the bisNDI compounds.

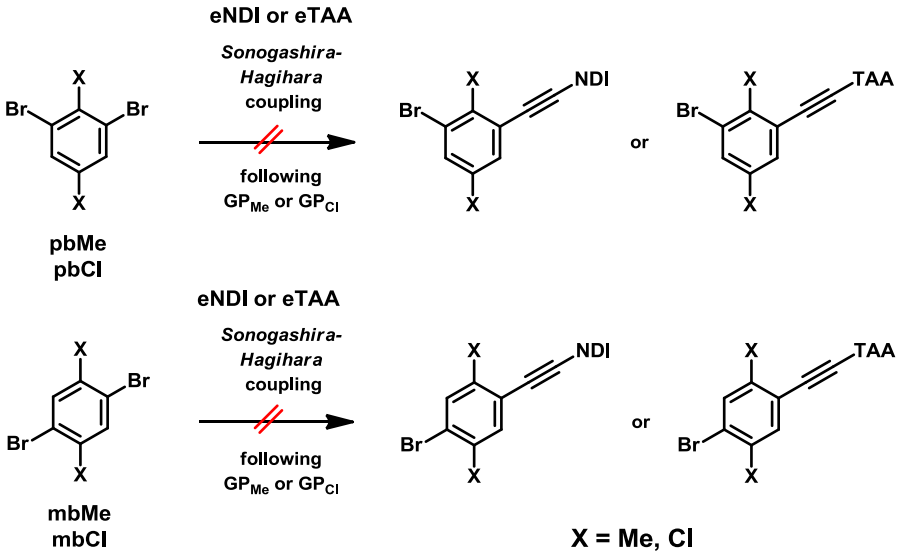

Scheme 30: Attempts to mono-couple **pb-/mbMe** or **pb-/mbCl** with **eTAA** or **eNDI** under **GP$_{Me/Cl}$** conditions.

Table 18: Reaction conditions tried to mono-couple **pb-/mbMe** or **pb-/mbCl** with **eTAA** or **eNDI**.

	Reaction Conditions	Reactant	Eq. NDI	Eq. TAA
GP$_{Me}$	$Pd(PPh_3)_2Cl_2$, CuI, P^tBu_3, HN^iPr_2, 1,4-dioxane, 60 °C, 3–5 d	**pbMe**	0.5	-
		mbMe	0.5	-
		pbMe	-	0.5
		mbMe	-	0.5
GP$_{Cl}$	$Pd(C_6H_5CN)_2Cl_2$, CuI, P^tBu_3, HN^iPr_2, 1,4-dioxane, 60 °C, 1–2 d	**pbCl**	0.5	-
		mbCl	-0.5	-
		pbCl		0.3
		mbCl		0.3

Therefore the synthesis of the TM was tried in different order. **pb-/mbMe** or **pb-/mbCl** were treated with 0.3 eq. of **eTAA** following the corresponding GP. Under this condition, again just doubly coupled products, namely **p-/mMe** or **p-/mCl**, were formed. But here, compared to the coupling attempts with **eNDI**, TLC analysis showed that the reaction time seemed to be much shorter. The latter led to the use of a "dilution principle apparatus"[194] (6.2.5, Scheme 34) and the creation of **GP$_{DPA}$**: Here the catalytic system, consisting of a Pd-source, CuI and NEt_3, and the bridges were heated under reflux and 0.1–0.2 eq. **eTAA** was added over a period of about 5 h dropwise to a reservoir of condensate, which slowly flowed back to the reaction

mixture. Using this experimental set-up, the highly diluted alkyne solution meets a highly concentrated solution of bridging units, which statistically leads to the mono-coupled product. Since $Pd(C_6H_5CN)_2Cl_2$ decomposes slowly at temperatures of ca. 75–80 °C, the more stable Pd source $Pd(PPh_3)_2Cl_2$ was chosen. In Addition to that, instead of 1-4-dioxane with a boiling point of 101 °C, THF with a boiling point of 66 °C was used to perform the reaction under mild conditions.

By use of these optimizations, coupling of **pb-/mbOMe'** or **mbOMe'46** with 0.1–0.2 eq. of **eTAA** the mono-substituted methoxy compounds **17**, **18** and **19** were synthesized in yields of 65 %, 84 % and 72 %, respectively (Scheme 31, Table 19). Additionally **17** could be formed using a step-by-step halogen exchange route starting from 1-bromo-3-iodo-2,5-dimethoxybenzene presented in chapter 3.1.3 (Scheme 24). Using $\mathbf{GP_{DPA}}$ and 0.2 eq. of **eTAA** and **mb-/pbMe** the methyl compounds **20** and **21** were obtained in ca. 75 % yield. The chloro compounds **22** and **23** could even be isolated with very good yields of ca. 95 %.

The last step of the synthesis of the methoxy, methyl and chloro dyads is a *Sonogashira-Hagihara* coupling with **eNDI** (Scheme 31). For every kind of substituent OMe to Cl the specific GP was used. Coupling **17**, **18** and **19** following $\mathbf{GP_{OMe}}$ with 1.0–2.1 eq. of **eNDI** the dyads **pOMeNDI**, **mOMeNDI** and **mOMeNDI46** were synthesized in yields of 79 %, 91 % and 80 % respectively (Table 19). Using 1.1–2.0 eq. of **eNDI** and **20**/**21**, the methyl compounds **pMeNDI** and **mMeNDI** were achieved in high yields of ca. 95 %. The chloro compounds **pClNDI** and **mClNDI** were isolated in good yields of ca. 85 %.

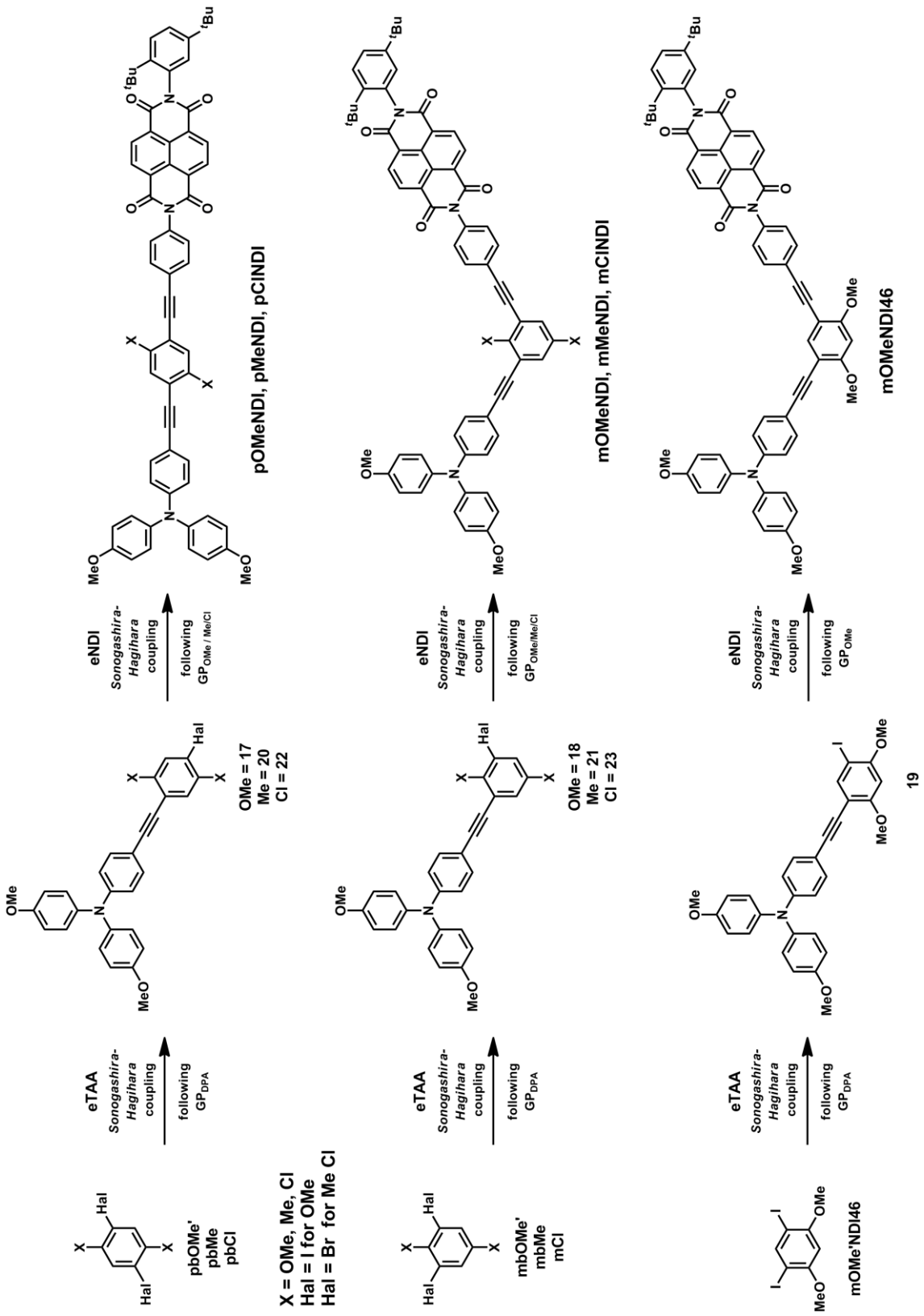

Scheme 31: Synthesis of the methoxy, methyl and chloro dyads by *Sonogashira-Hagihara* coupling of first **eTAA** and then **eNDI**.

Table 19: *Sonogashira-Hagihara* conditions used for the synthesis of the mono TAA substituted intermediate compounds and the TM.

	Reaction Conditions	Reactant	Eq. NDI	Eq. TAA	Product	Yield in %
GP_{DPA}	$Pd(PPh_3)_2Cl_2$, CuI, NEt_3, THF, 80 °C, 1 d	**pbOMe'**	-	0.1	**17**	65
		mbOMe'	-	0.2	**18**	84
		mbOMe'46	-	0.2	**19**	72
		pbMe	-	0.2	**20**	74
		mbMe	-	0.2	**21**	80
		pbCl	-	0.2	**22**	95
		mbCl	-	0.2	**23**	94
GP_{OMe}	$Pd(PPh_3)_2Cl_2$, CuI, NEt_3, THF, 60 °C, 1 d	**17**	1.0	-	**pOMeNDI**	79
		18	2.0	-	**mOMeNDI**	91
		19	2.1	-	**mOMeNDI46**	80
GP_{Me}	$Pd(PPh_3)_2Cl_2$, CuI, P^tBu_3, HN^iPr_2, 1,4-dioxane, 60 °C, 1–2 d	**20**	2.0	-	**pMeNDI**	97
		21	1.1	-	**mMeNDI**	93
GP_{Cl}	$Pd(C_6H_5CN)_2Cl_2$, CuI, P^tBu_3, HN^iPr_2, 1,4-dioxane, 60 °C, 1–2 d	**22**	1.0	-	**pClNDI**	93
		23	1.0	-	**mClNDI**	81
GP_{CN}	$Pd(PPh_3)_2Cl_2$, CuI, NEt_3, THF, 60 °C, 1–2 d	**pbCN**	0.5	-	**24**	37
		mbCN	0.5	-	**25**	70
		24	-	3.0	**pCNNDI**	90
		25	-	3.0	**mCNNDI**	91
GP_{NO_2}	$Pd(PPh_3)_2Cl_2$, CuI, NEt_3, toluene, 60 °C, 1 d	**$pbNO_2$**	-	0.3	**26**	65
		$mbNO_2$	-	0.3	**27**	79
		$pbNO_2$	0.3	-	**28**	42
		$mbNO_2$	0.3	-	**29**	58
		28	-	2.0	**$pbNO_2$**	59
		29	-	2.0	**$mbNO_2$**	56

Synthesis of the CN and NO_2 Substituted Dyads

The nitro compounds were first synthesized in analogy to the OMe–Cl dyads. Following **GP_{NO_2}** the bridging units **mb-/pbNO_2** were mono coupled with 0.3 eq. **eTAA** (Scheme 32). For this reaction procedure no 'dilution principle apparatus' was needed, if the solution of the alkyne was slowly added dropwise. It was noteworthy, that the yield of the resulting single substituted TAA derivatives were satisfying, receiving **26** and **27** in yields of ca. 70 % (Table 19). In contrast to the next step, the *Sonogashira* cross coupling reaction with **eNDI**, resulted in very low yields of the TM. Only ca. 1 % of **p-/mNO_2NDI** was could be isolated. The reason for this low yield could not be clarified.

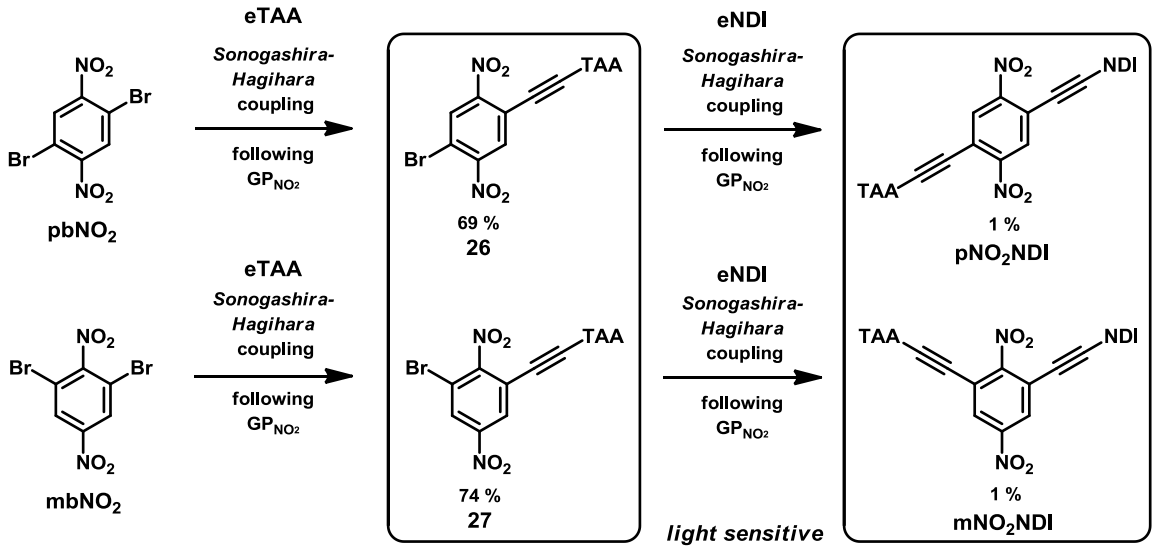

Scheme 32: Synthesis of the nitro dyads via *Sonogashira-Hagihara* coupling with first **eTAA** and then **eNDI**.

Besides the miserable yields of the last step, this synthesis route bared another major disadvantage. The workup procedure of the intermediate **26** and **27** as well as those of the TM **p-** and **mNO_2NDI** had to be done under exclusion of light, since all these four compounds decomposed under irradiation with light.

For these reasons the synthesis of the TM was tried in different order. **pb-** and **mbNO_2** were cross coupled with 0.3 eq. **eNDI** to **28** and **29** respectively (Scheme 33). Using **GP_{NO_2}** (no "dilution principle apparatus" was used) the solution of the alkyne was added slowly dropwise. This might be a reason why **28** and **29** were just obtained in ca. 50 % yield. However, **28** and **29** both did not show any signs of light sensitivity, which simplified the workup procedure significantly. In addition to that, the purification via recycling GPC is very effective and fast. This is the mai reason why reason **p-/mCNNDI** were synthezised in the

same manner. Starting with the addition of the acceptor unit the cyano compounds **24** and **25** were synthesized and yielded in 37 % and 70 %, respectively.

The last step of the synthesis of the cyano and nitro dyads was a *Sonogashira-Hagihara* coupling with **eTAA**. For the two different substituents (CN or NO_2) the respective GP was used. When coupling **24** and **25** following **GP_{CN}** with 3.0 eq. of **eTAA**, the dyads **pCNNDI** and **mCNNDI** were synthesized in high yields of ca. 90 %. Using 2.0 eq. of **eTAA** and **28** and **29** the nitro compounds **pNO_2NDI** and **mNO_2NDI** were obtained in moderate yields of ca. 55 %.

Although the last presented synthesis sequence of the nitro compounds partially had a significant lower yield in the first step and recycling GPC had to be used for isolation of the intermediate product, it is favored because of two major reasons: the first being that the intermediate compounds **24** and **25** are not light sensitive and thus one light excluding workup process was avoided. The second reason being that the overall yield of **pNO_2NDI** and **mNO_2NDI** is still clearly higher than in the first shown synthetic route.

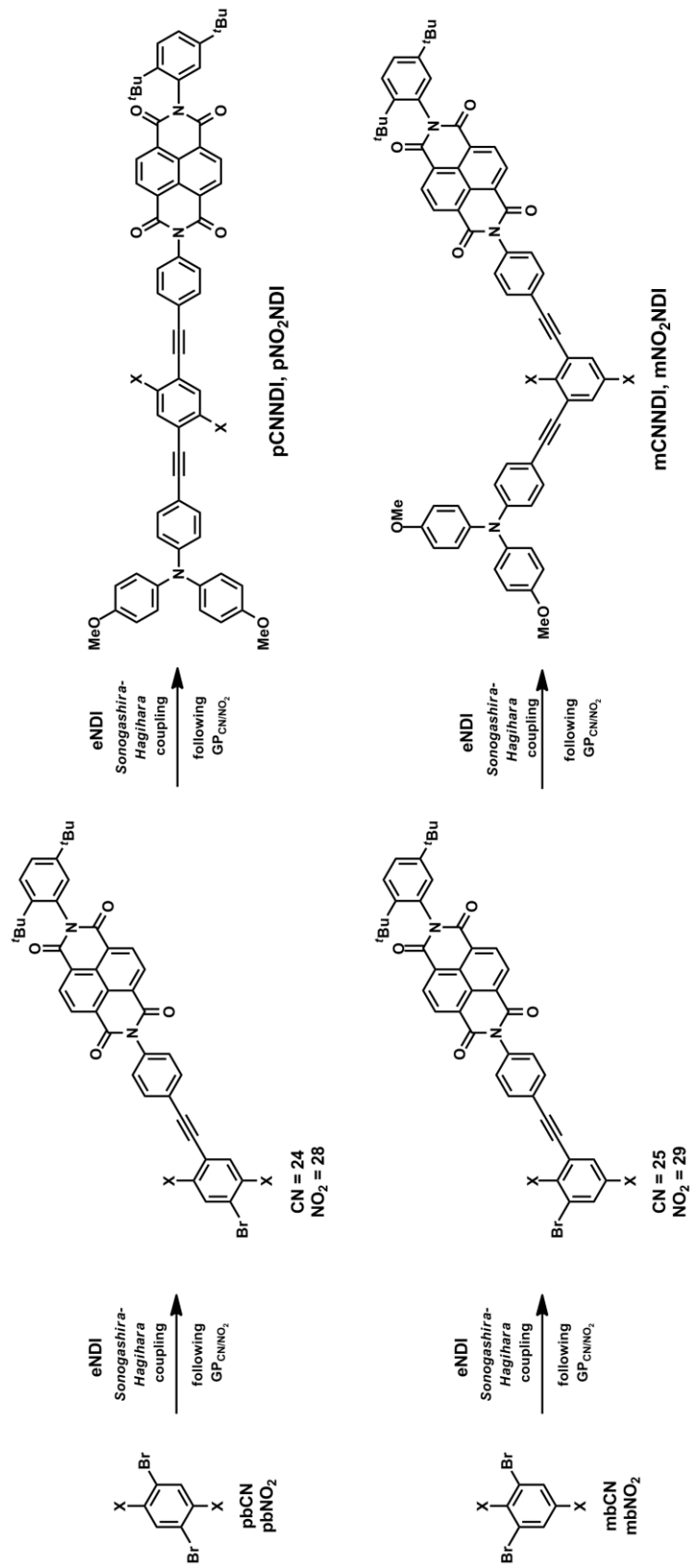

Scheme 33: Synthesis of the cyano and nitro dyads by *Sonogashira-Hagihara* coupling of first **eNDI** and then **eTAA**.

4.2 Steady-State Absorption Spectroscopy

In order to obtain information about the electronic excited state of the dyads and their references, steady-state UV/Vis absorption spectra were measured in solvents of different polarity, namely toluene, DCM and MeCN. The absorption maxima ($\tilde{\nu}_{max}$ and λ_{max}) and extinction coefficients (ε_{max}) of the characteristic absorption bands for toluene and DCM are listed in Table 20, those for MeCN are listed in Table 21. The absorption behavior will be discussed exemplary for toluene in more detail, since most essential observations can be transferred directly to the other solvents. The main differences when changing the solvent are worked out later. First, the absorption spectra of the donor references **sX** (shortly) and acceptor references **sXNDI** will be treated, then, with the insights gained, the dyads will be discussed.

The absorption spectra of the donor references **sX** were already discussed in section 3.2.2 and the obtained results are used in the following discussion (Figure 13, A and Table 8). Briefly summarized: **sOMe–sCl** and **sOMe46** show typical broad π-π*-absorptions of the TAA with maximum absorption energy of ca. 28000 cm^{-1} (357 nm) and a maximum molar absorption coefficient of ca. 30000 M^{-1} cm^{-1}. The absorption is a collective signal of mainly two transitions, one with the transition moment along the bridge axis (named "*z*-band") and one perpendicular within the π-π*-system of the dianisyl part (named "*x*-band"). Increasing the electron withdrawing character of X leads to an electron deficient bridge and therefore a hypsochromic shift of the transition and for **sCN**/**sNO$_2$** to the appearance of a separate CT band. Consequently, **sCN** and **sNO$_2$** show a transition at 23700 cm^{-1} (422 nm) and 20200 cm^{-1} (495 nm), respectively.

The absorption spectra of the acceptor references **sXNDI** in toluene are depicted in Figure 39, A. All references exhibit similar absorption characteristics, that is a strong absorption which is caused by the typical NDI π–π* transition with its vibronic fine structure.[195-198] The absorption consists of a double peak at ca. 26000 cm^{-1} (385 nm) and 28000 cm^{-1} (357 nm), and a shoulder at ca. 31000 cm^{-1} (323 nm). Remarkably, the position of the absorption maxima are nearly unaffected by the benzene unit and its substituents X. From this it can be concluded that the NDI is highly decoupled to the rest of the dyad. The decoupling originates from the nodal plane of the NDI HOMO and LUMO along the molecular axis and the almost perpendicular arrangement of the *N*-phenylene bridge attached to the NDI (see 4.6.1).

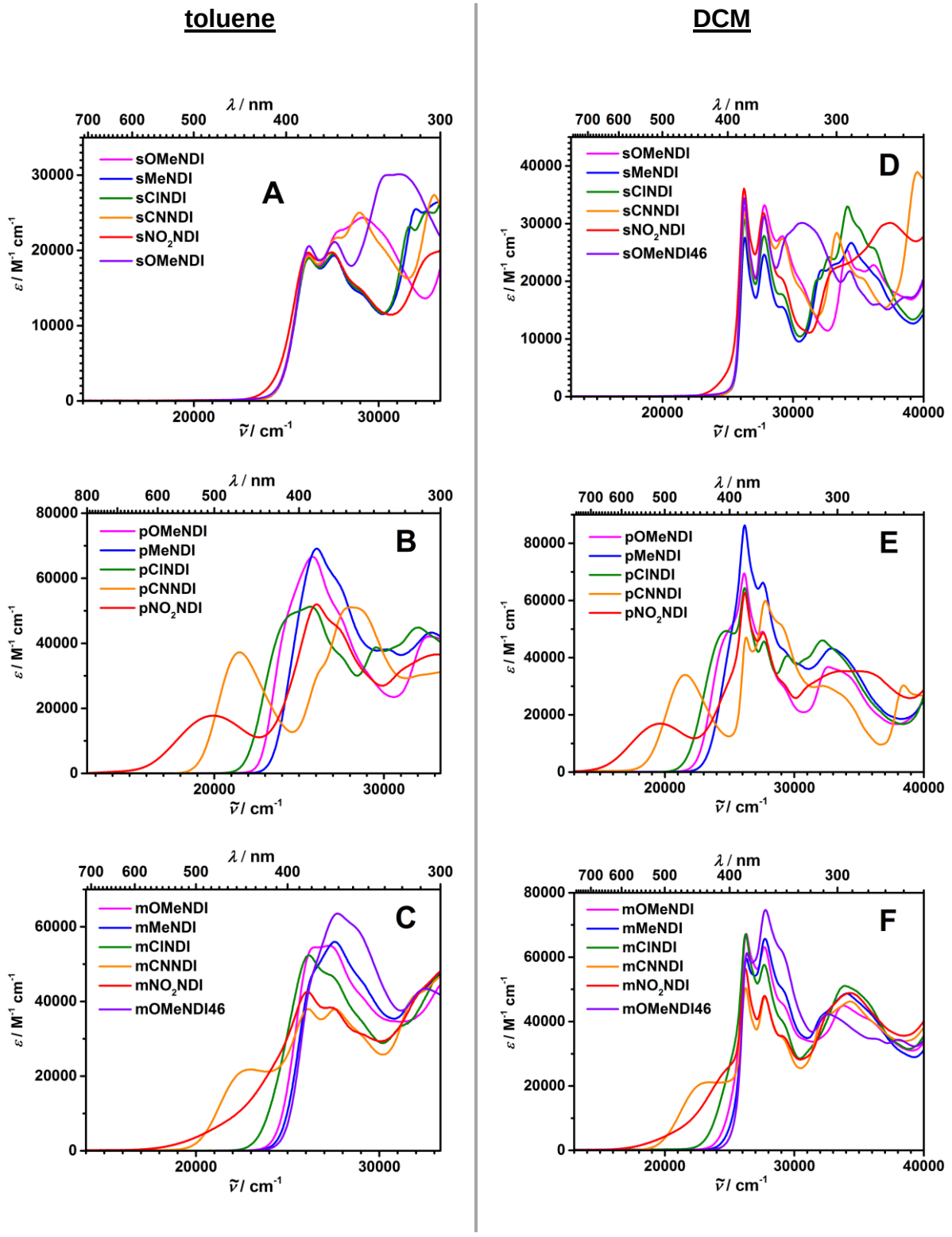

Figure 39: Left: Absorption spectra of the reference compounds **sXNDI** (A), *para*-compounds **pXNDI** (B) and *meta*-compounds **mXNDI** (C) in toluene. Right: Absorption spectra of the reference compounds **sXNDI** (D), *para*-compounds **pXNDI** (E) and *meta*-compounds **mXNDI** (F) in DCM.

Table 20: Absorption maxima ($\tilde{\nu}_{max}$ and λ_{max}) and extinction coefficients (ε_{max}) of the characteristic absorption bands of references **sXNDI**, the *para*-compounds **pXNDI** and the *meta*-compounds **mXNDI** in toluene and DCM.

		$\tilde{\nu}_{max}$ (λ_{max}) / ε_{max} / cm^{-1} (nm) / M^{-1} cm^{-1}	$\tilde{\nu}_{max}$ (λ_{max}) / ε_{max} / cm^{-1} (nm) / M^{-1} cm^{-1}	$\tilde{\nu}_{max}$ (λ_{max}) / ε_{max} / cm^{-1} (nm) / M^{-1} cm^{-1}
toluene	**sOMeNDI**	-	26200 (382) / 19500	27800 (360) / 22600
	sMeNDI	-	26200 (382) / 19100	27500 (363) / 19300
	sClNDI	-	26200 (382) / 19000	27600 (363) / 19500
	sCNNDI	-	26200 (382) / 19300	27700 (361) / 21600
	sNO$_2$NDI	-	26200 (382) / 19700	27500 (363) / 19700
	sOMeNDI46	-	26200 (382) / 20600	27500 (363) / 21100
	pOMeNDI	-	26000 (385) / 69100	27200 (368) / 45100[a]
	pMeNDI	-	25800 (388) / 66600	27200 (368) / 45100[a]
	pClNDI	-	25600 (391) / 51200	27500 (363) / 35800[a]
	pCNNDI	21500 (465) / 37200	26200 (382) / 31300[a]	28000 (357) / 51100
	pNO$_2$NDI	19900 (503) / 17700	26000 (385) / 52000	27200 (368) / 45100[a]
	mOMeNDI	-	26500 (377) / 54500	27200 (368) / 54900
	mMeNDI	-	26500 (377) / 48100[a]	27600 (362) / 55900
	mClNDI	-	26100 (383) / 52300	27400 (365) / 46800
	mCNNDI	23000 (435) / 21800	26100 (383) / 38000	27600 (362) / 37900
	mNO$_2$NDI	-	26100 (383) / 42600	27300 (366) / 38400
	mOMeNDI46	-	26400 (379) / 47600[a]	27700 (361) / 74600
DCM	**sOMeNDI**	-	26300 (380) / 27600	27800 (360) / 24600
	sMeNDI	-	26300 (380) / 30700	27800 (360) / 27900
	sClNDI	-	26200 (382) / 32000	27800 (360) / 31200
	sCNNDI	-	26300 (380) / 32800	27800 (360) / 33200
	sNO$_2$NDI	-	26200 (382) / 36100	27700 (361) / 31800
	sOMeNDI46	-	26300 (380) / 34400	27800 (360) / 31200
	pOMeNDI	-	26100 (383) / 69500	27500 (364) / 49100
	pMeNDI	-	26200 (382) / 86300	27600 (362) / 66300
	pClNDI	24700 (405) / 49400	26200 (382) / 64400	27600 (362) / 45600
	pCNNDI	21600 (463) / 34000	26300 (380) / 47000	27700 (261) / 59800
	pNO$_2$NDI	19600 (510) / 16900	26200 (382) / 62600	27600 (362) / 48700
	mOMeNDI	-	26300 (381) / 67300	27700 (361) / 63100
	mMeNDI	-	26300 (381) / 59500	27700 (361) / 65700
	mClNDI	-	26200 (382) / 67100	27700 (361) / 57600
	mCNNDI	23400 (427) / 21100	26200 (382) / 50400	27700 (361) / 47500
	mNO$_2$NDI	-	26200 (382) / 56300	27700 (361) / 48000
	mOMeNDI46	-	26300 (381) / 61300	27800 (360) / 74600

[a] ±200 cm^{-1}, shoulder in the absorption spectrum.

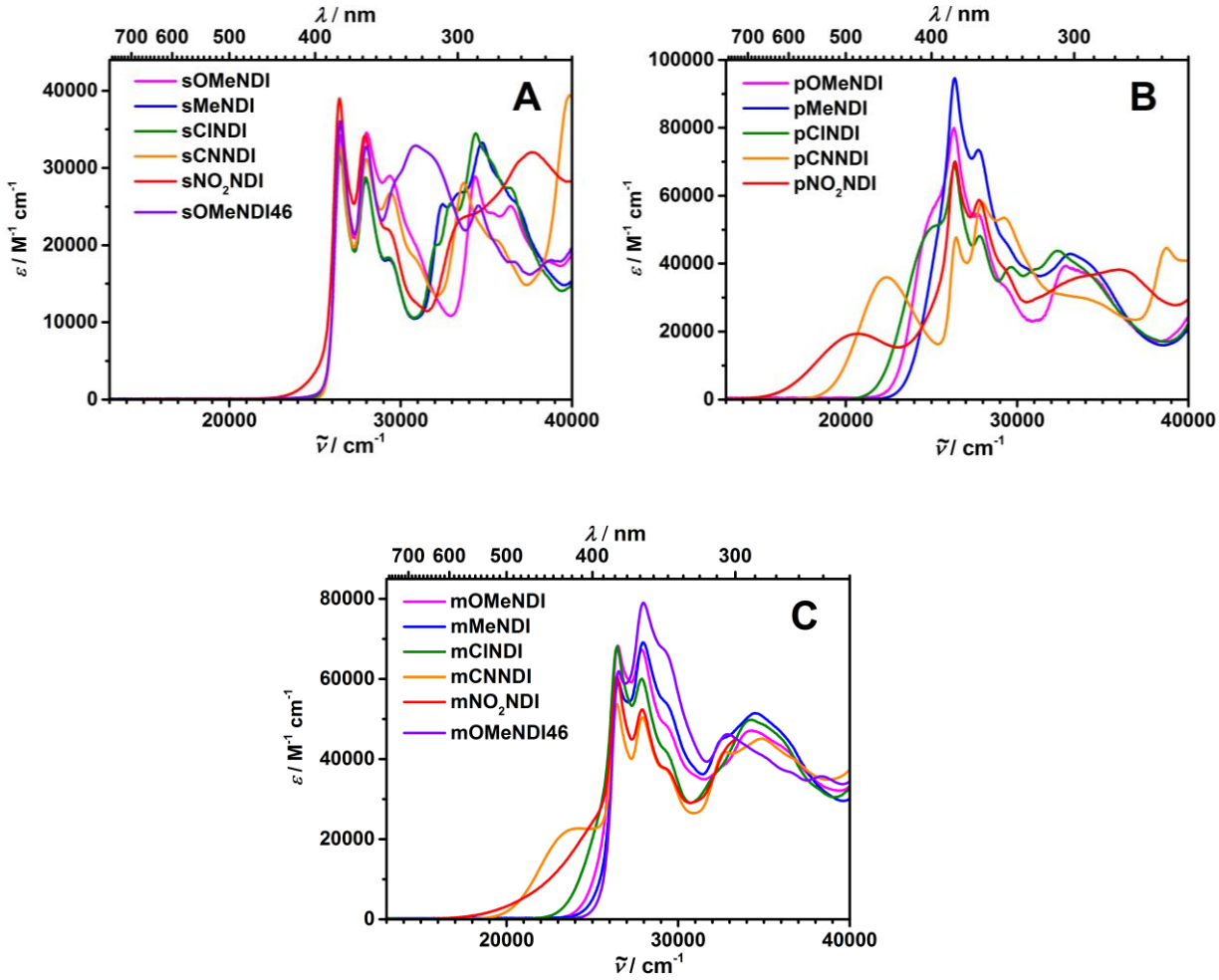

Figure 40: Absorption spectra of the reference compounds **sXNDI** (A) *para*-compounds **pXNDI** (B) and *meta*-compounds **mXNDI** (C) in MeCN.

The onsets of absorption of all references are at the same position except for **sNO$_2$NDI**, which has a somewhat broader slope and a bathochromic onset-shift of ca 200 cm^{-1}. The extinction coefficients of the NDI associated maxima are almost identical for **sMeNDI**, **sClNDI** and **sNO$_2$NDI**. Whereas **sOMeNDI** and **sCNNDI** show additional intense absorptions at ca. 29000 cm^{-1} (345 nm) which superimpose with parts of the NDI absorption resulting in higher ε_{max} values at ca. 28000 cm^{-1} (357 nm). Additionally, **sOMeNDI46** has a slightly higher ε_{max} of the NDI and an additional broad absorption at ca. 30000 cm^{-1} (333 nm).

Table 21: Absorption maxima ($\tilde{\nu}_{max}$ and λ_{max}) and extinction coefficients (ε_{max}) of the characteristic absorption bands of references **sXNDI**, the *para*-compounds **pXNDI** and the *meta*-compounds **mXNDI** in MeCN.

	$\tilde{\nu}_{max}$ (λ_{max}) / ε_{max} / cm^{-1} (nm) / cm^{-1} M^{-1}	$\tilde{\nu}_{max}$ (λ_{max}) / ε_{max} / cm^{-1} (nm) / cm^{-1} M^{-1}	$\tilde{\nu}_{max}$ (λ_{max}) / ε_{max} / cm^{-1} (nm) / cm^{-1} M^{-1}
sOMeNDI	-	26500 (379) / 34300	28000 (357) / 34600
sMeNDI	-	26500 (377) / 32000	28000 (357) / 28500
sClNDI	-	26500 (377) / 32100	28000 (357) / 28800
sCNNDI	-	26500 (377) / 32800	28000 (357) / 31200
sNO_2NDI	-	26400 (379) / 39000	27900 (358) / 34200
sOMeNDI46	-	26500 (377) / 36100	28000 (357) / 32800
pOMeNDI	-	26300 (380) / 79900	27600 (362) / 54700
pMeNDI	-	26400 (379) / 94600	27700 (361) / 48100
pClNDI	-	26400 (379) / 68700	27800 (360) / 48100
pCNNDI	22400 (446) / 36000	26500 (377) / 47700	28000 (357) / 58100
pNO_2NDI	20600 (485) / 19400	26400 (379) / 70100	27800 (360) / 58800
mOMeNDI	-	26500 (377) / 68300	27900 (358) / 67300
mMeNDI	-	26500 (377) / 59500	28000 (357) / 69100
mClNDI	-	26500 (377) / 68100	27900 (358) / 60100
mCNNDI	24200 (413) / 22700	26500 (377) / 53700	27900 (358) / 50400
mNO_2NDI	-	26500 (377) / 60700	27900 (358) / 52400
mOMeNDI46	-	26500 (377) / 62000	28000 (357) / 79000

The absorption spectra of the dyads **pXNDI** and **mXNDI** show strong absorptions at 26000–28000 cm^{-1} (385–357 nm) which are caused by superposition of the NDI π–π^* absorption with its typical vibrionic fine structure and the π–π^* excitations of the TAA (Figure 39, B and C). Like references **sX** both series of dyads show a progressive red shift on going from X = Me, OMe, Cl, CN to NO_2. Since one or both OMe groups at the bridge are assigned to be rotated out of plane, the electron withdrawing features caused by the electronegativity of the oxygen dominate, which leads to absorption maxima below those of the respective methyl compounds (see chapter 3.2.2).[159]

The overall absorption features of the **p-/mXNDI** is related to 4 different types of absorptions, two for each chromphore. In case of the TAA, one one absorption is associated to the TAA without involving the bridge, the other with involving the benzene unit. The same is true for the NDI associated absorptions.

Accordingly, by subtracting the absorption spectrum of **sXNDI** from those of **p-/mXNDI** it is possible to simulate the absorption features caused of the remaining (TAA involving) part of the molecule. The resulting difference spectra are shown in Figure 41.

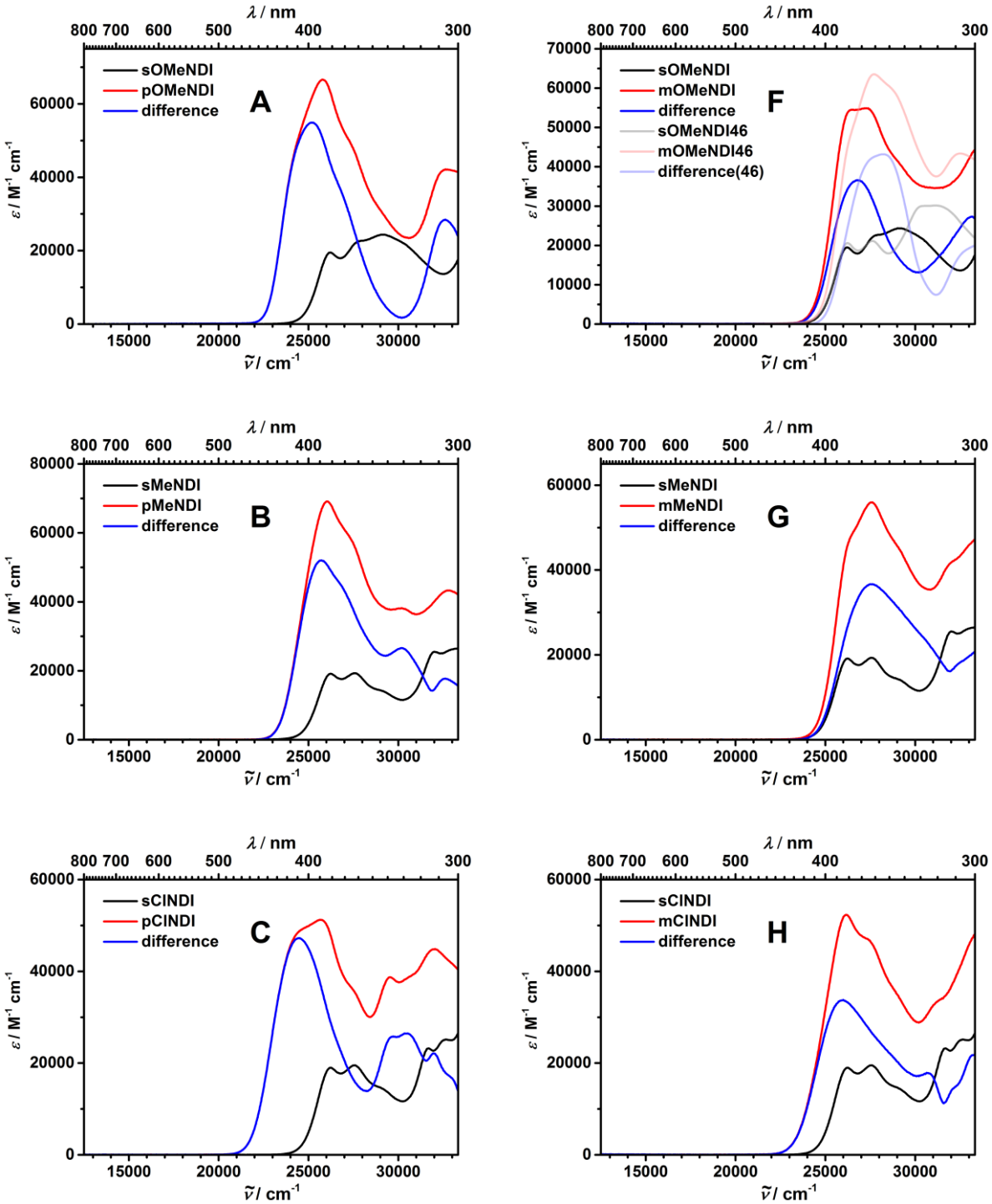

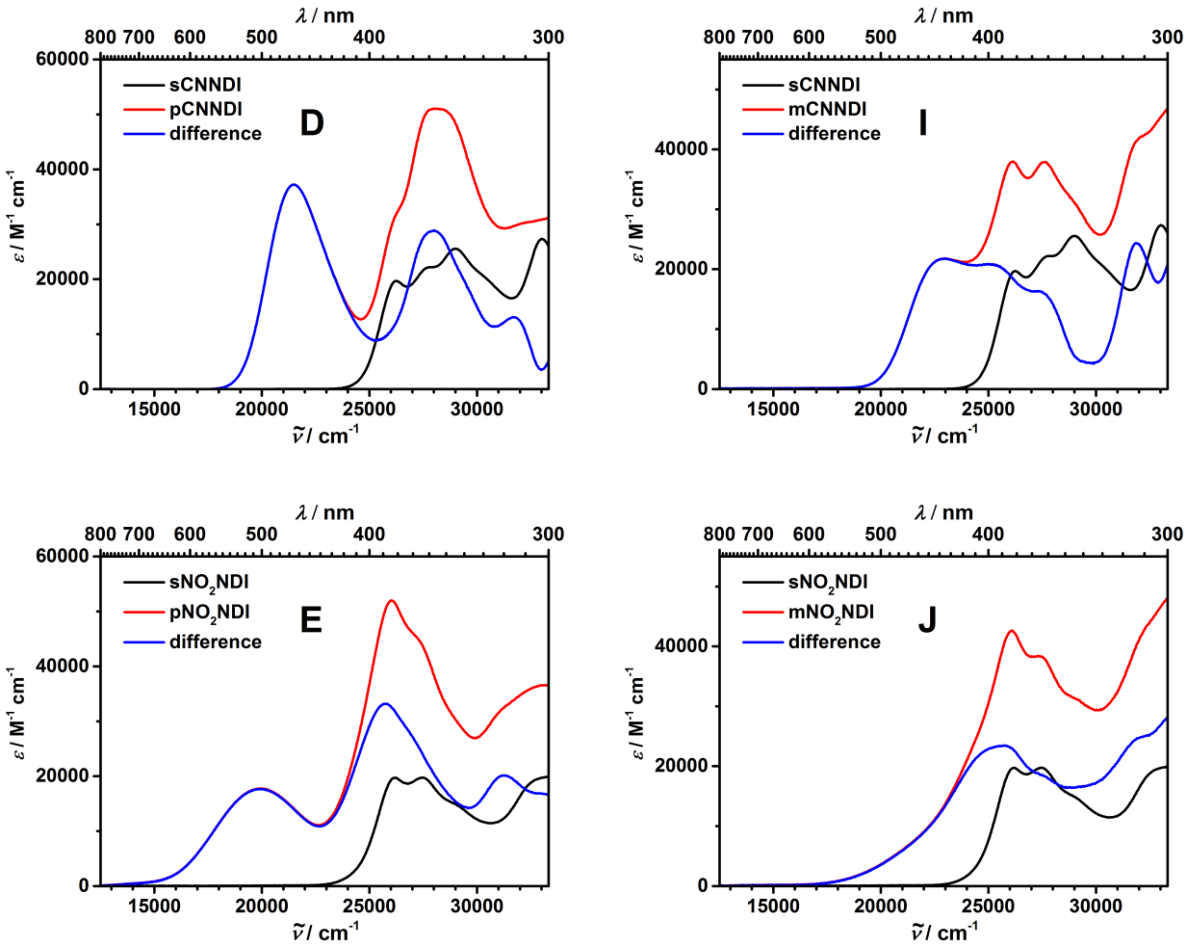

Figure 41: Left: Absorption spectra of the references **sXNDI**, the *para*-dyads **pXNDI** and the resulting difference spectra in toluene (A–E). Right: Absorption spectra of the references **sXNDI**, the *para*-dyads **pXNDI** and the resulting difference spectra in toluene (F–J). The transparent absorption spectra in F belong to references **sXNDI46**, the *meta*-dyad **mOMeNDI46** and the resulting difference spectra.

The absorption spectra of the *meta*-dyads **mXNDI** are in a first approximation the sum of the absorption spectra of the fragments **sX** and the **sXNDI**, which indicates little electronic interaction between the NDI and the TAA in the electronic ground state. Nevertheless, comparing the reference spectra of **sX** to the corresponding difference spectra, a small bathochromic shift of the TAA associated bands and a different band shape of the absorption is observable, indicating an influence of the NDI to the rest of the molecule. However, this influence could also be due to the benzene unit, which links the bridge and the NDI, and does not result from the NDI itself.

As in the case of **sCN** the combination of an electron deficient bridge with the TAA donor leads in **mCNNDI** to a particularly low-lying and thus clearly visible CT band at 23600 cm^{-1} (424 nm). In all the other cases, the partial CT character becomes obvious when looking at

the difference absorption spectra. Remarkably, the CT band of the TAA in **mNO$_2$NDI** can no longer be identified as an isolated band. It is assigned to be shifted close to the transitions at higher wavenumbers resulting in a broad absorption.

The absorption spectra of the *para*-dyads **pXNDI** are different. Here, the characteristic absorptions of the NDI units remain at ca. 26000 cm^{-1} (385 nm) to 28000 cm^{-1} (357 nm), whereas the TAA associated CT bands are (compared to the references **sX**) bathochromically shifted of about 300 cm^{-1}, demonstrating that the position of the NDI, or more precisely, that of the connecting benzene unit attached to the benzene bridge, influences the absorption behavior significantly.

Using the tangent to the rising flank of the difference spectra also enables estimating the E_{00} energy of this (partial) CT state. The evaluated data are given in Table 22.

Table 22: E_{00} energy of CT state of the *meta*- and *para*-compounds estimated by using the tangent to the rising flank of the difference spectra.

para	E_{00} / cm^{-1} (eV)	***meta***	E_{00} / cm^{-1} (eV)
pOMeNDI	22800 (2.83 eV)	**mOMeNDI**	24500 (3.04 eV)
pMeNDI	23300 (2.89 eV)	**mMeNDI**	24800 (3.07 eV)
pClNDI	21800 (2.70 eV)	**mClNDI**	23400 (2.90 eV)
pCNNDI	19100 (2.37 eV)	**mCNNDI**	20200 (2.50 eV)
pNO$_2$NDI	18500 (2.29 eV)	**mNO$_2$NDI**	18500 (2.29 eV)
		mOMeNDI46	25100 (3.11 eV)

In toluene, DCM and MeCN the shape of the spectra are considerably different. While increasing the solvent polarity the broad and featureless absorption bands of the NDI in toluene become sharp and resolved in DCM and MeCN. This sharpening of the absorption is mainly caused by the NDI, since the solvent polarity does not change the shape of the reference **sX** significantly. It is probably due to aromatic solvent-specific effects such as exciplex formation, as observed several times before.[199]

Only weak negative solvatochromism is indicated by the shift of the main NDI π-π^* absorption bands from toluene to MeCN of ca. 300 cm^{-1}. However, the maxima of the TAA CT bands of the **CN** compounds and **sNO$_2$** are shifted by about 1000 cm^{-1} and 700 cm^{-1}, respectively, proving their CT character.

In all tested solvents (toluene, DCM, and MeCN) the nitro dyads **p-/mNO$_2$NDI** decompose under irradiation with light. This is shown exemplary for **mNO$_2$NDI** in toluene and DCM. The corresponding spectra are depicted in Figure 42 (A for toluene and B for DCM). Black curves show the spectra without light exposure (0 min), red lines after of irradiation of light for 60 min. The decomposition progress can be observed by a color change from red to green, caused by a decrease of the characteristic absorptions of the NDI and TAA bands between ca. 24000 cm^{-1} (417 nm) and 30000 cm^{-1} (333 nm) and a simultaneous appearing of two broad bands between 12000 cm^{-1} (833 nm) and 24000 cm^{-1} (417 nm). An identification of the decomposition product(s) was not possible.

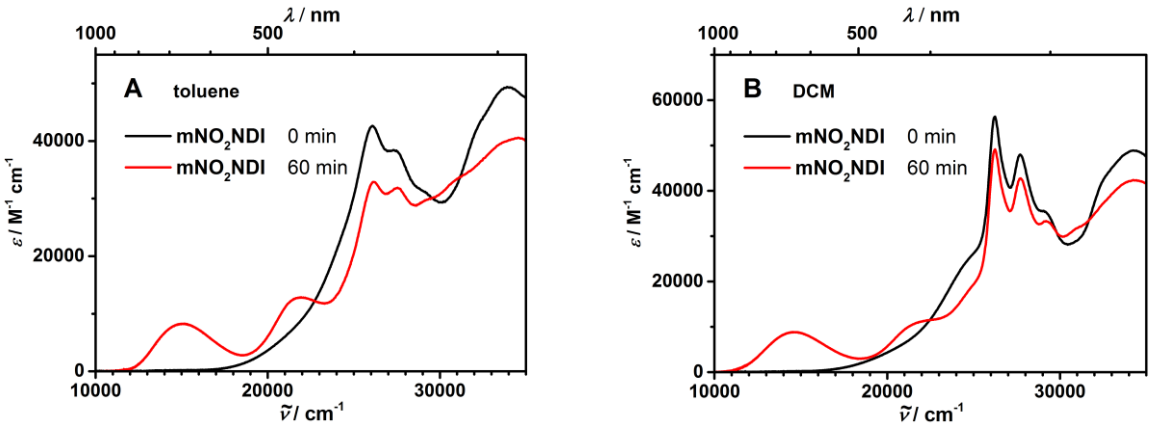

Figure 42: Absorption spectra of **mNO$_2$NDI** in toluene (A) and DCM (B) without (black lines) and after 60 min (red) of light exposure.

Unfortunately, decomposition of the two nitro dyads **p-** and **mNO$_2$NDI** did also occur in other optical measurements, like SEC and transient absorption measurements. Thus further measurements with respect to the charge transfer dynamics taking place after excitation, could not be carried out.

4.3 Electrochemistry (CV, SWV, DPV)

In order to investigate the electrochemical properties of the dyads **m-/pXNDI**, as well as the reference compounds and **sXNDI**, and to determine the energy of CS states, electrochemical measurements were performed. In Figure 43 the cyclic voltammograms (CV) of all TM are displayed. Figure 44 shows the square wave voltammograms (SWV) of the methoxy compounds (A) and the differential pulse voltammograms (DPV) of the nitro compounds (B). The SWV were recorded in order to resolve the process in the oxidative parts in the OMe compounds. The DPV for resolving reductive processes within the nitro compounds. All measurements were performed under argon atmosphere in DCM with TBAHF as supporting electrolyte and referenced against the ferrocen/ferrocenium (Fc/Fc^+) redox couple. The potentials are listed in Table 23. Chemical and electrochemical reversibility of the half-wave potentials were investigated by multi thin layer experiments and measurement at different scan rates, respectively.[165] In the following treatment of the redox behavior, special attention will be given to the half-wave processes referring to the first reduction of the NDI acceptor and the first oxidation of the TAA donor, respectively. Their energetic position and behavior play a key role in the possibility to form CS states in later transient absorption measurements.

The electrochemical properties of the donor references **sX** were already discussed in section 3.2.3 and the obtained results are used in the following (Figure 16, B and Table 10. Briefly summarized: All references **sX** and **sOMe46** show a first reversible oxidation of the TAA at ca. +300 mV and a second irreversible oxidation at ca. +1000 mV. In Addition to that **sCN** shows one additional irreversible reductive process at 1919 mV. **sNO_2** shows two reversible half-wave potentials at −1244 mV and −1064 mV. **sOMe** and **sOMeNDI46** show three additional oxidative processes at ca. 1000 mV, 1150 mV and 1400 mV. All these additional reductive/oxidative processes are related to reduction/oxidation of the substituents of the “bridging units”, and follow up reactions in case of **sOMe** and **sOMeNDI**.

Before discussing the dyads, the acceptor references, with NDI attached to the “bridging unit”, **sXNDI** and **sOMeNDI** will be discussed. The CV are depicted Figure 43 (A), all molecules exhibit a half-wave potential $E_{1/2}$ of approximately −1000 mV deriving from the first reduction (Red1) of the NDI. Another signal at ca. −1500 mV derives from the second oxidation (Red4) of the NDI unit. Both one-electron reductions are completely reversible and the redox potentials are comparable to similar NDI moieties of that kind.[78, 113, 196, 197, 200]

In the references, both the first and the second reduction of the NDI at about the same redox potential, nearly irrespective of the substituent X and is substitution pattern at the benzene unit (2,5- or 4,6-position).

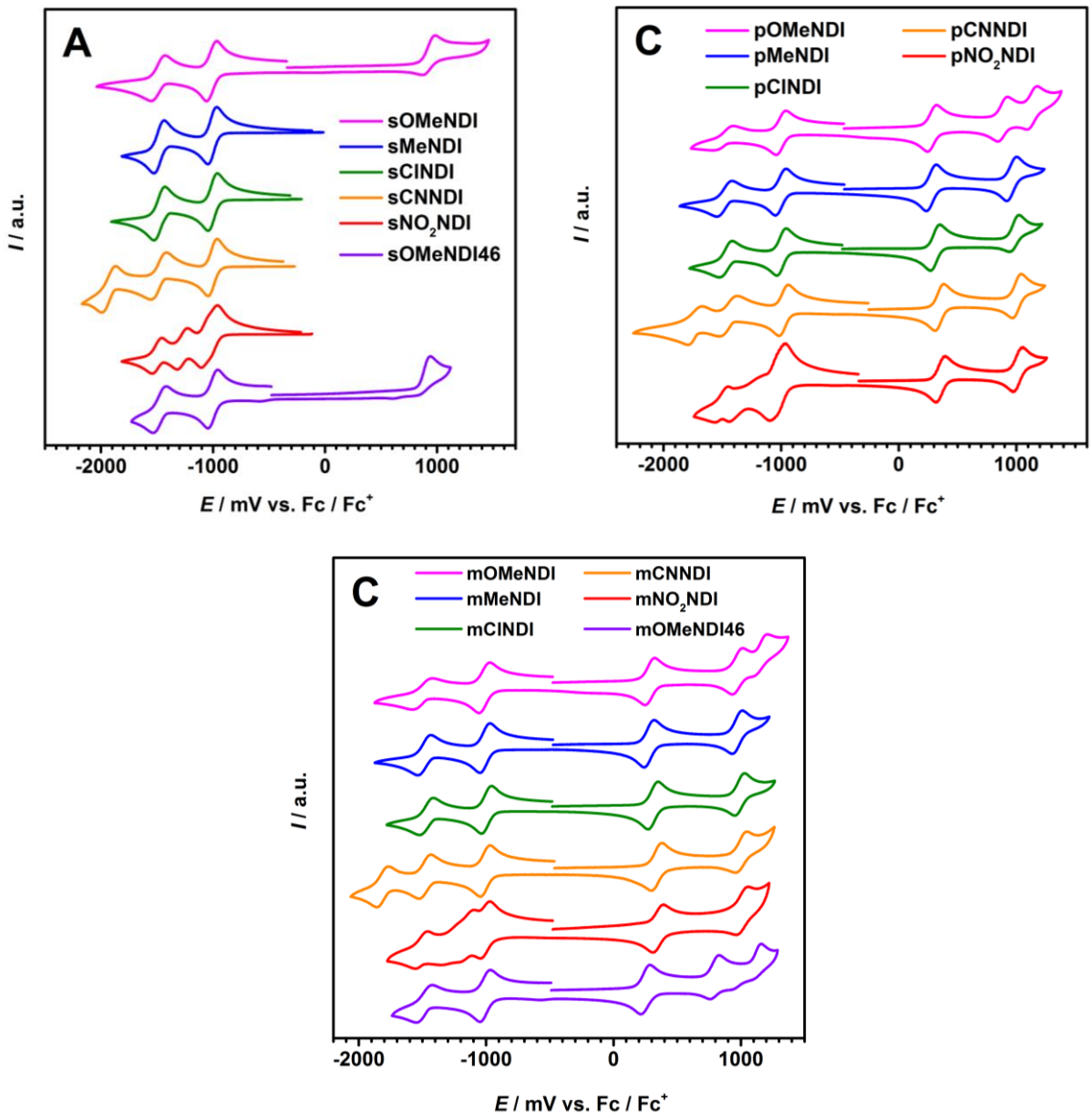

Figure 43: Cyclic voltammograms of the reference compounds **sXNDI** (A). Cyclic voltammograms of the *para*-compounds **pXNDI** (B). Cyclic voltammograms of the *meta*-compounds **mXNDI** (C). The voltammograms of all compounds **OMe** to **CN** were recorded in DCM/0.2 M TBAHF at a scan rate of 1000 mV s^{-1}. The NO_2 compounds were recorded at a scan rate of 100 mV s^{-1}. All potentials are referenced against Fc/Fc^+.

Only a slight increase of the redox potentials while changing the substituent X from OMe (Red1: −1011 mV) to CN (Red1: −1000 mV), indicating a slight decrease of electron density at the NDI by decreasing the electron-donating character of X, was detected. Note that for **sNO$_2$NDI**, the value rises again (Red1: −1033 mV), but this might result from the determination of the redox potential by DPV experiment (see below). However, one electronic property of the NDI unit becomes obvious. The NDI LUMO having a nodal plane

along the molecular axis reduces the electronic interaction with substituents attached to its nitrogen imide atoms. In fact, the redox potentials do not differ much from NDI which are not substituted with an additional benzene unit.[197, 200]

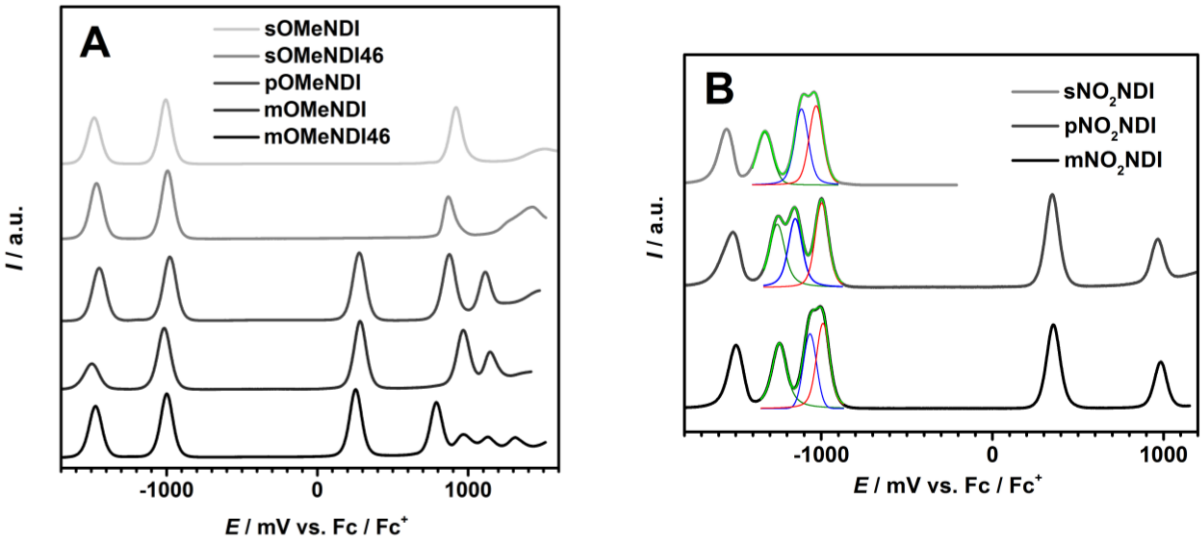

Figure 44: Square wave voltammograms of the OMe compounds in DCM/0.2 M TBAHF at a scan rate of 50 mV s^{-1} (A). Differential pulse voltammograms of the NO_2 compounds in DCM/0.2 M TBAHF at a scan rate of 2 mV s^{-1} (B). The colored lines (olive, blue, red) show the *Voigt* fits of the first 3 reductive signals and its resulting cumulative fits (green). All potentials are referenced against Fc/Fc^+.

sCNNDI shows an additional redox process at −1920 mV which is referring to a reduction of a CN group at the benzene unit. This reduction appears to be weakly irreversible under multi-layer thin film experiment. In the CV **sNO$_2$NDI** has a broad first reduction process at ca. −1000 mV, followed by a redox process at −1325 mV which corresponds to a reduction of a nitro group and finally the second reduction of the NDI at −1523 mV. In the DPV experiment the broad first reduction (ca. −1000 mV) gets more resolved and one can recognize two consecutive processes (Figure 44, B).

The reductive area in the DPV from ca. −800 mV to −1400 mV was simulated by three *Voigt* fits (the signal at −1325 mV was taken into account). The simulation clearly shows a reductive process at −1033 mV which is assigned to the first reduction of the NDI and a second one at −1102 mV that is assigned to a reduction of a nitro group.

In the CV **sOMeNDI** and **sOMeNDI46** show a strong irreversible oxidation at ca. +900 mV which are caused by oxidation processes of a OMe group at the benzene unit. In the SWV of **sOMeNDI** one redox process at +1507 mV, and of **sOMeNDI** two additional processes, at +1291 mV and 1427 mV were recorded (Figure 44, A). They are related to continuing

irreversible oxidations of the 2,5- and 4,6-dimethoxybenzene bridges and follow up reactions like polymerization at the electrode oxidations.[167, 168]

The *para*- and *meta*-dyads show a redox behavior that behaves like the combination of donor (**sX, sOMeNDI46**) and the acceptor (**sXNDI**) references. Like **sXNDI**, the dyads feature a reversible half-wave potential $E_{1/2}$ representing the first reduction at the NDI at ca. −1000 mV (Red1) and second at ca. −1500 mV (Red4). Like **sX** they feature a reversible half-wave potential $E_{1/2}$ representing the first oxidation at the TAA at ca. +300 mV (Ox1) and second irreversible oxidation at ca. +1000 mV (Ox2). **p/-mCNNDI** show an additional irreversible reduction process at ca. −1800 mV, which is caused by the reduction of a CN moiety.[169] **p-/mNO$_2$NDI** show a broad and undefined reduction signal in the CV. The DPV measurements show that this signal belongs to four reduction processes (Figure 44, B). First, the reduction of the NDI at ca. −1000 mV, then a reversible reduction at −1068 mV for the *meta*- and −1152 mV for the *para*-compound, respectively, and another reversible process at ca. −1500 mV, which is caused by the reduction of the second a nitro group.[171, 172] The fourth reduction is again related to the generation of the NDI dication. In the CV, **p-/mOMeNDI** shows an additional redox signal at ca. +1200 mV. In the SWV experiment **mOMeNDI46** exhibits even three additional oxidation processes at higher potential (+969 mV, +1135 mV and +1331 mV). The half-wave processes (Ox3 to Ox5) of the OMe compound are again assigned to continuing irreversible oxidations of the 2,5- and 4,6-dimethoxybenzene bridges and follow up reactions.[167, 168] However, a more precise assignment of the processes taking place was not possible.

There is only a slight increase of these half-wave potentials of the first NDI reduction by increasing electron-withdrawing ability from OMe (**pOMeNDI**-Red1: −1002 mV, **mOMeNDI**-Red1: −1013 mV) to CN (**pCNNDI**-Red1: −979 mV, **mCNNDI**-Red1: −993 mV). For the NO_2 compounds, the value drops again (**pNO$_2$NDI**-Red1: −992 mV, **mNO$_2$NDI**-Red1: −998 mV), but this might result from the determination of $E_{1/2}$ from the DPV. The only very small influence of X to the redox behavior of the NDI demonstrates that the NDI is mostly electronically decoupled from rest of the molecule and hardly affected by X. This characteristic is caused by the NDI LUMO having a nodal plane along the molecular axis reducing the electronic interaction with substituents attached to its nitrogen imide atoms.

The TAA referring redox processes are much more influenced by the bridging units or rather the EDG/EWG X attached to them. By increasing the electron-donating ability of X from OMe (ca. +280 mV) to NO_2 (ca. +350 mV) the corresponding half-wave potentials $E_{1/2}$ increase by ca. +70 mV showing that strong EDG like OMe increase the charge density at the benzene unit and the TAA and therefore the TAA get oxidized more easily. The opposite is true for e.g. **sNO$_2$**, the EWG NO_2 decreases the charge density at the TAA resulting in a higher half-wave potential.

The position X at the benzene unit is another criterion for the position of the first TAA oxidation. The 2,5-position of the OMe groups in **p-/mOMeNDI** lead to a first oxidation TAA at ca. +290 mV, in **mOMeNDI46** this potential drops to +252 mV, indicating that in the 4,6-position the OMe substituents have a better electronic communication to the TAA donor.

Table 23: Redox potentials[a] ($E_{1/2}$) and potential difference between the first reduction and oxidation ($\Delta E_{1/2}$) of **sXNDI**, **pXNDI** and **mXNDI** in DCM/0.2 M TBAHF.

	$E_{1/2}$ / mV									
	Red5[b]	**Red4**	**Red3**	**Red2**	**Red1**	**Ox1**	**Ox2**[b]	**Ox3**[b,c]	**Ox4**[b,c]	**Ox5**[b,c]
sOMeNDI	-	−1489	-	-	−1011	-	-	+925	-	+1507
sMeNDI	-	−1485	-	-	−1006	-	-	-	-	-
sClNDI	-	−1484	-	-	−1003	-	-	-	-	-
sCNNDI	−1920	−1481	-	-	−1000	-	-	-	-	-
sNO$_2$NDI	-	−1523	−1325	−1102	−1033	-	-	-	-	-
sOMe46NDI	-	−1472	-	-	−1001	-	-	+869	+1291	+1427
pOMeNDI	-	−1490	-	-	−1002	+286	+885	-	+1191	-
pMeNDI	-	−1489	-	-	−1004	+277	+963	-	-	-
pClNDI	-	−1479	-	-	−999	+309	+1012	-	-	-
pCNNDI	−1722	−1448	-	-	−979	+350	+1008	-	-	-
pNO$_2$NDI	-	−1497	−1245[d]	−1068[d]	−992	+358	1012	-	-	-
mOMeNDI	-	−1503	-	-	−1013	+288	+976		+1159	-
mMeNDI	-	−1476	-	-	−1010	+276	+968		-	-
mClNDI	-	−1469	-	-	−997	+313	+990	-	-	-
mCNNDI	−1803	−1467	-	-	−993	+343	+993	-	-	-
mNO$_2$NDI	-	−1516	−1257[d]	−1152[d]	−998	+351	+996	-	-	-
mOMeNDI46	-	−1499	-	-	−1020	+252	+789	+969	+1135	+1331

[a]All potentials are referenced against Fc/Fc$^+$. [b]Irreversible process. [c]Values determined by SWV. [d]Value determined by DPV.

The free energy of the charge separated state (ΔG_{CS}) for **pXNDI**, **mXNDI** and **mOMeNDI46** and were calculated using the *Weller* approach via equation (26) and the determined half-wave redox potentials.[201]

$$\Delta G_{cs} = \frac{N_A}{1000} ze \left[E_{ox}\left(\frac{D}{D^+}\right) - E_{red}\left(\frac{A}{A^-}\right)\right] - \frac{N_A e^2}{1000 \times 4\pi\varepsilon_0}\left[\left(\frac{1}{2r_D}+\frac{1}{2r_A}\right)\left(\frac{1}{\varepsilon_r}-\frac{1}{\varepsilon_s}\right)+\frac{1}{\varepsilon_r d_{DA}}\right] \quad (26)$$

with the radii of the donor and acceptor (r_D = 4.81 Å, r_A = 3.97 Å) and the center to center distance between them (d_{DA} = 22.99 Å for **pXNDI** / d_{DA} =19.53 Å for **mXNDI/mOMeNDI46**). The radii r_D and r_A were calculated from the corresponding *Connolly* Molecular Surfaces of the subunits optimization with *ChemBio3D Ultra*[202] and the distances d_{DA} were determined at a B3LYP/6-31G* level of theory using *Gaussian09*.[203] N_A is *Avogadro's* constant, *e* the elementary charge, *z* the number of transferred charges. [$E_{ox}(D/D^+)$-$E_{red}(A/A^-)$] reflects the redox-potential difference between the first oxidation of the donor $E_{1/2}$(Ox1) and first reduction of the acceptor $E_{1/2}$ (Red1), ε_0 is the vacuum permittivity, ε_r is the permittivity of the solvent used for cyclic voltammetry and ε_s is that for the solvent used in the photophysical experiment. Since the transient absorption measurements presented in the following are done in toluene and MeCN, those two solvents were chosen here. For toluene the ΔG_{CS} values for all molecules are in the range of 2.0 eV and are listed in Table 24. For the *para*-series a slight decrease from 2.11 eV for **pNO$_2$NDI** to 2.05 eV for **pOMeNDI** takes place. The same is true for the *meta*-series, which shows a slight decrease from 2.05 eV for **mCNNDI** to 2.02 mV for **mOMeNDI**. However, for **mNO$_2$NDI** a value of 2.02 eV was calculated. The lowest free energy with 1.99 eV was found for **mOMeNDI46**. Since the input parameters were the same for the calculation in MeCN, the obtained data in MeCN show the same trends. However, here free energy of the charge separated state has a value of ca. 1.0 eV.

Table 24: ΔG_{CS} values of **p-/mXNDI** and **mOMeNDI46** calculated by the *Weller* equation.

para	ΔG_{CS} (toluene) / eV	ΔG_{CS} (MeCN) / eV	***meta***	ΔG_{CS} (toluene) / eV	ΔG_{CS} (MeCN) / eV
pOMeNDI	2.05	1.00	**mOMeNDI**	2.02	1.01
pMeNDI	2.05	0.99	**mMeNDI**	2.01	0.99
pClNDI	2.07	1.02	**mClNDI**	2.03	1.02
pCNNDI	2.09	1.04	**mCNNDI**	2.05	1.04
pNO$_2$NDI	2.11	1.06	**mNO$_2$NDI**	2.02	1.06
			mOMeNDI46	1.99	0.96

4.4 Spectroelectrochemitsry

Spectroelectrochemitsry (SEC) measurements were performed to investigate the photophysical properties of the dyads in their cationic and anionic form. For this purpose a solution of the dyads was stepwise oxidized/reduced by applying a voltage to the solution. After each change UV/Vis/NIR absorption spectra was monitored. The spectra were recorded in DCM using TBAHF/0.2M as conducting salt. Here, only the spectra of the first oxidation and reduction are shown, since they proved to be reversible in the previous electrochemical investigations (see chapter above). Indeed, SEC of all compounds proved to be reversible as the back oxidation/reduction processes fully recover the neutral spectra. SEC of **p-/mNO$_2$NDI** was not possible due to decomposition taking place. The obtained spectroscopic data are listed in Table 25. The neutral compounds were already discussed in chapter 4.2 and the corresponding data are given in Table 20. On the left side of Figure 45 the evolution of the radical anion (red) and the radical cation (green) features when reducing or oxidizing the *para*-compounds **pXNDI** (X = OMe–CN) are depicted. The left side of Figure 46 shows the spectra of the *meta*-compounds **mXNDI** and the left side of Figure 47 of **mOMeNDI46**.

For all dyads one can see an appearing and increasing of four peaks at 12800 cm^{-1} (781 nm), 14200 cm^{-1} (704 nm), 16400 cm^{-1} (610 nm) and 20900 cm^{-1} (478 nm) upon stepwise reduction (red). The first three peak only grow to a small extinction coefficient (12800 cm^{-1}: ε = 6900 ± 2400 cm^{-1} M^{-1}, 14200 cm^{-1}: ε = 4000 ± 1500 cm^{-1} M^{-1}, 16400 cm^{-1}: ε = 615200 ± 2500 cm^{-1} M^{-1}), while the extinction coefficient of the fourth transition at 20900 cm^{-1} reach values of ε = 45700 cm^{-1} M^{-1} to ε = 69600 cm^{-1} M^{-1} (for **pCNNDI$^{\bullet-}$**). The energetic position and intensity distribution of the transition bands are characteristic for NDI anions. The differences in the intensity of the highest energy transitions are mainly caused by superposition of the NDI$^{\bullet-}$ absorption with bridge involving TAA absorptions (see **pCNNDI**, Figure 42, D). Simultaneous to the growth of the NDI$^{\bullet-}$ bands, the typical vibrionic structured π–π* NDI absorptions at 26200 cm^{-1} (381 nm) and 27700 cm^{-1} (361 nm) decrease, proving that during the reduction processes, the NDI anions get formed at the expense of the neutral NDI.

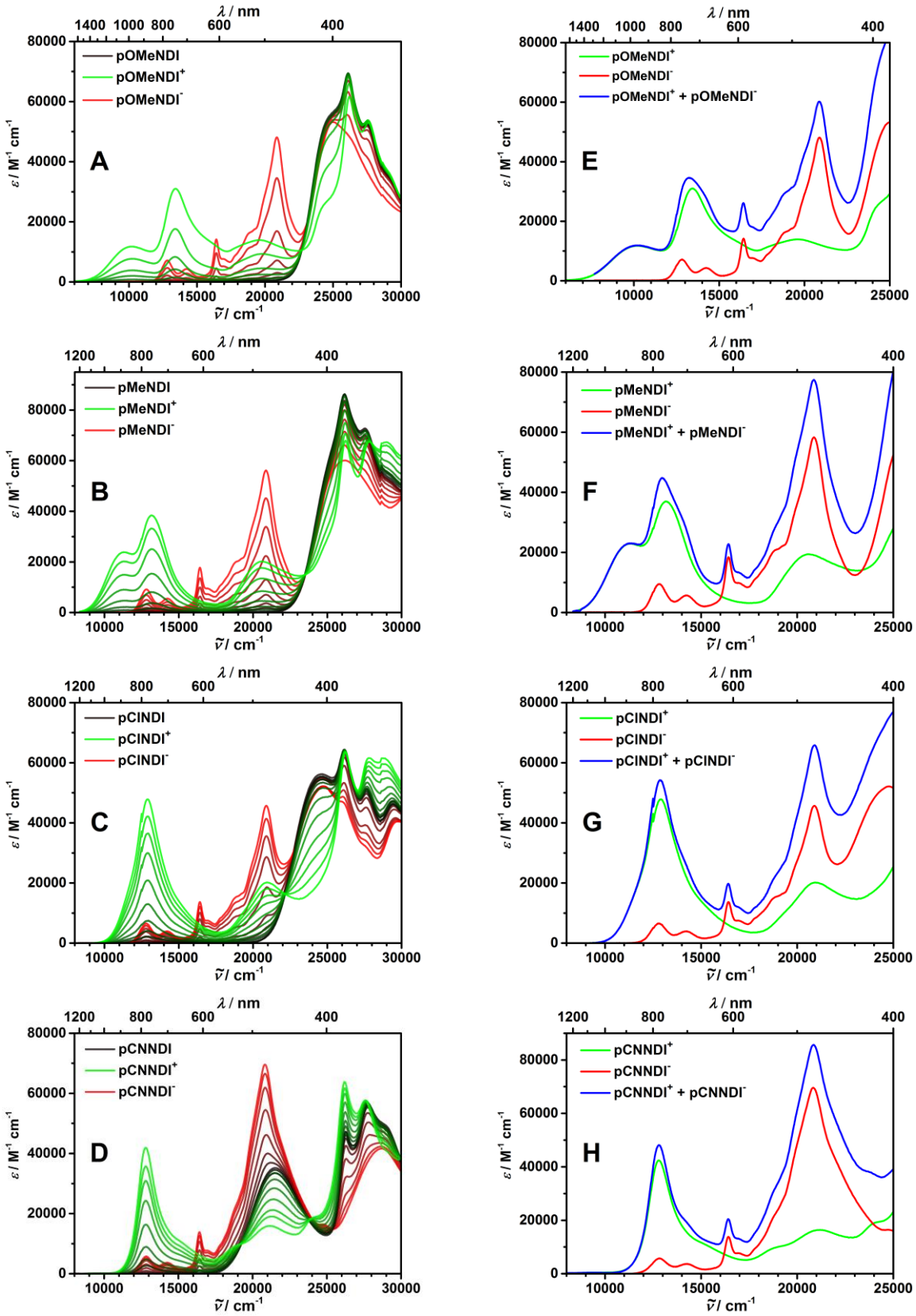

Figure 45: Left: Stepwise first oxidation (green) and first reduction (red) of the *para*-compounds (A–D) from spectroelectrochemistry. Right: Monoradical cation (green) and monocation spectrum (red) and the sum of both (blue; E–H). All spectra were recorded in DCM/0.2M TBAHF.

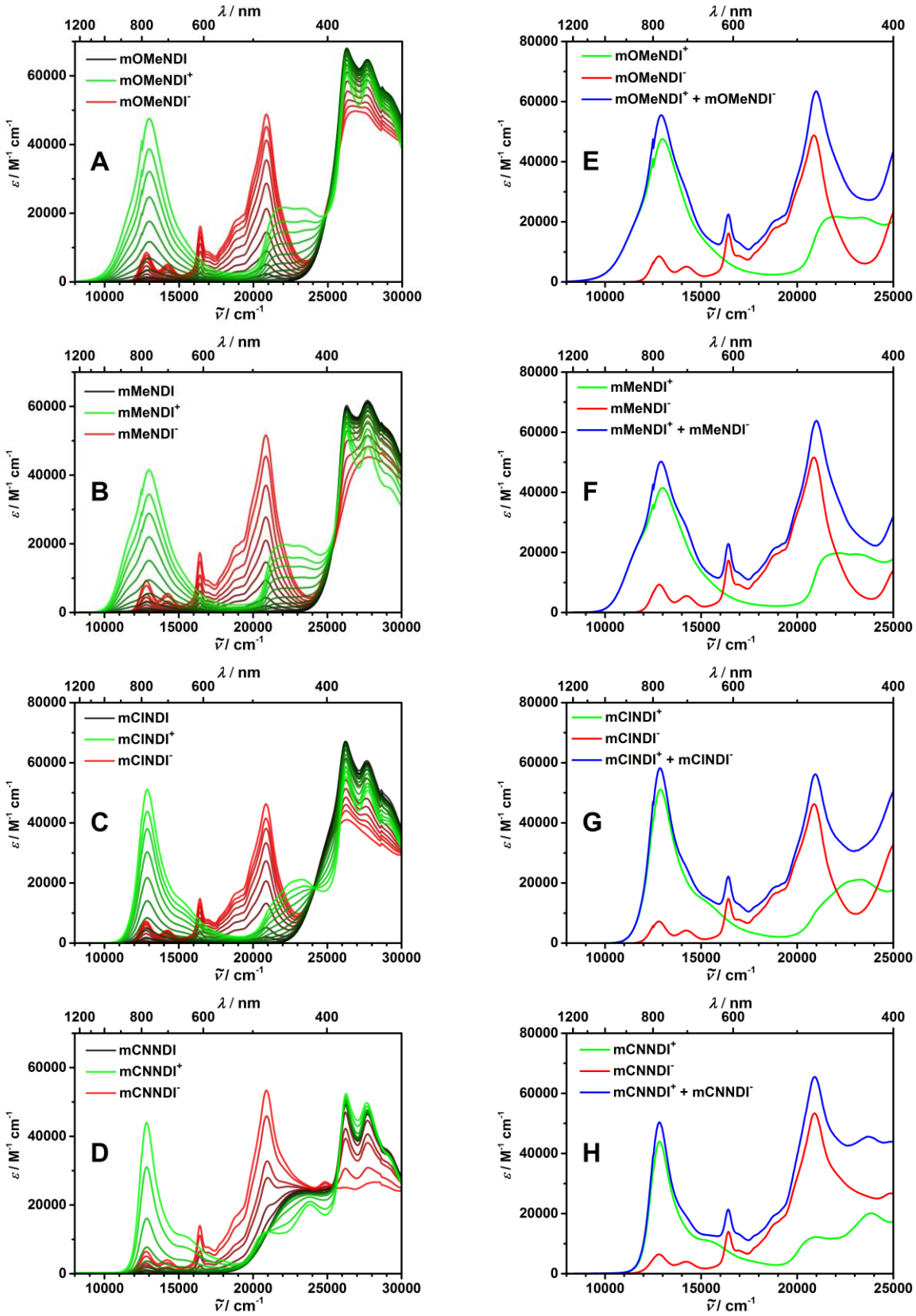

Figure 46: Left: Stepwise first oxidation (green) and first reduction (red) of the *meta*-compounds (A–D) from spectroelectrochemistry. Right: Monoradical cation (green) and monocation spectrum (red) and the sum of both (blue; E–H). All spectra were recorded in DCM/0.2M TBAHF.

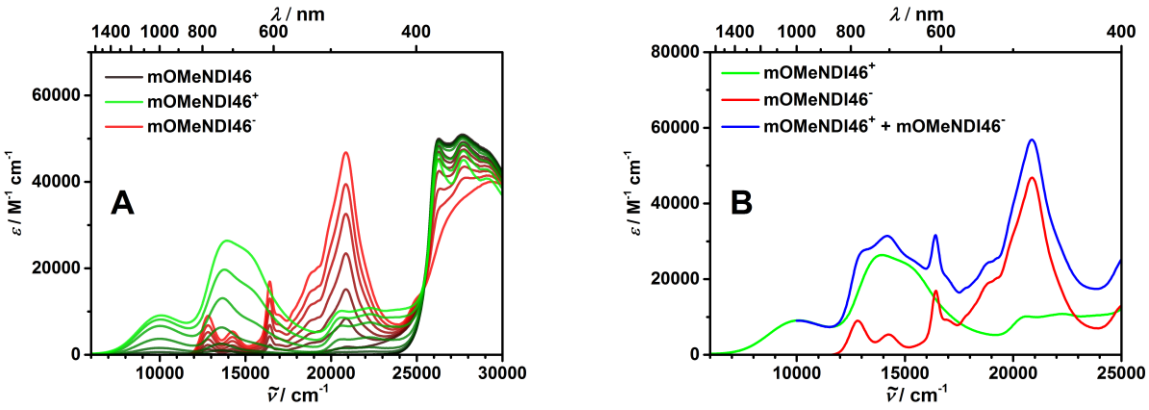

Figure 47: Stepwise first oxidation (green) and first reduction (red) of **mOMeNDI46** (A) from spectroelectrochemistry. Monoradical cation (green) and monocation spectrum (red) and the sum of both (blue; B). All spectra were recorded in DCM/0.2M TBAHF.

Upon stepwise oxidation of the dyads the situation gets more complex (green). Here, intense absorptions between ca. 7000 cm^{-1} (1430 nm) and 17000 cm^{-1} (588 nm) rise, which can be assigned to π–π* TAA radical cation transitions. This signal is a result of two excitations: one HOMO−1 → SOMO transition with transition moment oriented along the alkyne axis and one HOMO → SOMO transition with a transition moment perpendicular to it. The former gets influenced by the bridge and is therefore related to the substituents at the bridging unit ("bridge band"). The latter is not related to a π–π* transition within the dianisyl part of the TAA cation and is called in the following "π–π* band (cf. chemical oxidation of the bisTAAs in chapter 3.3.1) EWG (like CN) shift the HOMO−1 → SOMO transition to higher, EDG (like OMe) to lower energies, respectably. In case of **pClNDI$^{\bullet+}$**, **mMeNDI$^{\bullet+}$** and **mOMeNDI$^{\bullet+}$**, the HOMO and the HOMO−1 are almost degenerated and thus the absorptions sum up to one broad signal. The bridge band absorptions of **p-/mCNNDI$^{\bullet+}$** and **mClNDI$^{\bullet+}$** are hypsochromically shifted and exhibit a shoulder at higher wavenumbers. For **pMeNDI$^{\bullet+}$** the bridge band are bathochromically shifted by about 2000 cm^{-1}, showing the influence of X and the importance of the substitution pattern of the donor and acceptor at the bridging benzene unit (cf. **mMeNDI$^{\bullet+}$** has two degenerated transitions). For **pOMeNDI$^{\bullet+}$** and **mOMeNDI46$^{\bullet+}$**, the position of the maximum of the bridge band is even shifted by 2000 cm^{-1}. This shows that not only the *meta*-/*para*-orientation of the donor and acceptor, but also that of substituent X is crucial.

Table 25: Absorption maxima ($\tilde{\nu}_{max}$ and λ_{max}) and extinction coefficients (ε_{max}) of the characteristic absorption bands of the cationic and anionic *para*- (**pXNDI**) and *meta*-compounds (**mXNDI**) with OMe to CN substituents, determined by SEC

	TAA cation $\tilde{\nu}_{max}$ (λ_{max}) / ε_{max} / cm^{-1} (nm) / M^{-1} cm^{-1}	**TAA cation** $\tilde{\nu}_{max}$ (λ_{max}) / ε_{max} / cm^{-1} (nm) / M^{-1} cm^{-1}	**NDI anion** $\tilde{\nu}_{max}$ (λ_{max}) / ε_{max} / cm^{-1} (nm) / M^{-1} cm^{-1}
pOMeNDI	10200 (980) / 11800	13400 (746) / 31000	20900 (478) / 48100
pMeNDI	11200 (893) / 23800	13100 (763) / 38400	20900 (478) / 56200
pClNDI	-	12900 (775) / 47900	20900 (478) / 45700
pCNNDI	-	12800 (781) / 41800	20800 (481) / 69600
mOMeNDI	-	13000 (746) / 47500	20900 (478) / 47500
mMeNDI	-	13000 (746) / 41500	20900 (478) / 51600
mClNDI	-	12900 (775) / 51500	20900 (478) / 46300
mCNNDI	-	12800 (781) / 44000	20900 (478) / 53300
mOMeNDI46	10100 (990) / 9100	13900 (719) / 26400	20900 (478) / 46800

Between ca. 17000 cm^{-1} (588 nm) and 25000 cm^{-1} (400 nm) one can identify a rise of additional absorptions, whose origins could not be clarified. They are assigned to be higher excitations within the $TAA^{\bullet+}$, because "isolated" $TAA^{\bullet+}$ that are not attached to a further molecule moiety, show comparable absorptions.[96]

As already described in chapter 4.2, the signals of the neutral dyads between 25000–30000 cm^{-1} (400–333 nm) result from the superposition of the TAA and the NDI absorptions. When oxidizing dyads with X = OMe–Cl, the TAA associated π–π^* excitations in this area decrease. Consequently while the NDI peaks become clearer and sharper the total absorption somewhat decrease. In contrast to **p-/mCNNDI**, where large parts of the π–π^* TAA excitations of the neutral species show a strong influence of the bridge and are shifted to lower energy. Here, even an increase of the NDI structures takes place during oxidation, which is assigned to a superposition of the NDI transitions and a new, $TAA^{\bullet+}$ related, transition appears.

All compounds have in common that simultaneous to the growth of the $TAA^{\bullet+}$ bands, the neutral TAA bands decrease, which indicates that the TAA cation is directly formed at the expense of the neutral TAA, since no other intermediates were found.

The resulting features for oxidative and reductive species will help to identify the CS states, interpret the transient absorption spectra and to understand possible ET pathways. SEC experiments provide the possibility to estimate the spectra of the CS states in which the NDI is reduced and the TAA is oxidized. It can be simulated by the sum of the TAA cation and the

NDI anion spectra that were obtained by the measurements. On the right side of Figure 42 the radical anion (red) and the radical cation (green) and sum of them (blue) for **pXNDI** (X = OMe–CN) are depicted. The right side of Figure 43 shows the spectra of the *meta*-derivatives **mXNDI** and the right side of Figure 47 those of **mOMeNDI46**. The absorption maxima are hardly shifted by the sum of the separate spectra. The simulated CS spectra show three (four for the dyads with separated bridge band) dominating peaks between ca. 10000 cm^{-1} (1000 nm) and 23000 cm^{-1} (437 nm), namely the sharp and intense $NDI^{\bullet+}$ absorption at ca. 20900 cm^{-1}, the less intense one at 16400 cm^{-1} and the $TAA^{\bullet+}$ absorption between 10000 cm^{-1} and 15000 cm^{-1} (which is separated into two for the dyads with energetic low laying bridge band). The two small $NDI^{\bullet+}$ peaks at 12800 cm^{-1} and 14200 cm^{-1} are dominated by the overlaying $TAA^{\bullet+}$ absorptions and therefore no longer observable.

4.5 Steady-State Emission Spectroscopy

Although the dyads are practically non-fluorescent ($\phi < 0.01$) due to effective quenching of the excited state by photoinduced electron transfer processes, the references **sOMe**, **sMe**, **sCl** and **sCN** show distinct emission. In order to determine their excited state energies and thus estimate those of the dyads, steady-state fluorescence spectroscopy of the fragments were performed in toluene (Figure 48, A) and MeCN (Figure 48, B, not for **sCN**), therefore the molecules were excited at their respective absorption maxima. For both solvents the free energy difference ΔG^{00} was determined by calculating the average of the absorption and emission maxima. In addition to that, the fluorescence quantum yields ϕ were measured using optically dense samples in an integrating sphere. The obtained data are listed in Table 26.

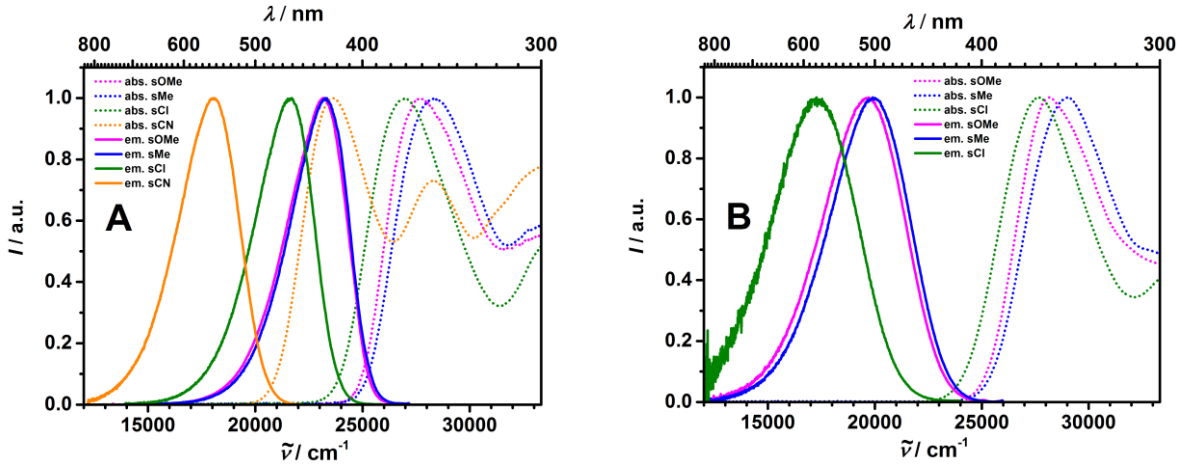

Figure 48: Normalized emission (solid lines) and absorption spectra (dotted lines) of the references **sOMe**, **sMe**, **sCl** and **sCN** in toluene (A). Normalized emission (solid lines) and absorption spectra (dotted lines) of the references **sOMe**, **sMe**, **sCl** in MeCN (B). The molecules were excited at (or near) their absorption maximum (see Table 26).

The reference compounds show the typical TAA fluorescence behavior, that is large *Stokes* shifts and mirror images to the energetic lowest absorption bands.[103, 183] The emissions are broad and featureless and strongly dependent on the solvent polarity. In toluene the emission maxima shift bathochromic with increasing the electron withdrawing strength of the substituents X. In toluene the maxima shift starting from 23300 cm^{-1} (429 nm) for **sMe** over 23200 cm^{-1} (431 nm) for **sOMe** and 21700 cm^{-1} (461 nm) for **sCl** to 18000 cm^{-1} (555 cm^{-1}) for **sCN**.

Thus, as in the absorption measurements, the dimethyl substituted benzene seems to exhibits better donor qualities than the dimethoxybenzene moiety. This can again be explained by the rotation of (at least) one OMe out of plane (see 3.2.2).

In MeCN investigation of **sCN** was not possible, since it is non-fluorescent, for the other references a bathochromic shift from 19900 cm^{-1} (503 nm) for **sMe** over 19700 cm^{-1} (508 nm) for **sOMe** to 17300 cm^{-1} (578 cm^{-1}) for **sCl** is observed, too. The high solvent dependency is a typical behavior for the emission from a charge transfer state, since the state is stabilized more efficiently in polar solvent. Accordingly, the free energy difference ΔG^{00} in MeCN is about 0.3 eV less than in toluene.

The fluorescence quantum yields (QY) show a strongly differing behavior. In toluene QY rises from 0.49 for **sMe** to 0.53 for **sOMe** and stays constant (ca. 0.64) for **sCl** and **sCN**. Remarkably, for **sCN** hardly any change of QY is observable when changing the excitation wavelength from the energetically lowest transition at 23600 cm^{-1} (423 nm) to 28300 cm^{-1} (353 nm). However in MeCN the QY somewhat drops from 0.41 for **sMe** to 0.36 for **sOMe**, then there is a drastically drop to 0.04 for **sCl** and for **sCN** determination of ϕ was not even possible.

Table 26: Fluorescence data of **sOMe**, **sMe**, **sCl** and **sCN** in toluene and MeCN (not for **sCN**).

		$\tilde{\nu}_{fl}$ (λ_{fl}) / cm^{-1} (nm)	$\tilde{\nu}_{abs}$ (λ_{abs}) / cm^{-1} (nm)	ϕ	ΔG^{00} / eV
toluene	**sOMe**	23200 (431)	27700 (361)	0.53	2.71
	sMe	23300 (429)	28500 (351)	0.49[a]	2.76
	sCl	21700 (461)	27000 (370)	0.65[a]	2.59
	sCN	18000 (555)	28300 (353) 23600 (423)	0.64 0.63	2.21
MeCN	**sOMe**	19700 (508)	28100 (356)	0.36	2.47
	sMe	19900 (503)	29000 (345)	0.41	2.53
	sCl	17300 (578)	27700 (361)	0.04	2.33

[a]Values determined by excitation at 28300 cm^{-1} (353 nm).

4.6 Electron Transfer Processes

At this point it is important to explain why the study of the ET will be restricted to the *meta*-dyads **mXNDI** (X = OMe–CN) and **mOMeNDI46**. Hence, some later findings have to be anticipated to explain these limitations.

The aim of the following part of this work is to investigate the dynamics of the charge separation (CS) and charge recombination (CR) after photoexcitation of the dyads. Therefore, the CS will be examined by fs-, the CR by ns-transient absorption (TA) spectroscopy. In both cases the dyads are excited by an intense laser pulse and the transient is probed with time delay. Unfortunately, it was not possible to investigate the photo dynamics taking place after excitation for the nitro dyads **p-/mNO$_2$NDI**, since they decomposed rapidly under these conditions. Therefore these dyads are not dealt with in this part.

The dyads of the *para*-series **pXNDI** (X = OMe–CN) did not show a transient absorption in the ns-time range. It is assumed, probably due to efficient coupling, that the CR processes are significantly faster compared to the *meta*-dyads. This assumption is supported by the knowledge gained in the first part of the work, which assigns markedly higher couplings to the *para*-connections. Since a complete picture of all charge transfer processes, starting from CS up to CR, is to be obtained, the investigation of the *para*-compounds was dispensed for the benefit of the *meta*-compounds **mXNDI** (X = OMe–CN) and **mOMeNDI46**, since the entire dynamic are detectable in the latter case.

4.6.1 TD-DFT Computations

In order to get first information of the charge transfer properties of **mXNDI** (X = OMe, Me, Cl, CN) TD-DFT computations were performed were performed.[6] The DFT optimizations of the ground state structure in the gas phase was done at B3LYP/6-31G* level. The obtained MOs for **mXNDI** are shown in Figure 53 to Figure 52. While the HOMO is in all cases located at the TAA moiety, the LUMO is at the NDI. In contrast to the LUMO extent, which has a strict limitation on the central naphthalene core, the HOMO has a significant MO contribution at the attached bridge in the ground state (S_0). Consequently, a reason for the influence of the substituents X on photophysical/electrochemical properties of the molecules is evident (e.g. steady state absorption, CV).

In order to estimate the inner reorganization energy, the charge transfer state S_2 (= CT) and the charge separated S_1 (= CS) of **mCNNDI** were also optimized (Figure 53), which gave 0.39 eV for the charge separation (CT → CS) and 0.43 eV for charge recombination (CS → S_0). Furthermore, it is apparent that the influences of the substituents X on the LUMO decreases when going from the S_0 to the S_1 state since the MO distributions becomes more TAA localized. For all three states the LUMO+1 is localized at the bridge having only small orbital coefficients at the benzene unit connected to the NDI (but not with the naphthalene itself), indicating the influence of X to the CT transition.

The dipole moment of the CS states (μ_{CS}) of all dyads were calculated to characterize the amount of charge separation. The dipole moment drops from 90.8 D for **mOMeNDI**, to 88.4 D for **mMeNDI** and 83.0 D for **mCNNDI**. However μ_{CS} for **mCNNDI** (90.7 D) is close to that obtained for **mOMeNDI**. A dipole difference of e.g. 90.8 D corresponds to a charge separation of 18.9 Å. Accordingly, compared to the calculated TAA nitrogen and NDI center distance of 19.5 Å, the high dipole moments indicate almost complete charge separation.

DFT calculations for **mOMeNDI** support an assumption which explains some photophysical properties of the methoxy compounds investigated in this work. The DFT optimizations show that the OMe group situated at the 2-position between the two alkynyl groups is turned out of the π-plane for steric reasons, that is, the oxygen p-type lone pair orbital cannot overlap with the benzene π-orbitals. This particular orientation of the methoxy group is probably present in the reference compounds and the methoxy compounds presented in the first part of this work, too. Therefore this particular OMe group acts as an electron acceptor through the oxygen electronegativity rather than an electron donor through the lone-pair orbital. This causes a slightly less electron rich benzene ring in comparison to the respective methyl derivative (e.g. **mMeNDI**).

[6] The TD-DFT computations were performed by Dr. Marco Holzapfel.[181]

mOMeNDI

LUMO+3 (-1.34 eV)

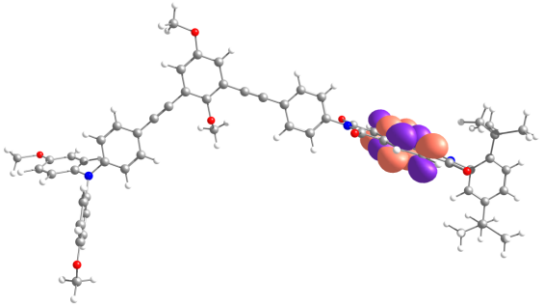

HOMO (-4.16 eV)

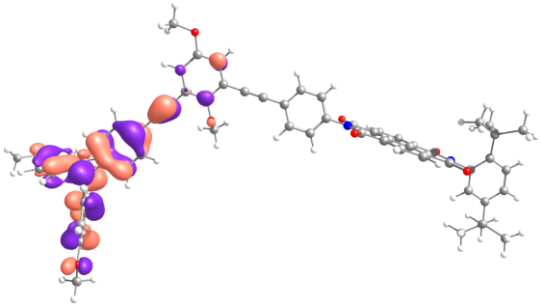

LUMO+2 (-1.50 eV)

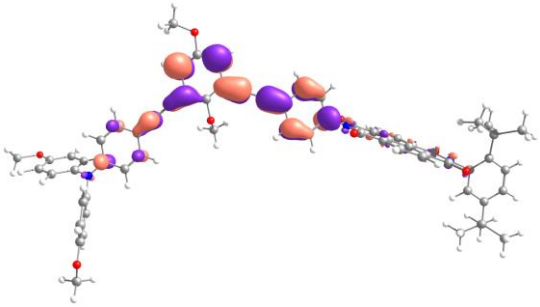

HOMO-1 (-4.99 eV)

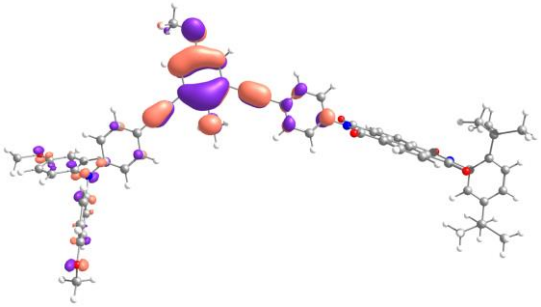

LUMO+1 (-1.81 eV)

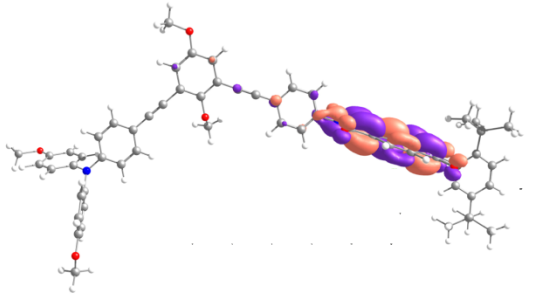

HOMO-2 (-5.10 eV)

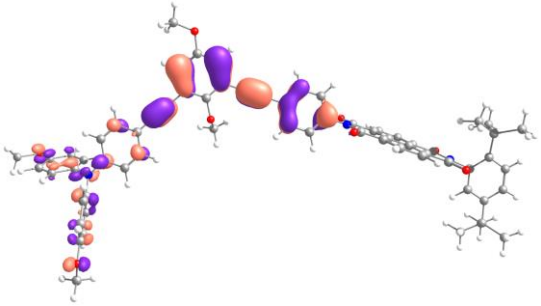

LUMO (-3.39 eV)

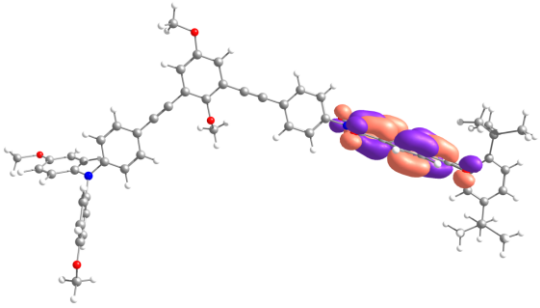

HOMO-3 (-5.60 eV)

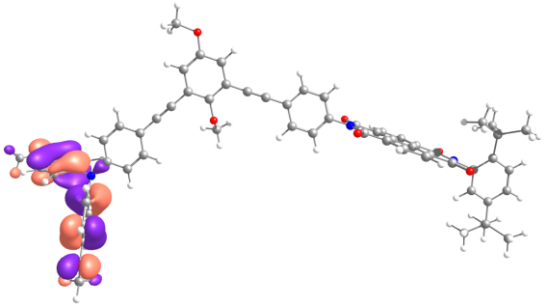

Figure 49: MOs of **mOMeNDI** calculated on basis of a B3LYP /6-31G* functional.

mMeNDI

LUMO+3 (-1.35 eV)

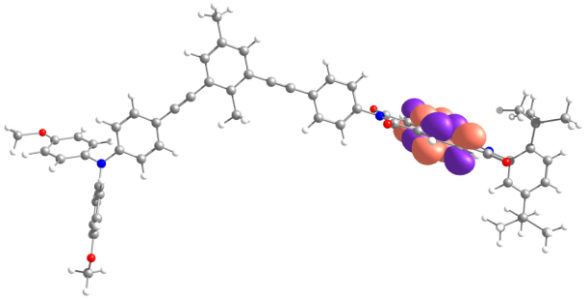

HOMO (-4.14 eV)

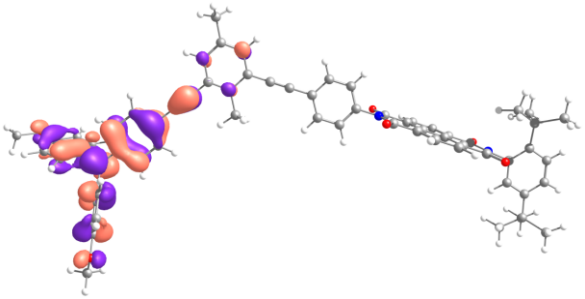

LUMO+2 (-1.50 eV eV)

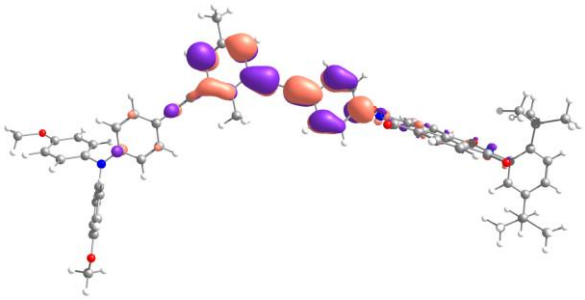

HOMO-1 (-5.06 eV)

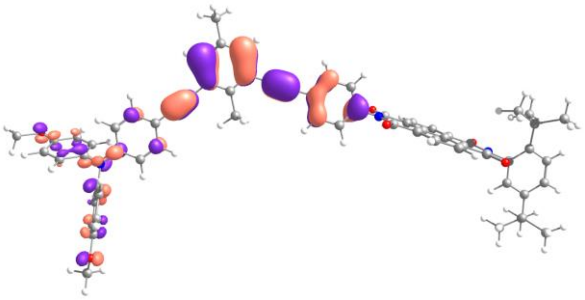

LUMO+1 (-1.83 eV)

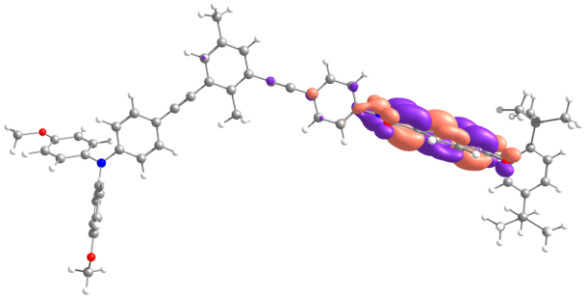

HOMO-2 (-5.20 eV)

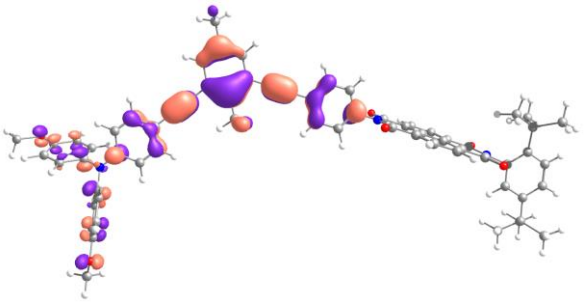

LUMO (-3.40 eV)

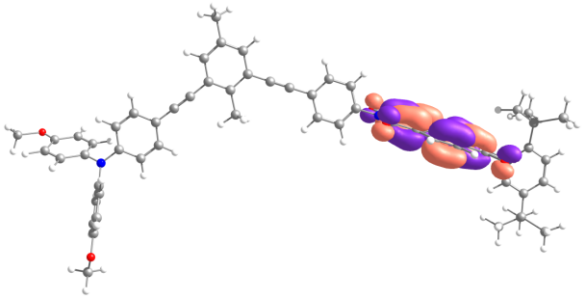

HOMO-3 (-5.58 eV)

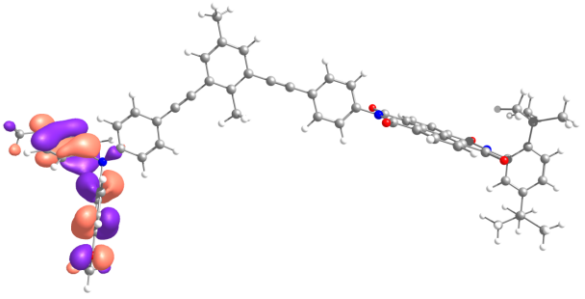

Figure 50: MOs of **mMeNDI** calculated on basis of a B3LYP /6-31G* functional.

mClNDI

LUMO+3 (-1.49 eV)

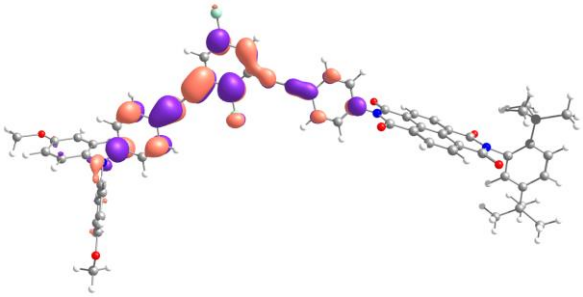

HOMO (-4.29 eV)

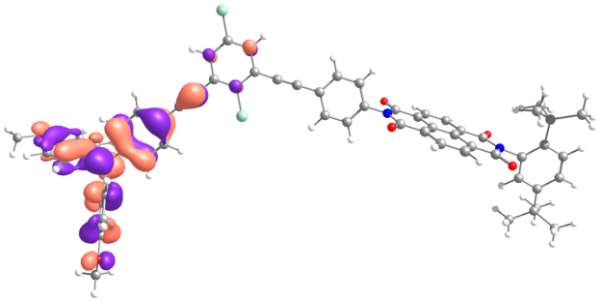

LUMO+2 (-1.77 eV)

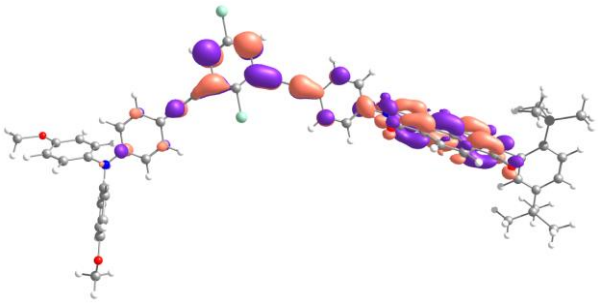

HOMO-1 (-5.34 eV)

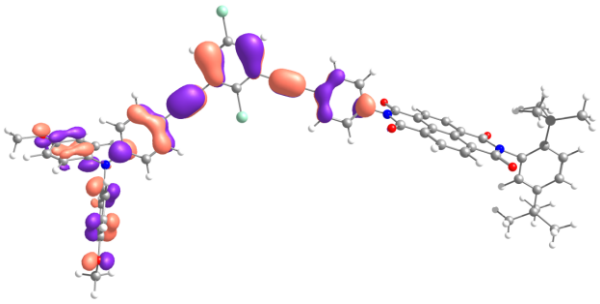

LUMO+1 (-1.96 eV)

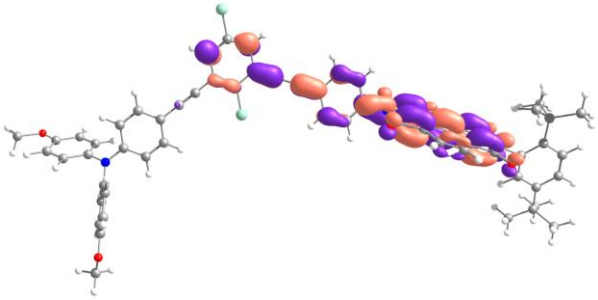

HOMO-2 (-5.43 eV)

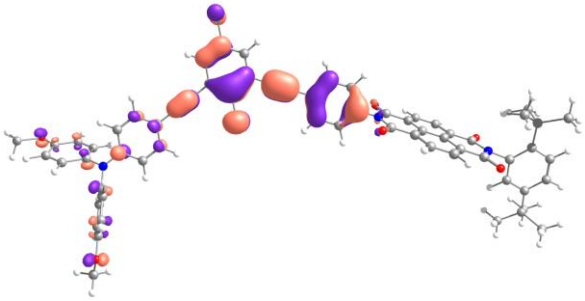

LUMO (-3.46 eV)

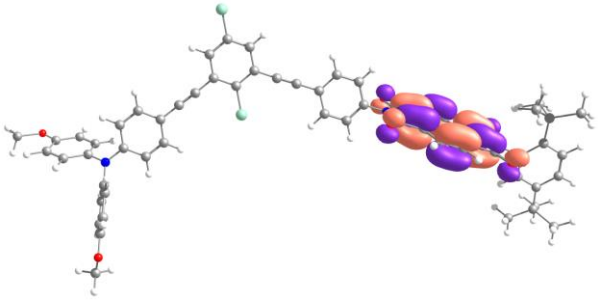

HOMO-3 (-5.67 eV)

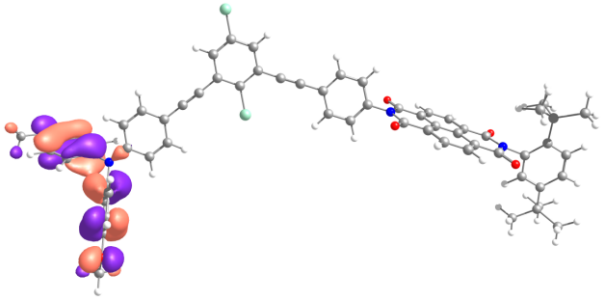

Figure 51: MOs of **mClNDI** calculated on basis of a B3LYP /6-31G* functional.

mCNNDI

LUMO+3 (-1.88 eV)

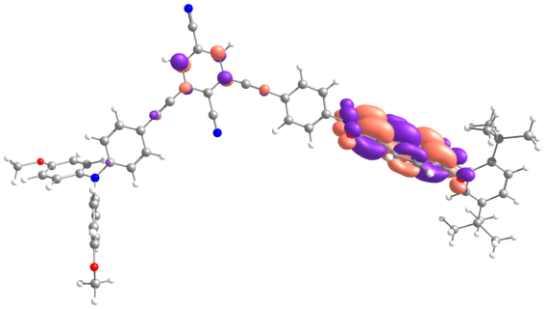

HOMO (-4.44 eV)

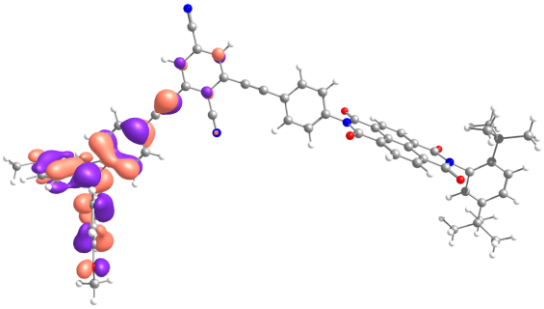

LUMO+2 (-2.10 eV)

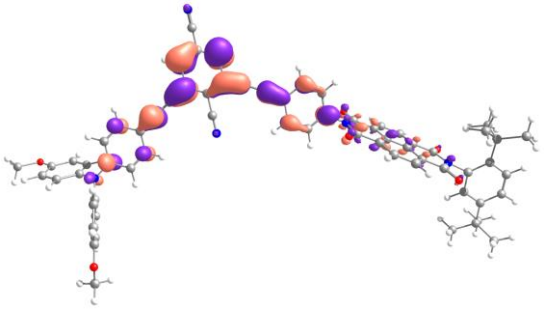

HOMO-1 (-5.55 eV)

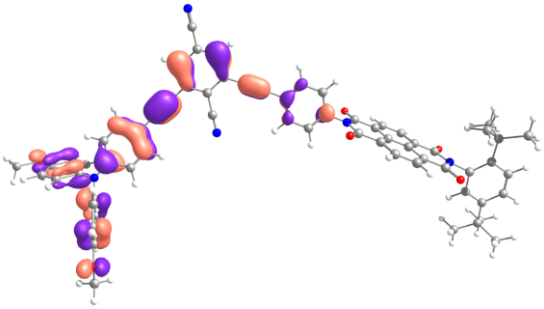

LUMO+1 (-2.48 eV)

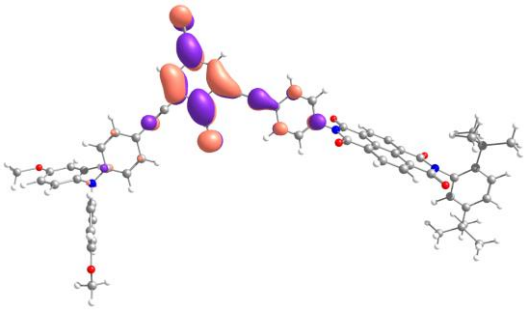

HOMO-2 (-5.73 eV)

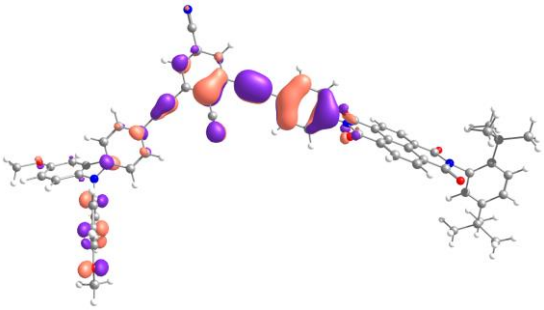

LUMO (-3.49 eV)

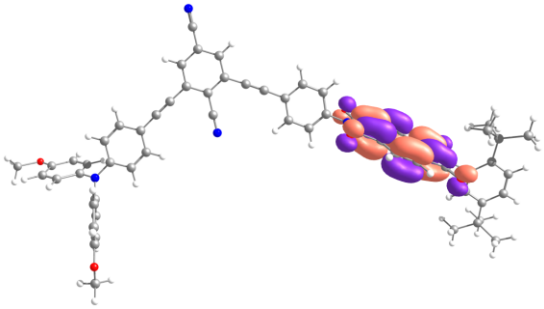

HOMO-3 (-5.75 eV)

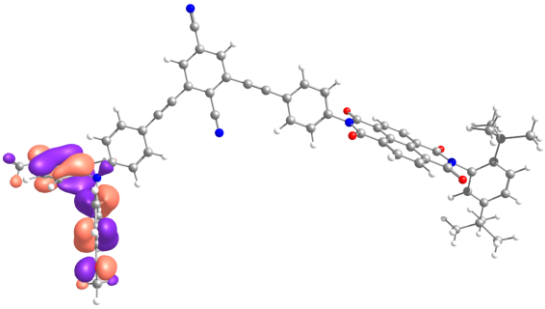

Figure 52: MOs of **mCNNDI** calculated on basis of a B3LYP /6-31G* functional.

mCNNDI

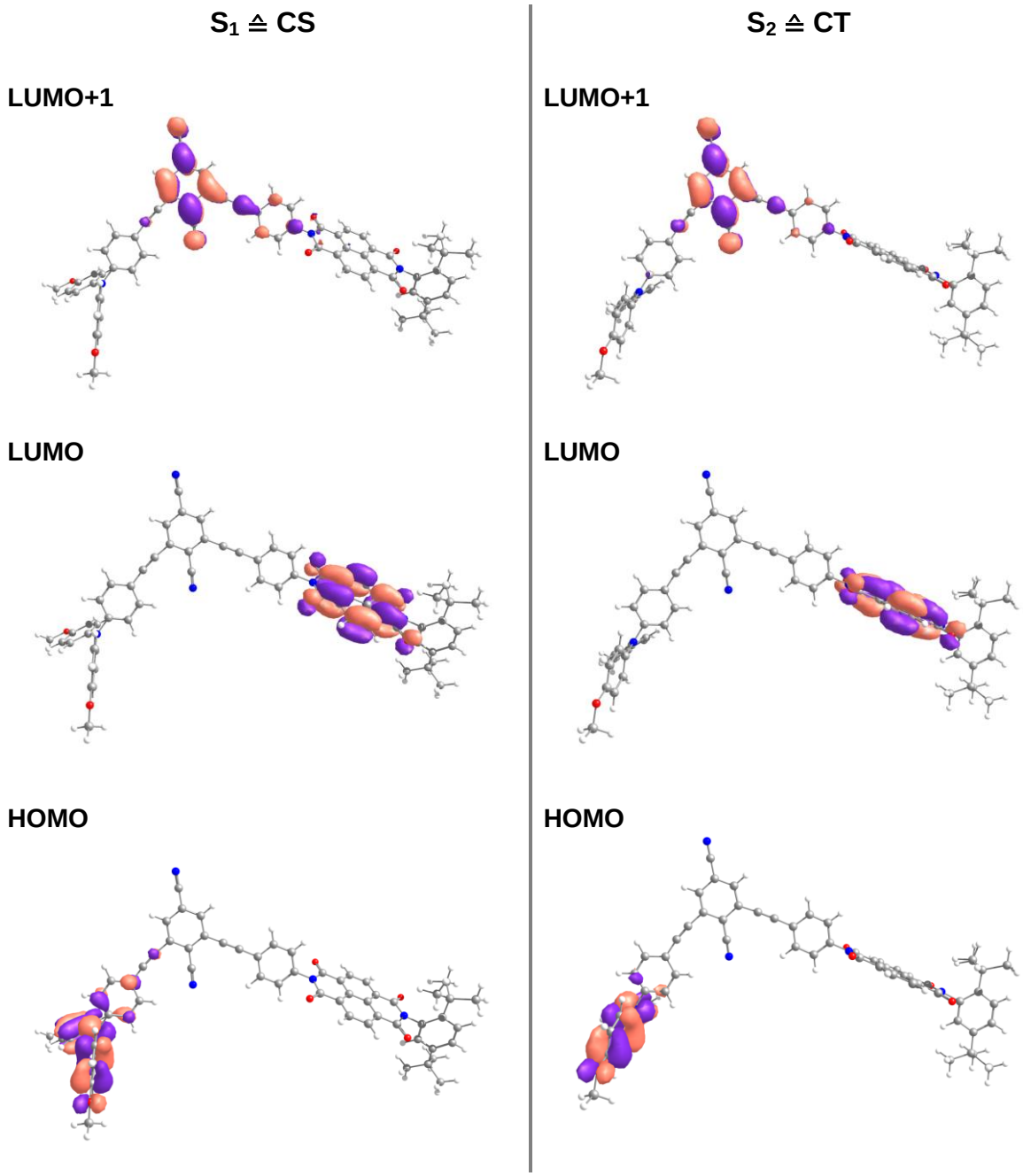

Figure 53: HOMO, LUMO and LUMO+1 of the S_1 and S_2 states of **pCNNDI** obtained by DFT calculations on basis of a B3LYP /6-31G* functional.

Table 27: Calculated dipole moment and the resulting distance of the charges in the CS state for the *meta*-compounds **mXNDI** with X = OMe–CN.

meta	μ_{CS} / D	d_{DA} from μ_{CS} / Å
mOMeNDI	90.8	18.9
mMeNDI	88.4	18.4
mClNDI	90.7	18.9
mCNNDI	83.0	17.2

An important parameter, when discussing the charge separation in context of *Marcus* theory is the electronic coupling V_{CS}. Assuming a coherent superexchange mechanism, lower virtual bridges states should promote ET. That is, the lower the local LUMO energy of the bridge, the larger the coupling.[204] Figure 54 shows a plot of the energies of LUMO+2 and HOMO-1 for the dyads **mXNDI**, representing the bridge states. The LUMO energies of the bridge shows the trend ε_{LUMO}(Me) > ε_{LUMO}(OMe) > ε_{LUMO}(Cl) > ε_{LUMO}(CN), thus the electronic coupling is expected to increase in the same sequence.

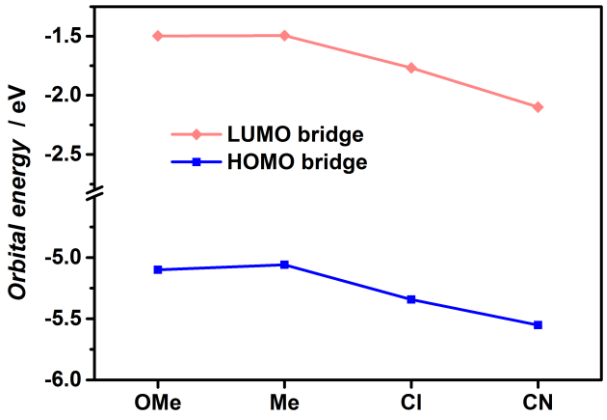

Figure 54: HOMO and LUMO energies of the bridges states in dyads **mXNDI** (X = OMe-CN).

4.6.2 ESR Spectroscopy

In order to get indications on the positions of the unpaired electrons in the CS-state, ESR measurements of the radical cations and anions of the *meta*-compounds **mXNDI** (x = OMe, Me, Cl CN) were performed.[7] by Dr. Ivo Krummenachen.[178] The measurements were done in *o*DCB at a concentration of ca. 1×10^{-4} M at rt. The radical cations and anions were generated by oxidation with tris(bromophenyl)ammonium hexachloroantimonate, the radical anions by reduction with cobaltocene.[173] The ESR spectra are presented in Figure 55 (cations on the left and the respective anions on the right). The *g* values were referenced to 1,1-diphenyl-2-picrylhydrazyl (DPPH, $g = 2.0036 \pm 0.0002$)[205] and the spectral simulations were performed using MATLAB and EasySpin 4.5.5.[206] The hyperfine coupling constants and *g*-values thus obtained are listed in Table 28. For the simulations of the anion spectra the chemically non-equivalent nitrogen atoms of the naphthalene diimide unit display virtually the same nitrogen hyperfine coupling constant, that is why only one value is given. For the same reason, the four hydrogen atoms of the NDI were treated as being equivalent, too.

As expected, the ESR measurements clearly show that in **mXNDI$^{\bullet-}$** the electron is located in the center of the NDI unit. This is confirmed by comparison of the hfc, *g*-values and line shape with similar NDI radical cations, e.g. without further substituents at the outer benzenes.[207-209] However, in the oxidized species **mXNDI$^{\bullet+}$** the radical is distributed over the TAA moiety. In accordance with literature, it is assumed with ca. 2/3 of the spin density distributed over the three phenyl groups.[210, 211]

All determined *g*-values are slightly larger than those of the free electron (2.0023). For **mOMeNDI$^{\bullet+}$** and **mOMeNDI$^{\bullet+}$** the *g*-factor has a value of 2.0033, and for **mClNDI$^{\bullet+}$** and **mCNNDI$^{\bullet+}$** of 2.0034. The nitrogen hfc are constant at 24.0 MHz for X = OMe, Me, Cl and somewhat with 24.9 MHz somewhat higher for **mCNNDI$^{\bullet+}$** (couplings to hydrogen atoms were not used for simulations of the spectra). For the anions with X = OMe a *g*-factor of at 2.0039, for X = Me–CN of 2.0038 was obtained. Here the nitrogen hfc rise slightly from 2.68 to 2.80 MHz, while the hydrogen hfc drops from 5.28 to 5.15 MHz when decreasing the donating character of X from OMe to CN. Although a minor influence of X on the obtained data is present, the impact of X is very small and the measurements show a very uniform picture of the radical cations and anions.

[7] The ESR measurements and the simulations of the spectra were done by Dr. Ivo Krummenachen.[178] I. Krummenacher, *Institute of Inorganic Chemitry, University of Wuerzburg*, Wuerzburg, Germany.

By separate ESR measurements of the cation and anion, no direct statement on the situation of the biracial in the CS state is possible, since e.g. an additional Coulomb interaction is disregarded. Nevertheless, it is assumed that the situation in the CS state is similar, since the two moieties (NDI and TAA) are highly decoupled and in all cases no distribution of the electron to the respective rest of the molecule was observed.

Table 28: Overview of the hyperfine coupling constants and g values determined by ESR spectroscopy in toluene at rt.

		g_{iso}	a (^{14}N) [MHz]	a (^{1}H) [MHz]
radical cations	**mOMeNDI**$^{\cdot+}$	2.0033	24.0[a]	-
	mMeNDI$^{\cdot+}$	2.0033	24.0[a]	-
	mClNDI$^{\cdot+}$	2.0034	24.0[a]	-
	mCNNDI$^{\cdot+}$	2.0034	24.9[a]	-
radical anions	**mOMeNDI**$^{\cdot-}$	2.0039	2.68[b]	5.28[c]
	mMeNDI$^{\cdot-}$	2.0038	2.64[b]	5.26[c]
	mClNDI$^{\cdot-}$	2.0038	2.67[b]	5.25[c]
	mCNNDI$^{\cdot-}$	2.0038	2.80[b]	5.15[c]

[a]Nitrogen hyperfine coupling constant for the triarylamine unit. [b]The chemically non-equivalent nitrogen atoms of the naphthalene bisimide unit display virtually the same nitrogen hyperfine coupling constant, which is why only one value is given. [c]The four hydrogen atoms of the naphthalene bisimide unit were treated as being equivalent.

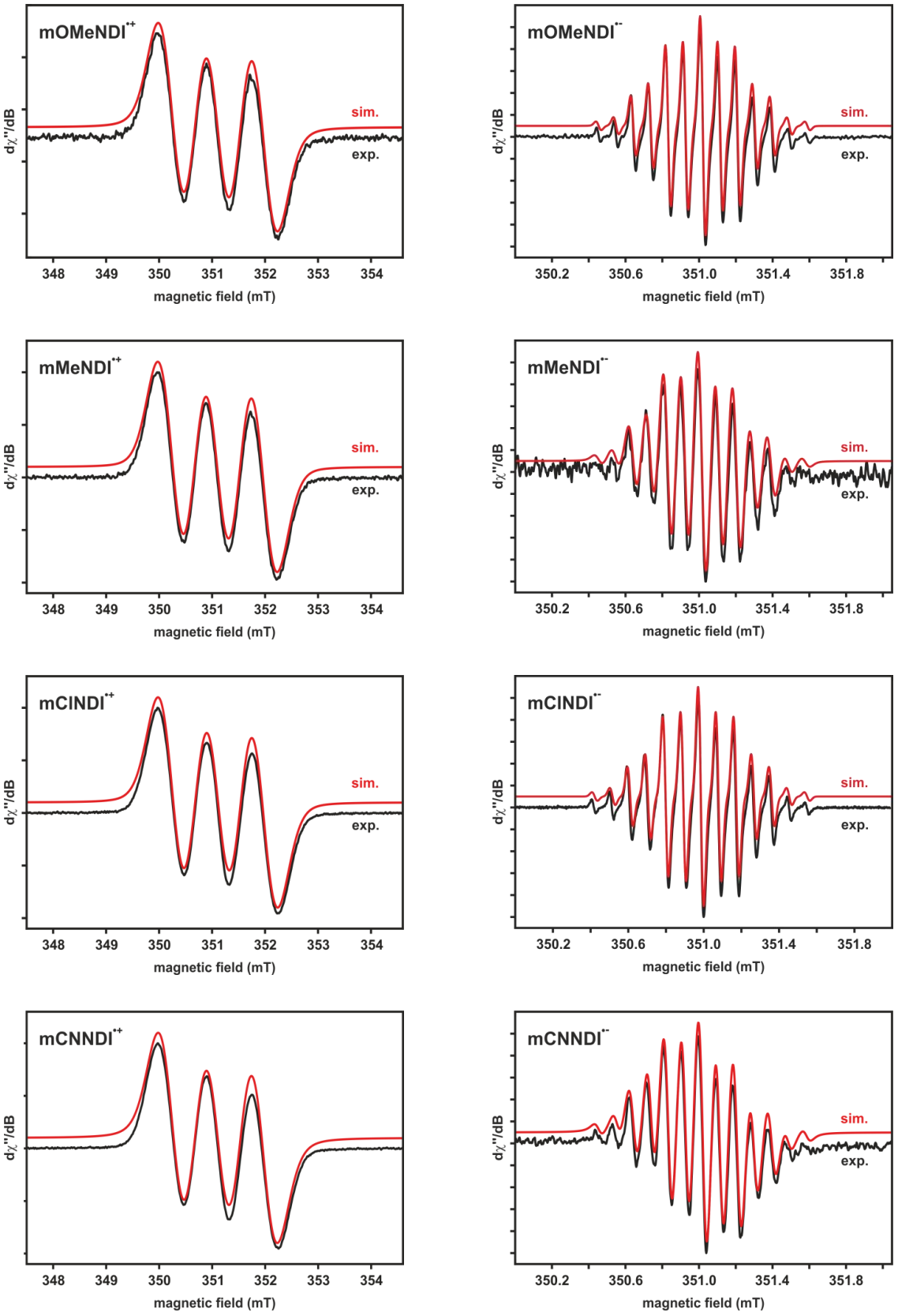

Figure 55: ESR spectra (black) of the radical cations (left) and radical anions (right) of the *meta*-dyads **mOMeNDI**, **mMeNDI**, **mClNDI** and **mCNNDI** in *o*DCB and their simulated spectra (red).

4.6.3 fs-Pump-Probe Spectroscopy

The photoinduced dynamics of dyads **mXNDI** (X = OMe, Me, Cl, CN) and **mOMeNDI46**, the two donor fragments **sOMe**/**sCN** and the three acceptor fragments **sOMeNDI**, **sCNNDI** and **sOMeNDI46** were investigated by fs-transient absorption (TA) spectroscopy in toluene.[8] The molecules were excited by pulses with an approximate duration of 140 fs. **mXNDI**, **sOMe** and **sCN** were pumped at wavenumbers which excite the CT state involving the TAA donor (4.2, Figure 41). This was done for **mCNNDI** at 23000 cm^{-1} (435 nm), which exclusively excites the CT state. For the other molecules excitation without involving the NDI absorption was not possible, thus **mClNDI** and **mOMeNDI** were excited in the rising flank of the CT band which has weak overlap with the NDI absorption at 25000 cm^{-1} (400 nm). It allows exciting the CT state to ca. 75 % for **mOMeNDI** and ca. 85 % for **mClNDI**. However, in case of **mMeNDI** and **mOMeNDI46** this was not possible, since the NDI absorption superimposes more with the CT absorption, and 26400 cm^{-1} (379 nm) and 27700 cm^{-1} (361 nm), respectively, was chosen which excites ca. 60 % of the CT state. **sOMe** was excited at 27700 cm^{-1} (361 nm) and **sCN** at 23500 cm^{-1} (426 nm). The acceptor references **sOMeNDI**, **sCNNDI** and **sOMeNDI46** were excited at the NDI maxima at 26200 cm^{-1} (382 nm). All transient spectra were probed by a white light continuum (ca. 140 fs) between 12500–25000 cm^{-1} (800–400 nm), except for **mOMeNDI46** where 15200–33300 cm^{-1} (660–300 nm) was chosen. Transient maps were recorded by delaying the probe pulse with quasilogarithmic time steps from 20 fs up to 8 ns. These transient maps were chirp corrected and analyzed by a global deconvolution which gave the minimum number of independent spectral components in form of evolution associated difference spectra (EADS) and the difference associated difference spectra (DADS).[9]

Before discussing the pump-probe spectra of dyads **mXNDI** and **mOMeNDI46** concerning the charge separation (CS) in detail, the photopyhsics of the donor fragments **sOMe** and **sCN** (Figure 56), as well as the acceptor fragments **sOMeNDI**, **sCNNDI** and **sOMeNDI46** (Figure 58) will be discussed, which will be helpful for understanding the dynamics of the dyads. The state diagram in Figure 57 summarizes the photophysical processes after excitation of the methoxy references.

For **sOMe** global analysis yields four components (Figure 56). First the formation of a broad excited state absorption (ESA) between 13000–22000 cm^{-1} (769–455 nm) and an emissive signal with a minimum at 24000 cm^{-1} (417 nm) takes place. The absorption is assigned to be correlated to a singlet excited species, which decays with τ_1 = 6.1 ps into a state with slightly different ESA shape and slightly shifted GSB minimum at 23300 cm^{-1} (429 nm). The

[8] The measurements were performed by Alexander Schmiedel.[212]
[9] The chirp corrections and deconvolution of the spectra were done by D. Marco Holzapfel.[181]

absorption of this state shows a somewhat more pronounced signal at 14000 cm^{-1} (714 nm), which indicates the formation of a positive partial charge at the TAA unit, thus a CT has to be formed with a negative partial charge at the dimethoxybenzene unit (bOMe).[166, 213] However, no spectral identification of the negative charged dimethoxybenzene was possible. The emissive signal possibly results from superposition of the ESA with fluorescence from TAA. This assumption is underpinned by the position of the minimum at 23200 cm^{-1} (429 nm), which matches the emission spectra of **sOMe** in chapter 4.5 (Figure 48). The CT state transforms with τ_2 = 99 ps into a very similar CT state, which might be the result of vibrational/rotational or solvent relaxation processes.[48, 214]

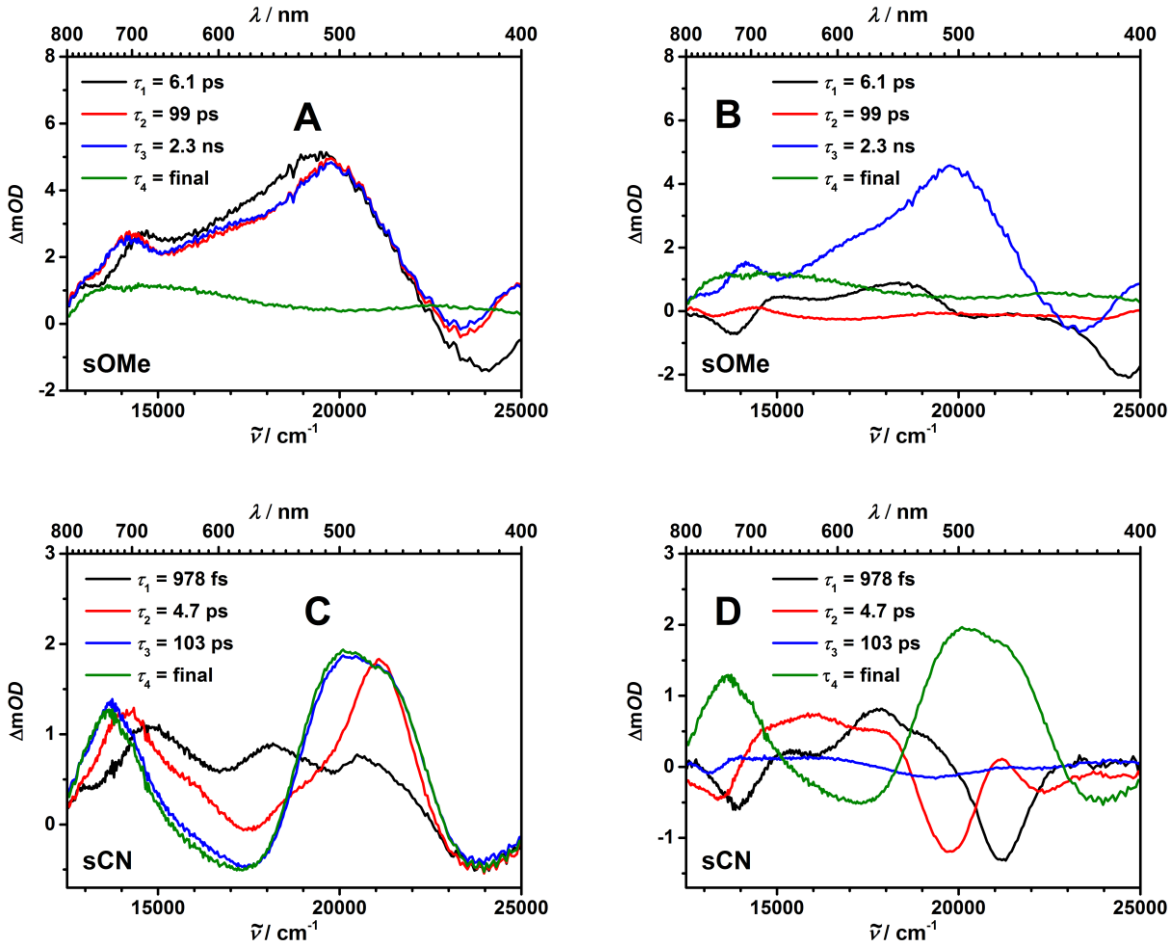

Figure 56: Evolution associated difference spectra (EADS) of **sOMe** (A) and **sCN** (C) in toluene, obtained from a global analysis of the transient map. Difference associated difference spectra (DADS) of **sOMe** (B) and **sCN** (D). **sOMe** was excited at 27700 cm^{-1} (361 nm), **sCN** at 23500 cm^{-1} (426 nm).

This third species decays with a lifetime of τ_3 = 2.3 ns into the last detected species within this fs-setup, that is a long lived (possibly triplet) state with very broad absorption features

and low maximum at ca. 16000 cm^{-1} (625 nm). These EADS are very similar to those observed for TAA with cyclophane attached to it, previously observed by *Lambert et al.*[166]

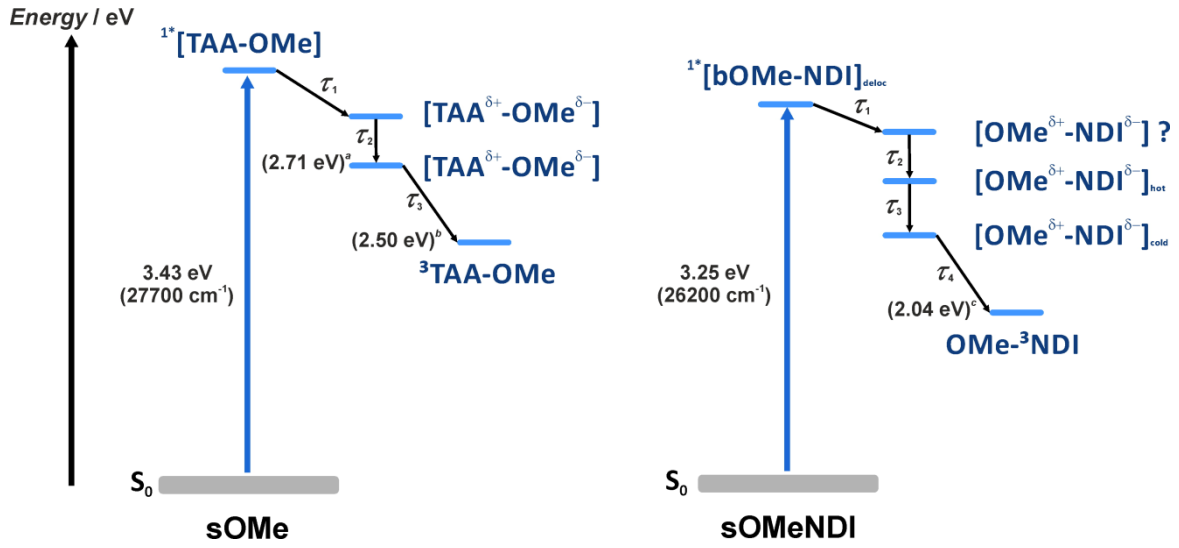

Figure 57: State diagrams for the photophysical dynamics in reference compounds **sOMe** (left) and **sOMeNDI** (right). (a) Determined by stead state absorption and fluorescence measurements. (b) Triplett energy of dianisylaminobiphenyl in toluene at 77 K.[103] (c) Triplett energy of NDI, averaged from EtOH at 77 K (2.05 eV)[215] and 2-methyl-THF at 77 K (2.03 eV).[216]

Although global analysis for **sCN** yields four components, too (Figure 56), the photoinduced dynamics are considerably different. First a broad ESA with three maxima at 14900 cm^{-1} (671 nm), 18100 cm^{-1} (552 nm) and 20700 cm^{-1} (483 nm), and a GSB at 23600 cm^{-1} (424 nm) is formed. The species shows a fast decay with τ_1 = 978 fs into the subsequent state, which has a strong ESA at 14100 cm^{-1} (671 nm), 21100 cm^{-1} (552 nm) and a minimum between 16700–18200 cm^{-1} (599–550 nm). After a lifetime of τ_2 = 4.7 ps it leads to a spectrum with a broad EAS between 18500–22500 cm^{-1} (541–444 nm) and a significant emissive signal between 15000–18500 cm^{-1} (667–541 nm). With τ_3 = 103 ps the last species is formed, which has a very similar spectrum. The origin of the fs-TAA spectra and states for **sCN** could not be clarified. Nevertheless, it is assumed that (at least) the two last spectra are a superposition of (possibly CT associated) ESA and the fluorescence of the TAA, since the maximum of the emissive signal at 18000 cm^{-1} (555 nm) has position as the emission maximum obtained by fluorescence spectroscopy in chapter 4.5 (Figure 48). Finally it is worth mentioning, that no formation of triplet state could be observed for **sCN**.

For the acceptor substituted reference sOMeNDI global analysis yields five components (Figure 58). After excitation, a broad ESA with a maximum at 21000 cm^{-1} (476 nm) and a small peak at 12900 cm^{-1} (775 nm) are detected. It is assigned to be a somehow delocalized

state (where adjacent units may be involved), since no absorption at ca. 16500 cm^{-1} (605 nm), which is typically observed for a locally excited NDI singlet state, is present. Fs-transient absorption measurements of similar NDI compounds support this interpretation.[198]

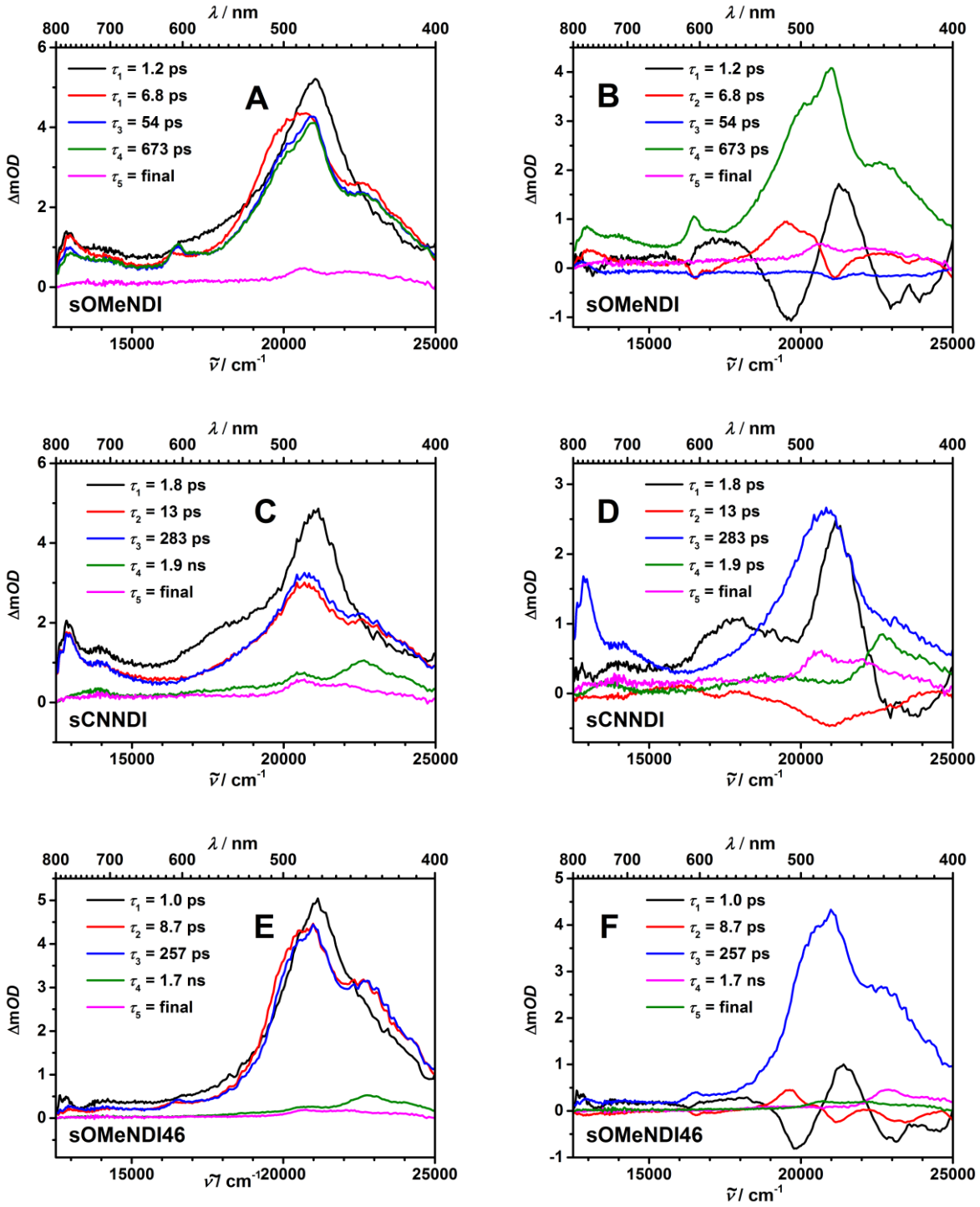

Figure 58: Evolution associated difference spectra (EADS) of **sOMeNDI** (A), **sCNNDI** (C) and **sOMeNDI46** (E) in toluene, obtained from a global analysis of the transient map. Difference associated difference spectra (DADS) of **sOMeNDI** (B), **sCNNDI** (D) and **sOMeNDI46** (F) in toluene. The molecules were excited at 26200 cm^{-1} (382 nm).

The delocalized state decays within τ_1 = 1.2 ps into a state where, at least to a small extent, absorption at 16500 cm^{-1} (625 nm) and thus a contribution of negative charged NDI is present. The ESA is broader at 21000 cm^{-1} (476 nm) and shows a shoulder at 22000 cm^{-1} (455 nm). It is conceivable that this state is best described by a negatively charged NDI unit and a positively charged adjacent benzene unit (one attached to the imide nitrogen). It decays with a time constant of τ_2 = 6.8 ps into a subsequent CT state, with rather long lifetime of τ_3 = 54 ps. Here the CT is "fully developed", indicated by sharp and intense absorptions which are related to a partial negative charged NDI. Unfortunately the signature of the partial positive charged dimethoxybenzene unit was not detected. This CT state transforms into another CT state with very similar absorption and a lifetime of τ_4 = 673 ps. It is assumed that here a cooling process from a hot to a cool state occurs which is caused by e.g. vibrational/rotational or solvent relaxation processes. Finally, the last EADS recorded with this fs-setup corresponds to a long lived triplet NDI state with broad absorption features and low maxima at ca. 21600 cm^{-1} (463 nm) and 22200 cm^{-1} (450 nm).[198, 216, 217] As **sOMe,** the EADS of **sOMeNDI** are similar to those observed for NDI with cyclophane attached to it, previously studied by *Lambert et al.*[166]

Although the fs-TA spectra of **sOMeNDI** and **sCNNDI** appear to be similar at first sight, there are fundamental differences on closer examination. Global analysis yields five components (Figure 58), the first of which shows broad ESA with a maximum at 21000 cm^{-1} (476 nm) and a small peak at 12900 cm^{-1} (775 nm). As for **sOMeNDI,** it is assigned to be a somehow delocalized state. A locally NDI excited singlet state could not be detected. The species shows a fast decay τ_1 = 1.8 ps into the subsequent state, which has a slightly shifted absorption maximum at 20700 cm^{-1} (483 nm) with a shoulder at 22600 cm^{-1} (442 nm) and a small peak at 12900 cm^{-1} (775 nm). Here, no spectral evidence for the formation of a partial negative charged NDI and CT state is observed. Possibly, caused by the cyan groups at the benzene acting as acceptors themselves, the formation of a CT state is no longer energetically possible. Therefore the spectrum is assigned to correlate to a NDI centered excited state. It decays with τ_2 = 13 ps into a state (with τ_3 = 282 ps) of very similar band shape, accordingly it is assumed that a relaxation process takes place. With τ_4 = 283 ps, this state leads to species with low absorption intensities and a absorption maxima at 22600 cm^{-1} (442 nm) and 20500 cm^{-1} (442 nm). Studies of *Zuilhof et al.* on NDI led to the conclusion that the absorption spectra might be a sum of the NDI triplet spectrum (see following EADS) and another transient, whose origin remained unclear.[218] One possible explanation could be the formation of excimers consisting of two NDI. However, the last EADS clearly belongs to a long lived triplet NDI with broad absorption features and low maxima at ca. 21600 cm^{-1} (463 nm) and 22200 cm^{-1} (450 nm).[198, 217]

Fs-TA spectra of **sOMeNDI46** are very similar to those of **sOMeNDI** and therefore no detailed interpretation is given. However, it should be noted that **sOMeNDI46**, like **sCNNDI**, shows the existence of a species with a long lifetime of ca. 2 ns before the final species, while there is no such species detected in **sOMeNDI**.

Table 29: Lifetimes of the EADS deduced from deconvolution of the fs-transient absorption measurements in toluene. Lifetimes which are too long for accurate measurement with the fs-setup are not given. Rate constants and electronic coupling of the CS state for the dyads **mXNDI** (X = OMe–CN).

	Excitation / nm	EADS1 τ_1 / ps	EADS2 τ_2 / ps	EADS3 τ_3 / ps	EADS4 τ_4 / ps	k_{CS} (= 1/τ_2) / 10^{10} s^{-1}	V_{CS} / cm^{-1}
sOMe	361	6.1	99	2310	-	-	-
sCN	425	0.98	4.7	103	-	-	-
sOMeNDI	382	1.2	6.8	54	673	-	-
sCNNDI	382	1.8	13	283	1890	-	-
sOMeNDI46	381	1.0	8.7	257	1670	-	-
mMeNDI	379	1.9	35	2200	-	2.86	34
mOMeNDI	400	2.6	23	-	-	4.34	30
mClNDI	400	2.1	14	-	-	7.14	32
mCNNDI	435	1.9	8.9	-	-	11.2	22
mOMeNDI46	361	3.2	24	1200	-	-	-

In the following the results of the fs-TA measurements of **mOMeNDI** (Figure 60) and **mCNNDI** (Figure 63), will be explained. The main conclusions can be transferred to **mMeNDI** (Figure 61), **mClNDI** (Figure 62) and **mOMeNDI46** (Figure 64) too, since they behave analogously. Figure 59 summarizes the photophysical processes for the dyads leading to the CS state.

For dyad **mOMeNDI** the global analysis yields three components (Figure 60). The first EADS has a time constants of τ_1 = 2.6 ps and shows a strong ESA with maxima at 20800 cm^{-1} (480 nm), 18500 cm^{-1} (540 nm) and a less intense ESA at 12500–14300 cm^{-1} (700–800 nm). The next obtained EADS has a lifetime of τ_2 = 23 ps and possess a similar spectral shape. Here the band at 18500 cm^{-1} (540 nm) is less pronounced and the spectrum gets more defined, thus it is assumed that a relaxation process from a hot to a cold state takes place. The spectral features of these two EADS are very similar to the ones observed for TAA-NDI dyads with cyclophane bridges. According to the characteristic TAA radical cation absorption at 12500–14300 cm^{-1} (700–800 nm) these two states are ascribed to a CT state which involves the bridging moiety. [166, 213] For the sake of completeness it has to be mentioned that in the second EADS, a somewhat increased absorption at 16400 cm^{-1} (610 nm) can be identified. The development of this band would require a CT state with participation of a negatively charged NDI and a positively charged bridge. This in turn would mean that the second EADS possibly has to be approximated by a superposition of two probably CT-like states which are populated from either the donor or the acceptor involving excitation.

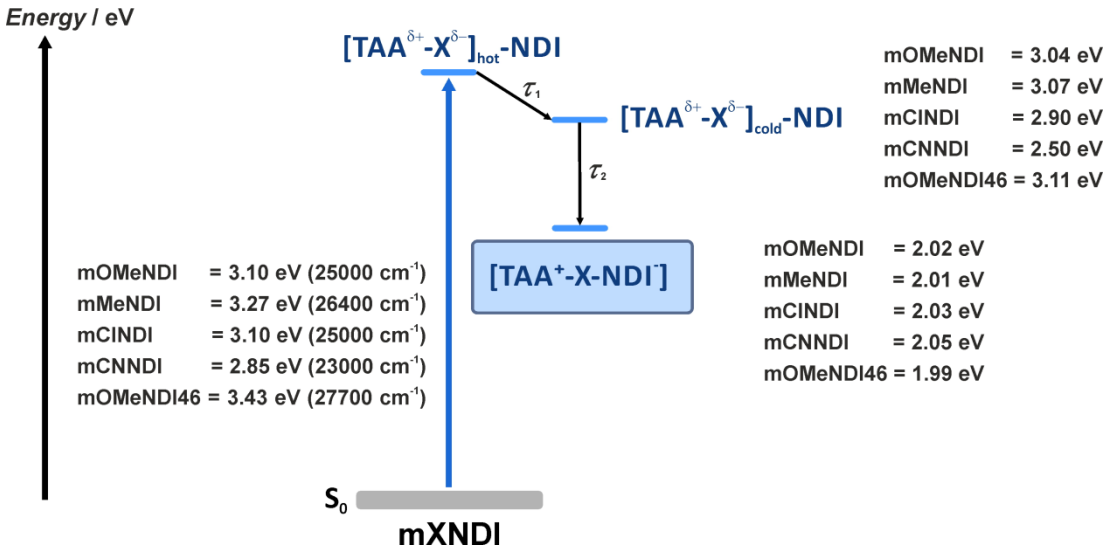

Figure 59: Energy scheme for the photophysical dynamics in dyads **mXNDI** (X = OMe–CN). The energies of the CT states were estimated from the steady-state absorption spectra (section 4.5). The energies of the CS states were determined by *Weller* approximation.

The EADS that follows is distinctly different from the previous one. It shows three typical signatures which prove the formation of the CS state. It shows the typical ESA of a NDI radical anion, that are a strong one at 21200 cm^{-1} (475 nm), a weaker one at 16400 cm^{-1} (610 nm) and a broad ESA at 12900–13800 cm^{-1} (725–775 nm) caused by the TAA radical cation.[99, 113, 166, 219, 220] The rise of the spectrum is related to the time decay of the foregoing EADS with τ_3 = 23 ps, and it remains present for the time range of the fs-TAA measurements.

For **mCNNDI** (Figure 62) global analysis also provides three components, the two first EADS are clearly different compared to the ones obtained for **mOMeNDI**. Excitation of **mCNNDI** gives an EADS with a pronounced ESA at 21300 cm^{-1} (470 nm) and a broader EAS at ca. 14500 cm^{-1} (690 nm) with a lifetime of τ_1 = 23 ps. Since **mCNNDI** was exclusively excited at the CT band at 23000 cm^{-1} (435 nm) and thus neither a local TAA or local NDI state can be excited at the chosen wavenumber, the spectrum is related to a CT state which involves the TAA as a donor and the bridge as the acceptor, respectively. It is followed by an EADS with shifted maxima at 20800 cm^{-1} (480 nm) and 13700 cm^{-1} (730 nm), with a lifetime of τ_2 = 8.9 ps. The spectral changes are again assigned to a transition from a hot CT (first EADS) which relaxes into a cold CT state (second EADS). Such a relaxation should be accompanied by a continuous shift of the spectra. While a global analysis cannot reproduce/analyze continuous shifts, the decay associate difference spectra (DADS) show the typical sine like signature at 13300–16700 cm^{-1} (750-600 nm) for such a behavior. The last EADS obtained in the fs-time range is again clearly correlated to a CS state were the positive charge is located at the TAA and the negative at the NDI, respectively. [99, 113, 166, 219] As for **mOMeNDI**, the rise of the third EADS proceeds with the decay of the second.

The transient spectra of **mMeNDI** and **mClNDI** behave analogously as those of the other dyads. However, for **mMeNDI** one additional EADS was found, since there are two EADS which correspond to a CS state. The rise time of the first CS state is τ_2 = 35 ps and it transforms with τ_3 = 2.2 ns into a state of very similar EAS. It is assumed that at this point a relaxation process from hot to cold CS takes place.

The fs-TA measurements of **mOMeNDI46** were performed to investigate the dependency of the CS dynamics on the position of X at the bridging unit. Here, the excited species were probed between 15200–33300 cm^{-1} (660–300 nm). All EADS show a broad GSB with a maximum at 27800 cm^{-1} (360 nm), whose intensity is nearly constant for whole time range. The first two EADS show EAS between 15200–25000 cm^{-1} which are very similar in shape and lifetime to those obtained for **mOMeNDI**, which suggests that the same process is present. Then there are two EADS which correspond to a CS state. The first gets formed with rise time of τ_2 = 24 ps and transforms with τ_3 = 1.2 ns into a state of very similar EAS. Although ESA between 11800–15200 cm^{-1} (850–660 nm), which is related to the TAA radical

cation, was not probed, due to the high consistency of the measurements (and all other measurements like CV and SEC and later ns-TA), it is assumed that the CS is formed.

In summary it should be noted that the final CS spectra show a uniform band shape. While the positions of the NDI peaks seem to be unaffected by the substituents X constant at 21200 cm^{-1} (475 nm) and at 16400 cm^{-1} (610 nm), there are obvious differences of the TAA absorptions (for OMe–CN) at ca. 13300 cm^{-1} (750 nm). **mMe** shows a two-band structure and a weak absorption. Increasing the electron withdrawing character to **mCN** is associated with an increase of absorption intensity and a sharpening of the TAA radical cation band. Simultaneously the two-band structure vanishes in favor of a single absorption peak.
A possible explanation of this behavior is given in chapter 4.6.5, where the normalized simulated CS state spectra obtained by SEC, the last spectra of the fs-setup pump-probe measurements and the first spectra recorded by ns-laser flash spectroscopy for each dyad are compared with each other (Figure 68).

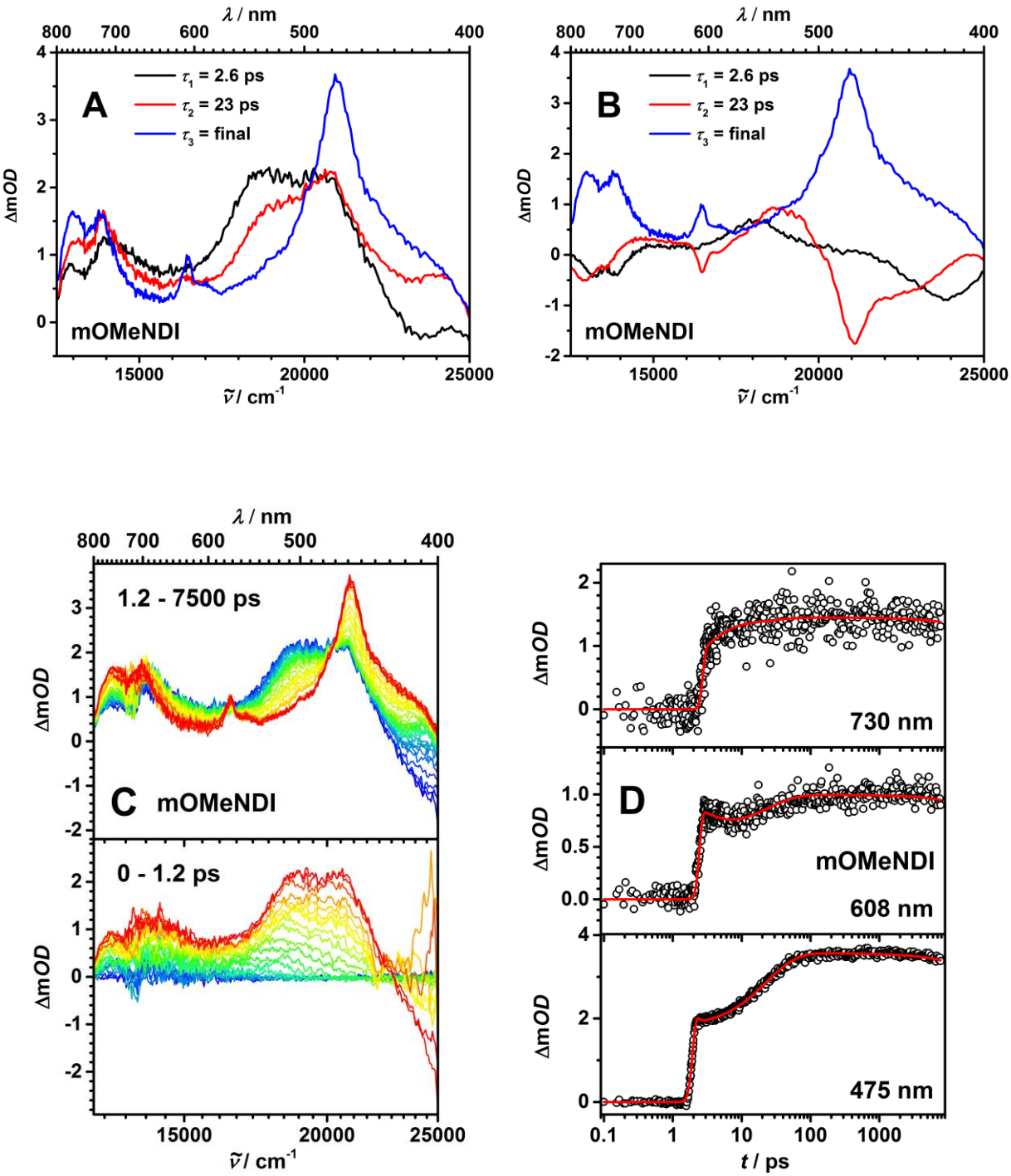

Figure 60: Evolution associated difference spectra (EADS) of **mOMeNDI** obtained from a global analysis of the transient map (A). Difference associated difference spectra (DADS; B). Fs-Transient absorption spectra corrected for chirp and scattered pump light. Early spectra are depicted in blue and at later times in red colors (C). Decay profiles at selected wavelengths for which the zero time delay was set arbitrarily (D). The sample was excited at 25000 cm^{-1} (400 nm) in toluene.

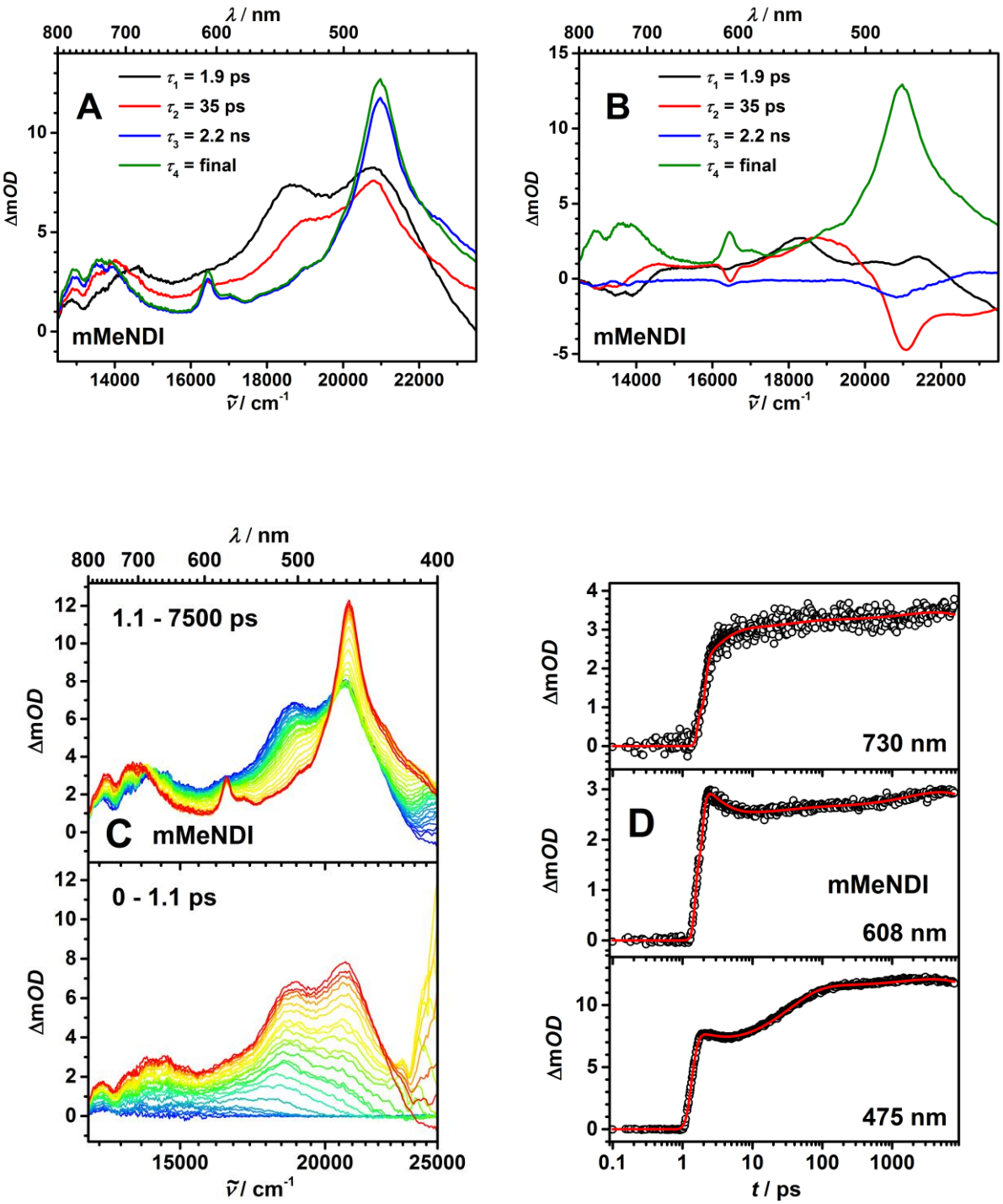

Figure 61: Evolution associated difference spectra (EADS) of **mMeNDI** obtained from a global analysis of the transient map (A). Difference associated difference spectra (DADS; B). Fs-Transient absorption spectra corrected for chirp and scattered pump light. Early spectra are depicted in blue and at later times in red colors (C). Decay profiles at selected wavelengths for which the zero time delay was set arbitrarily (D). The sample was excited at 26400 cm^{-1} (379 nm) in toluene.

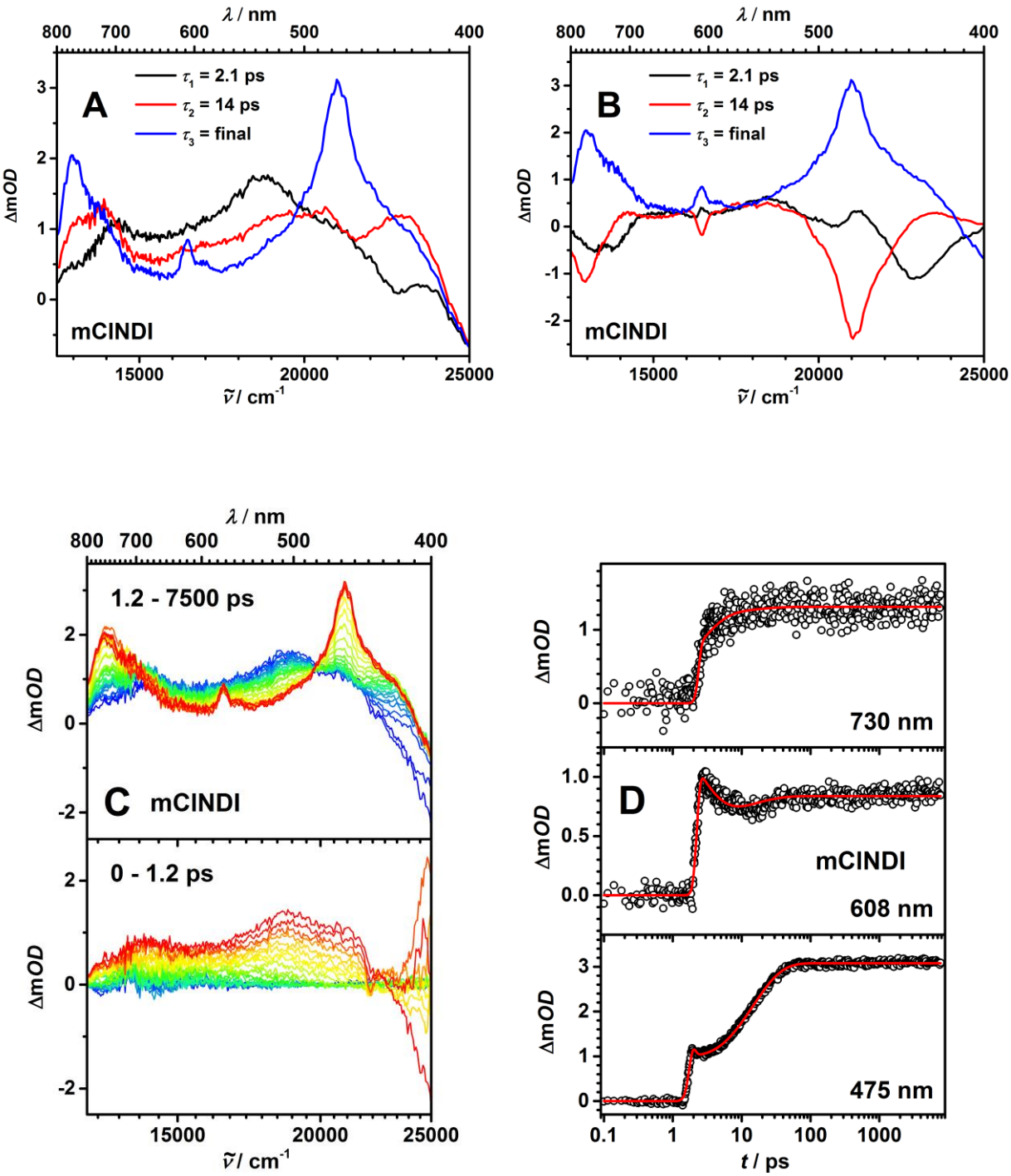

Figure 62: Evolution associated difference spectra (EADS) of **mCINDI** obtained from a global analysis of the transient map (A). Difference associated difference spectra (DADS; B). Fs-Transient absorption spectra corrected for chirp and scattered pump light. Early spectra are depicted in blue and at later times in red colors (C). Decay profiles at selected wavelengths for which the zero time delay was set arbitrarily (D). The sample was excited at 25000 cm^{-1} (400 nm) in toluene.

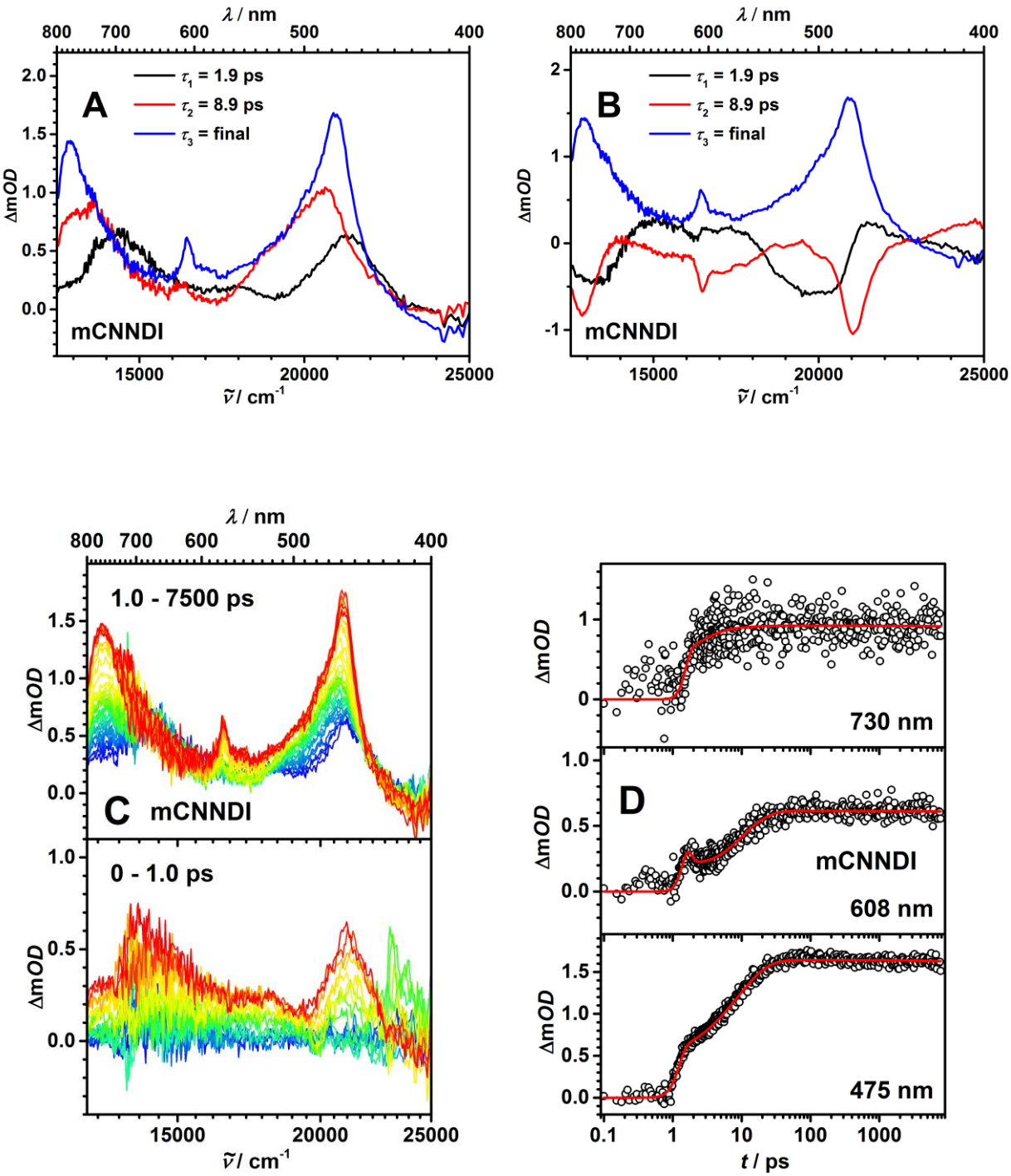

Figure 63: Evolution associated difference spectra (EADS) of **mCNNDI** obtained from a global analysis of the transient map (A). Difference associated difference spectra (DADS; B). Fs-Transient absorption spectra corrected for chirp and scattered pump light. Early spectra are depicted in blue and at later times in red colors (C). Decay profiles at selected wavelengths for which the zero time delay was set arbitrarily (D). The sample was excited at 23000 cm^{-1} (435 nm) in toluene.

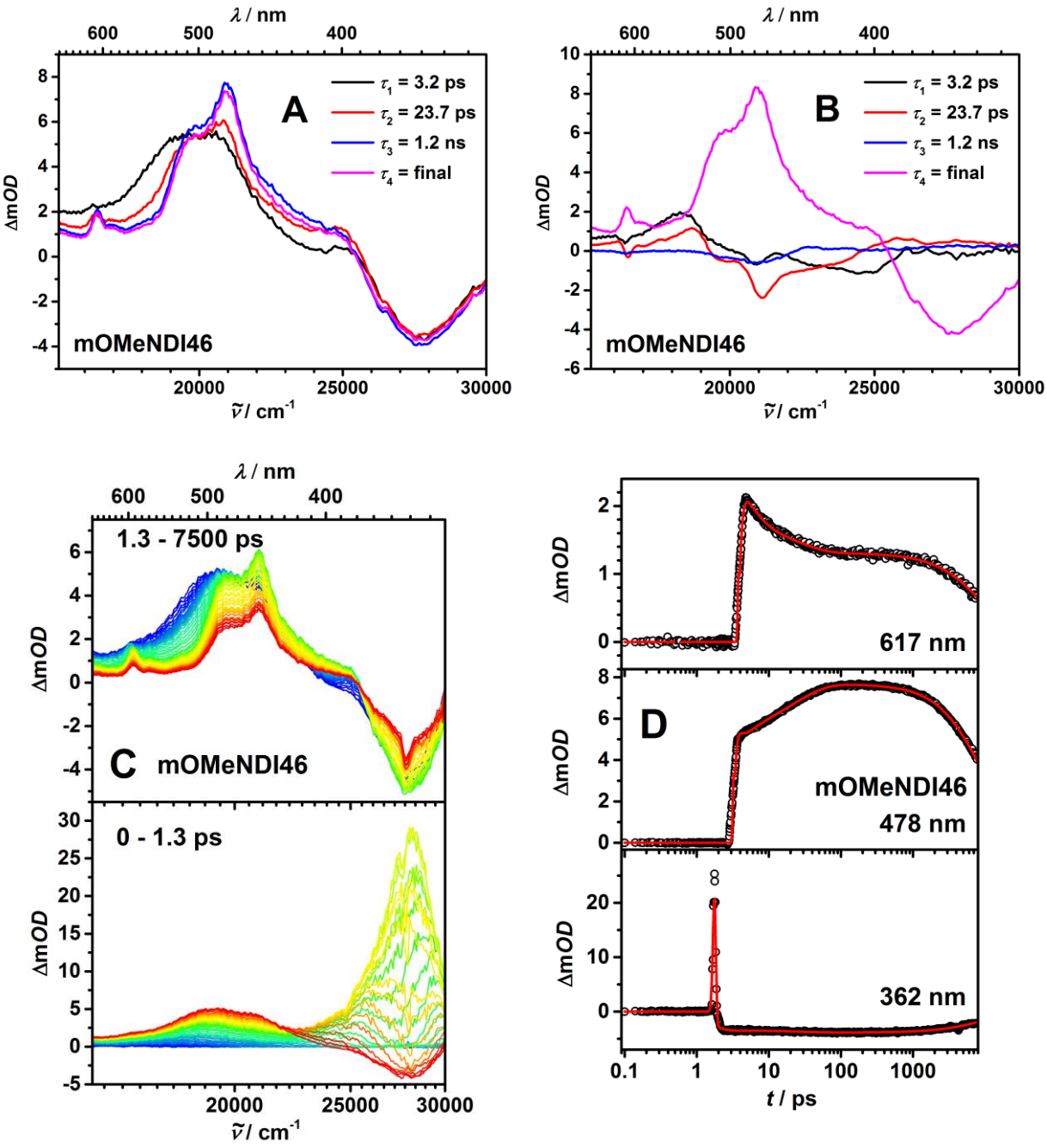

Figure 64: Evolution associated difference spectra (EADS) of **mOMeNDI46** obtained from a global analysis of the transient map (A). Difference associated difference spectra (DADS; B). Fs-Transient absorption spectra corrected for chirp and scattered pump light. Early spectra are depicted in blue and at later times in red colors (C). Decay profiles at selected wavelengths for which the zero time delay was set arbitrarily (D). The sample was excited at 27700 cm^{-1} (361 nm) in toluene.

4.6.4 Discussion of the Charge Separation

From the DFT calculations the internal reorganization energy λ_i for the charge separation CT → CS was estimated to be 0.39 eV. The outer reorganization energy λ_o of nonpolar toluene is estimated to be ca. 0.1 eV based on the *Born* model.[221, 222] Accordingly, the overall reorganization energy λ for the charge separation has a value of ca. 0.5 eV. From the E_{00} energies of the CT states (4.2, Table 26) and the energy of the CS states ΔG_{CS} which were estimated from the redox potentials via *Weller* equation (4.3, Table 24), it appears that the CS process of all compounds is in the *Marcus* inverted or at best optimal region because $\lambda \leq |\Delta G_{CT\rightarrow CS}|$.[223, 224] Here, the intrinsic *Marcus* barrier for charge separation is larger for the more exergonic charge separation process and decreases from X = Me over OMe, Cl to CN. This is exactly the sequence that is observed for the rise time of the CS states: τ(Me) = 35 ps, τ(OMe) = 23 ps, τ(Cl) = 14 ps and τ(CN) = 8.9 ps. The (at first) contradictory fact of finding **mOMeNDI** placed below **mMeNDI** (because OMe should be the better electron donor than Me), can be explained by the findings obtained by DFT calculations (4.6.1). Remarkably a 4,6-configuration of the methoxy compounds hardly influences the CS. The CS states of both **mOMeNDI** and **mOMeNDI46** are formed with almost exactly the same rise times.

Another important parameter when discussing ET rates in context of *Marcus* theory is the electronic coupling *V*. Assuming a coherent superexchange mechanism, lower virtual bridge states should promote ET, that is, the more electron deficient or the lower the local LUMO energy of the bridge, the larger the coupling. Accordingly, the substituents X at the bridge should regulate the magnitude of *V*. The DFT computed LUMO energies of the bridge (Figure 54) decrease gradually from X = OMe to CN, thus the electronic coupling is expected to increase in the same sequence.

The electronic couplings of the charge separation processes V_{CS} can also be estimated by use of *Bixon-Jortner* theory and the following equation.[225, 226]

$$k_{ET} = 4\pi^2 hc^2 V^2 \sum_{j=0}^{\infty} \frac{e^{-S} S^j}{j!} \sqrt{\frac{1}{4\pi hc\lambda_o kT}} \exp\left[-\frac{hc\left(j\tilde{\nu}_v+\lambda_o+\Delta G^{00}\right)^2}{4\lambda_o kT}\right] \qquad (27)$$

$$\text{with } S = \frac{\lambda_v}{\tilde{\nu}_v}$$

The *Huang-Rhys* factor *S* is given as the quotient of the inner reorganization energy λ_v and average molecular quantum mode $\tilde{\nu}_v$. The first has a value of 0.39 eV (from the DFT calculations) and the latter has as a typical value 1500 cm^{-1} (0.16 eV).[227-229] The solvent reorganization energy λ_o equals 0.1 eV and the rates were taken from Table 29 as $k_{CS} = 1/\tau_2$. Calculation gave couplings of V_{CS}(Me) = 30 cm^{-1}, V_{CS}(OMe) = 34 cm^{-1}, V_{CS}(Cl) = 32 cm^{-1} and V_{CS}(CN) = 22 cm^{-1}. On the one hand these values are on the order of those evaluated recently for TAA-NDI dyads with cyclophane or triazole bridges.[91, 113] On the other hand, contrary to the expectation, these couplings appear not to vary systematically with the bridge substituents. However, it must be mentioned, that a precise determination of the couplings V_{CS} is only possible to a limited extent, caused by the strongly approximate character of the input parameters. Therefore, it is supposed that the *Marcus* (inverted) barrier plays the decisive role for the charge separation kinetics.

4.6.5 ns-Laser Flash Spectroscopy

After discussion of the charge separation dynamics (CS) for **mXNDI** (X = OMe–CN) and **mOMeNDI46**, attention will be paid to the charge recombination (CR) in these dyads. As already mentioned above, the *para*-dyads **pXNDI** did not show TA in the ns-time range, thus they are excluded in this discussion.

The CR was investigated by ns-transient absorption measurements in toluene and MeCN, to investigate the influence of the solvent. First the CR at zero magnetic field will be presented, second the influence of applied magnetic field on the CS state and the possible magnetic field effects (MFE) will be evaluated. Finally, the data obtained will be discussed in the subsequent chapter by means of an appropriate model (4.6.6).

At Zero Magnetic Field

Decay traces were recorded at 4 nm steps between 25000 cm^{-1} (400 nm) to 11800 cm^{-1} (850 nm) for toluene and 400 nm (25000 cm^{-1}) to 833 nm (12000 cm^{-1}) for MeCN. All samples were excited by laser pulses from a Nd:YAG laser at 28200 cm^{-1} (355 nm). The decay traces in toluene were measured up to 40 μs with a time resolution of 4 ns for **mXNDI** and up to 20 μs with a time resolution of 2 ns for **mOMeNDI46**. Those in MeCN were measured up to 20 μs with a time resolution of 2 ns, too. The amplitudes of the decay lifetimes were normalized to 1 to make the comparison easier. The decay traces were used to reconstruct a transient map. The transient spectra and the decay curves at 21000 cm^{-1} (476 nm, maximum absorption of NDI radical anion) of **mXNDI** and **mOMeNDI46** in toluene are displayed in Figure 65 and Figure 66, respectively. Those in MeCN are depicted in Figure 67.

All transient spectra show the signatures of the NDI radical anion and the TAA radical cation, which are a strong absorption at 21000 cm^{-1} (476 nm) and a weaker one at 16500 cm^{-1} (608 nm) that are typical of NDI radical anion,[166, 196, 197, 219, 230] and an absorption between 11800–15400 cm^{-1} (850–650 nm) which is related to the TAA radical cation.[78, 90, 96, 166, 213] The rise of the CS absorption corresponding to its formation takes place within the instrument response and is related to the last EADS obtained in the above described fs-experiments. At all wavelengths the signal decays biexponentially with a short and a long lifetime, as exemplified for 21000 cm^{-1} (476 nm). The origin of the biexponential decay can be understood by a so-called “relaxation mechanism” caused by singlet triplet equilibrium in the CS state.[107, 231] However, at this point the resulting data is presented and underlying processes are discussed in more detail in the subsequent chapter (4.6.6).

The lifetimes of the CS states of **mXNDI** in toluene were extracted from the biexponential tail of the decay curves. Since one tifetime of the decays of **mOMeNDI46** in toluene and **mXNDI** in MeCN consistis very short instruments response function (IRF) had to be taken into account and the decays were fitted by reconvolution fits.

In toluene the charge recombination (CR) in all *meta*-compounds **mXNDI** possess two lifetimes (Table 30). The shorter lifetime τ_1 is about 200–300 ns and the longer τ_2 ca. 4000–6000 ns. Although no distinct correlation between substituent X and the lifetimes was possible, the amplitudes clearly change systematically. Starting from **mMeNDI** (τ_1 = 0.33 / τ_2 = 0.67) over **mOMeNDI** (τ_1 = 0.45 / τ_2 = 0.55) to **mClNDI** (τ_1 = 0.47 / τ_2 = 0.53) and **mCNNDI** (τ_1 = 0.76 / τ_2 = 0.24) the contribution of the shorter lifetime rose. The longer lifetimes were extremely dependent on oxygen, thus the sample had to be degassed thoroughly. This dependency underpins the assumption that a triplet state is involved in the CR dynamics. The quantum yields (QY) of CS state formation were determined by actinometry at 28200 cm^{-1} (355 nm) vs. benzophenone (in benzene).[232] In **mOMeNDI–mClNDI** the CS state gets populated with ca. 50 % efficiency while in **mCNNDI** the QY of CS state formation drops to 31 % (Table 30). However, a comparison of the data obtained for **mCNNDI** to **mOMeNDI–mClNDI** is only conditionally valid, since the difference may arise from the excitation wavelength. On the one hand, as can be seen from the difference spectra of the absorption in Figure 41 (section 4.2), for **mOMeNDI–mClNDI** a pump pulse at 28200 cm^{-1} (355 nm) excites NDI and the TAA associated CT absorptions in the ratio of approximately 1:1. On the other hand, for **mCNNDI** significantly less absorption of the CT band is available (ratio of ca. 2:1). However, NDI and CT excitations may offer a different pathway to populate the CS state, thus NDI excitation seems to be not as efficient for CS as excitation in the CT band.

Table 30: Decay times (*τ*) and amplitudes (*a*) for **mXNDI** (X = OMe–CN, Figure 65, E-H) and **mOMeNDI46** (Figure 66, B) in toluene at 476 nm (21000 cm^{-1}) detection wavelength. Quantum yields (QY) of the formation of the CS state for **mXNDI** (X = OMe–CN) in toluene.

	τ_1 / τ_2 in ns	a_1 / a_2[c]	QY of CS[a]
mOMeNDI[a]	294 / 3980	0.46 / 0.54	51 %
mMeNDI[a]	246 / 4100	0.33 / 0.67	51 %
mClNDI[a]	282 / 6480	0.48 / 0.52	49 %
mCNNDI[b]	178 / 4950	0.75 / 0.25	31 %
mOMeNDI46[a]	12.4 / 7290	0.986 / 0.014	-

[a]Excitation at 355 nm (28200 cm^{-1}). [b]Excitation at 460 nm (21700 cm^{-1}). [c]Normalized to one.

toluene

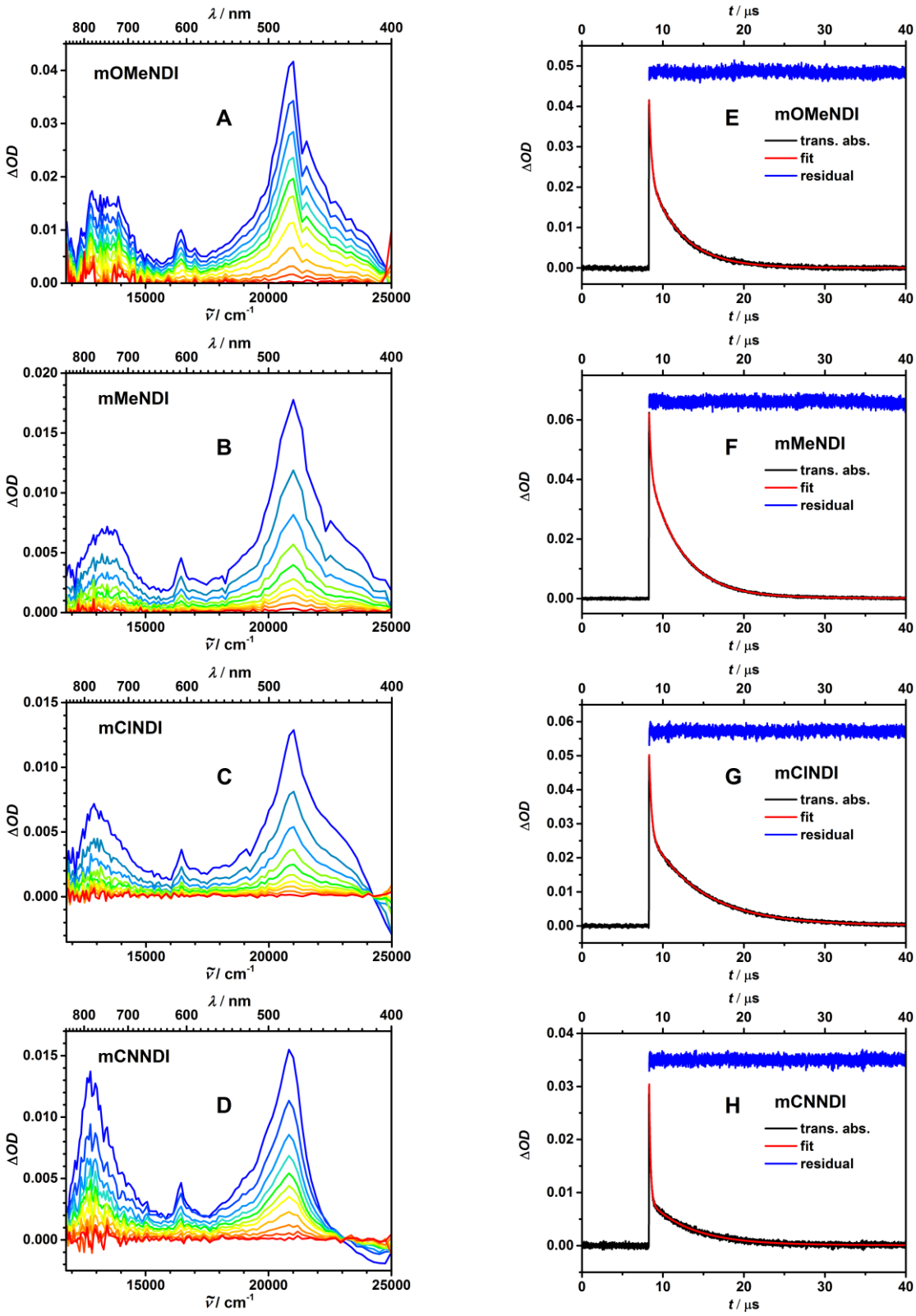

Figure 65: Left: Transient absorption spectra of **mXNDI** (X = OMe, Me, Cl and CN) in toluene (A–D). Early spectra are depicted in blue and at later times in red colors. Right: Decay traces (black), tail fits (red) and the residuals (blue) at 476 nm (21000 cm^{-1}) in toluene and excitation at 355 nm (28200 cm^{-1}; E–H).

Ns-TA measurements of **mOMeNDI46** in toluene were performed to investigate the dependency of the CR dynamics on the position of X at the bridging unit. As already mentioned above, the lifetime of **mOMeNDI46** was determined by reconvolution fit. The decay trace was deconvoluted with four fit functions: a *Gaussian* shaped instruments response function (IRF) which has a full width at half maximum (FWHM) of 12 ns and three exponential functions. The first exponential function was necessary for the description the short increase of the signal at the beginning, the other two to describe the biexponential decay. Since the decay consists of two very different lifetimes and the reconvolution is based on the extrapolation of the fit functions to time zero (rise of the signal), the amplitude of the short lifetime might appear to be too large in comparison to the decay traces depicted in (Figure 66).

The obtained TA spectra are significantly different compared to those of **mXNDI**. Although the typical NDI radical anion absorptions at 21000 cm^{-1} (476 nm) and 16500 cm^{-1} (608 nm) are present, the shape of the first-mentioned ESA is clearly different, having a broad shoulder at ca. 19600 cm^{-1} (510 nm). The ESA between 11800–15400 cm^{-1} (850–650 nm), which is related to the TAA radical cation, is pronounced very weakly. Therefore, it cannot be definitively clarified whether a CS state is formed with a positive charge at the TAA unit, but it is assumed. This assumption is supported by the previous measurements such as CV and SEC, since here no findings were obtained which suggest a contrary assumption. The presence of such a weak EAS at between 11800–15400 cm^{-1} (850–650 nm) will be recaptured later in this chapter.

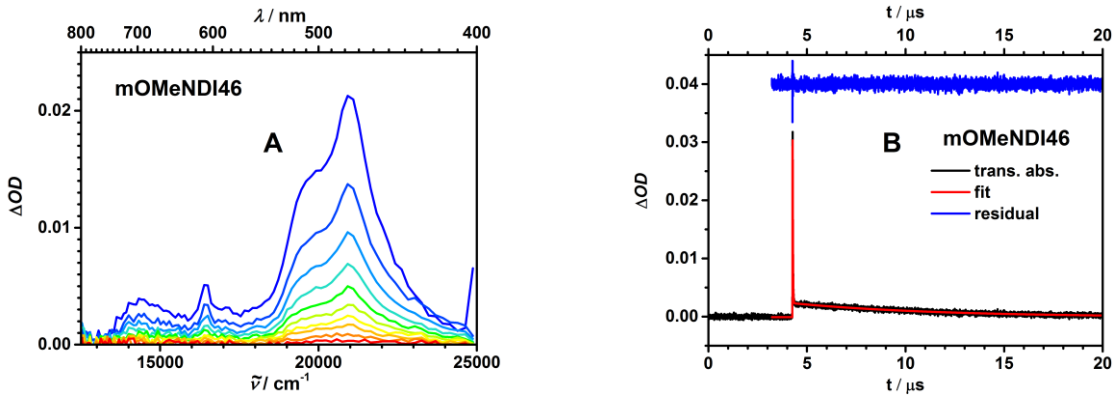

Figure 66: Transient absorption spectra of **mOMeNDI46** in toluene (A). Early spectra are depicted in blue and at later times in red colors. Decay trace (black), reconvolution fit (red) and the residual (blue) at 476 nm (21000 cm^{-1}) in toluene and excitation at 355 nm (28200 cm^{-1}; B).

Remarkably, compared to the other dyads **mOMeNDI46** possess two lifetimes of τ_1 = 12.4 and τ_2 = 7290 ns, with amplitudes of a_1 = 0.99 and a_2 = 0.01, respectively (Table 32). Thus the short lifetime τ_1 is more than an order of magnitude smaller compared to the other *meta*-dyads, while the longer time τ_2 has about the same value.

In MeCN (Figure 67, A–D) the same signatures of NDI radical anion and TAA radical cation are observed and the dyads (**mXNDI**) possess a uniform decay behavior, which does not seem to vary systematically with the bridge substituents. The lifetimes of the CS state were determined by reconvolution fit in the same way as described for **mOMeNDI46** in toluene above. Reconvolution fit of the decays at 21000 cm^{-1} (476 nm) gave lifetimes of τ_1 = 7.3 ns and τ_2 = 1230 ns for **mOMeNDI** (Table 31). For **mMeNDI** the lifetimes τ_1 = 5.8 ns and τ_2 = 1470 ns, for **mCNNDI** τ_1 = 6.6 and τ_2 = 880 ns, and for **mClNDI** τ_1 = 4.9 ns and τ_2 = 1170 ns were found. All dyads exhibit amplitudes of ca. 0.991 for the short lifetime and 0.001 for the long lifetime. Nevertheless, the longer time has to be taken into account, since a monoexponentially fit was not possible.
However, a change of solvent from nonpolar toluene to polar MeCN is associated with a strong decrease of the lifetimes. The short lifetime τ_1 is about two orders of magnitude smaller in MeCN compared to toluene, the long lifetime τ_2 of about a quarter.
For **mOMeNDI46** it was not possible to obtain ns-TA spectra in MeCN and it is assumed that the CR process in this dyad is too fast to be detected within this setup, since the measurements in toluene were already much faster compared to the **mXNDI** derivatives.

Table 31: Decay times (τ) and amplitudes (a) for **mXNDI** (X = OMe–CN) in MeCN at 476 nm (21000 cm^{-1}) detection wavelength.

	τ_1 / τ_2 / ns	a_1 / a_2 [c]
mOMeNDI	7.3 / 1230	0.999 / 0.001
mMeNDI	5.8 / 1490	0.998 / 0.002
mClNDI	6.4 / 880	0.999 / 0.001
mCNNDI	4.9 / 1170	0.999 / 0.001

[a]Excitation at 355 nm (28200 cm). [a]Excitation at 460 nm (21700 cm).
[c]Normalized to one.

MeCN

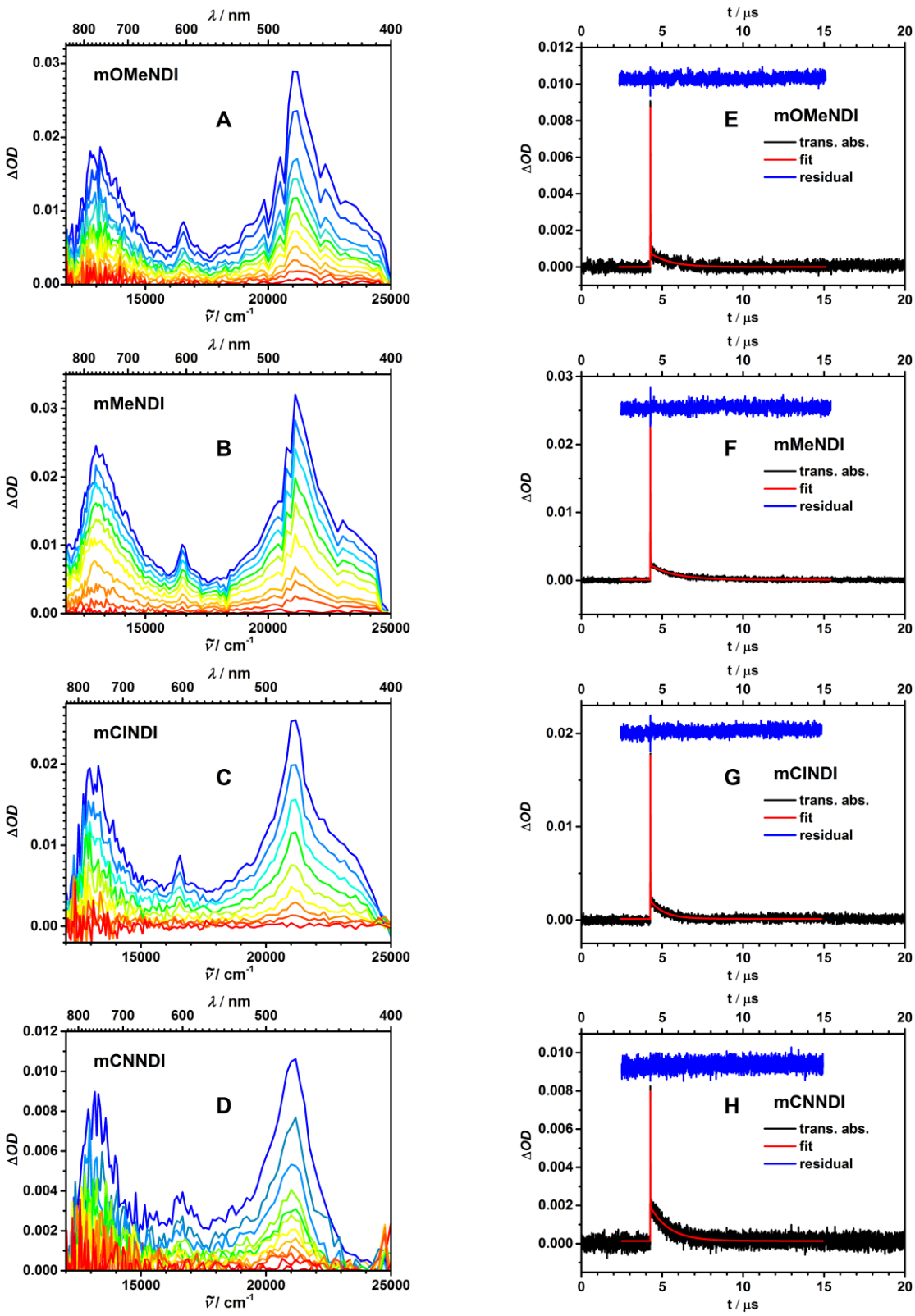

Figure 67: Left: Transient absorption spectra of **mXNDI** (X = OMe, Me, Cl and CN) in MeCN (A–D). Early spectra are depicted in blue and at later times in red colors. Right: Decay traces (black), reconvolution fits (red) and the residuals (blue) at 476 nm (21000 cm^{-1}) in MeCN and excitation at 355 nm (28200 cm^{-1}; E–H).

The next section deals with the comparison of the spectra of the CS state of **mXNDI** and **mOMeNDI46** which were obtained by SEC (simulated by addition of the cation and anion spectra, Chapter 4.4, Figure 45), which were recorded as the last spectra of the fs-setup pump-probe measurements (4.6.3, Figure 60–Figure 65) and which were received as the first spectra recorded by ns-laser flash spectroscopy in toluene and MeCN (the latter not for **mOMeNDI**, see above). All mentioned spectra are depicted in Figure 68.

As already mentioned in the respective chapters, all spectra show the strong absorption of the NDI radical anion at 21000 cm^{-1} (476 nm) and a weaker one at ca 16500 cm^{-1} (608 nm), as well as the TAA radical cation absorption between 11800–15400 cm^{-1} (850–650 nm), clearly indicating that the CS state is formed in the TA measurements (Figure 68). However for **mOMeNDI–mClNDI** (A–D) and especially **mOMeNDI46** (E) the latter one is significantly less pronounced in the TA measurements, compared to those obtained by SEC simulating the TA spectra. In addition to that the absorptions measured in MeCN are slightly shifted to higher energies.

The origins of the differences are assigned to be related to e.g. the type of solvent used. The SEC was performed in DCM, the fs-TA absorption measurements in nonpolar toluene and those in the ns-time regime in toluene or MeCN. Furthermore one has to note, that the SEC measurements were performed with tetrabutylammonium hexafluorophosphate as a conducting salt, which might affect the absorption spectra by strongly increasing the polarity. Another reason for the deviation of the spectra might be second order diffraction. The ground state bleach for **mOMeNDI–mClNDI** and **mOMeNDI46** is estimated to be located at ca. 27000 cm^{-1} (370 nm), thus at twice the wavelength a negative second order signal may superimpose with the ESA. This effect is assigned to be a main reason for the difference of the SEC measurements, compared to the TA spectra, which gets obvious when looking at Figure 68, D, where the spectra of **mCNNDI** are depicted. Since the GSB of **mCNNDI** is located at lower energies at ca. 23800 cm^{-1} (420 nm) the negative second order signal is no longer in the detection area, accordingly the spectra of all four different measurements show the best consistency.

Comparable effects of a decrease in intensity of the TAA radical cation band in TA measurements for similar dyads were also previously observed by *Lambert et al.* and reported in literature.[103, 166]

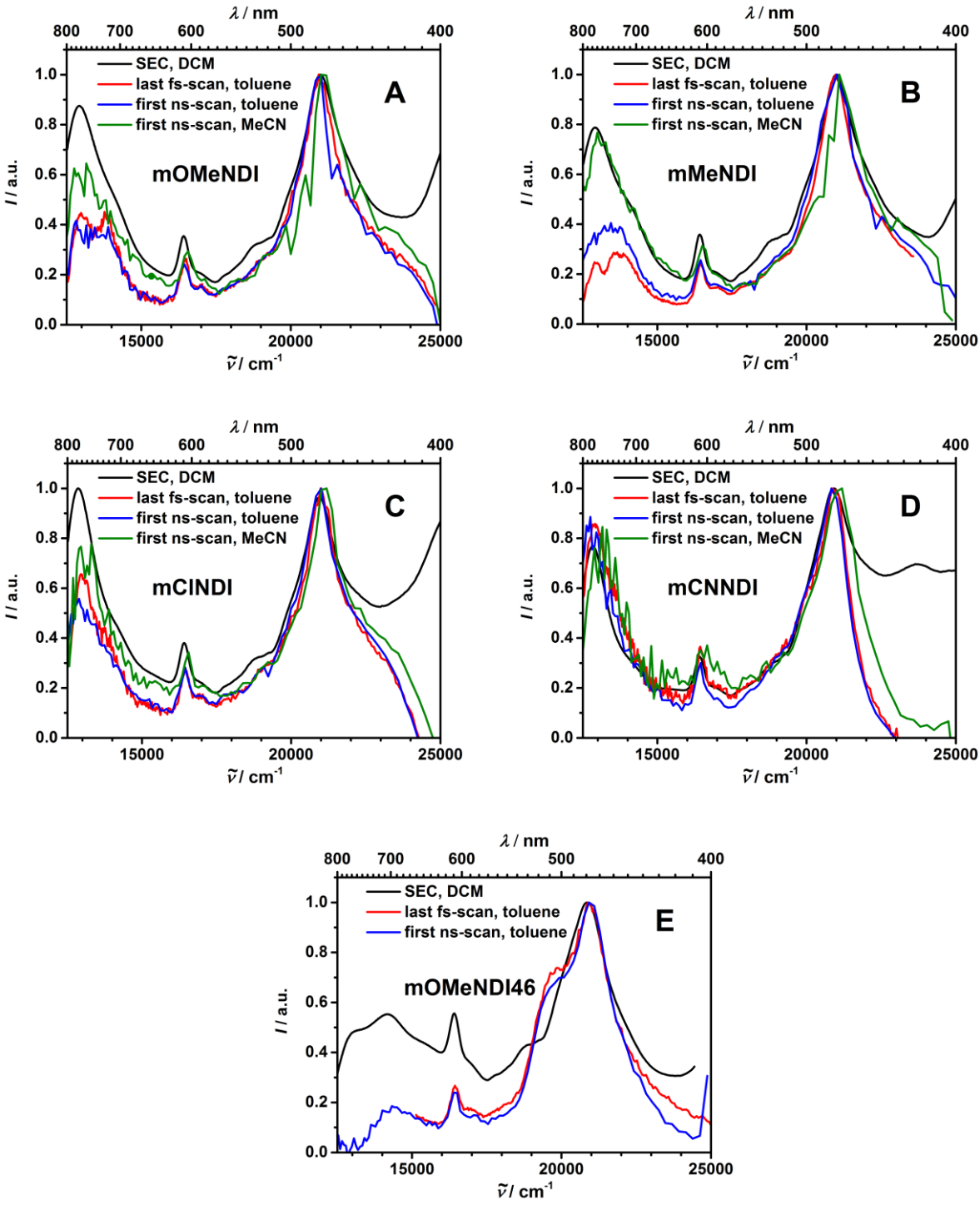

Figure 68: Spectra of the CS state of **mXNDI** (X = OMe–CN; A–D) and **mOMeNDI46** (E) obtained by SEC (simulated by addition of the cation and anion spectra, black line), as the last spectra of the fs-setup pump-probe measurements (red line) and the first spectra recorded by ns-laser flash spectroscopy in toluene (blue line) and MeCN (green line, not for **mOMeNDI46**).

At Non-zero Magnetic Field

In this section, the measurements of the charge recombination (CR) while applying an external magnetic field will be presented. The detailed interpretation is given in the subsequent chapter.

mOMeNDI, **mMeNDI** and **mClNDI** were excited by laser pulses from a Nd:YAG laser at 355 nm (28200 cm^{-1}). **mCNNDI** was excited by laser pulses from an Nd:YAG laser with an optical parametric oscillator at 460 nm (21700 cm^{-1}). **mOMeNDI46** did not show any magnetic field effect (MFE) and is consequently not discussed further in this section.

The decay traces were measured up to 40 μs with a time resolution of 4 ns at 476 nm (21000 cm^{-1}) detection wavelength. The MFE on the charge recombination dynamics was probed by applying ca. 100 different magnetic fields *B* between 0 and 1800 mT to the sample and measure the decay after every variation of the magnetic field. The step size between different magnetic fields was stepwise increased from 0.1 mT from (0–1 mT), to e.g. 0.3 mT (between 2–7 mT), 1.0 mT (between 10–19 mT), 10.0 mT (between 100–190 mT) and 100 mT (between 500–800 mT). The error of determining *B* was assigned to ±0.02 mT for magnetic fields between 0–400 mT and ±1 mT for fields between 400–1800 mT. The magnetic field dependent decays for **mXNDI** (X = OMe, Me, Cl and CN) were subtracted by a small long-time offset (individually for each decay curve), normalized to one and the decay maximum was given the time zero.

As shown in Figure 69, in toluene the dyads **mXNDI** show a strong MFE, which can be separated in two magnetic field ranges, dependent on the decay behavior while increasing *B*. The depiction of the measurement for **mOMeNDI** is divided in the field ranges 0–33.0 mT (A) and 33.0–1800 mT (B). **mMeNDI** is separated in 0–18.9 mT (C) and 18.9–1800 mT (D), **mClNDI** in 0–22.6 mT (E) and 22.6–1800 mT (F), and **mClNDI** in 0–22.0 mT (G) and 22.0–1800 mT (H). In order to make the MFE clearly visible, the decay curves are only displayed between 0–12 μs (Figure 69). In the figures presenting the decay curves at low magnetic field (left side of Figure 69), it becomes clear that at times shorter than ca. 3 μs, the decay is becoming slower when increasing the field strength, however at longer times the decay becomes faster.

In contrast, at higher *B* (right side of Figure 69) the opposite trend of the time traces is visible. Here, the decays become faster for shorter times than ca. 5 μs and slower for longer times. The respective changes are particularly pronounced in the vicinity of the turning point, which is exactly the upper limit of the first and the lower limit of the second field range, respectively (**mOMeNDI** 33.0, **mMeNDI** 18.9 mT, **mClNDI** 22.6 mT **mClNDI** 22.0 mT). The decay times and amplitudes at the three characteristic magnetic fields (0 mT, turning points and 1800 mT) are given in Table 32.

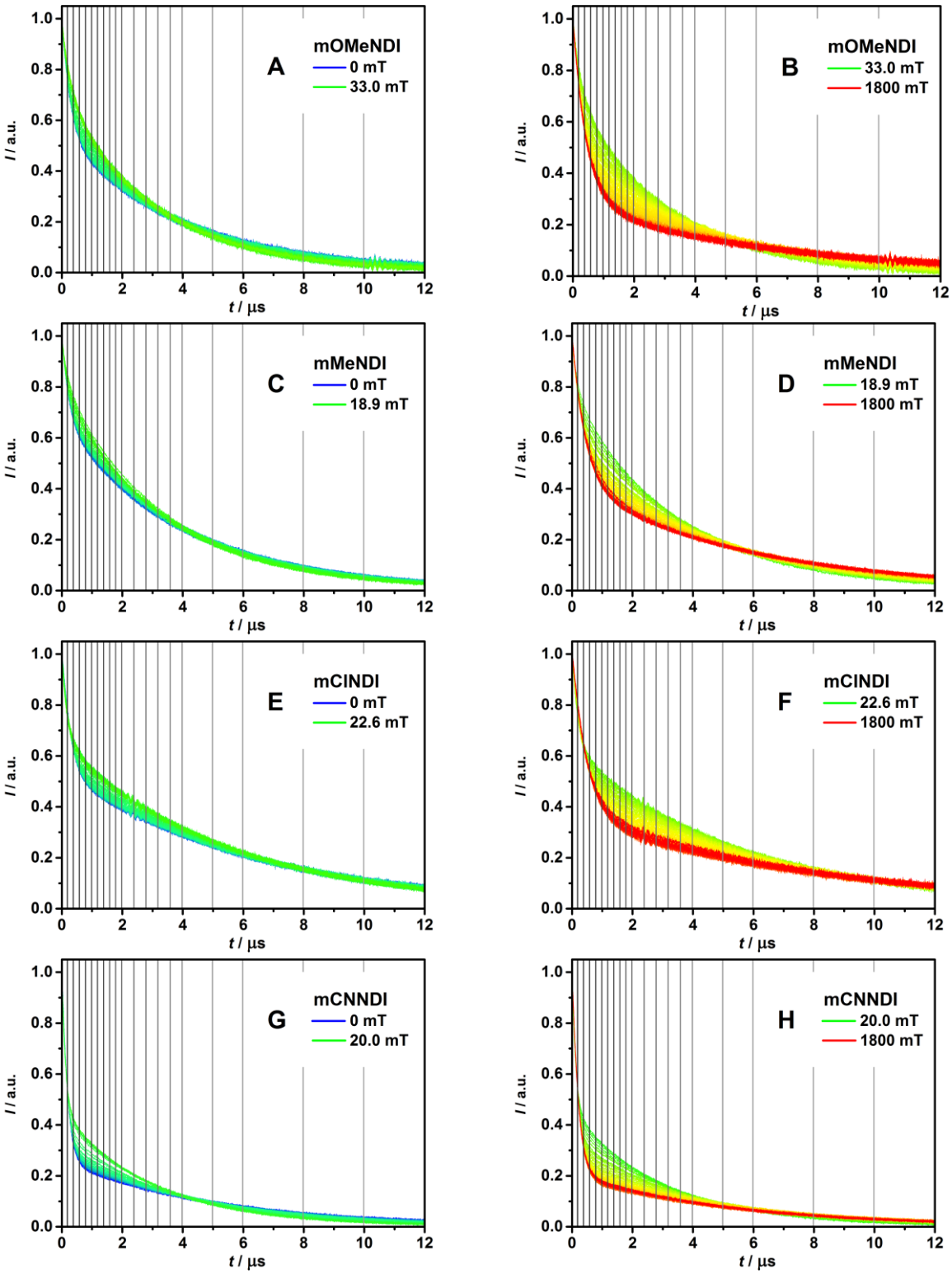

Figure 69: Divided magnetic field dependent decay curves for **mOMeNDI** (0–33.0 mT (A) and 33.0–1800 mT (B)), **mMeNDI** (0–18.9 mT (C), 18.9–1800 mT (D)), **mClNDI** (0–22.6 mT (E), 22.6–1800 mT (F)) and **mClNDI** in (0–22.0 mT (G) and 22.0–1800 mT (H)) at 476 nm. The increase of magnetic field is indicated by color change from blue to green (in A, C, E, G) and green to red (in B, D, F, H). The vertical grey lines show the position of the time slices, which are depicted in Figure 70. All measurements were done in toluene.

The MFE behavior gets most obvious when looking at the double log plot of amplitude vs. magnetic field at different times (0–9.98 μs), as given in Figure 70. The position of the time slices in the decay measurements are indicated by grey vertical lines (Figure 69). The time intervals chosen become continuously larger, starting with 0.20 μs at the beginning to 2.00 μs towards later times.

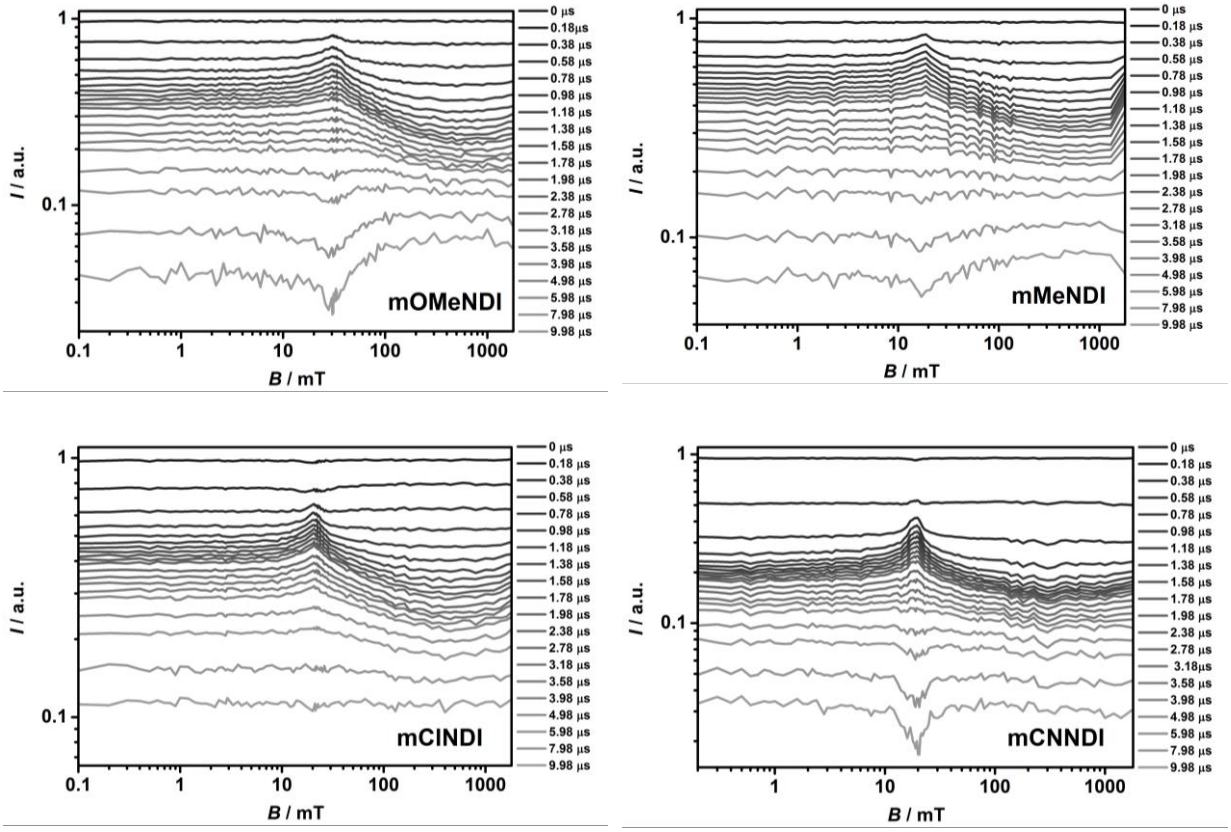

Figure 70: Double log plot of time slices through the sets of experimental curves at different times between 0 and 9.98 μs.

For **mXNDI** (X = OMe–CN) no change of amplitudes while increasing *B* from 0.1 to ca 10 mT takes place, resulting in vertical lines for each time trace (Figure 70). A further rise of *B* from 10 mT to the first turning point (at 33.0 mT for **mOMeNDI**, 18.9 mT for **mMeNDI**, 22.5 mT for **mClNDI** and 22.0 mT for **mClNDI**) is associated with three different possible trends of the lines: the amplitude can rise, stay constant or drop. For X = OMe, Me, CN the absorption for times between ca. 0.18–3.18 μs increases, at ca. 3.18 μs no change occurs and for times between ca. 3.18–9.18 μs the absorption drops. For **mClNDI** the latter case (if at all) can still be seen for 9.18 μs. When applying continuously higher fields *B* from the first turning point to ca. 700 mT a contrarious development for values above and below 3.18 μs (9.18 μs for **mClND**I) begins. For 0.18–3.18 μs the amplitudes drop to values lower than those obtained

at the beginning of the decay, for 3.18–9.18 μs the opposite is true and even higher values are reached. Here, indeed a second turning point becomes obvious, since a further increase from 700 mT to 1800 mT is again associated with an increase above ca. 3.18 μs and a decrease below. The respective lifetimes at this second turning point are listed in Table 32. An attempt to interpret this observation will be given later in this work.

Table 32: Decay times (τ) and amplitudes (a) for **mXNDI** (X = OMe–CN) in toluene at 476 nm (21000 cm^{-1}) detection wavelength and four characteristic magnetic fields.

	Zero-field	*1st turning point*	*2nd turning point @ 700 mT*	**1800 mT**
	τ_1 / τ_2 in ns (a_1 / a_2)	τ_1 / τ_2 in ns (a_1 / a_2)	τ_1 / τ_2 in ns (a_1 / a_2)	τ_1 / τ_2 in ns (a_1 / a_2)
mOMeNDI[a]	294 / 3980 (0.46 / 0.54)	**33.0 mT** 319 / 3170 (0.29 / 0.71)	451 / 6800 (0.73 / 0.27)	489 / 6400 (0.70 / 0.30)
mMeNDI[a]	246 / 4100 (0.33 / 0.67)	**18.9 mT** 294 / 3520 (0.18 / 0.82)	446 / 5960 (0.59 / 0.41)	477 / 5620 (0.56 / 0.44)
mClNDI[a]	282 / 6480 (0.48 / 0.52)	**22.6 mT** 209 / 5710 (0.36 / 0.64)	509 / 8690 (0.66 / 0.44)	463 / 8220 (0.61 / 0.39)
mCNNDI[b]	178 / 4950 (0.75 / 0.25)	**20.0 mT** 126 / 3110 (0.55 / 0.45)	210 / 5330 (0.81 / 0.19)	193 / 5020 (0.79 / 0.21)
mOMeNDI46	12.4 / 7290 (0.99 / 0.01)	-	-	-

[a]Excitation at 355 nm (28200 cm^{-1}). [b]Excitation at 460 nm (21700 cm^{-1}).

For **mMeNDI** the MFE on the CR dynamic was also investigated in polar MeCN, were the signal to noise ratio is significantly worse. As already shown in the previous section, the reconvolution fit of the decay at zero magnetic field consists of a very short lifetime (5.8 ns) with high amplitude (0.999) and a long lifetime (1490 ns) with low amplitude (0.002). The same holds true for the decays when applying a magnetic field, as can be seen in Figure 71, A. It is apparent, that the MFE is distinctly less pronounced in MeCN compared to toluene. Enlargement of the time area of 0–600 ns helps to clarify the changes in decay behavior when increasing the magnetic field (Figure 71 C and D). In times shorter than ca. 250 ns, the decays become slower and at longer times somewhat faster when increasing the magnetic field from 0 to 16.9 mT (Figure 71 C). A progressive increase above 16.9 mT leads to an opposing behavior in the respective time ranges. Thus in MeCN (16.9 mT) the position of the turning point is in very good agreement to those in toluene (18.9 mT) and only slightly shifted to lower magnetic field.

Besides the position of the turning point at somewhat lower magnetic, the MFE in MeCN the measurements shows an analogous development of the decay curves compared to toluene. This analogy will largely persist when looking at the double log plot of amplitude vs. magnetic field at different times (Figure 71, B). Caused by the faster decays only the amplitudes of the time slices between 0.4–1400 ns are imaged. First, there is no change while increasing the magnetic field from 0.1 to ca. 10 mT, resulting in vertical lines for each time trace. A further increase of the magnetic field to the first turning point at 16.9 mT is again associated with three different possible trends of the lines. The one at 160 ns does not change (blue line), those above ca. 160 ns rise and those below drop in intensity. Because of the bad signal to noise ratio the trace at 1400 ns is colored in green, it demonstrates exemplary the latter case. On the one hand, as in toluene, at higher field strength the respective opposite behavior is observed. On the other hand a second turning point at ca. 700 mT is hardly detectable. Nevertheless, for completeness, the reconvolution fit at this magnetic field, together with those at 0 mT, 16.9 mT and 1800 mT are given in Table 33.

Compared to 0 mT, at 16.9 mT the short lifetime τ_1 rises to 19.0 mT while its amplitude decreases to 0.940 and the longer lifetime τ_2 drops to 940 ns. From there on a further increase of *B* results in a continuous increase of τ_2 to 13900 ns. In contrast, after a drop from 19.0 ns at 16.9 mT to ca. 8 ns at 700 mT, τ_1 remaines nearly unaffected.

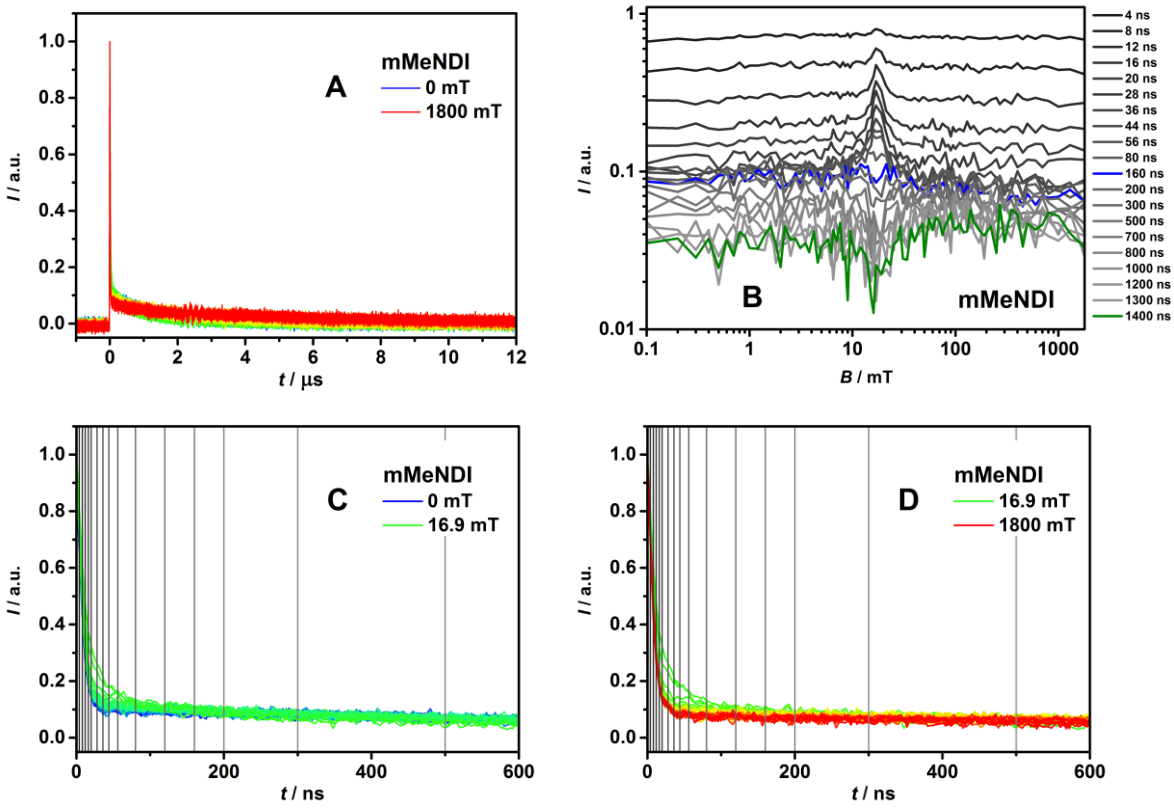

Figure 71: Magnetic field dependent decays for **mMeNDI** in MeCN at 0–1800mT (A). Increase of the magnetic field is associated with a color change from rom blue to red. Double log plot of time slices through the sets of experimental curves at different times between 4 ns and 1400 ns (B). Magnified (from 0–600 ns) magnetic field dependent decay curves divided in 0–16.9 mT (C) and 16.9–1800 mT (D), the vertical grey lines show the position of the time slices, which are depicted in B.

Table 33: Decay times (τ) and amplitudes (a) for **mMeNDI** in MeCN at 476 nm (21000 cm^{-1}) detection wavelength and four characteristic magnetic fields.

	τ_1 / τ_2 in ns (a_1 / a_2)	τ_1 / τ_2 in ns (a_1 / a_2)	τ_1 / τ_2 in ns (a_1 / a_2)	τ_1 / τ_2 in ns (a_1 / a_2)
	0 mT	**16.9 mT**	**700 mT**	**1800 mT**
mMeNDI[a]	5.80 / 1490	19.0 / 940	7.91 / 7589	7.70 / 13900
	(0.998 / 0.012)	(0.940 / 0.060)	(0.989 / 0.011)	(0.992 / 0.008)

[a]Excitation at 355 nm (28200 cm^{-1}).

4.6.6 Discussion of the Charge Recombination

From the DFT calculations the internal reorganization λ_i energy for the charge recombination CS $\rightarrow$ S_0 was estimated to be 0.43 eV. The outer reorganization energy λ_o of nonpolar toluene is estimated to be ca. 0.1 eV based on the *Born* model. Accordingly, the overall reorganization energy λ for the CR has a value of ca. 0.5 eV. The energies of the CS states ΔG_{CS} which were estimated from the redox potentials via *Weller* equation have a value of ca. 2.0 eV (4.3, Table 24). Thus it appears that the CR process of all compounds in toluene is in the *Marcus* inverted region because $\lambda < |\Delta G_{CS\rightarrow S0}|$. For **mMeNDI** in MeCN the situation is different. The outer reorganization energy λ_o of polar MeCN is estimated to be ca. 1.4 eV, resulting in an overall reorganization energy λ for the CR of ca. 1.8 eV. From the energy of the CS states ΔG_{CS} (ca. 1.0 eV, Table 24) it appears that the CR process is now clearly in the *Marcus* normal region because $\lambda > |\Delta G_{CS\rightarrow S0}|$.This change of the *Marcus* region leads to a distinct reduction of the ET barrier and thus to an acceleration of the CR process for **mXNDI**.

For *meta*-compound **mOMeNDI46** it was possible to detect the CR with the ns-setup in toluene. According to the findings in chapter 3 the 4,6-conformation of the OMe groups in **mOMeNDI46** strongly increases the coupling between the redox centers. Thus, in nonpolar toluene the CR is much faster than in **mXNDI**, while in polar MeCN (smaller ET barrier) it assumed to be so fast, that it is no longer detectable with the used setup. If the coupling is further increased, as in case of the *para*-dyads **pXNDI**, ET processes are accelerated so much that they can neither be detected in toluene nor in MeCN. All dyads show a biexponential decay of the CS state. This biexponential decay is a result of an intersystem crossing from the initially singlet populated singlet CS state to the triplet CS state. The charge recombination to the S_0 state from ^{3}CS states is spin forbidden and thus can only take place from the singlet state. For the depopulation of the triplet state again an intersystem crossing to the singlet state has to take place, which prolongs the lifetime of the CS state and leads to a biexponential decay.

The impact of a magnetic field on the CS state dynamics of dyads with radical centers far away from eachother and negligible exchange interaction (degenerated singlet and triplet CS states at zero field), was already described in the introduction (1.7.1). In summary: applying a magnetic field results in a splitting of the triplet sublevels into T_+, T_0 and T_- based on the *Zeeman* effect, as shown in Figure 72 (right). *Hayashi* and *Nagakura* proposed a relaxation mechanism which describes the dynamics between the singlet and triplet states of the CS state.[107] At zero flied the CS dynamics are governed by a fast S-T equilibrium driven by isotropic hyperfine interaction, which is a coherent process. The splitting leads to a decrease

of the interconversion between $T_{+/-}$ and S and T_0, respectively, because these processes are now governed by spin relaxation of the radicals and only the S-T_0 transition remains coherent.[107, 231, 233] Accordingly, the decay of the CS state becomes steadily slower with increasing magnetic field.

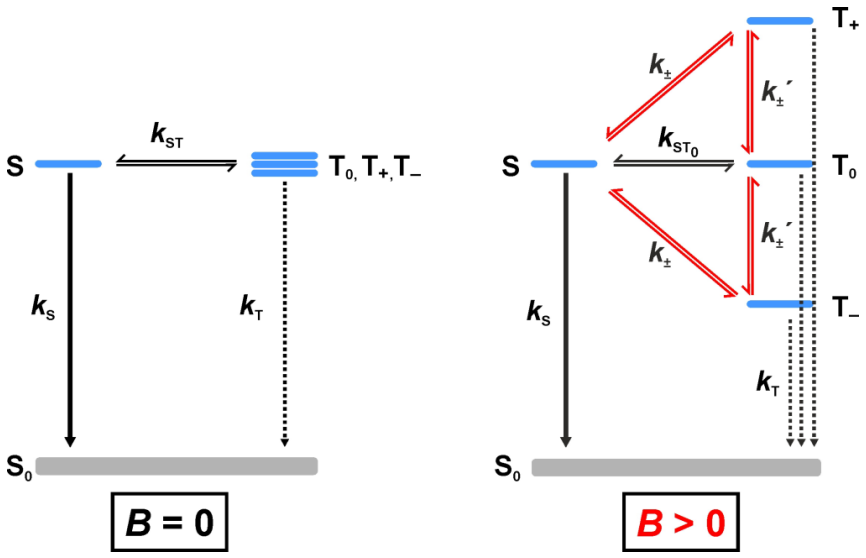

Figure 72: State diagram of the CS state with (at zero field) degenerate singlet and triplet states at zero magnetic field (left) and non-zero field (right).

The population of the states can be described by the following differential rate equations (28), which can be solved numerically (e.g. by using MATLAB). The assignment of the rate constant to the respective interconversion was already described in the introduction.

$$\frac{d[S]}{dt} = -(k_S+2k_\pm+k_{ST_0})[S]+k_{ST_0}[T_0]+k_\pm([T_+]+[T_-])$$

$$\frac{d[T_0]}{dt} = k_{ST_0}[S]-(k_T+2k_\pm+k_{ST_0})[T_0]+k_\pm([T_+]+[T_-]) \quad (28)$$

$$\frac{d[T_+]}{dt} = k_\pm[S]+k_\pm[T_0]-(k_T+2k_\pm)[T_+]$$

$$\frac{d[T_-]}{dt} = k_\pm[S]+k_\pm[T_0]-(k_T+2k_\pm)[T_-]$$

A relaxation mechanism of that kind is suitable to only a limited extent to describe the dynamics of the CS states within the dyads presented in this work. Especially the strong shortening of the decay times at 20–30 mT cannot be explained adequately.

Therefore the model of relaxation mechanism has to be expanded taking an energy difference between singlet and triplet levels even at zero field into account.

In the following, the effects of the magnetic field on the CS states, where the singlet CS and the triplet CS are non-degenerate at zero magnetic field will be presented (Figure 73, A). This case occurs if the radical centers are closer and exchange interaction is sizable. Here, the energy difference between singlet and triplet levels is given by E_S-E_T = 2J where J is the exchange interaction. There are two scenarios possible in which the triplet state is either below or above the singlet state, defined by the sign of J, which is usually positive for states with strongly overlapping orbitals. Nevertheless it may be negative for radical pairs with vanishing orbital overlap due of perturbations by energetically nearby lying localized triplet states with similar energy. For the dyads **mXNDI**, J is assumed to be positive. If the exchange interaction is much larger than the average hfc, spin interconversion is no longer coherent. It is then based on an incoherent stochastic relaxation process which is at least an order of magnitude slower than the coherent spin flip. It is particularly dominant at larger S-T separations and in addition to that slows down the spin-flip drastically with S-T separation increasing. Applying a magnetic field leads to a *Zeeman* splitting of the three sublevels of the triplet manifold, T_+, T_0 and T_- which increases linearly with the field strength B (Figure 73, upper picture). While T_0 remains unaffected by the field being separated by 2J from S, the state energy of T_- decreases continuously, resulting in steadily increasing energy gap between S and T_-. For T_+ the situation is different. First, at fields smaller than 2J the energetic separation S-T_+ decreases with increasing magnetic field. Then, at B = 2J the T_+ level is isoenergetic to the S level. In this situation spin interconversion between S and T_+ is coherent (Figure 73, B) and thus the interconversion is much faster than before. Obviously, in this case, the incoherent processes get overcompensated by the coherent process.

This can directly be observed by means of the decay curves in Figure 69 and Figure 71,C/D. Here, the magnetic fields of the “first turning points” are equal to 2J. In addition to that, the same is true for the amplitude vs. magnetic field at different times plots in Figure 70 and Figure 71,B. Increasing the magnetic fields further (B > $2J$) T_+ rises in energy and the separation to S also increases (Figure 73, C) and at higher fields the spin interconversion between S and T_+ is again incoherent and thus slowing down the dynamics in the CS state.

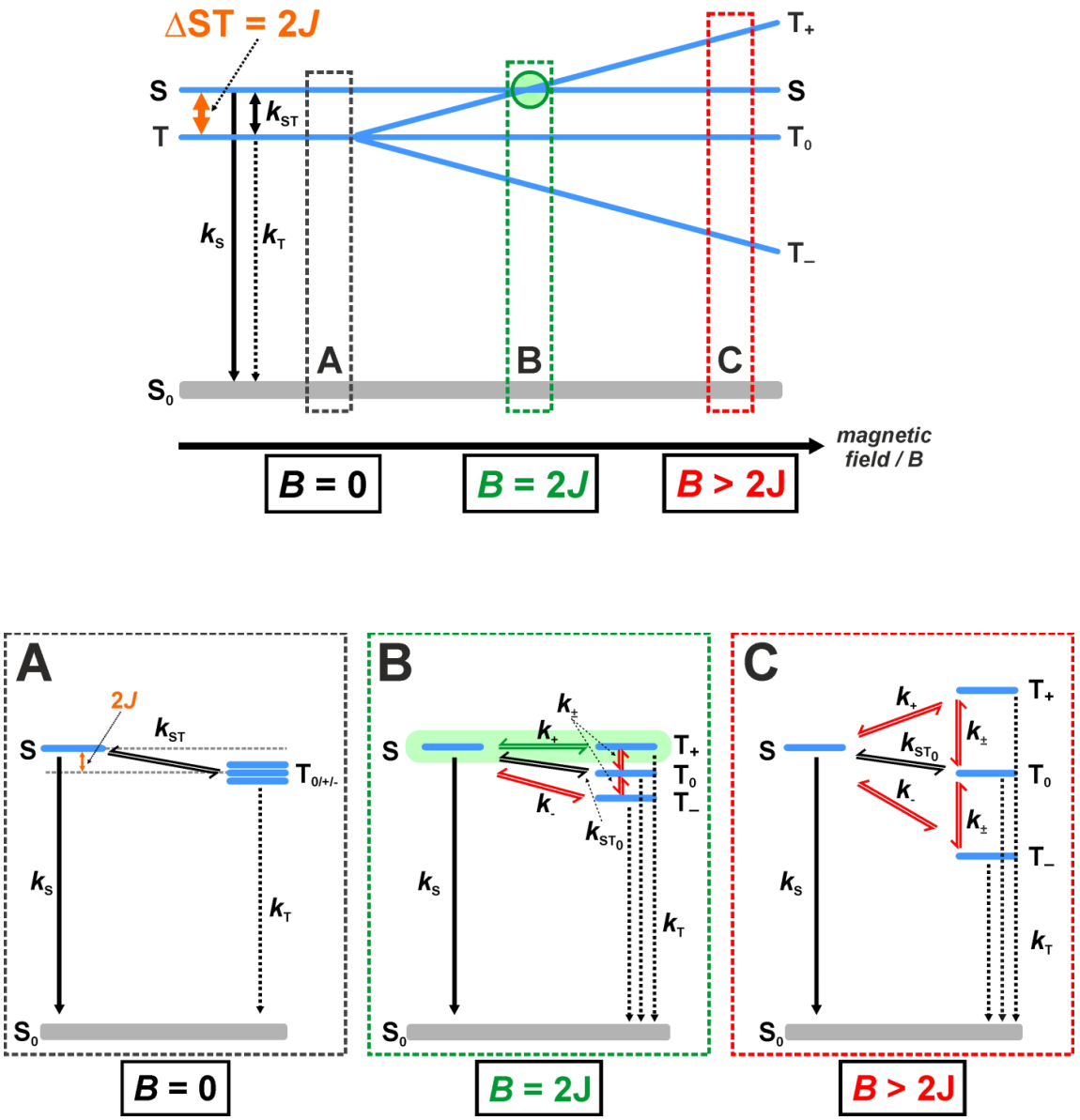

Figure 73: Upper picture: Energy diagram as a function of magnetic field for a (at zero-field) non-degenerated triplet and singlet CS state. Lower pictures: Energy diagram and rate constants at zero magnetic field (A), at B = 2*J* (B) and at B > 2*J* (C).

In Figure 73, the state diagram of the three limiting cases $B = 0$ (A), $B = 2J$ (B) and $B > 2J$, are depicted. In case A the rate of S-T interconversion for a non-degenerated CS state can solely be described by k_{ST0}. Whereas, however, the CS dynamics at $B > 0$ for degenerated states ($2J = 0$) could be described by introducing one additional magnetic field dependent parameter $k_\pm$ (Chapter 1.7.1) the situation for non-degenerated states ($2J > 0$) is much more complex. As can be seen from e.g. Figure 73,C the interconversion between each T_0, T_+, T_- and S has to be associated with its own rate constant; which are k_{ST0} for S-T_0 (unaffected by magnetic fields), k_+ for S-T_+ and k_- for S-T_-. Since the separation between T_0-T_+ and T_0-T_- have the same magnitude, these interconversions are described by one rate constant $k_\pm$.

In the following, the dynamics of spin chemistry were treated in the context of the above outlined *Hayashi-Nagakura* scheme in a classical way by solving differential rate equations numerically using MATLAB,[234] which in the past turned out to provide a good phenomenological basis. An adaptation of the numerical solving approach to the extended model with a non-degenerate singlet and triplet CS state at low fields has not yet been realized, thus the model with degenerated CS state (Figure 72) and equations (28) were used as a first approximation.

With regard to the kinetics, $k_{ST0,}$ k_S and $k_{T,}$ as well as the initial spin population of the singlet triplet states $p_{S,0}$ must be independent of the magnetic field and thus are regarded as global parameters.[109] Due to the spin conservation rule no charge recombination from the triplet states to the S_0 state is allowed, thus k_T equals 0.[109] The remaining global parameters were determined by fitting the numerical solutions to 16 selected kinetic decay curves at various magnetic fields. Therefore a MatLab script was developed, where 16 selected experimental curves are fitted simultaneously using a sum of square minimizing tool, where the sum of squares difference between the model output and data feeds to the algorithm and expresses the quality of the fit (resnorm).[78]

Besides the assumption k_T = 0, three additional approaches can simplify the fitting procedure. First, the field k_{ST0} at zero in the degenerated model for similar DA-compounds is expected to be in the order of 10^7–10^8 s^{-1}, driven by the isotropic hyperfine interaction.[106] Since the theoretical description is not exactly valid for the system where the singlet and triplet levels are non-degenerated the exchange interconversion must be decreased and k_{ST0} be smaller. Second, in the limit of zero field it can be assumed that $k_{\pm} \approx k_{ST0}$. Third, it was assumed that the ^{1}CS state is initially nearly exclusively populated.

To determine the best value of the initial singlet character $p_{S,0}$ of the CS state for a given global test value of k_{ST0} and k_S the total root mean square (resnorm) values over the decay curves at 16 standard fields were minimized for individually values of $k_{\pm}$. For each dyad a large number of fits with varying global parameters were needed to optimize $p_{S,0}$, k_{ST0} and k_S. The final values are listed in Table 34.

Table 34: Global fitting parameters k_{ST0}, k_S and $p_{S,0}$ derived from simulating 16 selected decay curves. $k_\pm$ values of four characteristic magnetic fields obtained by fit of the decay curves by use of the global parameters.

	$2J$ / mT	k_{ST0} / 10^5 s^{-1}	k_S / 10^6 s^{-1}	$p_{S,0}$	$k_\pm$ / 10^5 s^{-1}			
					(0 mT)	(@ $2J$)	(700 mT)	(1800 mT)
mOMeNDI	33.0	3.9	1.64	0.94	3.91	9.79	0.63	0.70
mMeNDI	18.9	5.8	1.36	0.99	5.80	15.2	1.29	1.59
mClNDI	22.6	2.6	1.07	0.99	2.60	4.83	0.84	1.27
mCNNDI	20.0	1.1	3.40	0.87	1.20	2.75	0.63	0.83

It was found that the values of k_{ST0} are as expected significantly lower for **mXNDI** compared to the degenerated situation of the CS states. They are in an order of 10^5 s^{-1}, which suggests that k_{ST0} is exclusively caused by spin relaxation. In addition to that, it decreases in the sequence: $k_{ST0}(Me) = 5.8 \times 10^5$ s^{-1}, $k_{ST0}(OMe) = 3.9 \times 10^5$ s^{-1}, $k_{ST0}(Cl) = 2.6 \times 10^5$ s^{-1} and $k_{ST0}(CN) = 1.1 \times 10^5$ s^{-1}. This tendency shows that the substituents X seem to have a decisive influence on the S-T_0 spin flip, while this is not observable for k_S. For the latter no clear trend of rate constants is observable and values of $k_S(Me) = 1.36 \times 10^5$ s^{-1}, $k_S(OMe) = 1.64 \times 10^5$ s^{-1}, $k_S(Cl) = 1.07 \times 10^5$ s^{-1} and $k_S(CN) = 3.4 \times 10^5$ s^{-1} were obtained.

The initial population consists mainly of a singlet population for ($p_{S,0}(OMe) = 0.94$, $p_{S,0}(Me) = 0.99$, $p_{S,0}(Cl) = 0.99$). However, for **mCNNDI** a triplet population of 0.13 was needed to obtain reasonable fits. One has to note, that deviation from these values has a high impact on the quality of the fit. The fit of the cyano compound was very difficult, since no global values could be found that produced good fits in all areas of the magnetic field. With global values achieving accurate simulations of the low and high magnetic fields, a simulation of the decay curves around the changing point ($B = 2J$) was not possible. The same applies to the exact reverse case, which describes a good simulation accuracy of the change point. Therefore, averaging of the global parameters had to be accepted, in order to obtain reasonable fits over the entire magnetic.

All (ca. 100) decay curves were fitted individually with these global parameters to determine the $k_\pm$ value for every single magnetic field. The evaluated rate constants were plotted vs. the magnetic field B in a double logarithmic plot (Figure 74, left). A more detailed description of the procedure of determination of all rate constants, including the MATLAB script, is given in literature.[78]

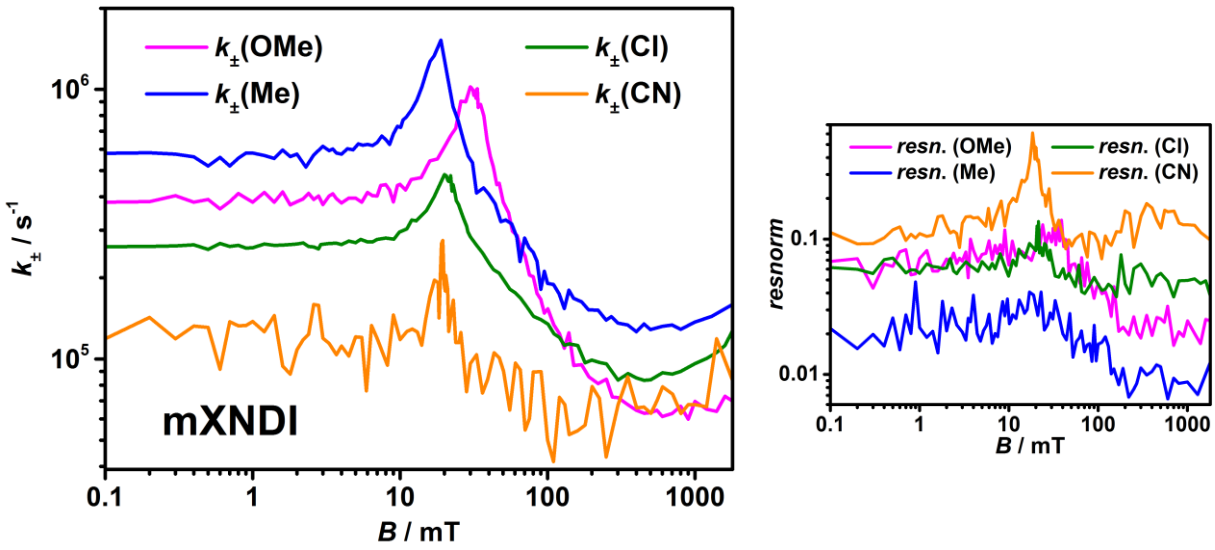

Figure 74: Left: Magnetic field dependence of $k_{\pm}$ for **mOMeNDI**, **mMeNDI**, **mClNDI** and **mCNNDI** obtained by fitting the CS decay curves. Right: Resnorms of the fittings, representing their quality.

For all dyads a similar progression of the plot was found. First, at ca. 0–10 mT there is a plateau positioned at about $k_{\pm} = k_{ST0,}$ then there is a three-fold increase of $k_{\pm}$ at ca. 20 mT for X = Me–CN and 30 mT for OMe (Table 34). Then a drop of the $k_{\pm}$ values under those at low magnetic field and finally a small increase, for highest magnetic fields possible with this setup, is observed. This treatment thus shows a good phenomenological consistency of the position of the 2*J* resonance (located at exactly the same magnetic field) and the other turning points, in comparison to the above shown representations (Figure 69 and Figure 70). Nevertheless some errors have to be considered. On the right side of Figure 74 the resorms of the respective fits are plotted. Especially for the methyl dyad this analytical method shows only slight deviations of the fits from the measured decays and provides good results. For the methoxy and chloro dyads the resnorms are significant higher and in addition to that, magnetic field-dependent variations in the quality of the fit are observable. At high magnetic fields (100–1800 mT) where relaxation processes dominate but also at small fields (0–10 mT), lowest resnorms and thus good fits were found. Not surprisingly the deviations around B = 2*J* are the largest, since the isoenergetic position of S and T_+ cannot be adequately considered in this relaxation mechanism, which exactly reveals the biggest disadvantage of this approach. For **mCNNDI** it has to be mentioned, that the fits show a large deviation from the decay curve and thus high resnorm values. Especially at the vicinity of *B* = 2*J* the error is very high, however a qualitative description of the characteristics of the MFE is still possible.

Surprisingly, $k_{\pm}$ increases for all dyads from 800–1800mT. This behavior was already observed in the amplitude vs. magnetic field at different times plots in Figure 70 and Figure 71, B. It is assumed that here a new interconversion process is added or the existing one is modified in an unknown way. As a new contribution the Δg mechanism could possibly be considered. It is a field dependent interconversion, caused by differing isotropic *g* values of the two radical centers, with $k_{\Delta g} = \frac{\Delta g \mu_B B_0}{2\hbar}$.[235, 236] Since, however, the *g*-factors of the radical at the donor and the acceptor were determined to 2.0033 and 2.0038, respectively (see ESR analysis in 3.3.2), they have nearly the same value and thus this process should only be sizable at very high fields. Since the fields applied were of relatively low strength, this process should be neglectable. Therefore, unfortunately no reasonable explanation was found to interpret the unforeseen increase of spin interconversion at high fields.

Another observation, which requires an explanation, concerns the magnitude of the 2*J* coupling. While 2*J* was determined to ca. 20 mT for **mXNDI** with X = Me–Cl, for **mOMeNDI** a distinctly larger value 2*J* = 30 mT was found. Although 2*J* values in the right order of magnitude were obtained by TD-DFT calculations, a sufficiently accurate simulation of the 2*J* failed so far, since these values are very sensitive to the geometry used for the optimization of the excited states. This sensitivity is much larger than the variation of 2*J* along the series of dyads investigated in this work. Thus, a deeper analysis is not possible at the moment.

One possible explanation can be found following the argumentation by *Anderson*, which was already presented in the introduction (see chapter 1.7.2).[120] Based on perturbation theory, the exchange interaction is related to the square of electronic coupling to energetically nearby lying states. Unfortunately, there is no information about the energies of other states than those presented here. Assuming that there are triplet CT counterparts for all singlet CT states that precede the formation of the CS states, a significant change of the exchange coupling 2*J* might be possible, since these ^{3}CT states should have slightly lower energies than the ^{1}CT states and might perturb the ^{3}CS states.

The electronic couplings of the charge recombination processes V_{CR} were estimated by use of *Bixon-Jortner* theory and equation (**27**) given in chapter 4.6.4.[225, 226] With an inner reorganization energy λ_v of 0.43 eV derived from DFT calculations, an average molecular quantum mode $\tilde{\nu}_v$ with a typical value of 1500 cm^{-1} (0.16 eV)[227-229] and a solvent reorganization energy λ_o of 0.1 eV (toluene). The charge recombination rates constants were taken from simulation of the decay curves at B = 0 mT (Figure 75). These fits were done according to the *Hayashi-Nagakura* relaxation scheme, not with the global rate constants (k_S, k_{ST0}) determinated above, but with parameters individually adapted to the decay curves and assuming that $k_{\pm} \approx k_{ST0}$ (Table 35). It is noticeable, that k_S and k_{ST0}, especially for **mCNNDI**, show a difference to those obtained by the global fits. This difference is caused by the

method of determining the global parameters as described above, where for example an averaging of k_S and k_{ST0} was accepted.

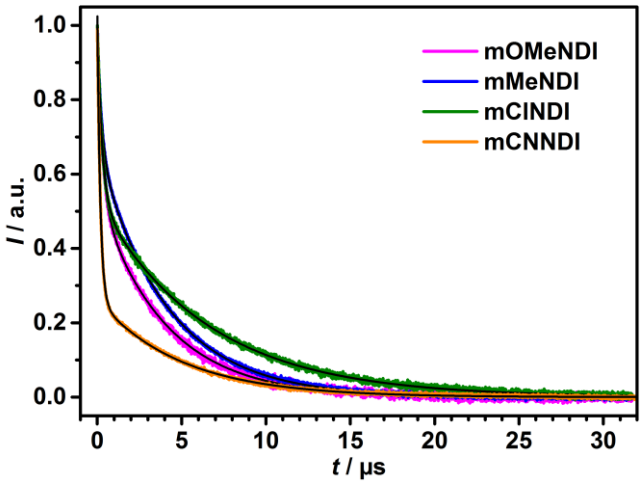

Figure 75: Transient absorption decay traces for **mXNDI** (X = OMe–CN) at 21000 cm^{-1} (476 nm) at B = 0 mT and fit (black lines).

Table 35: Global fitting parameters k_{ST0}, k_S and $p_{S,0}$ derived from simulating of the decay curves at B = 0 mT.

	k_{ST0} / 10^5 s^{-1}	k_S / 10^6 s^{-1}	$p_{S,0}$	V_{CR} / cm^{-1}
mOMeNDI	5.04	1.88	0.97	4.5
mMeNDI	6.42	1.41	1.00	4.1
mClNDI	1.88	2.64	0.61	5.7
mCNNDI	2.32	4.36	0.88	7.3

The charge recombination rates $k_{CR} = k_S$ follow a trend in the same order as charge separation $k_{CS} = 1/\tau_2$, that is, k_S(Me) < k_S(OMe) < k_S(Cl) < k_S(CN), as can also be seen in Figure 76. For the CS it was suggested above that the rate depends on the ET barrier in the *Marcus* inverted region, and that the coupling V_{CS} plays a subordinated role. For CR the charged redox centers are identical in all cases and ΔG should be practically a constant for all derivatives.

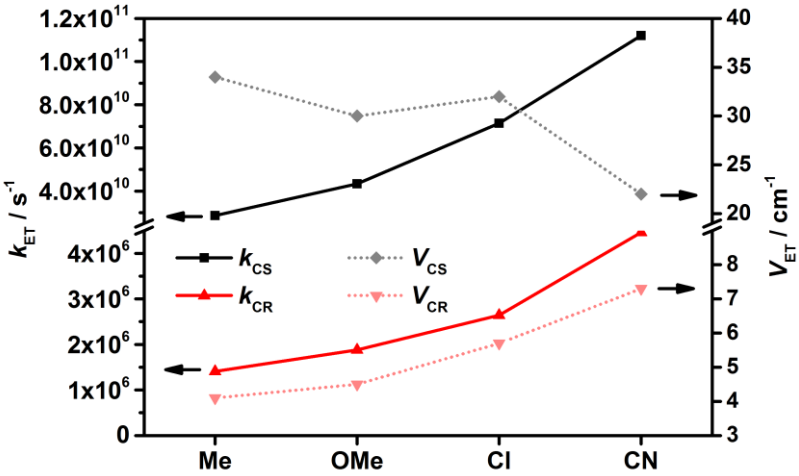

Figure 76: Rate constants (k_{ET}, solid lines) and couplings (V_{CS}, dotted lines) for photoinduced charge separation (black) and charge recombination (red).

The calculations of the electronic couplings gave values of V_{CR}(Me) = 4.1 cm^{-1}, V_{CR}(OMe) = 4.5 cm^{-1}, V_{CR}(Cl) = 5.7 cm^{-1} and V_{CR}(CN) = 7.3 cm^{-1}, and follow the trend of the recombination rate, thus the couplings and not the barrier seem to play the decisive role in this case. V_{CR} increases slightly when increasing the electron accepting character of X at the benzene unit, presumably caused by an increasingly lower bridge-LUMO which improves the electron transfer via virtual states. The couplings are distinctly smaller than those for CS because here the recombination takes place between charges being localized at the two redox centers, whereas in CS process one has to consider a CT state where the negative charge is already partially localized at the bridge and has to move over a significant smaller distance to the acceptor to form the CS state.

The smaller electronic coupling together with the larger barrier in the inverted region makes charge recombination slower than charge separation by more than factor 10^4. One has to note, that this ratio only concerns the charge recombination of the singlet CS state. The entire recombination process is governed by the slow spin equilibrium of the CS state resulting in a second much longer lifetime component τ_2 which is in the microsecond time regime.

4.7 Conclusion and Future Outlook

In this chapter the ET processes of charge separation and charge recombination of *meta*-substituted dyads **mXNDI** (with X = OMe–CN) were investigated. The charge recombination was additionally influenced using an external magnetic field in order to study the charge recombination processes occurring with respect to the singlet-triplet spin multiplicity.

The global analysis of the spectra obtained by fs-TA spectroscopy, regarding the CS processes showed, that first a CT state is formed, which involves the bridging moiety. Then the formation of a CS state could be detected. This CS process is in the *Marcus* inverted or at best optimal region for all compounds. The rise time of the CS states increases with increase of electron-withdrawing strength of the substituent X at the bridging unit.
The CR was examined by ns-TA spectroscopy. Therefore the lifetimes of the CS state were extracted from the biexponential tail fits or reconvolution fits of the decay curves. The biexponential decay can be explained by singlet-triplet equilibrium in the CS state. In toluene the CR of **mXNDI** and **mOMeNDI46** were found to be in the *Marcus* inverted region, with those of **mOMeNDI46** being significantly faster. In MeCN the charge recombination for all dyads is much faster and in the *Marcus* normal region. For **mOMeNDI46** it is assumed that the CR is sped up so strongly that it could not be recorded with the time resolution of the ns-setup. Although, exemplified shown for **mMeNDI**, application of an external magnetic field *B* led to a magnetic field effect (MFE) in toluene and MeCN, discussion was sololey focused on toluene since the MFE significantly more pronounced.
Regarding the findings of the first part of this work, the significantly faster CR in **mOMeNDI46** is assigned to be a result of the strong electron donating OMe substituents attached to positions with high molecular orbital contribution, thus probably effectively increasing the coupling *V.* Using weaker EDG (e.g. X = Me–CN) would probably reduce *V* and simultaneously decelerate the CR in **mXNDI46**. Hence, the recombination could be slowed down so that an examination of this series is possible. By this approach the dependency of the substitution pattern at the central benzene ring on the MFE could be studied in more detail.
For the investigation of **mXNDI**, it was particularly noticeable that at first an acceleration of the decay behavior, followed by a considerable slowdown with increasing B was observable. It was shown that the turning point of this trend corresponds to the size of the singlet-triplet splitting within the CS state, with an energy difference E_S-E_T = 2*J,* with *J* being the singlet-triplet exchange interaction. Simulation of the decay curves using a relaxation scheme proposed by *Hayashi and Nagakura* for a *degenerated* singlet-triplet at zero-field (2*J* = 0) confirmed this assumption and helped to determin the involved rate constants. For X = Me–

Cl, 2*J* values of ca. 20 mT were obtained and for X = OMe 2*J* was determined to 30 mT. The origin of this deviation could not be clarified and further investigation is needed. Since these fitting procedures are based on the relaxation scheme of a degenerate situation, where all field dependent interconversion processes defined by one rate constant $k_{\pm}$, only the energetic position of the 2*J* resonance could be reproduced qualitatively well. However, the simulations of the decay curves, especially for **mClNDI** and **mCNNDI**, are very imprecise.
In order to obtain an improvement, the mathematical description of the dynamic equilibrium has to be adapted to the non-degenerated relaxation scheme. A differentiation of k_+, k_- and k_+ is necessary, with k_+ and k_+ being the rate constant for the T_+, T_- and S interconversion, respectively and $k_{\pm}$ being the rate constant for T_+ T_- and T_0 interconversion. To maybe facilitate the simulation, some assumptions can be made: The first is to assume that at low magnetic fields (0 to ca. 5 mT) $k_{ST0} \approx k_+ = k_- = k_{\pm}$. At high field (above ca. 100 mT) $k_+ = k_- = k_{\pm}$ (and $< k_{ST0}$) should be a good assumption, since the energetic spacing between the sublevels T_- and T_+ and the singlet state is quite large. Most importantly, from ca. 5 mT to ca. 100 mT, that is, in the range of the level crossing of S and T_+, the relation $k_- = k_{\pm} \neq k_+$ must hold, since k_+ describes the level crossing effect but both k_- and $k_{\pm}$ interactions between states that are energetically further apart.

Both parts of this work, the investigation of the HT in cationic MV bisTAA compounds, as well as the investigation of the ET in DA compounds, revealed a decisive influence of the benzene bridging unit on the appearing ET processes.
For the HT in the ground state of the MV compound, the *para*-connectivity showed highest transfer rates due to high electronic coupling *V*, which was also tunable by variation of the substituents X. Electron-donating substituents X strongly increased the electronic coupling in **pX** and thus increased the transfer rates. For the *meta*-series **mX** lowest transfer rates and no impact of the substituents X was observed. Finally, the *meta*46-series **mX46** showed an intermediate behavior in between. With strong electron-donating substituents X, ET transfer rates equal to those of the *para*-series were found. Decreasing the donating character of X resulted in a strong decrease of the transfer rates and a behavior comparable to those of the *meta*-series was found.
For the ET in the exited states of the DA compounds, the *para*-connectivity seemed to be most efficient, as well. In fact, due to the very fast ET dynamics, an investigation of the CR processes in the ns-time regime was not even possible. Hence, the investigation was restricted to the *meta*-series. On the one hand, in accordance to the MV compounds, **mXNDI** (X = OMe-CN) showed significantly slower ET dynamics than the *para*-compounds. On the other hand, the substituents X showed an influence on the charge transfer rates *k* and couplings *V* of both the CS and CR. For the CS, a decrease in electron-donating character of

X, results in an increase of the rate constants *k*cs, while the coupling *V*cs decreased. In case of the CR, the electronic coupling V_{CR} and transfer rate k_{CR} increased.

Again, the *meta*46-compound **mOMeNDI46** displaying traits of *para*- and *meta*-compounds, having a much faster ET dynamic in the excited state than the *meta*-series **mXNDI**, but having its CR still being detectable in the ns-time regime just as the *para*-series **pXNDI**.

5 SUMMARY

In the first part of this thesis, the synthesis of a series of bistriarylamine (bisTAA) compounds was presented. On the one hand, the substitution pattern of the TAA at the benzene bridging unit was varied from *meta*- to *para*-position (**pX** and **mX**), on the other hand, the energetic position of the bridging unit was tuned by use of two electron-donating or electron-accepting substituents X (with X = OMe, Me, Cl, CN, NO_2) in 2,5-position. In case of the *meta*-series, compounds with X in 4,6-position were synthesized (**mX46**). The photophysical and electrochemical properties of the neutral compounds were investigated.
The cationic mixed valence (MV) bisTAA compounds could be generated by oxidation. Thermally induced hole transfer (HT) in the groud state was investigated by temperature depending ESR spectroscopy. While the HT rate *k* and HT barrier Δ*G* in **mX** are unaffected by the substituents X, *k* and Δ*G* in the **pX** series increase simultaneously with increasing electron-donating strength of X. This, at first contradictory observation can be explained by an increasingly important solvent dynamic effect and an additional, effective barrier. The optically induced HT was examined by UV/Vis/NIR spectroscopy. The **pX**-series revealed an increase of the electronic coupling *V*, and correspondingly a decrease of ΔG, with an increase of the electron donating character of X. For **mX**, a spectroscopic determination of these parameters was not possible. **mX46** showed an intermediate behavior, MV compounds with strong electron-donating X, obtained coupling of similar magnitude as **pX**, which could be explained by means of DFT calculations, with regard to the molecular orbitals.

In the second part of this work, the synthesis of a series of dyads with triarylamine (TAA) as a donor and naphthalene diimide (NDI) as an acceptor was presented. Again, the substitution pattern of the redox centers at the benzene bridging unit was varied in the form of a *meta*- or *para*-position (**pXNDI** or **mXNDI**) and the energetic position of the bridging unit was varied by X (with X = OMe, Me, Cl, CN, NO_2) attached in the 2,5-position. Additionally, compound **mOMe46NDI** with methoxy substitution in 4,6-position was synthesized. The photophysical and electrochemical properties of these compounds were investigated. The electron transfer (ET) processes of charge separation (CS) and charge recombination (CR) of these were investigated by means of transient absorption (TA) spectroscopy in toluene. This was not possible for the nitro-compounds **p-/mNO$_2$NDI**, since they decomposed under irradiation. In addition to that, the CR of **pXNDI** was not detectable by ns-setup, which is why the focus was given to the **mXNDI** series (with X = OMe–CN).The CS was examined by fs-TA spectroscopy, where the formation of a CS state could be detected. The rise time of the CS states decreases with increasing electron-withdrawing substituents X. CR was examined with ns-TA spectroscopy and shows a biexponential decay behavior, which is caused by

singlet-triplet equilibrium in the CS state. By applying an external magnetic field, the decay behavior was decisively changed and the singlet-triplet splitting could be determined. This finding could also be confirmed by simulating the decay curves.

In both parts of this work, the decisive influence of the benzene bridging unit on the appearing ET processes became obvious. For the HT in the ground state of the MV compound, as well as for the ET in the exited states of the DA compounds, the highest transfer rates were found for the *para*-series **pX** and **pXNDI**, and much smaller rates for the *meta*-series **mX** and **mXNDI**. The *meta*46-compounds **mX46** and **mOMeNDI46** showed an intermediate behavior in both parts of this work.

6 EXPERIMENTAL SECTION

6.1 Materials and Methods

6.1.1 Steady-State Absorption Spectroscopy

- JASCO V-670 UV/Vis/NIR spectrometer (software SpectraManager v. 2.08.04)
- Agilent Technologies Cary 5000 UV-Vis-NIR spectrophotometer (software Agilent Cary WinUV Analysis and Bio v.4.2)

All solvents were of spectroscopic grade and were used without further purification (Acros Organics, Uvasolv from Merck, Sigma Aldrich, Spectronorm from VWR), only $PhNO_2$ was destilled prior to use.[237]Absorption spectra were recorded in 10 × 10 mm quartz-cuvettes with teflon stopper (Hellma or Starna) at rt. The neat solvent was used as reference. Aggregation of the samples could be excluded by a concentration independent behavior of the spectra (10^{-7}–10^{-5} M).

6.1.2 Electrochemistry

All electrochemical measurements were performed in DCM with tetrabutylammonium hexafluorophosphate (TBAHFP, 0.2 M) as supporting electrolyte. DCM was first dried over calcium chloride, distilled from calcium hydride and stored over activated alumina or molecular sieve prior to use. TBAHFP was synthesized according to literature,[238] recrystallized from ethanol/water and dried under high vacuum.

6.1.2.1 Cyclic Voltammetry (CV), Square Wave Voltammetry (SWV) and Differential Pulse Voltammetry (DPV)

- BAS CV-50 W electrochemical workstation including corresponding software (v. 2.31)
- Gamry Instruments Reference 600 Potentiostat/Galvanostat/ZRA (v. 6.2.2, Warminster, PA, USA)

The cyclic voltammograms of all compounds (2 mM) were measured under an argon atmosphere in DCM with tetrabutylammonium hexafluorophosphate (TAHFP, 0.2 M) as

conducting salt. A conventional three electrode set-up consisting of a platinum disc working electrode (Ø = 1 mm), a Ag/AgCl 'LEAK FREE' reference electrode (Warner Instruments, Hamden, CT, USA) and a platinum wire counter electrode was used. The measurement cell was dried in an oven and flushed with argon before use. The reference electrode was referenced against the ferrocene/ferrocenium (Fc/Fc^+) redox couple. In the CV meassurements chemical and electrochemical reversibility of the redox processes were checked by multi thin layer experiments and measurements at different scan rates (from 25–1000 mV s^{-1}), respectively. The SWV measurements were performed at a scan rate of 50 mV s^{-1}. The DPV measurements were performed at a scan rate of 2 mV s^{-1}.

6.1.2.2 Spectroelectrochemistry (SEC)

- JASCO V-670 UV/Vis/NIR spectrometer (software SpectraManager v. 2.08.04)
- Agilent Technologies Cary 5000 UV-Vis-NIR spectrophotometer (software Agilent Cary WinUV Analysis and Bio v.4.2)
- Princeton Applied Research Model 283 potentiostat

UV/Vis/NIR-spectroelectrochemistry was performed at rt in a custom built three electrode quartz-cell sample compartment implemented in a Jasco V-670 or a Cary 5000 UV-Vis-NIR spectrometer. For the Jasco spectrometer the cell consists of a platinum disc working electrode (Ø = 6 mm), a gold covered stainless steel (V2A) plate as counter electrode and an AgCl-covered silver wire as pseudo-reference. The cell used in the Cary spectrometer consists of a platinum disc working electrode (Ø = 6 mm) and platinum counter electrode and pseudo-reference. The cell volume was flushed with argon before use. All experiments were measured in reflexion mode with a path length of 100 µm and a concentration of 1 mM of the solutes.

6.1.3 Redox Titrations / Chemical Oxidation

- Agilent Technologies Cary 5000 UV-Vis-NIR spectrophotometer (software Agilent Cary WinUV Analysis and Bio v.4.2)

Redox titrations monitored by UV/Vis/NIR spectroscopy were performed in three different solvents ($PhNO_2$, *o*DCB and DCM) using a Cary 5000 UV-Vis-NIR absorption spectrometer (Agilent technologies) and 10 × 10 mm quartz-cuvettes with Teflon stopper (Hellma or

Starna). $PhNO_2$ was distilled prior to use,[237] *o*DCB (Acros) and DCM (Uvasol from Merck) were of spectroscopic grade and were used without further purification. $SbCl_5$ (Acros Organics or Merck) was used as oxidant in all cases. The bistriarylamine solution (ca. 1.5 µM) was titrated with a solution of $SbCl_5$ in the respective solvent (ca. 1 mM) using a microliter pipette (Eppendorf). The pure solvent was used as reference.

6.1.4 fs-Pump-Probe Spectroscopy

- Newport-Spectra-Physics Solstice one box amplified ultrafast Ti:Sapphir laser system with a fundamental wavenumber of 12 500 cm^{-1} (800 nm), a pulse length of 100 fs and a repetition rate of 1 kHz
- Newport-Spectra-Physics TOPAS-C optical parametric amplifier as the source for the pump pulses with a pulse length of 140 fs
- Ultrafast Systems Helios transient absorption spectrometer with a CMOS sensor (1.5 nm intrinsic resolution, 350–800 nm sensitivity range) and an InGaAs sensor (3.5 nm intrinsic resolution, 800–1600 nm sensitivity range)

The the fs-pump-probe spectroscopy was performed by Alexander Schmiedel.[212] All experiments were performed in quartz cuvettes from Spectrocell (Oreland, PA) with an optical path length of 2 mm equipped with a micro-stirrer to allow stirring during the measurement. All samples were dissolved in the solvent as indicated, filtered and degassed for at least 15 min before each measurement.The laser beam from the Solstice amplifier was split into two parts. One part was used to seed an optical parametric amplifier (Newport-Spectra-Physics, TOPAS) as the source for the pump pulse with a pump energy of 100–250 nJ, and a wavenumber of 20800 cm^{-1} (480 nm) and 26500 cm^{-1} (378 nm) with a pulse length of 140 fs. The second fraction of the Ti:sapphire output was focused into a moving calcium fluoride-plate to produce a white light continuum in the visible between 25000 cm^{-1} (400 nm) and 11800 cm^{-1} (850 nm) which acted as the probe pulse. The measurements were done under magic angle conditions. The probe pulses were detected via a transient absorption spectrometer (Ultrafast Systems, Helios) with a CMOS sensor. A typically instrument response function (IRF) was in the range of 150–350 fs depending on the used solvent and the pump wavelength. By means of a computer-controlled linear stage (retro reflector in double pass setup) the relative temporal delay between pump and probe pulse was varied in 20 fs steps from 0 fs to 4 ps and from 4 ps to 8 ns in logarithmic steps with a maximum step size of 200 ps. The stability of the samples was verified by recording the steady-state absorption spectra before and after the time-resolved measurements.

The time resolved spectra were analysed by global fitting with GLOTARAN (v. 1.2).[239, 240] For this purpose a sequential model was applied yield the evolution associated difference spectra (EADS). The white light dispersion (chirp) was corrected by fitting a third order polynomial to the crossphase modulation signal of the pure solvent under otherwise identical experimental conditions. Singular value decomposition was used to estimate the number of components and the quality of the fits.

6.1.5 ns-Laser Flash Spectroscopy

- Edinburgh LP 920 laser flash spectrometer with a 450 W ozone-free Xe arc lamp including a photomultiplier (Hamamatsu R955), digital storage oscilloscope (Tektronix TD3012B) and software (L900 v. 7.3.5)
- Continuum Minilite II Nd:YAG laser operating at 10 Hz, 3–5 ns pulse duration, pulse energy 8 mJ at 355 nm (28200 cm^{-1})
- EKSPLA NT340 Nd:YAG laser with integrated optical parametric oscillator operating at 10 Hz, 3–6 ns pulse duration, pulse energy 8 mJ at 460 nm (21700 cm^{-1})
- GMW Associates C-frame electromagnet 5403 (pole diameter = 76 mm, pole face = 38 mm, axial hole in poles 6.35 mm, pole gap = 12 mm), Sorensen (DLM40-75E) power supply
- Hall-Sensor (Single-Axis Magnetic Field Transductor YM12-2-5-5T, SENIS GmbH)

At Zero Field (B = 0)

ns-Transient absorption spectra were measured with an Edinburgh LP 920 laser flash spectrometer consisting of a Continuum Minilite II Nd:YAG laser or a EKSPLA NT340 Nd:YAG laser with intergrated optical parametric oscillator and a Xe flash lamp for detection of the spectra. All solvents were of spectroscopic grade and were used without further purification and degassed by bubbling argon through the solution for at least 2 h. The srew cap with septum was exchanged for one without in a glove box. Measurements were carried out in 10 × 10 mm quartz-cuvettes (Hellma or Starna). The samples were excited with ca. 5 ns laser pulses at 28200 cm^{-1} (355 nm) and all measurements were done using the fluorescence correction implemented in the L900 software. The transient maps were obtained by measuring decay profiles in 4 nm or 5 nm steps between ca. 11800 cm^{-1} (850 nm) and 25000 cm^{-1} (400 nm). The instrument response (ca. 8 ns) of the set-up was determined by measuring the scattered light using a LUDOX AS-30 colloidal silica suspension in water. Decay curves were fitted with the tailfit function of the spectrometer

software. Measurements were performed at different concentrations (10^{-6}–10^{-5} M) and pulse energies (0.2–1.2 mJ) to avoid bimolecular deactivation processes. The stability of the samples was verified by recording the steady-state absorption spectra before and after the time-resolved measurements.

At Non-zero Field (B > 0)

For the field-dependent measurements the aforementioned laser pump-probe set-up was equipped with an electromagnet. The pump and probe beams were perpendicular to each other, while the pump beam was focused through the poles and the probe white light was directed through the open faces of the C-frame. The magnetic field strength was controlled by a Hall-sensor which was placed at the side of the pole face. The magnetic field effect (MFE) on the charge recombination dynamics was probed by applying ca. 100 different magnetic fields *B* between 0 and 1800 mT to the sample and measure the decay after every variation of the magnetic field. The step size between different magnetic fields was stepwise increased from 0.1 mT from (0–1 mT), to e.g. 1.0 mT (between 10–19 mT), 10.0 mT (between 100–190 mT) and 100 mT (between 500–800 mT). The error of determining *B* was assigned to ±0.02 mT for magnetic fields between 0–400 mT and ±1 mT for fields between 400–1800 mT. A more detailed description of the setup is reported in literature.[78, 113] The sample preparation and further transient absorption conditions are analogous to those described for the zero field measurements. The stability of the samples was verified by recording the steady-state absorption spectra before and after the time-resolved measurements.
The magnetic field dependent decays were subtracted by a small long-time offset (individually for each decay curve, determined by the tailfit function of the spectrometer software), normalized to one and the decay maximum was given the time zero.

Actinometry

The quantum yield of CS state formation were determined by actinometry at 28200 cm^{-1} (355 nm) vs. benzophenone (in benzene).[232] The following equation was used: $\Phi_{CS} = \Phi_{ref} \times ((\Delta OD_{CS} \times \varepsilon_{ref}) / (\Delta OD_{ref} \times \varepsilon_{CS}))$. For ε_{ref} of the transient absorption signal at 18900 cm^{-1} (530 nm) of benzophenone[232] the value of 7220 L mol^{-1} cm^{-1} was used. The triplet state quantum yield for benzophenone Φ_{ref} is according to literature 1.[241] The ε_{CS} values for the CS states were extracted from spectroelectrochemistry measurements

(section 4.4). The ΔOD_{CS} and ΔOD_{ref} values were determined by an average of four different measurements at four different laser intensities.

6.1.6 Steady-State Emission Spectroscopy

- Edinburgh Instruments FLS980 fluorescence lifetime spectrometer (software F980 version 1.2.2) with a 450 W Xenon lamp / PMT (R928P)

Steady state emission spectra at room temperature were recorded in 10 × 10 mm quartz-cuvettes with Teflon stopper (Hellma or Starna). All solvents were of spectroscopic grade and were used without further purification. Aggregation of the samples could be excluded by measuring with strongly diluted samples (< 0.05 OD). The dissolved samples were purged with argon for 30 min.

The quantum yields were determined using diluted samples in an integrating sphere and equation (29).[242]

$$\phi = \frac{\int E_{\text{sample}}}{\int Ex_{\text{sample}} - \int Ex_{\text{solvent}}} \tag{29}$$

where ϕ is the quantum yield, E_{sample} is the emission spectrum of the sample, Ex_{sample} is the spectrum of the light used to excite the sample and Ex_{solvent} is the spectrum of the light used for excitation with only the solvent in the sphere.

6.1.7 ESR Spectroscopy

The measurements were done by Dr. Boryana Mladenova[177] and Dr. Ivo Krummenacher.[178] The ESR line shape analysis was performed using a program designed by Dr. Daniel Kattnig.[179]

The temperature dependent ESR measurements of the MV compounds were performed on a Bruker ELEXSYS E-500 X-band ESR spectrometer or on a Bruker ELEXSYS E-580 CW/FT spectrometer equipped with a digital Bruker-temperature control unit. Variable temperatures were kept constant at ±0.5 K. Experimental details concerning the sample preparation and handling, the ESR-spectroscopic measurements, and the evaluation of the rate constants from line-broadening effects are all explained in detail literature.

The ESR measurements of the DA compounds were carried out at room temperature using a Bruker ELEXSYS E580 CW ESR spectrometer at X-band (9.86 GHz). The *g* values were referenced to 1,1-diphenyl-2-picrylhydrazyl (DPPH, g = 2.0036 ± 0.0002).[205] The spectral simulations were performed using MATLAB 8.3 and the EasySpin 4.5.5 toolbox.[206]

6.1.8 DFT Calculations

The calculations were done by Dr. Marco Holzapfel.[181] They were performed at the density functional level, by use of a polarizable continuum model accounting for solvent effects,[192, 193] a hybrid functional with 35% exact-exchange admixture and a SVP basis set and using Gaussian09.[203] The time dependent (TD-DFT) calculations were done at the same level of theory.

6.1.9 Microwave Oven

- *µCHEMIST microPREP Microwave Digestion System ATC-FO 300* from MLS (Leutkirch, Germany)

Microwave reactions were performed in a microwave oven with a fibre optical thermometer sensor (ATC-FO, 0–270 °C), which controls the reaction temperature by regulation of the output power (0–1200 W) of the microwave oven. The reaction mixture was placed in a pressure quartz vessel (max. 12 bar).

6.1.10 Recycling Gel Permeation Chromatography (GPC)

- JASCO Gel Permeation Chromatography System: interface box (LC-NetII ADC), HPLC pump (PU-2080 plus), in-line degasser (DG-2080-53), solvent selection valve unit (LV-2080-03), multi wavelength UV/Vis detector 195 –700 nm (UV-2077), software Chrompass (v. 6.1)
- Shimadzu Gel Permeation Chromatography System: system controller (CBM-20A), solvent delivery unit (LC-20AD), on-line degasser (DGU-20A9), diode array detector (SPD-M20A), software LCsolution (v. 1.25)

Gel permeation chromatography (GPC) was done using two preparative GPC columns (styrene-divinylbenzene-copolymer, 50 and 500 Å, 600 × 20.8 mm) from PSS (Mainz, Germany).The flow rate was 4 ml min^{-1} and the used solvent was HPLC grade $CHCl_3$ (Fisher Chemical or HiPerSolv Chromanorm from VWR Chemicals).

6.1.11 NMR Spectroscopy

- Avance III HD 400 FT-Spectrometer (^{1}H: 400.13 MHz, ^{13}C: 100.61 MHz) with a Bruker Ultrashield magnet
- Avance III HD 400 FT-Spectrometer (^{1}H: 400.03 MHz, ^{13}C: 100.59 MHz) with a Bruker Ascend magnet
- Avance III HD 600 FT-Spectrometer (^{1}H: 600.13 MHz, ^{13}C: 150.90 MHz) with an Oxford Instruments magnet (with cryoprobe unit, CPDCH 13C)
- Avance III HD 600 FT-Spectrometer (^{1}H: 600.43 MHz, ^{13}C: 150.98 MHz) with a Bruker Ascend magnet

^{1}H and ^{13}C NMR spectra were acquired in deuterated solvents as indicated (e. g. chloroform-*d* ($CDCl_3$), dichloromethane-d_2 (CD_2Cl_2), acetone-d_6 ($(CD_3)_2CO$) and dimethylsulfoxide-d_6 ($(CD_3)_2SO$). Chemical shifts are given in ppm relative to residual non-deuterated solvent signal (^{1}H in ppm: $CDCl_3$: δ 7.26, DCM: δ 5.32, $(CD_3)_2CO$: δ 2.05, $(CD_3)_2SO$: δ 2.50; ^{13}C: $CHCl_3$: δ 77.16, DCM: 53.84, $(CD_3)_2CO$: δ 29.84, $(CD_3)_2SO$: 39.52).[243] The deuterated solvents were used as received (Deutero, Acros Organics). The proton signals are abbreviated as follows: s = singlet, d = doublet, t = triplet, m = multiplet, dd = doublet of doublet. Multiplet signals or overlapping signals in proton NMR spectra that could not be assigned to first order couplings are given as (-). The declaration order for the proton spectra is: chemical shift (spin multiplicity, coupling constant, number of protons and correlation of the proton in the molecule). The carbon signals are abbreviated as follows: CH_3 = primary, CH_2 = secondary, CH = tertiary, C_q = quaternary.

6.1.12 Mass Spectrometry

- Bruker Daltonics microTOF focus (ESI)
- Bruker Daltonics autoflex II LRF (MALDI)
- Finnigan MAT 90 (EI)

MALDI spectra were recorded in positive mode (POS) using a DCTB (*trans*-2-[3-(4-*tert*-butylphenyl)-2-methyl-2-propenylidene]malononitrile) matrix. All mass spectrometry peaks are reported as m/z. For calculation of the respective mass values of the isotopic distribution, the software "Bruker Daltonics IsotopePattern" from the software Compass 1.1 from Bruker Daltonics GmbH, Bremen was used. Calculated (calc.) and measured (exp.) peak values always correspond to the first peak of the isotopic distribution.

6.1.13 Microanalysis (CHN)

- vario MICRO cube CHNS instrument from Elementar (Hanau, Germany)

Elemental analyses were performed at the Institut für Anorganische Chemie, Universität Würzburg. V_2O_5 was added to enhance the combustion process.

6.1.14 Crystal Structure Determination

The crystallographic analysis was performed by Dr. Marius Schäfer[148] by use of an APEX 2 CCD detector and multi-layer mirror monochromated and MoKα-radiation. The structure was solved with an intrinsic phasing method (ShelXT)[244], expanded by Fourier-expansion and refined usining the programs SHELX and ShelXLe GUI.[245, 246] Non-hydrogen atoms were anisotropically refined and hydrogen atoms were assigned to idealized geometric positions. Figure 11 was created using the program POV-RAY.[247]

Crystal data for **pOMe**: $C_{58}H_{50}N_2O_6$; formula weigt M_r = 871.00 g·mol^{-1}; orange block; dimensions 0.40 × 0.35 × 0.30 mm^3; triclinic space group *P*-1; unit cell dimensions: *a* = 8.7974(13) Å, *b* = 11.2009(16) Å, *c* = 13.2374(19) Å, α = 66.402(4)°, β = 77.604(4)°, γ = 73.349(4)°, volume = 1137.8(3) Å^3; *Z* = 1, calculated density ρ_{calcd} = 1.271 g cm^{-3}, absorbtion coefficient μ = 0.082 mm^{-1}, *F*(000) = 460, temperature = 100(2) K; final R indices [I > 2σ(I)] R_1 = 0.00659, wR^2= 0.1850; R indices (all data) R_1 = 0.0817, wR^2 = 0.2020; 4830 independent reflections [2θ ≤ 53.62°] and 301 parameters; Goodness-of-fit on F^2 = 1.020; maximum/minimum residual electron density (e·Å^{-3}) 0.521 / –0.433.

6.2 Synthesis

Commercial compounds including solvents were purchased from Acros Organics, Alfa Aesar, Chempur, Fisher Chemical, Fluorochem, Fluka, Merck, Sigma-Aldrich, VWR Chemicals and used without further purification.

All reactions specified as being performed under nitrogen atmosphere were performed in air-free conditions (nitrogen, dried with Sicapent® from Merck, oxygen was removed by copper oxide catalyst R3-11 from BASF) using standard Schlenk techniques. Solvent for oxygen and/or moisture sensitive reactions were freshly distilled under nitrogen from the appropriate dehydrating agent (sodium/benzophenone for THF and 1,4-dioxane, sodium for toluene and CaH_2 for DCM) and sparged with dry nitrogen before use. Solvents for chromatography and work-up procedures were of technical grade and distilled prior to use. Flash chromatography[248] was performed on silica gel (Macherey-Nagel “Silica 60 M”, 40–63 µm) wet-packed in glass columns.

6.2.1 Synthesis of the TAA and the NDI units

N,*N*-Bis(4-methoxyphenyl)-*N*-[4-(trimethylsilylethynyl)phenyl]amine (**2**),[113] *N*,*N*-bis(4-methoxyphenyl)-*N*-[4-ethynylphenyl]amine (**eTAA**)[113] and *N*-(2,5-di-*tert*-butylphenyl)-*N*’-(4ethynylphenyl)-naphthalene-1,8:4,5-tetracarboxy diimid (**eNDI**)[113] were synthesized following reported procedures.

***N*,*N*-Bis(4-methoxyphenyl)-*N*-(4-bromophenyl)amine (1)**

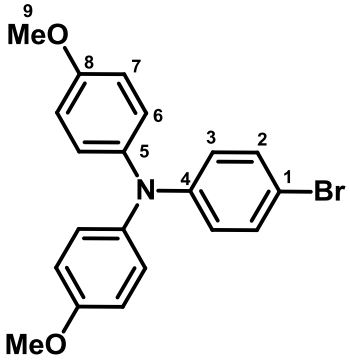

CA: [194416-45-0].

Synthesis according to literature.[124]

Under a nitrogen atmosphere 4-iodanisol (5.71 g, 24.4 mmol), 1,10-phenanthroline (82.0 mg, 453 µmol), CuI (86.0 mg, 453 µmol) and powdered KOH (1.77 g, 31.6 mmol) were suspended in dry toluene (10 ml) and the mixture was degassed for 15 min. After the addition of 4-bromoaniline (2.00 g, 11.6 mmol) the mixture was stirred for 5 d under reflux. The solvent was removed *in vacuo*, the residue was dissolved in DCM (50 ml) and washed with H_2O (2 × 50 ml). The combined organic phase was dried with $MgSO_4$ and the solvent was removed *in vacuo*. The crude product was purified by flash chromatography on silica gel (PE:EA, 2:1) and recrystallized from EtOH/H_2O.

Yield: 2.91 mg (7.57 mmol, 65 %), colorless solid.

Formula: $C_{20}H_{18}BrNO_2$ [384.27].

^{1}H-NMR (400.1 MHz, $(CD_3)_2CO$):

δ [ppm] = 7.28 (AA´, 2 H, H-2), 7.06 (AA´, 4 H, H-6), 6.91 (BB´, 4 H, H-7), 6.75 (BB´, 2 H, H-3), 3.79 (s, 6 H, H-9).

^{13}C-NMR (100.6 MHz, $(CD_3)_2CO$):

δ [ppm] = 157.5 C-8, 149.3 C-1, 141.2 C-5, 132.6 C-2, 127.9 C-7, 122.1 C-3, 115.8 C-6, 112.2 C-4, 55.8 C-9.

6.2.2 Synthesis of the Bridging Units

2,4-Dibromo-3,6-dimethoxyaniline (**3**),[249] 1,3-diiodo-4,6-dimethoxybenzene (**mbOMe'46**),[128] 2,5-dibromo-*para*-xylene (**pbMe**),[250] 2,4-Dibromo-3,6-dimethylaniline (**6**),[251] 2,6-dibromo-*para*-xylene (**mbMe**),[251] 2,4-Dibromo-3,6-dichloroaniline (**7**),[252] 1,3-dibromo-2,5-dichlorobenzene (**mbCl**),[252] 2,5-dibromoterephthalic acid (**9**),[253] 1,4-dibromo-2,5-dinitrobenzene (**pbNO$_2$**),[138, 139] and 2,6-dibromo-4-nitroaniline (**14**)[254] and were synthesized following reported procedures.

2,5-Dibromo-1,4-dimethoxybenzene (pbOMe) / 2-bromo-1,4-dimethoxy-benzene (sbOMe)

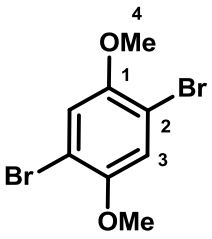

pbOMe

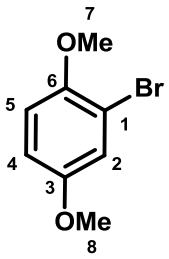

sbOMe

CA: **pbOMe** [2674-34-2].
sbOMe [25245-34-5].

Synthesis according to literature.[255]

1,4-Dimethoxybenzene (5.00 g, 36.2 mmol) was suspended in glacial acetic acid (8 ml). The mixture was cooled (0 °C) and bromine (12.9 g, 81.0 mmol) in glacial acetic acid (25 ml) was added slowly. After stirring for 3 h at rt a mixture of crushed ice (50 g) and water (100 ml) was added. The aqueous solution was extracted with DCM (3 × 30 ml) and the combined organic phase was dried over $MgSO_4$. After evaporation of the solvent the solid crude product was purified by flash chromatography on silica gel (PE:DCM, 2:1 → 1:2).

Yield: **pbOMe** 7.06 g (23.9 mmol, 66 %), colorless solid.
sbOMe 645 mg (2.97 mmol, 8 %), colorless oil.

Formula: **pbOMe** $C_8H_8Br_2O_2$ [295.96].
sbOMe $C_8H_9BrO_2$ [217.06].

^{1}H-NMR (pbOMe, 400.1 MHz, $CDCl_3$):
δ [ppm] = 7.08 (s, 2 H, H-3), 3.83 (s, 6 H, H-4).

^{13}C-NMR (pbOMe, 100.6 MHz, $CDCl_3$):
δ [ppm] = 150.5 C-1, 117.1 C-3, 110.5 C-2, 57.1 C-4.
EI-MS (pbOMe): calc.: $[M]^+$ 295.9 m/z
exp.: $[M]^+$ 295.8 m/z

^{1}H-NMR (sbOMe, 400.1 MHz, $CDCl_3$):

δ [ppm] = 7.13 (dd, $^{4}J_{HH}$ = 2.6 Hz, $^{5}J_{HH}$ = 0.5 Hz, 1 H, H-2), 6.85 (dd, $^{3}J_{HH}$ = 8.9 Hz, $^{5}J_{HH}$ = 0.5 Hz, 1 H, H-5), 6.81 (dd, $^{3}J_{HH}$ = 8.9 Hz, $^{4}J_{HH}$ = 2.6 Hz, 1 H, H-4).

2,6-Dibromo-4-methoxyphenole (4)

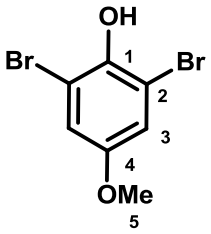

CA: [2423-74-7].

Synthesis according to literature.[125]

To a solution of 4-methoxyphenole (1.21 g, 9.75 mmol) in a mixture of DCM (98 ml) and MeOH (39 ml) BTMA-Br_3 (7.60 g, 19.5 mmol) was added. The mixture was stirred for 18 h at rt. The solvent was removed *in vacuo* and the crude product was purified by flash chromatography on silica gel (DCM:PE, 3:7).

Yield: 2.14 g (7.60 mmol, 78 %), colorless solid.

Formula: $C_7H_6Br_2O_2$ [281.93].

^{1}H-NMR (400.1 MHz, $CDCl_3$):

δ [ppm] = 7.03 (s, 2 H, H-3), 5.49 (s, 1 H, O*H*), 3.74 (s, 3 H, H 5).

^{13}C-NMR (100.6 MHz, $CDCl_3$):

δ [ppm] = 153.8 C-4, 143.9 C-1, 117.9 C-3, 109.8 C-2, 56.2 C-4.

EI-MS: calc.: $[M]^+$ 281.9 m/z
exp.: $[M]^+$ 281.9 m/z

1,3-Dibromo-2,5-methoxybenzene (mbOMe)

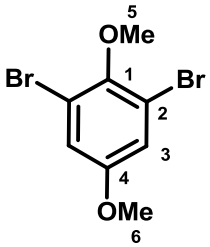

CA: [74076-59-8].

a) Synthesis according to literature.[251]

2,4-Dibromo-3,6-dimethoxyaniline (**3**, 1.84 g, 5.92 mmol) was added to a solution of EtOH (14 ml) and benzene (2.5 ml). The suspension was heated and conc. H_2SO_4 (4 ml) and then sodium nitrite (857 mg, 12.4 mmol) were added. When the foaming stopped, the reaction was heated under reflux for 3 h until the gas formation stopped. After cooling to rt the solution was acidified with aqueous HCl solution and extracted with DCM (3 × 30 ml). The combined organic phase was washed with H_2O (2 × 30 ml) and dried on $MgSO_4$. The crude product was purified by flash chromatography on silica gel (DCM:PE, 1:1)

Yield: 1.49 g (5.05 mmol, 85 %), colorless oil.

b) Synthesis according to literature.[256]

2,6-Dibromo-4-methoxyphenole (**4**, 200 mg, 709 µmol) and dimethyl sulfate (202 µl, 268 mg, 2.13 mmol) were added slowly to a solution of sodium hydroxide (85.0 mg, 2.13 mmol) in water (10 ml). The mixture was stirred for 30 min at rt and then heated under reflux for 30 min to destroy excess dimethyl sulfate. After cooling to rt the solution was extracted with DCM (3 × 15 ml). The combined organic phase was washed with H_2O (2 × 15 ml) and dried on $MgSO_4$. The crude product was purified by flash chromatography on silica gel (DCM:PE, 1:1)

Yield: 150 mg (5.75 mmol, 71 %), colorless oil.

Formula: $C_8H_8Br_2O_2$ [295.96].

^{1}H-NMR (400.1 MHz, $CDCl_3$):

δ [ppm] = 7.05 (s, 2 H, H-3), 3.83 (s, 3 H, H-5), 3.75 (s, 3 H, H-6).

^{13}C-NMR (100.6 MHz, $CDCl_3$):

δ [ppm] = 156.5 C-4, 148.2 C-1, 118.3 C-3, 60.9 C-5, 56.1 C-6, 53.6 C-2.

EI-MS: calc.: $[M]^+$ 295.9 m/z
exp.: $[M]^+$ 295.9 m/z

1,4-Diiodo-2,5-dimethoxybenzene (pbOMe')

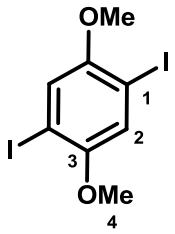

CA: [51560-21-5].

Synthesis according to literature.[129, 257]

1,4-Dimethoxybenzene (2.00 g, 14.8 mmol), iodine (3.04 g, 12.0 mmol) and periodic acid (1.36 g, 5.96 mmol) were dissolved in a mixture of acetic acid (27 ml), water (5.9 ml), DCM (5.3 ml) and sulfuric acid (1.2 ml). The mixture was heated for 15 h at 75°C and then cooled with an ice bath. The resulting precipitate was separated by filtration, washed with a saturated aqueous Na_2SO_3 solution (20 ml) and water (20 ml) and dried *in vacuo*. The crude product was purified by flash chromatography on silica gel (PE:DCM, 2:1).

Yield: 4.51 g (11.6 mmol, 80 %), colorless solid.

Formula: $C_8H_8I_2O_2$ [389.96].

^{1}H-NMR (400.1 MHz, $CDCl_3$):

δ [ppm] = 7.19 (s, 2 H, H-2), 3.82 (s, 6 H, H-4).

^{13}C-NMR (100.6 MHz, $CDCl_3$):

δ [ppm] = 153.5 C-3, 121.8 C-2, 85.6 C-1, 57.4 C-4.

EI-MS: calc.: $[M]^+$ 389.9 m/z
exp.: $[M]^+$ 390.0 m/z

1-Iodo-2,5-dimethoxybenzene (sbOMe')

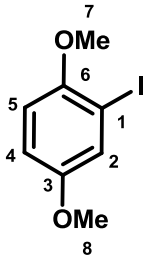

CA: [25245-35-6].

Synthesis according to literature.[130, 131]

1,4-Dimethoxybenzene (383 mg, 2.77 mmol) was dissolved in a mixture of MeOH, water and conc. sulfuric acid (100:20:3). Periodic acid (128 mg, 562 µmol) and iodine (281 mg, 1.11 mmol) wer added and the mixture was stirred for 3 h at 55 °C. After additional stirring for 12 h at rt a saturated aqueous sodium thiosulfate solution was added to destroy the excess iodine. The mixture was cooled with an ice bath and filtered. The filtrate was extracted with DCM (2 × 25 ml) and washed with a saturated aqueous Na_2SO_3 solution (25 ml). The solvent was removed *in vacuo* and the crude product was purified by flash chromatography on silica gel (PE:DCM, 3:2).

Yield: 278 mg (1.05 mmol, 38 %), colorless oil.

Formula: $C_8H_9IO_2$ [264.06].

^{1}H-NMR (400.1 MHz, $CDCl_3$):

δ [ppm] = 7.34 (d, $^4J_{HH}$ = 3.0 Hz,1 H, H-2), 6.87 (dd, $^3J_{HH}$ = 8.9 Hz, $^4J_{HH}$ = 3.0 Hz, 1 H, H-4), 6.76 (d, $^3J_{HH}$ = 8.9 Hz, 1 H, H-5), 3.82 (s, 3 H, H-7), 3.76 (s, 3 H, H-8).

^{13}C-NMR (100.6 MHz, $CDCl_3$):

δ [ppm] = 154.5 C-3, 152.9 C-6, 125.0 C-2, 114.9 C-4, 111.8 C-5, 86.2 C-1, 57.2 C-7, 56.1 C-8.

EI-MS: calc.: $[M]^+$ 264.0 m/z
exp.: $[M]^+$ 263.9 m/z

1-Bromo-3-iodo-2,5-dimethoxybenzene (5)

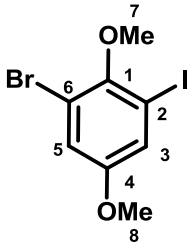

CA: [/].

Synthesis according to literature.[258]

1,3-Dibromo-2,5-methoxybenzene (200 mg, 676 µmol) was dissolved in dry diethyl ether (4 ml), cooled to −78 °C and *t*-butyllithium (1.56 ml, 4.06 mmol, 2.6 M in toluene) was added dropwise. After stirring for 45 min at −78 °C, a cooled solution of iodine (1.03 g, 4.05 mmol) in dry diethyl ether (13 ml) was added. The mixture was slowly warmed to rt and stirred for 60 min. A saturated aqueous $Na_2S_2O_3$ solution (20 ml) and added and the mixture was extracted with DCM (3 × 30 ml). The organic layer was washed with water (2 × 30 ml) and dried over $MgSO_4$. The solvent was removed *in vacuo* and the crude product was purified by flash chromatography on silica gel (PE:DCM, 1:1).

Yield: 225 mg (656 µmol, 97 %), colorless oil.

Formula: $C_8H_8IBrO_2$ [342.96].

^{1}H-NMR (400.1 MHz, $CDCl_3$):

δ [ppm] = 7.26 (d, $^4J_{HH}$ = 2.8 Hz, 1 H, H-5), 7.09 (d, $^4J_{HH}$ = 2.8 Hz, 1 H, H-3), 3.81 (s, 3 H, H-8), 3.76 (s, 3 H, H-7).

^{13}C-NMR (100.6 MHz, $CDCl_3$):

δ [ppm] = 156.8 (C_q), 150.7 (C_q), 124.0 (CH), 119.4 (CH), 116.3 (C_q), 91.8 (C_q), 60.9 (CH_3), 56.1 (CH_3).

EI-MS: calc.: $[M]^+$ 343.9 m/z
exp.: $[M]^+$ 343.9 m/z

1,3-Diiodo-2,5-dimethoxybenzene (mbOMe')

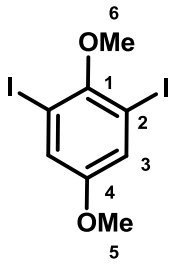

CA: [744216-14-6].

Synthesis according to literature.[134]

Under a nitrogen atmosphere CuI (38.6 mg, 203 µmol) and NaI (6.08 g, 40.5 mmol) were added to 1,4-dioxane (8 ml) and the mixture was degassed for 10 min. *Trans-N,N*-dimethy-1,2-cyclohexandiamin (57.7 mg, 405 µmol) and **mbOMe** (300 mg, 1.01 mmol) were added and the mixture was heated at 110 °C for 3 d. After cooling to rt the solvent was removed *in vacuo*. To the residue was added ammonium hydroxide (30 %, 20 ml) and water (40 ml). The aqueous phase was extracted with dichloromethane (3 × 20 ml). The organic phase was dried over $MgSO_4$ and the solvent was removed *in vacuo*. The crude product was purified by chromatography on silica gel (PE:DCM, 1:1).

Yield: 294 mg (754 µmol, 73 %), colorless solid.

Formula: $C_8H_8I_2O_2$ [389.96].

^{1}H-NMR (400.1 MHz, $CDCl_3$):

δ [ppm] = 7.30 (s, 2 H, H-3), 3.80 (s, 3 H, H-6), 3.73 (s, 3 H, H-5).

^{13}C-NMR (100.6 MHz, $CDCl_3$):

δ [ppm] = 156.9 (C_q), 153.1 (C_q), 125.2 (CH), 89.8 (C_q), 61.0 (CH_3), 56.1 (CH_3).

EI-MS: calc.: $[M]^+$ 389.9 m/z
exp.: $[M]^+$ 389.7 m/z

2,6-Dibromoterephthalic acid (8)

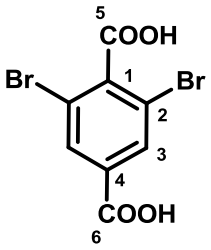

CA: [22191-58-8].

Synthesis according to literature.[253]

2,6-Dibromo-*p*-xylene (**mbMe**, 2.64 g, 10.0 mmol) and $KMnO_4$ (7.90 g, 50.0 mmol) were added in pyridine (20 ml) and water (10 ml) and the mixture was heated for reflux. Then $KMnO_4$ (3.00 g, 19.0 mmol) dissolved in water (10 ml) was added in 4 steps in 30 min intervals. After refluxing for 2 d, the result was filtered through celite. The mixture was concentration by vacuum distillation and an aqueous HCl solution (10 %, 10 ml) was added to the filtrate. The resulting precipitate was extracted by EA (3 × 10 ml), dried over $MgSO_4$, filtered and the solvent was evaporated *in vacuo*.

Yield: 1.90 g (5.86 mmol, 59 %), colorless solid.

Formula: $C_8H_4Br_2O_4$ [323.92].

^{1}H-NMR (400.1 MHz, $(CD_3)_2SO$):

δ [ppm] = 8.10 (s, 2 H, H-3). *The signal of the protons of the carboxyl group is missing. This is probably due to an exchange of the protons in the solvent.*

^{13}C-NMR (100.6 MHz, $(CD_3)_2SO$):

δ [ppm] = 166.6 (C_q), 164.5 (C_q), 142.2 (C_q), 134.0 (C_q). 132.1 (CH), 118.7 (C_q).

EI-MS: calc.: $[M]^+$ 323.8 m/z
exp.: $[M]^+$ 323.9 m/z

2-Bromoterephthalic acid (10)

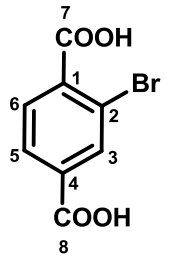

CA: [586-35-6].

Synthesis according to literature.[253]

2-Bromo-*p*-xylene (1.85 g, 10.0 mmol) and $KMnO_4$ (7.90 g, 50.0 mmol) were suspended in pyridine (20 ml) and water (10 ml) and the mixture was heated for reflux. Then $KMnO_4$ (3.00 g, 19.0 mmol) dissolved in water (10 ml) was added in 4 steps in 30 min intervals. After refluxing for 2 d, the result was filtered through celite. The mixture was concentration by vacuum distillation and an aqueous HCl solution (10 %, 10 ml) was added to the filtrate. The resulting precipitate was extracted by EA (3 × 10 ml), dried over $MgSO_4$, filtered and the solvent was evaporated *in vacuo*.

Yield: 1.53 mg (6.24 mmol, 62 %), colorless solid.

Formula: $C_8H_5BrO_4$ [245.03].

^{1}H-NMR (400.1 MHz, $(CD_3)_2SO$):

δ [ppm] = 13.6 (bs, 2 H, COO*H*), *8*.13 (d, $^4J_{HH}$ = 1.5 Hz, 1 H, H-3), 7.96 (dd, $^3J_{HH}$ = 8.0 Hz, $^4J_{HH}$ = 1.5 Hz, 1 H, H-5), 7.82 (d, $^3J_{HH}$ = 8.0 Hz, 1 H, H-6).

^{13}C-NMR (100.6 MHz, $CDCl_3$):

δ [ppm] = 167.1 (C_q), 165.5 (C_q), 137.8 (C_q), 134.2 (C_q), 134.0 (CH), 130.6 (CH), 128.46 (CH), 119.7 (C_q).

EI-MS: calc.: $[M]^+$ 243.9 m/z
exp.: $[M]^+$ 243.8 m/z

2,6-Dibromotetrephthalamide (11)

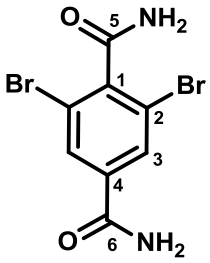

CA: [/].

Synthesis according to literature.[259]

The mixture of 2,6-dibromotetrephthalic acid (**8**, 750 mg, 2.32 mmol), thionyl chloride (14 ml) and a drop of DMF was refluxed for 3 h. The solvent was removed *in vacuo*, and the crude product was dissolved in 1,4-dioxane (15 ml). Ammonium hydroxide (15 ml, conc.) was added dropwise to the mixture and stirred overnight at rt. The precipitate was filtered off and washed with 1,4-dioxane to afford the pure product as a colorless solid.

Yield: 613 mg (1.96 mmol, 87 %), colorless solid.

Formula: $C_8H_6Br_2N_2O_2$ [321.95].

^{1}H-NMR (400.1 MHz, $(CD_3)_2SO$):
δ [ppm] = 8.19 (s, 1 H, N*H*), 8.09 (s, 2 H, H-3), 8.08 (s, 1 H, N*H*), 7.81 (s, 1 H, N*H*), 7.65 (s, 1 H, N*H*).

^{13}C-NMR (100.6 MHz, $(CD_3)_2SO$):
δ [ppm] = 167.0 C-5, 164.6 C-6, 142.9 C-1, 136.5 C-4, 130.6 C-3, 119.5 C-2.

EI-MS: calc.: $[M]^+$ 321.9 m/z
exp.: $[M]^+$ 321.8 m/z

2,5-Dibromoterephthalamide (12)

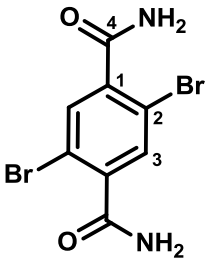

CA: [50880-39-2].

Synthesis according to literature.[259]

The mixture of 2,5-dibromoterephthalic acid (**9**, 4.00 g, 12.4 mmol), thionyl chloride (55 ml) and five drops of DMF was refluxed for 3 h. The solvent was removed *in vacuo*, and the crude product was dissolved in 1,4-dioxane (60 ml). Ammonium hydroxide (50 ml, conc.) was added dropwise to the mixture and stirred overnight at rt. The precipitate was filtered off and washed with 1,4-dioxane to afford the pure product as a colorless solid.

Yield: 3.60 g (11.2 mmol, 91 %), colorless solid.

Formula: $C_8H_6Br_2N_2O_2$ [321.95].

^{1}H-NMR (400.1 MHz, $(CD_3)SO$):

δ [ppm] = 7.98 (s, 2 H, N-*H*), 7.67 (s, 2 H, N-*H*), 7.63 (s, 2 H, H-3).

^{13}C-NMR (100.6 MHz, $(CD_3)SO$):

δ [ppm] = 167.2 C-4, 140.9 C-1, 132.3 C-3, 117.7 C-2.

EI-MS: calc.: $[M]^+$ 321.9 m/z
exp.: $[M]^+$ 321.9 m/z

2-Bromoterephthalamide (13)

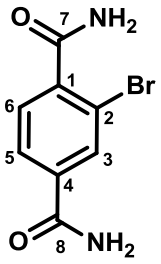

CA: [337507-04-7].

Synthesis according to literature.[259]

The mixture of 2-bromoterephthalic acid (**10**, 757 mg, 3.09 mmol), thionyl chloride (14 ml) and a drop of DMF was refluxed for 3 h. The solvent was removed *in vacuo*, and the crude product was dissolved in 1,4-dioxane (15 ml). Ammonium hydroxide (15 ml, conc.) was added dropwise to the mixture and stirred overnight at rt. The precipitate was filtered off and washed with 1,4-dioxane to afford the pure product as a colorless solid.

Yield: 414 mg (1.73 mmol, 55 %), colorless solid.

Formula: $C_8H_7BrN_2O_2$ [243.01].

^{1}H-NMR (400.1 MHz, $(CD_3)SO$):

δ [ppm] = 8.12 (s, 1 H, N-*H*), 8.10 (d, $^4J_{HH}$ = 1.6 Hz, 1 H, H-3), 7.92 (s, 1 H, N-*H*), 7.88 (dd, $^3J_{HH}$ = 7.9 Hz, $^4J_{HH}$ = 1.6 Hz, 1 H, H-5), 7.63 (s, 1 H, N-*H*), 7.54 (s, 1 H, N-*H*), 7.47 (d, $^3J_{HH}$ = 7.9 Hz, 1 H, H-6).

^{13}C-NMR (100.6 MHz, $(CD_3)SO$):

δ [ppm] = 168.6 C-7, 165.9 C-8, 141.7 C-1, 136.1 C-4, 131.6 C-3, 128.4 C-6, 126.6 C-5, 118.6 C-2.

EI-MS: calc.: $[M]^+$ 242.0 m/z

exp.: $[M]^+$ 241.9 m/z

2,6-Dibromoterephthalonitrile (mbCN)

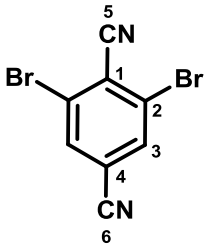

CA: [/].

Synthesis according to literature.[89, 259]

2,6-Dibromoterephthalamide (**11**, 300 mg, 923 µmol) was dissolved in phosphorus oxychloride (12 ml) and heated at 125 °C for 12 h. The cooled mixture was slowly poured into ice water (50 ml) and stirred for 15 min. The resulting precipitate was filtered off , washed with water and dried *in vacuo.*

Yield: 182 mg (636 µmol, 82 %), colorless solid.

Formula: $C_8H_2Br_2N_2$ [285.92].

^{1}H-NMR (400.1 MHz, $CDCl_3$):

δ [ppm] = 7.93 (s, 2 H, H-3).

^{13}C-NMR (100.6 MHz, $CDCl_3$):

δ [ppm] = 134.7 C-3, 127.7 C-2, 123.3 C-1, 118.2 C-6, 114.84 C-6, 114.76 C-5.

EI-MS: calc.: $[M]^+$ 285.9 m/z

exp.: $[M]^+$ 285.8 m/z

2,5-Dibromoterephthalonitrile (pbCN)

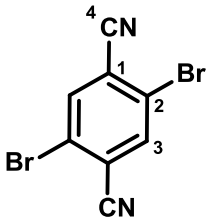

CA: [18870-11-6].

Synthesis according to literature.[89, 259]

2,5-Dibromoterephthalamide (**12**, 200 mg, 823 µmol) was dissolved in phosphorus oxychloride (12 ml) and heated at 125 °C for 12 h. The cooled mixture was slowly poured into ice water (50 ml) and stirred for 15 min. The resulting precipitate was filtered off, washed with water and dried *in vacuo.*

Yield: 182 mg (636 µmol, 82 %), colorless solid.

Formula: $C_8H_2Br_2N_2$ [285.92].

^{1}H-NMR (400.1 MHz, $CDCl_3$):

δ [ppm] = 7.96 (s, 2 H, H-3).

^{13}C-NMR (100.6 MHz, $CDCl_3$):

δ [ppm] = 138.0 C-3, 124.4 C-2, 121.3 C-1, 114.7 C-4.

EI-MS: calc.: $[M]^+$ 285.9 m/z

exp.: $[M]^+$ 285.8 m/z

2-Bromoterephthalonitrile (sbCN)

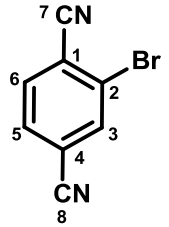

CA: [18870-13-8].

Synthesis according to literature.[89, 259]

2-Bromoterephthalamide (**13**, 170 mg, 699 µmol) was dissolved in phosphorus oxychloride (11 ml) and heated at 125 °C for 12 h. The cooled mixture was slowly poured into ice water (50 ml) and stirred for 15 min. The resulting precipitate was filtered off, washed with water and dried *in vacuo.*

Yield: 96.0 mg (464 µmol, 66 %), colorless solid.

Formula: $C_8H_3BrN_2$ [207.03].

^{1}H-NMR (400.1 MHz, $CDCl_3$):

δ [ppm] = 8.00 (dd, $^4J_{HH}$ = 1.5 Hz, $^5J_{HH}$ = 0.5 Hz, 1 H, H-3), 7.79 (dd, $^3J_{HH}$ = 8.1 Hz, $^5J_{HH}$ = 0.5 Hz, 1 H, H-6), 7.73 (dd, $^3J_{HH}$ = 8.1 Hz, $^4J_{HH}$ = 1.5 Hz, 1 H, H-5).

^{13}C-NMR (100.6 MHz, $CDCl_3$):

δ [ppm] = 136.4 C-3, 134.8 C-6, 131.1 C-5, 126.3 C-2, 120.4 C-1, 117.9 C-4, 115.9 C-7, 115.8 C-8.

EI-MS: calc.: $[M]^+$ 205.9 m/z
exp.: $[M]^+$ 206.0 m/z

2-Bromo-4-nitroaniline (15)

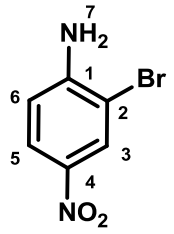

CA: [13296-94-1].

Synthesis according to literature.[254, 260]

To a cooled (0 °C) solution of 4-nitroaniline (5.00 g, 36.2 mmol) in DMF (75 ml) NBS (6.44 g, 36.2 mmol) was added in small portions. The mixture was stirred for 30 min at 0 °C. The ice-bath was removed and stirring was continued at RT for additional 12 h. The mixture was poured into water (200 ml) and extracted with DCM (3 × 75 ml). The combined organic phase was dried over $MgSO_4$ and the solvent was removed *in vacuo*. The crude product was purified by flash chromatography on silica gel (PE:EA, 1:1)

Yield: 4.12 g (19.0 mmol, 52 %), yellow solid.

Formula: $C_6H_5BrN_2O_2$ [217.02].

^{1}H-NMR (400.1 MHz, $CDCl_3$):

δ [ppm] = 8.38 (d, $^4J_{HH}$ = 2.5 Hz, 1 H, H-3), 8.03 (dd, $^3J_{HH}$ = 9.0, $^4J_{HH}$ = 2.5 Hz, 1 H, H-5), 6.74 (d, $^3J_{HH}$ = 9.0 Hz, 1 H, H-6), 4.82 (s, 2 H, H-7).

^{13}C-NMR (100.6 MHz, $(CD_3)_2SO$):

δ [ppm] = 152.4 C-1, 136.3 C-4, 128.9 C-3, 125.1 C-5, 113.4 C-6, 105.0 C-2.

EI-MS: calc.: $[M]^+$ 216.0 m/z
exp.: $[M]^+$ 215.9 m/z

1,3-Dibromo-2,5-dinitrobenzene ($mbNO_2$)

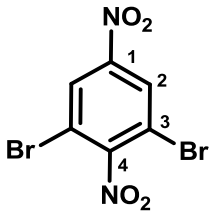

CA: [20024-98-0].

Synthesis according to literature.[142]

A solution of 2,6-dibromo-4-nitroaniline (**14**, 500 mg, 1.69 mmol) in trifluoroacetic acid (20 ml) was heated under reflux. H_2O_2 (30 %, 6 ml) was added over a period of 15 min. The mixture was heated under reflux for additional 15 min, cooled to rt and poured on crushed ice and water (20 ml). The resulting precipitate was collected by filtration.

Yield: 467 mg (1.43 mmol, 85 %), colorless solid.

Formula: $C_6H_2Br_2N_2O_4$ [325.90].

^{1}H-NMR (400.1 MHz, $CDCl_3$):

δ [ppm] = 8.51 (s, 2 H, H-2).

^{13}C-NMR (100.6 MHz, $CDCl_3$):

δ [ppm] = 154.9 (C-4), 147.9 (C-1), 128.2 (C-2), 115.1 (C-3).

EI-MS: calc.: $[M]^+$ 325.8 m/z

exp.: $[M]^+$ 325.8 m/z

2-Bromo-1,4-dinitrobenzene (sbNO$_2$)

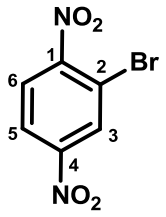

CA**:** [13296-65-6].

Synthesis according to literature.[142]

A solution of 2-bromo-4-nitroaniline (**15**, 500 mg, 2.34 mmol) in trifluoroacetic acid (20 ml) was heated under reflux. H_2O_2 (30 %, 6 ml) was added over a period of 15 min. The mixture was heated under reflux for additional 15 min, cooled to rt and poured on crushed ice and water (20 ml). The resulting precipitate was collected by filtration and recrystallized from EtOH/water.

Yield: 519 g (2.10 mmol, 91 %), beige solid.

Formula: $C_6H_3BrN_2O_4$ [247.00].

^{1}H-NMR (400.1 MHz, $CDCl_3$):

δ [ppm] = 8.62 (d, $^4J_{HH}$ = 2.3 Hz, 1 H, H-3), 8.33 (dd, $^3J_{HH}$ = 8.8 Hz, $^4J_{HH}$ = 2.3 Hz, 1 H, H-5), 7.97 (d, $^3J_{HH}$ = 8.8 Hz, 1 H, H-6).

^{13}C-NMR (100.6 MHz, $CDCl_3$):

δ [ppm] = 153.4 C-1, 149.1 C-4, 130.4 C-3, 126.3 C-6, 123.6 C-5, 115.6 C-2.

EI-MS: calc.: $[M]^+$ 245.9 m/z

exp.: $[M]^+$ 245.9 m/z

6.2.3 General Procedures for *Sonogashira-Hagihara* Coupling

GP_{OMe}:

***Sonogashira-Hagihara* Coupling with with $Pd(PPh_3)_2Cl_2$, CuI and NEt_3 in tetrahydrofuran[98, 261-263]**

Under a nitrogen atmosphere the aryl iodide, $Pd(PPh_3)_2Cl_2$ and CuI were dissolved in NEt_3. The alkyne was added to the solution in THF and the mixture was degassed. The reaction mixture was stirred at 60 °C for 1 d in the dark.

GP_{Me}:

***Sonogashira-Hagihara* Coupling with with $Pd(PPh_3)_2Cl_2$, CuI, P^tBu_3 and HN^iPr_2 1,4-dioxane[90, 261-263]**

Under a nitrogen atmosphere the alkyne, the aryl bromide, $Pd(C_6H_5CN)_2Cl_2$, CuI, P^tBu_3 and HN^iPr_2 were dissolved in 1,4-dioxane and degassed. The reaction mixture was stirred at 60 °C for 1–2 d in the dark. The solvent was removed *in vacuo.*

GP_{Cl}:

***Sonogashira-Hagihara* Coupling with $Pd(C_6H_5CN)_2Cl_2$, CuI, P^tBu_3 and HN^iPr_2 in 1,4-dioxane[90, 261-263]**

Under a nitrogen atmosphere the alkyne, the aryl bromide, $Pd(C_6H_5CN)_2Cl_2$, CuI, P^tBu_3 and HN^iPr_2 were dissolved in 1,4-dioxane and degassed. The reaction mixture was stirred at 60 °C for 1–2 d in the dark.

GP_{CN}:

***Sonogashira-Hagihara* Coupling with with $Pd(PPh_3)_2Cl_2$, CuI and NEt_3 in tetrahydrofuran[145, 261-263]**

Under a nitrogen atmosphere the alkyne, $Pd(PPh_3)_2Cl_2$ and CuI were dissolved in NEt_3. The aryl iodide was added to the solution in THF and the mixture was degassed. The reaction mixture was stirred at 60 °C for 1–2 d in the dark.

GP_{NO_2}:

***Sonogashira-Hagihara* Coupling with $Pd(PPh_3)_2Cl_2$, CuI and NEt_3 in toluene[261-264]**

Under a nitrogen atmosphere the alkyne, the aryl bromide, $Pd(PPh_3)_2Cl_2$ CuI and NEt_3 were dissolved in toluene and degassed. The reaction mixture was stirred at 60 °C for 1 d in the dark.

GP_{DPA}:

***Sonogashira-Hagihara* Coupling with $Pd(PPh_3)_2Cl_2$, CuI and NEt_3 in tetrahydrofuran[98, 261-263], "dilution principle apparatus (DPA)"[194]**

Under a nitrogen atmosphere the aryl halogenide, $Pd(PPh_3)_2Cl_2$, and CuI were dissolved in NEt_3. By use of the "dilution principle apparatus" (Scheme 34) a solution of the alkyne in THF was added slowly to the refluxing reaction mixture. After complete addition of the alkyne, the mixture was stirred at 60 °C for 8 h in the dark.

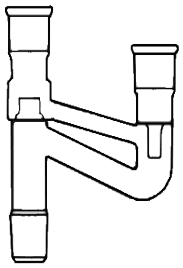

Scheme 34: "Dilution principle apparatus".

Workup for all GPs:

The solvent was removed *in vacuo.* The residue was dissolved in DCM and was washed with water. The organic phase was dried over $MgSO_4$ and the solvent removed *in vacuo*. The crude product was purified by flash column chromatography on silica gel and if necessary with preparative recycling GPC ($CHCl_3$, 4 ml min^{-1}).

6.2.4 Synthesis of the bisTAAs and their References

1-{4-[*N*,*N*-Di(4-methoxyphenyl)amino]phenylethynyl}(3-bromo-2,5-dimethoxy)-benzene (16)

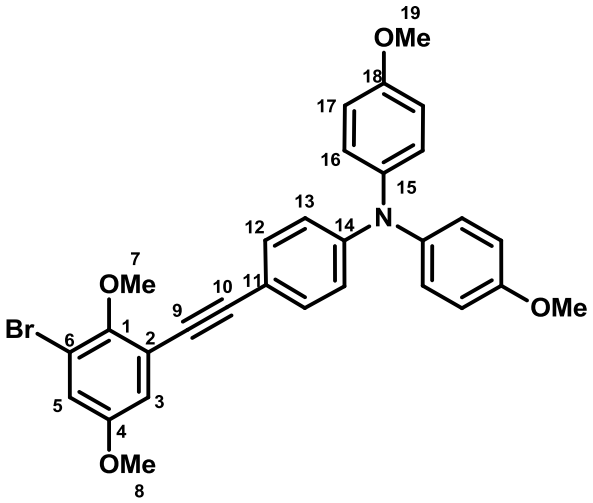

CA: [/].

Following **GP$_{OMe}$**: 1-Iodo-3-bromo-2,5-dimethoxybenzene (**5**, 240 mg, 700 µmol), CuI (2.67 mg, 14.0 µmol), $Pd(PPh_3)_2Cl_2$ (19.7 mg, 28.0 µmol) were added to NEt_3 (6 ml). **eTAA** (346 mg, 1.05 mmol) in THF (6 ml) was added to this solution. Flash chromatography on silica gel (PE:DCM, 1:2).

Yield: 356 mg (654 µmol, 93 %), yellow oil.

Formula: $C_{30}H_{26}BrNO_4$ [544.44].

^{1}H-NMR (400.1 MHz, $(CD_3)_2CO$):

δ [ppm] = 7.35 (AA´, 2 H, H-12), 7.13 (d, $^4J_{HH}$ = 3.0 Hz, 1 H, H-3), 7.12 (AA´, 4 H, H-16), 7.00 (d, $^4J_{HH}$ = 3.0 Hz, 1 H, H-5), 6.94 (BB´, 4 H, H-17), 6.79 (BB´, 2 H, H-13), 3.91 (s, 3 H, H-7 o. H-8), 3.81 (s, 3 H, H-7 o- H-8), 3.80 (s, 6 H, H-19).

^{13}C-NMR (100.6 MHz, CD_2Cl_2):

δ [ppm] = 157.8 (C_q), 156.8 (C_q), 152.4 (C_q), 150.4 (C_q), 140.5 (C_q), 133.2 (CH), 128.4 (CH), 120.4 (C_q), 119.5 (CH), 118.9 (CH), 118.1 (C_q), 117.7

(CH), 115.8 (CH), 113.5 (C_q), 96.0 (C_q), 84.2 (C_q), 61.2 (CH_3), 56.3 (CH_3), 55.7 (CH_3).

EI-MS: calc.: $[M]^+$ 543.1 m/z
exp.: $[M]^+$ 543.1 m/z

1-{4-[*N*,*N*-Di(4-methoxyphenyl)amino]phenylethynyl}(3-bromo-2,5-dimethoxy)-benzene (18)

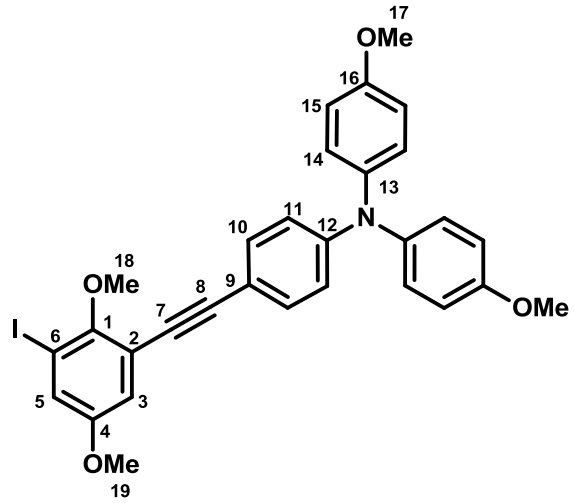

CA: [/].

a)
Synthesis according to literature.

Compound **16** (246 mg, 452 µmol) was dissolved in dry diethyl ether (7 ml) and cooled to −78 °C and *t*-butyllithium (521 µl, 1.36 mmol, 2.6 M in toluene) was added dropwise. After stirring for 45 min at −78 °C, a cooled solution of iodine (688 mg, 2.71 mmol) in dry diethyl ether (15 ml) was added. The mixture was slowly warmed to rt and stirred for 60 min. A saturated aqueous $Na_2S_2O_3$ solution (20 ml) was added and the mixture was extracted with DCM (3 × 30 ml). The combined organic layer was washed with water (2 × 30 ml) and over with $MgSO_4$. The solvent was removed *in vacuo* and the crude product was purified by flash chromatography on silica gel (PE:DCM, 1:2).

Yield: 231 mg (391 µmol, 87 %), yellow solid.

b)

Following **GP_{DPA}**: 1,3-Diiodo-2,5-dimethoxybenzene (**mbOMe'**, 992 mg, 2.54 mmol), CuI (1.38 mg, 7.25 µmol), $Pd(PPh_3)_2Cl_2$ (10.2 mg, 14.5 µmol) were dissolved in THF (35 ml) and NEt_3 (20 ml). **eTAA** (120 mg, 363 µmol) dissolved in THF (20 ml) was added. Flash chromatography on silica gel (DCM:PE, 1:1).

Yield: 180 mg (304 µmol, 84 %), yellow solid.

Formula: $C_{30}H_{26}INO_4$ [591.44].

^{1}H-NMR (400.1 MHz, CD_2Cl_2):

δ [ppm] = 7.35 (AA´, 2 H, H-10), 7.33 (d, $^4J_{HH}$ = 3.0 Hz, 1 H, H-5), 7.12 (AA´, 4 H, H-14), 7.03 (d, $^4J_{HH}$ = 3.0 Hz, 1 H, H-3), 6.95 (BB´, 4 H, H-15), 6.79 (BB´, 2 H, H-11), 3.90 (s, 3 H, H-18 o. H-19), 3.81 (-, 9 H, H-18 o. H-19 a. H-17).

^{13}C-NMR (100.6 MHz, CD_2Cl_2):

δ [ppm] = 157.1 (C_q), 156.2 (C_q), 154.6 (C_q), 149.7 (C_q), 140.2 (C_q), 132.7 (CH), 127.8 (CH), 124.9 (CH), 118.9 (CH), 118.31 (C_q), 118.28 (CH), 115.2 (CH), 113.2 (C_q), 95.4 (C_q), 92.0 (C_q), 83.9 (C_q), 61.3 (CH_3), 56.3 (CH_3), 55.8 (CH_3).

EI-MS: calc.: $[M]^+$ 591.1 m/z
exp.: $[M]^+$ 591.1 m/z

1-{4-[*N*,*N*-Di(4-methoxyphenyl)amino]phenylethynyl}(2,5-dimethoxy)benzene (sOMe)

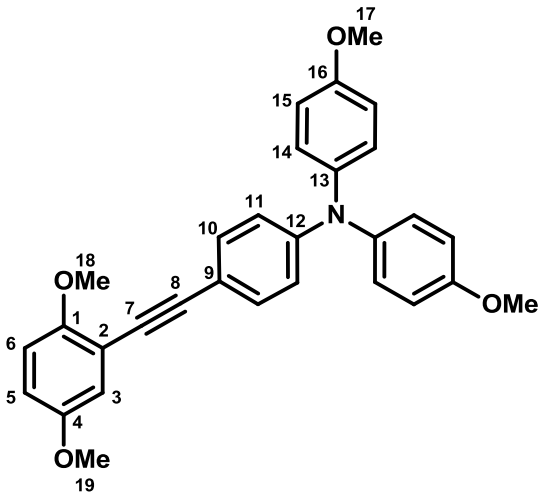

CA: [/].

Following **GP$_{OMe}$**: 2-Iodo-1,4-dimethoxybenzene (**sbOMe'**, 60.0 mg, 227 µmol), CuI (433 µg, 2.72 µmol), $Pd(PPh_3)_2Cl_2$ (3.19 mg, 4.54 µmol) were added to NEt_3 (2 ml) **eTAA** (90.0 mg, 237 µmol) in THF (2 ml) was added to this solution. Flash chromatography on silica gel (EA:PE, 1:4).

Yield: 70.0 mg (150 µmol, 66 %), light brown solid.

Formula: $C_{30}H_{27}NO_4$ [465.54].

^{1}H-NMR (400.1 MHz, $(CD_3)_2CO$):

δ [ppm] = 7.31 (AA´, 2 H, H-10), 7.11 (AA´, 4 H, H-14), 6.98 (d, $^4J_{HH}$ = 3.0 Hz, 1 H, H-3), 6.97–6.92 (-, 5 H, H-6, H-15), 6.89 (dd, $^3J_{HH}$ = 9.0, $^4J_{HH}$ = 3.0 Hz, 1 H, H-5), 6.79 (BB´, 2 H, H-11), 3.83 (s, 3 H, H-18), 3.80 (s, 6 H, H-17), 3.76 (s, 3 H, H-19).

^{13}C-NMR (100.6 MHz, $(CD_3)_2CO$):

δ [ppm] = 157.7 (C_q), 155.3 (C_q), 154.3 (C_q), 150.0 (C_q), 140.8 (C_q), 133.1 (CH), 128.3 (CH), 119.2 (CH), 118.5 (CH), 115.9 (CH), 115.8 (CH), 114.8 (C_q), 114.4 (C_q), 113.2 (CH), 94.5 (C_q), 85.4 (C_q), 56.6 (CH_3), 56.0 (CH_3), 55.7 (CH_3).

ESI-MS (high resolution):

calc.: $[M]^+$ 465.19346 m/z

exp.: $[M]^+$ 465.19309 m/z Δ = 0.80 ppm

1,4-Bis{4-[*N*,*N*-di(4-methoxyphenyl)amino]phenylethynyl}(2,5-dimethoxy)-benzene (pOMe)

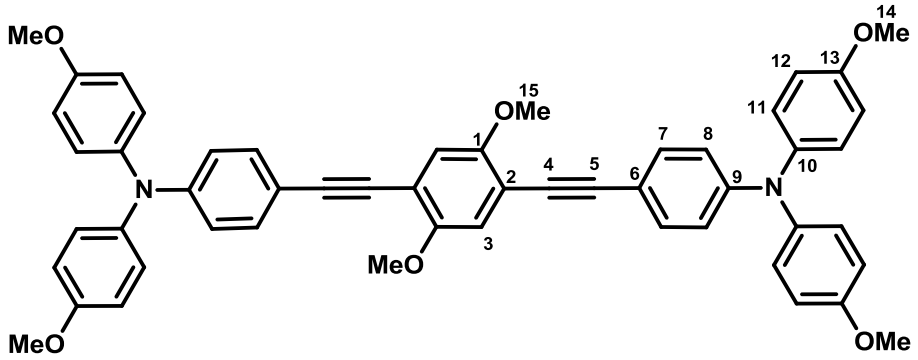

CA: [500023-90-5].

Following **GP$_{OMe}$**: 1,4-Diiodo-2,5-dimethoxybenzene (**pbOMe**, 60.0 mg, 154 µmol), CuI (586 µg, 3.08 µmol), $Pd(PPh_3)_2Cl_2$ (4.32 mg, 6.15 µmol) were added to NEt_3 (2 ml) **eTAA** (111 mg, 338 µmol) in THF (2 ml) was added to this solution. Flash chromatography on silica gel (PE:EA, 3:1).

Yield: 101 mg (127 µmol, 83 %), yellow solid.

Formula: $C_{52}H_{44}N_2O_6$ [792.92].

^{1}H-NMR (600.1 MHz, CD_2Cl_2):

δ [ppm] = 7.30 (AA´, 4 H, H-7), 7.08 (AA´, 8 H, H-11), 7.00 (s, 2 H, H-3), 6.86 (BB´, 8 H, H-12), 6.82 (BB´, 4 H, H-8), 3.86 (s, 6 H, H-15), 3.79 (s, 12 H, H-14).

^{13}C-NMR (150.9 MHz, CD_2Cl_2):

δ [ppm] = 157.0 (C_q), 154.1 (C_q), 149.5 (C_q), 140.3 (C_q), 132.6 (CH), 127.7 (CH), 119.0 (CH), 115.7 (CH), 115.2 (CH), 113.8 (C_q), 113.6 (C_q), 95.9 (C_q), 84.9 (C_q), 56.7 (CH_3), 55.8 (CH_3).

ESI-MS (high resolution):

calc.: $[M]^+$ 792.31905 m/z

exp.: $[M]^+$ 792.31939 m/z Δ = 0.43 ppm

1,3-Bis{4-[*N*,*N*-di(4-methoxyphenyl)amino]phenylethynyl}(2,5-dimethoxy)-benzene (mOMe)

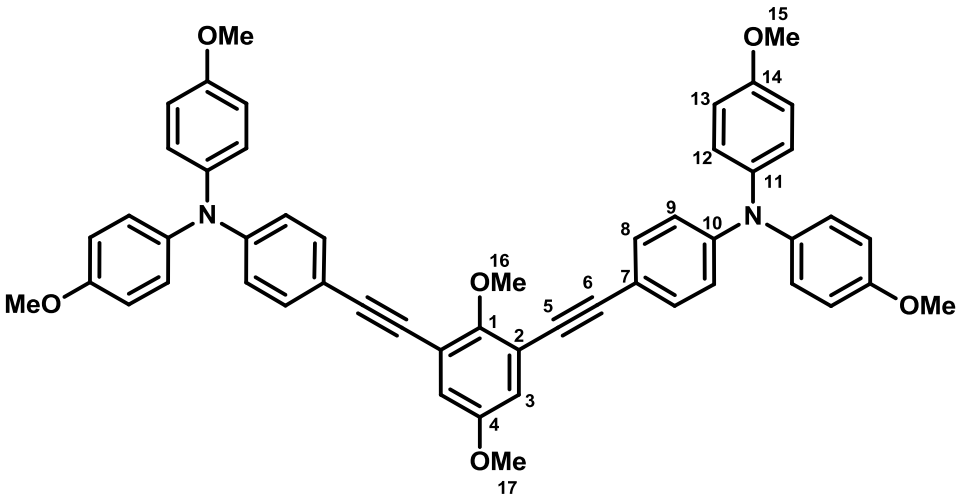

CA: [/].

a)

Following **GP$_{OMe}$**: 1,3-Diiodo-2,5-dimethoxybenzene (**mbOMe**, 110 mg, 282 µmol), $Pd(PPh_3)_2Cl_2$ (7.92 mg, 11.3 µmol) and CuI (1.07 mg, 5.64 µmol) were dissolved in NEt_3 (4 ml). **eTAA** (204 mg, 619 µmol) in THF (4 ml) was added to the solution. Flash chromatography on silica gel (DCM).

Yield: 200 mg (252 µmol, 89 %), yellow solid.

b)

Following **GP$_{OMe}$**: Compound **17** (100 mg, 169 µmol), $Pd(PPh_3)_2Cl_2$ (4.75 mg, 6.76 µmol) and CuI (644 µg, 3.38 µmol) were dissolved in NEt_3 (3 ml). **eTAA** (100 mg, 304 µmol) in THF (3 ml) was added to the solution. Flash chromatography on silica gel (DCM).

Yield: 116 mg (146 µmol, 86 %), yellow solid.

Formula: $C_{52}H_{44}N_2O_6$ [792.92].

^{1}H-NMR (600.1 MHz, CD_2Cl_2):

δ [ppm] = 7.32 (AA´, 4 H, H-8), 7.08 (AA´, 8 H, H-12), 6.94 (s, 2 H, H-3), 6.87 (BB´, 8 H, H-13), 6.82 (BB´, 4 H, H-9), 4.00 (s, 3 H, H-16), 3.79 (s, 12 H, H-15), 3.78 (s, 3 H, H-17).

^{13}C-NMR (150.9 MHz, CD_2Cl_2):

δ [ppm] = 157.0 (C_q), 155.8 (C_q), 155.4 (C_q), 149.6 (C_q), 140.3 (C_q), 132.7 (CH), 127.7 (CH), 119.01 (C_q), 119.00 (CH), 118.0 (CH), 115.2 (CH), 113.6 (C_q), 94.6 (C_q), 84.2 (C_q), 61.6 (CH_3), 56.1 (CH_3), 55.8 (CH_3).

ESI-MS (high resolution):

calc.: $[M]^+$ 792.31939 m/z

exp.: $[M]^+$ 792.31953 m/z Δ = 0.18 ppm

1-{4-[*N*,*N*-Di(4-methoxyphenyl)amino]phenylethynyl}(2,4-dimethoxy)benzene (sOMe46)

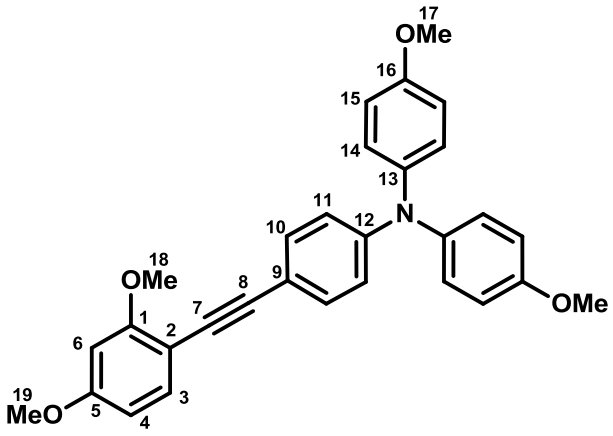

CA: [/].

Following **GP$_{OMe}$**: 1-Iodo-2,4-dimethoxybenzene (**sbOMe'46**, 110 mg, 417 µmol), CuI (1.15 mg, 6.04 µmol), $Pd(PPh_3)_2Cl_2$ (8.51 mg, 12.1 µmol) were added to NEt_3 (4 ml) **eTAA** (169 mg, 513 µmol) in THF (6 ml) was added to this solution. Flash chromatography on silica gel (DCM).

Yield: 101 mg (217 µmol, 52 %), brown solid.

Formula: $C_{30}H_{27}NO_4$ [456.54].

^{1}H-NMR (400.1 MHz, $(CD_3)_2CO$):

δ [ppm] = 7.34 (d, $^{3}J_{HH}$ = 8.4 Hz, 1 H, H-3), 7.28 (AA´, 2 H, H-10), 7.09 (AA´, 4 H, H-14), 6.93 (BB´, 4 H, H-15), 6.78 (BB´, 2 H, H-11), 6.59 (d, $^{4}J_{HH}$ = 2.4 Hz, 1 H, H-6), 6.52 (dd, $^{3}J_{HH}$ = 8.5, $^{4}J_{HH}$ = 2.4 Hz, 1 H, H-4), 3.86 (s, 3 H, H-18 o.H-19), 3.83 (s, 3 H, H-18 o.H-19), 3.76 (s, 6 H, H-17).

^{13}C-NMR (100.6 MHz, $(CD_3)_2CO$):

δ [ppm] = 162.1 (2 × C_q), 157.6 (C_q), 149.5 (C_q), 140.9 (C_q), 134.6 (CH), 132.8 (CH), 128.1 (CH), 119.5 (CH), 115.7 (CH), 115.6 (C_q), 106.2 (C_q), 106.1 (CH), 99.2 (CH), 92.8 (C_q), 85.5 (C_q), 56.1 (CH_3), 55.8 (CH_3), 55.7 (CH_3).

ESI-MS (high resolution):

calc.: $[M]^+$ 465.19346 m/z

exp.: $[M]^+$ 465.19309 m/z Δ = 0.80 ppm

1,3-Bis{4-[*N*,*N*-di(4-methoxyphenyl)amino]phenylethynyl}(4,6-dimethoxy)-benzene (mOMe46)

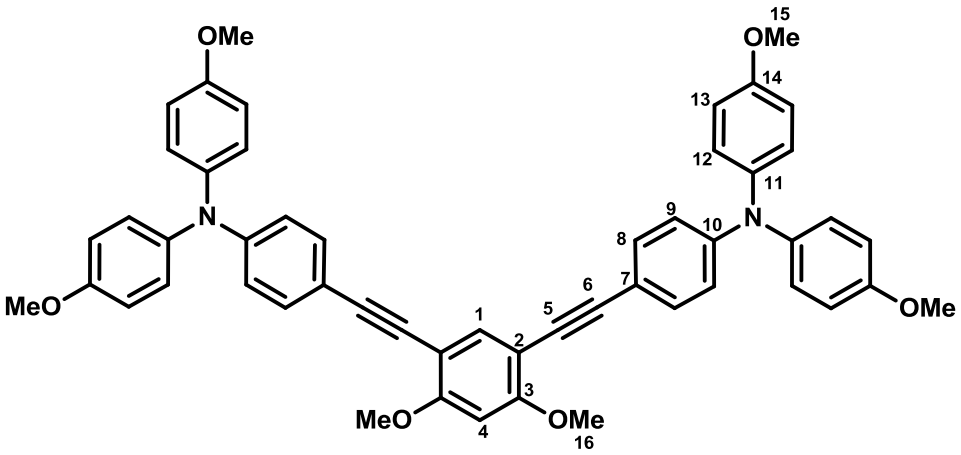

CA: [/].

Following **GP$_{OMe}$**: 1,3-Diiodo-4,6-dimethoxybenzene (**mbOMe'46**, 134 mg, 344 µmol), CuI (1.31 mg, 6.87 µmol), $Pd(PPh_3)_2Cl_2$ (9.65 mg, 13.7 µmol) were added to NEt_3 (5 ml). **eTAA** (249 mg, 756 µmol) in THF (6 ml) was added to this solution. Flash chromatography on silica gel (PE:DCM, 1:4 → DCM).

Yield: 240 mg (303 µmol, 88 %), yellow solid.

Formula: $C_{52}H_{44}N_2O_6$ [792.92].

^{1}H-NMR (600.1 MHz, $CD_3)_2SO$):

δ [ppm] = 7.42 (s, 1 H, H-4), 7.26 (AA´, 4 H, H-8), 7.08 (AA´, 8 H, H-12), 6.94 (BB´, 8 H, H-13), 6.72 (s, 1 H, H-1), 6.68 (BB´, 4 H, H-9), 3.91 (s, 6 H, H-16), 3.75 (s, 12 H, H-15).

^{13}C-NMR (150.9 MHz, $CD_3)_2SO$):

δ [ppm] = 160.8 (C_q), 156.3 (C_q), 148.5 (C_q), 139.2 (C_q), 136.2 (CH), 132.1 (CH), 127.5 (CH), 117.7 (CH), 115.1 (CH), 113.0 (C_q), 104.2 (C_q), 96.2 (CH), 92.5 (C_q), 83.7 (C_q), 56.61 (CH_3), 56.3 (CH_3).

ESI-MS (high resolution):

calc.: $[M]^+$ 792.31939 m/z

exp.: $[M]^+$ 792.32006 m/z Δ = 0.85 ppm

1-{4-[*N*,*N*-Di(4-methoxyphenyl)amino]phenylethynyl}(2,5-dimethyl)benzene (sMe)

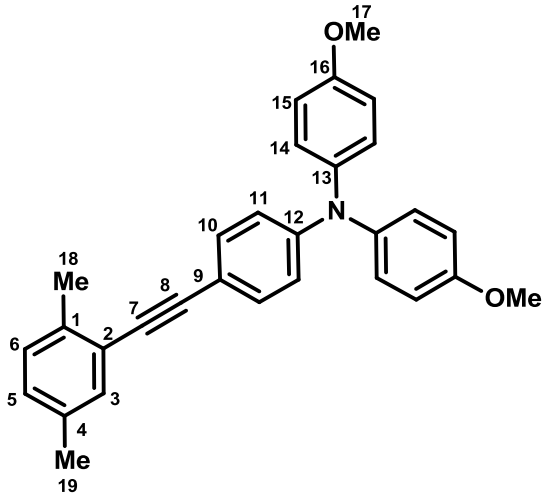

CA: [875667-88-2].

Following **GP$_{Me}$**: 2-Bromo-*para*-xylene (**sbMe**, 70.0 mg, 378 µmol), **eTAA** (137 mg, 416 µmol), CuI (2.88 mg, 15.1 µmol), $Pd(PPh_3)_2Cl_2$ (15.9 mg, 22.7 µmol), HN^iPr_2 (68.9 mg,

681 µmol) and P^tBu_3 (115 µl of a 1.00 M solution in *n*-hexane, 115.0 µmol) were added to 1,4-dioxane (4 ml). Flash chromatography on silica gel (EA:PE, 1:4).

Yield: 100 mg (231 µmol, 61 %), pale green oil.

Formula: $C_{30}H_{27}NO_2$ [433.54].

^{1}H-NMR (400.1 MHz, $(CD_3)_2CO$):

δ [ppm] = 7.33 (AA´, 2 H, H-10), 7.26 (d, $^4J_{HH}$ = 1.6 Hz, 1 H, H-3), 7.15 (d, $^3J_{HH}$ = 7.8 Hz, 1 H, H-6), 7.11 (AA´, 4 H, H-15), 7.06 (dd, $^3J_{HH}$ = 7.78, $^4J_{HH}$ = 1.6 Hz, 1 H, H-5), 6.94 (BB´, 4 H, H-14), 6.79 (BB´, 2 H, H-11), 3.80 (s, 6 H, H-17), 2.41 (s, 3 H, H-18) 2.28 (s, 3 H, H-19).

^{13}C-NMR (100.6 MHz, $(CD_3)_2CO$):

δ [ppm] = 157.7 (C_q), 150.0 (C_q), 140.8 (C_q), 137.2 (C_q), 136.0 (C_q), 133.1 (CH), 132.6 (CH), 130.3 (CH), 129.7 (CH), 128.3 (CH), 124.1 (C_q), 119.3 (CH), 115.8 (CH), 114.6 (C_q), 94.5 (C_q), 87.7 (C_q), 55.7 (CH_3), 20.7 (CH_3), 20.3 (CH_3).

1,4-Bis{4-[*N*,*N*-di(4-methoxyphenyl)amino]phenylethynyl}(2,5-dimethyl)benzene (pMe)

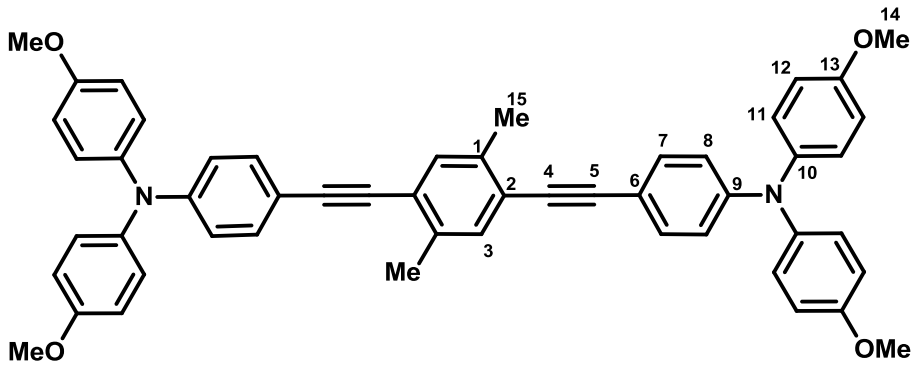

CA: [866864-08-6].

Following **GP_{Me}**: 2,5-Dibromo-*para*-xylene (**pbMe**, 55.0 mg, 208 µmol), **eTAA** (151 mg, 458 µmol), CuI (3.17 mg, 17.0 µmol), $Pd(C_6H_5CN)_2Cl_2$ (9.56 mg, 25.0 µmol), HN^iPr_2 (76.0 mg, 750 µmol) and P^tBu_3 (167 µl of a 1.00 M solution in *n*-hexane, 167 µmol) were added to 1,4-dioxane (4 ml). Flash chromatography on silica gel (PE:DCM, 1:2) and recrystallization from acetone/water.

Yield: 130 mg (171 µmol, 82 %), pale green solid.

Formula: $C_{52}H_{44}N_2O_4$ [760.92].

^{1}H-NMR (600.1 MHz, CD_2Cl_2):

δ [ppm] = 7.30 (-, 6 H, H-3 a. H-7), 7.08 (AA´, 8 H, H-11), 6.86 (BB´, 8 H, H-12), 6.82 (BB´, 4 H, H-8), 3.79 (s, 12 H, H-14), 2.42 (s, 6 H, H-15).

^{13}C-NMR (150.9 MHz, CD_2Cl_2):

δ [ppm] = 157.0 (C_q), 149.4 (C_q), 140.4 (C_q), 137.3 (C_q), 132.6 (CH), 132.5 (CH), 127.6 (CH), 123.3 (C_q), 119.2 (CH), 115.1 (CH), 114.1 (C_q), 95.6 (C_q), 87.4 (C_q), 55.8 (CH_3), 20.2 (CH_3).

1,3-Bis{4-[*N*,*N*-di(4-methoxyphenyl)amino]phenylethynyl}(2,5-dimethyl)benzene (mMe)

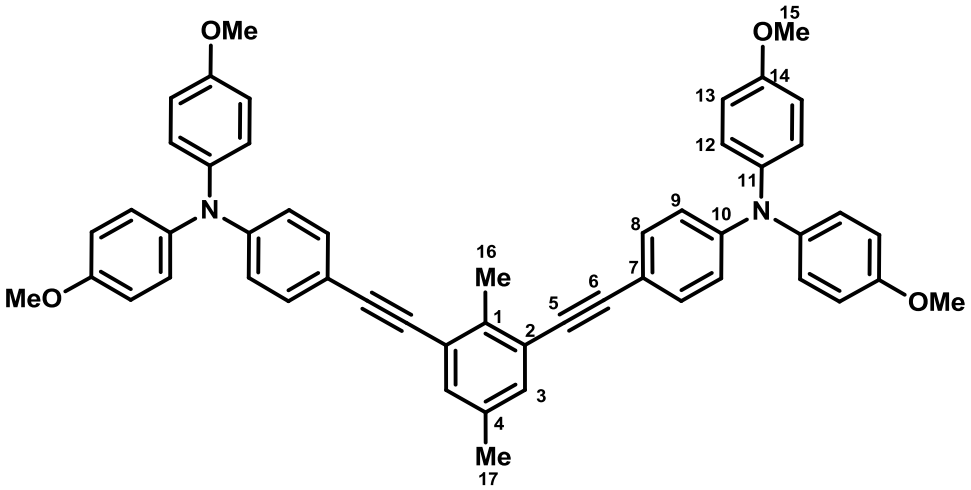

CA: [/].

Following **GP$_{Me}$**: 2,6-Dibromo-*para*-xylene (**mbMe**, 55.0 mg, 208 µmol), **eTAA** (151 mg, 458 µmol), CuI (3.17 mg, 17.0 µmol), $Pd(Ph_3)_2Cl_2$ (17.6 mg, 25.0 µmol), HN^iPr_2 (76.0 mg, 750 µmol) and P^tBu_3 (167 µl of a 1.00 M solution in *n*-hexane, 167 µmol) were added to 1,4-dioxane (4 ml). Flash chromatography on silica gel (DCM:PE, 3:1).

Yield: 103 mg (135 µmol, 66 %), pale green solid.

Formula: $C_{52}H_{44}N_2O_4$ [760.92].

^{1}H-NMR (600.1 MHz, CD_2Cl_2):

δ [ppm] = 7.31 (AA´, 4 H, H-8), 7.24 (dd, $^4J_{HH}$ = 0.6 Hz, $^5J_{HH}$ = 0.4 Hz, 2H, H-3), 7.08 (AA´, 8 H, H-12), 6.86 (BB´, 8 H, H-13), 6.82 (BB´, 4 H, H-9), 3.79 (s, 12 H, H-15), 2.61 (d, $^5J_{HH}$ = 0.4 Hz, 3 H, H-16), 2.29 (d, $^4J_{HH}$ = 0.6 Hz, 3 H, H-17).

^{13}C-NMR (150.9 MHz, CD_2Cl_2):

δ [ppm] = 156.9 (C_q), 149.4 (C_q), 140.4 (C_q), 138.7 (C_q), 135.5 (C_q), 132.6 (CH), 132.2 (CH), 127.6 (CH), 124.1 (C_q), 119.2 (CH), 115.1 (CH), 114.1 (C_q), 94.1 (C_q), 87.2 (C_q), 55.8 (CH_3), 20.7 (CH_3), 18.9 (CH_3).

ESI-MS (high resolution):

calc.: $[M]^+$ 760.32956 m/z

exp.: $[M]^+$ 760.32931 m/z Δ = 0.45 ppm

Microanalysis (CHN):

calc.: C-%: 82.08, H-%: 5.83, N-%: 3.68

exp.: C-%: 81.84, H-%: 5.83, N-%: 3.53

1,3-Bis{4-[*N*,*N*-di(4-methoxyphenyl)amino]phenylethynyl}(4,6-dimethyl)benzene (mMe46)

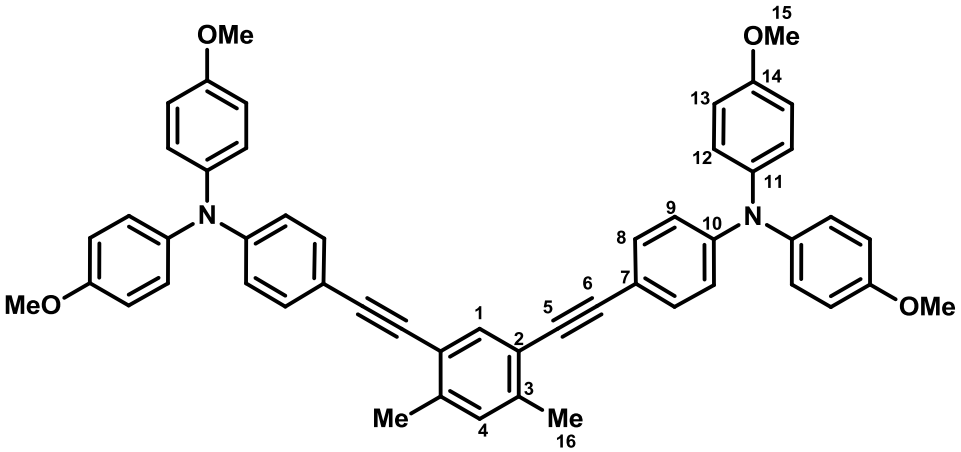

CA: [/].

Following **GP_{Me}**: 4,6-Dibromo-*meta*-xylene (**mbMe46**, 60.0 mg, 227 µmol), **eTAA** (165 mg, 500 µmol), CuI (3.46 mg, 18.2 µmol), $Pd(Ph_3)_2Cl_2$ (10.5 mg, 27.3 µmol), HN^iPr_2 (83.0 mg, 818 µmol) and P^tBu_3 (182 µl of a 1.00 M solution in *n*-hexane, 182 µmol) were added to 1,4-dioxane (4.5 ml). Flash chromatography on silica gel (DCM:PE, 3:1).

Yield: 79.0 mg (104 µmol, 60 %), yellow solid.

Formula: $C_{52}H_{44}N_2O_4$ [760.92].

^{1}H-NMR (600.1 MHz, CD_2Cl_2):

δ [ppm] = 7.53 (s, 1 H H-1), 7.29 (AA´, 4 H, H-8), 7.10 (s, 1 H, H-14), 7.07 (AA´, 8 H, H-12), 6.86 (BB´, 8 H, H-13), 6.83 (BB´, 4 H, H-9), 3.79 (s, 12 H), 2.44 (s, 6 H).

^{13}C-NMR (150.9 MHz, CD_2Cl_2):

δ [ppm] = 156.9 (C_q), 149.3 (C_q), 140.4 (C_q), 140.0 (C_q), 134.5 (CH), 132.5 (CH), 131.1 (CH), 127.6 (CH), 121.4 (CH), 119.2 (C_q), 115.1 (C_q), 114.2 (CH), 94.0 (C_q), 86.6 (C_q), 55.8 (CH_3), 20.8 (CH_3).

ESI-MS ($M^{+\bullet}$, high resolution):

calc.: 760.3296 m/z

exp.: 760.3291 m/z Δ = 0.66 ppm

1-{4-[*N*,*N*-Di(4-methoxyphenyl)amino]phenylethynyl}(2,5-dichloro)benzene (sCl)

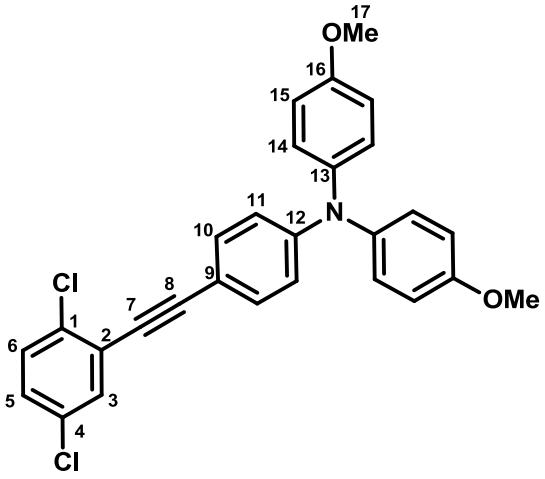

CA: [/].

Following **GP$_{Cl}$**: 1-Bromo-2,5-dichlorobenzene (**sbCl**, 52.8 mg, 234 µmol), **eTAA** (70.0 mg, 213 µmol), CuI (1.93 mg, 10.1 µmol), $Pd(C_6H_5CN)_2Cl_2$ (5.30 mg, 13.8 µmol), HN^iPr_2 (47.3 mg, 468 µmol) and P^tBu_3 (30.8 µl of a 1.00 M solution in *n*-hexane, 30.8 µmol) were added to 1,4-dioxane (5 ml). Flash chromatography on silica gel (PE:DCM, 1:1).

Yield: 67.0 mg (141 µmol, 66 %), yellow solid.

Formula: $C_{28}H_{21}Cl_2NO_2$ [474.39].

^{1}H-NMR (400.1 MHz, $(CD_3)_2CO$):

δ [ppm] = 7.61 (dd, $^4J_{HH}$ = 2.6 Hz, $^5J_{HH}$ = 0.3 Hz, 1 H, H-3), 7.52 (dd, $^3J_{HH}$ = 8.6 Hz, $^5J_{HH}$ = 0.3 Hz, 1 H, H-6), 7.39 (dd, $^3J_{HH}$ = 8.6 Hz, $^4J_{HH}$ = 2.6 Hz, 1 H, H-5), 7.38 (AA´, 2 H, H-10), 7.14 (AA´, 4 H, H-14), 6.96 (BB´, 4 H, H-15), 6.79 (BB´, 2 H, H-11), 3.81 (s, 6 H, H-17).

^{13}C-NMR (100.6 MHz, $(CD_3)_2CO$):

δ [ppm] = 158.0 (C_q), 150.9 (C_q), 140.4 (C_q), 134.3 (C_q), 133.5 (CH), 133.04 (C_q), 132.99 (CH), 131.6 (CH), 130.0 (CH), 128.6 (CH), 126.1 (C_q), 118.7 (CH), 115.8 (CH), 112.8 (C_q), 97.9 (C_q), 84.3 (C_q), 55.7 (CH_3).

ESI-MS (high resolution):

calc.: $[M]^+$ 473.09439 m/z

exp.: $[M]^+$ 473.09417 m/z Δ = 0.47 ppm

1,4-Bis{4-[*N*,*N*-di(4-methoxyphenyl)amino]phenylethynyl}(2,5-dichloro)benzene (pCl)

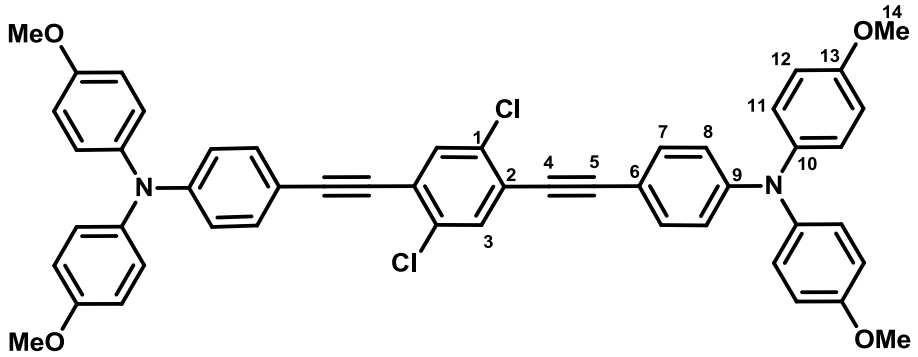

CA: [/].

Following **GP$_{Cl}$**: 1,4-Dibromo-2,5-dichlorobenzene (**pbCl**, 60.0 mg, 197 µmol), **eTAA** (130 mg, 394 µmol), CuI (3.64 mg, 19.0 µmol), $Pd(C_6H_5CN)_2Cl_2$ (9.82 mg, 26.0 µmol), HN^iPr_2 (88.0 mg, 866 µmol) and P^tBu_3 (57.0 µl of a 1.00 M solution in *n*-hexane, 57.0 µmol) were added to 1,4-dioxane (8 ml). Flash chromatography on silica gel (PE:DCM, 1:1).

Yield: 50.0 mg (62.4 µmol, 32 %), yellow solid.

Formula: $C_{50}H_{38}Cl_2N_2O_4$ [801.75].

^{1}H-NMR (600.1 MHz, $(CD_3)_2CO$):

δ [ppm] = 7.69 (s, 2 H, H-3), 7.38 (AA´, 4 H, H-7), 7.14 (AA´, 8 H, H-11), 6.96 (BB´, 8 H, H-12), 6.79 (BB´, 4 H, H-8), 3.81 (s, 12 H, H-14).

^{13}C-NMR (150.9 MHz, $(CD_3)_2CO$):

δ [ppm] = 158.0 (C_q), 150.1 (C_q), 140.4 (C_q), 134.0 (C_q), 133.6 (CH), 133.4 (CH), 128.7 (CH), 124.9 (C_q), 118.6 (CH), 115.9 (CH), 112.7 (C_q), 99.4 (C_q), 84.6 (C_q), 55.8 (CH_3).

ESI-MS (high resolution):

calc.: $[M]^+$ 800.22032 m/z

exp.: $[M]^+$ 800.22052 m/z Δ = 0.26 ppm

1,3-Bis{4-[*N*,*N*-di(4-methoxyphenyl)amino]phenylethynyl}(2,5-dichloro)benzene (mCl)

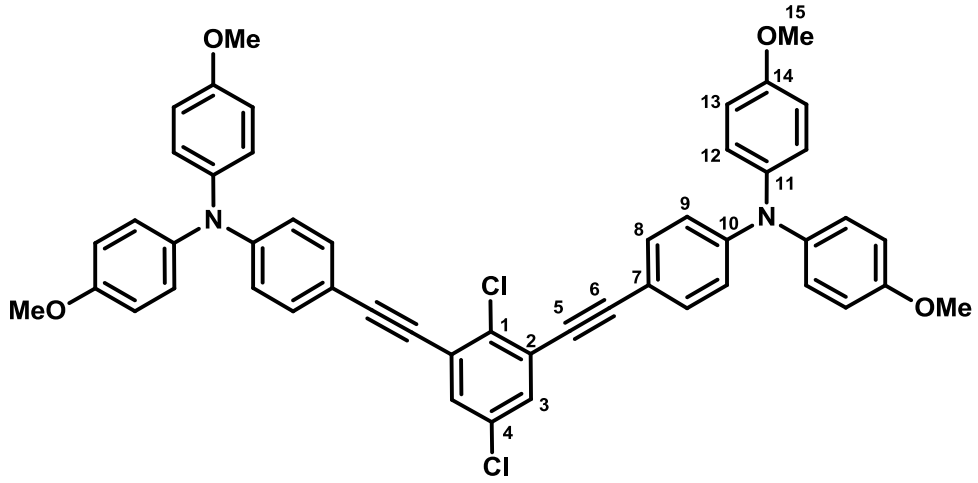

CA: [/].

Following **GP$_{Cl}$**: 1,3-Dibromo-2,5-dichlorobenzene (**mbCl**, 70.0 mg, 230 µmol), **eTAA** (152 mg, 460 µmol), CuI (4.24 mg, 22.0 µmol), Pd($C_6H_5CN)_2Cl_2$ (11.5 mg, 30.0 µmol), HN^{i}Pr$_2$ (102 mg, 1.01 mmol) and P^{t}Bu$_3$ (67.0 µl of a 1.00 M solution in *n*-hexane, 67.0 µmol) were added to 1,4-dioxane (8,5 ml). Flash chromatography on silica gel (PE:DCM, 1:2).

Yield: 64.0 mg (79.8 µmol, 35 %), yellow solid.

Formula: $C_{50}H_{38}Cl_2N_2O_4$ [801.75].

^{1}H-NMR (600.1 MHz, $(CD_3)_2CO$):

δ [ppm] = 7.54 (s, 2 H, H-3), 7.38 (AA´, 4 H, H-8), 7.13 (AA´, 8 H, H-12), 6.95 (BB´, 8 H, H-13), 6.79 (BB´, 4 H, H-9), 3.81 (s, 12 H, H-15).

^{13}C-NMR (150.9 MHz, $(CD_3)_2CO$):

δ [ppm] = 158.0 (C_q), 150.9 (C_q), 140.4 (C_q), 135.2 (C_q), 133.6 (CH), 132.7 (C_q), 131.9 (CH), 128.6 (CH), 126.7 (C_q), 118.7 (CH), 115.8 (CH), 112.6 (C_q), 98.3 (C_q), 84.4 (C_q), 55.8 (CH_3).

ESI-MS (high resolution):

calc.: $[M]^+$ 800.22032 m/z

exp.: $[M]^+$ 800.22070 m/z Δ = 0.47 ppm

1-{4-[*N*,*N*-Di(4-methoxyphenyl)amino]phenylethynyl}(2,5-dicyano)benzene (sCN)

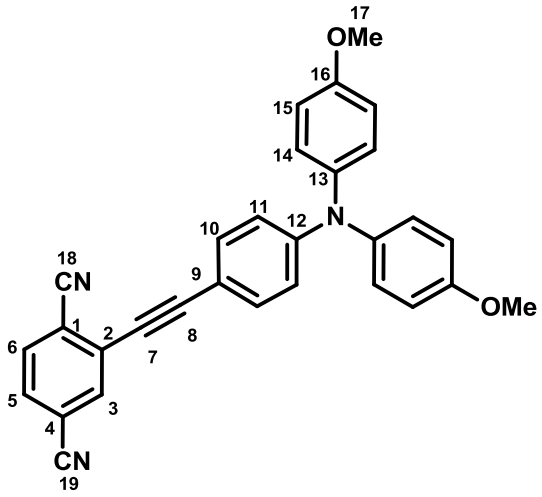

CA: [/].

Following **GP$_{CN}$**: **eTAA** (76.0 mg, 231 µmol), CuI (773 µg, 4.06 µmol), Pd(PPh$_3$)$_2$Cl$_2$ (5.70 mg, 8.11 µmol) were added to NEt$_3$ (4 ml) 2-Bromoterephthonitrile (**sbCN**, 40.0 mg, 193 µmol) in THF (2 ml) was added to this solution. Flash chromatography on silica gel (PE:DCM, 1:2).

Yield: 82.0 mg (180 µmol, 93 %), orange solid.

Formula: $C_{30}H_{21}N_3O_2$ [455.51].

^{1}H-NMR (600.1 MHz, (CD$_3$)$_2$CO):

δ [ppm] = 8.11 (dd, $^4J_{HH}$ = 1.6 Hz, $^5J_{HH}$ = 0.6 Hz, 1 H, H-3), 8.06 (dd, $^3J_{HH}$ = 8.1 Hz, $^5J_{HH}$ = 0.6 Hz, 1 H, H-6), 7.93 (dd, $^3J_{HH}$ = 8.1 Hz, $^4J_{HH}$ = 1.6 Hz, 1 H, H-5), 7.41 (AA´, 2 H, H-10), 7.16 (AA´, 4 H, H-14), 6.97 (BB´, 4 H, H-15), 6.80 (BB´, 2 H, H-11), 3.81 (s, 6 H, H-17).

^{13}C-NMR (150.9 MHz, (CD$_3$)$_2$CO):

δ [ppm] = 158.2 (C_q), 151.5 (C_q), 140.1 (C_q), 135.8 (CH), 134.7 (CH), 133.9 (CH), 132.0 (CH), 129.3 (C_q), 128.8 (CH), 118.9 (C_q), 118.3 (CH), 117.6 (C_q), 117.4 (C_q), 117.1 (C_q), 115.9 (CH), 111.4 (C_q), 100.2 (C_q), 84.1 (C_q), 55.8 (CH_3).

ESI-MS (high resolution):

calc.: $[M]^+$ 455.16283 m/z

exp.: $[M]^+$ 455.16296 m/z Δ = 0.29 ppm

1,4-Bis{4-[*N*,*N*-di(4-methoxyphenyl)amino]phenylethynyl}(2,5-dicyano)benzene (pCN)

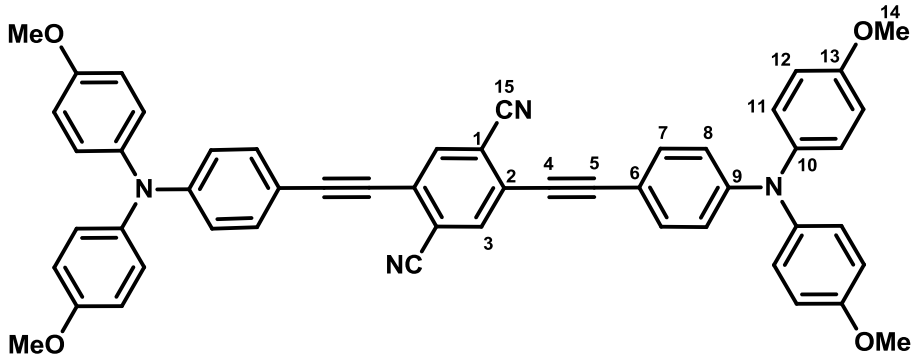

CA: [/].

Following **GP$_{CN}$**: **eTAA** (127 mg, 385 µmol), CuI (1.54 mg, 8.08 µmol), $Pd(PPh_3)_2Cl_2$ (11.3 mg, 16.0 µmol) were added to NEt_3 (7 ml). 2,5-Dibromoterephthonitrile (**pbCN**, 55.0 mg, 192 µmol) in THF (2 ml) was added to this solution. Flash chromatography on silica gel (PE:DCM, 1:2).

Yield: 80.0 mg (102 µmol, 53 %), red solid.

Formula: $C_{52}H_{38}N_4O_4$ [782.88].

^{1}H-NMR (600.1 MHz, CD_2Cl_2):

δ [ppm] = 8.12 (s, 2 H, H-3), 7.42 (AA´, 4 H, H-7), 7.17 (AA´, 8 H, H-11), 6.97 (BB´, 8 H, H-12), 6.80 (BB´, 4 H, H-8), 3.81 (s, 12 H, H-14).

^{13}C-NMR (150.9 MHz, $(CD_3)_2CO$):

δ [ppm] = 158.2 (C_q), 151.5 (C_q), 140.1 (C_q), 136.5 (CH), 133.9 (CH), 128.8 (CH), 127.0 (C_q), 118.9 (C_q), 118.3 (CH), 116.7 (C_q), 115.9 (CH), 111.4 (C_q), 101.6 (C_q), 84.6 (C_q), 55.8 (CH_3).

ESI-MS (high resolution):

calc.: $[M]^+$ 782.28876 m/z

exp.: $[M]^+$ 782.28841 m/z Δ = 0.45 ppm

1,4-Bis{4-[*N*,*N*-di(4-methoxyphenyl)amino]phenylethynyl}(2,5-dicyano)benzene (mCN)

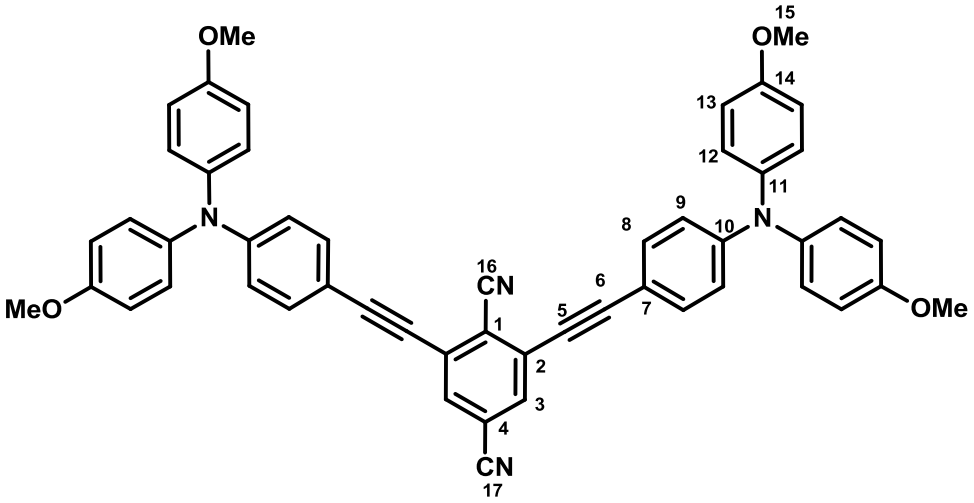

CA: [/].

Following **GP$_{CN}$**: **eTAA** (177 mg, 539 µmol), CuI (1.96 mg, 10.3 µmol), $Pd(PPh_3)_2Cl_2$ (14.4 mg, 21.0 µmol) were added to NEt_3 (10 ml). 2,6-dibromotetrephthonitrile (**mbCN**, 70.0 mg, 245 µmol) in THF (3 ml) was added to this solution. Flash chromatography on silica gel (PE:DCM, 1:2).

Yield: 105 mg (134 µmol, 70 %), red solid.

Formula: $C_{52}H_{38}N_4O_4$ [782.88].

^{1}H-NMR (600.1 MHz, $(CD_3)_2CO$):

δ [ppm] = 7.99 (s, 2 H, H-3), 7.43 (AA´, 4 H, H-8), 7.17 (AA´, 8 H, H-12), 6.97 (BB´, 8 H, H-13), 6.80 (BB´, 4 H, H-9), 3.81 (s, 12 H, H-15).

^{13}C-NMR (150.9 MHz, $(CD_3)_2CO$):

δ [ppm] = 158.2 (C_q), 151.6 (C_q), 140.1 (C_q), 134.0 (CH), 133.8 (CH), 130.1 (C_q), 128.8 (CH), 120.1 (C_q), 118.3 (CH), 117.5 (C_q), 117.1 (C_q), 116.3 (C_q), 115.9 (CH), 111.3 (C_q), 100.5 (C_q), 84.2 (C_q), 55.8 (CH_3).

ESI-MS (high resolution):

calc.: $[M]^+$ 782.28876 m/z

exp.: $[M]^+$ 782.28926 m/z Δ = 0.64 ppm

1-{4-[*N*,*N*-Di(4-methoxyphenyl)amino]phenylethynyl}(2,5-dinitro)benzene (sNO$_2$)

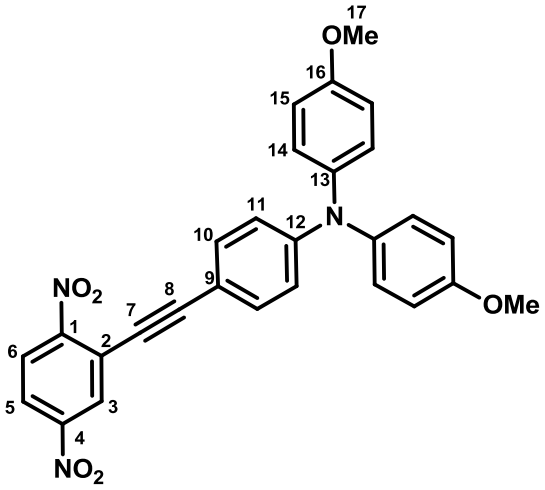

CA: [/].

Following **GP$_{NO_2}$**: 2-Bromo-1,4-dinitrobenzene (**sbNO$_2$**,100 mg, 405 µmol), **eTAA** (147 mg, 446 µmol), CuI (9.00 mg, 47.3 µmol), $Pd(PPh_3)_2Cl_2$ (9.91 mg, 14.1 µmol) and triethylamine (2 ml) were added to toluene (8 ml). Flash chromatography on silica gel (PE:DCM, 1:2).

Yield: 120 mg (242 µmol, 60 %), red (black) solid.

Formula: $C_{28}H_{21}N_3O_6$ [495.48].

^{1}H-NMR (400.1 MHz, $(CD_3)_2CO$):

δ [ppm] = 8.54 (dd, $^4J_{HH}$ = 1.7, $^5J_{HH}$ = 1.2 Hz, 1 H, H-3), 8.36 (-, 2 H, H-5, H-6), 7.44 (AA´, 2 H, H-10), 7.17 (AA´, 4 H, H-14), 6.97 (BB´, 4 H, H-15), 6.79 (BB´, 2 H, H-11), 3.82 (s, 6 H, H-17).

^{13}C-NMR (100.6 MHz, $(CD_3)_2CO$):

δ [ppm] = 158.2 (C_q), 153.1 (C_q), 151.6 (C_q), 150.37 (C_q), 140.1 (CH), 134.1 (C_q), 129.6 (CH), 128.8 (CH), 127.1 (CH), 123.8 (CH), 121.0 (C_q), 118.2 (CH), 115.9 (CH), 111.6 (C_q), 101.9 (C_q), 83.1 (C_q), 55.7 (CH_3).

ESI-MS (high resolution):

calc.: $[M]^+$ 495.14249 m/z

exp.: $[M]^+$ 495.14226 m/z Δ = 0.46 ppm

1,4-Bis{4-[*N*,*N*-di(4-methoxyphenyl)amino]phenylethynyl}(2,5-dinitro)benzene (pNO_2)

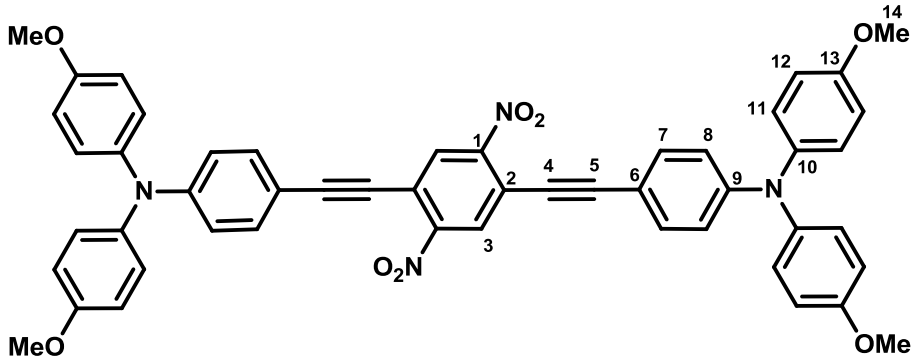

CA: [/].

Following **GP_{NO_2}**: 1,4-Dibromo-2,5-dinitrobenzene (**$pbNO_2$**, 70.0 mg, 215 µmol), **eTAA** (156 mg, 473 µmol), CuI (9.00 mg, 47.0 µmol), $Pd(C_6H_5CN)_2Cl_2$ (9.91 mg, 46.0 µmol) and triethylamine (2 ml) were added to toluene (8 ml). Flash chromatography on silica gel (PE:DCM, 1:2).

Yield: 85.0 mg (103 µmol, 59 %), red solid.

Formula: $C_{50}H_{38}N_4O_8$ [822.86].

^{1}H-NMR (600.1 MHz, CD_2Cl_2):

δ [ppm] = 8.28 (s, 2 H, H-3), 7.36 (AA´, 4 H, H-7), 7.11 (AA´, 8 H, H-11), 6.88 (BB´, 8 H, H-12), 6.81 (BB´, 4 H, H-8), 3.80 (s, 12 H, H-14).

^{13}C-NMR (150.9 MHz, CD_2Cl_2):

δ [ppm] = 157.4 (C_q), 150.9 (C_q), 150.5 (C_q), 139.7 (C_q), 133.7 (CH), 130.6 (CH), 128.1 (CH), 118.5 (C_q), 118.2 (CH), 115.3 (CH), 111.3 (C_q), 103.3 (C_q), 83.6 (C_q), 55.8 (CH_3).

ESI-MS (high resolution):

calc.: $[M]^+$ 822.26842 m/z

exp.: $[M]^+$ 822.26806 m/z Δ = 0.44 ppm.

1,3-Bis{4-[*N*,*N*-di(4-methoxyphenyl)amino]phenylethynyl}(2,5-dinitro)benzene (mNO_2)

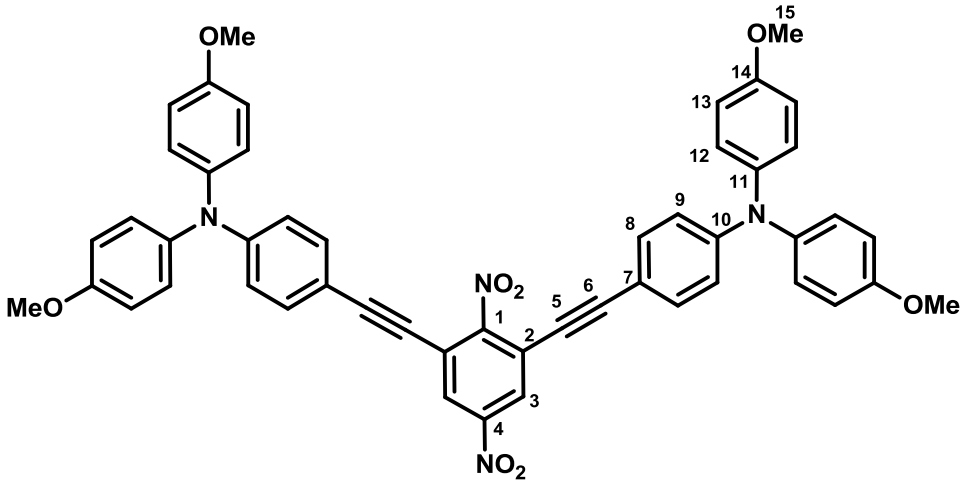

CA: [/].

Following **GP_{NO_2}**: 1,3-Dibromo-2,5-dinitrobenzene (**$mbNO_2$**, 100 mg, 307 µmol), **eTAA** (222 mg, 675 µmol), CuI (9.00 mg, 47.0 µmol), $Pd(PPh_3)_2Cl_2$ (9.91 mg, 14.0 µmol) and triethylamine (2 ml) were added to toluene (8 ml). Flash chromatography on silica gel (PE:DCM, 1:2).

Yield: 108 mg (131 µmol, 43 %), red solid.

Formula: $C_{50}H_{38}N_4O_8$ [822.86].

^{1}H-NMR (600.1 MHz, CD_2Cl_2):

δ [ppm] = 8.27 (s, 2 H, H-3), 7.30 (AA´, 4 H, H-8), 7.10 (AA´, 8 H, H-12), 6.87 (BB´, 8 H, H-13), 6.79 (BB´, 4 H, H-9), 3.79 (s, 12 H, H-15)

^{13}C-NMR (150.9 MHz, CD_2Cl_2):

δ [ppm] = 157.4 (C_q), 155.4 (C_q), 150.9 (C_q), 148.2 (C_q), 139.7 (C_q), 133.5 (CH), 128.1 (CH), 126.0 (CH), 119.8 (C_q), 118.2 (CH), 115.3 (CH), 110.6 (C_q), 100.9 (C_q), 80.3 (C_q), 55.8 (CH_3).

ESI-MS (high resolution):

calc.: $[M]^+$ 822.26842 m/z

exp.: $[M]^+$ 822.26836 m/z Δ = 0.07 ppm

6.2.5 Synthesis of the DA Compounds and their NDI-substituted References

sOMeNDI

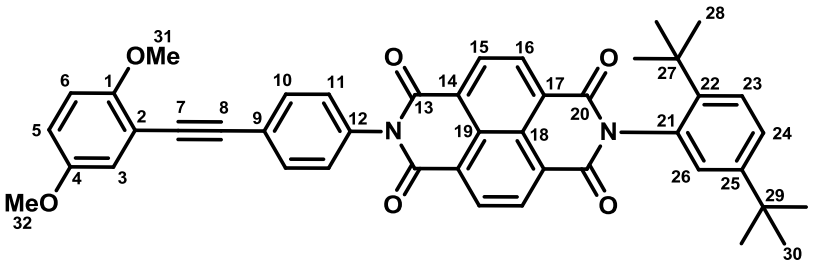

CA: [/].

Following **GP$_{OMe}$**: 1-Iodo-2,5-dimethoxybenzene (**sbOMe'**, 55.0 mg, 208 µmol), CuI (397 µg, 2.08 µmol), $Pd(PPh_3)_2Cl_2$ (2.92 mg, 4.16 µmol) were added to NEt_3 (2 ml). **eNDI** (104 mg, 187 µmol) in THF (2 ml) was added to this solution. Flash chromatography on silica gel (DCM).

Yield: 78.0 mg (113 µmol, 60 %), red solid.

Formula: $C_{44}H_{38}N_2O_6$ [690.78].

^{1}H-NMR (400.1 MHz, CD_2Cl_2):

δ [ppm] = 8.84 (-, 4 H, H-15 a. H-16), 7.75 (AA´, 2 H, H-10), 7.64 (d, $^3J_{HH}$ = 8.6 Hz, 1 H, H-23), 7.53 (dd, $^3J_{HH}$ = 8.6 Hz, $^4J_{HH}$ = 2.4 Hz, 1 H, H-24), 7.36 (BB´, 2 H, H-11), 7.07 (dd, $^4J_{HH}$ = 2.8 Hz, $^5J_{HH}$ = 0.6 Hz 1 H, H-3), 7.06 (d, $^4J_{HH}$ = 2.2 Hz, 1 H, H-26), 6.92 (dd, $^3J_{HH}$ = 9.0 Hz, $^4J_{HH}$ = 2.8 Hz, 1 H, H-5), 6.85 (dd, $^3J_{HH}$ = 9.0 Hz, $^5J_{HH}$ = 0.6 Hz 1 H, H-6), 3.90 (s, 3 H, H-31), 3.80 (s, 3 H, H-32), 1.34 (s, 9 H, H-28), 1.28 (s, 9 H, H-30).

^{13}C-NMR (100.6 MHz, CD_2Cl_2):

δ [ppm] = 164.3 (C_q), 163.3 (C_q), 155.0 (C_q), 153.7 (C_q), 151.0 (C_q), 144.5 (C_q), 135.1 (C_q), 133.0 (C_q), 132.8 (CH), 131.7 (2 × CH), 129.4 (CH), 129.3 (CH), 128.0 (CH), 127.72 (C_q), 127.70 (C_q), 127.6 (C_q), 127.4 (C_q), 126.9 (CH), 124.8 (C_q), 118.4 (CH), 116.4 (CH), 112.8 (C_q), 112.6

(CH), 92.5 (C_q), 87.5 (C_q), 56.8 (CH_3), 56.1 (CH_3), 35.9 (C_q), 34.6 (C_q), 31.8 (CH_3), 31.3 (CH_3).

ESI-MS (high resolution):

calc.: $[M + H]^+$ 691.28026 m/z

exp.: $[M + H]^+$ 691.28058 m/z Δ = 0.46 ppm

sOMeNDI46

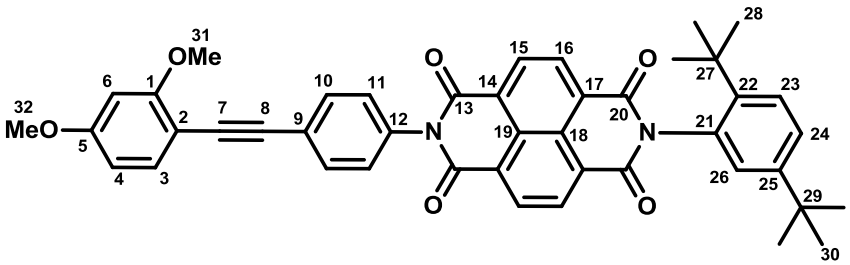

CA: [/].

Following **GP_{OMe}**: 1-Iodo-2,4-dimethoxybenzene (**sbOMe'46**, 80.0 mg, 303 µmol), CuI (793 µg, 4.17 µmol), $Pd(PPh_3)_2Cl_2$ (5.85 mg, 8.33 µmol) were added to NEt_3 (4 ml). **eNDI** (165.0 mg, 500 µmol) in THF (4 ml) was added to this solution. Flash chromatography on silica gel (PE:DCM, 1:2).

Yield: 140 mg (203 µmol, 68 %), orange solid.

Formula: $C_{44}H_{38}N_2O_6$ [690.78].

^{1}H-NMR (400.1 MHz, CD_2Cl_2):

δ [ppm] = 8.84 (-, 4 H, H-15 a. H-16), 7.71 (AA´, 2 H, H-10), 7.64 (d, $^3J_{HH}$ = 8.6 Hz, 1 H, H-23), 7.53 (dd, $^3J_{HH}$ = 8.6 Hz, $^4J_{HH}$ = 2.3 Hz, 1 H, H-24), 7.45 (dd, $^3J_{HH}$ = 8.1 Hz, $^5J_{HH}$ = 0.5 Hz 1 H, H-3), 7.34 (BB´, 2 H, H-11), 7.05 (d, $^4J_{HH}$ = 2.1 Hz, 1 H, H-26), 6.54–6.51 (-, 2 H, H-3 a. H-6), 3.92 (s, 3 H, H-31), 3.80 (s, 3 H, H-32), 1.34 (s, 9 H, H-28), 1.27 (s, 9 H, H-30).

^{13}C-NMR (100.6 MHz, CD_2Cl_2):

δ [ppm] = 164.3 (C_q), 163.3 (C_q), 162.1 (C_q), 161.8 (C_q), 151.0 (C_q), 144.5 (C_q), 134.7 (CH), 134.6 (C_q), 133.0 (C_q), 132.6 (CH), 131.70 (CH), 131.69 (CH), 129.4 (CH), 129.2 (CH), 128.0 (CH), 127.71 (C_q), 127.69 (C_q), 127.6 (C_q), 127.4 (C_q), 126.9 (CH), 125.3 (C_q), 105.5 (CH), 104.7 (C_q), 98.8 (CH), 91.3 (C_q), 87.8 (C_q), 56.3 (CH_3), 55.9 (CH_3), 35.9 (C_q), 34.6 (C_q), 31.8 (CH_3), 31.3 (CH_3).

ESI-MS (high resolution):

calc.: $[M + H]^+$ 691.2803 m/z

exp.: $[M + H]^+$ 691.2796 m/z Δ = 1.01 ppm

1-{4-[*N*,*N*-Di(4-methoxyphenyl)amino]phenylethynyl}(4-iodo-2,5-dimethoxy)-benzene (17)

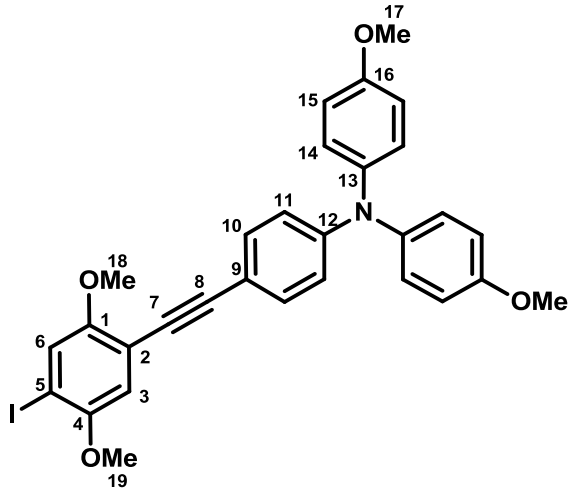

CA: [/].

Following **GP_{DPA}**: 2,5-Diiodo-1,4-dimethoxybenzene (**pbOMe'**, 1.42 g, 3.64 mmol), CuI (1.38 mg, 7.25 µmol), $Pd(PPh_3)_2Cl_2$ (10.2 mg, 14.5 µmol) were dissolved in THF (35 ml) and NEt_3 (20 ml). **eTAA** (120 mg, 364 µmol) dissolved in THF (20 ml) was added. Flash chromatography on silica gel (DCM).

Yield: 143 mg (242 µmol, 66 %), yellow solid.

Formula: $C_{30}H_{26}INO_4$ [591.44].

^{1}H-NMR (400.1 MHz, $CDCl_3$):

δ [ppm] = 7.41 (s, 1 H, H-6), 7.31 (AA´, 2 H, H-10), 7.11 (AA´, 4 H, H-14), 7.03 (s, 1 H, H-3), 6.95 (BB´, 4 H, H-15), 6.78 (BB´, 2 H, H-11), 3.87 (s, 3 H, H-18 o. H-19), 3.85 (s, 3 H, H-18 o. H-19), 3.81 (s, 6 H, H-17).

^{13}C-NMR (100.6 MHz, $CDCl_3$):

δ [ppm] = 157.8 (C_q), 155.6 (C_q), 153.4 (C_q), 150.2 (C_q), 140.7 (C_q), 133.1 (CH), 128.4 (CH), 128.3 (C_q), 123.4 (CH), 119.1 (CH), 115.8 (CH), 115.7 (CH), 114.8 (C_q), 114.4 (C_q), 95.7 (C_q), 84.9 (C_q), 57.3 (CH_3), 57.0 (CH_3), 55.8 (CH_3).

MALDI-MS: calc.: $[M]^+$ 591.09 m/z
exp.: $[M]^+$ 591.17 m/z

1-{4-[*N*,*N*-Di(4-methoxyphenyl)amino]phenylethynyl}(3-iodo-4,6-dimethoxy)-benzene (19)

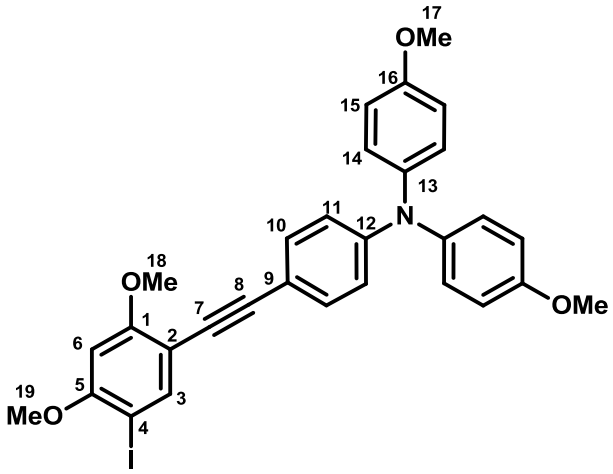

CA: [/].

Following **GP$_{DPA}$**: 1,3-Diiodo-4,6-dimethoxybenzene (**mbOMe'46**, 1.30 g, 3.34 mmol), CuI (2.54 mg, 13.3 µmol), $Pd(PPh_3)_2Cl_2$ (18.8 mg, 26.8 µmol) were dissolved in THF (45 ml) and NEt_3 (20 ml). **eTAA** (220 mg, 668 µmol) dissolved in THF (20 ml) was added. Flash chromatography on silica gel (DCM:PE, 1:1 → 2:1).

Yield: 285 mg (482 µmol, 72 %), brown solid.

Formula: $C_{30}H_{26}INO_4$ [591.44].

^{1}H-NMR (400.1 MHz, $(CD_3)_2SO$):

δ [ppm] = 7.70 (s, 1 H, H-3), 7.26 (AA´, 2 H, H-10), 7.08 (AA´, 4 H, H-14), 6.94 (BB´, 4 H, H-15), 6.69 (s, 1 H, H-6), 6.78 (BB´, 2 H, H-11), 3.89 (s, 3 H, H-18 o.H-19), 3.88 (s, 3 H, H-18 o.H-19), 3.75 (s, 6 H, H-17).

^{13}C-NMR (100.6 MHz, $(CD_3)_2SO$):

δ [ppm] = 161.3 (C_q), 159.0 (C_q), 156.3 (C_q), 148.5 (C_q), 141.3 (CH), 139.2 (C_q), 132.1 (CH), 127.5 (CH), 117.6 (CH), 115.1 (CH), 112.8 (C_q), 106.3 (C_q), 96.6 (CH), 93.1 (C_q), 83.2 (C_q), 74.0 (C_q), 56.7 (CH_3), 56.1 (CH_3), 55.3 (CH_3).

MALDI-MS: calc.: $[M]^+$ 591.090 m/z
exp.: $[M]^+$ 591.071 m/z

pOMeNDI

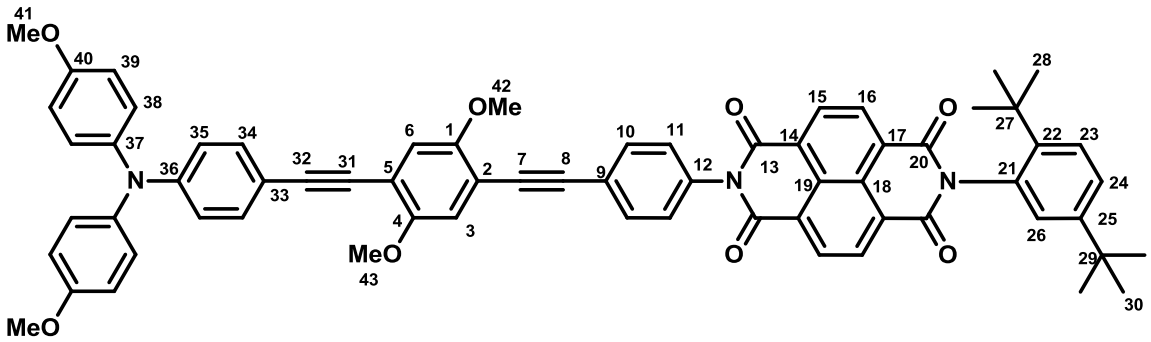

CA: [/].

Following **GP_{OMe}**: Compound **17** (59.0 mg, 99.8 µmol), CuI (190 µg, 998 nmol), $Pd(PPh_3)_2Cl_2$ (1.40 mg, 2.00 µmol) were added to NEt_3 (2 ml). **eNDI** (55.3 mg, 99.7 µmol) in THF (2 ml) was added to this solution. Flash chromatography on silica gel (DCM) and GPC.

Yield: 80.0 mg (78.6 µmol, 79 %), green solid.

Formula: $C_{66}H_{55}N_3O_8$ [1018.16].

^{1}H-NMR (600.1 MHz, CD_2Cl_2):

δ [ppm] = 8.84 (-, 4 H, H-15 a. H-16), 7.76 (AA´, 2 H, H-10), 7.64 (d, $^{3}J_{HH}$ = 8.7 Hz, 1 H, H-23), 7.53 (dd, $^{3}J_{HH}$ = 8.4 Hz, $^{4}J_{HH}$ = 2.2 Hz, 1 H, H-24), 7.37 (BB´, 2 H, H-11), 7.32 (AA´, 2 H, H-34), 7.10 (AA´, 4 H, H-38), 7.07 (s, 1 H, H-6), 7.06 (d, $^{4}J_{HH}$ = 2.2 Hz, 1 H, H-26), 7.03 (s, 1 H, H-3), 6.88 (BB´, 4 H, H-39), 6.82 (BB´, 2 H, H-35), 3.91 (s, 3 H, H-42), 3.90 (s, 3 H, H-43), 3.80 (s, 6 H, H-41), 1.34 (s, 9 H, H-28), 1.27 (s, 9 H, H-30).

^{13}C-NMR (150.9 MHz, CD_2Cl_2):

δ [ppm] = 164.3 (C_q), 163.3 (C_q), 157.0 (C_q), 154.5 (C_q), 154.0 (C_q), 151.0 (C_q), 149.6 (C_q), 144.5 (C_q), 140.3 (C_q), 135.2 (C_q), 133.0 (C_q), 132.8 (CH), 132.7 (CH), 131.7 (2 × CH), 129.4 (CH), 129.3 (CH), 128.0 (CH), 127.8 (C_q), 127.71 (C_q), 127.69 (C_q), 127.6 (C_q), 127.4 (CH), 126.9 (CH), 124.6 (C_q), 118.9 (CH), 115.9 (CH), 115.8 (CH), 115.2 (CH), 114.8 (C_q), 113.6 (C_q), 112.5 (C_q), 96.3 (C_q), 93.7 (C_q), 87.6 (C_q), 84.7 (C_q), 56.82 (CH_3), 56.80 (CH_3), 55.8 (CH_3), 35.9 (C_q), 34.6 (C_q), 31.8 (CH_3), 31.3 (CH_3).

ESI-MS (high resolution):

calc.: $[M + H]^+$ 1017.39837 m/z

exp.: $[M + H]^+$ 1017.39890 m/z Δ = 0.52 ppm

mOMeNDI

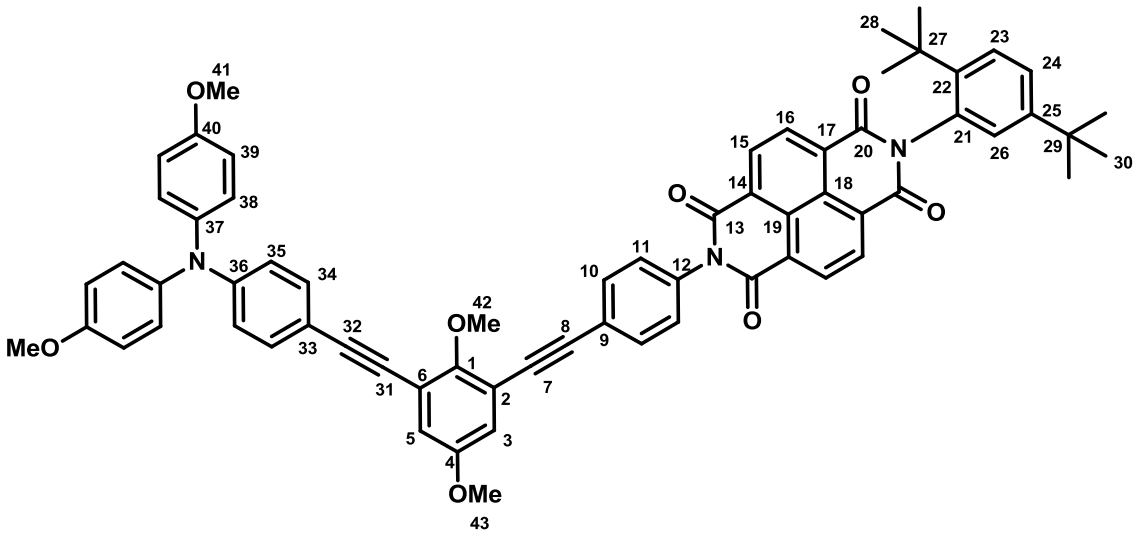

CA: [/].

Following **GP$_{OMe}$**: Compound **18** (90.0 mg, 152 µmol), CuI (580 µg, 3.04 µmol), Pd(PPh$_3$)$_2$Cl$_2$ (4.27 mg, 6.09 µmol) were added to NEt$_3$ (4 ml). **eNDI** (168 mg, 304 µmol) in THF (6 ml) was added to this solution. Flash chromatography on silica gel (DCM) and GPC.

Yield: 141 mg (138 µmol, 91 %), green solid.

Formula: $C_{66}H_{55}N_3O_8$ [1018.16].

^{1}H-NMR (600.1 MHz, CD_2Cl_2):

δ [ppm] = 8.85 (-, 4 H, H-15 a. H-16), 7.78 (AA´, 2 H, H-10), 7.64 (d, $^3J_{HH}$ = 8.6 Hz, 1 H, H-23), 7.53 (dd, $^3J_{HH}$ = 8.6 Hz, $^4J_{HH}$ = 2.3 Hz, 1 H, H-24), 7.38 (BB´, 2 H, H-11), 7.33 (AA´, 2 H, H-34), 7.10 (AA´, 4 H, H-38), 7.05 (d, $^4J_{HH}$ = 2.2 Hz, 1 H, H-26), 7.03 (d, $^4J_{HH}$ = 3.1 Hz, 1 H, H-5), 7.02 (d, $^4J_{HH}$ = 3.1 Hz, 1 H, H-3), 6.87 (BB´, 4 H, H-39), 6.83 (BB´, 2 H, H-35), 4.06 (s, 3 H, H-42), 3.82 (s, 3 H, H-43), 3.80 (s, 6 H, H-41), 1.34 (s, 9 H, H-28), 1.27 (s, 9 H, H-30).

^{13}C-NMR (150.9 MHz, $CDCl_3$):

δ [ppm] = 164.3 (C_q), 163.3 (C_q), 157.0 (C_q), 156.2 (C_q), 155.4 (C_q), 151.0 (C_q), 149.6 (C_q), 144.5 (C_q), 140.3 (C_q), 135.4 (C_q), 133.0 (C_q), 132.9 (CH), 132.7 (CH), 131.72 (CH), 131.71 (CH), 129.5 (CH), 129.3 (CH), 128.0 (CH), 127.74 (CH), 127.72 (C_q), 127.70 (C_q), 127.6 (C_q), 127.4 (C_q),

126.9 (CH), 124.5 (C_q), 119.3 (C_q), 119.00 (CH), 118.97 (CH), 118.3 (CH), 118.1 (C_q), 115.2 (CH), 113.5 (C_q), 95.0 (C_q), 92.7 (C_q), 86.9 (C_q), 84.0 (C_q), 61.8 (CH_3), 56.2 (CH_3), 55.8 (CH_3), 35.9 (C_q), 34.6 (C_q), 31.8 (CH_3), 31.3 (CH_3).

ESI-MS (high resolution):

calc.: $[M + H]^+$ 1017.39837 m/z

exp.: $[M + H]^+$ 1017.40130 m/z Δ = 2.88 ppm

mOMeNDI46

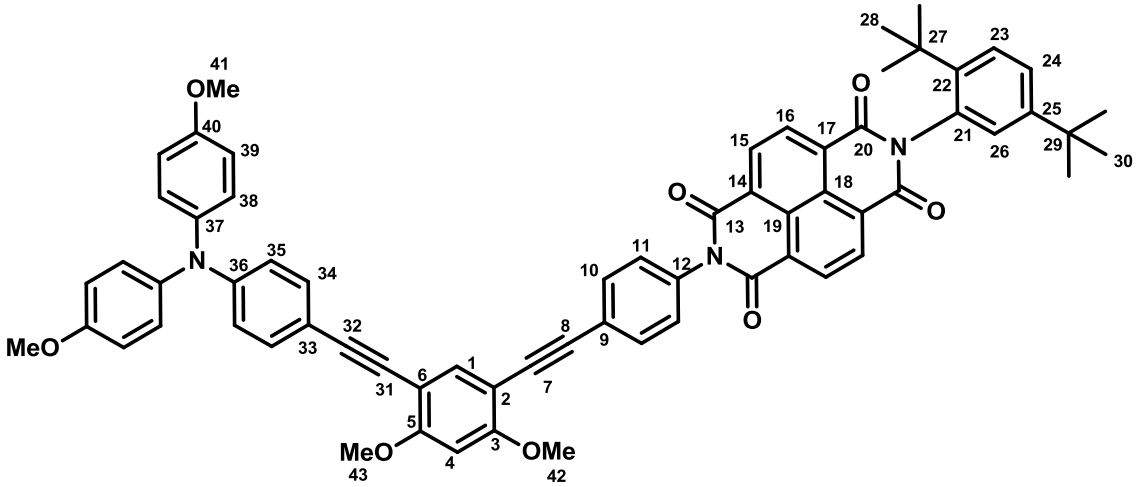

CA: [/].

Following **GPo$_{Me}$**: Compound **19** (85.0 mg, 144 µmol), CuI (547 µg, 2.87 µmol), $Pd(PPh_3)_2Cl_2$ (4.27 mg, 6.09 µmol) were added to NEt_3 (4 ml). **eNDI** (149 mg, 269 µmol) in THF (5 ml) was added to this solution. Flash chromatography on silica gel (DCM:EA, 100:1).

Yield: 117 mg (115 µmol, 80 %), green solid.

Formula: $C_{66}H_{55}N_3O_8$ [1018.16].

^{1}H-NMR (600.1 MHz, CD_2Cl_2):

δ [ppm] = 8.84 (-, 4 H, H-15 a. H-16), 7.72 (AA´, 2 H, H-10), 7.64 (d, $^3J_{HH}$ = 8.6 Hz, 1 H, H-23), 7.60 (s, 1 H, H-4), 7.53 (dd, $^3J_{HH}$ = 8.6 Hz, $^4J_{HH}$ = 2.3 Hz, 1 H, H-24), 7.34 (BB´, 2 H, H-11), 7.29 (AA´, 2 H, H-34), 7.08

(AA´, 4 H, H-38), 7.05 (d, $^4J_{HH}$ = 2.2 Hz, 1 H, H-26), 6.86 (BB´, 4 H, H-39), 6.82 (BB´, 2 H, H-35), 6.51 (s, 1 H, H-1), 3.99 (s, 3 H, H-42), 3.97 (s, 3 H, H-43), 3.79 (s, 6 H, H-41), 1.34 (s, 9 H, H-28), 1.27 (s, 9 H, H-30).

^{13}C-NMR (150.9 MHz, $CDCl_3$):

δ [ppm] = 164.3 (C_q), 163.3 (C_q), 162.0 (C_q), 161.8 (C_q), 156.9 (C_q), 151.0 (C_q), 149.1 (C_q), 144.5 (C_q), 140.5 (C_q), 137.9 (CH), 134.8 (C_q), 133.0 (C_q), 132.6 (CH), 132.5 (CH), 131.70 (CH), 131.69 (CH), 129.4 (CH), 129.2 (CH), 128.0 (CH), 127.8 (C_q), 127.71 (C_q), 127.69 (C_q), 127.6 (CH), 127.4 (C_q), 126.9 (CH), 125.0 (C_q), 119.2 (CH), 115.1 (CH), 114.3 (C_q), 105.8 (C_q), 104.7 (C_q), 95.5 (CH), 93.2 (C_q), 91.6 (C_q), 86.9 (C_q), 83.7 (C_q), 56.53 (CH_3), 56.49 (CH_3), 55.82 (CH_3), 35.9 (C_q), 34.6 (C_q), 31.8 (CH_3), 31.3 (CH_3).

ESI-MS (high resolution):

calc.: $[M + H]^+$ 1017.3984 m/z

exp.: $[M + H]^+$ 1017.3976 m/z Δ = 0.79 ppm

sMeNDI

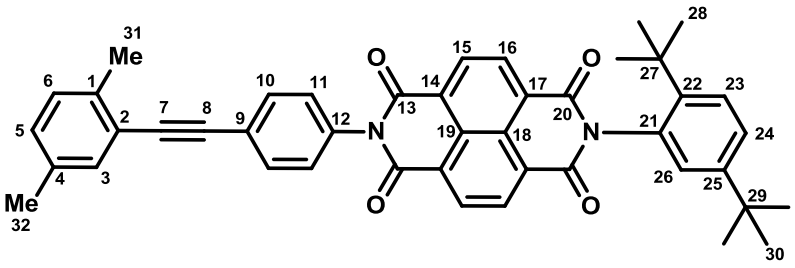

CA: [/].

Following **GP$_{Me}$**: 2-Bromo-*para*-xylene (**sbMe**, 70.0 mg, 378 µmol), **eNDI** (210 mg, 379 µmol), CuI (1.08 mg, 5.67 µmol), $Pd(PPh_3)_2Cl_2$ (5.31 mg, 7.57 µmol), HN^iPr_2 (68.9 mg, 681 µmol) and P^tBu_3 (57.1 µl of a 1.00 M solution in *n*-hexane, 57.1 µmol) were added to 1,4-dioxane (4 ml). Flash chromatography on silica gel (DCM).

Yield: 186 mg (282 µmol, 75 %), yellow solid.

Formula: $C_{44}H_{38}N_2O_4$ [658.78].

^{1}H-NMR (600.1 MHz, CD_2Cl_2):

δ [ppm] = 8.85 (-, 4 H, H-15 a. H-16), 7.76 (AA´, 2 H, H-11), 7.64 (d, $^{3}J_{HH}$ = 8.6 Hz, 1 H, H-23), 7.53 (dd, $^{3}J_{HH}$ = 8.6 Hz, $^{4}J_{HH}$ = 2.3 Hz, 1 H, H-24), 7.38–7.35 (-, 3 H, H-3 a. H-10), 7.17 (d, $^{3}J_{HH}$ = 7.8 Hz, 1 H, H-6), 7.11 (dd, $^{3}J_{HH}$ = 7.8 Hz, $^{4}J_{HH}$ = 1.6 Hz, 1 H, H-5), 7.05 (d, $^{4}J_{HH}$ = 2.2 Hz, 1 H, H-26), 2.51 (s, 3 H, H- 31), 2.34 (s, 3 H, H-32), 1.34 (s, 9 H, H-28), 1.28 (s, 9 H, H-30).

^{13}C-NMR (150.9 MHz, CD_2Cl_2):

δ [ppm] = 164.3 (C_q), 163.3 (C_q), 151.0 (C_q), 144.5 (C_q), 137.7 (C_q), 135.7 (C_q), 135.0 (C_q), 133.0 (C_q), 132.8 (CH), 132.7 (CH), 131.7 (2 × CH), 130.0 (CH), 129.8 (CH), 129.5 (CH), 129.2 (CH), 128.0 (CH), 127.72 (C_q) 127.71 (C_q), 127.6 (C_q), 127.4 (C_q), 126.9 (CH), 124.9 (C_q), 122.7 (C_q), 92.3 (C_q), 90.2 (C_q), 35.9 (C_q), 34.6 (C_q), 31.8 (CH_3) 31.3 (CH_3), 20.9 (CH_3) 31.3 (CH_3).

ESI-MS (high resolution):

calc.: $[M + H]^+$ 659.29043 m/z

exp.: $[M + H]^+$ 659.29065 m/z Δ = 0.33 ppm

1-{4-[*N*,*N*-Di(4-methoxyphenyl)amino]phenylethynyl}(4-bromo-2,5-dimethyl)-benzene (20)

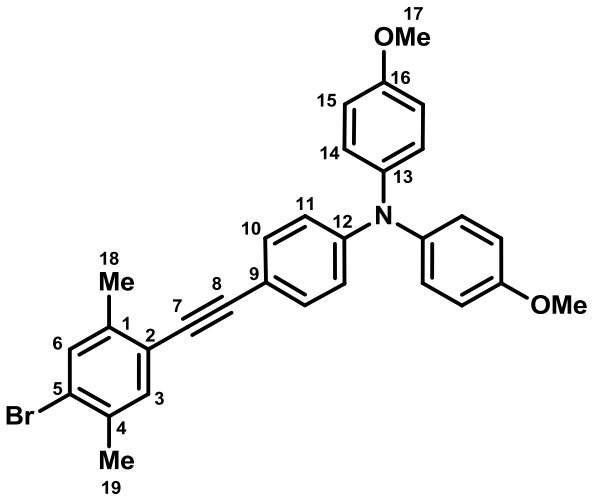

CA: [/].

Following **GP_{DPA}**: 2,5-Dibromo-*para*-xylene (**pbMe**, 1.00 g, 3.79 mmol), CuI (2.89 mg, 15.2 µmol), $Pd(PPh_3)_2Cl_2$ (21.3 mg, 30.3 µmol) were dissolved in THF (35 ml) and NEt_3 (20 ml). **eTAA** (250 mg, 759 µmol) dissolved in THF (20 ml) was added. Flash chromatography on silica gel (DCM:PE, 1:1).

Yield: 288 mg (562 µmol, 74 %), yellow solid.

Formula: $C_{30}H_{26}BrNO_2$ [512.44].

^{1}H-NMR (400.1 MHz, $(CD_3)_2CO$):

δ [ppm] = 7.48 (-, 1 H, H-3), 7.38 (s, 1 H, H-6), 7.34 (AA´, 2 H, H-10), 7.11 (AA´, 4 H, H-14), 6.95 (BB´, 4 H, H-15), 6.79 (BB´, 2 H, H-11), 3.80 (s, 6 H, H-17), 2.42 (s, 3 H, H-18), 2.33 (s, 3 H, H-19).

^{13}C-NMR (100.6 MHz, $(CD_3)_2CO$):

δ [ppm] = 157.8 (C_q), 150.3 (C_q), 140.7 (C_q), 139.8 (C_q), 135.9 (C_q), 134.1 (CH), 133.8 (CH), 131.1 (CH), 128.4 (CH), 124.6 (C_q), 123.9 (C_q), 119.1 (CH), 115.8 (CH), 114.1 (C_q), 95.7 (C_q), 86.6 (C_q), 55.7 (CH_3), 21.2 (CH_3), 20.0 (CH_3).

MALDI-MS: calc.: $[M]^+$ 513.11 m/z
exp.: $[M]^+$ 513.12 m/z

1-{4-[*N*,*N*-Di(4-methoxyphenyl)amino]phenylethynyl}(3-bromo-2,5-dimethyl)-benzene (21)

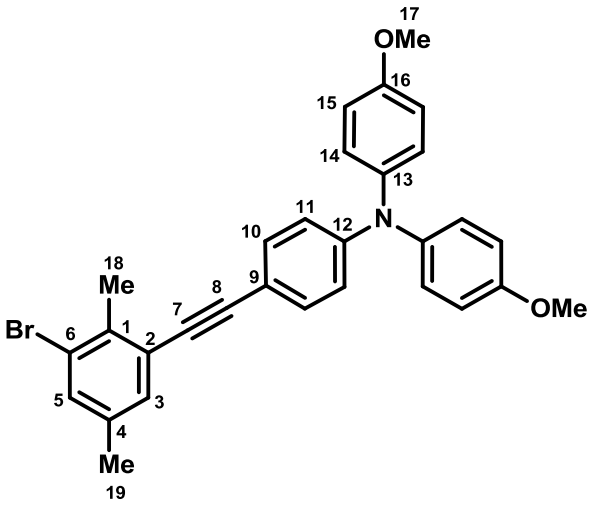

CA: [/].

Following **GP$_{DPA}$**: 2,6-Dibromo-*para*-xylene (**mbMe**, 1.00 g, 3.79 mmol), CuI (2.89 mg, 15.2 µmol), $Pd(PPh_3)_2Cl_2$ (21.3 mg, 30.3 µmol) were dissolved in THF (35 ml) and NEt_3 (20 ml). **eTAA** (250 mg, 759 µmol) dissolved in THF (20 ml) was added. Flash chromatography on silica gel (DCM:PE, 1:1).

Yield: 310 mg (605 µmol, 80 %), yellow solid.

Formula: $C_{30}H_{26}BrNO_2$ [512.44].

^{1}H-NMR (400.1 MHz, $(CD_3)_2CO$):

δ [ppm] = 7.39 (s, 1 H, H-3), 7.34 (AA´, 2 H, H-10), 7.29 (s, 1 H, H-5), 7.11 (AA´, 4 H, H-14), 6.94 (BB´, 4 H, H-15), 6.79 (BB´, 2 H, H-11), 3.80 (s, 6 H, H-17), 2.53 (s, 3 H, H-18), 2.29 (s, 3 H, H-19).

^{13}C-NMR (100.6 MHz, $(CD_3)_2CO$):

δ [ppm] = 157.8 (C_q), 150.3 (C_q), 140.6 (C_q), 138.2 (C_q), 136.4 (C_q), 133.5 (CH), 133.2 (CH), 132.3 (CH), 128.4 (CH), 126.0 (C_q), 125.4 (C_q), 119.1 (CH), 115.8 (CH), 113.8 (C_q), 95.3 (C_q), 87.2 (C_q), 55.7 (CH_3), 21.0 (CH_3), 20.3 (CH_3).

MALDI-MS: calc.: $[M]^+$ 513.11 m/z
exp.: $[M]^+$ 513.11 m/z

pMeNDI

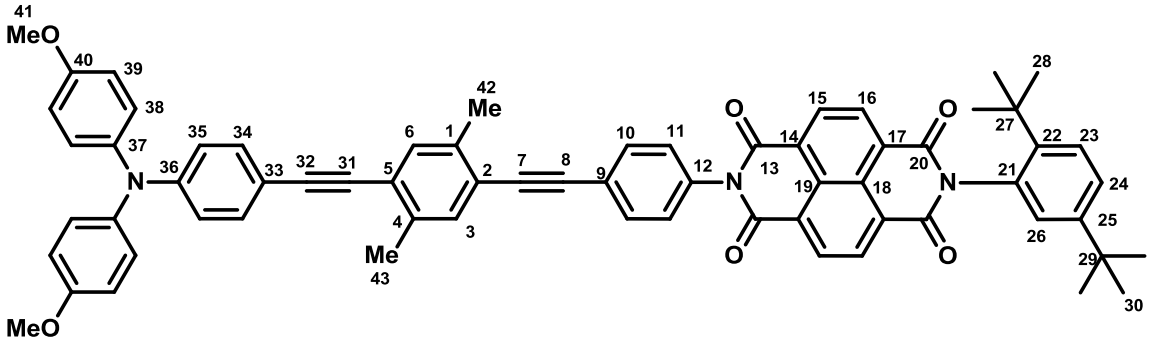

CA: [/].

Following **GP$_{Me}$**: Compound **20** (80.0 mg, 156 µmol), **eNDI** (173 mg, 312 µmol), CuI (446 µg, 2.34 µmol), $Pd(PPh_3)_2Cl_2$ (2.19 mg, 3.12 µmol), HN^iPr_2 (28.4 mg, 281 µmol) and P^tBu_3 (23.6 µl of a 1.00 M solution in *n*-hexane, 23.6 µmol) were added to 1,4-dioxane (4 ml). Flash chromatography on silica gel (DCM) and GPC.

Yield: 150 mg (152 µmol, 97 %), green solid.

Formula: $C_{66}H_{55}N_3O_6$ [986.16].

^{1}H-NMR (600.1 MHz, CD_2Cl_2):

δ [ppm] = 8.85 (-, 4 H, H-15 a. H-16), 7.76 (AA´, 2 H, H-10), 7.64 (d, $^3J_{HH}$ = 8.6 Hz, 1 H, H-23), 7.53 (dd, $^3J_{HH}$ = 8.6 Hz, $^4J_{HH}$ = 2.3 Hz, 1 H, H-24), 7.42 (s, 1 H, H-6) 7.38–7.36 (-, 3 H, H-3 a. H-11), 7.29 (AA´, 2 H, H-34), 7.09 (AA´, 4 H, H-38), 7.05 (d, $^4J_{HH}$ = 2.2 Hz, 1 H, H-26), 6.87 (BB´, 4 H, H-39), 6.83 (BB´, 2 H, H-35), 3.80 (s, 6 H, H-41), 2.50 (s, 3 H, H-42), 2.46, (s, 3 H, H-43), 1.34 (s, 9 H, H-28), 1.28 (s, 9 H, H-30).

^{13}C-NMR (150.9 MHz, CD_2Cl_2):

δ [ppm] = 164.3 (C_q), 163.3 (C_q), 157.0 (C_q), 151.0 (C_q), 149.5 (C_q), 144.6 (C_q), 140.4 (C_q), 138.0 (C_q), 137.5 (C_q), 135.1 (C_q), 133.00 (CH), 132.97 (C_q), 132.8 (CH), 132.6 (CH), 132.5 (CH), 131.7 (2 × CH), 129.5 (CH), 129.3 (CH), 128.0 (CH), 127.72 (C_q), 127.71 (C_q), 127.66 (CH), 127.63 (C_q), 127.4 (C_q), 126.9 (CH), 124.7 (C_q), 124.4 (C_q), 123.3 (C_q), 119.1 (CH), 115.2 (CH), 113.9 (C_q), 96.0 (C_q), 93.7 (C_q), 90.0 (C_q), 87.2 (C_q),

55.8 (CH_3), 35.9 (C_q), 34.6 (C_q), 31.9 (CH_3), 31.3 (CH_3), 20.24 (CH_3), 20.23 (CH_3).

ESI-MS (high resolution):

calc.: $[M + H]^+$ 985.40854 m/z

exp.: $[M + H]^+$ 985.40651 m/z Δ = 2.06 ppm

mMeNDI

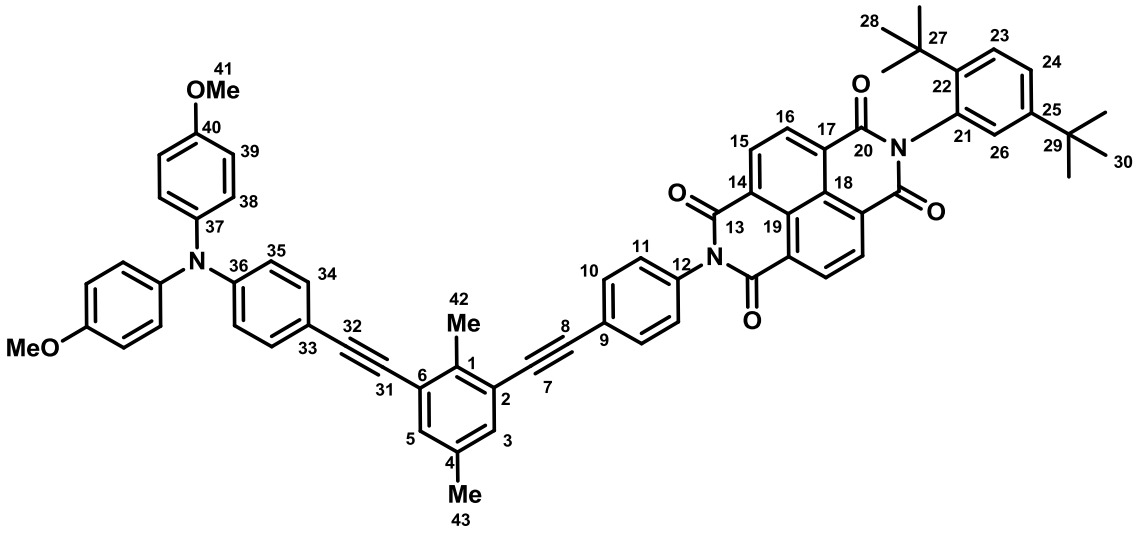

CA: [/].

Following **GP$_{Me}$**: Compound **21** (100 mg, 195 µmol), **eNDI** (119 mg, 215 µmol), CuI (557 µg, 2.92 µmol), $Pd(PPh_3)_2Cl_2$ (2.74 mg, 3.90 µmol), HN^iPr_2 (35.5 mg, 351 µmol) and P^tBu_3 (29.3 µl of a 1.00 M solution in *n*-hexane, 29.3 µmol) were added to 1,4-dioxane (5 ml). Flash chromatography on silica gel (DCM) and GPC.

Yield: 180 mg (182 µmol, 93 %), green solid.

Formula: $C_{66}H_{55}N_3O_6$ [986.16].

^{1}H-NMR (600.1 MHz, CD_2Cl_2):

δ [ppm] = 8.84 (-, 4 H, H-15 a. H-16), 7.76 (AA´, 2 H, H-11), 7.64 (d, $^3J_{HH}$ = 8.7 Hz, 1 H, H-23), 7.53 (dd, $^3J_{HH}$ = 8.6 Hz, $^4J_{HH}$ = 2.3 Hz, 1 H, H-24), 7.37 (BB´, 2 H, H-10), 7.35–7.32 (-, 4 H, H-3 a. H-5 a. H-34), 7.09 (AA´, 4 H, H-38), 7.05 (d, $^4J_{HH}$ = 2.2 Hz, 1 H, H-26), 6.87 (BB´, 4 H, H-39),

6.83 (BB´, 2 H, H-35), 3.79 (s, 6 H, H-41), 2.68 (s, 3 H, H-42), 2.33, (s, 3 H, H-43), 1.34 (s, 9 H, H-28), 1.28 (s, 9 H, H-30).

^{13}C-NMR (150.9 MHz, CD_2Cl_2):

δ [ppm] = 164.3 (C_q), 163.3 (C_q), 157.0 (C_q), 151.0 (C_q), 149.4 (C_q), 144.6 (C_q), 140.4 (C_q), 139.3 (C_q), 135.7 (C_q), 135.1 (C_q), 133.00 (CH), 132.97 (C_q), 132.8 (CH), 132.6 (CH), 132.5 (CH), 131.7 (2 × CH), 129.5 (CH), 129.3 (CH), 128.0 (CH), 127.72 (C_q), 127.71 (C_q), 127.66 (CH), 127.63 (C_q), 127.4 (C_q), 126.9 (CH), 124.7 (C_q), 124.4 (C_q), 123.3 (C_q), 119.1 (CH), 115.2 (CH), 113.9 (C_q), 94.4 (C_q), 92.4 (C_q), 89.9 (C_q), 87.0 (C_q), 55.8 (CH_3), 35.9 (C_q), 34.6 (C_q), 31.9 (CH_3), 31.3 (CH_3), 20.7 (CH_3), 18.9 (CH_3).

ESI-MS (high resolution):

calc.: $[M + H]^+$ 985.40854 m/z

exp.: $[M + H]^+$ 985.40844 m/z Δ = 0.10 ppm

sClNDI

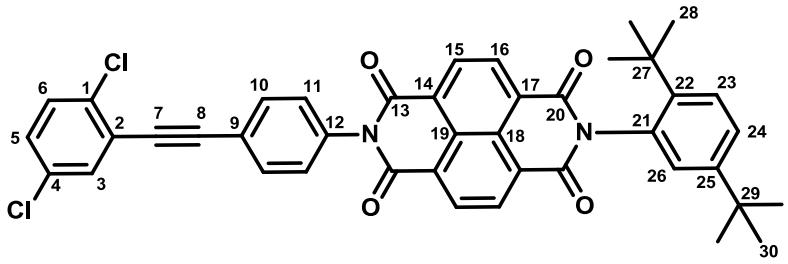

CA: [/].

Following **GP$_{Cl}$**: Bromo-2,5-dichlorobenzene (**sbCl**, 70.0 mg, 310 µmol), **eNDI** (172 mg, 310 µmol), CuI (2.83 mg, 14.9 µmol), $Pd(C_6H_5CN)_2Cl_2$ (7.73 mg, 20.2 µmol), HN^iPr_2 (69.0 mg, 682 µmol) and P^tBu_3 (47.0 µl of a 1.00 M solution in *n*-hexane, 47.0 µmol) were added to 1,4-dioxane (4 ml). Flash chromatography on silica gel (DCM).

Yield: 177 mg (253 µmol, 82 %), yellow solid.

Formula: $C_{42}H_{32}Cl_2N_2O_4$ [699.62].

^{1}H-NMR (600.1 MHz, CD_2Cl_2):

δ [ppm] = 8.85 (-, 4 H, H-15 a. H-16), 7.79 (AA´, 2 H, H-11), 7.65–7.62 (-, 2 H, H-3 a. H-23), 7.53 (dd, $^{3}J_{HH}$ = 8.6 Hz, $^{4}J_{HH}$ = 2.2 Hz, 1 H, H-24), 7.42 (d, $^{3}J_{HH}$ = 8.6 Hz, 1 H, H-6), 7.40 (BB´, 2 H, H-10), 7.31 (dd, $^{3}J_{HH}$ = 8.6 Hz, $^{4}J_{HH}$ = 2.5 Hz, 1 H, H-5), 7.05 (d, $^{4}J_{HH}$ = 2.2 Hz, 1 H, H-26), 1.34 (s, 9 H, H-28), 1.27 (s, 9 H, H-30).

^{13}C-NMR (150.9 MHz, CD_2Cl_2):

δ [ppm] = 164.3 (C_q), 163.3 (C_q), 151.0 (C_q), 144.5 (C_q), 135.9 (C_q), 134.8 (C_q), 133.2 (CH), 133.1 (CH), 133.0 (C_q), 132.8 (C_q), 131.74 (CH), 131.71 (CH), 130.9 (CH), 130.2 (CH), 129.5 (CH), 129.4 (CH), 128.0 (CH), 127.72 (C_q) 127.71 (C_q), 127.66 (C_q), 127.3 (C_q), 126.9 (CH), 124.7 (C_q), 123.7 (C_q), 95.0 (C_q), 86.4 (C_q), 35.9 (C_q), 34.6 (C_q), 31.8 (CH_3) 31.3 (CH_3).

ESI-MS (high resolution):

calc.: $[M + H]^+$ 699.18119 m/z

exp.: $[M + H]^+$ 699.18154 m/z Δ = 0.50 ppm

1-{4-[*N*,*N*-Di(4-methoxyphenyl)amino]phenylethynyl}(4-bromo-2,5-dichloro)-benzene (22)

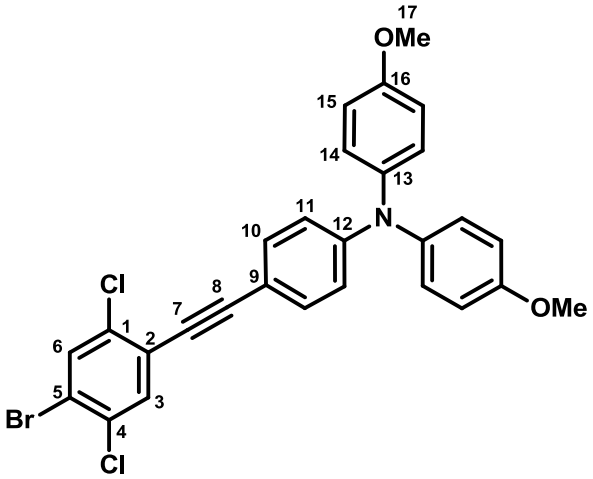

CA: [/].

Following **GP_{DPA}**: 1,4-Dibromo-2,5-dichlorobenzene (**pbCl**, 1.00 g, 3.28 mmol), CuI (2.50 mg, 13.1 µmol), $Pd(PPh_3)_2Cl_2$ (18.4 mg, 26.2 µmol) were dissolved in THF (35 ml) and NEt_3

(20 ml). **eTAA** (216 mg, 656 µmol) dissolved in THF (20 ml) was added. Flash chromatography on silica gel (DCM:PE, 1:2).

Yield: 346 mg (625 µmol, 95 %), yellow oil/solid.

Formula: $C_{28}H_{20}BrCl_2NO_2$ [553.27].

^{1}H-NMR (400.1 MHz, $(CD_3)_2CO$):

δ [ppm] = 7.90 (d, $^5J_{HH}$ = 0.3 Hz, 1 H, 6-H), 7.77 (d, $^5J_{HH}$ = 0.3 Hz, 1 H, 3-H), 7.38 (AA´, 2 H, H-10), 7.14 (AA´, 4 H, H-14), 6.96 (BB´, 4 H, H-15), 6.78 (BB´, 2 H, H-11), 3.81 (s, 6 H, H-17).

^{13}C-NMR (100.6 MHz, $(CD_3)_2CO$):

δ [ppm] = 158.0 (C_q), 150.1 (C_q), 140.4 (C_q), 134.8 (C_q), 134.6 (CH), 134.0 (CH), 133.57 (CH), 133.55 (C_q), 128.7 (CH), 125.3 (C_q), 122.3 (C_q), 118.6 (CH), 115.9 (CH), 112.4 (C_q), 98.9 (C_q), 83.7 (C_q), 55.7 (CH_3).

MALDI-MS: calc.: $[M]^+$ 553.00 m/z
exp.: $[M]^+$ 553.00 m/z

1-{4-[*N*,*N*-Di(4-methoxyphenyl)amino]phenylethynyl}(2-bromo-2,5-dicloro)-benzene (23)

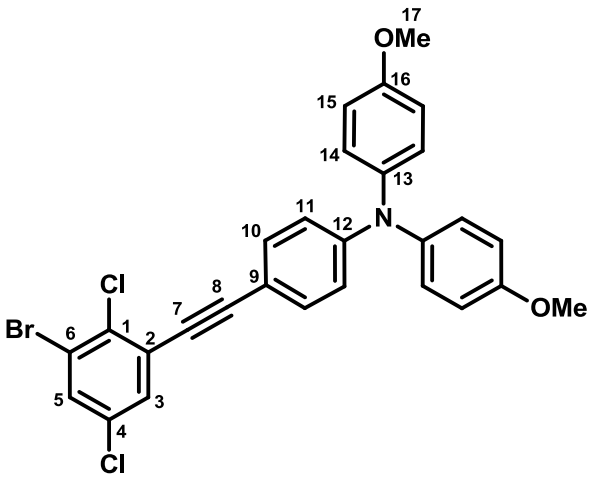

CA: [/].

Following **GP_{DPA}**: 1,3-Dibromo-2,5-dichlorobenzene (**mbCl**, 1.00 g, 3.28 mmol), CuI (2.50 mg, 13.1 µmol), $Pd(PPh_3)_2Cl_2$ (18.4 mg, 26.2 µmol) were dissolved in THF (35 ml) and NEt_3 (20 ml). **eTAA** (216 mg, 656 µmol) dissolved in THF (20 ml) was added. Flash chromatography on silica gel (DCM:PE, 1:2).

Yield: 340 mg (615 µmol, 94 %), yellow solid.

Formula: $C_{28}H_{20}BrCl_2NO_2$ [553.27].

^{1}H-NMR (400.1 MHz, $(CD_3)_2CO$):

δ [ppm] = 7.73 (d, $^4J_{HH}$ = 2.4 Hz, 1 H, 5-H), 7.60 (d, $^4J_{HH}$ = 2.4 Hz, 1 H, 3-H), 7.36 (AA´, 2 H, H-10), 7.12 (AA´, 4 H, H-14), 6.94 (BB´, 4 H, H-15), 6.78 (BB´, 2 H, H-11), 3.80 (s, 6 H, H-17).

^{13}C-NMR (100.6 MHz, $(CD_3)_2CO$):

δ [ppm] = 158.0 (C_q), 150.1 (C_q), 140.3 (C_q), 134.5 (C_q), 133.6 (CH), 133.4 (C_q), 133.0 (CH), 132.1 (CH), 128.6 (CH), 127.4 (C_q), 124.1 (C_q), 118.6 (CH), 115.8 (CH), 112.3 (C_q), 98.9 (C_q), 84.5 (C_q), 55.7 (CH_3).

MALDI-MS: calc.: $[M]^+$ 553.00 m/z

exp.: $[M]^+$ 552.99 m/z

pClNDI

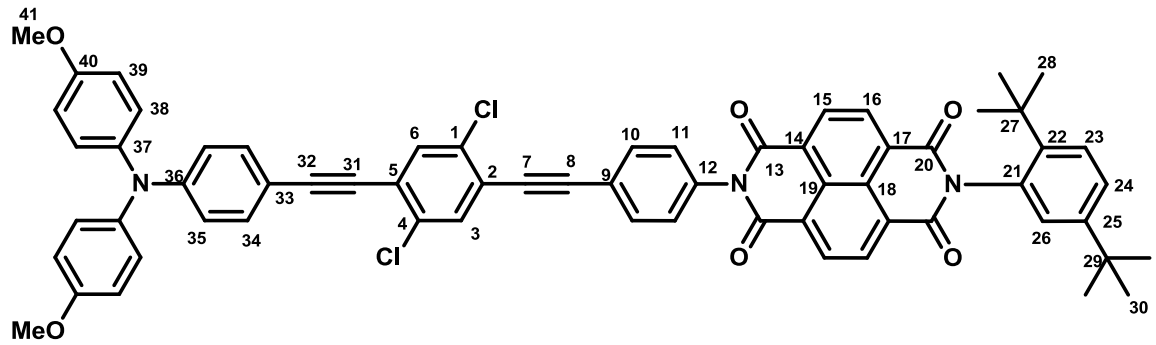

CA: [/].

Following **GP_{Cl}**: Compound **22** (100 mg, 181 µmol), **eNDI** (100 mg, 180 µmol), CuI (1.65 mg, 8.66 µmol), $Pd(C_6H_5CN)_2Cl_2$ (4.51 mg, 11.7 µmol), HN^iPr_2 (40.2 mg, 398 µmol) and P^tBu_3

(27.1 µl of a 1.00 M solution in *n*-hexane, 27.1 µmol) were added to 1,4-dioxane (5 ml). Flash chromatography on silica gel (DCM) and GPC.

Yield: 171 mg (167 µmol, 93 %), green solid.

Formula: $C_{64}H_{49}Cl_2N_3O_6$ [1027.00].

^{1}H-NMR (600.1 MHz, CD_2Cl_2):

δ [ppm] = 8.85 (-, 4 H, H-15 a. H-16), 7.80 (AA´, 2 H, H-10), 7.67 (s, 1 H, H-3), 7.64 (d, $^3J_{HH}$ = 8.6 Hz, 1 H, H-23), 7.61 (s, 1 H, H-6), 7.53 (dd, $^3J_{HH}$ = 8.6 Hz, $^4J_{HH}$ = 2.3 Hz, 1 H, H-24), 7.40 (BB´, 2 H, H-11), 7.35 (AA´, 2 H, H-34), 7.10 (AA´, 4 H, H-38), 7.06 (d, $^4J_{HH}$ = 2.2 Hz, 1 H, H-26), 6.88 (BB´, 4 H, H-39), 6.83 (BB´, 2 H, H-35), 3.80 (s, 6 H, H-41), 1.34 (s, 9 H, H-28), 1.28 (s, 9 H, H-30).

^{13}C-NMR (150.9 MHz, CD_2Cl_2):

δ [ppm] = 164.3 (C_q), 163.3 (C_q), 157.2 (C_q), 151.0 (C_q), 150.2 (C_q), 144.5 (C_q), 140.0 (C_q), 135.9 (C_q), 134.3 (C_q), 133.8 (C_q), 133.5 (CH), 133.10 (CH), 133.07 (CH), 133.04 (CH), 133.0 (C_q), 131.74 (CH), 131.71 (CH), 129.45 (CH), 129.44 (CH), 128.0 (CH), 127.9 (CH), 127.72 (C_q), 127.70 (C_q), 127.66 (C_q), 127.3 (C_q), 126.9 (CH), 125.4 (C_q), 123.7 (C_q), 123.2 (C_q), 118.6 (CH), 115.2 (CH), 112.3 (C_q), 99.2 (C_q), 96.1 (C_q), 86.6 (C_q), 84.4 (C_q), 55.8 (CH_3), 35.9 (C_q), 34.6 (C_q), 31.9 (CH_3), 31.3 (CH_3).

ESI-MS (high resolution):

calc.: $[M + H]^+$ 1025.29929 m/z

exp.: $[M + H]^+$ 1025.29840 m/z Δ = 0.87 ppm

mClNDI

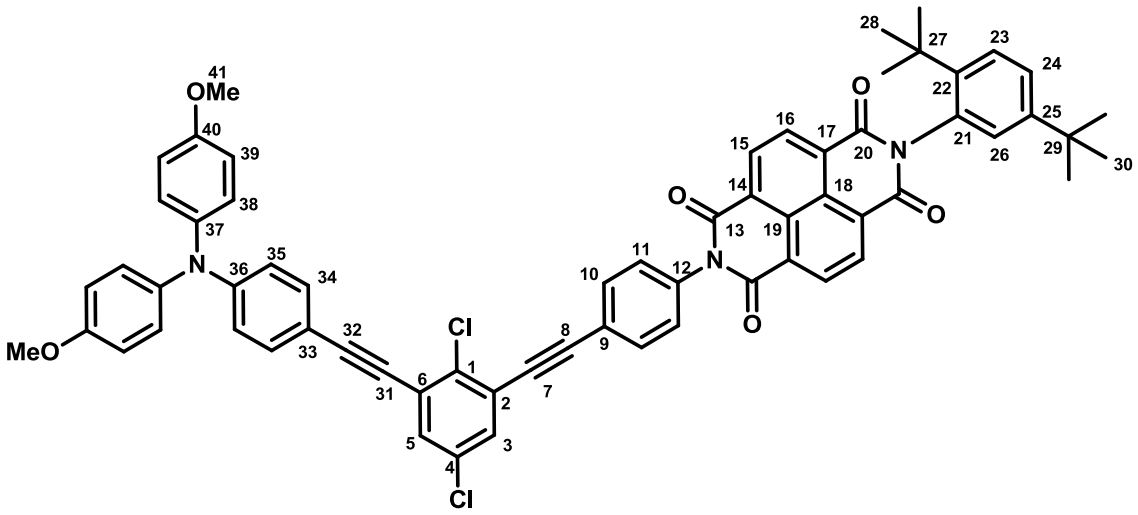

CA: [/].

Following **GP$_{Cl}$**: Compound **23** (80.0 mg, 145 µmol), **eNDI** (80.0 mg, 144 µmol), CuI (1.32 mg, 6.93 µmol), $Pd(C_6H_5CN)_2Cl_2$ (3.61 mg, 9.41 µmol), HN^iPr_2 (32.2 mg, 318 µmol) and P^tBu_3 (21.7 µl of a 1.00 M solution in *n*-hexane, 21.7 µmol) were added to 1,4-dioxane (4 ml). Flash chromatography on silica gel (DCM) and GPC.

Yield: 123 mg (120 µmol, 81 %), green solid.

Formula: $C_{64}H_{49}Cl_2N_3O_6$ [1027.00].

^{1}H-NMR (600.1 MHz, CD_2Cl_2):

δ [ppm] = 8.84 (-, 4 H, H-15 a. H-16), 7.80 (AA´, 2 H, H-10), 7.64 (d, $^3J_{HH}$ = 8.6 Hz, 1 H, H-23), 7.54 (d, $^4J_{HH}$ = 2.5 Hz, 1 H, H-3), 7.53 (dd, $^3J_{HH}$ = 8.6 Hz, $^4J_{HH}$ = 2.3 Hz, 1 H, H-24), 7.51 (d, $^4J_{HH}$ = 2.5 Hz, 1 H, H-5), 7.40 (BB´, 2 H, H-11), 7.36 (AA´, 2 H, H-34), 7.10 (AA´, 4 H, H-38), 7.06 (d, $^4J_{HH}$ = 2.2 Hz, 1 H, H-26), 6.88 (BB´, 4 H, H-39), 6.83 (BB´, 2 H, H-35), 3.80 (s, 6 H, H-41), 1.34 (s, 9 H, H-28), 1.28 (s, 9 H, H-30).

^{13}C-NMR (150.9 MHz, CD_2Cl_2):

δ [ppm] = 164.3 (C_q), 163.3 (C_q), 157.2 (C_q), 151.0 (C_q), 150.2 (C_q), 144.5 (C_q), 140.1 (C_q), 135.9 (C_q), 135.7 (C_q), 133.2 (CH), 133.1 (CH), 133.0 (C_q), 132.5 (CH), 132.3 (C_q), 132.0 (CH), 131.74 (CH), 131.71 (CH), 130.0 (CH), 129.5 (CH), 128.0 (CH), 127.9 (CH), 127.72 (C_q), 127.70 (C_q),

127.66 (C_q), 127.3 (C_q), 126.9 (CH), 126.3 (C_q), 125.1 (C_q), 123.6 (C_q), 118.6 (CH), 115.2 (CH), 112.3 (C_q), 97.8 (C_q), 95.1 (C_q), 86.5 (C_q), 84.1 (C_q), 55.8 (CH_3), 35.9 (C_q), 34.6 (C_q), 31.9 (CH_3), 31.3 (CH_3).

ESI-MS (high resolution):

calc.: $[M + H]^+$ 1025.29929 m/z

exp.: $[M + H]^+$ 1025.29995 m/z Δ = 0.64 ppm

sCNNDI

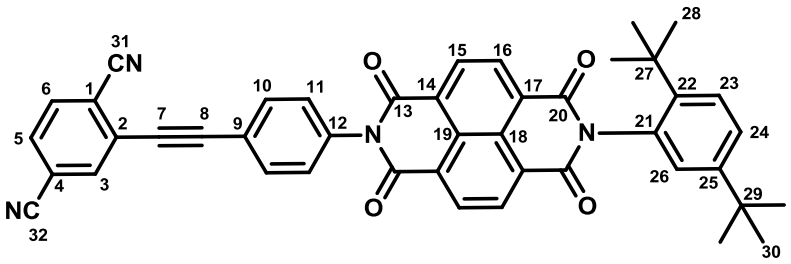

CA: [/].

Following **GP$_{CN}$**: **eNDI** (161 mg, 290 µmol), CuI (966 µg, 5.07 µmol), $Pd(PPh_3)_2Cl_2$ (7.12 mg, 10.1 µmol) were added to NEt_3 (5 ml) 2-Bromotetrephthonitrile (**sbCN**, 50.0 mg, 242 µmol) in THF (3 ml) was added to this solution. Flash chromatography on silica gel (DCM).

Yield: 122 mg (179 µmol, 74 %), yellow solid.

Formula: $C_{44}H_{32}N_4O_4$ [680.75].

^{1}H-NMR (400.1 MHz, CD_2Cl_2):

δ [ppm] = 8.85 (-, 4 H, H-15 a. H-16), 7.99 (dd, $^4J_{HH}$ = 1.6 Hz, $^5J_{HH}$ = 0.6 Hz, 1 H, H-3), 7.86 (AA´, 2 H, H-11), 7.84 (dd, $^3J_{HH}$ = 8.1 Hz, $^5J_{HH}$ = 0.6 Hz, 1 H, H-6), 7.74 (dd, $^3J_{HH}$ = 8.1 Hz, $^4J_{HH}$ = 1.6 Hz, 1 H, H-5), 7.64 (d, $^3J_{HH}$ = 8.6 Hz, 1 H, H-23), 7.53 (dd, $^3J_{HH}$ = 8.6 Hz, $^4J_{HH}$ = 2.2 Hz, 1 H, H-24), 7.44 (BB´, 2 H, H-10), 7.05 (d, $^4J_{HH}$ = 2.2 Hz, 1 H, H-26), 1.34 (s, 9 H, H-28), 1.27 (s, 9 H, H-30).

^{13}C-NMR (150.9 MHz, CD_2Cl_2):

δ [ppm] = 164.2 (C_q), 163.2 (C_q), 151.0 (C_q), 144.5 (C_q), 136.7 (C_q), 135.8 (CH), 133.9 (CH), 133.5 (CH), 132.9 (C_q), 132.0 (CH), 131.8 (CH), 131.7 (CH), 129.6 (CH), 129.5 (CH), 128.4 (C_q), 128.0 (CH), 127.73 (C_q), 127.71 (C_q) 127.70 (C_q), 127.25 (C_q), 126.9 (CH), 122.5 (C_q), 119.6 (C_q), 117.1 (C_q), 117.0 (C_q), 116.5 (C_q), 97.5 (C_q), 85.2 (C_q), 35.9 (C_q), 34.6 (C_q), 31.8 (CH_3) 31.3 (CH_3).

ESI-MS (high resolution):

calc.: $[M + H]^+$ 681.24963 m/z

exp.: $[M + H]^+$ 681.24975 m/z Δ = 0.18 ppm

Compound (24)

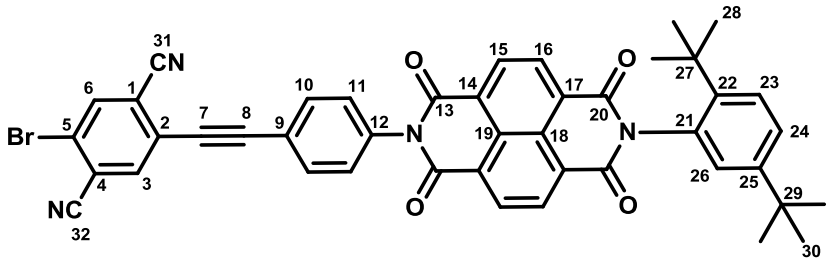

CA: [/].

Following **GP_{CN}**: 2,5-Dibromotetrephthonitrile (**pbCN**, 140.0 mg, 490 µmol), CuI (979 µg, 5.14 µmol), $Pd(PPh_3)_2Cl_2$ (7.22 mg, 10.3 µmol) were added to NEt_3 (7 ml) **eNDI** (136 mg, 245 µmol) in THF (3 ml) was added to this solution. Flash chromatography on silica gel (DCM).

Yield: 152.0 mg (68.5 µmol, 82 %), yellow solid.

Formula: $C_{44}H_{31}BrN_4O_4$ [759.65].

^{1}H-NMR (400.1 MHz, CD_2Cl_2):

δ [ppm] = 8.85 (-, 4 H, H-15 a. H-16), 8.05 (d, $^5J_{HH}$ = 0.4 Hz, 1 H, H-6), 7.97 (d, $^5J_{HH}$ = 0.4 Hz, 1 H, H-3), 7.85 (AA´, 2 H, H-11), 7.64 (d, $^3J_{HH}$ = 8.6 Hz, 1 H, H-23), 7.53 (dd, $^3J_{HH}$ = 8.6 Hz, $^4J_{HH}$ = 2.3 Hz, 1 H, H-24), 7.44 (BB´,

2 H, H-10), 7.06 (d, $^4J_{HH}$ = 2.2 Hz, 1 H, H-26), 1.34 (s, 9 H, H-28) 1.28 (s, 9 H, H-30).

^{13}C-NMR (100.6 MHz, CD_2Cl_2):

δ [ppm] = 164.7 (C_q), 163.2 (C_q), 151.0 (C_q), 144.5 (C_q), 137.4 (CH), 137.2 (CH), 136.8 (C_q), 133.5 (CH), 132.9 (C_q), 131.8 (CH), 131.7 (CH), 129.7 (CH), 129.4 (CH), 128.0 (CH), 127.71 (C_q), 127.70 (C_q), 127.69 (C_q), 127.2 (C_q), 127.0 (C_q), 126.9 (CH), 124.9 (C_q), 122.3 (C_q), 120.5 (C_q), 120.4 (C_q), 115.7 (C_q), 115.3 (C_q), 98.5 (C_q), 84.6 (C_q), 35.9 (C_q), 34.6 (C_q), 31.8 (CH_3) 31.3 (CH_3).

EI-MS: calc.: $[M - C_4H_9]^+$ 703.1 m/z
exp.: $[M - C_4H_9]^+$ 703.0 m/z

Compound (25)

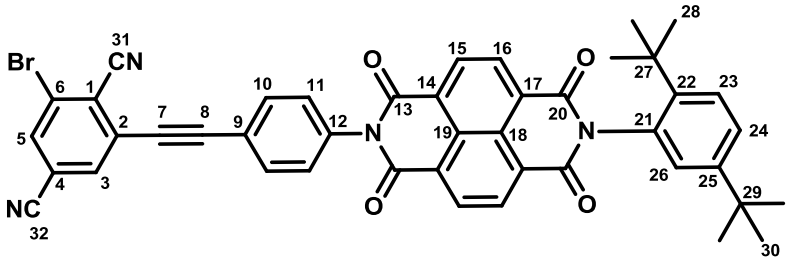

CA: [/].

Following **GP_{CN}**: 2,6-Dibromotetrephthonitrile (**mbCN**, 140.0 mg, 490 µmol), CuI (979 µg, 5.14 µmol), $Pd(PPh_3)_2Cl_2$ (7.22 mg, 10.3 µmol) were added to NEt_3 (7 ml) **eNDI** (136 mg, 245 µmol) in THF (3 ml) was added to this solution. Flash chromatography on silica gel (DCM).

Yield: 130 mg (171 µmol, 70 %), yellow solid.

Formula: $C_{44}H_{31}BrN_4O_4$ [759.65].

^{1}H-NMR (400.1 MHz, CD_2Cl_2):

δ [ppm] = 8.85 (-, 4 H, H-15 a. H-16), 7.95 (d, $^4J_{HH}$ = 1.4 Hz, 1 H, H-5), 7.93 (d, $^4J_{HH}$ = 1.4 Hz, 1 H, H-3), 7.86 (AA´, 2 H, H-11), 7.64 (d, $^3J_{HH}$ = 8.6 Hz, 1

H, H-23), 7.53 (dd, $^{3}J_{HH}$ = 8.6 Hz, $^{4}J_{HH}$ = 2.3 Hz, 1 H, H-24), 7.45 (BB´, 2 H, H-10), 7.06 (d, $^{4}J_{HH}$ = 2.2 Hz, 1 H, H-26), 1.34 (s, 9 H, H-28) 1.28 (s, 9 H, H-30).

^{13}C-NMR (100.6 MHz, CD_2Cl_2):

δ [ppm] = 164.2 (C_q), 163.2 (C_q), 151.0 (C_q), 144.5 (C_q), 137.0 (C_q), 135.4 (CH), 134.2 (CH), 133.6 (CH), 132.9 (C_q), 131.8 (CH), 131.7 (CH), 130.4 (C_q), 129.7 (CH), 129.4 (CH), 128.0 (CH), 127.72 (C_q), 127.71 (C_q), 127.70 (C_q) 127.2 (C_q), 126.9 (CH), 126.6 (C_q), 122.7 (C_q), 122.1 (C_q), 117.7 (C_q), 115.9 (C_q), 115.3 (C_q), 98.7 (C_q), 85.0 (C_q), 35.9 (C_q), 34.6 (C_q), 31.8 (CH_3) 31.3 (CH_3).

EI-MS: calc.: $[M - C_4H_9]^+$ 703.1 m/z
exp.: $[M - C_4H_9]^+$ 703.0 m/z

pCNNDI

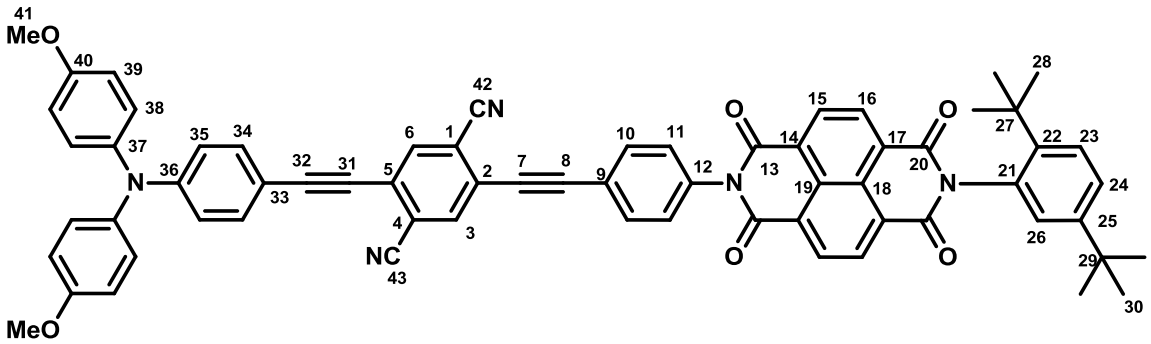

CA: [/].

Following **GP_{CN}**: Compound **24** (48.0 mg, 63.2 µmol), CuI (253 µg, 1.33 µmol), $Pd(PPh_3)_2Cl_2$ (1.86 mg, 2.65 µmol) were added to THF (2.5 ml). **eTAA** (62.4 mg, 190 µmol in NEt_3 (4 ml) was added to this solution. Flash chromatography on silica gel (DCM → DCM + 1 % MeOH).

Yield: 57.0 mg (56.5 µmol, 89 %), red solid.

Formula: $C_{66}H_{49}N_5O_6$ [1008.13].

^{1}H-NMR (600.1 MHz, CD_2Cl_2):

δ [ppm] = 8.85 (-, 4 H, H-15 a. H-16), 7.93 (d, $^{5}J_{HH}$ = 0.5 Hz, 1 H, H-6), 7.88 (d, $^{5}J_{HH}$ = 0.6 Hz, 1 H, H-3), 7.85 (AA´, 2 H, H-10), 7.64 (d, $^{3}J_{HH}$ = 8.6 Hz, 1 H, H-23), 7.53 (dd, $^{3}J_{HH}$ = 8.6 Hz, $^{4}J_{HH}$ = 2.2 Hz, 1 H, H-24), 7.43 (BB´, 2 H, H-11), 7.40 (AA´, 2 H, H-34), 7.12 (AA´, 4 H, H-38), 7.06 (d, $^{4}J_{HH}$ = 2.2 Hz, 1 H, H-26), 6.89 (BB´, 4 H, H-39), 6.83 (BB´, 2 H, H-35), 3.80 (s, 6 H, H-41), 1.34 (s, 9 H, H-28), 1.28 (s, 9 H, H-30).

^{13}C-NMR (150.9 MHz, CD_2Cl_2):

δ [ppm] = 164.2 (C_q), 163.2 (C_q), 157.4 (C_q), 150.1 (C_q), 150.9 (C_q), 144.5 (C_q), 139.7 (C_q), 136.6 (C_q), 136.2 (CH), 135.7 (CH), 133.6 (CH), 133.4 (CH), 132.9 (C_q), 131.8 (CH), 131.7 (CH), 129.6 (CH), 129.4 (CH), 128.12 (C_q), 128.10 (CH), 128.0 (CH), 127.71 (C_q), 127.69 (C_q), 127.68 (C_q), 127.2 (C_q), 126.9 (CH), 125.3 (C_q), 122.6 (C_q), 119.4 (C_q), 118.6 (C_q), 118.2 (CH), 116.2 (C_q), 116.1 (C_q), 115.3 (CH), 110.8 (C_q), 102.5 (C_q), 98.3 (C_q), 85.6 (C_q), 84.1 (C_q), 55.8 (CH_3), 35.9 (C_q), 34.6 (C_q), 31.8 (CH_3), 31.3 (CH_3).

ESI-MS (high resolution):

calc.: $[M + H]^+$ 1007.36774 m/z

exp.: $[M + H]^+$ 1007.36809 m/z Δ = 0.35 ppm

mCNNDI

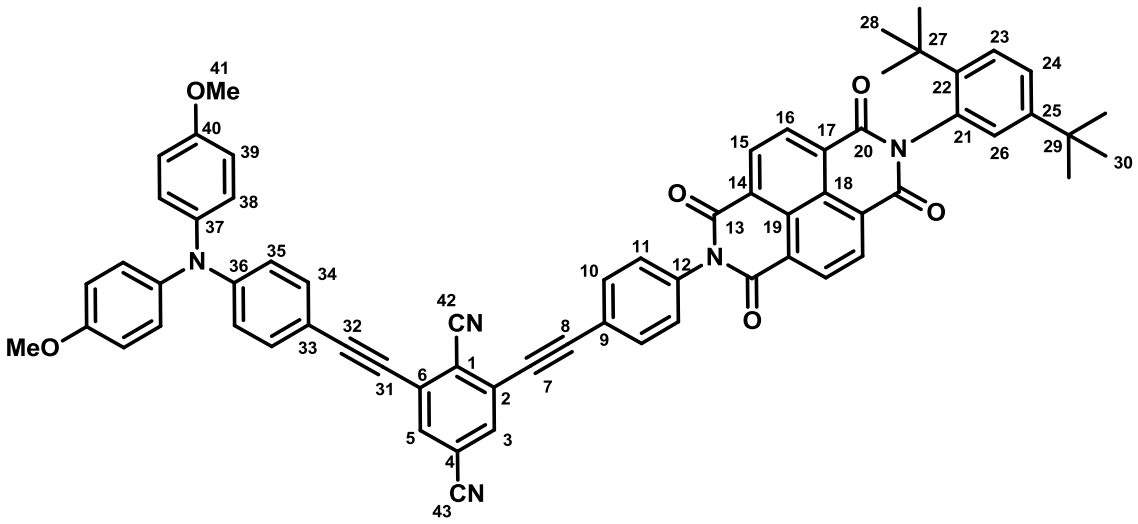

CA: [/].

Following **GP_{CN}**: Compound **25** (70.0 mg, 92.1 µmol), CuI (369 µg, 1.94 µmol), $Pd(PPh_3)_2Cl_2$ (2.72 mg, 3.87 µmol) were added to THF (5 ml). **eTAA** (91.0 mg, 276 µmol in NEt_3 (6 ml) was added to this solution. Flash chromatography on silica gel (DCM → DCM + 1 % MeOH).

Yield: 84.0 mg (83.3 µmol, 90 %), red solid.

Formula: $C_{66}H_{49}N_5O_6$ [1008.13].

^{1}H-NMR (400.1 MHz, CD_2Cl_2):

δ [ppm] = 8.85 (-, 4 H, H-15 a. H-16), 7.86 (AA´, 2 H, H-10), 7.79 (d, $^4J_{HH}$ = 1.5 Hz, 1 H, H-5), 7.77 (d, $^4J_{HH}$ = 1.5 Hz, 1 H, H-3), 7.65 (d, $^3J_{HH}$ = 8.6 Hz, 1 H, H-23), 7.53 (dd, $^3J_{HH}$ = 8.6 Hz, $^4J_{HH}$ = 2.3 Hz, 1 H, H-24), 7.43 (BB´, 2 H, H-11), 7.40 (AA´, 2 H, H-34), 7.13 (AA´, 4 H, H-38), 7.08 (d, $^4J_{HH}$ = 2.2 Hz, 1 H, H-26), 6.90 (BB´, 4 H, H-39), 6.84 (BB´, 2 H, H-35), 3.80 (s, 6 H, H-41), 1.35 (s, 9 H, H-28), 1.29 (s, 9 H, H-30).

^{13}C-NMR (100.6 MHz, CD_2Cl_2):

δ [ppm] = 164.2 (C_q), 163.2 (C_q), 157.4 (C_q), 150.94 (C_q), 150.89 (C_q), 144.5 (C_q), 139.7 (C_q), 136.7 (C_q), 133.9 (CH), 133.6 (CH), 133.5 (CH), 133.2 (CH), 132.9 (C_q), 131.7 (CH), 131.7 (CH), 130.1 (C_q), 129.6 (CH), 129.4 (CH), 128.8 (C_q), 128.1 (CH), 128.0 (CH), 127.69 (C_q), 127.67 (C_q), 127.65 (C_q), 127.2 (C_q), 126.9 (CH), 122.4 (C_q), 120.9 (C_q), 118.2 (CH), 116.8 (C_q), 116.7 (C_q), 115.7 (C_q), 115.3 (CH), 110.7 (C_q), 101.1 (C_q), 97.5 (C_q), 85.4 (C_q), 83.7 (C_q), 55.8 (CH_3), 35.8 (C_q), 34.6 (C_q), 31.8 (CH_3), 31.3 (CH_3).

ESI-MS (high resolution):

calc.: $[M + H]^+$ 1007.36774 m/z

exp.: $[M + H]^+$ 1007.36702 m/z Δ = 0.71 ppm

sNO$_2$NDI

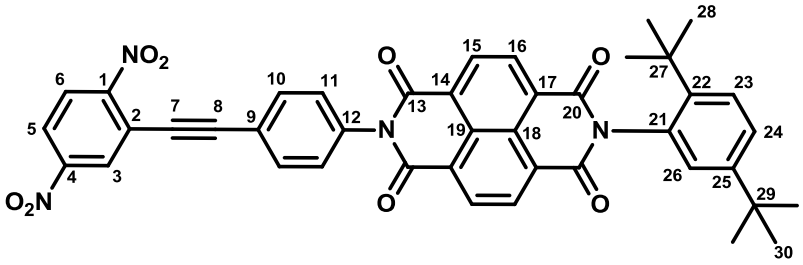

CA: [/].

Following **GP$_{NO_2}$**: 2-Bromo-2,5-dinitrobenzene (**sbNO$_2$**, 80.0 mg, 324 µmol), **eNDI** (180 mg, 324 µmol), CuI (4.75 mg, 24.9 µmol), Pd($C_6H_5CN)_2Cl_2$ (5.23 mg, 13.6 µmol) and triethylamine (2 ml) were added to toluene (6 ml). Flash chromatography on silica gel (DCM).

Yield: 150 mg (208 µmol, 64 %), yellow solid.

Formula: $C_{42}H_{32}N_4O_8$ [720.73].

^{1}H-NMR (600.1 MHz, CD_2Cl_2):

δ [ppm] = 8.85 (-, 4 H, H-15 a. H-16), 8.64 (dd, $^4J_{HH}$ = 2.4 Hz, $^5J_{HH}$ = 0.5 Hz, 1 H, H-3), 8.31 (dd, $^3J_{HH}$ = 9.0 Hz, $^4J_{HH}$ = 2.4 Hz, 1 H, H-5), 8.25 (dd, $^3J_{HH}$ = 9.0 Hz, $^5J_{HH}$ = 0.5 Hz, 1 H, H-6), 7.85 (AA´, 2 H, H-11), 7.64 (d, $^3J_{HH}$ = 8.6 Hz, 1 H, H-23), 7.53 (dd, $^3J_{HH}$ = 8.6 Hz, $^4J_{HH}$ = 2.2 Hz, 1 H, H-24), 7.44 (BB´, 2 H, H-10), 7.05 (d, $^4J_{HH}$ = 2.2 Hz, 1 H, H-26), 1.34 (s, 9 H, H-28), 1.27 (s, 9 H, H-30).

^{13}C-NMR (150.9 MHz, CD_2Cl_2):

δ [ppm] = 164.3 (C_q), 163.2 (C_q), 153.0 (C_q), 151.1 (C_q), 149.9 (C_q), 144.5 (C_q), 136.8 (C_q), 133.6 (CH), 133.0 (C_q), 131.8 (CH), 131.7 (CH), 130.1 (CH), 129.6 (CH), 129.5 (CH), 128.0 (CH), 127.73 (C_q), 127.71 (2 × C_q), 127.2 (C_q), 126.9 (CH), 126.6 (CH), 124.0 (CH), 122.7 (C_q), 120.4 (C_q), 99.1 (C_q), 84.2 (C_q), 35.9 (C_q), 34.6 (C_q), 31.8 (CH_3) 31.3 (CH_3).

ESI-MS (high resolution):

calc.: $[M + H]^+$ 721.22929 m/z

exp.: $[M + H]^+$ 721.22866 m/z Δ = 0.84 ppm

1-{4-[*N*,*N*-Di(4-methoxyphenyl)amino]phenylethynyl}(4-bromo-2,5-dinitro)-benzene (26)

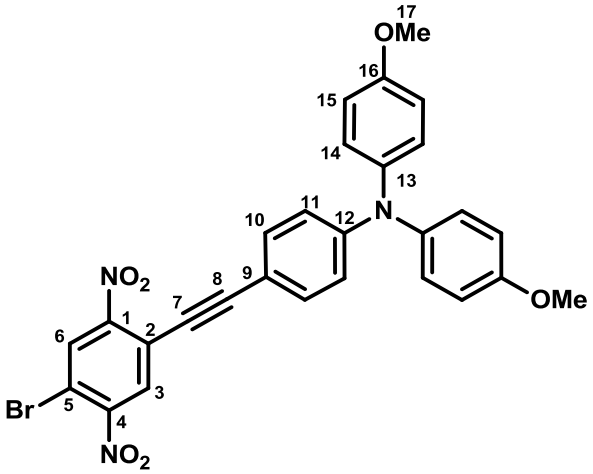

CA: [/].

Following **GP$_5$**: 1,4-Dibromo-2,5-dinitrobenzene (**pbNO$_2$**, 237 mg, 727 µmol), CuI (7.12 mg, 37.4 µmol), $Pd(PPh_3)_2Cl_2$ (7.84 mg, 11.2 µmol) and triethylamine (2 ml) were added to toluene (8 ml). **eTAA** (80.0 mg, 243 µmol) in toluene (5 ml) was added dropwise to this solution. Flash chromatography on silica gel (DCM:PE, 2:1) and GPC.

Yield: 90.0 mg (157 µmol, 65 %), red solid.

Formula: $C_{28}H_{20}BrN_3O_6$ [574.38].

^{1}H-NMR (400.1 MHz, CD_2Cl_2):

δ [ppm] = 8.41 (d, $^5J_{HH}$ = 0.2 Hz, 1 H, 6-H), 8.07 (d, $^5J_{HH}$ = 0.2 Hz, 1 H, 3-H), 7.36 (AA´, 2 H, H-10), 7.11 (AA´, 4 H, H-14), 6.88 (BB´, 4 H, H-15), 6.80 (BB´, 2 H, H-11), 3.80 (s, 6 H, H-17).

^{13}C-NMR (100.6 MHz, CD_2Cl_2):

δ [ppm] = 157.5 (C_q), 152.0 (C_q), 151.1 (C_q), 149.8 (C_q), 139.6 (C_q), 133.7 (CH), 131.7 (CH), 130.7 (CH), 128.2 (CH), 120.5 (C_q), 119.1 (CH), 115.3 (CH), 112.3 (C_q), 110.8 (C_q), 104.0 (C_q), 82.7 (C_q), 55.8 (CH_3).

EI-MS: calc.: $[M]^+$ 575.2 m/z
exp.: $[M]^+$ 575.2 m/z

1-{4-[*N*,*N*-Di(4-methoxyphenyl)amino]phenylethynyl}(3-bromo-2,5-dinitro)-benzene (27)

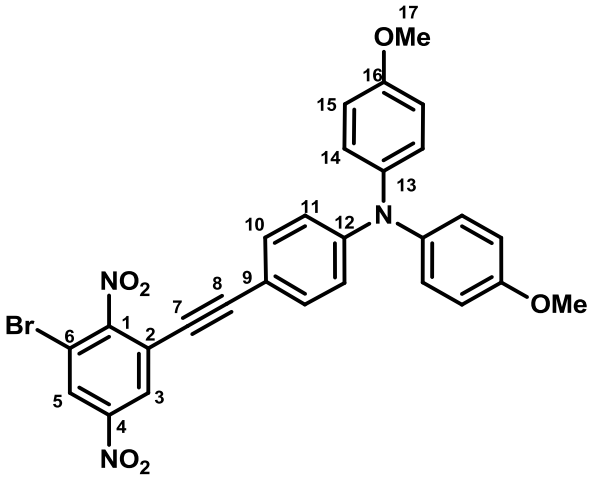

CA: [/].

Following **GP$_5$**: 1,3-Dibromo-2,5-dinitrobenzene (**mbNO$_2$**, 148 mg, 454 µmol), CuI (4.45 mg, 23.4 µmol), $Pd(PPh_3)_2Cl_2$ (4.90 mg, 6.98 µmol) and triethylamine (2 ml) were added to toluene (6 ml). **eTAA** (50.0 mg, 152 µmol) in toluene (3 ml) was added dropwise to this solution. Flash chromatography on silica gel (DCM:PE, 2:1).

Yield: 69.0 mg (120 µmol, 79 %), red solid.

Formula: $C_{28}H_{20}BrN_3O_6$ [574.38].

^{1}H-NMR (400.1 MHz, CD_2Cl_2):

δ [ppm] = 8.39 (d, $^4J_{HH}$ = 2.3 Hz, 1 H, 3-H o. 5-H), 8.38 (d, $^4J_{HH}$ = 2.3 Hz, 1 H, 3-H o. 5-H), 7.28 (AA´, 2 H, H-10), 7.10 (AA´, 4 H, H-14), 6.88 (BB´, 4 H, H-15), 6.79 (BB´, 2 H, H-11), 3.80 (s, 6 H, H-17).

^{13}C-NMR (100.6 MHz, CD_2Cl_2):

δ [ppm] = 157.5 (C_q), 152.0 (C_q), 151.1 (C_q), 149.8 (C_q), 139.6 (C_q), 133.7 (CH), 131.7 (CH), 130.7 (CH), 128.2 (CH), 120.5 (C_q), 118.1 (CH), 115.3 (CH), 112.3 (C_q), 110.8 (C_q), 104.0 (C_q), 82.7 (C_q), 55.7 (CH_3).

EI-MS: calc.: $[M]^+$ 575.1 m/z
exp.: $[M]^+$ 575.2 m/z

Compound 28

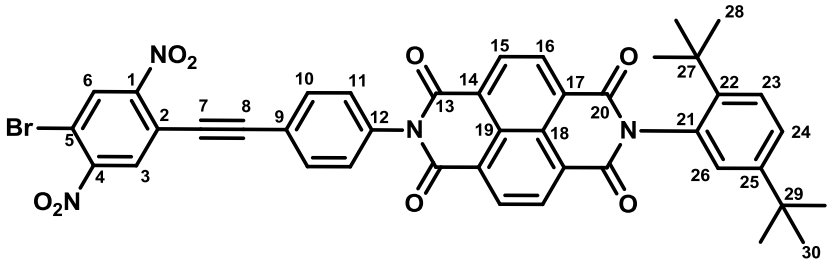

CA: [/].

Following **GP_{NO_2}**: 1,4-Dibromo-2,5-dinitrobenzene (**$pbNO_2$**, 310 mg, 951 µmol), **eNDI** (132 mg, 238 µmol), CuI (3.49 mg, 18.3 µmol), $Pd(PPh_3)_2Cl_2$ (3.84 mg, 5.47 µmol) and triethylamine (2 ml) were added to toluene (6 ml). Flash chromatography on silica gel (DCM) and GPC.

Yield: 80.0 mg (100 µmol, 42 %), yellow solid.

Formula: $C_{42}H_{31}BrN_4O_8$ [799.62].

^{1}H-NMR (400.1 MHz, CD_2Cl_2):

δ [ppm] = 8.85 (-, 4 H, H-15 a. H-16), 8.51 (s, 1 H, H-3), 8.22 (s, 1 H, H-6), 7.84 (AA´, 2 H, H-11), 7.64 (d, $^3J_{HH}$ = 8.6 Hz, 1 H, H-23), 7.53 (dd, $^3J_{HH}$ = 8.6 Hz, $^4J_{HH}$ = 2.2 Hz, 1 H, H-24), 7.44 (BB´, 2 H, H-10), 7.05 (d, $^4J_{HH}$ = 2.2 Hz, 1 H, H-26), 1.34 (s, 9 H, H-28) 1.27 (s, 9 H, H-30).

^{13}C-NMR (100.6 MHz, CD_2Cl_2):

δ [ppm] = 164.2 (C_q), 163.2 (C_q), 152.1 (C_q), 151.0 (C_q), 150.6 (C_q), 144.5 (C_q), 136.9 (C_q), 133.6 (CH), 132.9 (C_q), 131.9 (CH), 131.8 (CH), 131.7 (CH), 131.3 (CH), 129.7 (CH), 129.5 (CH), 128.0 (CH), 127.73 (C_q), 127.72 (C_q) 127.71 (C_q), 127.2 (C_q), 126.9 (CH), 122.5 (C_q), 119.4 (C_q), 114.4 (C_q), 10.2 (C_q), 83.7 (C_q), 35.9 (C_q), 34.6 (C_q), 31.8 (CH_3) 31.3 (CH_3).

EI-MS: calc.: $[M - NO]^+$ 770.1 m/z
exp.: $[M - NO]^+$ 770.2 m/z

Compound 29

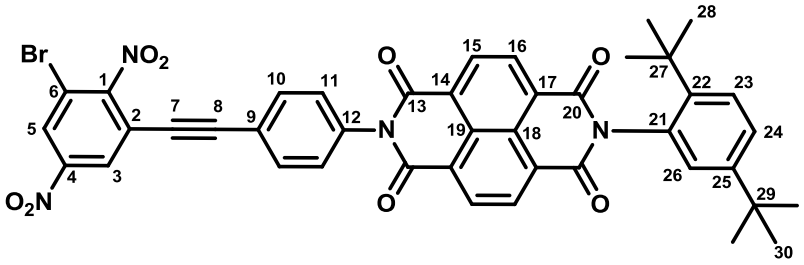

CA: [/].

Following **GP$_{NO_2}$**: 1,3-Dibromo-2,5-dinitrobenzene (**mbNO$_2$**, 310 mg, 951 µmol), **eNDI** (132 mg, 238 µmol), CuI (3.49 mg, 18.3 µmol), $Pd(PPh_3)_2Cl_2$ (3.84 mg, 5.47 µmol) and triethylamine (2 ml) were added to toluene (6 ml). Flash chromatography on silica gel (DCM) and GPC.

Yield: 110 mg (138 µmol, 58 %), yellow solid.

Formula: $C_{42}H_{31}BrN_4O_8$ [799.62].

^{1}H-NMR (400.1 MHz, CD_2Cl_2):

δ [ppm] = 8.85 (-, 4 H, H-15 a. H-16), 8.54 (d, $^4J_{HH}$ = 2.2 Hz, 1 H, H-5), 8.53 (d, $^4J_{HH}$ = 2.2 Hz, 1 H, H-3), 7.77 (AA´, 2 H, H-11), 7.64 (d, $^3J_{HH}$ = 8.6 Hz, 1 H, H-23), 7.53 (dd, $^3J_{HH}$ = 8.6 Hz, $^4J_{HH}$ = 2.3 Hz, 1 H, H-24), 7.43 (BB´, 2 H, H-10), 7.05 (d, $^4J_{HH}$ = 2.2 Hz, 1 H, H-26), 1.34 (s, 9 H, H-28) 1.27 (s, 9 H, H-30).

^{13}C-NMR (100.6 MHz, CD_2Cl_2):

δ [ppm] = 164.2 (C_q), 163.2 (C_q), 156.0 (C_q), 151.0 (C_q), 148.2 (C_q), 144.5 (C_q), 137.1 (C_q), 133.6 (CH), 132.9 (C_q), 131.8 (CH), 131.7 (CH), 129.7 (CH), 129.5 (CH), 128.9 (CH), 128.0 (CH), 127.731 (C_q), 127.726 (C_q), 127.71 (C_q) 127.5 (CH), 127.2 (C_q), 126.9 (CH), 121.7 (C_q), 119.8 (C_q), 114.6 (C_q), 98.8 (C_q), 81.3 (C_q), 35.9 (C_q), 34.6 (C_q), 31.8 (CH_3) 31.3 (CH_3).

MALDI-MS: calc.: $[M - NO]^+$ 770.1 m/z
exp.: $[M - NO]^+$ 770.2 m/z

pNO$_2$NDI

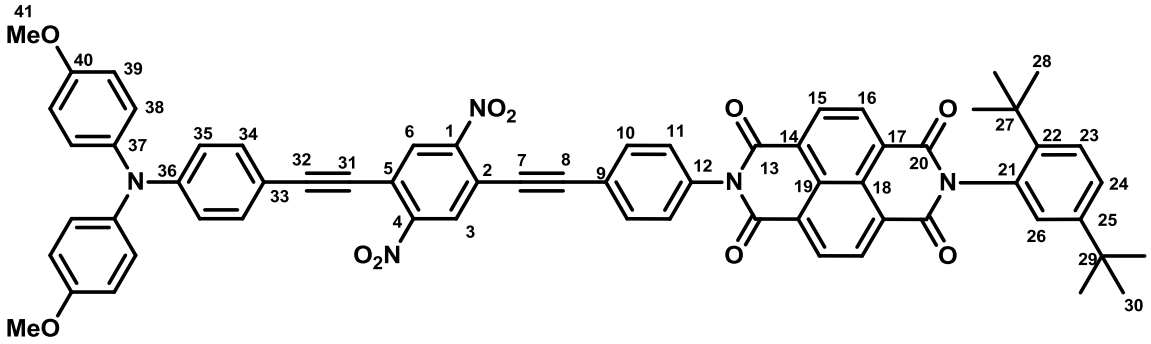

CA: [/].

Following **GP$_{NO_2}$**: Compound **28** (82.0 mg, 103 µmol), **eTAA** (67.6 mg, 205 µmol), CuI (1.50 mg, 7.88 µmol), $Pd(PPh_3)_2Cl_2$ (1.66 mg, 2.36 µmol) and triethylamine (2 ml) were added to toluene (4 ml). Flash chromatography on silica gel (DCM → DCM+ 1 % EA).

Yield: 64.0 mg (61.1 µmol, 59 %), red solid.

Formula: $C_{64}H_{49}N_5O_{10}$ [1048.10].

^{1}H-NMR (600.1 MHz, CD_2Cl_2):

δ [ppm] = 8.85 (-, 4 H, H-15 a. H-16), 8.42 (d, $^5J_{HH}$ = 0.4 Hz 1 H, H-6), 8.35 (d, $^5J_{HH}$ = 0.4 Hz 1 H, H-3), 7.84 (AA´, 2 H, H-10), 7.64 (d, $^3J_{HH}$ = 8.6 Hz, 1 H, H-23), 7.53 (dd, $^3J_{HH}$ = 8.6 Hz, $^4J_{HH}$ = 2.3 Hz, 1 H, H-24), 7.43 (BB´, 2 H, H-11), 7.40 (AA´, 2 H, H-34), 7.12 (AA´, 4 H, H-38), 7.05 (d, $^4J_{HH}$ = 2.2 Hz, 1 H, H-26), 6.90 (BB´, 4 H, H-39), 6.82 (BB´, 2 H, H-35), 3.80 (s, 6 H, H-41), 1.34 (s, 9 H, H-28), 1.27 (s, 9 H, H-30).

^{13}C-NMR (150.9 MHz, CD_2Cl_2):

δ [ppm] = 164.3 (C_q), 163.2 (C_q), 157.5 (C_q), 151.2 (C_q), 151.1 (C_q), 151.0 (C_q), 150.4 (C_q), 144.5 (C_q), 139.6 (C_q), 136.7 (C_q), 133.8 (CH), 133.5 (CH), 132.9 (C_q), 131.8 (CH), 131.7 (CH), 131.3 (CH), 130.7 (CH), 129.6 (CH), 129.5 (CH), 128.2 (CH), 128.0 (CH), 127.73 (C_q), 127.71 (C_q), 127.70 (C_q), 127.3 (C_q), 126.9 (CH), 122.9 (C_q), 120.3 (C_q), 118.1 (CH), 117.1 (C_q), 115.3 (CH), 111.0 (C_q), 104.6 (C_q), 99.6 (C_q), 84.7 (C_q), 83.7 (C_q), 55.8 (CH_3), 35.9 (C_q), 34.6 (C_q), 31.8 (CH_3), 31.3 (CH_3).

ESI-MS (high resolution):

calc.: $[M + Na]^+$ 1070.337164 m/z

exp.: $[M + Na]^+$ 1070.33895 m/z Δ = 1.67 ppm

mNO$_2$NDI

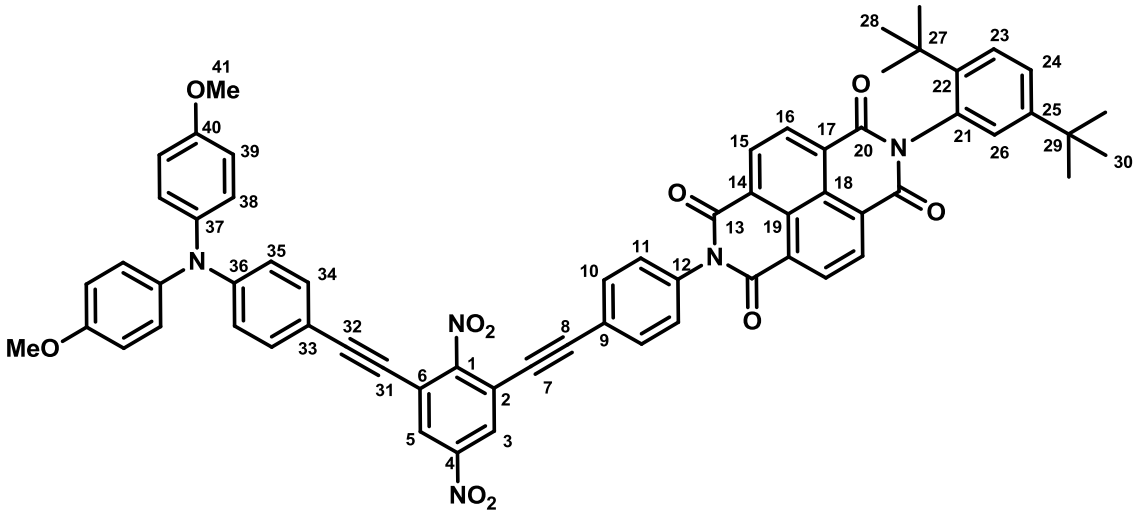

CA: [/].

Following **GP$_{NO_2}$**: Compound **29** (95.0 mg, 119 µmol), **eTAA** (78.0 mg, 237 µmol), CuI (1.74 mg, 9.14 µmol), $Pd(PPh_3)_2Cl_2$ (1.92 mg, 2.73 µmol) and triethylamine (2 ml) were added to toluene (7 ml). Flash chromatography on silica gel (DCM → DCM + 1 % EA).

Yield: 70.0 mg (66.8 µmol, 56 %), red solid.

Formula: $C_{64}H_{49}N_5O_{10}$ [1048.10].

^{1}H-NMR (400.1 MHz, (CD_2Cl_2)):

δ [ppm] = 8.85 (-, 4 H, H-15 a. H-16), 8.40 (-, 2 H, H-3 a. H-5), 7.78 (AA´, 2 H, H-10), 7.64 (d, $^3J_{HH}$ = 8.6 Hz, 1 H, H-23), 7.53 (dd, $^3J_{HH}$ = 8.6 Hz, $^4J_{HH}$ = 2.3 Hz, 1 H, H-24), 7.42 (BB´, 2 H, H-11), 7.32 (AA´, 2 H, H-34), 7.11 (AA´, 4 H, H-38), 7.05 (d, $^4J_{HH}$ = 2.2 Hz, 1 H, H-26), 6.89 (BB´, 4 H, H-39), 6.81 (BB´, 2 H, H-35), 3.80 (s, 6 H, H-41), 1.34 (s, 9 H, H-28), 1.27 (s, 9 H, H-30).

^{13}C-NMR (100.6 MHz, CD_2Cl_2):

δ [ppm] = 164.2 (C_q), 163.2 (C_q), 157.4 (C_q), 155.8 (C_q), 150.99 (C_q), 150.98 (C_q), 148.2 (C_q), 144.5 (C_q), 139.7 (C_q), 136.8 (C_q), 133.6 (CH), 133.5 (CH), 132.9 (C_q), 131.8 (CH), 131.7 (CH), 129.6 (CH), 129.5 (CH), 128.1 (CH), 128.0 (CH), 127.73 (C_q), 127.71 (2 × C_q), 127.4 (CH), 127.2 (C_q), 126.9 (CH), 126.5 (CH), 122.2 (C_q), 120.1 (C_q), 118.8 (CH), 118.1 (C_q), 115.3 (CH), 110.4 (C_q), 101.5 (C_q), 97.8 (C_q), 82.1 (C_q), 80.2 (C_q), 55.8 (CH_3), 35.9 (C_q), 34.6 (C_q), 31.8 (CH_3), 31.3 (CH_3).

ESI-MS (high resolution):

calc.: $[M]^+$ 1047.34739 m/z

exp.: $[M]^+$ 1047.34635 m/z Δ = 0.99 ppm

7 LITERATURE

[1] G. McDermott, S. M. Prince, A. A. Freer, A. M. Hawthornthwaite-Lawless, M. Z. Papiz, R. J. Cogdell, N. W. Isaacs, *Nature* **1995**, *374*, 517-521.

[2] M. Medina, *FEBS J.* **2009**, *276*, 3942-3958.

[3] J. Deisenhofer, O. Epp, K. Miki, R. Huber, H. Michel, *Nature* **1985**, *318*, 618-624.

[4] R. Huber, *Angew. Chem.* **1989**, *101*, 849-871.

[5] J. Deisenhofer, H. Michel, *Angew. Chem.* **1989**, *101*, 872-892.

[6] L. M. Utschig, D. M. Tiede, O. G. Poluektov, *Biochemistry* **2010**, *49*, 9682-9684.

[7] V. Krishnan, *Resonance* **1997**, *2*, 77-86.

[8] S. N. Datta, B. Mallik, *Int. J. of Quantum Chem.* **1997**, *61*, 865-879.

[9] T. Ameri, P. Khoram, J. Min, C. J. Brabec, *Adv. Mater.* **2013**, *25*, 4245-4266.

[10] H. Kang, G. Kim, J. Kim, S. Kwon, H. Kim, K. Lee, *Adv. Mater.* **2016**, *28*, 7821-7861.

[11] K. A. Mazzio, C. K. Luscombe, *Chem. Soc. Rev.* **2015**, *44*, 78-90.

[12] S. Günes, H. Neugebauer, N. S. Sariciftci, *Chem. Rev.* **2007**, *107*, 1324-1338.

[13] M. V. Jean-Pierre Launay, *Electrons in Molecules From Basic Principles to Molecular Electronics*, Oxford, **2014**.

[14] N. Sekar, R. P. Ramasamy, *Electrochem. Soc. Interface* **2015**, *24*, 67-73.

[15] R. M. Metzger, *Chem. Rev.* **2003**, *103*, 3803-3834.

[16] N. J. Tao, *Nat. Nanotechnol.* **2006**, *1*, 173-181.

[17] A. Nitzan, M. A. Ratner, *Science* **2003**, *300*, 1384-1389.

[18] J. H. Burroughes, D. D. C. Bradley, A. R. Brown, R. N. Marks, K. Mackay, R. H. Friend, P. L. Burns, A. B. Holmes, *Nature* **1990**, *347*, 539-541.

[19] J. Zaumseil, H. Sirringhaus, *Chem. Rev.* **2007**, *107*, 1296-1323.

[20] S. Moeller, C. Perlov, W. Jackson, C. Taussig, S. R. Forrest, *Nature* **2003**, *426*, 166-169.

[21] P. Gawrys, D. Boudinet, M. Zagorska, D. Djurado, J.-M. Verilhac, G. Horowitz, J. Pécaud, S. Pouget, A. Pron, *Synth. Met.* **2009**, *159*, 1478-1485.

[22] P. Gawrys, D. Djurado, J. n. Rimarčík, A. Kornet, D. Boudinet, J.-M. Verilhac, V. r. Lukeš, I. Wielgus, M. Zagorska, A. Pron, *J. Phys. Chem. B* **2010**, *114*, 1803-1809.

[23] W. B. Davis, W. A. Svec, M. A. Ratner, M. R. Wasielewski, *Nature* **1998**, *396*, 60-63.

[24] G. L. Closs, J. R. Miller, *Science* **1988**, *240*, 440-447.

[25] M. J. Ondrechen, *Int. Rev. Phys. Chem.* **1995**, *14*, 1-14.

[26] J. W. Verhoeven, H. J. van Ramesdonk, M. M. Groeneveld, A. C. Benniston, A. Harriman, *ChemPhysChem* **2005**, *6*, 2251-2260.

[27] A. Heckmann, C. Lambert, *Angew. Chem., Int. Ed.* **2012**, *51*, 326-392.

[28] D. E. Richardson, H. Taube, *Coord. Chem. Rev.* **1984**, *60*, 107-129.

[29] D. G. Evans, A. Nitzan, M. A. Ratner, *J. Chem. Phys.* **1998**, *108*, 6387-6393.

[30] H. Heitele, *Angew. Chem.* **1993**, *105*, 378-398.

[31] D. F. Calef, P. G. Wolynes, *J. Phys. Chem.* **1983**, *87*, 3387-3400.

[32] W. C. W. Leu, A. E. Fritz, K. M. Digianantonio, C. S. Hartley, *J. Org. Chem.* **2012**, *77*, 2285-2298.

[33] P. Karafiloglou, J.-P. Launay, *J. Phys. Chem. A* **1998**, *102*, 8004-8012.

[34] H. C. Schmidt, M. Spulber, M. Neuburger, C. G. Palivan, M. Meuwly, O. S. Wenger, *J. Org. Chem.* **2016**, *81*, 595-602.

[35] T. Weyland, K. Costuas, L. Toupet, J.-F. Halet, C. Lapinte, *Organometallics* **2000**, *19*, 4228-4239.

[36] K. Lancaster, S. A. Odom, S. C. Jones, S. Thayumanavan, S. R. Marder, J.-L. Brédas, V. Coropceanu, S. Barlow, *J. Am. Chem. Soc.* **2009**, *131*, 1717-1723.

[37] G. C. Solomon, D. Q. Andrews, R. P. Van Duyne, M. A. Ratner, *ChemPhysChem* **2009**, *10*, 257-264.

[38] Y. J. Chang, T. J. Chow, *Tetrahedron* **2009**, *65*, 9626-9632.

[39] T. Markussen, R. Stadler, K. S. Thygesen, *Nano Lett.* **2010**, *10*, 4260-4265.

[40] P. Sautet, C. Joachim, *Chem. Phys. Lett.* **1988**, *153*, 511-516.

[41] S.-H. Ke, W. Yang, H. U. Baranger, *Nano Lett.* **2008**, *8*, 3257-3261.

[42] X. Li, A. Staykov, K. Yoshizawa, *Bull. Chem. Soc. Jpn.* **2012**, *85*, 181-188.

[43] S. F. Nelsen, M. N. Weaver, A. E. Konradsson, J. P. Telo, T. Clark, *J. Am. Chem. Soc.* **2004**, *126*, 15431-15438.

[44] R. Hoffmann, *Accounts of Chemical Research* **1971**, *4*, 1-9.

[45] D. M. D'Alessandro, F. R. Keene, *Chem. Soc. Rev.* **2006**, *35*, 424-440.

[46] J.-P. Launay, *Chem. Soc. Rev.* **2001**, *30*, 386-397.

[47] A. Moneo, J. P. Telo, *J. Phys. Org. Chem.* **2012**, *25*, 1139-1143.

[48] B. Albinsson, J. Martensson, *Phys. Chem. Chem. Phys.* **2010**, *12*, 7338-7351.

[49] R. A. Marcus, *J. Chem. Phys.* **1956**, *24*, 966-978.

[50] R. A. Marcus, *Disc. Faraday Soc.* **1960**, *29*, 21-31.

[51] R. A. Marcus, *J. Chem. Phys.* **1965**, *43*, 679-701.

[52] N. S. Hush, *Coord. Chem. Rev.* **1985**, *64*, 135-157.

[53] N. S. Hush, *Electrochim. Acta* **1968**, *13*, 1005-1023.

[54] B. S. Brunschwig, C. Creutz, N. Sutin, *Chem. Soc. Rev.* **2002**, *31*, 168.

[55] S. F. Nelsen, M. D. Newton, *J. Phys. Chem. A* **2000**, *104*, 10023-10031.

[56] R. J. Cave, M. D. Newton, *Chem. Phys. Lett.* **1996**, *249*, 15-19.

[57] M. A. Reed, C. Zhou, C. J. Muller, T. P. Burgin, J. M. Tour, *Science* **1997**, *278*, 252-254.

[58] M. Mayor, H. B. Weber, J. Reichert, M. Elbing, C. von Haenisch, D. Beckmann, M. Fischer, *Angew. Chem., Int. Ed.* **2003**, *42*, 5834-5838.

[59] M. Mayor, C. Von Hanisch, H. B. Weber, J. Reichert, D. Beckmann, *Angew. Chem., Int. Ed.* **2002**, *41*, 1183-1186.

[60] H. B. Weber, J. Reichert, F. Weigend, R. Ochs, D. Beckmann, M. Mayor, R. Ahlrichs, H. von Lohneysen, *Chem. Phys.* **2002**, *281*, 113-125.

[61] C. Kergueris, J. P. Bourgoin, S. Palacin, D. Esteve, C. Urbina, M. Magoga, C. Joachim, *Phys. Rev. B: Condens. Matter Mater. Phys.* **1999**, *59*, 12505-12513.

[62] C. Kergueris, J. P. Bourgoin, S. Palacin, *Nanotechnology* **1999**, *10*, 8-13.

[63] L. Venkataraman, Y. S. Park, A. C. Whalley, C. Nuckolls, M. S. Hybertsen, M. L. Steigerwald, *Nano Lett.* **2007**, *7*, 502-506.

[64] E. Lortscher, C. J. Cho, M. Mayor, M. Tschudy, C. Rettner, H. Riel, *ChemPhysChem* **2011**, *12*, 1677-1682.

[65] W. Kaminski, R. Topolnicki, P. Hapala, P. Jelinek, R. Kucharczyk, *Org. Electron.* **2016**, *34*, 254-261.

[66] M. Kiguchi, H. Nakamura, Y. Takahashi, T. Takahashi, T. Ohto, *J. Phys. Chem. C* **2010**, *114*, 22254-22261.

[67] D. Q. Andrews, G. C. Solomon, R. H. Goldsmith, T. Hansen, M. R. Wasielewski, R. P. Van Duyne, M. A. Ratner, *J. Phys. Chem. C* **2008**, *112*, 16991-16998.

[68] T. Markussen, J. Schiötz, K. S. Thygesen, *J. Chem. Phys.* **2010**, *132*, 224104.

[69] T. Markussen, R. Stadler, K. S. Thygesen, *Phys. Chem. Chem. Phys.* **2011**, *13*, 14311-14317.

[70] C. M. Guedon, H. Valkenier, T. Markussen, K. S. Thygesen, J. C. Hummelen, S. J. van der Molen, *Nat. Nanotechnol.* **2012**, *7*, 305-309.

[71] D. A. Lovey, R. H. Romero, *Chem. Phys. Lett.* **2012**, *530*, 86-92.

[72] A. A. Kocherzhenko, F. C. Grozema, L. D. A. Siebbeles, *J. Phys. Chem. C* **2010**, *114*, 7973-7979.

[73] C. J. Lambert, *Chem. Soc. Rev.* **2015**, *44*, 875-888.

[74] N. Gorczak, N. Renaud, S. Tarkuc, A. J. Houtepen, R. Eelkema, L. D. A. Siebbeles, F. C. Grozema, *Chem. Sci.* **2015**, *6*, 4196-4206.

[75] N. Gorczak, N. Renaud, E. Galan, R. Eelkema, L. D. A. Siebbeles, F. C. Grozema, *Phys. Chem. Chem. Phys.* **2016**, *18*, 6773-6779.

[76] C. Patoux, C. Coudret, J.-P. Launay, C. Joachim, A. Gourdon, *Inorg. Chem.* **1997**, *36*, 5037-5049.

[77] R. H. Goldsmith, M. R. Wasielewski, M. A. Ratner, *J. Phys. Chem. B* **2006**, *110*, 20258-20262.

[78] J. H. Klein, D. Schmidt, U. E. Steiner, C. Lambert, *J. Am. Chem. Soc.* **2015**, *137*, 11011-11021.

[79] T. Tada, K. Yoshizawa, *ChemPhysChem* **2002**, *3*, 1035-1037.

[80] C. Rovira, D. Ruiz-Molina, O. Elsner, J. Vidal-Gancedo, J. Bonvoisin, J.-P. Launay, J. Veciana, *Chem. Eur. J.* **2001**, *7*, 240-250.

[81] C. Franco, P. M. Burrezo, V. Lloveras, R. Caballero, I. Alcon, S. T. Bromley, M. Mas-Torrent, F. Langa, J. T. Lopez Navarrete, C. Rovira, J. Casado, J. Veciana, *J. Am. Chem. Soc.* **2017**, *139*, 686-692.

[82] S. F. Nelsen, A. E. Konradsson, Y. Teki, *J. Am. Chem. Soc.* **2006**, *128*, 2902.

[83] S. F. Nelsen, R. F. Ismagilov, D. R. Powell, *J. Am. Chem. Soc.* **1996**, *118*, 6313-6314.

[84] S. F. Nelsen, R. F. Ismagilov, D. R. Powell, *J. Am. Chem. Soc.* **1997**, *119*, 10213-10222.

[85] S. F. Nelsen, R. F. Ismagilov, D. A. Trieber, II, *Science* **1997**, *278*, 846-849.

[86] S. F. Nelsen, R. F. Ismagilov, *J. Phys. Chem. A* **1999**, *103*, 5373-5378.

[87] S. F. Nelsen, R. F. Ismagilov, K. E. Gentile, D. R. Powell, *J. Am. Chem. Soc.* **1999**, *121*, 7108-7114.

[88] D. R. Kattnig, B. Mladenova, G. Grampp, C. Kaiser, A. Heckmann, C. Lambert, *J. Phys. Chem. C* **2009**, *113*, 2983-2995.

[89] S. Amthor, C. Lambert, *J. Phys. Chem. A* **2006**, *110*, 3495-3504.

[90] S. Amthor, C. Lambert, *J. Phys. Chem. A* **2006**, *110*, 1177-1189.

[91] B. Mladenova, D. R. Kattnig, C. Kaiser, J. Schaefer, C. Lambert, G. Grampp, *J. Phys. Chem. C* **2015**, *119*, 8547-8553.

[92] S. Barlow, C. Risko, S.-J. Chung, N. M. Tucker, V. Coropceanu, S. C. Jones, Z. Levi, J.-L. Bredas, S. R. Marder, *J. Am. Chem. Soc.* **2005**, *127*, 16900-16911.

[93] S. A. Odom, K. Lancaster, L. Beverina, K. M. Lefler, N. J. Thompson, V. Coropceanu, J.-L. Bredas, S. R. Marder, S. Barlow, *Chem. - Eur. J.* **2007**, *13*, 9637-9646.

[94] K. Lancaster, S. A. Odom, S. C. Jones, S. Thayumanavan, S. R. Marder, J.-L. Bredas, V. Coropceanu, S. Barlow, *J. Am. Chem. Soc.* **2009**, *131*, 1717-1723.

[95] Y. Su, X. Wang, X. Zheng, Z. Zhang, Y. Song, Y. Sui, Y. Li, X. Wang, *Angew. Chem., Int. Ed.* **2014**, *53*, 2857-2861.

[96] S. Amthor, B. Noller, C. Lambert, *Chem. Phys.* **2005**, *316*, 141-152.

[97] C. Lambert, M. Moos, A. Schmiedel, M. Holzapfel, J. Schaefer, M. Kess, V. Engel, *Phys. Chem. Chem. Phys.* **2016**, *18*, 19405-19411.

[98] C. Lambert, G. Noell, J. Schelter, *Nat. Mater.* **2002**, *1*, 69-73.

[99] B. Strehmel, S. Amthor, J. Schelter, C. Lambert, *ChemPhysChem* **2005**, *6*, 893-896.

[100] V. Coropceanu, C. Lambert, G. Noell, J. L. Brédas, *Chem. Phys. Lett.* **2003**, *373*, 153.

[101] A. Heckmann, S. Amthor, C. Lambert, *Chem. Comm.* **2006**, 2959-2961.

[102] J. Schaefer, Diploma thesis, University of Wuerzburg **2012**.

[103] S. Takahashi, K. Nozaki, M. Kozaki, S. Suzuki, K. Keyaki, A. Ichimura, T. Matsushita, K. Okada, *J. Phys. Chem. A* **2008**, *112*, 2533-2542.

[104] A. L. Thompson, T.-S. Ahn, K. R. J. Thomas, S. Thayumanavan, T. J. Martinez, C. J. Bardeen, *J. Am. Chem. Soc.* **2005**, *127*, 16348-16349.

[105] L. G. Heinz, O. Yushchenko, M. Neuburger, E. Vauthey, O. S. Wenger, *J. Phys. Chem. A* **2015**, *119*, 5676-5684.

[106] J. W. Verhoeven, *J. Photochem. Photobiol., C* **2006**, *7*, 40-60.

[107] H. Hayashi, S. Nagakura, *Bull. Chem. Soc. Jpn.* **1984**, *57*, 322-328.

[108] U. Werner, Y. Sakaguchi, H. Hayashi, G. Nohya, R. Yoneshima, S. Nakajima, A. Osuka, *J. Phys. Chem.* **1995**, *99*, 13930-13937.

[109] Y. Mori, Y. Sakaguchi, H. Hayashi, *J. Phys. Chem. A* **2002**, *106*, 4453-4467.

[110] H. Hayashi, K. Ito, S. Nagakura, *Bull. Chem. Soc. Jpn.* **1966**, *39*, 199.

[111] J. H. Klein, Doctor thesis, University of Wuerzburg **2015**.

[112] T. Miura, D. Fujiwara, K. Akiyama, T. Horikoshi, S. Suzuki, M. Kozaki, K. Okada, T. Ikoma, *J. Phys. Chem. Lett.* **2017**, *8*, 661-665.

[113] F. Zieschang, M. H. Schreck, A. Schmiedel, M. Holzapfel, J. H. Klein, C. Walter, B. Engels, C. Lambert, *J. Phys. Chem. C* **2014**, *118*, 27698-27714.

[114] E. A. Weiss, M. A. Ratner, M. R. Wasielewski, *J. Phys. Chem. A* **2003**, *107*, 3639-3647.

[115] S. Shaakov, T. Galili, E. Stavitski, H. Levanon, A. Lukas, M. R. Wasielewski, *J. Am. Chem. Soc.* **2003**, *125*, 6563-6572.

[116] A. M. Scott, T. Miura, A. B. Ricks, Z. E. X. Dance, E. M. Giacobbe, M. T. Colvin, M. R. Wasielewski, *J. Am. Chem. Soc.* **2009**, *131*, 17655-17666.

[117] A. M. Scott, A. Butler Ricks, M. T. Colvin, M. R. Wasielewski, *Angew. Chem., Int. Ed.* **2010**, *49*, 2904-2908, S2904/2901-S2904/2922.

[118] E. A. Weiss, M. J. Ahrens, L. E. Sinks, A. V. Gusev, M. A. Ratner, M. R. Wasielewski, *J Am Chem Soc* **2004**, *126*, 5577-5584.

[119] A. Weller, H. Staerk, R. Treichel, *Faraday Discuss. Chem. Soc.* **1984**, *78*, 271-278.

[120] P. W. Anderson, *Phys. Rev.* **1959**, *115*, 2-13.

[121] R. R. Tykwinski, *Angew Chem Int Ed Engl* **2003**, *42*, 1566-1568.

[122] E.-I. Negishi, L. Anastasia, *Chem. Rev.* **2003**, *103*, 1979-2017.

[123] C. Lambert, G. Noell, E. Schmaelzlin, K. Meerholz, C. Braeuchle, *Chem. Eur. J.* **1998**, *4*, 2129-2135.

[124] H. B. Goodbrand, N.-X. Hu, *J. Org. Chem.* **1998**, *64*, 670-674.

[125] A. Carbone, C. L. Lucas, C. J. Moody, *J. Org. Chem.* **2012**, *77*, 9179-9189.

[126] M. R. An der Heiden, H. Plenio, S. Immel, E. Burello, G. Rothenberg, H. C. J. Hoefsloot, *Chem. - Eur. J.* **2008**, *14*, 2857-2866.

[127] F. Barrios-Landeros, J. F. Hartwig, *J. Am. Chem. Soc.* **2005**, *127*, 6944-6945.

[128] J. Pavlinac, M. Zupan, S. Stavber, *Synthesis* **2006**, *2006*, 2603-2607.

[129] A. Schaate, P. Roy, T. Preuße, S. J. Lohmeier, A. Godt, P. Behrens, *Chem. Eur. J.* **2011**, *17*, 9320-9325.

[130] M. Azadi-Ardakani, T. W. Wallace, *Tetrahedron* **1988**, *44*, 5939-5952.

[131] S. Ciampi, T. Böcking, K. A. Kilian, J. B. Harper, J. J. Gooding, *Langmuir* **2008**, *24*, 5888-5892.

[132] I. C. Gerber, J. G. Angyan, M. Marsman, G. Kresse, *J. Chem. Phys.* **2007**, *127*, 054101/054101.

[133] L. Skulski, *Molecules* **2000**, *5*, 1331-1371.

[134] A. Klapars, S. L. Buchwald, *J. Am. Chem. Soc.* **2002**, *124*, 14844-14845.

[135] Z. Xie, S.-J. Yoon, S. Y. Park, *Adv. Funct. Mater.* **2010**, *20*, 1638-1644.

[136] H. Huang, C. Lin, T. Chao, H. Lee, C. Cheng, *U.S. Pat. Appl. Publ.* **2011**, US 20110198571 A20110198571.

[137] C. L. Jackson, D. F. Calhane, *Am. Chem. J.* **1902**, *28*, 451.

[138] C. J. Sunde, G. Johnson, C. F. Kade, *J. Org. Chem.* **1939**, *04*, 548-554.

[139] G. S. Hammond, F. J. Modic, *J. Am. Chem. Soc.* **1953**, *75*, 1385.

[140] M. D. Morrison, J. J. Hanthorn, D. A. Pratt, *Org. Lett.* **2009**, *11*, 1051-1054.

[141] C. S. Popeney, A. L. Rheingold, Z. Guan, *Organometallics* **2009**, *28*, 4452-4463.

[142] R. Adams, M. D. Nair, *J. Am. Chem. Soc.* **1956**, *78*, 5932-5938.

[143] G. A. Guerrero-Vasquez, N. Chinchilla, J. M. G. Molinillo, F. A. Macias, *J. Nat. Prod.* **2014**, *77*, 2029-2036.

[144] H. Huang, C. Karlsson, M. Stroemme, M. Sjoedin, A. Gogoll, *Beilstein J. Org. Chem.* **2016**, *12*, 89-96.

[145] Y. Yamaguchi, Y. Matsubara, T. Ochi, T. Wakamiya, Z.-i. Yoshida, *J. Am. Chem. Soc.* **2008**, *130*, 13867-13869.

[146] Y. Yamaguchi, T. Ochi, Y. Matsubara, Z.-i. Yoshida, *J. Phys. Chem. A* **2015**, *119*, 8630-8642.

[147] S. Etienne, M. Matt, T. Oster, M. Samadi, M. Beley, *Tetrahedron* **2008**, *64*, 9619-9624.

[148] M. Schaefer, *Institute of Inorganic Chemitry, University of Wuerzburg*, Wuerzburg, Germany.

[149] G. M. Brown, G. R. Freeman, R. I. Walter, *J. Am. Chem. Soc.* **1977**, *99*, 6910-6915.

[150] C. Kaiser, Doctor thesis, University of Wuerzburg **2014**.

[151] M. Schaefer, J. Schaefer, R. D. Dewhurst, W. C. Ewing, M. Krahfuss, M. W. Kuntze-Fechner, M. Wehner, C. Lambert, H. Braunschweig, *Chem. Eur. J.* **2016**, *22*, 8603-8609.

[152] M. Schaefer, N. A. Beattie, K. Geetharani, J. Schaefer, W. C. Ewing, M. Krahfuss, C. Hoerl, R. D. Dewhurst, S. A. Macgregor, C. Lambert, H. Braunschweig, *J. Am. Chem. Soc.* **2016**, *138*, 8212-8220.

[153] *D.M.S. UV Atlas of Organic Compounds*, Butterworth (Weinheim) Verlag Chemie, **1966**.

[154] C. Reichardt, T. Welton, in *Solvents and Solvent Effects in Organic Chemistry*, Wiley-VCH Verlag GmbH & Co. KGaA, **2010**, pp. 549-586.

[155] N. N. Dhaneshwar, S. S. Tavale, L. M. Pant, *Acta Crystallogr., Sect. B* **1976**, *B32*, 2159-2162.

[156] G. W. R. Bartindale, M. M. Crowder, K. A. Morley, *Acta Crystallogr.* **1959**, *12*, 111-115.

[157] E. Miler-Srenger, C. Stora, T. Avignon, *Acta Crystallogr., Sect. B* **1978**, *B34*, 1221-1226.

[158] L. Radom, W. J. Hehre, J. A. Pople, G. L. Carlson, W. I. Fateley, *J. Chem. Soc., Chem. Commun.* **1972**, 308-309.

[159] G. M. Anderson, III, P. A. Kollman, L. N. Domelsmith, K. N. Houk, *J. Am. Chem. Soc.* **1979**, *101*, 2344-2352.

[160] G.-T. Li, Z.-K. Li, Q. Gu, S.-L. You, *Org. Lett.* **2017**, *19*, 1318-1321.

[161] T. F. Koetzle, G. J. B. Williams, *J. Am. Chem. Soc.* **1976**, *98*, 2074-2078.

[162] L. E. McCandlish, J. C. Hanson, G. H. Stout, *Acta Crystallogr., Sect. B* **1976**, *B32*, 1793-1801.

[163] L. Lv, B. B. Snider, Z. Li, *J. Org. Chem.* **2017**, *82*, 5487-5491.

[164] F. Barrière, W. E. Geiger, *J. Am. Chem. Soc.* **2006**, *128*, 3980-3989.

[165] R. Carlier, J. Simonet, *Bull. Soc. Chim. Fr.* **1988**, 831-833.

[166] C. Kaiser, A. Schmiedel, M. Holzapfel, C. Lambert, *J. Phys. Chem. C* **2012**, *116*, 15265-15280.

[167] J. C. Forgie, D. Rochefort, *RSC Advances* **2013**, *3*, 12035-12038.

[168] M. Choy de Martinez, O. P. Marquez, J. Marquez, F. Hahn, B. Beden, P. Crouigneau, A. Rakotondrainibe, C. Lamy, *Synth. Met.* **1997**, *88*, 187-196.

[169] J. P. Telo, A. l. Moneo, M. F. N. N. Carvalho, S. F. Nelsen, *J. Phys. Chem. A* **2011**, *115*, 10738-10743.

[170] A. Moneo, M. Fernanda N. N. Carvalho, J. P. Telo, *J. Phys. Org. Chem.* **2012**, *25*, 559-565.

[171] A. Cyr, P. Huot, J.-F. Marcoux, G. Belot, E. Laviron, J. Lessard, *Electrochim. Acta* **1989**, *34*, 439-445.

[172] N. A. Macías-Ruvalcaba, J. P. Telo, D. H. Evans, *J. Electroanal. Chem.* **2007**, *600*, 294-302.

[173] N. G. Connelly, W. E. Geiger, *Chem. Rev.* **1996**, *96*, 877-910.

[174] J. Fiedler, S. Zalis, A. Klein, F. Hornung, W. Kaim, *Inorg. Chem.* **1996**, *35*, 3039-3043.

[175] F. Zieschang, doctor thesis, University of Wuerzburg **2014**.

[176] I. R. Gould, D. Noukakis, L. Gomez-Jahn, R. H. Young, J. L. Goodman, S. Farid, *Chem. Phys.* **1993**, *176*, 439-456.

[177] B. Mladenova, *Institute of Physical and Theoretical Chemistry, Graz University of Technology*, Graz, Austria.

[178] I. Krummenacher, *Institute of Inorganic Chemitry, University of Wuerzburg*, Wuerzburg, Germany.

[179] D. Kattnig, *Physical and Theoretical Chemistry Laboratory, University of Oxford*, Oxford, U.K.

[180] J. P. Telo, S. F. Nelsen, Y. Zhao, *J. Phys. Chem. A* **2009**, *113*, 7730-7736.

[181] M. Holzapfel, *Institute of Organic Chemistry and Center for Nanosystems Chemistry, University of Wuerzburg*, Wuerzburg, Germany.

[182] A. Heckmann, C. Lambert, *Angew. Chem. Int. Ed. Engl.* **2012**, *51*, 326-392.

[183] C. Lambert, S. Amthor, J. Schelter, *J. Phys. Chem. A* **2004**, *108*, 6474-6486.

[184] V. Gladkikh, A. I. Burshtein, I. Rips, *J. Phys. Chem. A* **2005**, *109*, 4983-4988.

[185] G. E. McManis, A. Gochev, M. J. Weaver, *Chem. Phys.* **1991**, *152*, 107-120.

[186] H. A. Ahmed, G. Thyagarajan, *Proc. Indian Natl. Sci. Acad., Part A* **1989**, *55*, 661-669.

[187] V. G. Nikiforov, V. S. Lobkov, *J. Struct. Chem.* **2009**, *50*, 789-794.

[188] J. K. Vij, F. Hufnagel, T. Grochulski, *J. Mol. Liq.* **1991**, *49*, 1-16.

[189] I. Rips, J. Jortner, *J. Chem. Phys.* **1987**, *87*, 2090-2104.

[190] T. Gennett, D. F. Milner, M. J. Weaver, *J. Phys. Chem.* **1985**, *89*, 2787-2794.

[191] S. Mallikarjun, N. E. Hill, *Trans. Faraday Soc.* **1965**, *61*, 1389-1398.

[192] M. Kaupp, M. Renz, M. Parthey, M. Stolte, F. Wurthner, C. Lambert, *Phys. Chem. Chem. Phys.* **2011**, *13*, 16973-16986.

[193] M. Renz, K. Theilacker, C. Lambert, M. Kaupp, *J. Am. Chem. Soc.* **2009**, *131*, 16292-16302.

[194] F. Voegtle, *Chem. Ztg.* **1972**, *96*, 396.

[195] T. C. Barros, S. Brochsztain, V. G. Toscano, P. Berci Filho, M. J. Politi, *J. Photochem. Photobiol., A* **1997**, *111*, 97-104.

[196] G. Andric, J. F. Boas, A. M. Bond, G. D. Fallon, K. P. Ghiggino, C. F. Hogan, J. A. Hutchison, M. A. P. Lee, S. J. Langford, J. R. Pilbrow, G. J. Troup, C. P. Woodward, *Aust. J. Chem.* **2004**, *57*, 1011-1019.

[197] S. V. Bhosale, C. H. Jani, S. J. Langford, *Chem. Soc. Rev.* **2008**, *37*, 331-342.

[198] P. Ganesan, J. Baggerman, H. Zhang, E. J. R. Sudhölter, H. Zuilhof, *J. Phys. Chem. A* **2007**, *111*, 6151-6156.

[199] H. Miyasaka, H. Masuhara, N. Mataga, *J. Phys. Chem.* **1985**, *89*, 1631-1636.

[200] S.-L. Suraru, F. Wurthner, *Angew Chem Int Ed Engl* **2014**, *53*, 7428-7448.

[201] A. Weller, *Z. Phys. Chem.* **1982**, *133*, 93-98.

[202] C. D. Ultra, 2.0.2.1076 ed., Cambridge, **2010**.

[203] R. E. Gaussian 09, M. J. Frisch, G. W. Trucks, H. B. Schlegel, G. E. Scuseria, M. A. Robb, J. R. Cheeseman, G. Scalmani, V. Barone, B. Mennucci, G. A. Petersson, H. Nakatsuji, M. Caricato, X. Li, H. P. Hratchian, A. F. Izmaylov, J. Bloino, G. Zheng, J. L. Sonnenberg, M. Hada, M. Ehara, K. Toyota, R. Fukuda, J. Hasegawa, M. Ishida, T. Nakajima, Y. Honda, O. Kitao, H. Nakai, T. Vreven, J. A. Montgomery, Jr., J. E. Peralta, F. Ogliaro, M. Bearpark, J. J. Heyd, E. Brothers, K. N. Kudin, V. N. Staroverov, R. Kobayashi, J. Normand, K. Raghavachari, A. Rendell, J. C. Burant, S. S. Iyengar, J. Tomasi, M. Cossi, N. Rega, J. M. Millam, M. Klene, J. E. Knox, J. B. Cross, V. Bakken, C. Adamo, J. Jaramillo, R. Gomperts, R. E. Stratmann, O. Yazyev, A. J. Austin, R. Cammi, C. Pomelli, J. W. Ochterski, R. L. Martin, K. Morokuma, V. G. Zakrzewski, G. A. Voth, P. Salvador, J. J. Dannenberg, S. Dapprich, A. D. Daniels, Ö. Farkas, J. B. Foresman, J. V. Ortiz, J. Cioslowski, D. J. Fox, *Gaussian, Inc., Wallingford CT* **2009**.

[204] A. Arrigo, A. Santoro, M. T. Indelli, M. Natali, F. Scandola, S. Campagna, *Phys. Chem. Chem. Phys.* **2014**, *16*, 818-826.

[205] N. D. Yordanov, *Appl. Magn. Reson.* **1996**, *10*, 339-350.

[206] S. Stoll, A. Schweiger, *J. Magn. Reson.* **2006**, *178*, 42-55.

[207] K. J. Reszka, M. Takayama, R. H. Sik, C. F. Chignell, I. Saito, *Photochem. Photobiol.* **2005**, *81*, 573-580.

[208] J. F. Penneau, B. J. Stallman, P. H. Kasai, L. L. Miller, *Chem. Mater.* **1991**, *3*, 791-796.

[209] S. F. Nelsen, *J. Am. Chem. Soc.* **1967**, *89*, 5925-5931.

[210] F. A. Neugebauer, S. Bamberger, W. R. Groh, *Chem. Ber.* **1975**, *108*, 2406-2415.

[211] S. Bamberger, D. Hellwinkel, F. A. Neugebauer, *Chem. Ber.* **1975**, *108*, 2416-2421.

[212] A. Schmiedel, *Institute of Organic Chemistry and Center for Nanosystems Chemistry, University of Wuerzburg*, Wuerzburg, Germany.

[213] J. H. Klein, T. L. Sunderland, C. Kaufmann, M. Holzapfel, A. Schmiedel, C. Lambert, *Phys. Chem. Chem. Phys.* **2013**, *15*, 16024-16030.

[214] M. Maroncelli, *J. Mol. Liq.* **1993**, *57*, 1-37.

[215] J. E. Rogers, L. A. Kelly, *J. Am. Chem. Soc.* **1999**, *121*, 3854-3861.

[216] S. Green, M. A. Fox, *J. Phys. Chem.* **1995**, *99*, 14752-14757.

[217] B. M. Aveline, S. Matsugo, R. W. Redmond, *J. Am. Chem. Soc.* **1997**, *119*, 11785-11795.

[218] P. Ganesan, J. Baggerman, H. Zhang, E. J. R. Sudhoelter, H. Zuilhof, *J. Phys. Chem. A* **2007**, *111*, 6151-6156.

[219] A. S. Lukas, P. J. Bushard, E. A. Weiss, M. R. Wasielewski, *J. Am. Chem. Soc.* **2003**, *125*, 3921-3930.

[220] S. Suzuki, R. Sugimura, M. Kozaki, K. Keyaki, K. Nozaki, N. Ikeda, K. Akiyama, K. Okada, *J. Am. Chem. Soc.* **2009**, *131*, 10374-10375.

[221] S. R. Greenfield, W. A. Svec, D. Gosztola, M. R. Wasielewski, *J. Am. Chem. Soc.* **1996**, *118*, 6767-6777.

[222] E. Vauthey, P. Suppan, E. Haselbach, *Helv. Chim. Acta* **1988**, *71*, 93-99.

[223] P. Siders, R. A. Marcus, *J. Am. Chem. Soc.* **1981**, *103*, 741-747.

[224] P. Siders, R. A. Marcus, *J. Am. Chem. Soc.* **1981**, *103*, 748-752.

[225] M. Bixon, J. Jortner, *J. Chem. Phys.* **1968**, *48*, 715-726.

[226] J. Jortner, *J. Chem. Phys.* **1976**, *64*, 4860-4867.

[227] I. R. Gould, D. Noukakis, L. Gomez-Jahn, R. H. Young, J. L. Goodman, S. Farid, *Chem. Phys.* **1993**, *176*, 439-456.

[228] D. Veldman, S. p. M. A. Chopin, S. C. J. Meskers, R. A. J. Janssen, *J. Phys. Chem. A* **2008**, *112*, 8617-8632.

[229] D. B. MacQueen, K. S. Schanze, *J. Am. Chem. Soc.* **1991**, *113*, 7470-7479.

[230] J. E. Rogers, L. A. Kelly, *J. Am. Chem. Soc.* **1999**, *121*, 3854-3861.

[231] T. Klumpp, M. Linsenmann, S. L. Larson, B. R. Limoges, D. Buerssner, E. B. Krissinel, C. M. Elliott, U. E. Steiner, *J. Am. Chem. Soc.* **1999**, *121*, 1076-1087.

[232] J. K. Hurley, N. Sinai, H. Linschitz, *Photochem. Photobiol.* **1983**, *38*, 9-14.

[233] M. T. Rawls, G. Kollmannsberger, C. M. Elliott, U. E. Steiner, *J. Phys. Chem. A* **2007**, *111*, 3485-3496.

[234] MATLAB, The MathWorks, Inc. R2011b, Natick, Massachusetts, United States, **2011**.

[235] R. Haberkorn, M. E. Michel-Beyerle, *Biophys. J.* **1979**, *26*, 489-498.

[236] B. Brocklehurst, *Chem. Soc. Rev.* **2002**, *31*, 301-311.

[237] W. L. F. Armarego, C. L. L. Chai, in *Purification of Laboratory Chemicals (Sixth Edition)*, Butterworth-Heinemann, Oxford, **2009**.

[238] S. Dummling, E. Eichhorn, S. Schneider, B. Speiser, M. Wuerde, *Curr. Sep.* **1996**, *15*, 53-56.

[239] I. H. M. van Stokkum, D. S. Larsen, R. van Grondelle, *Biochim. Biophys. Acta* **2004**, *1657*, 82-104.

[240] S. L. J. J. Snellenburg, R. Seger, K. M. Mullen, I. H. M. van Stokkum, *J. Stat. Softw.* **2012**, *49*, 1-22.

[241] I. Carmichael, G. L. Hug, *J. Phys. Chem. Ref. Data* **1986**, *15*, 1-250.

[242] C. Wuerth, M. Grabolle, J. Pauli, M. Spieles, U. Resch-Genger, *Nat. Protoc.* **2013**, *8*, 1535-1550, 1516 pp.

[243] G. R. Fulmer, A. J. M. Miller, N. H. Sherden, H. E. Gottlieb, A. Nudelman, B. M. Stoltz, J. E. Bercaw, K. I. Goldberg, *Organometallics* **2010**, *29*, 2176-2179.

[244] G. M. Sheldrick, *Acta Crystallogr., Sect. C: Struct. Chem.* **2015**, *71*, 3-8.

[245] G. M. Sheldrick, *Acta Crystallogr., Sect. A: Found. Crystallogr.* **2008**, *64*, 112-122.

[246] C. B. Huebschle, G. M. Sheldrick, B. Dittrich, *J. Appl. Crystallogr.* **2011**, *44*, 1281-1284.

[247] C. Cason, *Persistence of Vision Pty. Ltd.*, **2009**.

[248] W. C. Still, M. Kahn, A. Mitra, *J. Org. Chem.* **1978**, *43*, 2923-2925.

[249] C. C. Nawrat, C. J. Moody, *Org. Lett.* **2012**, *14*, 1484-1487.

[250] M. C. Bonifacio, C. R. Robertson, J.-Y. Jung, B. T. King, *J. Org. Chem.* **2005**, *70*, 8522-8526.

[251] T. Otsubo, D. Stusche, V. Boekelheide, *J. Org. Chem.* **1978**, *43*, 3466-3470.

[252] S. Huang, X. Jin, Z. Lou, D. Poon, J. Tellew, Y. Wan, X. Wang, Y. Xie, WO 2011/025927 A1, **2011**.

[253] H. Huang, C. Lin, T. Chao, H. Lee, C. Cheng, in *U.S. Pat. Appl. Publ.*, US 20110198571 A1, **2011**.

[254] R. G. Shepherd, *J. Org. Chem.* **1947**, *12*, 275-283.

[255] H. E. Ungnade, K. T. Zilch, *J. Org. Chem.* **1950**, *15*, 1108-1112.

[256] S. Tsutsui, H. Tanaka, K. Sakamoto, *Organometallics* **2004**, *23*, 3719-3726.

[257] M. Yan, L. Ge, W. Gao, J. Yu, X. Song, S. Ge, Z. Jia, C. Chu, *Adv. Funct. Mater.* **2012**, *22*, 3899-3906, S3899/3891-S3899/3892.

[258] R. P. Hsung, C. E. D. Chidsey, L. R. Sita, *Organometallics* **1995**, *14*, 4808-4815.

[259] J.-Z. Cheng, C.-C. Lin, P.-T. Chou, A. Chaskar, K.-T. Wong, *Tetrahedron* **2011**, *67*, 734-739.

[260] J. Lv, Q. Liu, J. Tang, F. Perdih, K. Kranjc, *Tetrahedron Lett.* **2012**, *53*, 5248-5252.

[261] S. Takahashi, Y. Kuroyama, K. Sonogashira, N. Hagihara, *Synthesis* **1980**, *1980*, 627-630.

[262] W. B. Austin, N. Bilow, W. J. Kelleghan, K. S. Y. Lau, *J. Org. Chem.* **1981**, *46*, 2280-2286.

[263] K. Sonogashira, Y. Tohda, N. Hagihara, *Tetrahedron Lett.* **1975**, *16*, 4467-4470.

[264] D. V. Kosynkin, J. M. Tour, *Org. Lett.* **2001**, *3*, 993-995.

8 TABLE OF FORMULARS

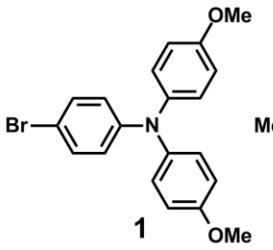

1

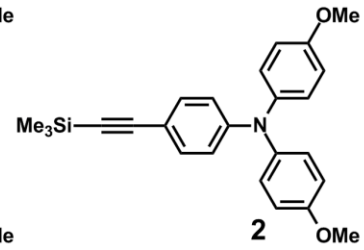

2

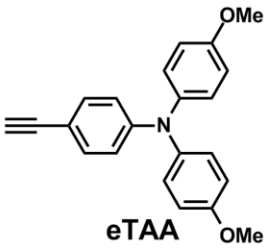

eTAA

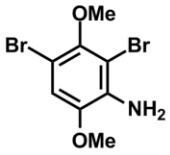

3

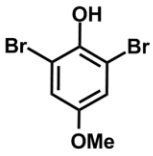

4

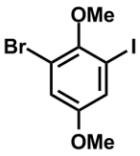

5

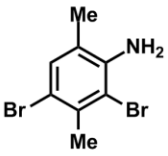

6

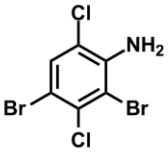

7

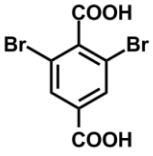

8

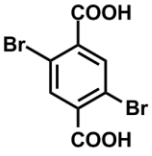

9

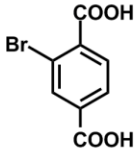

10

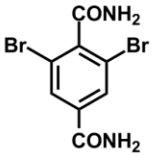

11

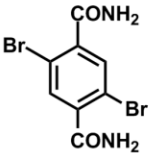

12

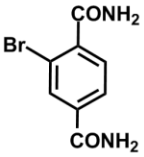

13

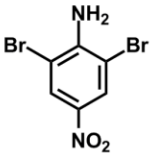

14

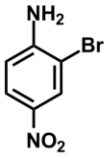

15

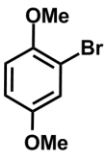

sbOMe

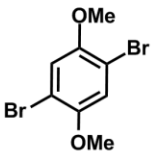

pbOMe

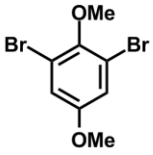

mbOMe

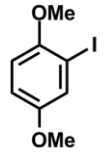

sbOMe'

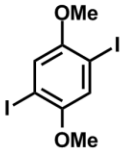

pbOMe'

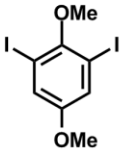

mbOMe'

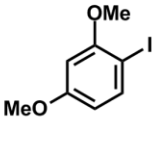

sbOMe'46

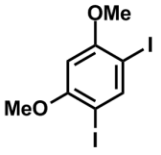

mbOMe'46

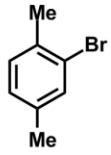

sbMe

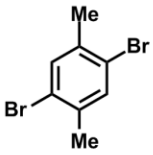

pbMe

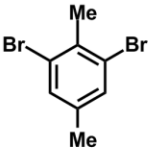

mbMe

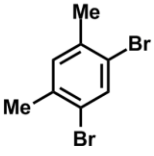

mbMe46

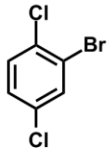

sbCl

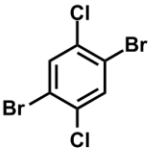

pbCl

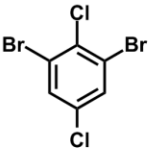

mbCl

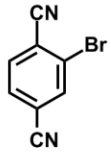

sbCN

pbCN

mbCN

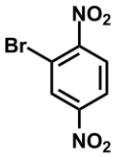

sbNO2

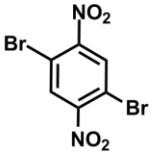

pbNO2

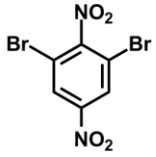

mbNO2

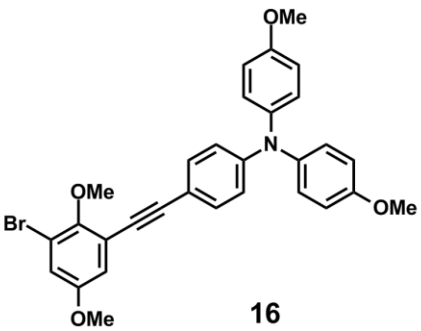

16

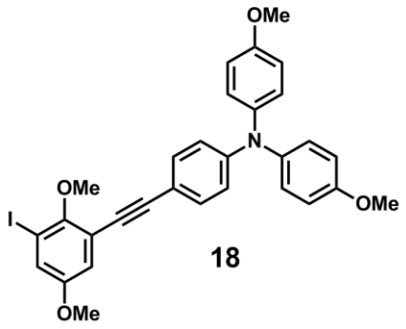

18

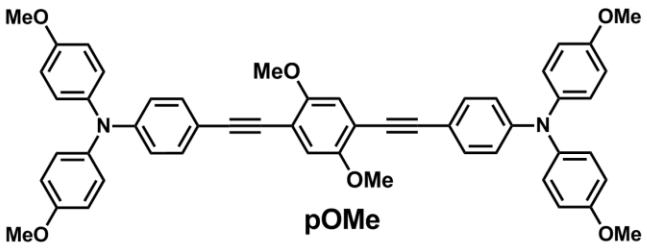

pOMe

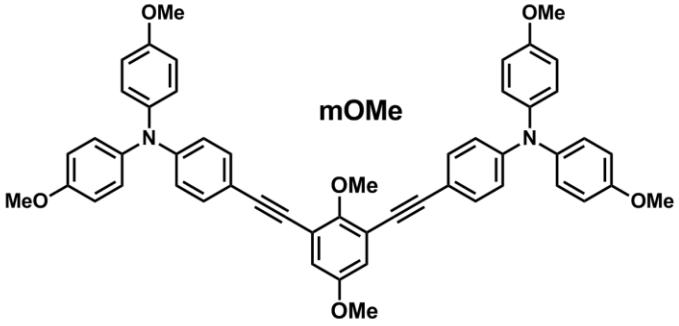

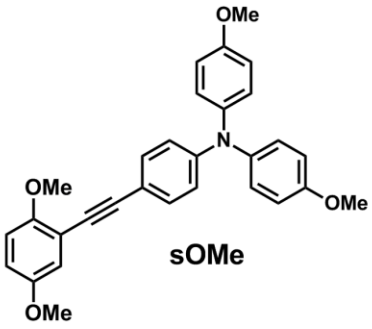

sOMe

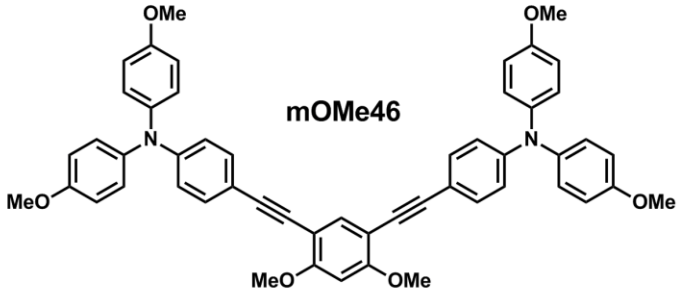

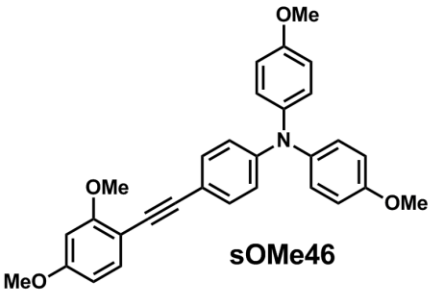

sOMe46

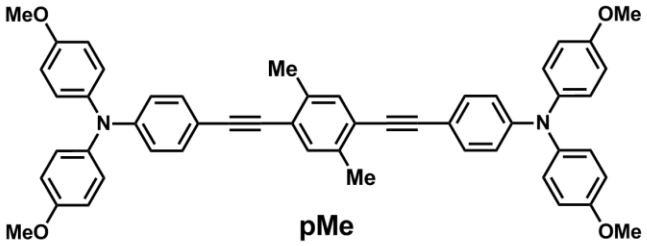

pMe

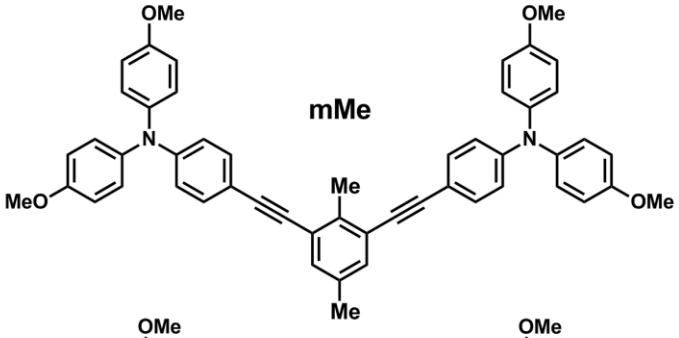

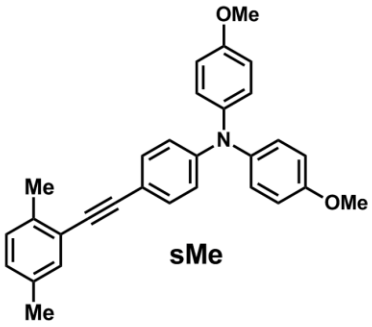

sMe

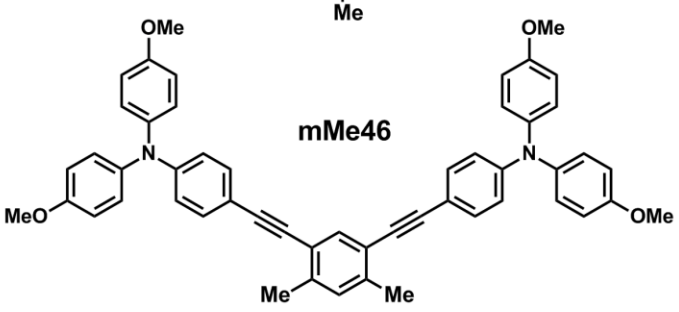

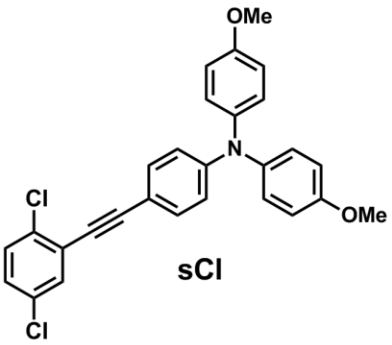
OMe
N
Cl
Cl
OMe
sCl

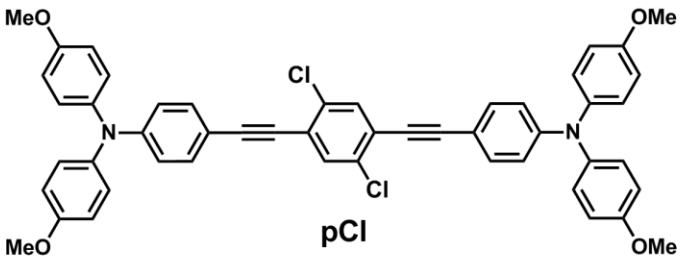
MeO
OMe
Cl
N
Cl
N
MeO
OMe
pCl

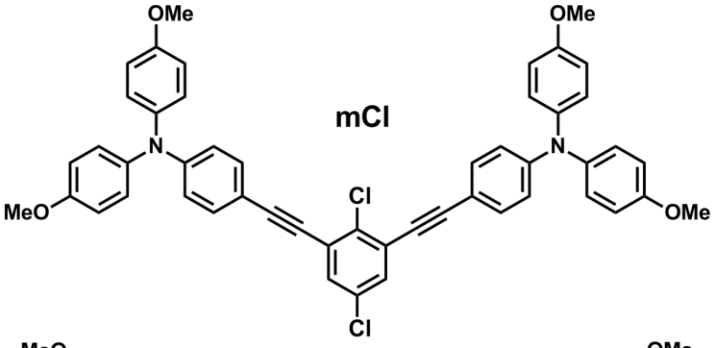
OMe
OMe
N
N
MeO
Cl
OMe
Cl
mCl

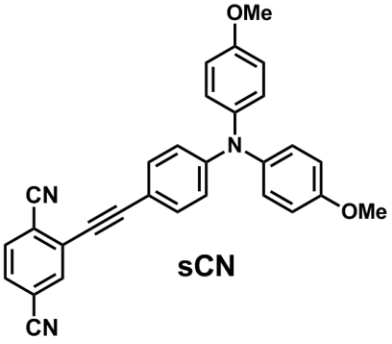
OMe
N
CN
CN
OMe
sCN

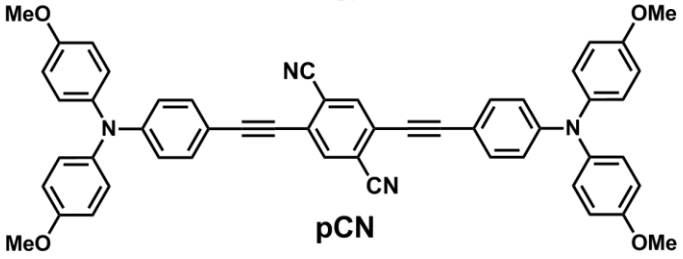
MeO
OMe
NC
N
N
CN
MeO
OMe
pCN

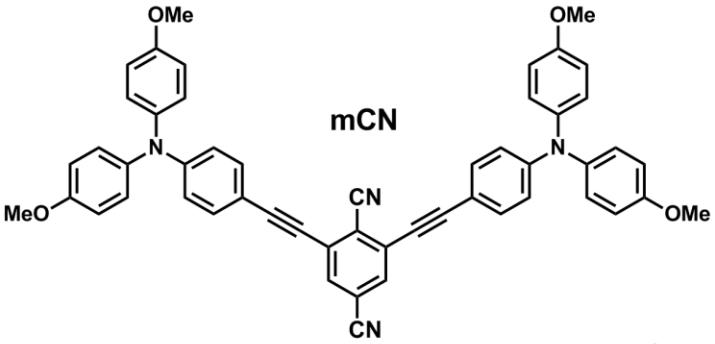
OMe
OMe
N
N
MeO
CN
OMe
CN
mCN

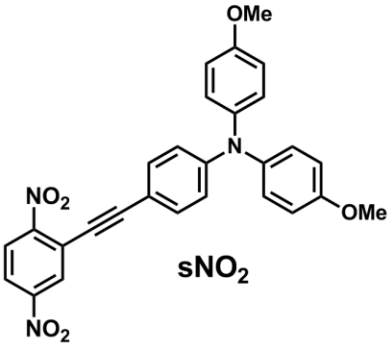
OMe
N
NO2
NO2
OMe
sNO2

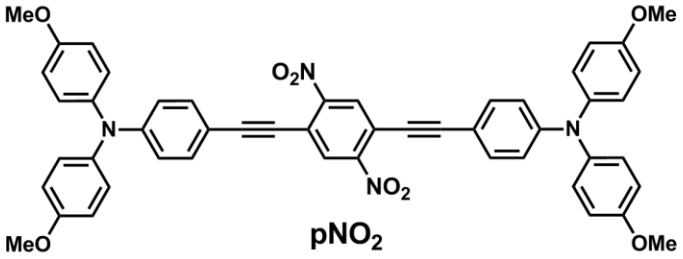
MeO
OMe
O2N
N
N
NO2
MeO
OMe
pNO2

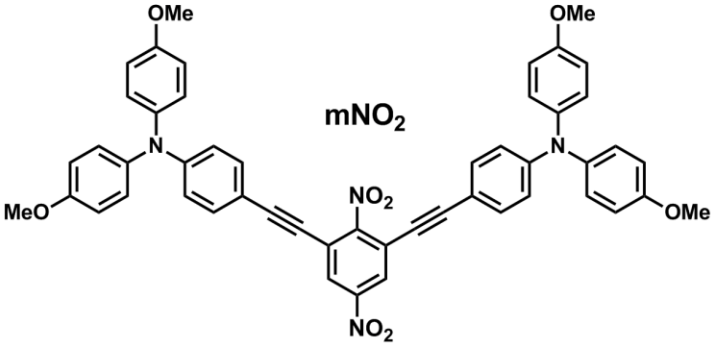
OMe
OMe
N
N
MeO
NO2
OMe
NO2
mNO2

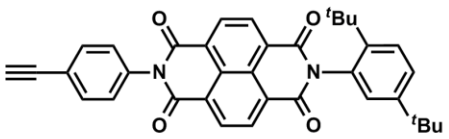

eNDI

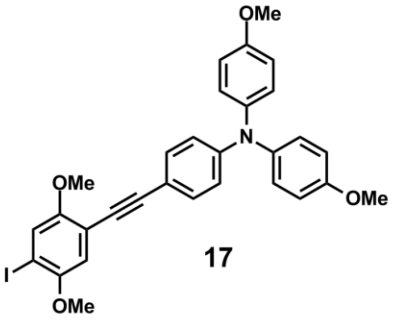

17

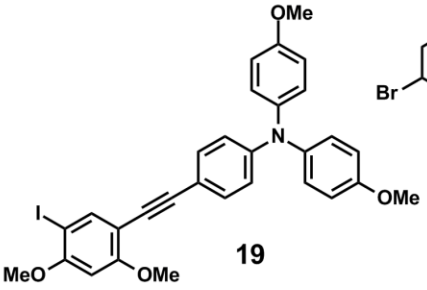

19

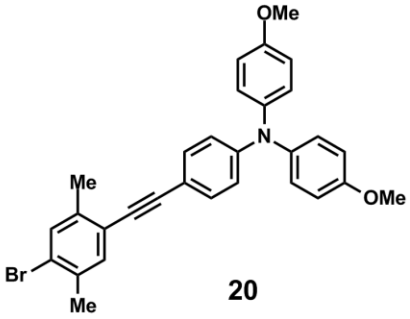

20

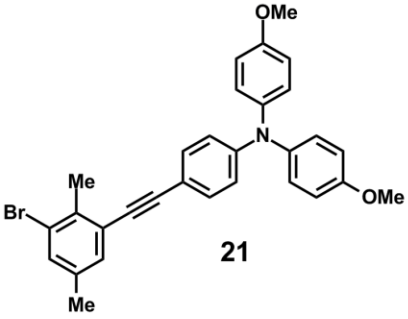

21

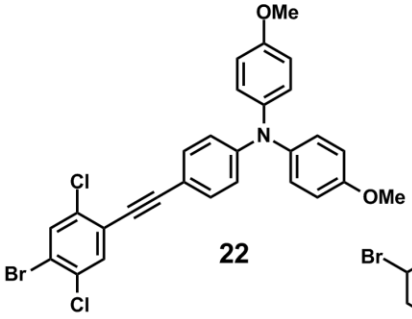

22

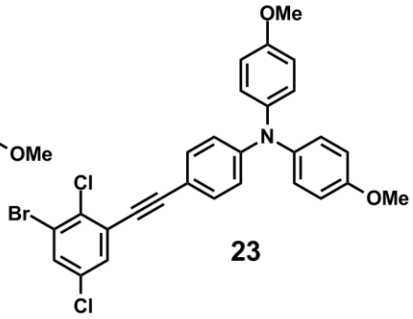

23

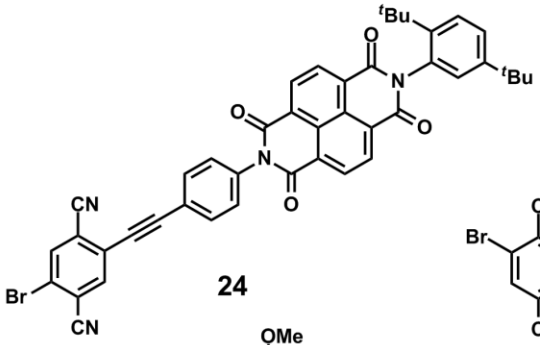

24

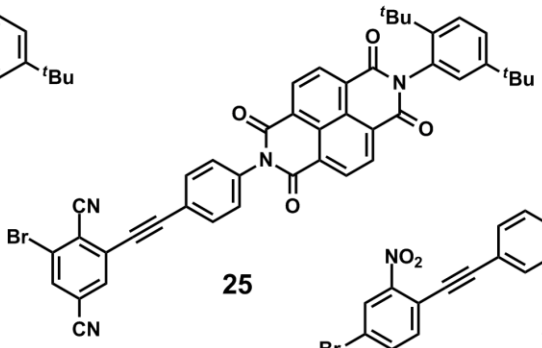

25

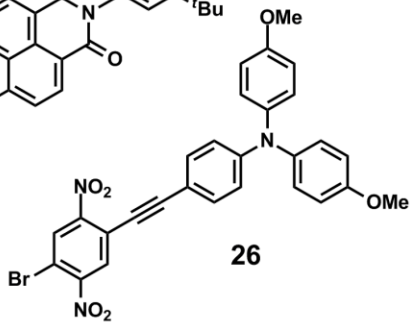

26

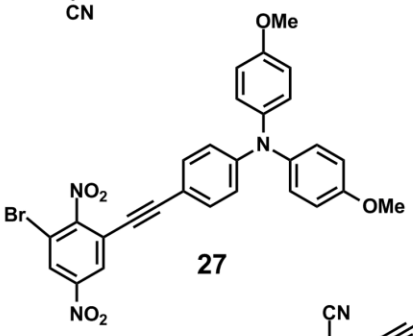

27

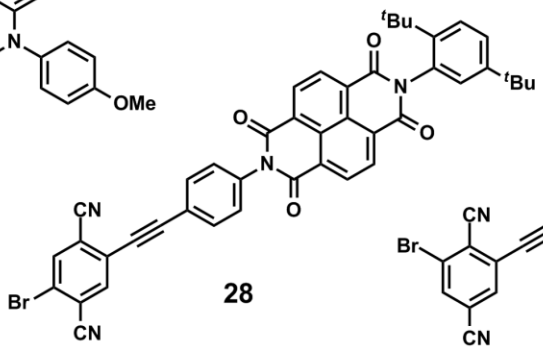

28

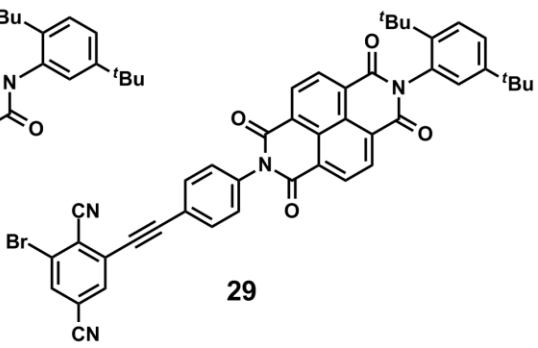

29

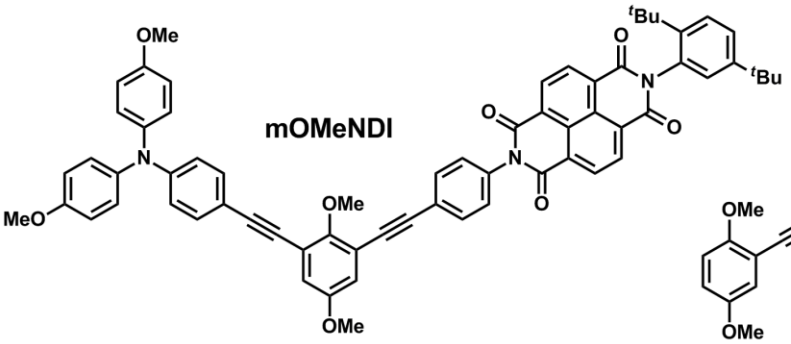
mOMeNDI

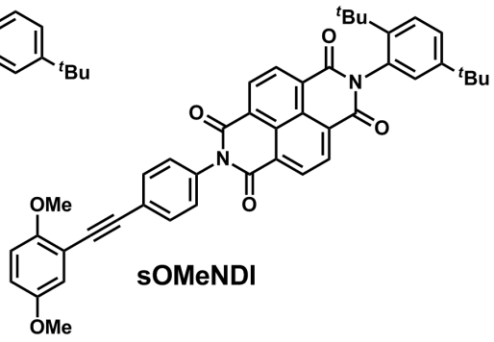
sOMeNDI

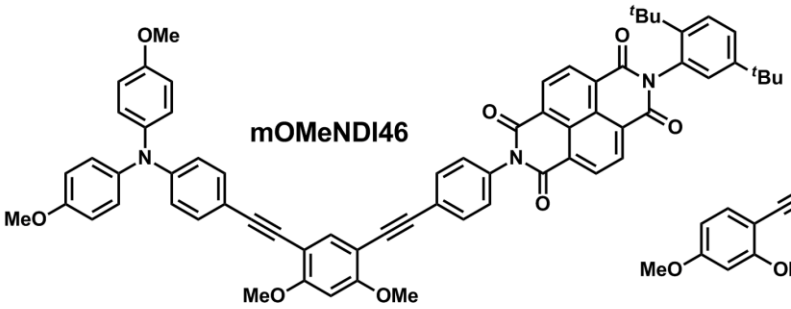
mOMeNDI46

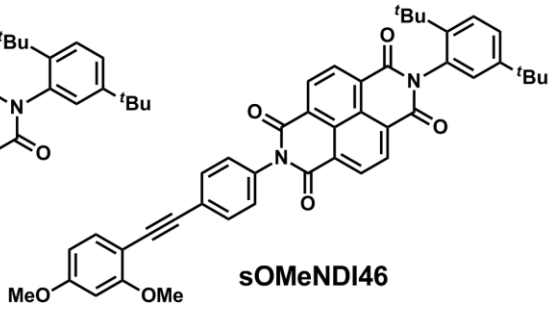
sOMeNDI46

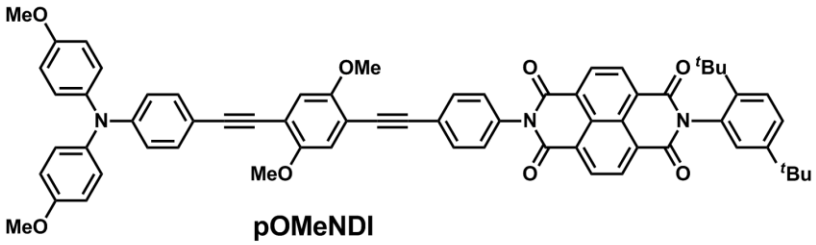
pOMeNDI

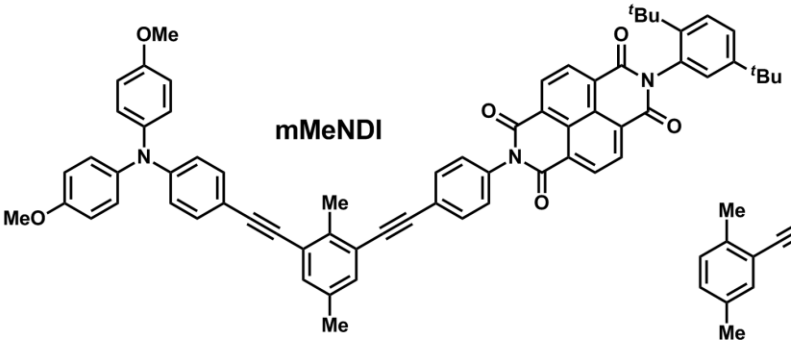
mMeNDI

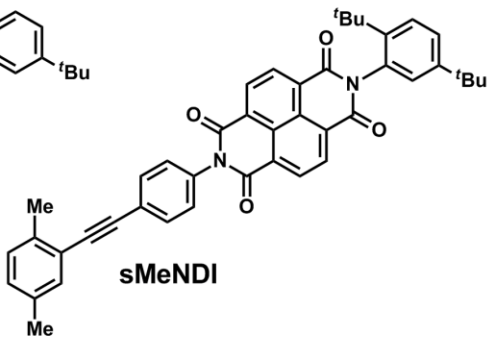
sMeNDI

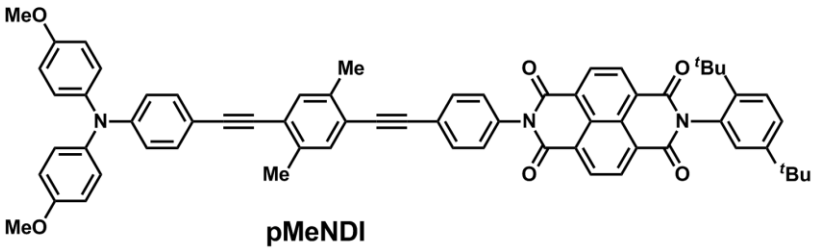
pMeNDI

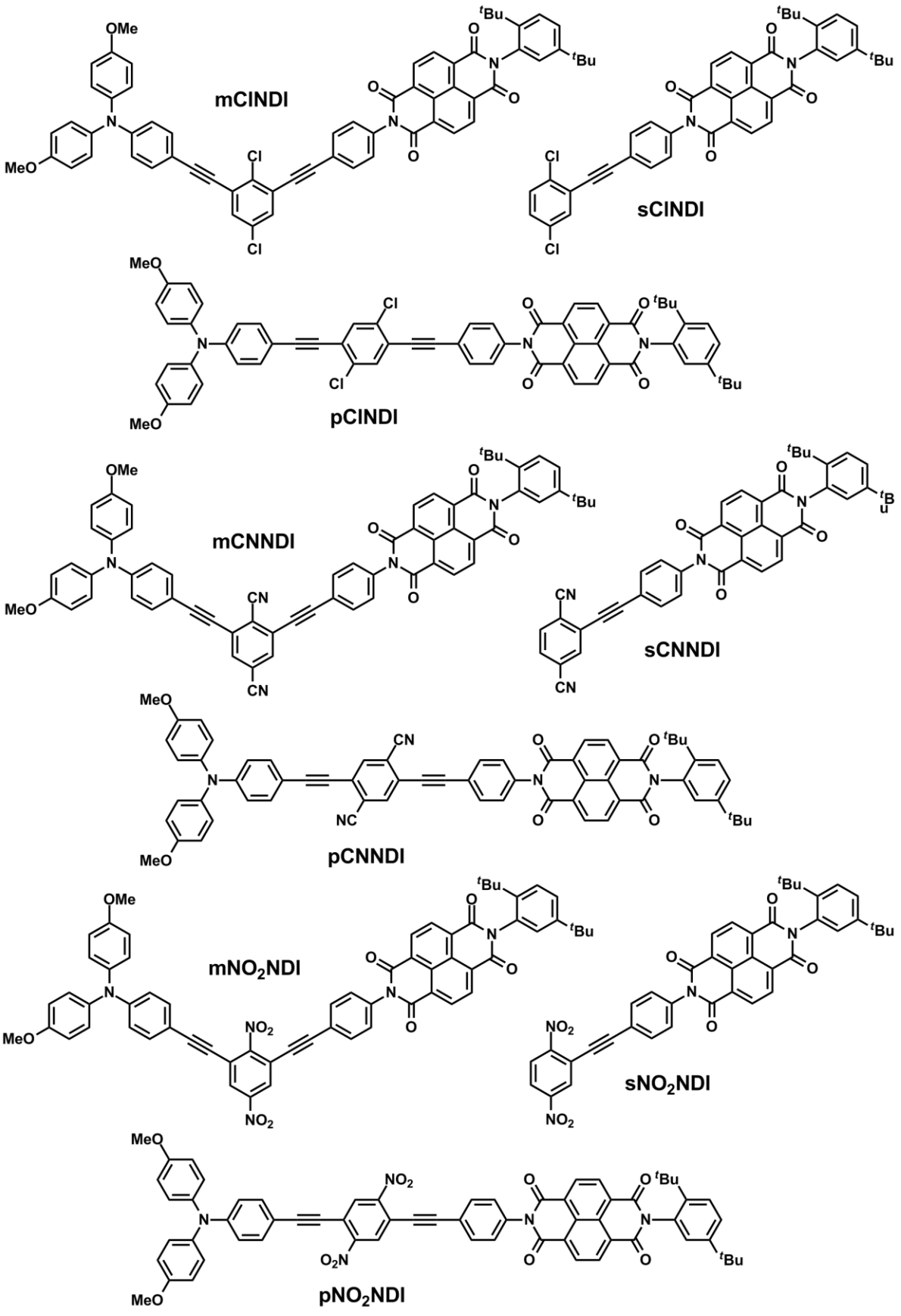
mClNDI
sClNDI
pClNDI
mCNNDI
sCNNDI
pCNNDI
mNO2NDI
sNO2NDI
pNO2NDI

9 ZUSAMMENFASSUNG

Im ersten Teil dieser Arbeit wurde die erfolgreiche Synthese einer Serie von bisTriarylamin (bisTAA) Verbindungen vorgestellt. Zum einen wurde das Substitutionmuster an der Benzol Brückeneinheit in Form einer *meta*- bzw. *para*-Ständigkeit der Redoxzentren (**pX** bzw. **mX**), und zum anderen die energetische Lage der Brückeneinheit durch zwei elektronenschiebende oder ziehende Substituenten X (mit X = OMe, Me, Cl, CN, NO_2) in 2,5-Position variiert. Im Falle der *meta*-Serie wurden auch einige in 4,6-Position substituierte Verbinungen hergestellt (**mX46**). Die neutral Verbindungen wurden bezüglich ihrer elektrochemischen und photophysikalischen Eigenschaften untersucht.
Durch Oxidation konnten die gemischt valenten (MV), kationischen bisTAA-Verbindungen erzeugt werden. Der thermisch induzierte Lochtransfer (HT) wurde durch temperaturabhängige ESR-Spektroskopie untersucht. Während die HT-Rate *k* und HT-Barriere Δ*G* in **mX** unbeeinflusst von den Substituenten X sind, steigen gleichzeitig *k und* Δ*G* in der **pX**-Serie mit zunehmenden Elektonenschub von X an. Diese zunächst widersprüchliche Beobachtung konnte durch einen ansteigenden Einfluss von Lösungsmitteleffekten und dadurch resultierend, einer zusätzlichen effektiven Barriere erklärt werden.
Der optisch induzierte Lochtransfer wurde mittels UV/Vis/NIR-Spektroskopie untersucht. Die **pX**-Serie zeigte eine Zuhname der elektronischen Kopplung *V* und dementsprechende eine Abnahme von Δ*G,* mit Anstieg des elektonenschiebenden Charakters von X. Für **mX** war eine spektroskopische Bestimmung dieser Parameter nicht möglich. Die **mX46**-Serie zeigte ein intermediäres Verhalten, wobei MV-Verbindungen mit stark elektronenschiebenden X eine ähnliche hohe Kopplungen wie **pX** aufwiesen, was mit Hilfe von DFT-Rechnungen bezüglich der Molekülorbitale erklärt werden konnte.

Im zweiten Teil dieser Arbeit wurde die Synthese einer Serie von Verbindungen mit Triarylamin (TAA) als Donor und Naphthalindiimid (NDI) als Akzeptor vorgestellt. Auch hier wurde zum einen das Substitutionmuster an der Benzol-Brückeneinheit in Form einer *meta*- bzw. *para*-Ständigkeit der Redoxzentren (**pXNDI** bzw. **mXNDI**) variieeiet und die energetische Lage der durch X (mit X = OMe, Me, Cl, CN, NO_2) in 2,5-Position variiert. Außerdem wurde die in 4,6-Position substituierte Verbinungen **mOMe46NDI** hergestellt. Alle Verbindungen wurden bezüglich ihrer elektochemischen und photophysikalischen Eigenschaften untersucht.
Die Elektronentransferprozesse der Ladungsseparierung (CS) und Ladungsrekombination (CR) dieser Verbindungen sollten mittels transienter Absorptionsspektroskopie (TA) in Toluol untersucht werden. Für die Nitroverbindungen **p-/mNO_2NDI** war dies nicht möglich, da sich

diese unter Bestrahung zersetzten. Die CR von **pXNDI** waren nicht im ns-Bereich detektierbar, weshalb sich auf die **mXNDI**-Serie (mit X = OMe–CN) konzentriert wurde.
Die CS wurde mittels fs-TA untersucht. Nach optischer Anregung konnte die Bildung eines CS-Zustandes detektiert werden, dessen Bildungsgeschwindigkeit hin zu elektronen-ziehenden Substituenten X steigt. Die CR wurde mit ns-TA untersucht. Sie findet in der *Marcus* invertierten Region statt und zeichnet sich wird durch ein biexponentialles Abklingverhaten, was durch ein Singulet-Triplett Gleichgewicht im CS-Zustand zustande kommt, aus. Durch Anlegen eines externen Magnetfeldes ließ sich das Abklingverhalten entscheidend verändern und es konnte eine Singulett-Triplett Aufspaltung nachgewiesen werden. Dieser Befund konnte weiterhin durch Simulation der Abklingkurven bestätigt werden.

In beiden Teilen dieser Arbeit konnte ein entscheidender Einfluss der Benzolbrücke auf die auftretenden Ladungstransferprozesse gezeigt werden. Für den HT in Grundzustand der MV bisTAA Verbindungen, sowie der ET im angeregten Zustand der Donor-Akzeptor-Verbindungen, wurden die höchsten ET-Raten für die *para*-Serien **pX** und **pXNDI** gefunden, während die *meta*-Serien **mX** und **mXNDI** deutlch kleine Transferraten aufwiesen. In beiden Studien zeigten die *meta*46-Verbindungen **mX46** und **mOMeNDI46** ein intermediäres Verhalten, zwischen denen der *para*- und *meta*-Verbindungen.

10 APPENDIX

10.1 ln($k/T^{1/2}$) vs 1/T plots

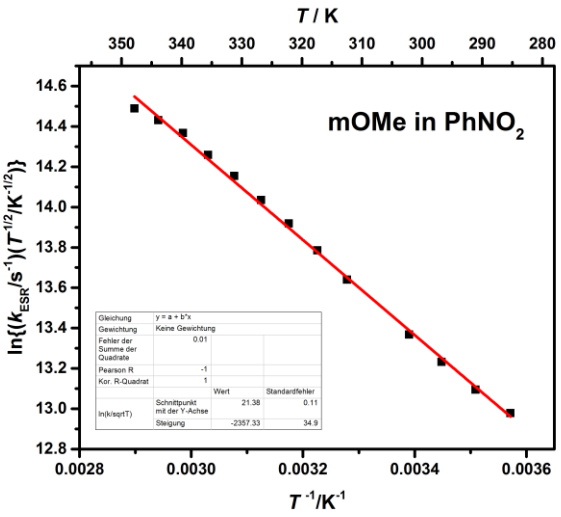

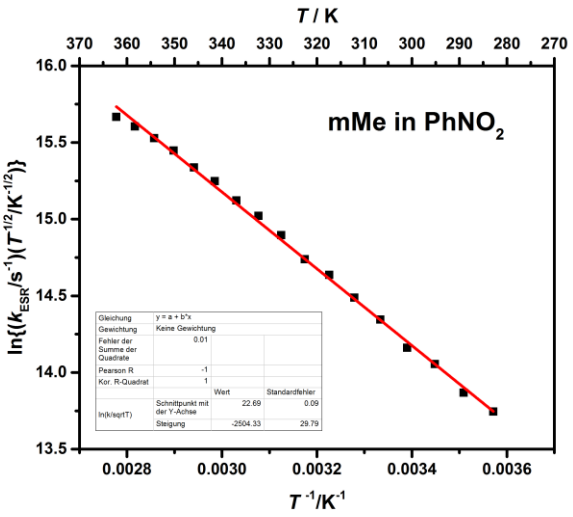

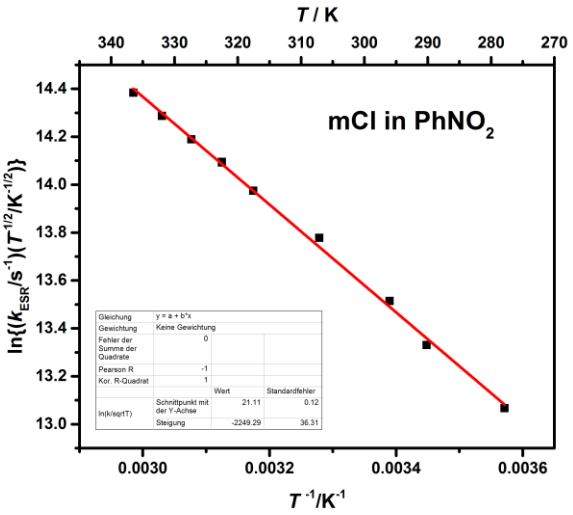

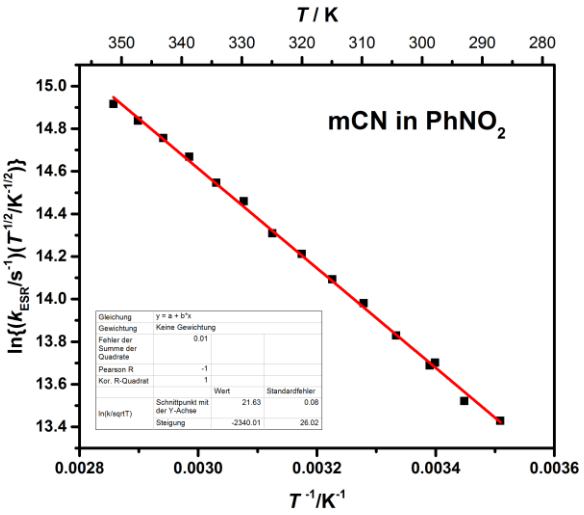

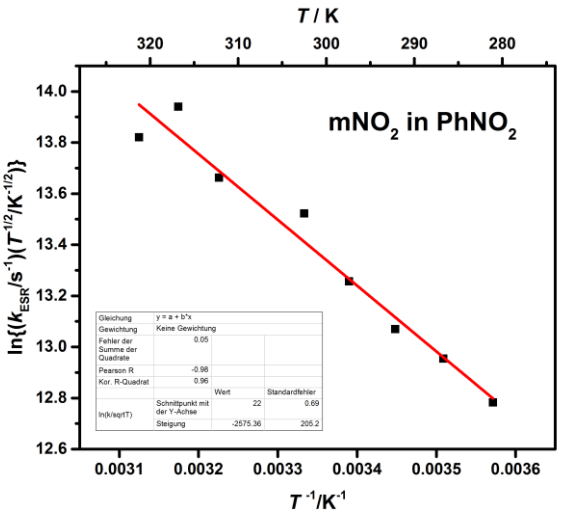

Figure A1: ln($k/T^{1/2}$) vs 1/T plots for the radical cations of the *meta*-compounds in $PhNO_2$.

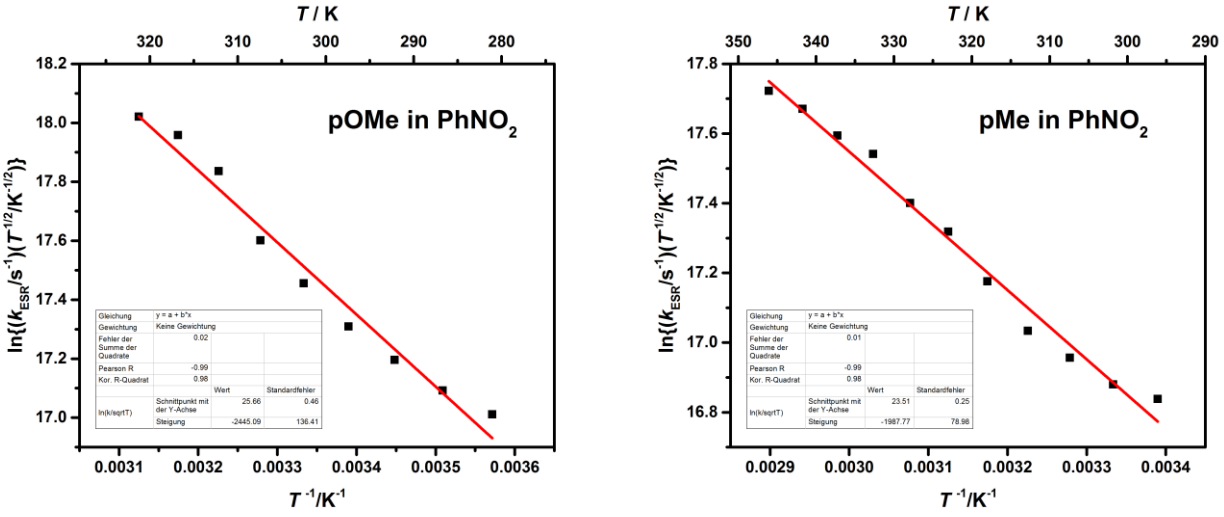

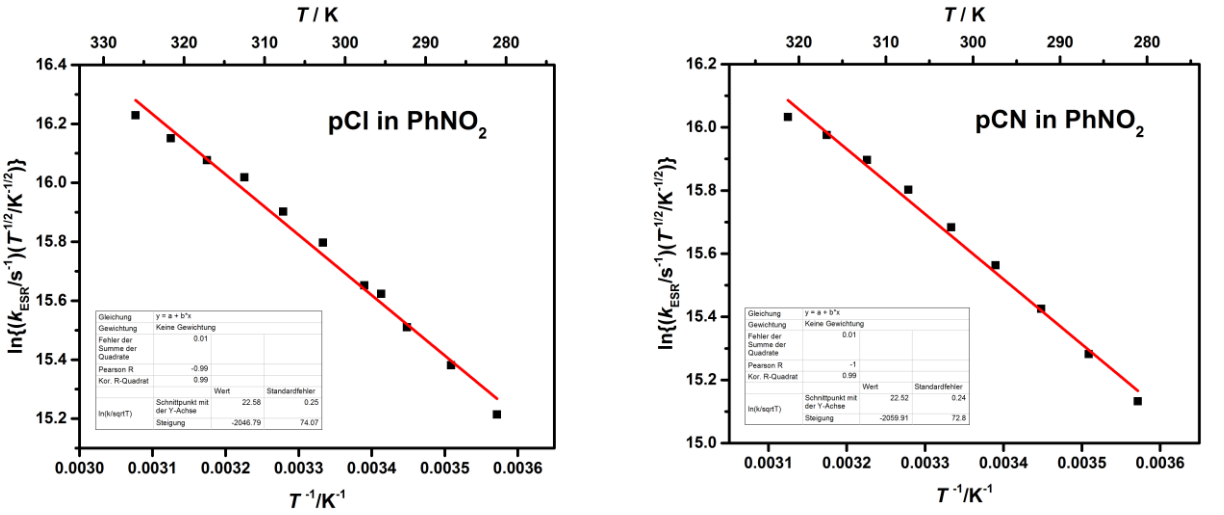

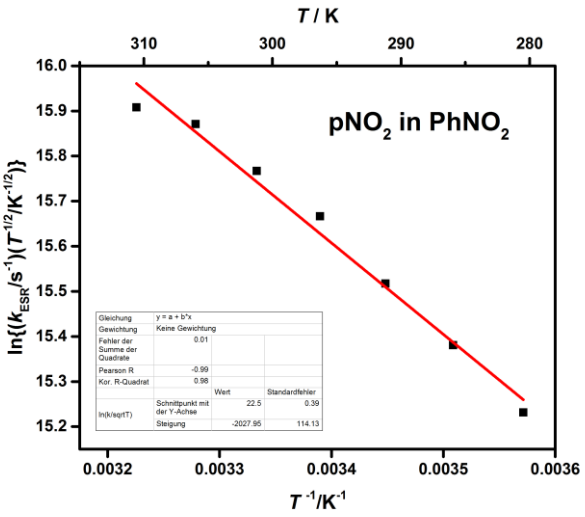

Figure A2: ln($k/T^{1/2}$) vs 1/T plots for the radical cations of the *para*-compounds in $PhNO_2$.

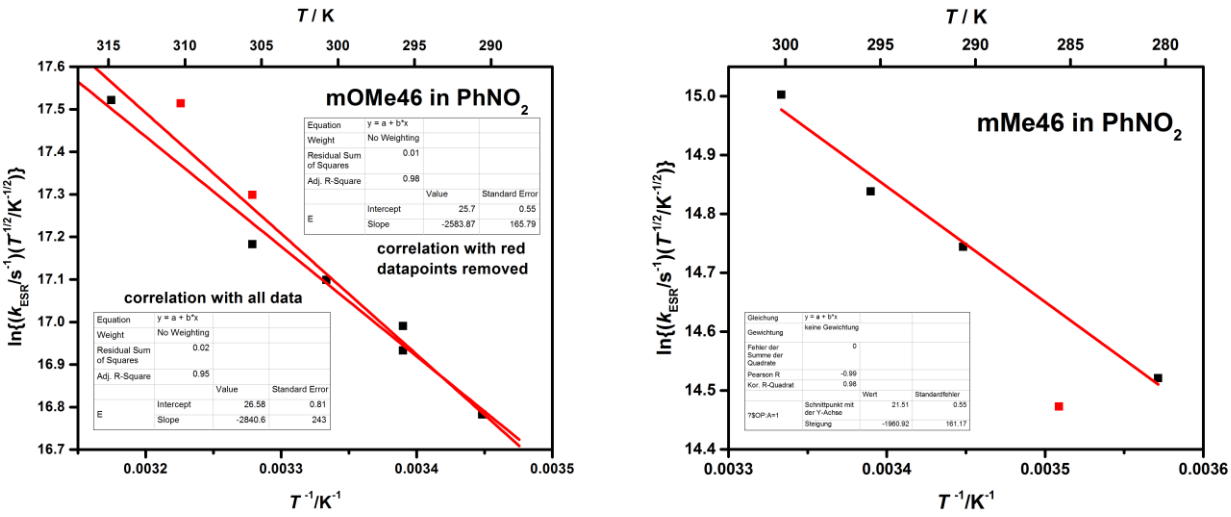

Figure A3: ln($k/T^{1/2}$) vs 1/T plots for the radical cations of **mOMe46** and **mMe46** in $PhNO_2$.

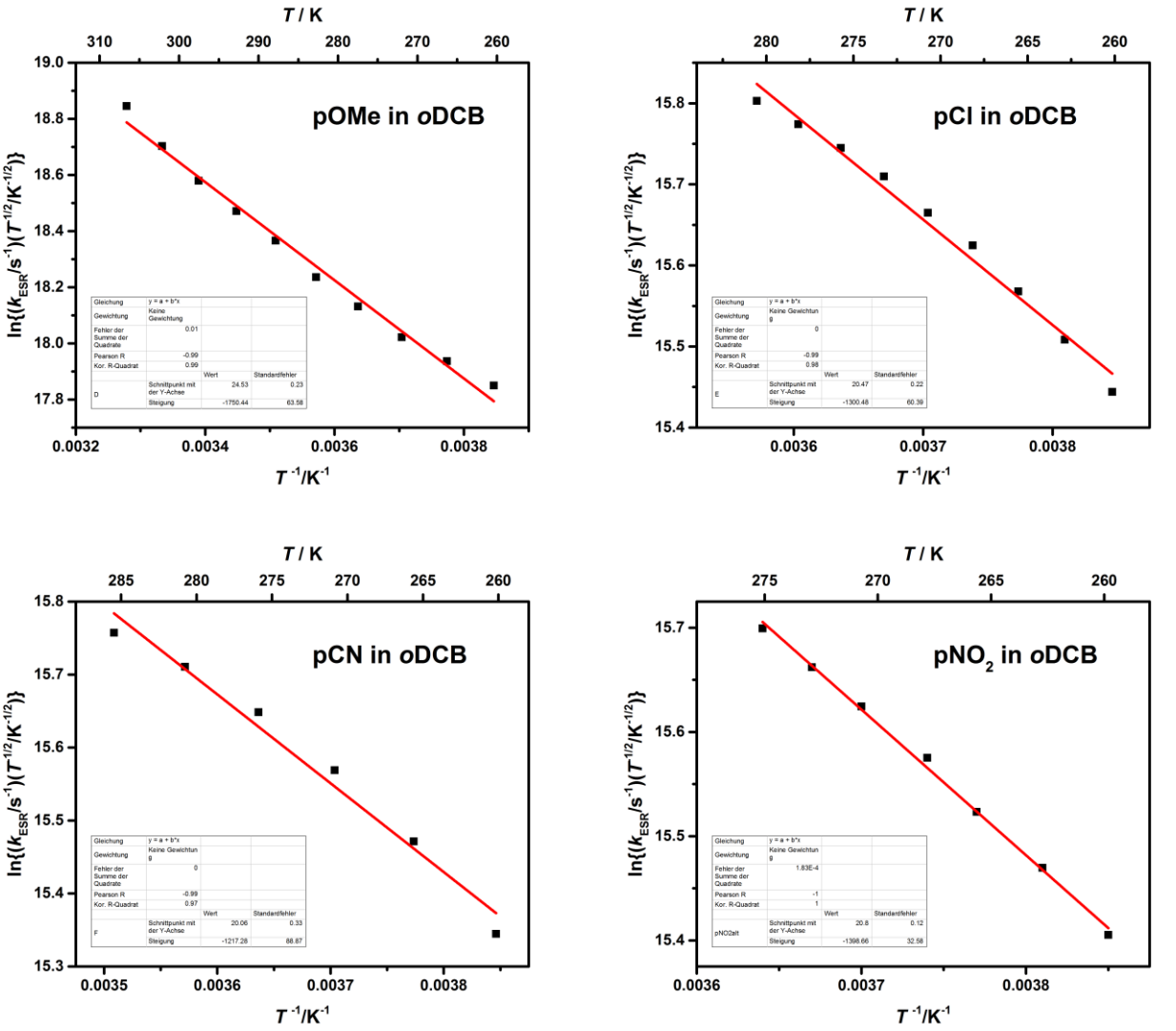

Figure A4: ln($k/T^{1/2}$) vs 1/T plots for the radical cations of **pOMe**, **pCl**, **pCN** and **pNO$_2$** in *o*DCB.

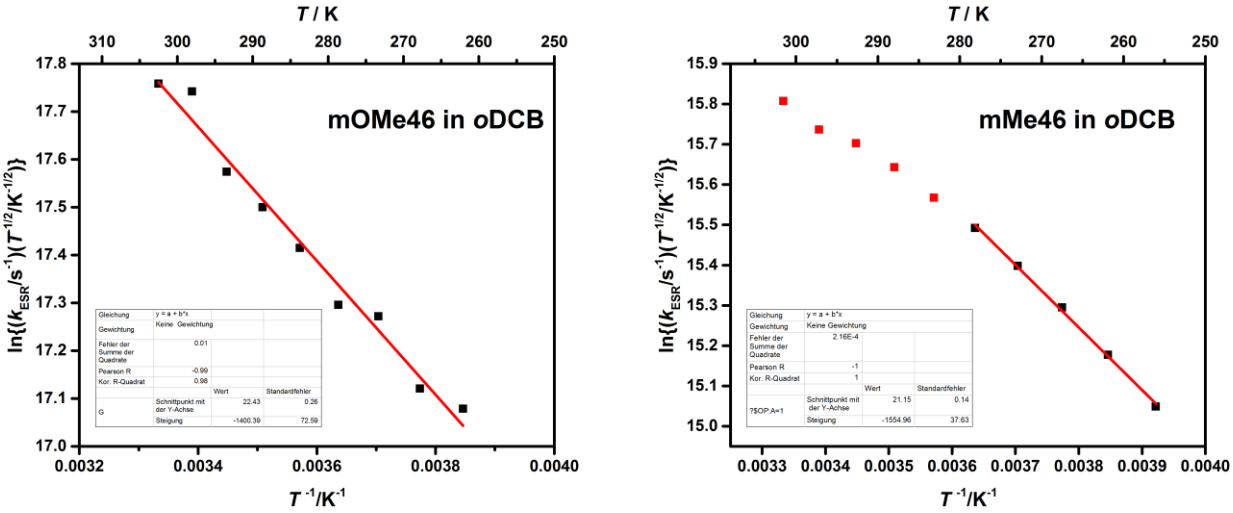

Figure A5: ln($k/T^{1/2}$) vs 1/T plots for the radical cations of **mOMe46** and **mMe46** in *o*DCB.

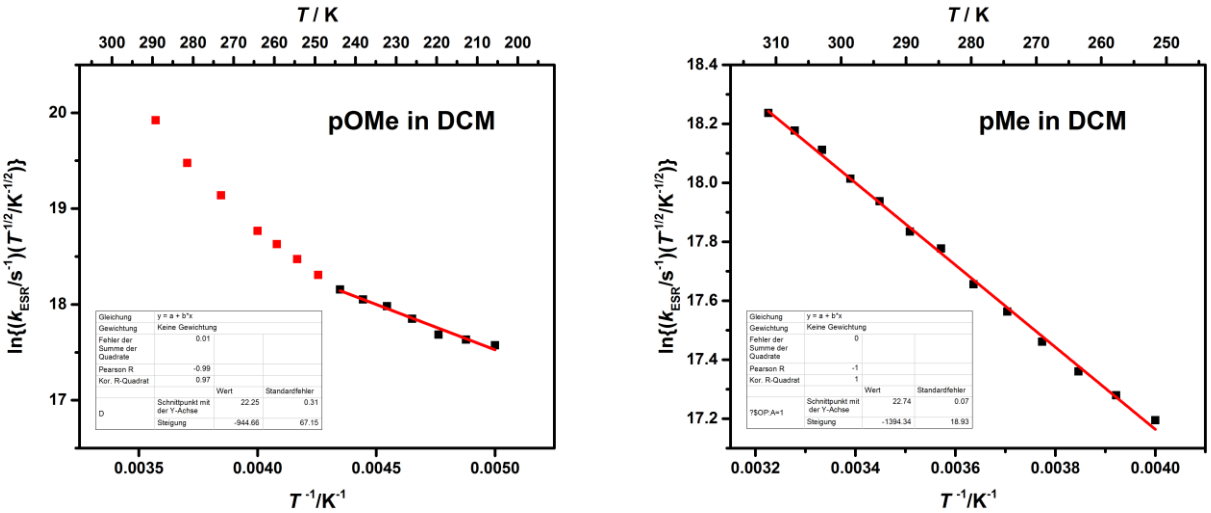

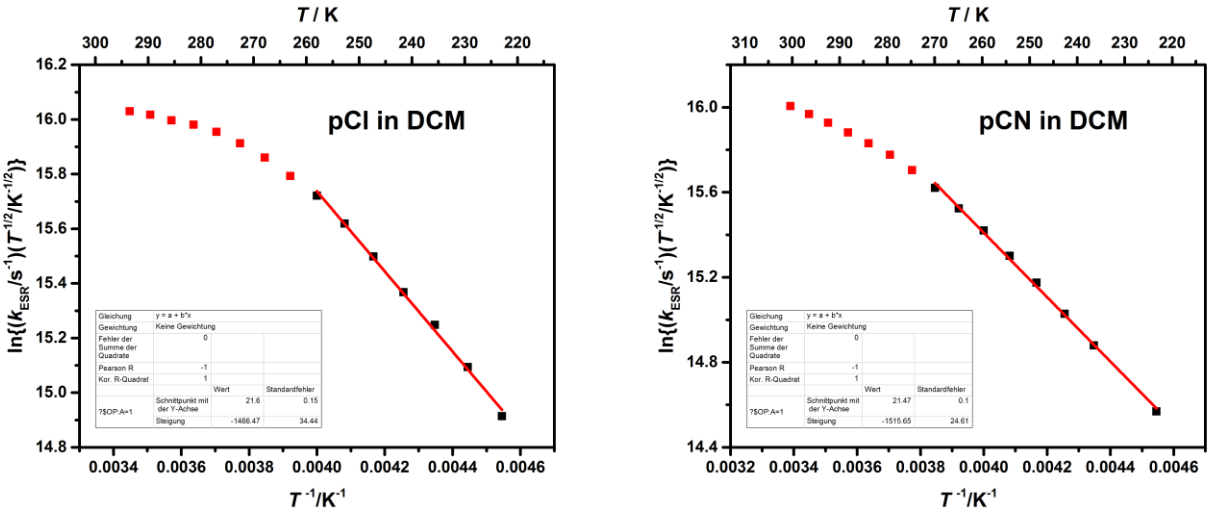

Figure A6: ln($k/T^{1/2}$) vs 1/T plots for the radical cations of **pOMe**, **pMe**, **pCl** and **pCN** in DCM.

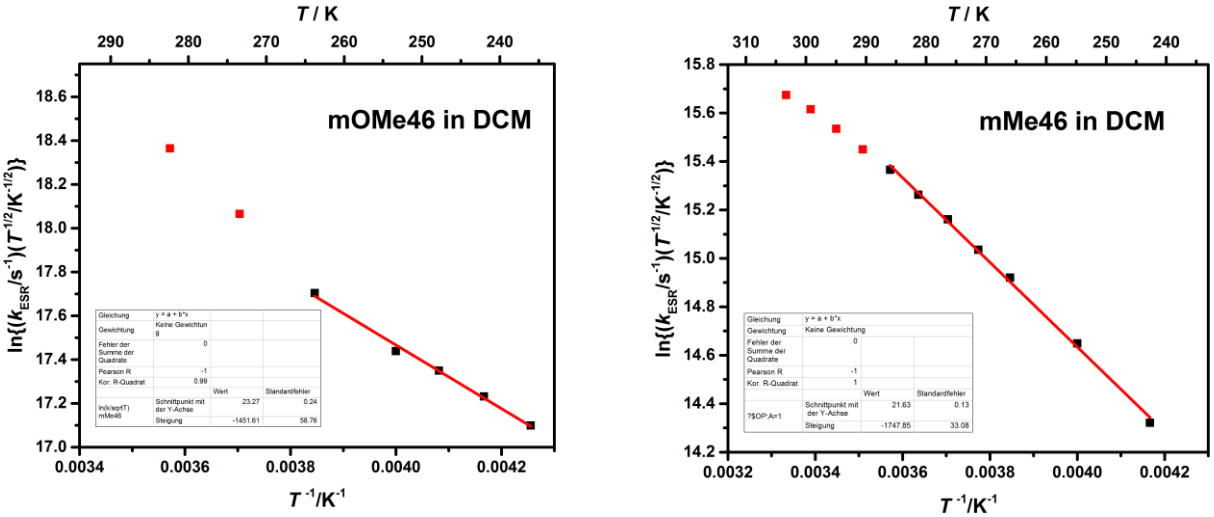

Figure A7: ln($k/T^{1/2}$) vs 1/T plots for the radical cations of **mOMe46** and **mMe46** in DCM.

10.2 List of Publications

Hole Transfer Processes in *meta*- and *para*-Conjugated Mixed Valence Compounds: Unforeseen Effects of Bridge Substituents and Solvent Dynamics
J. Schäfer, M. Holzapfel, B. Mladenova, D. Kattnig, I. Krummenacher, H. Braunschweig, G. Grampp, C. Lambert
J. Am. Chem. Soc. **2017**, *139*, 6200-6209.

Synthesis of Functionalized 1,4-Azaborinines by the Cyclization of Di-*tert*-butyliminoborane and Alkynes
M. Schäfer, N. A. Beattie, K. Geetharani, J. Schäfer, W. C. Ewing, M. Krahfuß, C. Hörl, R. D. Dewhurst, S. A. Macgregor, C. Lambert, H. Braunschweig
J. Am. Chem. Soc. **2016**, *138*, 8212-8220.

How fast is optically induced electron transfer in organic mixed valence systems?
C. Lambert, M. Moos, A. Schmiedel, M. Holzapfel, J. Schäfer, M. Keß, V. Engel
Phys. Chem. Chem. Phys. **2016**, *18*, 19405-19411.

Regioselective catalytic and stepwise routes to bulky, functional-group-appended, and luminescent 1,2-azaborinines
M. Schäfer, J. Schäfer, R. D. Dewhurst, W. C. Ewing, M. Krahfuss, M. W. Kuntze-Fechner, M. Wehner, C. Lambert, H. Braunschweig
Chem. Eur. J. **2016**, *22*, 8603-8609.

Investigations of the Degenerate Intra-molecular Charge Exchange in Symmetric Organic Mixed Valence Compounds: Solvent Dynamics of Bis(triarylamine)paracyclophane Redox Systems
B. Y. Mladenova, D. R. Kattnig, C. Kaiser, J. Schäfer, C. Lambert, G. Grampp
J. Phys. Chem. C **2015**, *119*, 8547-8553.

10.3 Poster Presentations

26th IUPAC International Symposium on Photochemistry, Osaka, Japan, April 2016 – "***Student Poster Award***"

Conjugated Oligomers and Polymers (KOPO), Würzburg, Deutschland, September 2015.

16th International Symposium on Novel aromatic Compounds (ISNA), Madrid, Spanien, Juli 2015.

3rd International "Solar Technologies Go Hybrid – SolTech" Meeting – Wildbad Kreuth, Germany, 2014.

Next Generation Solar Energy Congress, Erlangen, Deutschland, Dezember 2013.

International Conference on Photochemistry (ICP), Leuven, Belgien, Juli 2013.